TESLA Test Facility Linac
Design Report

Editor: D. A. Edwards

Version 1.0

1 March 1995

Abstract

The TESLA Test Facility will include capability for processing and measurement of 1.3 GHz superconducting accelerating structures, a 500–800 MeV linac based on these accelerating structures, and the cryogenic, power, diagnostic and other support systems appropriate to this effort. The main body of the linac will consist of four cryomodules each containing eight 1 meter nine-cell superconducting cavities operating at 1.3 GHz. The base accelerating gradient goal is 15 MV/m, leading to an electron energy of 500 MeV. If the TESLA 500 (500 GeV in the center of mass) figure of 25 MV/m is achievable in the Tesla Test Facility Linac, the output electron energy would be 800 MeV. Two injectors will be used; the first will produce the average current at low bunch charge appropriate to the TESLA 500 design, while the second, at the same average current, will provide the bunch intensity corresponding to the TESLA 500 specifications. Beam analysis areas will be provided for both the study of the injected beam and the high energy output beam. The Facility will be located at DESY, and will incorporate components and technical support provided by the collaborating institutions.

Contents

List of Tables

List of Figures

Preface

The TESLA collaboration embarked several years ago on a major effort to build a prototype linac for the superconducting cavity approach to a linear collider. A summary of the design to date is set down in this report. The primary reason for this report — and for its considerable scale — is to act as an aid and reference to the people who are carrying out the work.

The test facility is located at DESY, and in addition to the linac, includes a state-of-the-art infrastructure for superconducting cavity processing. The linac itself is intended to operate in the 500–800 MeV range, with the output energy determined by the accelerating gradient that can be achieved. The initial aim is 15 MV/m corresponding to the lower final energy figure, and the final goal is to reach the 25 MV/m figure chosen for TESLA 500,

At the time of this writing, cavity processing and performance measurements are underway in the new facility. Components and systems are flowing in from our collaborating institutions. The first major beam test of the linac with injector and one cryomodule is scheduled to take place by year's end.

It is a pleasure to acknowledge the contributions to our work of the over 250 scientists currently in the TESLA collaboration, many of whom have authored the text of this report. In standard "Design Report" style, their names do not appear, but fortunately, within the collaboration, the origin of the material is usually clear.

I also wish to thank the four individuals who have undertaken the project leadership role throughout the formulation of the plan documented here. They are, in succession, Donatus Degele, Maury Tigner, and Helen Edwards, with Martin Leenen as Deputy Project Leader providing continuity throughout. Finally, I thank Don Edwards for carrying out an editing task which grew far beyond its initial scale.

B. H. Wiik

Editor's Preface to Version 1.0

After a gestation period of over a year, this is the first version of the design report for the TESLA Test Facility Linac that can lay any claim to completeness. A project that is simultaneously under design and in construction is a moving target, and internal inconsistency is a likely consequence. But we have tried to update critical subjects — the layout, device coordinates, the cryogenic heat load budget, and the schedule are examples — to the date of publication.

Early on, we abandoned a slavish devotion to style and format; rather we concentrated on content. However, in a document of this size, with new material streaming in at the last minute, errors of one sort or another are inevitable. Changes in the source files are easy, so when you see an error, please let me know. When the error collection becomes sufficiently large, we will produce an update.

This version will be distributed in hard copy to everyone on the TESLA mailing list. This version, and its descendents, will be available on World Wide Web. To access the report via WWW go to URL http://info.desy.de:80/ and follow the path down through TTF to this report, which is available in postscript and in a number of compression styles.

The remarkable patience and cooperation of the many members of the collaboration who have written the material contained in this rather large report is deeply appreciated; I hope that I have not, in editorial zeal, obscured the technical content.

I am particularly indebted to Kai Desler, Dirk Hischke, Elaine Moore, and Ingrid Nikodem for their cheerful cooperation throughout the often tedious process of pulling this report together.

Don Edwards
edwards@desy.de

Chapter 1

Introduction

There is a widespread consensus within the high energy physics community that an electron–positron collider with a center of mass energy of 500 GeV and luminosity above 10^{33}cm^{-2}sec^{-1} should be considered as a possibility for the next accelerator facility after the LHC. Such a collider would provide for top analyses via $t\bar{t}$ production and discovery reach up to a Higgs mass of $\approx$350 GeV.

Worldwide, there are a number of groups pursuing different linear collider design efforts. These group activities have been reported in the yearly linear collider workshops, the accelerator conferences, and the usual journals. The TESLA activity is one of these R&D efforts, differing from the others in its choice both of superconducting accelerating structures and of low frequency (1.3 GHz). Several of these R&D groups, including TESLA, plan to have working prototype test facilities and well-developed collider designs in the 1997 time scale. After experience with implementation and operation of the test systems it will be possible to start to make relative evaluations of the different proposals, looking forward to the selection of the most promising technology.

Key in this selection will be technical merit, minimization of technical risk, and potential for optimization of performance. Equally important, however will be projected overall construction and operating costs.

In this competitive environment, the TESLA Collaboration has major challenges before it. Of highest priority is to prove the feasibility of reliably achieving accelerating gradients of 15 MV/m or more, and the clear potential for extrapolation to gradients of 25 MV/m, the TESLA 500 design goal.

(TESLA 500 would be the full-scale facility, to yield 500 GeV in the center of mass.) The TESLA Test Facility (TTF) is to prove that accelerating gradients greater than 15 MV/m are consistently obtainable, and that the cavities can be assembled into a linac test string (the TTF Linac or TTFL) that can be successfully operated with auxiliary systems to accelerate an electron beam to ≈500 MeV. The basic characteristics of the TTFL should be as consistent as possible with the parameters of the TESLA 500 design. The time scale for beam tests with four cryo modules of 8 cavities each is early 1997. The other collaborations are working to the same time scale.

In the Autumn of 1991, work began on the proposal for the TTF, to include state-of-the-art superconducting cavity processing capability, the electron linac that would reach 500 MeV at a gradient of 15 MeV/m as noted above, and necessary support and diagnostic equipment. The proposal was issued in April 1992.[1]

The TTF is to be located at DESY, with major components flowing in from the members of the collaboration. Since the proposal was issued, much of the processing and support facility has been completed, and plans for the linac have evolved considerably. This Conceptual Design Report is intended to summarize the present design status of the linac.

The design of the technical systems of the TTFL has developed substantially since the TTF Proposal. Though a complete description of the technical systems may not be possible within the bounds of reasonable effort and length, it is important that specific descriptions of the technical systems be given . This is needed so that everyone understands what is proposed to be built, whether it fits together, how to standardize it, just what is missing, needs to be changed, or is not necessary.

It is also necessary to define the experiments to be carried out on the TTFL. These experiments must to thought through and outlined in sufficient detail now so that the necessary diagnostics are built into the technical systems. This effort is especially important for those items needed in the cold cryostat and cryogenic system, where it will be difficult to make additions and modifications later.

The experiments that should be considered are not only the more typical beam experiments, but perhaps more importantly the cryogenic and RF measurements and operations to run the systems but may not require beam.

---

[1] *Proposal for a TESLA Test Facility*, TESLA Report 93-1, DESY 1992

The successful production of the cavity systems and the TTFL must be given first priority. To this end initial prototype components must be assembled to provide working subsystems and overall major systems in a timely manner. However once these efforts are underway, cost efficient designs must be explored and cost drivers for large scale production analyzed. Thus not only are successfully working systems a necessity, but convincing analysis of costs for the final TESLA 500 design must be carried out. In addition, prototypes of cost effective component designs should be tested when at all possible.

1.1 TESLA 500 and the TTFL

The various approaches to a next-generation linear collider design differ mainly in the choice of spot size, bunch charge, and frequency. The differences mainly come down to trade-offs between the amount of beam power that is required versus the spot size which must be provided at the interaction point. A higher beam intensity can be used to balance more relaxed beam emittance and final focus requirements. Typically, bunch intensities vary by an order of magnitude and vertical spot sizes by as much as a factor of 20. The different designs range from 1.3 to 30 GHz in accelerating structure excitation frequency.

The TESLA approach lies at the low frequency, high intensity end of the present parameter ranges. The use of superconducting RF cavities aids in reaching higher beam intensity. The beam power could as well be applied toward higher luminosity if more stringent emittance and focusing requirements were imposed. However, the major appeal of the superconducting RF approach is that it allows for more relaxed tolerances and less ambitious extrapolations from the state-of-the-art operation at the SLC.

The technical advantages of the superconducting RF cavities stem from their high Q values and low wall losses. This allows for the use of large aperture structures operating at relatively low frequency, with long pulse lengths and low peak RF power requirements. The large aperture of the cavities has the beneficial consequence of substantially reduced transverse and longitudinal wake field effects. As the aperture of an L-band cavity is ≈70 mm in diameter—about ten times larger than in some of the higher frequency designs—relaxed linac alignment and vibration tolerances should

result even at the higher bunch charge of this design. With a larger emittance, more dilution can be tolerated in the linac, in the optics after the linac, and in the final focus. Benefits for the detector include more longitudinal space after the last focusing element and a longer beam pulse with considerable time between bunch interactions.

Despite these attractive features, a major effort is needed to demonstrate that a superconducting linear collider can be built at a cost competitive with its normal conducting counterparts. The maximum accelerating gradient for niobium structures is in principle about 50 MeV/m, but in practice the achievable gradient is limited by field emission from localized regions on the cavity surface. In the last few years, there has been significant progress in the understanding of this field emission process and its cures, and the gradient produced by multicell cavities has moved up from the 5 MeV/m range to above 25 MeV/m. Estimates carried out by the TESLA collaboration indicate that a competitive balance may be reached at an accelerating gradient of 25 MeV/m.

A short summary of the suggested advantages and possible disadvantages and challenges of the TESLA approach is listed below.

Advantages:

- High efficiency — $\approx$23% of linac plug power delivered to the beam
- Large aperture $\rightarrow$ low wake fields
- High Q $\rightarrow$ long RF pulse, large bunch spacing, more bunches per RF pulse
- "Conventional" RF systems
- Large bunch charge aids in energy resolution
- Large vertical emittance permits:

    - Large alignment tolerances
    - Easier final focus
    - More longitudinal space for detector
    - May permit zero crossing angle
    - Easy collimation — large collimator opening, many σ

- large bunch spacing permits:

    - Collimator protection & injection error protection easier

- Multi-bunch servo & feedback easier for vibration compensation, energy control and other multi-bunch processes

– Possibly better detector backgrounds
– Result $\rightarrow$ Technical contingency—parameters, such as vertical spot size, are not pushed to extremes, or $\rightarrow$ easier extension to higher energy

Challenges:

– Cost and gradient improvements must be demonstrated in building the TTFL
– The complex cryogenic system
– Cryo/vacuum failure may result in cavity contamination; it should be demonstrated that, e.g., *in situ* high peak power processing can aid recovery (as has already been demonstrated in vertical tests with multicell cavities)
– Dark current capture may be a difficulty at the low TESLA frequency
– Lorentz force cavity detuning may be difficult to control
– Large damping ring and positron source may be required
– The implications of the large beam power must be examined (it is encouraging to note that 1.5 GHz storage ring cavities have handled beam currents as high as 26 mA at 5 GeV without any adverse effects. Recently, a 500 MHz single cell cavity was run in CESR at 5 GeV with a stored CW beam of 220 mA)

Some of these perceived advantages and challenges may be explored in the TTF program; others cannot. Tab. 1.1 illustrates the similarities and differences between TESLA 500 and the TTFL.

Two injectors are planned for the TTFL. The first, Injector I, is intended to be relatively straightforward in design, to provide the TESLA design current, but not the TESLA large bunch spacing and rather intense bunches. In its initial form, Injector I will employ a subharmonic buncher at one-sixth the linac frequency. The parameters of Injector I are shown in Tab. 1.2. The second, Injector II, is intended to provide the TESLA 500 spacing and bunch intensity. An RF photoemission gun is a candidate for Injector II; tentative parameters for this approach are shown in Tab. 1.3. Neither will have the transverse emittance ratio of TESLA 500.

Table 1.1: TESLA 500 – TTFL parameter comparison.

Parameter	TESLA 500	TTFL	
Linac Energy	250 GeV	500 MeV	
RF frequency	1.3 GHz	1.3 GHz	
Accel Gradient	25 MeV/m	15 MeV/m	
Q_0	5×10^9	3×10^9	
# Cryo modules	≈ 2500	4	
Energy spread, single bunch rms	1.5×10^{-3}	$\approx 10^{-3}$	
Energy variation, bunch to bunch rms	10^{-3}	$\approx 2 \times 10^{-3}$	
Bunch length rms	1 mm	1 mm	
Beam current	8 mA	8 mA	
Beam macro pulse length	0.8 ms	0.8 ms	
Lattice β typical	$\langle 66$ m$\rangle$	12 m max	
		Inj I	Inj II
Injection Energy	10 GeV	10 MeV	20 MeV
Emittances (x/y), $\gamma\sigma^2/\beta$	$20/1\mu$m	$\approx 5\mu$m	$\approx 20\mu$m
Beam size σ, end of linac	$50/12$ μm	250μm	500μm
Beam size σ, injection	$260/60$ μm	1.7 mm	3.5 mm
Bunch frequency	1 MHz	217 MHz	1MHz
Bunch separation	1 μsec	4.6 ns	1μsec
Particles per bunch	5×10^{10}	2.3×10^8	5×10^{10}

Table 1.2: Injector I

Gun Energy	250	keV
Output Energy	9.9	MeV
Accel Gradient (Capture Cav)	10	MV/m
Frequency Capture Cav	1300	Mhz
Phase spread, gun	± 150	deg
Prebuncher Frequency	216.7	MHz
Bunch Population	2.3×10^8	per bunch
RMS Phase Width	0.77	deg
Total Phase Width	3.2	deg
RMS Energy Spread	0.078	MeV
Total Energy Spread	0.3	MeV
Emittance $(4\gamma\sigma^2/\beta)$	16.8	mm-mrad
RMS bunch length	0.49	mm
$\Delta E/E$ RMS	0.8	%

Thus, there are a number of respects in which TESLA 500 and the TTFL are sufficiently similar, so that the TTFL experience will feed directly into the TESLA 500 design. There are some aspects of the full scale linear collider that will be difficult to check, and still others that cannot be seriously investigated. These distinctions are characterized in the following lists.

What the TTFL does check:

- Gradient achievable
- Cavity construction and processing techniques
- Input and HOM coupler designs
- RF control of multi-cavity systems
- Lorentz detuning effects and control
- *In situ* high peak power processing (HPP)
- Vacuum failure recovery potential
- Cryostat design
- Cryogenic operation and heat load (except possibly HOM)
- Dark current

Table 1.3:   Injector II: RF photoemission gun, accelerating section, and
                compressor nominal conditions.

Bunch spacing	1	μsec
Bunches per macropulse	800	
Electrons per bunch	5×10^{10}	
Brightness	4.8×10^{12}	A/m^2
Emittance, $\gamma\sigma^2/\beta$	20	mm-mrad
RF frequency	1.3	GHz
RF power—gun	2.5 typ, 4.5 max	MW
Solenoid focusing	0.14	T
field on axis		
Beam radius at cathode	3	mm
Bunch length, σ	4.33	mm
before compression		
Bunch length, σ	1 typ	mm
after compression		
Post gun kinetic energy	3.8 typ, 6 max	MeV
Injector output energy	20 typ	MeV
Gradient in acc sect	15 typ	MV/m
Momentum spread	4.2 typ	%
Longitudinal emittance	0.82 typ	MeV-deg
Laser pulse FWHM	28	ps
Photocathode QE	1	%
Micropulse energy	> 5	μJ
Time jitter	< 2	ps
Amplitude jitter	< 5	%
Pointing stability	< 100	μrad
Laser wavelength	< 300	nm

– Energy and position beam feedback and control
– Alignment and its stability (during thermal cycle also)
– BPM system
– First iteration on projected systems costs

What may be difficult to check:

– Q_0 and HOM measurements are not easy
– Wake field measurements only far off axis
– Cavity alignment via wake fields hard because of polarization
– TESLA 500 bunch charge hard to achieve in time scale of TTFL
– Accurate cost projection to mass production

What the TTFL does not check:

– Emittance growth
– Vibration sensitivity
– Many features of an overall TESLA 500 facility (damping, positrons, etc.)

1.2   Overview of the TTFL Program

The TESLA Test Facility is located in Building 28 (Halle 3) at DESY; a plan view of the layout is shown in Fig. 1.1. The linac itself is within a shielded enclosure in the upper part of the figure. An expanded view of the linac is shown in Fig. 1.2. The TTFL contains three major regions: the injector area, the main body of the linac, and the high energy beam analysis area. The injector area includes the electron gun, subharmonic prebuncher, the superconducting capture cavity, focusing lenses, and beam diagnostic equipment. The capture cavity is identical to one of the nine-cell structures in the main linac. The principal parameters of the injector (Injector I) have already been listed in Tab. 1.2.

Four cryomodules, each 12.2 m in length, comprise the main body of the linac. Each cryomodule contains eight nine-cell cavities and a "quadrupole package". Each cavity has an input coupler for RF power, two higher-order-mode (HOM) output couplers, and a tuning mechanism. Selected parameters of the cavities are given in Table 1.4. The quadrupole package includes a
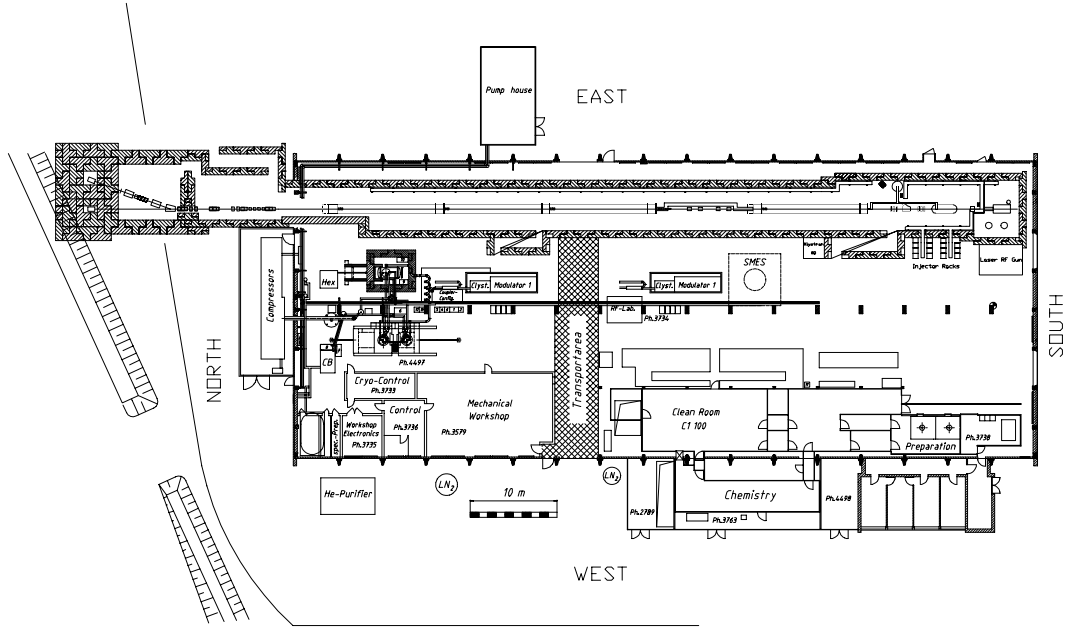
Figure 1.1: Layout of the TESLA Test Facility

Table 1.4: RF cavity parameters for the TTFL

Frequency	1.3	GHz
Cells per cavity	9	
Cavity length	1.036	m
Iris radius	35	mm
R/Q	1011	ohms/cavity
E_{peak}/E_{acc}	≈ 2.0	
RF power @ 25 MeV/m	206	kW/m
HOM k_{long}/cavity	8.5	V/pC (1mm bunch σ)
HOM k_{trans}/cavity	18	V/pC/m

500 MeV   10 - 15 MeV   250 keV

modules # 2 - # 4   module # 1   capture   gun
cavity

high energy   TTF linac   15 MeV
experimental   (4 modules / 32 cavities)   analysis
area   area
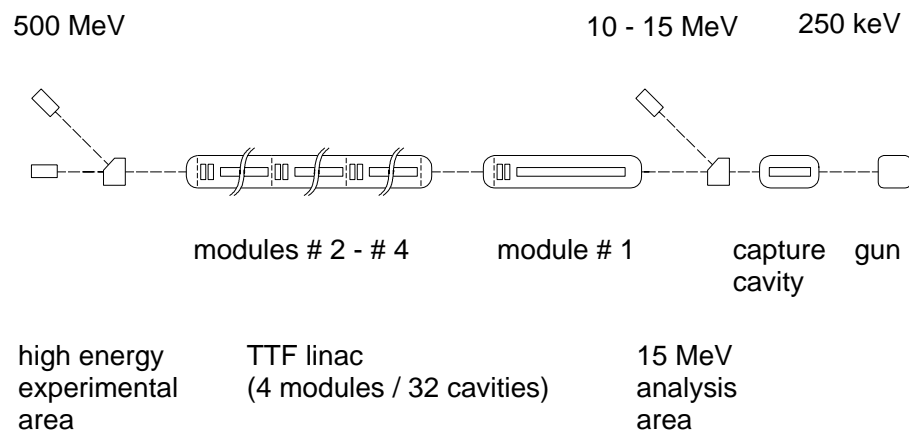
Figure 1.2: Schematic of the TTFL

Table 1.5:   Summary of the cryogenic system heat budget for TTFL (4 modules and injector). Budget is 1.5 times estimated loss.

	Static Losses	Total Losses 15 MV/m $Q=3 \times 10^9$	Total Losses 25 MV/m $Q= 5 \times 10^9$
Summary—2 K			
2 K load, W/m	0.23	1.28	1.78
Budget, 5 modules, W	21	115	160
Summary—4.5 K			
4.5 K load, W/m	1.16	1.27	1.33
Budget, 5 modules, W	104	114	120
Summary—70 K			
70 K load, W/m	6.4	10.4	11.3
Budget, 5 modules	576	936	1017
w/o HOM	576	684	765

quadrupole doublet, transverse steering, a transverse beam position monitor, and an HOM absorber.

RF power for the main body of the linac will be provided by two klystrons and two modulators. Each klystron/modulator will deliver 4.5 MW with a pulse length of up to 2 ms. The cavities will operate at a temperature of 1.8 K, with refrigeration provided by a system of 100 W capacity at 1.8 K, which can be increased to 200 W capacity by the addition of a heat exchanger. A summary of the cryogenic system budget is given in Tab. 1.5. The loads per unit length have averaged the accelerating structure loads over the entire length of the cryomodule. The total cryogenic system budget for the TTFL is 1.5 times 5 modules (counting the capture cavity and end effects).

A summary schedule for the TTFL is shown in Tab. 1.6. The column labeled "Original" is the schedule established in May 1993, while the column headed "Actual" is either the date at which the event occurred or the best schedule estimate at this writing.

The TTF program relies heavily on making substantial progress in achiev-

ing high field gradients in the cavities. To this end, a major effort has gone into the installation of a state-of-the-art facility to carry out the cavity processing procedures, as noted earlier.[2] Many of the milestones in Tab. 1.6 are associated with the equipment which was needed to proceed with a systematic investigation of the most effective cavity processing steps. The infrastructure that has been assembled in Halle 3 consists of:

- Cleanrooms spanning classes 10–10000, of total area $\approx 300 m^2$
- An automated chemical processing system for both inside and outside chemical etching
- A pure water rinsing system
- A very high pressure rinsing system
- A vacuum oven for titaniaum treatment to improve the thermal conduction properties of the cavities and RRR
- A vertical dewar cavity test setup and a 5 MW, 2 ms RF modulator for HPP of the cavities and for gradient measurements
- A horizontal test cryostat for one cavity, which will retest the individual cavities after the mounting of RF couplers and the helium vessel
- Cryogenics and controls to support the test program

A summary of the TTFL measurement program is outlined below; further detail will be found in the subsequent chapters of this report. The measurements may be considered to fall into three general categories: no beam, low bunch charge (Injector I), and high bunch charge (Injector II).

Major parts of the system can be checked without beam. These include pulsed mode operation and control of the low and high level RF systems with Lorentz force detuning compensation, and 16 cavities operated from one modulator system. Attempts at *in situ* HPP cavity processing and measurements of dark current can be performed. Cryogenic measurements of the static heat load, *in situ* Q_o measurements, and cooldown and warmup procedures can be developed and carried out. Measurements of alignment stability and vibration can be made.

With the low bunch charge injector, beam acceleration, control and stability of position, energy, and emittance with full beam current are possible. Cryogenic load measurements under full beam power loading can be carried

---

[2]*Proposal for a TESLA Test Facility, op cit*

out. Major vibrational effects on the beam and studies of beam losses and
associated radiation may be observed.

The high bunch charge injector allows for measurements of HOM losses,
wake field effects, and the possibility of observation of cavity misalignment
by mode excitation.

The lists below are organized under various subject headings, and, of
course, the lists cannot be complete. Entries concluding with an asterisk, '*',
need full bunch charge of Injector II.

Alignment-Vibration:

A–1 Measure cryomodule alignment stability during cooldown-warmup.

A–2 Measure vibration properties, i.e., vibration transfer function for cavi-
     ties, quadrupoles, and couplers.

Cryogenics:

K–1 Measure heat leak with and without beam and RF. Measure Q_o versus
     the accelerating gradient calorimetrically or, at least, be able to detect
     low Q (leading to $\approx 1/4$ watt in a cavity) and quenches.

K–2 Measure temperature profile for each cell and coupler on at least one
     cavity.

K–3 Measure operation as a function of temperature.

K–4 Measure HOM power deposited in He and in the beam tube absorber.*

Cavity performance:

C–1 Measure Q versus E_{acc} with time, with and without beam, both calori-
     metrically and electrically.

C–2 Attempt high power peak processing *in situ*.

C–3 Transfer full pulse power to beam at full pulse length.*

C–4 Measure HOM power deposited in liquid helium, coming out beam
     pipe and deposited in the HOM absorber, and coming out of the HOM
     couplers.*

C–5 Look for transverse mode excitation as a function of beam position. Try to measure module/cavity alignment by looking for beam position that yields minimum transverse mode excitation.*

C–6 Measure dark current. Measure radiation patterns and spectrum without beam for field emission and captured dark current.

RF system

R–1 Develop tuning procedures for cavity and input coupler (frequency, voltage, phase, coupling) with Lorentz force compensation.

R–2 Develop beam loading compensation, and be able to switch from no-beam to beam conditions.

R–3 Develop quench and arc protection.

R–4 Measure gradient and phase as functions of time in each cavity with and without beam.

R–5 Look for microphonics, including radiation pressure effects. Look for coupler vibration effects.

Beam

B–1 Measure energy, energy spread, and energy stability within the macropulse.

B–2 Measure emittance.

B–3 Repeat measurements above with Injector II. Need to measure bunch length at injector end to assure that injected beam is not leading to excessive energy spread.*

B–4 Measure emittance blowup off axis, off momentum.*

B–5 Observe single and multi-bunch wakefields. Is an off-energy witness bunch needed? Wakefield measurements are coupled to emittance (head-tail) and mode excitation measurements as well.*

B–6 Look for transverse mode excitation.*

Operation

O–1 Develop tuneup procedures, practice beam alignment, focusing, and energy optimization.

O–2 Check BPM system operation for sensitivity, linearity, off-center line, etc.

O–3 Make precise beam transmission measurements.

O–4 Measure radiation pattern with beam. Determine amount of radiation coming from poor quality injected beam.

O–5 Simulate fault conditions of subsystems, such as RF trips, magnet trips, and so on.

Table 1.6: Summary schedule for TTFL as of January 1995.

Item	Condition	Original Milestone 5.93	Actual or Expected
Two prototype cavities	available	8.93	8.93
Cryosystem vertical dewar	available		12.93
1st proto cavity RF test	start	11.93	1.94
lst cavity order (1-6)	release	10.93	2.94
TTF chemical processing	available		4.94
HPP RF modulator # 1	available	2.94	5.94
lst cavities	start delivery		11.94
Treatment, cavities 1–6	start	3.94	1.95
lst cavity horizontal test	start	5.94	4.95
lst cryomodule	start assembly	11.94	8.95
lst cryomodule	assembly complete		11.95
Feed can	delivery		7.95
1st cryomodule	cold test	4.95	11.95
Injector I	start test Saclay		3.95
Injector I	start oper DESY		10.95
Beam test 1st cryomodule	start	8.95	12.95
Final cavity order	release	6.95	
Final cryomodule order	release	6.95	
Assembly modules 2-4	start	5.96	
Modules 2-4	install in linac		3.97
Beam tests, 4 modules	start	4.97	
Injector II	start DESY oper		3.97
Beam, linac & Inj II	start		5.97

Chapter 2

Accelerator Physics Design

The first section of this chapter gives a description of the overall layout and shows the division of the linac into different segments each having its own beam optics considerations. The fact that beam matching between the different segments has finally to be achieved yields to constraints which we also describe. Section 2.2 will report on the first injector together with the rationale for the choice of its different subsystems including the low energy analysis area, Section 2.3 will cover the linac and Section 2.4 the high energy beam analysis area. The matching between injector and linac is dealt with as a special aspect of the linac optics. The problem of RF focusing is also covered by Section 2.3. The design of the high energy beam analysis area was determined by the need of beam diagnostic stations and the necessity of increasing the transverse beam dimensions before stopping the beam in the beam dumps. Injector II is not discussed in this chapter; a preliminary design is given in Chapter 3.

2.1   Linac Overview

The TTF Linac consists of a 250 keV room temperature injection, a short superconducting linac followed by a 10 MeV beam analysis area and an optics matching system, the capture cavity section and the linac itself consisting of four cryomodules with eight cavities each, and the 500 MeV beam analysis area.

    The warm part of the injector starts with a grid controlled thermionic gun

as the source. The anode voltage of 40 kV accelerates bunches ($2.3 \cdot 10^8$ e$^-$ in 50 degrees at 216.7 MHz) to an electron velocity of $\beta = 0.37$ with which the beam is injected into a 1 m long electrostatic preacceleration tube. At the end of this tube, the energy of 250 keV is a compromise between, in its lower limit, avoiding too strong space charge effects and, in its upper limit, the necessity of shortening the bunches by use of an energy modulating cavity followed by a drift. At 250 keV the bunch structure thus achieved can be transported along a few meters of beam line although the velocity of $\beta = 0.74$ still corresponds to a sensitivity to deflection by the earth magnetic field of almost 20 mrad.

The bunch compression is performed by means of a subharmonic buncher cavity (SHB) which is operated in the π-mode. Injection of the bunch is done at a time when the leading electrons see a decelerating field, then the field will change its direction during the bunch passage and therefore the late electrons will gain energy. The amplitude of energy modulation in the subharmonic buncher cavity depends on the distance between this cavity and the first accelerating cavity. Since the bunch compression is based on the change in velocity, the best injection phase into the SHB with respect to the zero-crossing point of the RF waveform will not be the longitudinal bunch center; some dephasing occurs as a result of the nonlinear dependence of the velocity β on the energy.

While transporting the longitudinally converging bunch through the beam line down to the entrance of the superconducting capture cavity, the transverse profile should be held at proper dimensions with respect to the beam tube diameter. At the same time, one also should avoid too small diameters since then the space charge forces increase drastically. Solenoids are used to provide the requisite focusing. A last solenoid should be used to match the transverse phase space to the capture cavity's acceptance.

The capture cavity is a standard superconducting TESLA 9–cell structure, is operated in the accelerating π–mode, and has a crucial influence on the beam quality at the end of the injector. As a standing wave, $\beta = 1$ cavity it has three major impacts on the beam optics. First, the large leakage field, which the injected electrons see in the beam tube in front of the first cell, acts as a decelerating field, at least for some part of the bunch. Second, the low velocity of the 250 keV ($\beta = 0.74$) electrons results in a phase slippage in the first cell. The consequence is an energy modulation but fortunately also a further bunch compression. The leading electrons gain more energy

than the trailing ones. And third, the field of a standing wave cavity has a strong focusing influence on the transverse dimensions of the electron beam. This is not only the decrease in the ratio of transverse to longitudinal momentum ('adiabatic damping') but also the existence of a net momentum transfer caused by the transverse Lorentz force on the electrons. Although a rough estimate of some of the effects can be made analytically, a complete simulation has been carried out using the tracking code PARMELA. This calculation also takes the space charge effects into account. The results are reported in Sect. 2.2.

The accelerated electron beam can be studied in the low energy beam analysis area behind the injection linac. It is planned to measure the transverse and longitudinal phase space volume and orientation. Therefore several diagnostic stations are used together with a focusing quadrupole triplet, either in the straight section (emittance measurement) or in a dispersive section (energy spread measurement) behind a bending magnet. Here the influence of the accelerating gradient and its focusing effect in the transverse phase space will be seen. The energy stability within the 800 μs macro pulse has also to be examined.

The first quadrupole triplet mentioned above will be used together with a second triplet, installed just in front of the main linac. This allows the matching of the beam to the optics lattice used along the linac. This matching strongly depends on the orientation of the injector beam in the transverse phase space. When entering the first triplet a converging beam is advantageous in order to avoid too large a beam diameter in this matching section.

The lattice along the TTF linac consists of cells, each having a superconducting quadrupole doublet and a beam position monitor followed by eight 1 m long superconducting cavities. For the first cell we omit the doublet since this is replaced by the matching system. One cell is basically represented by a focusing element 'F', a short intermagnet drift 'I', a defocusing element 'D' and finally a long drift 'O'. We refer to this arrangement as a FIDO lattice. The matching to this FIDO lattice is strongly disturbed by the RF focusing which has to be taken into account at least for the first main linac cavities. Section 2.3 gives the results of a detailed beam optics calculation.

Following the four cryomodules, the accelerated electron beam has to be transported through the high energy beam analysis area down to the end of the beam line, to the beam dump. It is planned to use one more quadrupole doublet together with the last superconducting doublet in order to measure

again both beam emittance and, in a dispersive section, energy spread. Further quadrupole singulets or doublets will be used in the two straight sections behind the analyzing magnet to increase the β–function by at least two orders of magnitude before stopping the beam in two separate dumps. Thus damage to the dump and its windows can be avoided. Section 2.4 deals with the detailed description of the beam transport calculation and includes the requirements for the analysis systems.

2.2   Injector

In this section, we outline the initial phase of the injector—Injector I as referred to in Chapter 1. The modifications needed to achieve Injector II will be treated in Chapter 3. The RF waveform, superconducting cavity gradient, and the beam time structure is shown in Fig. 2.1 for the two injectors.

The purpose of the phase 1 injector is to demonstrate that we can produce a beam with the correct properties with respect to acceleration, energy resolution and stability. The principal problems, therefore, arise from the operation of high-gradient superconducting cavities in pulsed mode and with heavy beam loading. Unlike problems concerning wakefields and higher-order mode dissipation, which will require the full TESLA bunch charge per bunch, the former problems can be studied with a beam of equivalent average current (8mA at 25 MV/m or 4.8 mA at 15 MV/m during 800 μs, this assumes the same Q_{ext} for both gradients) independently of the time structure of the pulse. Indeed the original TTF proposal mentions a scheme where bunch charges of 4×10^7 electrons are delivered at the maximum possible frequency of 1.3 GHz by RF chopping of a continuous 8 mA beam. Although that approach appears quite feasible we have adopted an alternative solution. It offers the promise of more flexible operation of the injector with the possibility of higher bunch populations at reduced micro-bunch frequency, although perhaps with diminishing beam quality for increasing bunch populations.

This latter solution consists of a gridded triode gun which produces short (<1 ns) pulses which are subsequently compressed longitudinally in a single-cell buncher cavity operating at a sub-harmonic of the accelerating cavity frequency (f_0 = 1.3 GHz). The sub-harmonic buncher (SHB) frequency is chosen to be $f_0/6$ = 216.7 MHz ensuring that the RF period is well in excess of the gun pulse duration. Following the SHB the beam passes through a
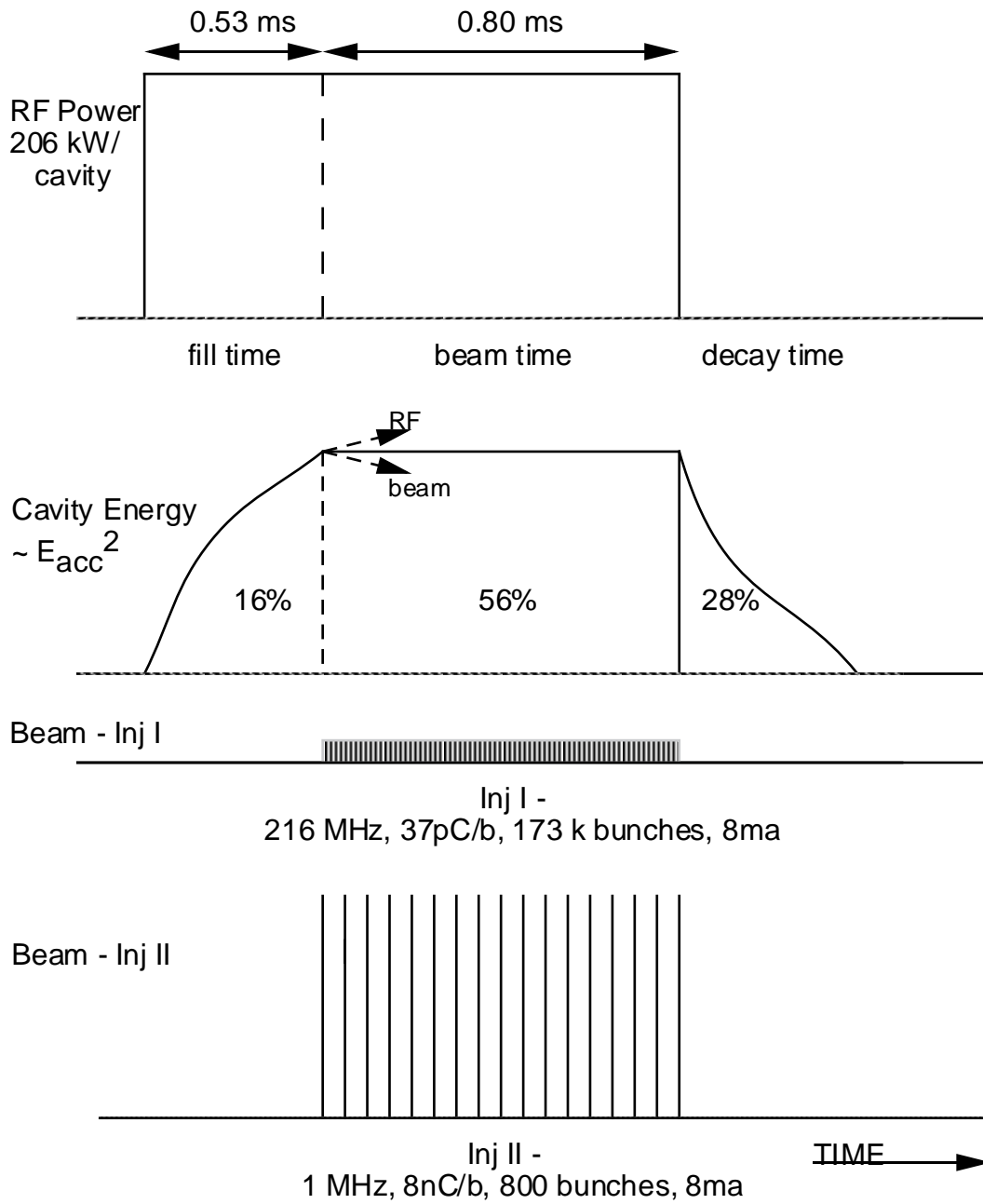
Figure 2.1:   RF waveform, cavity gradient, and beam time structure for Injectors I and II.

superconducting capture cavity which further bunches and accelerates the beam to the desired parameters for injection into the TTF linac. The superconducting capture cavity is a 9 cell, 1.3 GHz cavity identical in design to the cavities used for acceleration in TTF. The gun will be able to generate pulses at the frequency of the SHB and sub-multiples thereof so allowing operation of the injector at variable frequency. Modulation of the gun will be achieved by applying fast pulses, of variable repetition rate, from a wide-band amplifier to the gun cathode. This approach follows the design of the CLIO linac which has been built and successfully operated as an injector for the CLIO free electron laser at Orsay. [1]

For operation at 216.7 MHz and 8 mA average current the required charge per bunch is 37 pC (2.31×10^8 electrons). Such bunch charges can be easily produced in sub-nanosecond pulses from conventional thermionic guns. Taking, as example, a Gaussian pulse of 0.4 ns (FWHM) the peak gun current required would be of the order of 100 mA which, as experience at LAL shows, is easily achievable. As the superconducting capture cavity has a large leakage field which tends to decelerate the incoming beam the required gun voltage is higher than is conventionally used for an electron gun. Simulations using the PARMELA code indicate that a minimum voltage of 200 kV is required to ensure transmission of the beam through the capture cavity without loss. In order to avoid the need for special high voltage insulation procedures we have settled on an nominal operating voltage of 250 kV. This beam energy will be achieved by the use of a relatively low voltage (30 - 40 kV) gun followed by an electrostatic post-acceleration column as employed on the injector for the S-DALINAC accelerator at TH-Darmstadt.[2]

The choice of a superconducting capture cavity is dictated by the requirement for a minimum injection energy of 7 MeV (preferably higher). This minimum energy is needed in order to reduce the detrimental effects of space-charge on the beam as it is transported from the capture cavity to the first cryomodule of the main linac. To achieve a comparable injection energy with a room temperature structure would necessitate an additional multi-Megawatt klystron. The application of such a high-power pulse for the large TTF duty cycle (1%) was considered imprudent from the point of view

---

[1] J. C. Bourdon et al, *Commissioning the CLIO Injection System*, Nucl. Inst. & Methods **304**, 332 (1991).

[2] K. Alrutz-Ziemssen et al, *The High Current Injector for the Darmstadt Near-Infrared Free Electron Laser*, NIM A304, 300 (1991).

of heat dissipation in the structure. Finally, in view of the risks associated with a warm structure and in view of the injector construction schedule it was decided that a superconducting cavity was a more logical choice. In order to avoid the need to manufacture one special structure, we choose to use a cavity which is identical to those in the cryomodules. However, by consequence, the cavity is not then 'beta-matched' to the gun beam energy. The two 4.5 MW klystrons for the main linac contain sufficient excess power such as to allow some of this excess power to be used in the capture cavity. However we prefer to use an individual klystron for the injector in order to provide complete flexibility of the phase and amplitude control of the capture cavity. Such flexibility is considered to be crucial in obtaining optimum injector performance; this is expected to be particularly true in the early commissioning phase of the machine. Consequently the injector will make use of its own 300 kW klystron and associated modulator.

The beam will be transported from the capture cavity to the first cryomodule with a transport line containing two magnet triplets.

Many of the beam parameters for the injector are fixed by the need to test issues related to TESLA. The specification for the injector is given in Tab. 2.1. The energy spread is chosen to provide an acceptable fractional energy spread at the end of the linac. The emittance is chosen to provide a reasonable transverse beam spot size in the linac (< 3 mm.) The overall length of the injector is determined partly by the calculation of the required distances between the principal elements (gun, SHB, capture cavity...etc), the need to include sufficient diagnostics and focus elements, and by the space requirement for the high voltage gun and its associated power supplies. The latter is particularly large as the combination of the high voltage and long pulse duration result in the need for voluminous components which require large spatial separation to prevent high-voltage breakdown problems (see Chapter 3). In addition, space is provided for the insertion of a chicane which will be used to inject off-axis beams into the main linac from the phase-2 injector.

The layout of the principal components of the injector has been determined by simulation of the beam dynamics using the PARMELA code. Following measurements on the 40 kV electron gun (see chapter 3) we have performed simulations to extrapolate the gun output parameters to the exit of the electrostatic column, so providing us with reasonable input values for the PARMELA calculations. Our reference input conditions are shown in

Table 2.1: Specification for Injector I

Average macro-pulse current	8 mA (independent of pulse structure)
Pulse width	800 ms
Frequency	10 Hz
Minimum energy	7 MeV (higher preferred)
RMS bunch length	1 mm
RMS phase-width	1.6°
RMS energy spread	1%
Normalised rms emittance	5–10 mm-mrad
Nominal length	18 meters

Table 2.2:   Input beam parameters for PARMELA calculations.

Initial energy	250	keV
Normalised edge emittance	15	mm-mrad
β (Twiss parameter)	10.7	m/rad
α (Twiss parameter)	-8.05	
Bunch population	2.31×10^8	electrons
Initial phase spread	$\pm 150 \deg$	at 1.3 GHz

Tab. **??**.

The initial phase extent of the beam is taken to be $\pm 150 \deg$ at 1.3 GHz, which corresponds to a gun pulse width of 641 ps. The bunch population is that which corresponds to 8 mA average current at a bunch frequency of 216.7 MHz. As noted above, the PARMELA simulation is performed from the *exit of the electrostatic accelerating column* and not from the gun itself. The input parameters chosen are found by taking the measured beam parameters at the exit of the anode aperture (for 30 kV gun voltage) and simulating the evolution of these values as the beam passes through the electrostatic column. This simulation is done by approximating the electrostatic column as a low frequency (10 MHz) cavity of length equal to that of the column and with a field sufficient to provide a 220 keV energy gain at the end of the column. A

separate PARMELA run is then performed for this cavity alone to provide the column exit parameters for the injector simulation. The period of the 10 MHz cavity is much longer than both the bunch pulse width and its transit time through the column, so all particles see the same phase and receive the same energy. This approximation then provides us with an estimate of the expected beam parameters at the exit of the column, although it remains to be verified that these values are indeed produced at the end of the column, hereafter referred to as "point zero". The distance between point zero and the center of the SHB is set to 1285 mm which is considered the minimum necessary to allow for the required elements on the beamline (diagnostics, pumping, focus coil).

We have investigated the beam parameters at the exit of the capture cavity corresponding to capture cavity peak surface fields of between 14 MV/m and 30 MV/m, corresponding to maximum peak energy gains of 7 MeV/m and 15 MeV/m respectively. As the 9 cell capture cavity is operated in standing wave π mode there is only one phase parameter to play with in the PARMELA optimization. The fields of the capture cavity are determined by inputing the cylindrically symmetric cavity geometry of the full structure into SUPERFISH and calculating all of the on and off-axis field components. The calculated field distribution is then 'cut' into three distinct elements for the PARMELA calculation. These elements consist of a short length (17.4 cm) of beam pipe and the first 2 cells, one full cell, and finally the last 2 cells and the same short length of beam pipe. The reconstructed accelerating field is shown in Fig. 2.2. The field components of these elements are stored in a file and read during the PARMELA run. By reading the full cell five times and using each of the other elements at either side of these five cells we can construct the complete field of the entire 9 cell structure. Consequently the large leakage field, which has an important influence on the correct calculation of the beam dynamics, is properly accounted for and the beam parameters can be output at the exit of cells 2 through to 7. In order to gain an increased knowledge of the evolution of the beam parameters in the capture cavity, the first element has been further dissected to yield an output at both the center of the first cell and at the position of the second iris. Similarly, the last element has been cut to yield an output at the exit of cell 8. The field used for the calculation with the SHB is similarly that calculated from SUPERFISH using its design geometry (Chapter 3).

We have determined the distance to optimum bunching for SHB field
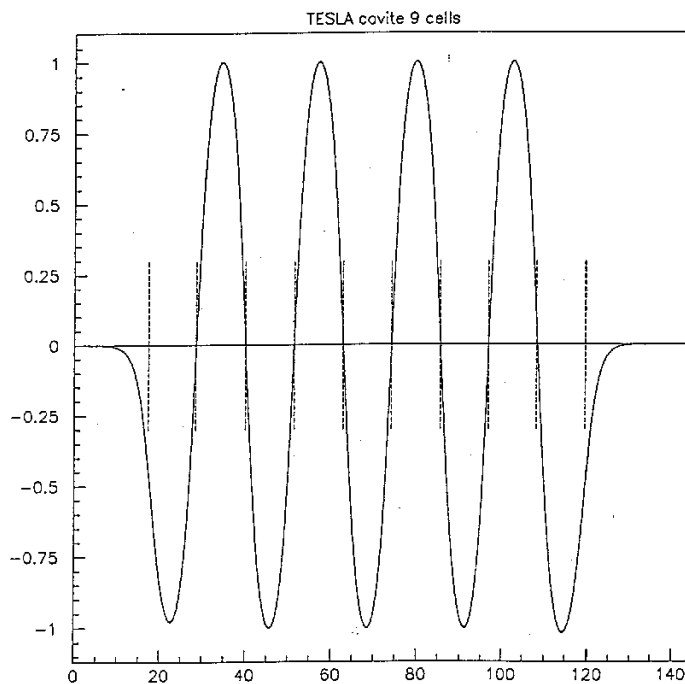
Figure 2.2:   Electric field distribution for 9 cell TESLA cavity. Dotted
lines indicate position of irises. Horizontal scale is centime-
ters.

amplitudes which correspond to reasonable SHB power requirements. This
field is the order of 1.5 MV/m and corresponds to a peak cavity voltage of
approximately 50 kV (see Chapter 3). As a linear head-tail energy spread
does not lead to the optimum bunching,[3] initial PARMELA runs were made
with the SHB alone to determine the best phase of the beam with respect
to the zero-crossing point of the SHB RF waveform (-17 deg). Taking ac-
count of the SHB period and the initial width of the pulse, the 50 kV cavity
voltage corresponds to a head-tail energy modulation of 42 kV. From sim-
ple kinematic considerations we can estimate that the distance to optimum

---

[3].M. B. James, *Production of High Intensity Electron Bunches for the SLAC Linear
Collider*, SLAC Report - 319, August 1987.

bunching, L, from the center of the SHB is given by

$$\Delta\phi = \omega L \left(\frac{1}{v_1} - \frac{1}{v_2} \right),$$ (2.1)

where v_1 and v_2 are the speeds of the head and tail particles respectively upon exit from the SHB, ω is the SHB angular frequency and $\Delta\phi$ is the initial phase spread. The final distance between the center of the SHB and the first iris of the capture cavity is found by repeated PARMELA runs for differing values of this distance and for different settings of the RF phase of the capture cavity until satisfactory beam values are found at the exit of the capture cavity. Our criterion for satisfactory beam values is that the final phase and energy spread of the beam should be less than that specified for the injector, and both as small as possible while permitting the maximum energy gain in the capture cavity. The initial charge distribution is that of a uniformly populated disc in phase space.

The final distance between the center of the SHB and the first iris of the capture cavity is found to be 2660 mm. This corresponds to the optimum bunching close to the third iris of the capture cavity. To preserve a reasonable transverse spot size we use four focusing coils between the gun output and the entrance to the capture cavity cryostat. The coils have peak fields of 150, 90, 180 and 190 Gauss respectively and their positions can be seen in Fig. 2.3.

The fields of the coils correspond to those of a real coil design and are not the artificial hard-edged fields generated by the "SOLENOID" option in PARMELA. The fourth of the coils is placed as close as possible to the entry of the cryostat to reduce the beam size in the capture cavity and so to minimize the risk of losses on the superconducting cavity walls. The final beam parameters at the exit of the capture cavity are shown in Tab. 2.3 for capture cavity surface fields of 20 and 30 MV/m (accelerating gradients of about 10 and 15 MV/m). It can be seen that in both cases the parameters meet the TTF injector specification. For the 30 MV/m case, the longitudinal and transverse phase space plots are shown in Fig. 2.4 and the population of the bunch as a function of phase and energy is shown in Fig. 2.5. The corresponding figures for 20 MV/m are shown in Fig. 2.6 and 2.7 respectively.

Calculations are in progress to determine the positions and required strengths of the two triplets to ensure that the beam exiting the capture cavity, for the range of accelerating gradients we have studied, can be matched

to the main linac.

In addition to our simulations with the reference input values we have performed calculations for changes in the values of various settings in turn. This allows us to the check how critical the injector performance is to those settings and to set stability limits on power supplies. To summarize briefly we find for the case of a capture cavity field of 20 MV/m the following:

1. Variations of 0.2% in the electron source voltage make no appreciable difference to the output values, whereas a 1% change results in an unacceptable increase in the final total phase extent. In order to leave a margin for error we therefore specify the high voltage power supply to be stable to $\pm 1 \times 10^{-3}$ during a pulse of 1 ms.

2. Changes of ± 40ps in the gun pulse width have no effect on the final beam values.

3. Changes of $\pm 10\%$ in the initial bunch populations have no effect on the final beam values

4. Changes of ± 1 deg in the phase of the SHB result in an increase of the final total phase extent of only 1.4 deg (4.5 deg in lieu of 3.1 deg). The SHB amplifier will be specified to have a phase stability of $\pm 0.5\%$ and an amplitude stability of 1% during a 2 ms pulse. (see Chapter3)

5. The effect of changes of ± 2 deg in the phase of the capture cavity field produces no detrimental effect onthe beam. Indeed a change of 10 deg in the reference phase is required to increase the rms energy spread to 1 %. Changes of 5 % in the capture cavity field amplitude change the beam energy by a corresponding amount while leaving the phase and energy spread essentially unchanged.

6. Changes of $\pm 5\%$ in the settings of the focus coil fields have little effect on the beam.

As well as investigating the sensitivity of the beam to small changes in external parameters we have verified that equally good "working points" exist at various operating fields for the capture cavity. Keeping all the positions of the main elements of the injector fixed we have shown that the required injector performance can be met for an energy gain of 8 MeV/m, 10 MeV/m
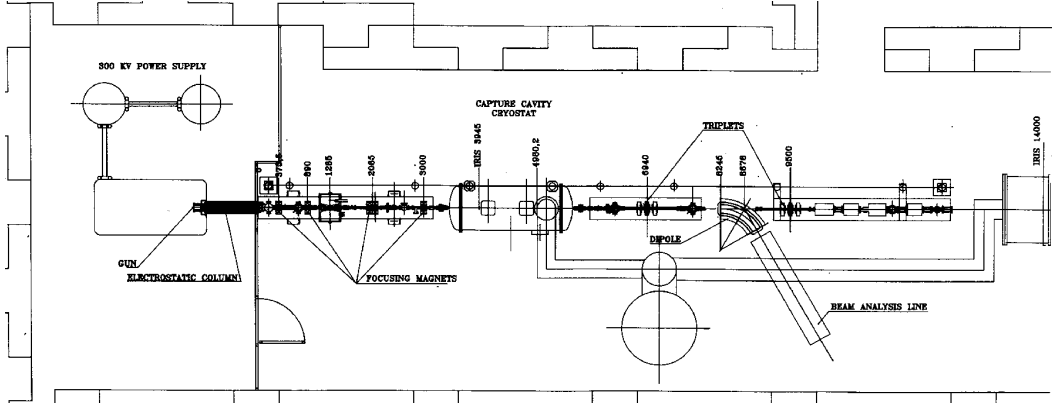
Figure 2.3:   Schematic layout of TTF Injector. Units are millimeters.

Table 2.3:   PARMELA calculated beam parameters for the reference case at the exit of the capture cavity.

Capture cavity field	20	30	MV/m
Energy	10.0	14.6	MeV
RMS phase width	0.76	0.80	deg
Total phase width	3.1	3.0	deg
RMS bunch length	0.49	0.51	mm
RMS energy spread, σ_E	0.073	0.12	MeV
Total energy spread	0.26	0.44	MeV
$\sigma E/E$	0.73	0.82	%
$4\gamma\beta\varepsilon_{rms}$	18.3	17.8	mm-mrad
RMS radius	0.49	0.82	mm
RMS divergence	-0.89	1.46	mrad
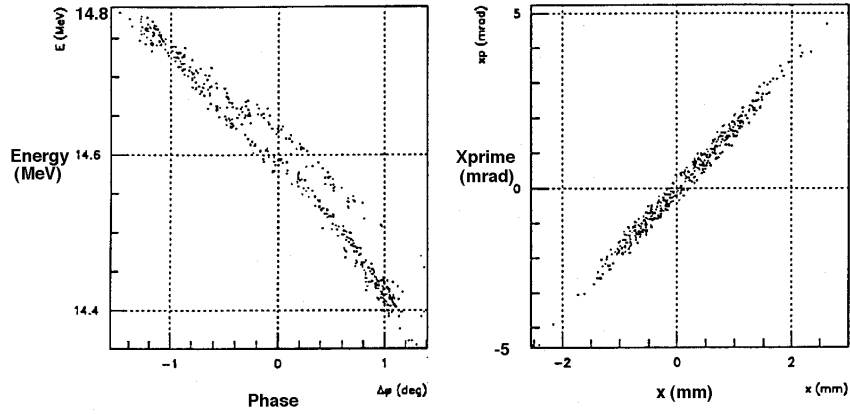
Figure 2.4:   Longitudinal phase space (left) and transverse phase space (right) at the exit of the capture cavity 5140 mm from exit of gun for surface field of 30 MV/m. Beam energy is 14.6 MeV.
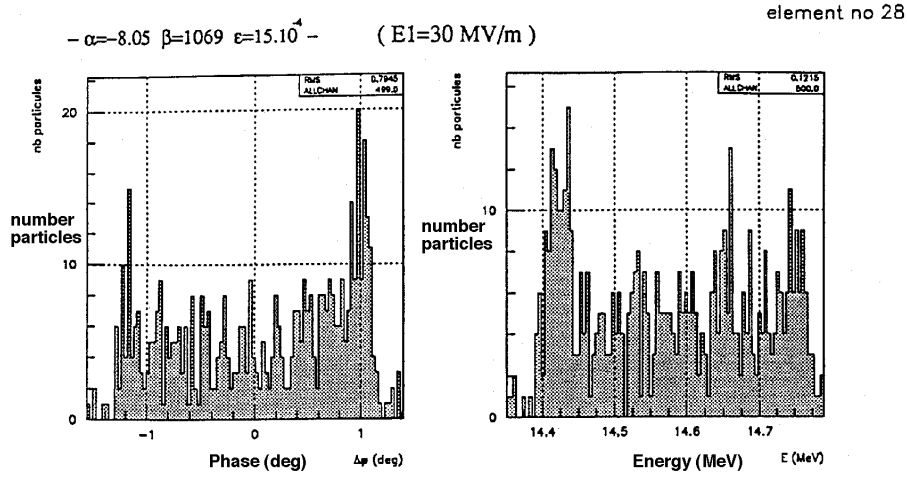
Figure 2.5:   Bunch population distribution as function of phase (left) and energy (right) at the exit of the capture cavity 5140 mm from exit of gun for surface field of 30 MV/m. Beam energy is 14.6 MeV.
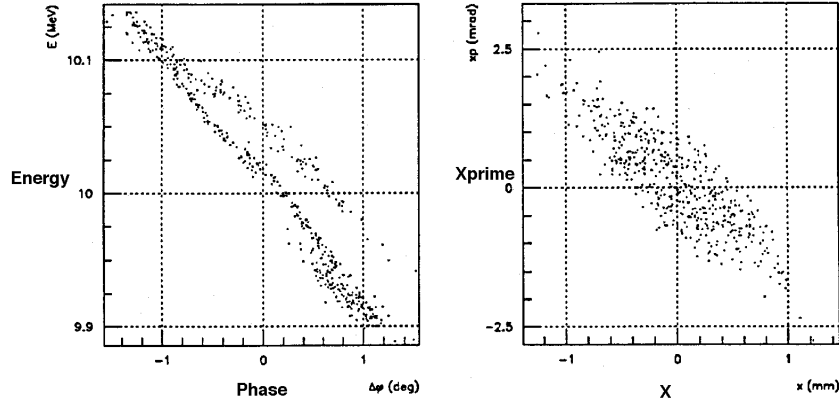
Figure 2.6:   Longitudinal phase space (left) and transverse phase space
              (right) at the exit of the capture cavity 5140 mm from exit of
              gun for surface field of 20 MV/m. Beam energy is 10.0 MeV.
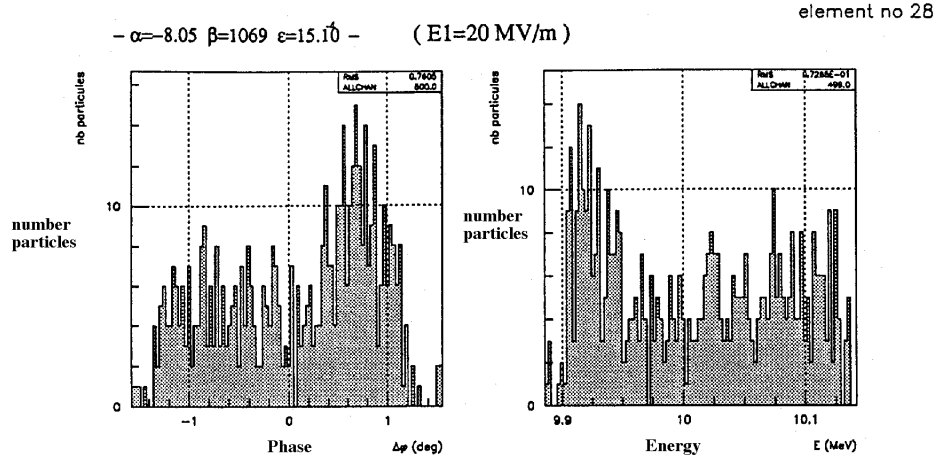
Figure 2.7:   Bunch population distribution as function of phase (left) and
              energy (right) at the exit of the capture cavity 5140 mm from
              exit of gun for surface field of 20 MV/m. Beam energy is
              10.0 MeV.

and 15 MeV/m by appropriate adjustments to the phase of the capture cavity
and amplitude of the SHB cavity.

As a nominal working point we have chosen to take a capture cavity field
of 20 MV/m. In principal this is easier to achieve and offers the benefit
of a convergent beam at the exit of the capture cavity (see Tab.2.3). The
reduced accelerating field is accompanied by a reduced RF focus effect thus
moving the beam waist further towards the first triplet. This has the added
advantage of making the matching of the beam from the injector to the
first cryomodule less sensitive to the settings of the first triplet. PARMELA
computations have shown that longitudinal de-bunching at the lower energy
(i.e. 10.0 MeV rather than 14.6 MeV) during the 9 m transport section is
negligible.

As described above, the exact beam parameters at the exit of the accel-
erating column are not fully known, consequently we have performed sim-
ulations for varying values of initial beam size, divergence and emittance
(radii up to 5 mm, divergences up to 24 mm-mrad, emittances up to 60
mm-mrad). These studies show that, although the required beam phase and
energy spread at the exit of the injector can always be met, the larger initial
divergences result in large beam sizes in the 250 keV beam line ant that
proper setting of the first lens at the exit of the column is needed to prevent
beam losses in the region between point zero and the sub-harmonic buncher.

2.3   Linac

The basics of the linac electron beam optics has been determined by a first
order beam transport calculation. We started with achieving a periodic so-
lution for the FIDO lattice as it has been defined above in Section 2.1, then
investigated the focusing effect of the standing wave accelerating cavities,
which is the replacement of the long drift 'O' by an acceleration section 'A',
and finally defined the matching system between injector and main linac.

The FIDO cell has been defined as shown in Fig. 2.8. The two magnets of
a quadrupole doublet with the strength $q \equiv B'l/B\rho$ are separated by a short
intermagnet drift d, and followed by a long drift L. The beam optics calcu-
lation has been done using the beam matrix σ[4] which is directly connected

---

[4]In this section, σ will denote the matrix defined here; elsewhere in the report, σ is
used to characterize the beam size
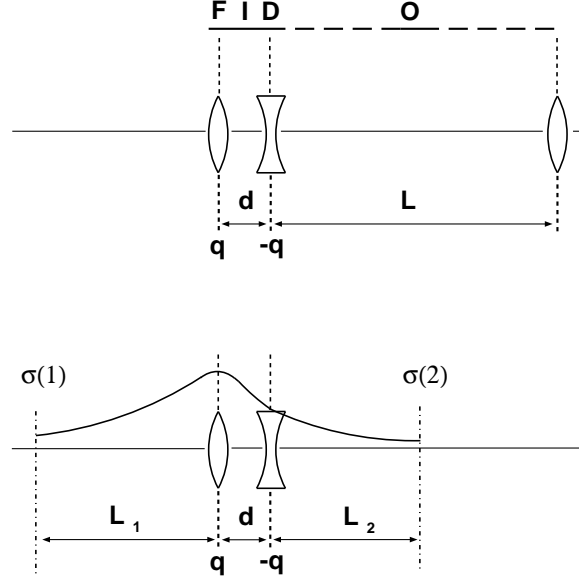
Figure 2.8:   The definition of the FIDO cell and the geometrical constraints for finding a periodic solution.

to the description by the *Twiss parameters*, where ε is the beam emittance.

$$\sigma = \left(\begin{array}{cc} \sigma_{11} & \sigma_{12} \\ \sigma_{21} & \sigma_{22} \end{array} \right) = \varepsilon \left(\begin{array}{cc} \beta & -\alpha \\ -\alpha & \gamma \end{array} \right) \tag{2.2}$$

With the transport matrix R the transformation between two points in the beam line is then described by

$$\sigma(2) = R \, \sigma(1) \, R^T \; ; \qquad R = \left(\begin{array}{cc} R_{11} & R_{12} \\ R_{21} & R_{22} \end{array} \right), \tag{2.3}$$

and a periodic solution of the FIDO cell can be calculated. Therefore we followed the situation shown in the lower part of Fig. 2.8, used the variables quadrupole strength q and length L_1, and observed the constraints that the nondiagonal elements of the beam matrix vanish, that the sum length $L_1 + L_2$ is equal to the length L of the long drift 'O' and that the phase advance per cell is $\pi/2$.

variables	fitting constraints
quadrupole strength q	$\sigma_{12}(1) = \sigma_{12}(2) = 0$
drift length L_1	$L_1 + L_2 = L$
	$\mathrm{acos}\left(\dfrac{tr(R)}{2}\right) = \pi/2$

The results for the FIDO lattice can be seen in Fig. 2.9 which shows the beam envelopes along the TTF linac, resulting from a first order beam transport calculation[5]. The beam injection energy is 10 MeV and the accelerating gradient was chosen to be 0 MV/m in order to have pure FIDO cells. Table 2.4 gives the values for the maximum beam size $\sqrt{\sigma_{11}}$, the maximum beam divergence $\sqrt{\sigma_{22}}$, and for the correlation $r_{12} = -\alpha/\sqrt{\beta\gamma}$ of the beam ellipse in the transverse phase space at a position corresponding to the entrance of the main linac. This is defined as 0.682 m in front of the first iris of the first accelerating cavity since this is the distance between the end of each module's quadrupole doublet and the first cavity iris in the following module. The correlation r_{12} measures the tilt of the ellipse and the intersection of it with the coordinate axes, e.g. $x_{int} = \sqrt{\sigma_{12}(1 - r_{12}^2)}$. At the same time, r_{12} gives the coordinates of the ellipse's projection on the axes, $(x_{max}, r_{12}\Theta_{max})$ and $(r_{12}x_{max}, \Theta_{max})$. The position of the waist in y-direction differs slightly from the one in x-direction. The difference depends on the length d of the short intermagnet section.

Switching on the superconducting cavities' field results in a drastic change of the beam envelopes. In part, this is caused by the so-called adiabatic damping which is just the fact that the momentum ratio $p_{x,y}/p_z$, with $p_{x,y}$ being the transverse momentum and $p_z c$ being the particle's energy, is decreasing. But standing wave accelerating structures introduce additional focusing[6]. Fig. 2.10 shows the beam envelopes again for the periodic solution but now with an accelerating gradient of 15 MV/m. The quadrupole strengths are scaled with the beam energy.

To emphasize the contribution of a real focusing, caused by the electromagnetic fields, to the net focusing in the accelerating cavities, we first

---

[5]T. Winkler, *XBEAM—A First Order Interactive Beam Transport Calculation*, Diploma Thesis 6/93, Institut für Kernphysik, TH-Darmstadt, Germany, unpublished.

[6]J. Rosenweig and L. Serafini, *Transverse Particle Motion in Radio-Frequency Linear Accelerators*, submitted to Physical Review E

Table 2.4:   Results for the FIDO lattice without acceleration.

Input Parameters			
Intermagnet Drift	d	0.10	m
Quadrupole Length	l_q	0.15	m
FIDO Cell Length	L	12.2	m
Beam Energy	E_{inj}	10.0	MeV
Output Parameters			
$\left(\begin{array}{l} \text{at the end of each module's quadrupole; given for} \\ \varepsilon_n = 5 \times 10^{-6} \text{ m rad} \end{array} \right)$			
Quadrupole Focal Strength	q	0.917	m^{-1}
Quadrupole Gradient/E	g/E	0.0204	T/m (MeV)$^{-1}$
x–Direction			
RMS Beam Size$\times \sqrt{E}$	$\sqrt{\sigma_{11}^x E}$	4.903	mm (MeV)$^{1/2}$
RMS Beam Divergence$\times \sqrt{E}$	$\sqrt{\sigma_{22}^x E}$	0.655	mrad (MeV)$^{1/2}$
Phase Space Orientation	r_{12}^x	0.6060	
y–Direction			
RMS Beam Size$\times \sqrt{E}$	$\sqrt{\sigma_{11}^y E}$	6.153	mm (MeV)$^{1/2}$
RMS Beam Divergence$\times \sqrt{E}$	$\sqrt{\sigma_{22}^y E}$	0.656	mrad (MeV)$^{1/2}$
Phase Space Orientation	r_{12}^y	-0.7734	
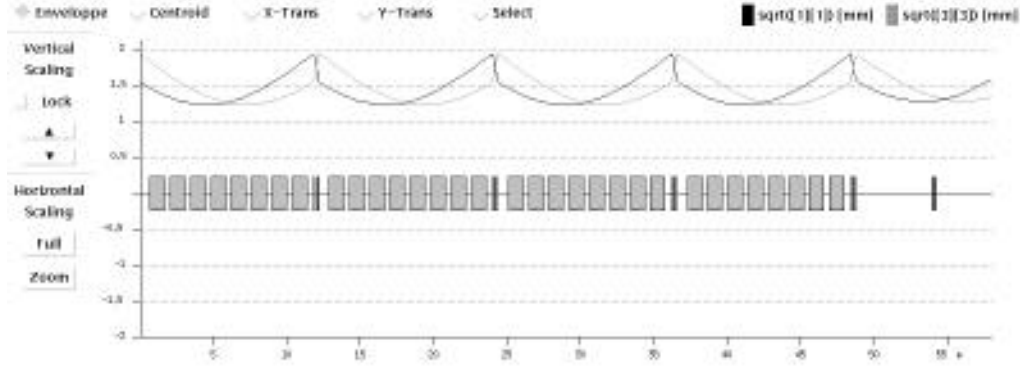
Figure 2.9:   The periodic solution for the FIDO lattice. The TTF accelerator's geometry is shown on axis and consists of four equal modules each containing eight superconducting cavities followed by a quadrupole doublet. Here, the accelerating fields are off.

compare the results shown in Fig. 2.10 with a calculation in which the accelerating cavity is described as a travelling wave structure. Here the energy of the reference trajectory is assumed to increase linearly over the entire cavity length which is a field free drift length without any externally applied magnetic field. Adiabatic damping has an influence on the beam envelopes but additional focusing does not occur. Fig. 2.11 gives the results and differs completely from the graph shown in Fig. 2.10. While the standing wave cavities pull the first waist towards the linac entrance, the adiabatic damping of travelling wave structures pushes the waist downstream. Thus, it is necessary to investigate the RF focusing and to describe the beam transfer matrix as it has been used for the TTF linac's superconducting cavities.

In standing wave cavities, an alternating focusing force acts on the off-axis particles due to the interference of the forward and the backward wave. Expressed in terms of the longitudinal field profile, this radial force is

$$F_r \cong -\frac{qr}{2}\frac{d}{dz}E_z, \tag{2.4}$$

where q is the charge of the particle and the total derivative is calculated with respect to z, the distance along the beam axis that the particle propagates. This is valid for an ultrarelativistic ($\beta c \cong c$) charged particle in a cylindrically
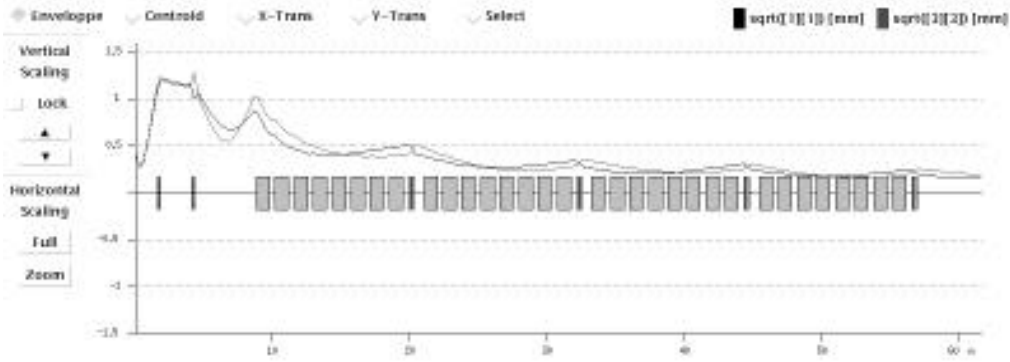
Figure 2.10:   The effect of the standing wave accelerating field on the periodic solution for the FIDO lattice.
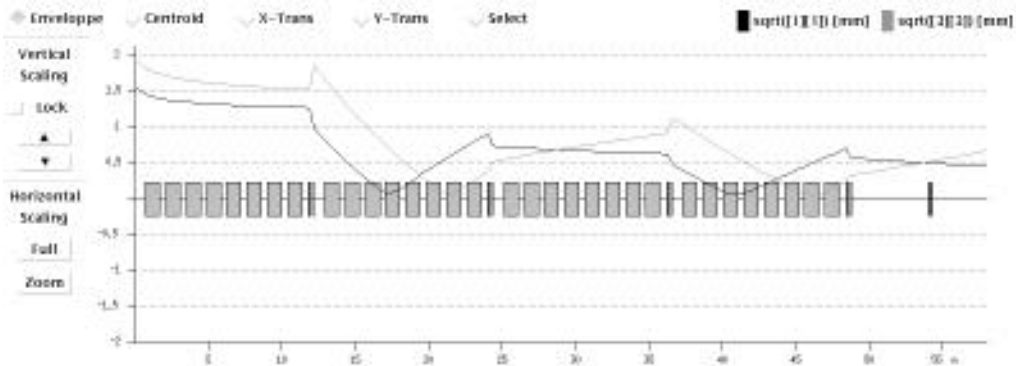
Figure 2.11:   The effect of the accelerating field of a travelling wave structure on the periodic solution for the FIDO lattice.

symmetric RF cavity, but only in an off-axis distance r for which the electric field E_r and the magnetic field H_ϕ are proportional to this distance. If we write the longitudinal field profile in the most general Floquet form[7],

$$E_z = E_0 \, \text{Re} \left[\sum_{n=-\infty}^{\infty} b_n e^{i(\omega t - k_n z)} \right], \qquad (2.5)$$

where E_0 is the average accelerating field experienced by an on-crest particle injected at the phase which gives maximum acceleration, $k_n = (\psi + 2\pi n)/d$ is the wave-number of the travelling wave associated with the n-th space harmonic considered with respect to the periodicity length d of the structure, and $\psi = l\pi/m$ is the phase advance per cavity cell (l, m being integers, $l \leq m$), then it is possible to average the periodic force derived from the last two equations which yields[8]

$$\overline{F}_r = \eta(\Delta\phi) \frac{(qE_0)^2}{8\gamma m_0 c^2} \, r. \qquad (2.6)$$

The function $\eta(\Delta\phi)$ contains the information about the longitudinal field distribution as obtained by electromagnetic design computer codes or from bench measurements. For the TESLA π-mode structures we find $\eta(\Delta\phi) = 1$, which is based on the fact that for standing wave structures the field coefficients in the Floquet form of the longitudinal field obey the relation $b_{-(n+1)} = b_n^*$. We also recognized that all coefficients but b_0 and b_{-1}, which both are equal to unity, vanish for a π-mode TESLA structure where no higher space harmonic exist. Therefore the calculated **average** force $\overline{F}_r$ is independent from the injection phase $\Delta\phi$, taken with respect to the maximum RF field. But nevertheless, a focusing effect has been observed also for π-mode structures; the reason will become clear in the following. So far, with the particle energy change

$$\frac{d\gamma}{dz} = \frac{q}{m_0 c^2} E_0 \cos(\Delta\phi) =: \gamma'_{max} \cos(\Delta\phi) \qquad (2.7)$$

we finally get the focusing strength parallel to either transverse axis as

[7]R. Helm and R. Miller in *Linear Accelerators*, Eds. Pierre M. Lapostolle and Albert L. Septier (North-Holland, Amsterdam, 1969.

[8]S. C. Hartmann and J. B. Rosenzweig, Phys. Rev. E **47**, 2031 (1993).

$$K = K_x = K_y = \frac{\eta(\Delta\phi)}{8}\left(\frac{\gamma'_{max}}{\gamma_i}\right)^2.$$ (2.8)

The first order beam transport matrix R_{trw} for a *travelling wave section* represents the adiabatic damping and can be written as two matrices, one describing a drift with a modified length L^* and the second one scaling the entry angle with the ratio γ_i/γ_f of the initial to the final energy. The length L refers to the cavity length and $\Delta\gamma$ is the change in energy.

$$R_{trw} = \begin{pmatrix} 1 & L\,\dfrac{\gamma_i}{\Delta\gamma}\,\ln\left(\dfrac{\gamma_f}{\gamma_i}\right) \\ 0 & \dfrac{\gamma_i}{\gamma_f} \end{pmatrix} = \begin{pmatrix} 1 & 0 \\ 0 & \dfrac{\gamma_i}{\gamma_f} \end{pmatrix}\begin{pmatrix} 1 & L^* \\ 0 & 1 \end{pmatrix}$$ (2.9)

The *standing wave cavity* accelerates the electron beam under the presence of a radial focusing force, as already mentioned above. The consequence is that the corresponding beam transport matrix R_{sw} is now the matrix of a focusing quadrupole with its strength K acting over the length L^*, which has been modified by the adiabatic damping. And again, this matrix has to be multiplied with the one scaling the resulting angle with the ratio γ_i/γ_f of the initial to the final energy.

$$R_{sw} = \begin{pmatrix} 1 & 0 \\ 0 & \dfrac{\gamma_i}{\gamma_f} \end{pmatrix}\begin{pmatrix} \cos\sqrt{K}\,L^* & \dfrac{1}{\sqrt{K}}\sin\sqrt{K}\,L^* \\ -\sqrt{K}\,\sin\sqrt{K}\,L^* & \cos\sqrt{K}\,L^* \end{pmatrix}$$ (2.10)

Now, the modified length L^* in the argument of the cosine and sine function is responsible for the clearly observed focusing effect of standing wave cavities. Going to off-crest injection of electrons reduces the final energy γ_f as well as the energy gain $\Delta\gamma$ and altogether increases the focusing length L^*.

The matrix R_{sw} describes the beam transport through the accelerating cavity but still does not include the existing transient force at the entrance and the exit of such a section. A sudden change in the field strength E_z from $E_z = 0$ to $E_z \neq 0$ or the other way round produces a kick which in first order can be described by a non-vanishing R_{21} element of an additional transport

matrix R_{kick}. Concentrating on one of the two transverse dimensions we can write the radial force F_r mentioned above as

$$\frac{dp_x}{dt} \cong -\frac{qr}{2}\frac{d}{dz}E_z \; , \tag{2.11}$$

which directly gives the change in transverse momentum

$$dp_x = -\gamma m_0 c \, \frac{d\gamma'}{2\gamma} \, r \tag{2.12}$$

with $d\gamma' = d(\gamma'_{max} \cos(\Delta\phi))$. Integration then yields

$$\frac{p_x}{p_z} = -\frac{\gamma'}{2\gamma} \cdot r =: R_{21} \cdot r. \tag{2.13}$$

Since the transient field behavior has neither an influence on the transverse position nor produces a scaling of the entry angle and if we assume the change in the gradient in a step like function (zero length) we finally get R_{kick}.

$$R_{kick} \;\; = \;\; \begin{pmatrix} 1 & 0 \\ \mp\dfrac{\gamma'}{2\gamma_{i(f)}} & 1 \end{pmatrix} \tag{2.14}$$

Thus, the complete beam transport matrix R for one single standing wave acceleration section is

$$R \;\; = \tag{2.15}$$

$$\begin{pmatrix} 1 & 0 \\ \dfrac{\gamma'}{2\gamma_f} & 1 \end{pmatrix} \begin{pmatrix} 1 & 0 \\ 0 & \dfrac{\gamma_i}{\gamma_f} \end{pmatrix} \begin{pmatrix} \cos\sqrt{K}\,L^* & \dfrac{1}{\sqrt{K}}\sin\sqrt{K}\,L^* \\ -\sqrt{K}\,\sin\sqrt{K}\,L^* & \cos\sqrt{K}\,L^* \end{pmatrix} \begin{pmatrix} 1 & 0 \\ -\dfrac{\gamma'}{2\gamma_i} & 1 \end{pmatrix}$$

where the off-crest phase $\Delta\phi$ effects the final energy γ_f and the length L^* according to
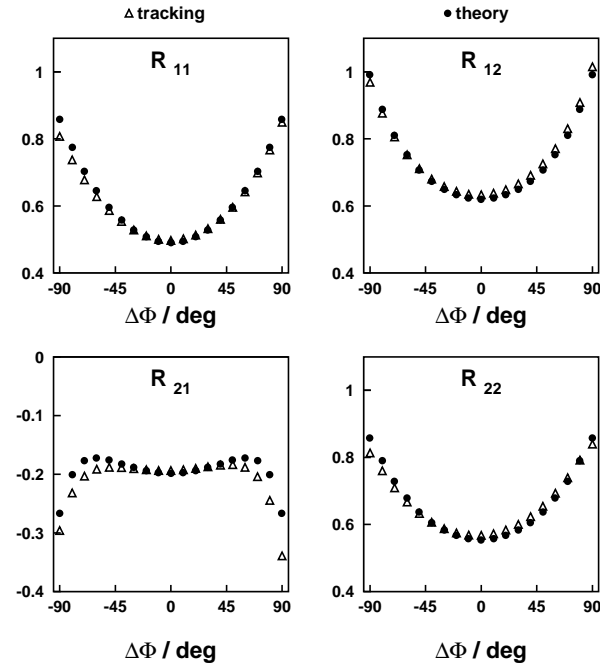
Figure 2.12: The calculation of the first order beam transport matrix elements according to the theoretical description (bullets) and using a modified field emission tracking program (triangles)

$$\Delta\gamma \;=\; \gamma'_{max}L\cos(\Delta\phi)$$

$$\gamma_f \;=\; \gamma_i + \Delta\gamma \tag{2.16}$$

$$L^* \;=\; \frac{\gamma_i}{\gamma'_{max}\cos(\Delta\phi)}\;\ln\left(1 + \frac{\gamma'_{max}\cos(\Delta\phi)}{\gamma_i}L\right)$$

The result is equivalent to the one given by Rosenzweig and Serafini[9]. In addition to this, a comparison with tracking calculations has been carried out. Using the electromagnetic fields of a 9-cell TESLA cavity, as determined from URMEL[10], all four elements of the first order beam transport matrix were calculated as a function of the off-crest phase $\Delta\phi$. For this purpose, a tracking program [11] has been modified which originally was developed for the investigation of dark currents in superconducting accelerating cavities. Single particles were placed in the 6-dimensional phase space and the comparison between these coordinates at the entrance and at the exit directly yields the transport matrix. Fig. 2.12 shows the results for an injection energy $\gamma_i = 10$ MeV / (m_0c^2), for an accelerating gradient of $\gamma'_{max} = 15$ MV/m and for the length $L = 1.038$ m of the 9-cell, 1.3 GHz, π-mode TESLA cavity.

Having the knowledge about RF focusing, one now can define the magnet system which takes care of matching the injector beam to the FIDA cell structure. The need to achieve the periodic solution for the beam enveloppes as close to the linac entrance as possible led us to the use of two lenses which were chosen to be symmetrically powered triplets. The first one, in front of the 45 degree dipole magnet of the spectrometer arm, will also be necessary for the 15 MeV energy and energy spread measurement.

The injector beam, as it is known from PARMELA[12] simulations (see above) and as in its phase space coordinates shown in Fig. 2.13, was first matched to the above mentioned FIDO lattice. The calculation was started just behind the capture cavity where the electron beam is almost round

---

[9] *op. cit.*

[10] T. Weiland, Nucl. Instr. Meth. **216**, 329 (1983)

[11] B. C. Yunn and R. Sundelin, *Field Emitted Electron Trajectories for the CEBAF Cavity*, 6th RF Superconductivity Workshop 1993, CEBAF, to be printed as workshop proc., ed. R. Sundelin.

[12] PARMELA, version 4.30 by B. Mouton, LAL/SEAR 93-455, Orsay, France.
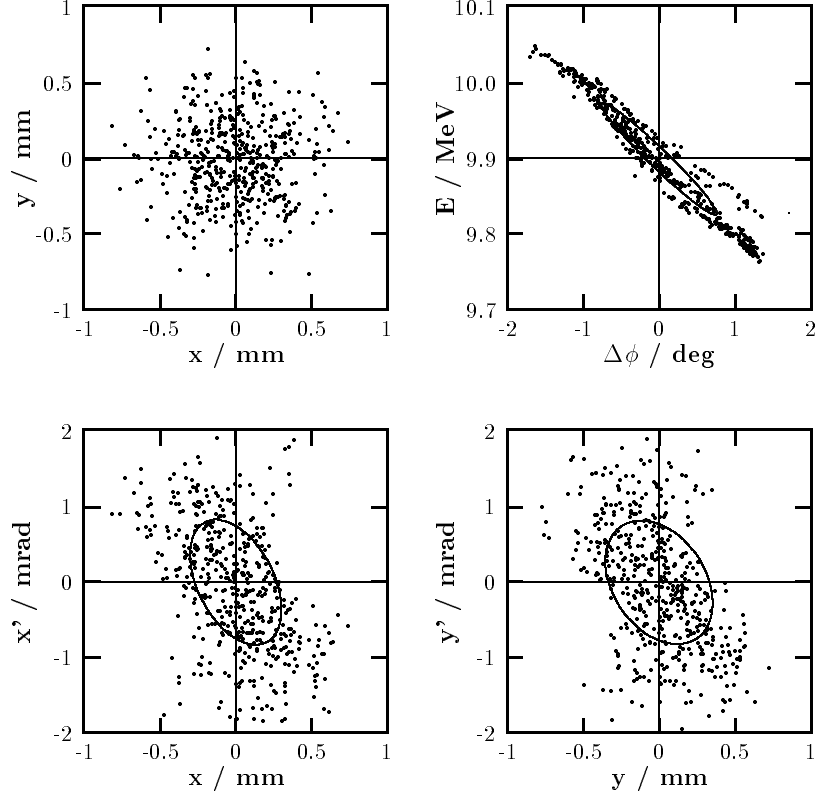
Figure 2.13:   The electron beam properties at the exit of the supercon-
                ducting capture cavity as they result from PARMELA sim-
                ulations. The four pictures show a cross section through the
                beam, and the longitudinal as well as the transverse phase
                space distribution. The ellipses shown correspond to 2σ-
                values.

and converging with respect to its transverse dimensions. The first triplet
produces a waist, for the horizontal and vertical direction slightly different
in z-position, and both triplets together scale the beam size down to some
proper value. Matching was achieved right from the beginning of the lattice.

The constraints were the beam parameters at the exit of the quadrupole
doublet in linac module #1. Fig. 2.14 shows the resulting envelopes together
with the schematic drawing of the beam line as Tab. 2.5 gives the input and
output properties and the calculated quadrupole strengths.

In a second step variations of the two lenses were used just in order to

Table 2.5:   The matching achieved between the TTF injector and the linac's FIDO lattice at an injection energy of 10 MeV.

Input Parameters $\left(\begin{array}{l}\text{determined using PARMELA, and 17.5 cm behind}\\\text{the last iris of the capture cavity}\end{array}\right)$			
x–Direction			
RMS Beam Size	$\sqrt{\sigma_{11}^x}$	0.484	mm
RMS Beam Divergence	$\sqrt{\sigma_{22}^x}$	0.884	mrad
Emittance (rms and norm.	$\varepsilon_{rms,n}^x$	4.57	mm mrad
y–Direction			
RMS Beam Size	$\sqrt{\sigma_{11}^y}$	0.476	mm
RMS Beam Divergence	$\sqrt{\sigma_{22}^y}$	0.904	mrad
Emittance (rms and norm.	$\varepsilon_{rms,n}^y$	4.65	mm mrad
Output Energy	E_{inj}	10.0	MeV
Magnet System Parameters			
Drift Capt.Cav. – 1$^{\text{st}}$ triplet	d_1	1.790	m
Quadrupole Length	l_q	0.06	m
Intermagnet Drift	d	0.08	m
Triplet Length	l_t	0.34	m
$(l_t = l_q + d + L_q + d + l_q)$			
Drift 1$^{\text{st}}$ triplet – 2$^{\text{nd}}$ triplet	d_2	2.220	m
Drift 2$^{\text{nd}}$ triplet – 1$^{\text{st}}$ cavity	d_3	4.330	m
Qudrupole Gradients	$q_{1,2,3}$	-0.784,-1.476,0.784	T/m
	$q_{4,5,6}$	0.601,-1.199,0.601	T/m
Output Parameters $\left(\begin{array}{l}\text{behind doublet in module \#1, i.e. 0.684 m}\\\text{upstream of first cavity iris in module \#2}\end{array}\right)$			
x–Direction			
RMS Beam Size	$\sqrt{\sigma_{11}^x}$	1.421	mm
RMS Beam Divergence	$\sqrt{\sigma_{22}^x}$	0.220	mrad
Phase Space Orientation	r_{12}^x	-0.664	
y–Direction			
RMS Beam Size	$\sqrt{\sigma_{11}^y}$	1.850	mm
RMS Beam Divergence	$\sqrt{\sigma_{22}^y}$	0.191	mrad
Phase Space Orientation	r_{12}^y	-0.740	
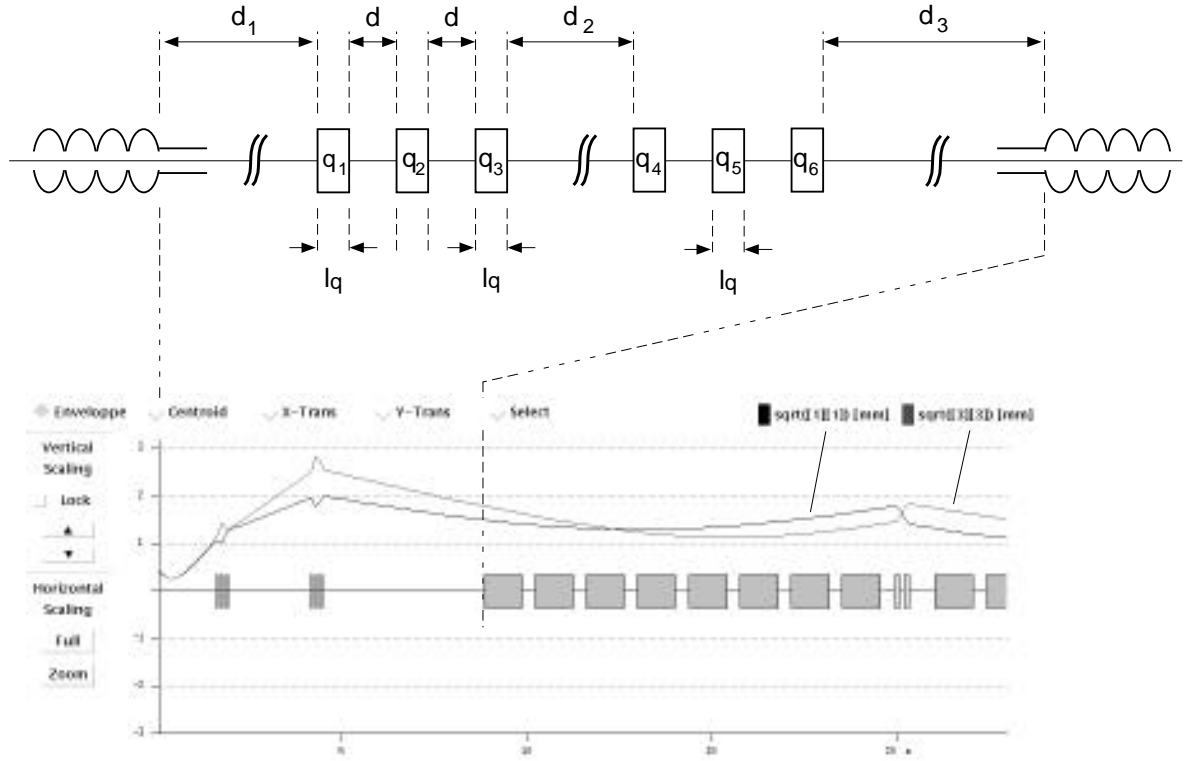
Figure 2.14:   Beam envelopes along the matching section for the FIDO lattice (no acceleration). The upper part of the figure exhibits the geometry.
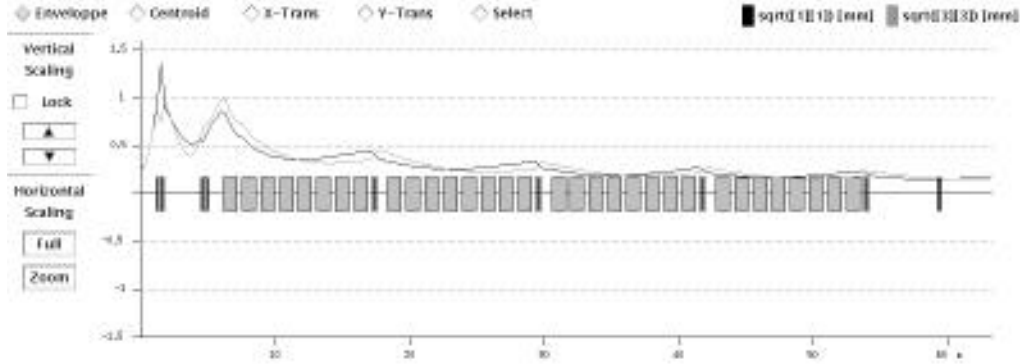
Figure 2.15: Beam envelopes along the matching section and linac at a gradient of 15 MeV/m.

achieve the matching to the FIDA lattice. Now, the fitting constraints were the beam parameters at the waists in module #2. The results of this matching procedure are given in Tab. 2.6 and shown in terms of beam envelopes in Fig. 2.15.

The results of the beam transport calculation along the TTFL, as reported above, show that the optics system consisting of a matching section between the injector and four cells of a modified FODO lattice in which the quadrupoles are grouped in pairs will fulfill the requirements. In the matching section, the beam can be held at a proper size, and along the linac, a cell to cell (that is, module to module) phase advance of 90 degrees is possible. Having realized a periodic lattice also allows the replacement of any of the modules by a warm section of equal length. Thus, the installation of a bunch compressor (as is needed for the above mentioned FEL plans) behind the first module and moving modules #2 to #4 downstream is possible. This situation is shown in Fig 2.16. The quadrupoles at the end of the first module and at the end of the warm section have the same focussing strength.

The four modules of the TTFL will be assembled one after another. As soon as the first module is installed, and initial cryogenic and RF tests have been performed, this module together with the injector will be operated with beam. This initial beam exercise will be particularly important for the optimization of the RF control system. The beam must be delivered to the beam analysis area, and so a temporary warm beam line is planned, with the FIDO optics replicated through the use of warm doublets. Therefore, the

Table 2.6: The matching achieved between the TTF injector and the linac's FIDA lattice at an accelerating gradient of 15 MeV/m

Input Parameters $\left(\begin{array}{c}\text{determined using PARMELA, and 17.5 cm behind}\\ \text{the last iris of the capture cavity}\end{array}\right)$			
x–Direction			
RMS Beam Size	$\sqrt{\sigma_{11}^x}$	0.484	mm
RMS Beam Divergence	$\sqrt{\sigma_{22}^x}$	0.884	mrad
Emittance (rms and norm.	$\varepsilon_{rms,n}^x$	4.57	mm mrad
y–Direction			
RMS Beam Size	$\sqrt{\sigma_{11}^y}$	0.476	mm
RMS Beam Divergence	$\sqrt{\sigma_{22}^y}$	0.904	mrad
Emittance (rms and norm.	$\varepsilon_{rms,n}^y$	4.65	mm mrad
Beam Energy	E_{inj}	10.0	MeV
Magnet Gradients			
Quadrupole Gradients	$q_{1,2,3}$	1.099,-2.090,1.099	T/m
	$q_{4,5,6}$	0.648,-1.297,0.648	T/m
Doublet Gradients	$q_{\#1,\#2}$	2.650,5.099	T/m
	$q_{\#3,\#4}$	7.547,10.0	T/m
Output Parameters $\left(\begin{array}{c}\text{behind doublet in module \#1, i.e. 0.684 m}\\ \text{upstream of first cavity iris in module \#2}\end{array}\right)$			
x–Direction			
RMS Beam Size	$\sqrt{\sigma_{11}^x}$	0.417	mm
RMS Beam Divergence	$\sqrt{\sigma_{22}^x}$	0.053	mrad
Phase Space Orientation	r_{12}^x	-0.588	
y–Direction			
RMS Beam Size	$\sqrt{\sigma_{11}^y}$	0.520	mm
RMS Beam Divergence	$\sqrt{\sigma_{22}^y}$	0.057	mrad
Phase Space Orientation	r_{12}^y	-0.791	

beam parameters at the end of the TTFL are well defined, and the detailed design of the high energy experimental area is possible.

2.4 Analysis Area

The Beam Analysis Area is shown in Fig. 2.17, after the last cryomodule and its terminating end cap.

The area has to fulfill three principal purposes:

- It serves as a room to measure the relevant beam parameters such as beam position, beam size and emittance, beam energy and energy spread, beam current and transmission through the linac, bunch length, shape, RF beam phase, and dark current from the cavities.

- It houses the beam dumps. Each beam line is terminated by a dump covered in all directions with heavy concrete shielding 3.2 m in thickness.

- It provides space for testing new diagnostic tools developed for TESLA.

In this section, we outline the techniques proposed for measurement of the beam parameters. The more extensive discussion of Chapter 9 will include the shielding and beam dumps, as well as further optics and component description. The Beam Analysis Area consists of three principal sections; we will refer to them below as Experimental Areas 1–3. About 12 meters beyond the linac, the beam line splits into two arms. The straight-on direction downstream stream of the split is assigned to the emittance measurement. The 20 degree bend is part of a magnetic spectrometer.

- Experimental Area 1 consists of four diagnostic stations, two quadrupole doublets, a horizontal and a vertical steerer, and the spectrometer dipole. The steering magnets are used to bring the beam back to the nominal axis if experiments with an off-axis beam in the cavities are performed. The first quadrupole doublet is used for emittance measurement; the second minimizes the beam size at the focus of the spectrometer.

- Experimental Area 2 is not used under normal operating conditions.

- Experimental Area 3 consists of a diagnostic station and two quadrupoles. The lens closely behind the spectrometer dipole can be used to make the dispersion small during set-up of the linac when the beam parameters (especially momentum) are not yet well known. This helps to keep the beam inside the vacuum tube through the downstream part of the line. For precise measurements, this lens can be turned off. The second quadrupole helps to control the spotsize at the beam dump in the spectrometer arm.

There are a variety of ways by which emittance can be measured; we will outline the one scanner method (quadrupole scan). The beam profile is measured as a function of the setting of a preceding lens. The profiler and the lens are separated by a distance L. The beam size is a parabolic function of the inverse focal length 1/f.

$$r^2 = \sigma_{11}\left(1 - \frac{L}{f}\right)^2 + 2\sigma_{12}L\left(1 - \frac{L}{f}\right) + \sigma_{22}L^2 \tag{2.17}$$

At least three measurements at different lens settings are necessary. The beam parameters σ_{11}, σ_{12}, and σ_{22} are determined by a fitting procedure. The emittance is given by

$$\varepsilon^2 = \sigma_{11}\sigma_{22} - \sigma_{12}^2. \tag{2.18}$$

Its accuracy depends on the precision of the beam size measurement, and on the number of data samples. Fig. 2.18 shows the result of a simulated quadrupole scan. Eleven profile measurements were performed. The errors of the measurements are distributed according to a Gaussian, with 10 μm standard deviation. In the case presented, the emittance can be determined with an error of 1%. However, for a more fluctuating sample the error can easily increase by an order of magnitude.

For the measurement of energy and energy spread, we make use of the spectrometer arm shown in Fig. 2.17. Particles with different energies move on different orbits in a dipole field perpendicular to the plane of motion. They are deflected by different angles. The bending radius ρ of the beam trajectory is given by

$$\frac{1}{\rho} = 0.2998\frac{B}{p} \tag{2.19}$$

where B is the magnetic field in Tesla, p is the momentum in GeV/c, and the radius of curvature ρ is in meters. To measure the nominal momentum or energy, ρ is kept fixed by varying the magnetic field according to the momentum. The orbit of particles with an energy slightly different from the nominal energy is displaced by a distance given by the dispersion function times the relative energy offset dE/E. The larger the energy offset, the larger the displacement from the nominal orbit. The dipole magnet acts as a weak focusing lens, including wedge and fringe field effects. The spatial separation dx at the focal point of two monoenergetic beams with an energy difference dE is given by

$$dx = \frac{\rho(1 - \cos\theta) + L\sin\theta}{E} dE \qquad (2.20)$$

where θ is the deflection angle at the median energy and L the distance between the endplate of the dipole and the focus. For $\theta = 20$ degrees, L=3.0 m, and ρ=3.23 m, we find a displacement dx of 1.5 mm per 1 MeV energy deviation at 800 MeV.

The RMS value of the profile of a monoenergetic beam at the focus is less than 100 μm. It will be broadened by the momentum spread of the particles. A SEM-grid measures the beam profile at the focus. Assuming an accuracy in the profile measurement of 10μm, a fractional energy spread of smaller than 10^{-4} can be resolved.

Fig. 2.19 shows the beam envelopes along the analysis area for a standard TTF beam ($\varepsilon_{x,n}$=3.9 mm mrad, $x_{max} = 0.18$ mm, $x'_{max} = 0.020$ mrad, $\varepsilon_{y,n}$=3.8 mm mrad, y_{max}=0.15 mm, y'_{max}=0.017 mrad, E = 800 MeV) with an energy spread of 10^{-3}.

Tab. 2.7 lists the corresponding parameters at the entrance and at three different locations (emittance measurement, energy spread measurement, dump) of the analysis area.

Table 2.7:   Optics parameters for the emittance and energy spread measurement.

	Before Last Cold Quad Doublet	Emittance Measurement	Energy Spread Measurement	Dump
Max beam size (x) mm	0.18	0.012	1.21	2.27
Max divergence, (x′) mrad	0.020	0.21	0.38	0.87
Max beam size (y) mm	0.15	0.23	0.26	1.21
Max divergence, (y′) mrad	0.017	0.13	0.011	0.21
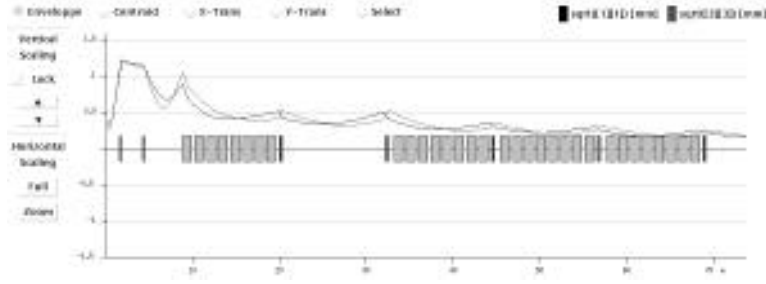
Figure 2.16: Beam envelopes along the the matching section, the 12.2 m warm section (planned for the bunch compressor) and the linac at a gradient of 15 MV/m
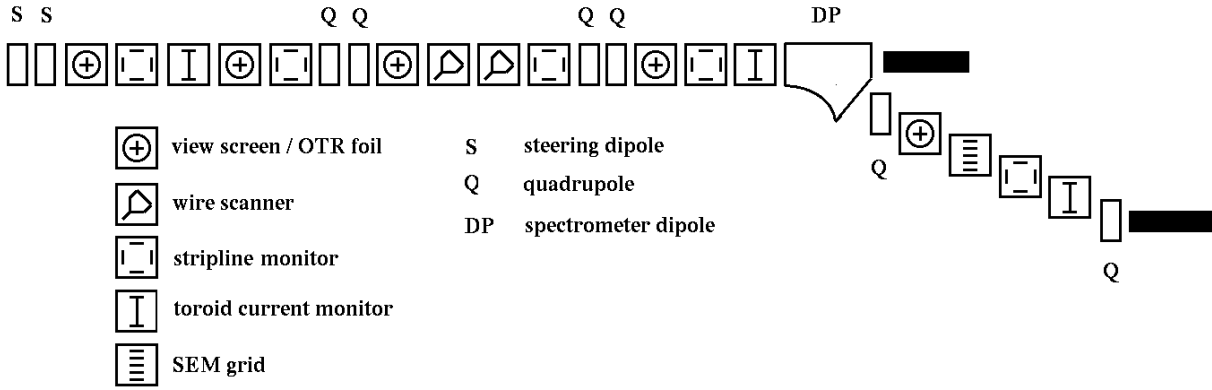
Figure 2.17: Beam Analysis Area
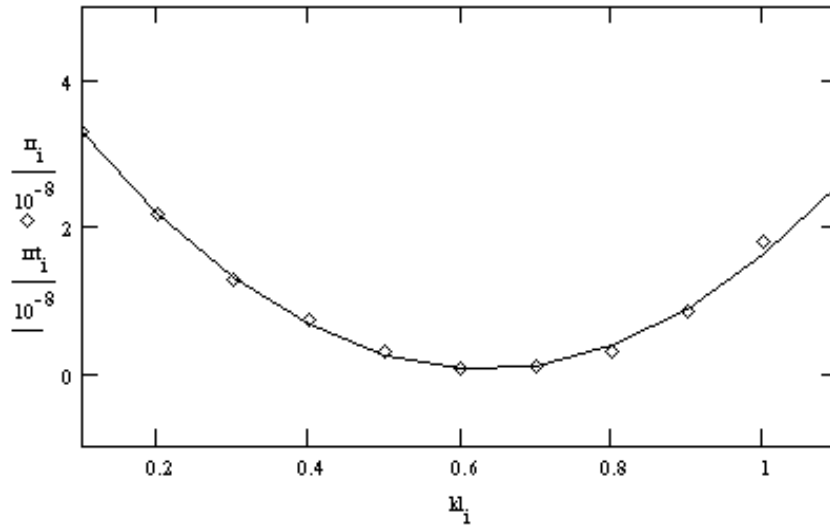
Figure 2.18:   Simulated quadrupole scan to determine the beam emittance. The square of the beam size (rms value) is plotted as a function of the quadrupole excitation (solid line: fit, diamonds: simulated data).
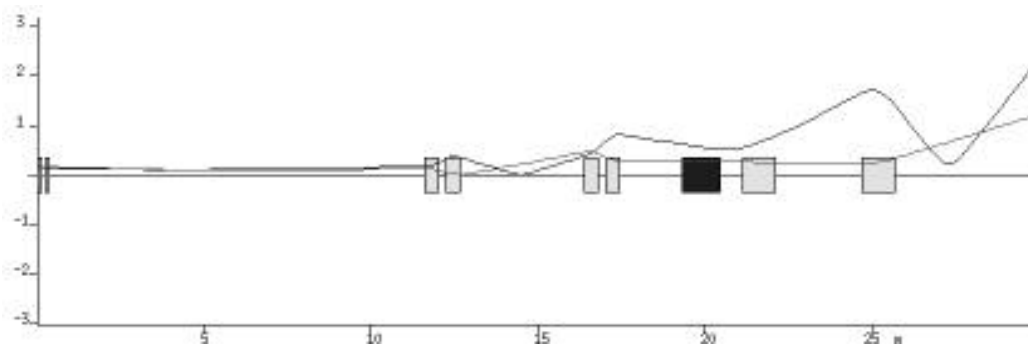
Figure 2.19:   Beam envelopes through the analysis area for TTF parame-
                ters. The calculation starts with the last quadrupole doublet.

Chapter 3

Injector

The goal of the injector is not so much to produce the exact beam charac-
teristics of a future TESLA 500 injector as to deliver a beam permitting the
study with the TTFL of the problems that TESLA designers will meet. It
should be "a well understood tool rather than a subject of experimentation."[1]
The production of a beam satisfying or closely approaching the TESLA 500
specifications is a difficult challenge because it requires 8000 bunches per
second each of charge 5×10^{10} electrons and with bunch length, σ_z, of 1 mm.
Because of this difficulty, it was decided to build the TTFL injector in two
steps:

1. Injector I will deliver 8 mA, 10 Hz macropulses at a bunch frequency
   of 216 MHz instead of the 1 MHz required for TESLA. The charge
   per bunch is thus reduced by a factor of 216. The space charge forces
   are then no longer a problem and the bunching scheme can be much
   simpler.

2. Injector II will deliver the same macropulse current at 1 MHz with the
   TESLA bunch population of 5×10^{10} electrons.

Injector I is the more straightforward to design and construct, and will
support a significant experimental program before Injector II is available. For
instance, Injector I will allow investigation of one essential issue of the TTFL;
namely, acceleration in pulsed RF mode, in the presence of cavity detuning by
Lorentz forces, with 16 cavities sharing the power of one klystron. However,

---

[1]A quotation from the NLCTA CDR.

Injector II is indispensable for a complete experimental program, such as study of wake field effects and the measurement of HOM power deposition in cryogenic components.

The energy required for injection into the TTFL is at least 10 MeV. This results from its optical configuration, which is the one chosen for TESLA and is not optimized for low energy transmission (the distance between focusing elements is 12 m). Furthermore, the RF focusing effect of the cavities, which scales like $1/E^2$, is very strong at low energy. The necessary preacceleration will be provided by a standard TESLA cavity in its own cryostat and powered separately by a 250 kW klystron. The injector will thus have the additional advantage of providing a complete test bench for an individual TESLA cavity either before the end of linac construction or, if necessary, after linac operation has begun.

For Injector I, direct injection from a 250 kV gun through a subharmonic buncher into the superconducting capture cavity of standard TESLA design permits satisfactory capture and acceleration of the electrons, if the gradient is about 10 MV/m. For Injector II, the electrons must be first accelerated to at least 3 MeV to reduce space charge forces. This will be achieved with an RF gun cavity triggered by a laser.

3.1 Injector I

3.1.1 Gun and Electrostatic Column

The required 250 keV electron beam will be produced using a gun of relatively low voltage (30 - 40 kV) followed by an electrostatic post-acceleration column to provide the additional energy. This approach is inspired by the use of such a column for the injector of the superconducting S-DALINAC at the Technische Hochschule Darmstadt (THD)[2]. The low voltage gun will be a modified version of an existing gun employed at Saclay and originally designed by R. Koontz. The gun will be a gridded triode with modulation of the cathode at a variable frequency permitting the operation of the injector at different micro-bunch time intervals. The repetition rate will be limited to sub-multiples of the sub-harmonic buncher frequency (216.7 MHz). The required charge per bunch for 8 mA average current operation at 216.7 MHz is

---

[2]K. Alrutz-Ziemssen et al, *op. cit.*

37 pC with reduced repetition rates requiring correspondingly higher bunch charges (e.g. one needs 0.1 nC at 72.2 MHz). The range of repetition frequency at which 8 mA average current can be produced will, of course, be limited by the gun performance (cathode emission, beam emittance, beam pulse duration and so on) but in principle it should be possible to produce a beam with a time structure close to that of TESLA (1 μs bunch spacing) albeit at much reduced average intensity. In order to ensure good bunching by the sub-harmonic buncher (SHB) it is necessary to have pulse-widths of short duration in comparison with the SHB RF period (4.6 ns). The modulation of the cathode will be achieved with a pulsed voltage (<100 V) signal from a wide-band amplifier (10 - 500 MHz) able to produce pulses at rates of up to 250 MHz. The duration of the pulses will be of the order of 1 ns depending upon the height of the required voltage. As we have performed our PARMELA runs for an initial pulse of base-width 641 ps, and in practice we expect to have "quasi-triangular" pulses, we will require a peak gun current of 115 mA to provide the necessary 37 pC charge.

3.1.1.1 The Electron Gun

The existing Saclay gun employs a classical Pierce-like geometry and uses an Eimac Y-845 cathode of 8 mm diameter. In its present configuration it provides approximately 100 mA for an anode-cathode (A-K) voltage difference of 40 kV. In order to increase the gun perveance to meet the needs of Injector I we plan to modify the geometry of the gun. Simulations with the SLAC code, EGUN[3] indicate that, by reducing the anode-cathode gap distance, g, from its original value of 96.5 mm (nominal) to 37.5 mm, the gun should be capable of producing currents in excess of 500 mA for an A-K voltage of 30 kV. Tests have been performed at Saclay on a spare gun in order to verify the results of the simulations. This spare gun has been modified so that an extended anode support allows the value of g to be reduced to 37.5 mm while still allowing use of the original anode-cathode insulation ceramic (Fig. 3.1). The measured currents confirm the results of the simulations. It should be noted that the EGUN calculations which we have performed have been done for the case of a simple diode gun, i.e., no grid is present in the simulation, and therefore the detrimental effect of the grid on the beam emittance is not

---

[3]W. B. Herrmansfeldt, *EGUN — An Electron Optics and Gun Design Program*, SLAC Report 331, 1988.
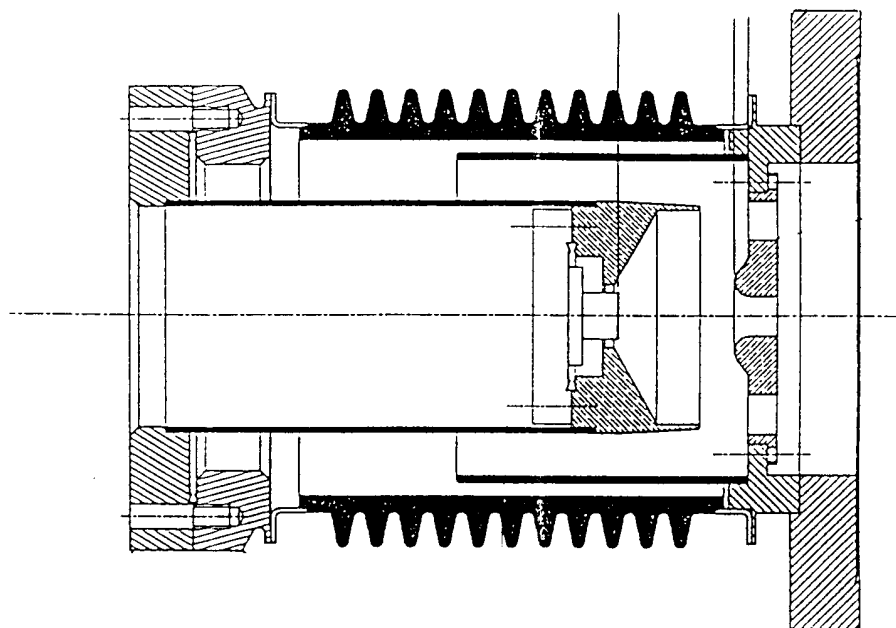
Figure 3.1:   Schematic of modified Saclay gun with reduced anode-
cathode gap.

calculated. Consequently the calculated emittances are much smaller than
the measured values and are not considered to be reliable.

With the reduced value of g there was some concern that the voltage dif-
ference between the "nose" of the focus electrode (FE) and the anode plate
might produce electrical breakdown during the 800 μs pulse. These fears
have since been allayed as tests show that the gun is capable of supporting
60 kV. However, before we were in a position to make voltage measurements
we took the precaution of machining a second focus electrode nose whose
length is only half that of the original. The simulations indicated that re-
moving half the FE nose would result in an increased diode current due to
an enhancement of the longitudinal electric field at the cathode surface. An
undesirable accompanying effect is that the focusing field is reduced result-
ing in a slightly increased beam divergence at the anode exit. We have now
been able to perform gun characteristic and emittance tests on both focus
electrode geometries and are in a position to evaluate both options for use

in TTF. The emittance of both guns has been measured, using a technique reported previously[4], for ranges of gun voltage between 25 and 35 kV and for ranges of current between 50 and 150 mA. The normalized emittance is seen to vary between 8 mm-mrad and 20 mm-mrad for both guns (whereas the intrinsic normalized emittance is 4 mm-mrad). However it is found that, for the gun with the reduced FE nose length, the increased divergence of the beam is greatly in excess of that predicted by EGUN (perhaps also due to the neglect of the grid in the calculation). In order to avoid excessive beam sizes/divergences at the exit of the column we prefer, therefore, to work with the original FE geometry.

3.1.1.2 The 300 kV Electrostatic Column

Present simulations have been concerned with the calculation of the beam trajectories with both the gun and the electrostatic column. A schematic of the column used at the THD is shown in Fig. 3.2. This column was manufactured by Dowlish Engineering (a subsidiary of EUROPA High Voltage Engineering) and is capable of operation to 300 kV. We propose to use a similar column as it provides an inexpensive solution to producing a 250 keV beam. The column consists of a series of field grading rings (35) separated by glass insulating discs. The voltages on the rings are determined by a chain of resistive dividers (34×30 MΩ) and the whole assembly is approximately one meter long. We are presently performing simulations to determine suitable potentials for the first few (5) field-grading rings and the diameters of their apertures. The selection of a reasonable mesh size for the EGUN calculation along with the limiting number of mesh point permitted by the code restricts the extent to which we can model the gun-column arrangement.

The performance of the TTF gun differs in some respects from that of the S-DALINAC. Principally, the required current for the TTF gun exceeds that of the S-DALINAC, which was limited to 50 mA maximum. The increased space-charge force has important consequences for the radial confinement of the beam along the column. The column itself provides little focusing and, because of the high voltage environment, it is impossible to use solenoidal magnetic focusing along the column as is traditionally used at the exit of lower voltage guns. Fig. 3.3 illustrates the beam trajectories for a 115 mA

---

[4]B. Aune et al, *A Device for Electron Gun Emittance Measurement*, IEEE Trans. Nucl. Sci. , Vol NS-32, No. 5, pp 1896–98 (1985)
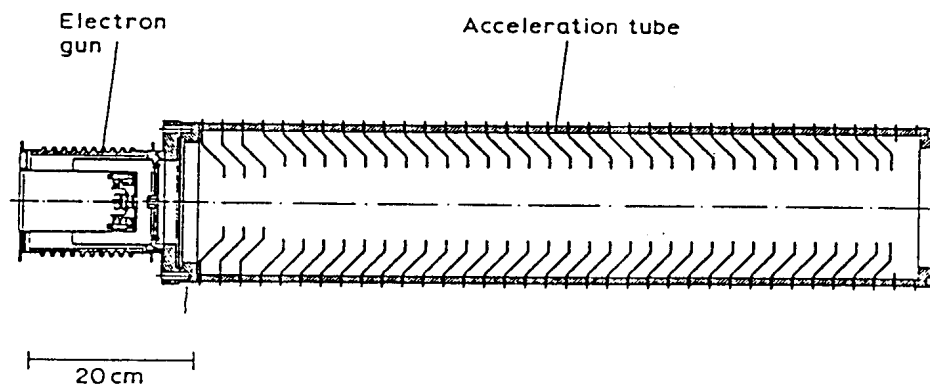
Figure 3.2: Schematic of electrostatic column used at THD

beam extracted through the anode aperture and transported across the first
five electrode gaps.

Although the modified Saclay gun is now able to provide sufficient current
levels to allow operation of the injector at 72.2 MHz and 8 mA, the EGUN
simulations to date indicate that such beams can not be transported through
the column without unacceptable growth in beam size and divergence. For
the initial mode of operation of the injector then we consider working only at
216.7 MHz. At a later stage, in order to transport higher currents along the
column and so permit operation at reduced repetition rate, we could employ
additional external focusing in the form of a small "Einzel" lens at the exit
of the anode aperture to provide an adjustable focusing force.

3.1.1.3   The Electron Gun Environment

The electron gun is installed inside of a Faraday cage which is connected to
the high voltage system. The electrostatic column is outside of this cage.
The electronic equipment necessary for the electron gun is inside of another
cage connected to the cathode. This second cage is inside the HV terminal
and is insulated from the terminal up to 40 kV. Inside of the second cage
we place the wide-band amplifier and the electronics needed to operate the
gun, i.e., the bias of the grid, the heating system for the cathode filament,
the pulse former for the macro-pulse on the grid, the pulse former for the
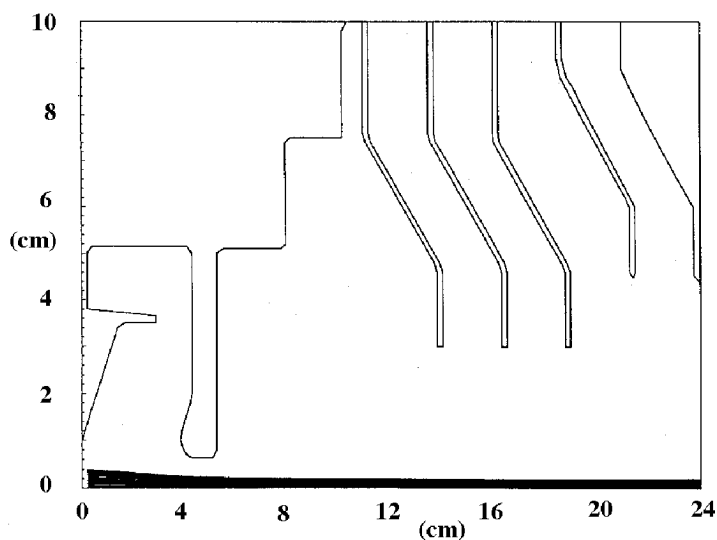
Figure 3.3:   EGUN simulation showing 115 mA beam traversing gun and first five rings of the electrostatic column. The potentials (kV) are 0, 30, 30, 38,46, 54, 63.

micro-pulse on the cathode and the fiber optics for control. The dimensions of the inner box are 0.75 m×0.7 m×0.6 m. The corners are rounded with a radius of 5 cm. The contents of the high voltage terminal, (outer box) are:

1. The gun.

2. A H.V. capacitor of 0.3 μF - 40 kV.

3. A H.V. power supply of 40 kV -1 mA.

4. A damping resistor between the capacitor and the gun in case of a short circuit.

5. A system of relay and resistor for discharging the capacitor.

6. An isolation transformer which can hold up to 40 kV and is rated at 220 V/220 V - 500 VA to feed the electronics inside the inner box.

7. Power supplies for the steering coils.

We reserve space inside the terminal to place a lens between the gun and the electrostatic column (if needed). There is a mechanical system for adjusting the position of the gun in the horizontal and vertical planes. Six insulators support the HV terminal. The dimensions of the terminal are 1 m$\times$1 m$\times$2 m.

3.1.1.4   The High Voltage System

The high voltage system for the gun and the electrostatic column is comprised of the following components. There is a power supply of 300 kV-1mA. rating to feed the electrostatic column. A 33 nF capacitor bank is needed to keep the voltage drop during the pulse within 10^{-3} of the nominal value of the voltage across the column. The gun itself is fed by another power supply of 40 kV-1mA rating. Fig.3.4 shows a schematic of the electrical circuitry. For the same reasons as above, we need a capacitance of 0.3 μF connected to the output of the 40 kV power supply. To protect the gun, the electrostatic column and the HV system, a high voltage damping resistor of 10 kΩ is placed between the 33 nF capacitor and the HV terminal. Another high voltage damping resistor protects the 300 kV power supply. It is connected between the capacitor and the power supply. There is also a resistor between the 40 kV capacitor and the cathode of the gun. To feed the elements inside of the HV terminal with mains power an isolation transformer is needed. The insulation between the primary and the secondary of the transformer is able to hold 300 kV. The rating of the transformer is 1 kVA. A minimum distance of one meter between all high voltage components and the surrounding walls must be respected and the same distance is needed between individual high voltage elements. Fig. 3.5 shows the layout of the elements. A system able to discharge the capacitors and the power supplies assures the safety of the equipment.

3.1.1.5   Gun Operation

The gun can be driven by the cathode and the grid. In case of normal operation, a macro-pulse of 800 μs and a few mA is applied to the grid. The level of this macro-pulse depends upon the bias voltage applied to the grid and the shape and the level of the current pulses emitted by the cathode. The

Gun Circuitry
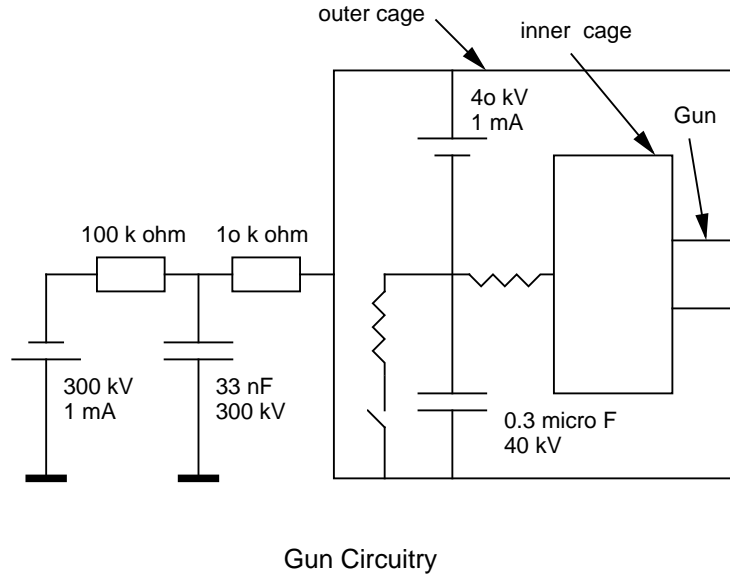
Figure 3.4:   Schematic of the high voltage system for gun and electro-static column.

current pulses are obtained by applying a micro-pulse of 1 to 2 nsec duration, 100V amplitude negative polarity, to the cathode. Those micro-pulses are driven from a wide band amplifier. Fig. 3.6 shows the structure of the macro and micro-pulses. The maximum repetition rate of the micro-pulses is 216.7 MHz, the repetition rate of the macro-pulses is 10 Hz. The repetition rate is controlled from ground level as with all electronic systems inside the HV terminal.

The micro-pulse applied to the cathode is the output of an amplifier stage. The amplifier delivers a negative pulse of 1 nsec full-width at half-height and 100 V into 50 ohm, i.e., 200 W peak power. The input pulse is obtained from a pulse former. It is synchronous with the 216.7 MHz signal and the global timing system of the machine. The output of the pulse former can be set to different repetition rates from 216.7 MHz down to 1 MHz. The 216.7 MHz and the control signals to set the repetition rate of the micro-pulses are sent from the ground level by means of optic fibers; the former is at the HV level.

The macro-pulse is furnished by another pulse former whose level can be controlled from the ground by an optic fiber. The width of this pulse is
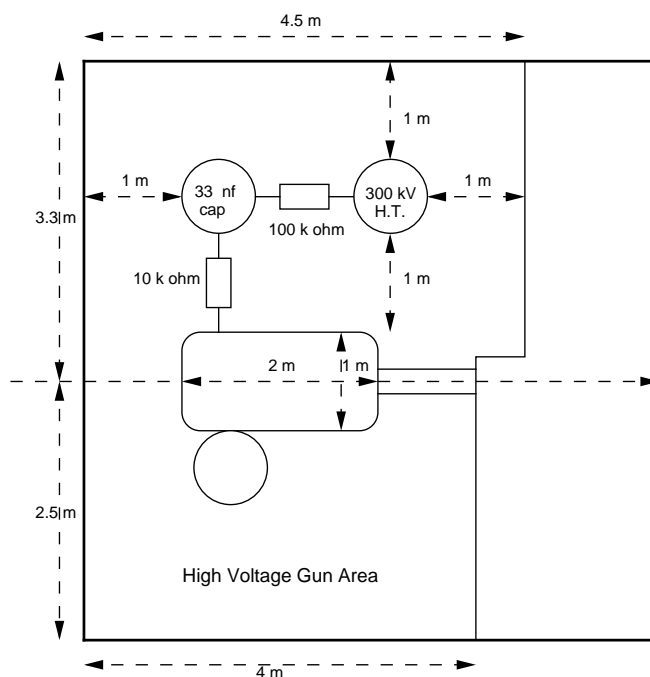
Figure 3.5:   Element layout for gun and column high voltage system.

also controlled from ground. An electronic system coupled to the current monitors can cut-off the pulse during operation in case of beam loss in the vacuum chamber of the linac. Beside the systems discussed above there is the heater system for the cathode filament. The output of this system is 6 to 7 V and 1 to 2 A. There is also electronic equipment for the grid bias. Its output can vary from 0 to 200 V and gives a few mA. All these systems are monitored from the ground by an optic fiber link. A special optical system is used to carry out the 216.7 MHz from ground to the HV deck. This allows the signal to be transmitted at high speed. The other links are achieved with a standard optic fiber. Fig. 3.7 shows the different sub-systems of the gun.

3.1.2   The Sub-Harmonic Buncher

The sub-harmonic bunching system consists of a high Q accelerating cavity, a pulse modulated radio-frequency amplifier, and an amplifier-to-cavity coaxial connection. Its purpose is to perform the phase compression of the current

Injector I Bunch Structure
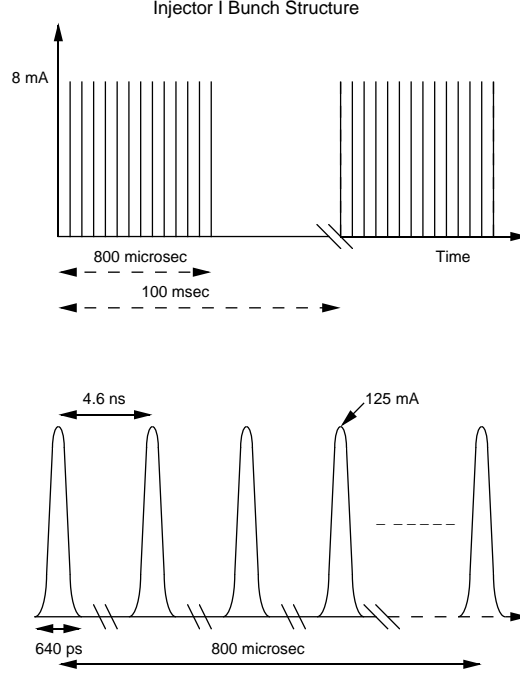
Figure 3.6: Injector pulse structure.

pulse generated by the gun (from 0.64 ns to 0.1 ns) before it is injected into the 1.3 GHz capture structure. The cavity is composed of an input coupling loop (for the amplifier), an additional loop (which can be connected to a matched load if necessary), two measuring loops (with couplings of 32 dB and 40 dB respectively), and two plungers for frequency tuning (one with a phase feedback loop and the other electrically controlled).

3.1.2.1 RF Characteristics

The cavity is a re-entrant coaxial resonator in TM_{010} mode, corresponding to the 6th sub-harmonic of the accelerator frequency. The maximum accelerating voltage required to pre-bunch the 250 keV electrons would be 100 kV which, as the cavity has a transit-time corrected shunt impedance, R_s, equal to 3.11 MΩ, would lead to a peak dissipated power of 1.6 kW and an average power of 32 W (we assume a pulse width of 2 ms and a repetition frequency of 10 Hz). The RF parameters have been calculated for a cavity made from
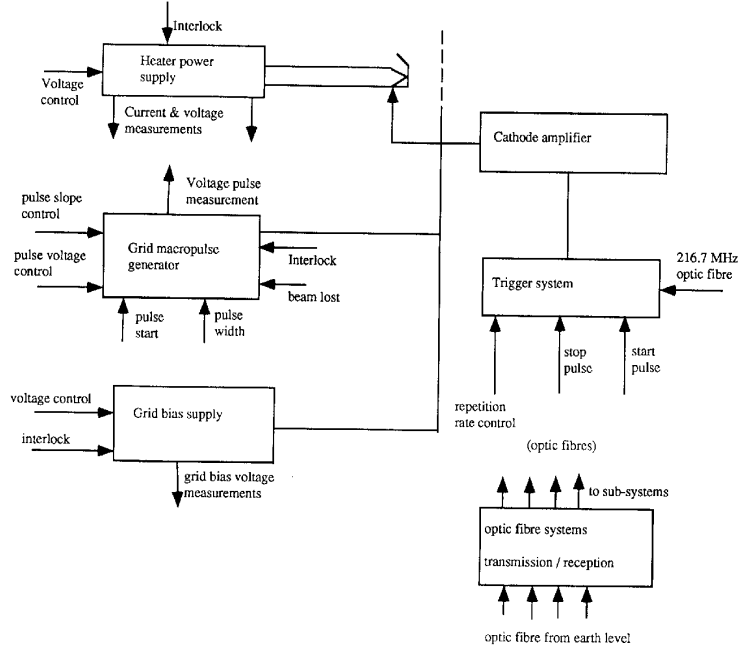
Figure 3.7: Block diagram of the gun systems

copper (using the SUPERFISH and URMEL codes) or from stainless steel (using URMEL). The calculated frequency has to be corrected to take into account errors induced by machining tolerances ($\Delta f = \pm 561$ kHz for $\Delta \ell = 0.05$ mm), the effects of temperature changes ($\Delta f = -3.47$ kHz/°C), variation of the dielectric constant between air pressure and vacuum ($\Delta f = +72$ kHz), and detuning due to beam-loading ($\Delta f < 2.9$ kHz, for average beam current of 8 mA).

3.1.2.2 Mechanical Characteristics

The cavity is composed of two half-cavities which in turn are constructed from separate machined parts. These separate parts are fabricated from plates and rolled sheets of 304L stainless steel which are then electron beam welded together. The connection between the two flanges (DN50) of the half

cavities is made with clawbolts and the required vacuum seal is made with a HELICOFLEX gasket. After RF acceptance measurements (frequency tuning) the inner surface of the cavity will be plated with a thin (20 μm) film of copper by electrolytic deposition. The side-walls of the cavity will be equipped with pipes and flanges of various diameters for the coupling loops (ϕ37 mm, length 45 mm), the tuning plungers (ϕ37 mm, length 63 mm) and the measurement loops (ϕ18 mm, length 32 mm). The temperature of the cavity will be stabilized by cooling water flowing in the pipes embedded inside of the re-entrant nose cones and in the side walls and body of the cavity. The dimensions of the cavity as calculated by SUPERFISH are inner diameter 480 mm, inner length 332 mm, and gap length 16 mm.

The two coupling loops are adjusted by rotation for which they have a special flange. They are built with a special 50Ω co-axial connector designed by SPINNER and the area of each loop is 2.4 cm^2. Their inductance is 97 nH. The servo controlled plunger is connected to the cavity with an accurate translator using a special ball-bearing screw designed at LAL and with a useful range of 100 mm. It could be cooled if necessary. The adjustable plunger is directly connected to the BALZERS flange of ϕ37 mm. Its adjustment is made by machining (or, optionally, by using the same type of translator as is used for the servo controlled plunger if necessary). The two measurement loops use a modified co-axial connector (PM BNC MECA2000). The cavity is shown schematically in Fig. 3.8 and its parameters summarized in Tab. 3.1.

3.1.2.3 The Amplifier

The amplifier feeds the cavity with an RF pulse (frequency 216 MHz) of nominal power equal to 2 kW and a repetition rate adjustable up to 10 Hz maximum. The useful width of the pulse is 1 ms (it is possible to adjust it up to 5 ms). The solid-state pre-amplifier stage has a gain of approximately 43 dB and provides 20 W of output power. It includes a pulse modulator to modulate the CW input signal and an analog attenuator that allows a dynamic range of at least 20 dB. The power is obtained with two 1 kW pulsed amplifiers of identical gain and phase characteristics so that they can be combined with a power output coupler to give the nominal 2 kW. An isolator, two 2-port couplers and a directional coupler are used to make the amplifier measurements and control. The power components use bipolar and MOS technology. A summary of the amplifier parameters is given in Tab. 3.2.

Table 3.1: Parameter summary for sub-harmonic cavity.

Nominal operating parameters	
Cavity type	reentrant coaxial
Frequency	216.7 MHz
Temperature	30°C
Input Power	<2 kW
RF pulse length	<2 ms
Vacuum	$< 1 \times 10^{-7}$torr
Mechanical parameters	
Length (flange-flange)	501.7 mm
Outer diameter	550 mm (flange DN500)
Material	304L stainless
Assembly	gasket and clawbolts
Cooling	6 water circuits
Electrical parameters	
Tuning frequency	216.63 MHz (air, 20°C, 60% relative humidity
Unloaded Q	24300 w/Cu plating
Shunt impedance	3.32 MΩ
VSWR at f_0	< 1.1
Time constant	18 μs
Transit time factor	0.95

216.7 MHz sub-harmonic bunching cavity.
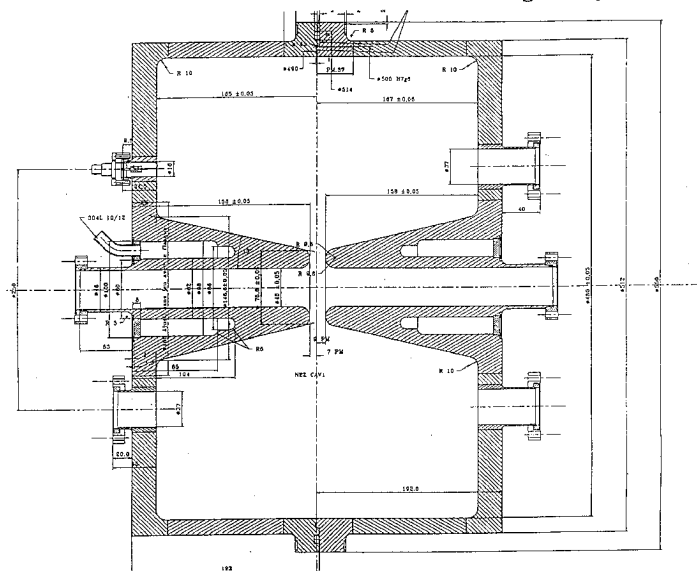
Figure 3.8: The subharmonic buncher cavity.

The control and analog information are directly usable in local mode in the four 19 inch racks that comprise the complete amplifier (22U); one for the modulator and driver, 1 for each 1 kW amplifier stage and 1 for output, protection and readouts. These controls and signals are also available on a separate unit for remote control of the injector.

3.1.3 Synchronization and Low-level RF distribution.

The components of the low-level RF distribution system are shown in Fig. 3.9. A high stability quartz oscillator ($\Delta f/f = \pm 3 \times 10^{-11}$/ day) at 9.027775 MHz generates, after multiplication, reference signals at 27 MHz, 54 MHz and 108 MHz. The phase-noise level at 108 MHz (10 Hz band-width) is better than 100 dB/Hz. The 216.7 MHz generator is a ceramic resonator (Ferranti CP0/L10) phase-locked to the 108 MHz output of the quartz oscillator. The 1.3 GHz generator (Ferranti VP0/L24C) is a cavity oscillator also phase-locked to the 108 MHz reference signal.

Table 3.2:   Summary of the amplifier parameters for the sub-harmonic buncher.

Input power	1 mW (0 dBm)
Frequency range	217 MHz $\pm$ 10 MHz
Gain flatness	± 0.2 dB
Output power	2 kW (1 to 5 ms, 10 Hz)
Amplitude stability	$\Delta V/V < \pm 0.5\%$
	(1 ms & pulse to pulse)
Phase stability	$\Delta f < \pm 0.5°$
	(1 ms & pulse to pulse)
Harmonic output	< 40 dB
Gain control (derated)	20 dB minimum
Gain control (rated)	3 dB minimum
Gain control (remote mode)	0 to 10 V/10 kΩ
Maximum input power	+13dBm
Operation class	A and AB
Input/output impedance	50Ω
Input connector	N female
Output connector	7/16 female
Cooling	forced air

Directional couplers extract a part of the incident RF power at the output of the cw 216.7 MHz generator, at the input of the sub-harmonic cavity (incident and reflected), at the interior of the 216.7 MHz cavity (loop coupling to the standing- wave field), and at the input to the capture cavity (incident). The 216.7 MHz cavity is water cooled. Transducers (platinum probes or thermistors) are used to control the inlet/outlet water temperatures of the cooling system (a feedback loop will be connected if necessary). The regulation is assured by an electro-pneumatic valve tied to an operational amplifier, the harmonic response of the system being close to 0.02 Hz and the accuracy = $\pm 0.1°$C. A motorized plunger (dynamic range = 245 kHz) is used to correct the cavity frequency shifts (effect of temperature, RF power, beam). A comparison is made between the phase of the incident signal to the

Inj I LLRF Dist & Amp and Phase Control
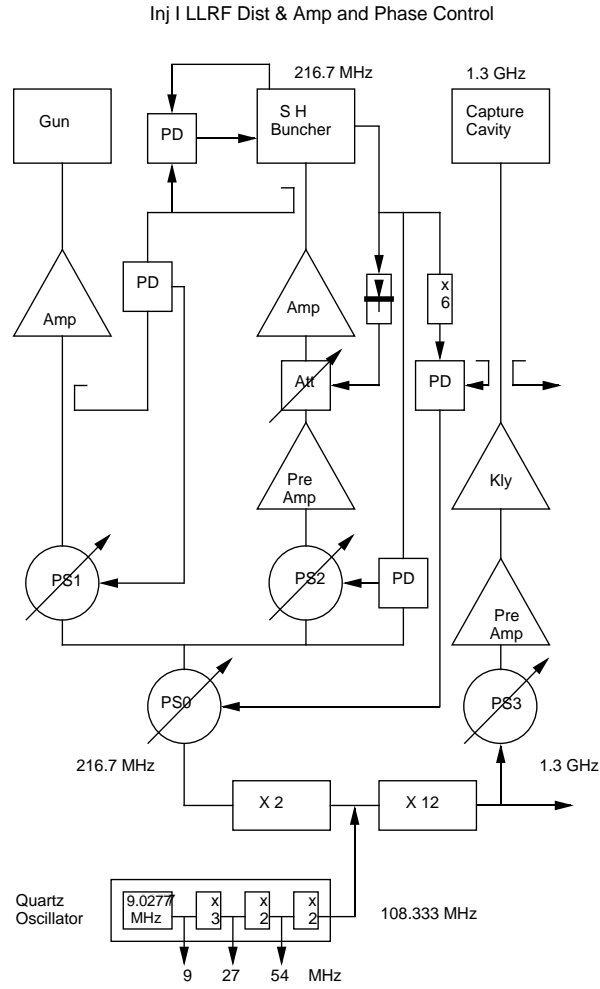
Figure 3.9: Injector low-level RF system.

cavity and the standing-wave field of the cavity and the signal obtained from this comparison is used to power the amplifier that feeds the DC motor of the plunger. The passband of this feedback loop is limited by the translator time constant to <1 Hz. After amplitude detection, the 216.7 MHz from the cavity is compared to a constant reference and the error signal from this comparison controls an analog attenuator of >20 dB dynamic range placed downstream of the cw driver of the RFTS pulsed power amplifier. The passband of this loop is limited by the cavity time constant to <10 kHz. The RF

Table 3.3:   Beam parameters downstream of capture cavity at 5141 mm
from end of gun column. (Last iris of capture cavity at 4985
mm from column)

Accel field	MV/m	8	10	12.5
Energy	MeV	7.9	10	12.3
$\sigma_{x,y}$	mm	0.9	0.5	0.32
$\sigma_{x',y'}$	mrad	0.4	0.9	0.9
ϵ (rms)	10^{-6}m	0.3	0.22	0.19
ϵ_n (rms)	10^{-6}	4.8	4.6	4.7
α		0.663	1.73	-1.2
β	m	2.7	1.11	0.56

phase of this cavity is compared to the master oscillator phase and fed back
to the cavity with the help of a fast analog phase-shifter (PS2) having a 10
MHz cut-off frequency which is placed upstream of the power amplifier. The
passband of the amplitude servo system is limited to <10kHz.

In a similar fashion, the 216.7 MHz cw signal phase feeding the pulsed
amplifier connected to the gun is compared to the 216.7 MHz pulsed signal
of the buncher cavity input coupler; the fast phase- shifter (PS1) for the gun
RF distribution is controlled by this signal. Ahead of the 216.7 MHz RF
distribution is another phase-shifter (PS0) of the same type. It adjusts the
phase of the SHB and the gun relative to the capture cavity. It is controlled
by a phase comparison between the capture cavity drive signal at 1.3 GHz and
a 216.7 MHz buncher cavity loop signal (after frequency multiplication by 6).
The control of the servo systems described above is assured by potentiometers
in the equipment racks in "local" mode or by the TTF control system in
"remote" mode.

3.1.4   Diagnostics and Analysis

3.1.4.1   Beam Parameters after Capture Cavity

The beam parameters at the output of the capture cavity as found by PARMELA
calculations are summarized in Tab. 3.3. Transverse phase space plots cor-
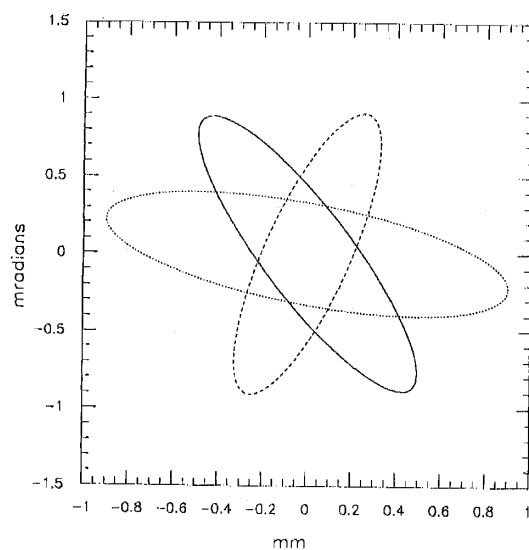
Figure 3.10: Transverse phase space plots at output of capture cavity for 10 MeV beam (solid line), 12.3 MeV (dashes) 7.9 MeV (dots)..

responding to the situation in Tab. 3.3 are shown in Fig. 3.10. The 2σ beam envelope is depicted in Fig. 3.11 in relation to the physical layout of the gun, buncher, capture cavity and various focusing elements. The envelope as a function of position from the end of the capture cavity through the analyzing beamline is shown in Fig. 3.12.
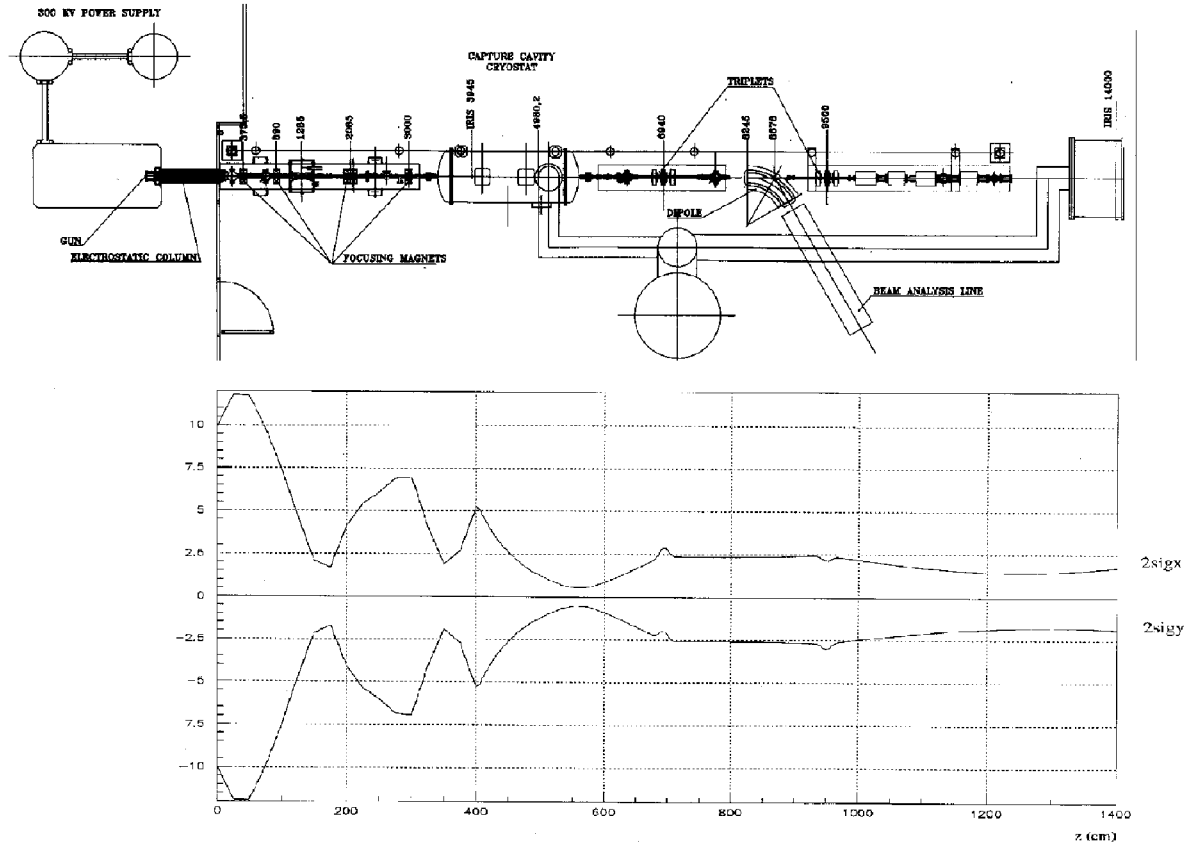
Figure 3.11:   Injector I layout and beam envelope (2σ) throughout Injector I as given by PARMELA calculations.
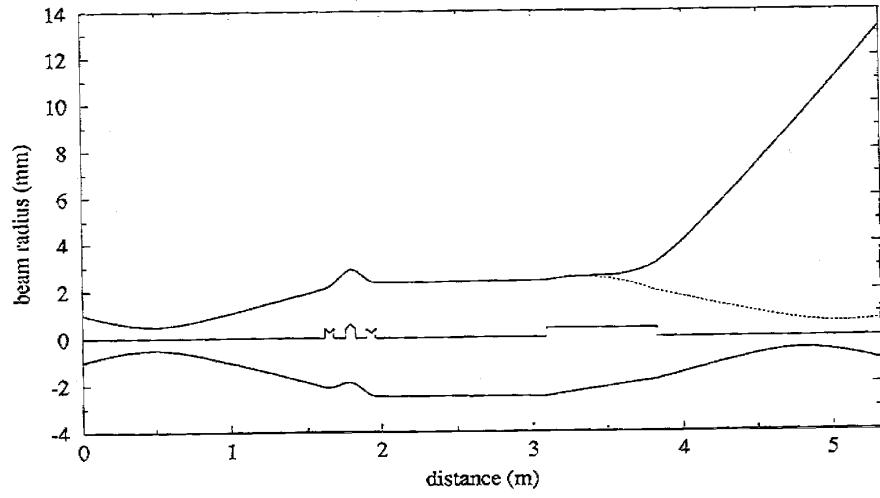
Figure 3.12:   Beam envelope (2σ) in the analyzing beamline as a function
of distance from output of the capture cavity. Dotted line: no
energy spread; solid line: σ_E 70 keV. Dipole focal distances
differ by 25 cm in the horizontal and in the vertical planes.

The diagnostics of the injection region can be divided into 8 regions:

1. Between end of gun and lens #1/buncher:
   capacitive pick up, view screen, steering

2. Between lens #1 and lens #2:
   insulated collimator, steering

3. Between lens #2 and lens #3/capture cavity:
   toroid, BPM, SEM grid, Faraday cup, collimator+X-ray detector, steering

4. Between capture cavity and 1st triplet:
   collimator+X-ray detector, BPM, toroid, view-screen, steering, steering in first triplet

5. Between 1st triplet and analysis magnet:
   BPM, phase monitor, OTR screen

6. Between analysis magnet and 2nd triplet:
   BPM (Berlin cavity), view/OTR screen, Faraday cup, steering in second triplet

7. Between 2nd triplet and first cryomodule:
   collimator+X-ray detector BPM , toroid - both of same type as at end of linac, dogleg steering. All elements removable to get at cryostat of 1st cryomodule. They are to be supplied at DESY except for the collimator and X-ray detector. Their exact layout will depend on space before the feed can. The dog-leg steering is required, especially for Injector II. The necessary space for the dog-leg (about 300 mm) must be incorporated in the layout.

8. In beam energy analysis line:
   toroid, OTR screen , SEM grid Faraday cup/beam dump.

Along the 250 kV beamline, earth's field cancelation will be accomplished by two pair of long rectangular Helmholtz coils. In the capture cavity cryostat, there is space for a possible superconducting solenoid lens upstream of the cavity and space for a BPM downstream.

3.1.4.2 Rationale for the Measurements

The rationale for the measurements is as follows. The beam from Injector I will be used mainly to check the correct acceleration under full current by the string of cavities of the linac. The most important prediction to check is the bunch to bunch energy fluctuation which should be less than $\pm 2 \times 10^{-3}$ for the TTFL, considerably less stringent than the $\pm 5 \times 10^{-4}$ specified for TESLA 500. The longitudinal phase space of the injector beam should permit a correct evaluation of this parameter. Parmela simulations give the following values: rms bunch length 0.7 deg, rms energy dispersion 70 keV for an energy of 10 MeV out of the capture cavity. The resulting energy spread, after acceleration to 500 MeV, is about 2×10^{-4}. It is thus of crucial importance to measure accurately the energy and energy dispersion of the injected beam at different times during the macropulse. A resolution of the order of 2 to 3×10^{-3} in the injector analysis station is sufficient. In addition the bunch phase variations will be monitored using a phase detector after the capture cavity. It is also useful to be able to measure the transverse emittance before and after the capture cavity. In addition the knowledge of the ellipse parameters before injection in the linac will help to set the matching optics. With an expected normalized rms emittance of 4 mm-mrad, the minimum rms beam sizes at the measurement locations will be about 1 mm in the 250 keV beam line and 0.2 mm at 10 MeV.

Thus, the principal parameters of interest can be listed as follows:

- transverse beam profile
- transverse emittance
- bunch length
- energy, and energy spread
- intensity
- beam position
- beam transmission losses

The relatively low beam energy (250 keV to 10 MeV) places stringent constraints on destructive monitors due to transparency and heating problems. The low range and severe multiple scattering of the 250 keV electrons make the design of these monitors particularly delicate. Heating of foils and of the movable Faraday cups (which have to be water cooled) is a particular issue at full beam current.

3.1.4.3   Summary of optical and diagnostic elements

We list in Tab. 3.4 a recapitulation of the diagnostic devices associated with the injector that will be discussed below. The locations and strengths, or nominal values, of the optical elements are given in Tab. 3.5 (location is the distance in mm from the end of 250 kV column).

3.1.4.4   Optical elements

Focusing coils, Solenoids: Four shielded solenoids are used between the gun exit and the entrance of the capture cavity. A phase advance of about 90 deg is planned in this channel. One lens (#2) will be made of two opposite solenoids to be non-rotating and will be used for measurement of beam emittance upstream of the capture cavity by monitoring the beam profile on the SEM-grid. Due to lack of space, the 3 others will be simple lenses, hence rotating. The main characteristics of the simple lenses are:

- Strength (integral of $B^2 \times dz$): 8×10^{-5} T^2 m
- Max field: 350 Gauss
- NI: 2500 Ampere-turns
- Length: 94 mm
- Gap: 74 mm
- Internal diameter: 70 mm
- External diameter:180 mm
- Current = 2 A, Voltage = 10 V

Triplets: Two triplets are used to transport the beam from the capture cavity to the first cryo module. They are composed of three identical quadrupoles.

- Length of each quadrupole: 60 mm
- Spacing between quadrupoles: 80 mm
- Bore radius: 20 mm
- Gradient: 3 T/m
- Current = 5 A , Voltage = 2 V
- D/A resolution: 16 bit

Table 3.4: Summary of Injector I diagnostic devices.

Capacitive pickup	1
View screen	2
View/OTR screen	1
OTR screen	2
Insulated collimator	1
Collimator+X-ray detector	3
Toroid	3
BPM	3
Phase monitor	2
SEM grid	2
Faraday cup	2
Faraday cup/beam dump	1
Steering - 250 kV	4
Steering - 10 MeV	3
Dog-leg	1
BPM-Berlin cavity	1
BPM/toroid package	1
(as at end of linac)	
Beam loss monitors	TBD
SC lens	1
Cold Berlin cavity	1

Table 3.5:   Disposition and strengths of elements in the Injector I analysis area.

Optical element	Location	Strength
lens #0 + steering	375	200 G
lens #1 + steering	890	200 G
lens #2 + steering	2085	200 G
lens #3 + steering	2950	200 G
steering	5200	
triplet #1 + steering	6700	
analysis magnet	8050	
triplet #2 + steering	9100	

Steering: There are four sets of H and V steering coils between the gun and the capture cavity. Conductors are drawn on printed circuit board formed into two half cylinders mounted inside the solenoids. The integrated strength of each coil is 9×10^{-3}T·m at a current of 4A and a voltage of 3V. Three sets of H and V steering coils are used between the capture cavity and the first cryo module. One is at the exit of the capture cavity, and two others are located inside the triplets. A dog leg system is planned to inject the beam 1 cm off-axis into the linac. This system will be used with the high charge beam. It will consist of two dipole magnets which will be installed between the second triplet and the first cryo module. The overall length of this system will be about 30 cm.

Analysis magnet: The magnet is of H-type geometry.

- Gap: 40 mm
- Field: 750 Gauss
- Angle: 60 deg
- Radius: 700 mm
- Pole face rotation: 18 deg (entrance and exit)

- Current = 20 A , Voltage = 15 V

The dispersion at the analyzing position is 1.6 cm/%. The magnet will be controlled by a 16 bit D/A with a regulation of 10^{-4}. It will be supplied with a trim coil and bipolar power supply that can correct fields to 10 G and a Hall probe if necessary.

3.1.4.5 Transverse Profile Measurements:

Three different types of beam profile measurements systems will be used: (a) view screens, (b) secondary electron emission monitor (SEM) grids and (c) optical transition radiation (OTR) measurements. These devices are destructive to the beam that intercepts them.

View screens: The view screens will consist of 25 mm square plates of alumina, one millimeter in thickness, which can be placed in the beam path at 45 degrees to the beam axis. The screens have a coating of indium oxide doped with chromium to enhance the signal, and prevent them from becoming electrically charged by the beam. The charging could lead to electrical breakdown to the vacuum chamber. The luminous signal obtained from these screens when the beam passes through them will thus allow fast qualitative information on the profile and position of the beam to be obtained. Three such screens will be employed. The first will be placed just downstream of the exit of the electrostatic column (see schematic of injector), the second will be placed just after the exit of the capture cavity and the third will be placed before the entrance of the linac. Screens will have in-out control, and will be viewed by a TV system both in real time and with a frame grabber for further recording and analysis. Screens will be readable one at a time only. Frame grabber information can be analyzed for position, spot size, and intensity information if the high level application program is provided.

Secondary Emission Monitors (SEM Grids): Two such monitors will be employed. The first will be placed after the second focusing coil (L_2) on the 250 keV beam line and before the capture cavity. The second will be used at the end of the beam energy analysis line for 10 MeV beam. Both monitors will display horizontal profiles only.

250 keV emittance grid: Due to the small range of 250 keV electrons in metals of high atomic number the low energy grid will consist of 32 strips

of titanium having a thickness of 15 μm and a width of 300 μm. The distance
between the centers of adjacent strips will be 0.7 mm. Secondary electron
emission from each of these strips will provide a signal proportional to the
current incident on that strip. Thus a "histogram" plot of the beam profile
will be available. By taking repeated measurements of the beam profile for
varying strengths of L_2 it will be possible to obtain the emittance of the
250 keV beam. L_2 will be a "non-rotating" lens to facilitate emittance data
reduction. The grid will make a measurement of the profile in only one
(horizontal) direction as it is assumed that the beam will be cylindrically
symmetric at this location. In the event of any uncertainty it will be possible
to rotate the grid through 90 degrees to check the measurement in the vertical
plane. To take space charge into account, emittance calculations will be made
by integration of the Kapchinski-Vladmirski envelope equation rather than
by matrix inversion.

10 MeV energy analysis grid: The second grid will be used for mea-
surements of the high energy beam emerging from the capture cavity. The
tuning-up procedure for the injector will require setting the RF phases and
amplitudes of the capture cavity and sub-harmonic buncher to provide a
beam having the necessary RF phase extent and energy spread. The trans-
verse profile of the beam in the focal plane of the dipole magnet will give the
corresponding energy spread. The dipole will have a dispersion of 16 mm for
1% energy spread. The SEM-grid will be composed of 40 wires of tungsten,
0.1 mm in diameter and spaced 2 mm apart. Thus it will allow a measure-
ment of total energy spread in the range of 5% and with 0.125% resolution.
Again, this grid will measure only in the horizontal plane. A vertical profile
might be measured by installing an additional OTR foil towards the end of
the analysis line.

Range, scattering, and heating in wires: For 250 keV electrons,
the range in carbon is 260 μm. For beryllium, 300 μm. Even use of wires of
thickness 50μm produces significant multiple scattering (angles of the order
of a radian) and prohibits the use of adjacent wire planes in horizontal and
vertical directions. Regarding instantaneous heating, at 250 keV, the specific
ionization is 3 MeV/(g cm^2), in contrast to the minimum ionization figure of
1.8 MeV/(g cm^2). For 4×10^{13} electrons per pulse, a spot size characterized

by $\sigma_x = \sigma_y = 2.5$mm, and 100 μm carbon wires, the heating by the 250 keV beam is less than 50 degrees Celsius. Concerning equilibrium temperature, one must find the balance between energy deposited by the beam and that removed by radiation and conduction. For the conditions listed here, a 100 μm carbon wire absorbs about 50 mW of beam power. The equilibrium temperature at which radiation balances the input power is about 650 degrees Celsius. For conduction in a long wire, the equilibrium temperature would be higher, about 1200 degrees Celsius. The melting point of carbon is 3500 degrees Celsius, so there is not expected to be any problem for beams and spot sizes expected at the injector.

Electronics for SEM grids: Electronics associated with both SEM grids allow for sampling of part of the macro pulse as short as 100 ns, though resolution of better than 1 μs is actually not required. Adjustable gain makes this system operational for the whole dynamic range of beam intensities and time windows.

Optical Transition Radiation Monitors (OTR): OTR measurements have already been shown to be valuable tool for charged particle beam diagnosis and some experience with these monitors has already been achieved at both Saclay and LAL. Three OTR monitors will be employed; The first will be installed after the first triplet and before the dipole magnet, the second will be placed before the entrance of the linac (sharing the same diagnostic port as the third view screen) and the third one in the analysis station. The backward transition radiation from thin (20μm to 30μm) aluminum foils will be used to provide images of the beam. This backward radiation is transmitted through appropriate optics and sent to an intensified CCD camera which allows sensitive observations and analysis to be made. The image intensifier can be used as a shutter and permits time resolution of the beam profile measurements in a window as small as 100 ns within the macropulse. As discussed above with SEM grids, by taking repeated measurements of the transverse profile of the beam for various settings of the triplet magnet, we will be able to determine the emittance of the beam emerging from the capture cavity by the three-gradients method and least squares analysis.

Intensified camera: The camera will be controlled through an RS 232 link from the CPU for gain control, with timing signals to control window trigger time and width. A frame grabber IPP(ELTEC) which provides information at CCIR standard with 640×512 points will be employed. The program monitoring the acquisition can transfer image files to a SUN station through Ethernet. Image analysis could therefore be done on the workstation. The OTR monitor and camera setup is shown in Fig. 3.13.
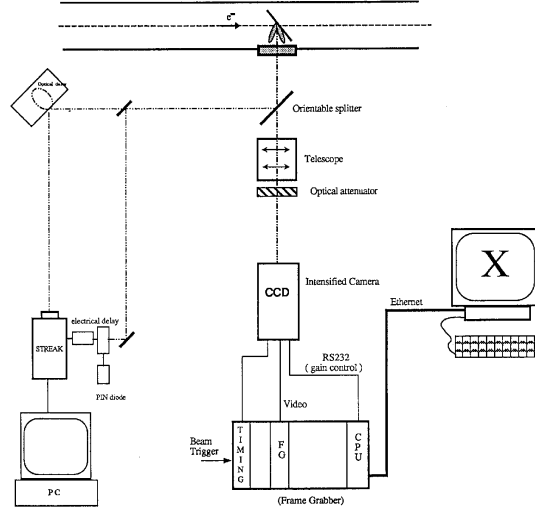
Figure 3.13: OTR monitor and camera setup.

Streak camera: In order to verify that the longitudinal phase extent of the bunch meets the specified requirements we intend to measure the bunch length using streak photography. The OTR signal will be measured using a streak camera of 2 ps resolution. A 2D analysis program of streak camera image is already available on a dedicated PC. A separate streak camera will need to be provided at DESY.

3.1.4.6   Intensity monitors

Three types of beam current monitors will be used: Capacitive pickup (nondestructive), Toroid (nondestructive), Faraday cup (destructive).

Capacitive pickup: A small capacitive pick/up monitor will be installed at the exit of the electrostatic column. This monitor, used with a fast (1 GHz) oscilloscope, will allow measurement of the charge current of the train of pulses from the gun.

Toroids: Three inductive toroids will be used to measure the beam intensity before and after the capture cavity and in the analysis line. They come as a piece of beam line interrupted by a ceramic gap, screened by a metallic cylinder. The magnetic core is made of Supermalloy (relative permeability > 60000); it is housed in a box providing electrical as well as magnetic shielding (three screens are used made of copper, mu-metal and iron). Calibration can be checked at any time by using an *in-situ* test wire.

- signal response: $2V/50\Omega$ for I = 10 mA
- resolution: 50 μA
- rise time: 0.8 μs
- droop: 13% for 1 ms
- number of turns: 300
- dimensions—main line: L = 160 mm , Diam. = 160 mm , Vac. flange CF35
- dimensions—analysis: L = 216 mm , Diam. = 250 mm , Vac. flange CF100

Beam loss monitoring: In comparing toroid measurements made at two locations, one can detect beam losses and provide a trip-off signal to the gun. The comparison is made by sampling the two signals every 10 μs. If the difference is found to be greater than 0.5 mA for three consecutive samples, the gun is returned to the low beam power regime, i.e. 10μs at 10 Hz. The full beam pulse length will be generated by increasing successive macropulses by 10 μs steps. If no beam loss is detected, it will then take 80 macropulses (i.e. 8 seconds) to reach the full pulse length. Thus this procedure allows that a charge equivalent to 30 μs, 8 mA, 10 Hz (i.e., 3.75% of the total beam) can be lost. It also permits the loss of 0.5 mA during the full pulse length. To avoid that the loss be repeated in the next pulse, the comparison, made at the end of the pulses, of integrated intensities will be able to trip off the gun.

Faraday Cups: During commissioning beam current will be monitored with insertable Faraday cups placed in the 250 kV beam line and before the second triplet. The shape is cylindrical with a depression in the center for capture of most of the secondary electrons. The cups will be made of copper, water-cooled, with a length and diameter of 20 mm. The repetition rate will be limited to 1 Hz when the cup after the capture cavity is introduced into the beam.

3.1.4.7   Beam Position Monitors (BPM):

The BPM's will be of the four button electrode type to measure horizontal and vertical position. Their design is based on those already in use at the European Synchrotron Radiation Facility. The BPM's will effectively provide a measurement which is an average over many micropulses of Injector I.

Three BPM's of this type will be installed at the following points; (i) the input to the capture cavity, (ii) the output of the capture cavity, and (iii) the input of the analyzing dipole magnet. The third of the BPM's will have an additional, fifth, button which will be used to measure the phase of the beam with respect to the RF.

Beam Position Measurement: The beam position accuracy will be determined to 0.1 mm within a range of 5 mm and with a resolution of <0.05 mm. The measurement will be performed using button electrodes. A beam position monitor (BPM) block will include 4 electrodes symmetrically distributed around the beam. The relation between the beam position and the relative signal strength obtained from the four electrodes is given by the following formulae. Here, A, B, C and D correspond to the respective electrode signals. As we look downstream along the beam along the positive z-axis, the positive x-axis is to the left and the positive y-axis is directed upward. Electrode A is inclined at an angle of 45 degrees clockwise from the x-axis, and the other electrodes are spaced at 90 degree intervals.

$$X = K\frac{(A+D)-(B+C)}{A+B+C+D} \tag{3.1}$$

and

$$Y = K\frac{(A+B)-(C+D)}{A+B+C+D} \tag{3.2}$$
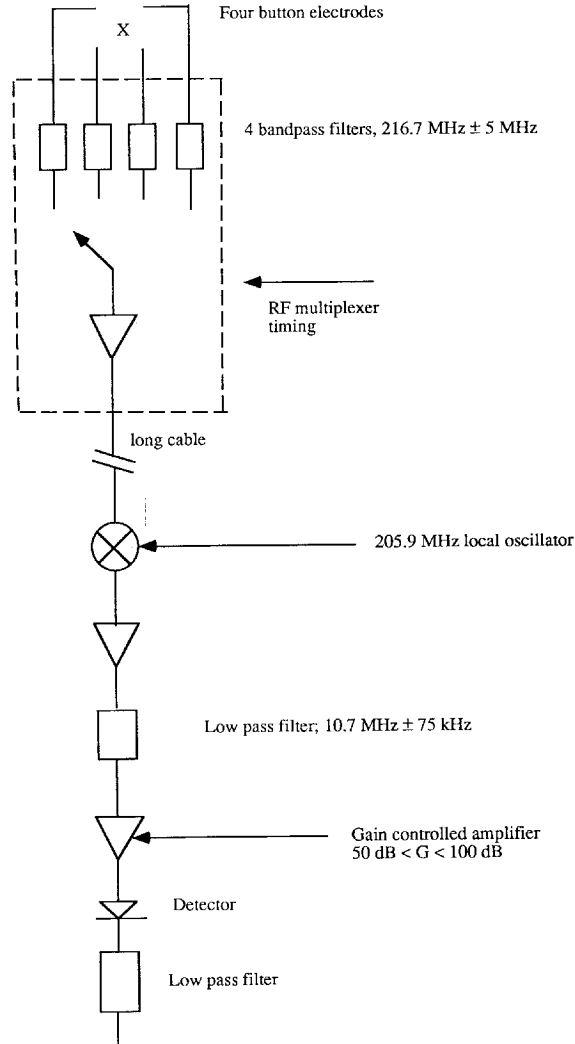
Figure 3.14:   Signal processing for the beam position monitors.

where K is a constant depending on the vacuum chamber radius (K is approximately 13.6 mm in our case). The above formulae are of sufficient precision for beam displacements of less than 5 mm from the axis.

The button electrodes, having a capacitance of 3 pF and being loaded with 50 Ω, show a characteristic frequency spectrum with increasing sensitivity up to 1 GHz with a cut-off frequency around 10 GHz. The electrode

sensitivity at 216.7 MHz is approximately 0.3 mV/mA. The signals from the four electrodes are filtered at 216.7 MHz and scanned by an RF multiplexer as outlined in Fig. 3.14. All four signals are then treated by a single chain of analog electronics. This chain performs amplifying, filtering and detection operations and yields time-multiplexed electrode signals at a DC amplitude of a few Volts. The advantage of having one single chain of electronics is that any drift (for example, gain or bandwidth offset) in the chain will affect all four signals in the same way. The de-multiplexing is done by a clock circuit which triggers an ADC card. The absolute gain of the electronic treatment chain has no importance. The timing and data acquisition is performed via the computer system.

Beam phase Measurement: It will be of interest to observe the stability of the phase of the beam with respect to the RF system. This will be done with the use of a fifth button electrode installed on the BPM block at the exit of the capture cavity. We will select the RF component of the electrode signal at 1.3 GHz with the aid of a band-pass filter. After frequency conversion to 108.33 MHz (1300 GHz / 12) we can measure the phase between the beam and the RF. The electronic treatment will permit observation of the sine and cosine video signals on an oscilloscope. This arrangement is shown in Fig. 3.15. There also is one more button just in front of the Faraday cup up stream of the capture cavity. This will be used for 250 keV beam phasing and time of flight with respect to the gun and buncher.

3.1.4.8   Collimators and Beam Loss Detectors

Collimators: Four collimators will be installed: one near the buncher cavity used as an emittance limiting aperture, one on each side of the capture cavity and one at the entrance of the main cryostat. The role of the later ones is to protect the SC cavities against missteering of the beam and to provide some vacuum separation between the cavities and the warm parts. The first one is made of copper, is water-cooled and insulated to provide measurement of the intercepted current. The three collimators near the SC cavities are made of niobium, 2 mm in thickness. The diameters of the collimators will be chosen after the measurement of the 250 keV beam emittance has been performed.
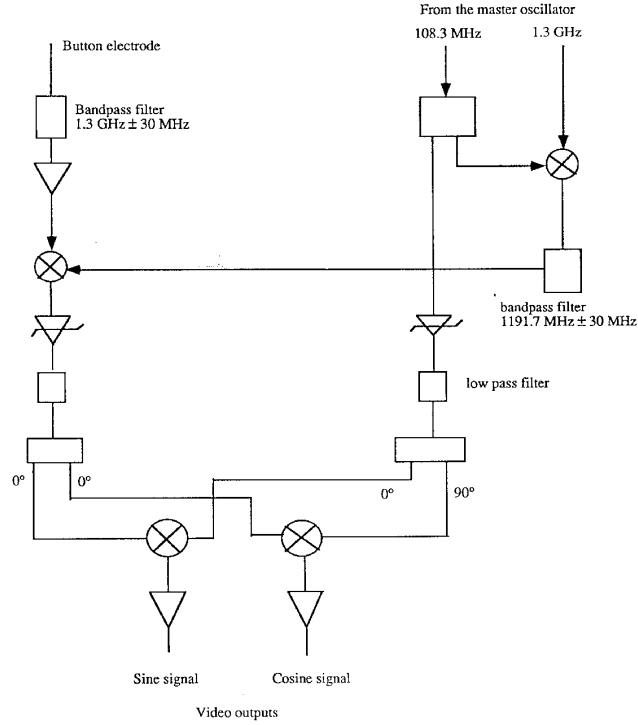
Figure 3.15:   Arrangement to measure stability of beam phase with respect to RF.

X-ray monitors: X-ray monitors are placed downstream of the collimators of the Nb type to provide an alarm in the event of beam scraping. Each monitor consists of four photodiodes which are sensitive to X-rays produced by electrons of several MeV (there is a doubt about their response at 250 keV). They have been calibrated with an electron beam of variable energy hitting a Nb target : the signal is directly proportional to the current and varies like the power 2.6 of the energy. The four signals are separately amplified so that their reading gives information on the location of the beam loss.

Beam Dump: A beam dump will be installed in the analyzing station. It is configured as a Faraday cup for current read-out. It will be made of

copper, water-cooled, and will have a length of 70 mm and a diameter of 80 mm.

3.2   Injector II

The principal parameters for Injector II were given in Tab. 1.3. The experimental program to construct and commission the photoinjector will have three phases. The first phase, a collaborative effort among Argonne National Laboratory, Fermilab, and UCLA, involves the testing of the photoinjector under essentially single-pulse operation to address single bunch beam dynamics issues, and to complete the optimization of the emittance compensation and magnetic compression assemblies. Optics for splitting and delaying the photocathode excitation laser pulse to provide a train of as many as ten pulses will be fitted towards the end of Phase I to begin the study of wakefield and beam loading effects. It is intended to complete this initial phase by mid-1996.

Phase II will commence with the installation of a prototype laser system at Fermilab in 1996. The laser will permit the production of a train of up to 1000 pulses spaced 1μs apart, allowing testing of the photoinjector under conditions identical, except for emittance, to those of the TESLA 500 linear collider. The TESLA 500 parameter list calls for 800 pulses; the larger number of pulses stated here is an allowance for stabilization, if necessary.

Phase III entails delivery and installation of the laser system, photoinjector, linac section, magnetic compression chicane and diagnostics to the TTF at DESY in the winter of 1996-97. The aim is to complete commissioning of Injector II in the Spring of 1997.

3.2.1   Beam Dynamics Considerations

The need for substantial bunch charge with good beam quality requires that the RF accelerating gradient in the photoinjector be relatively high to reduce space charge induced emittance growth, and that emittance compensation described by Carlsten *et al* [5] be implemented to reduce the correlated space charge emittance growth. RF contributions to the emittance must be carefully controlled, requiring that nonlinear variations of the accelerating field in

---

[5]B. E. Carlsten, NIM **A285**, p313-9, (1989)
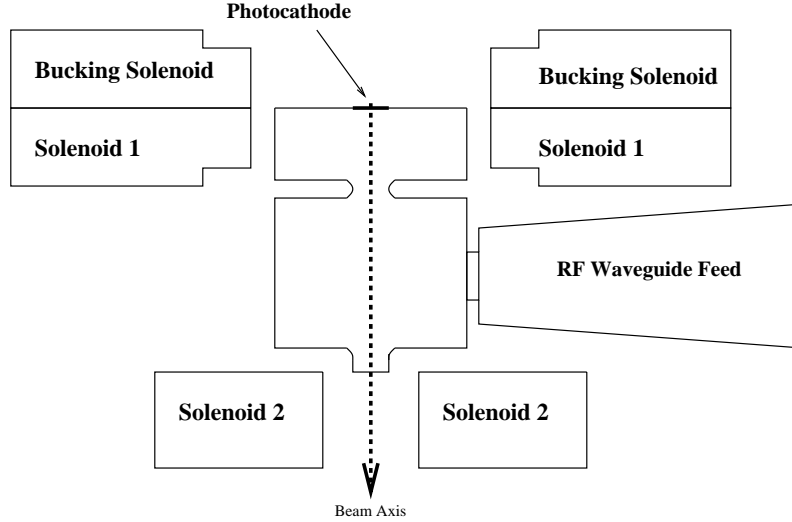
Figure 3.16:   Sketch showing location of focussing and bucking solenoids

both the radial and longitudinal direction be minimized, and that the beam dimensions and accelerating gradient be carefully optimized.

The Carlsten emittance compensation scheme requires that the bunch be given a focussing kick early on to start the gradual reclosure of the phase space "fan" that results from the longitudinal variation of the transverse space charge fields. The variation of the space charge fields results in a correlated emittance growth that can be partially reversed with a focussing kick from a linear lens. Ideally, the kick should take place ahead of the beam's exit from the RF photoinjector, as the time-dependent defocussing that takes place within the RF structure, which can interfere with the proper implementation of emittance compensation, depends on the square of the transverse beam size [6] and will be significantly smaller if the beam is focussed as close to the cathode as possible. As the emittance compensation scheme is sensitive both to the strength and to the longitudinal position of the focussing kick, a second solenoid, downstream of the RF feed for the full cell, is added to allow exploration of the efficacy of the compensation as a function of lens strength and position, with the ratio of the currents in the upstream and

---

[6]K. J. Kim, NIM **A275**, p201-18, (1989)

downstream solenoids determining the effective magnetic center of the lens, and the sum of the currents determining the overall focal length. A bucking coil to cancel the longitudinal magnetic field on the cathode completes the focussing assembly. Figure 3.16 provides a schematic representation of where the three solenoids are positioned. The beveled edge on the downstream side of the first focussing solenoid is to accommodate two laser ports at $\pm 54^o$ to the axis. The bucking coil manifests the same bevel for symmetry, not for mechanical clearance reasons.

The first focussing solenoid and bucking coil have opposing fields, and geometries determined mostly by the space available between the laser ports, the gun exterior, and the cathode plane. The third solenoid follows immediately after the full cell of the gun and has no such space constraints. The solenoid was designed to provide sufficient on-axis focussing strength to allow emittance compensation of beams with normalized energies up to $\gamma = 9.0$ on exit from the gun. The maximum on-axis field of the solenoid is 1415 gauss.

A short section is introduced after the photoinjector to allow the positioning of a six way cross for diagnostics, a vacuum gate valve, and a short drift, to allow the emittance compensation the required time to act before accelerating the beam further, thus "freezing out" the space charge forces.
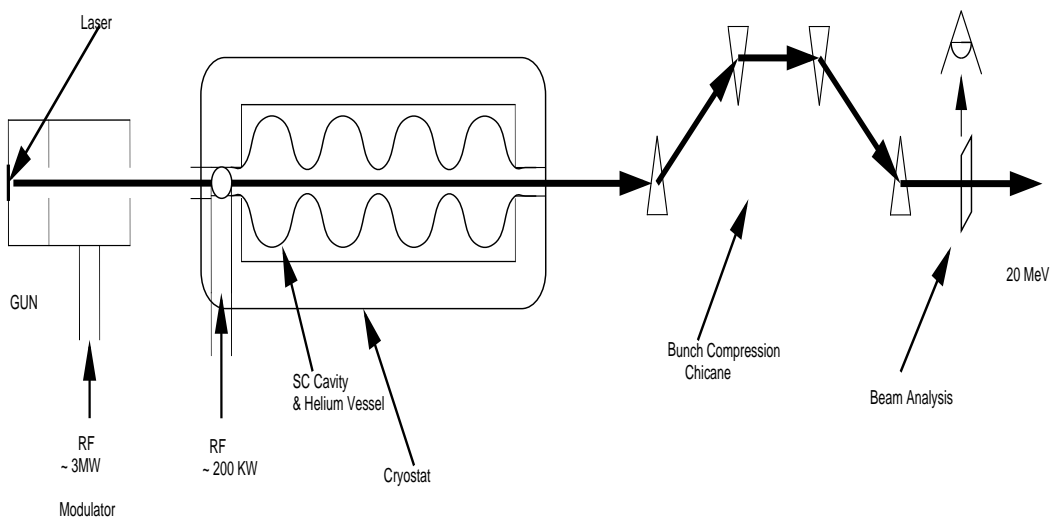
Figure 3.17: Schematic of the photoinjector for Injector II
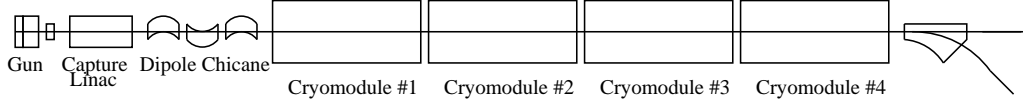
Figure 3.18:   Layout of beamline components for the Tesla Test Facility

As the photoinjector must be optimized to deliver the required transverse beam quality with reasonable RF power, the optimum accelerating gradient will require a long bunch length to reduce the space charge emittance growth during the relatively long acceleration time. As a result, compression of the beam must be undertaken once the beam reaches moderate energy. Magnetic compression requires that the beam pass through a dispersive optical element, making use of a linear energy-phase correlation to reduce the bunch length. Space charge forces will degrade all three emittances during compression, resulting in poor beam quality if compression proceeds for too long or at too low a beam energy. It is therefore optimal to compress at the highest energy possible (thereby reducing the space charge forces) that beamline space allows. The TTF experimental area has rather limited space, motivating the choice to place a magnetic compression chicane at a lower energy (20 MeV). The proposed photoinjector is sketched in Fig. 3.17 and its relationship to the entire linac is depicted in figure 3.18.

Detailed simulations of the photoinjector performance were completed using a modified version of PARMELA that accepts field maps for both RF cavity fields and static solenoid fields.The modified code also calculates the effects due to image charges on a metallic photocathode, and has several diagnostics tailored specifically to reveal the underlying phase space dynamics of emittance compensation.

Compression is estimated using the longitudinal emittance of the beam and assuming an ideal linear transformation on the phase space to produce the compressed bunch. Emittance growth resulting from compression is es-

timated from Carlsten's analysis [7] assuming a short bunch with a radially
uniform charge distribution:

$$\epsilon_N = \frac{ISG}{4I_A\beta^2\gamma^2} \qquad (3.3)$$

where I is the peak compressed current, S is the path length over which the
compressor dipole fields act on the beam, G is a geometric factor between
0.2 and 0.5, and the Alfven current $I_A = 4\pi\epsilon_o m_e c^3/e$.

Tab. 3.6 details the predicted performance of the photoinjector setup.
Emittance values quoted are one sigma normalized values enclosing 100% of
the stated bunch charge. (In each case, this represents 80% of the total ini-
tially launched charge, with the 20% excess "guard charge" being collimated
away.) Two different operating scenarios were examined: high bunch charge
(8 nC/bunch) operation for testing of HOM energy deposition in supercon-
ducting RF linac structures, and low bunch charge (1 nC/bunch) operation
for injecting into a free electron laser (FEL). Significant effort was devoted to
optimizing the 10 nC scenario, both for highest beam quality, and for lowest
possible RF power consumption. The low charge (1 nC) case was derived
by scaling the bunch radius and length to preserve the bunch core charge
density, thereby allowing the emittance compensating lens configuration and
strength to remain essentially unchanged. Although the 1 nC case outlined
below has not been fully optimized, good beam quality ($\epsilon = 2.5\pi$ mm-mr)
and moderately high peak current (80 Amperes) are present before com-
pression, which contributes approximately 0.52 π mm-mr to the transverse
emittance while raising the peak current to 120 Amperes.

Shown in Fig. 3.19 are the evolution of the transverse beam emittance and
beam size throughout the injector for the high bunch charge case. Five emit-
tance traces are shown, representing the one-sigma normalized emittances
of 100%, 95%, 90%, 80%, and 70% of the bunch particles. (viz. An 80%
emittance represents the emittance the bunch would have if the outermost
20% of the beam particles were collimated away) The onset of emittance
compensation is clearly visible in the decrease of all emittances after the
solenoid focussing kick. Longitudinal and transverse phase space plots at the
end of the injector beamline (prior to compression) are shown in Fig. 3.20
and Fig. 3.21. For reference, the gun exit is located at $z = 20.7$ cm, and is

---

[7]B. E. Carlsten, *Emittance Growth in Bunched Beams in Bends*, unpublished, (1993)

Table 3.6:   Predicted performance of photoinjector for Injector II

Parameter	Symbol	Predicted Value
Before Compression		
Bunch Charge	Q_b	8 nC = $5 \times 10^{10} e^-$
Laser pulse length FWHM	Γ_t	28 ps
Launch Phase (w.r.t. $E_z = 0$)	ϕ_o	45°
Beam radius at cathode	r_o	3.0 mm
Peak field on cathode	$E_{z,max}$	35 MV/m
Post-Gun Gamma	γ_1	8.5
Post-Linac Gamma	γ_f	35.7
Transverse emittance, normalized	ϵ_n	11 mm-mr
Longitudinal Emittance (100% RMS)	ϵ_z	820 deg-keV
Momentum Spread	σ_p/p_o	4.2 %
Bunch Length	σ_b	4.33 mm
Peak Current	I_p	276 Amperes
After Compression, from theory		
Transverse Emittance, normalized	ϵ_n	15. mm-mr
Bunch Length	σ_b	1 mm
Peak Current	I_p	958 Amperes
After compression, from PARMELA		
Transverse Emittance	ϵ_n	26 mm-mr
Bunchlength rms	σ_b	0.5 mm
Momentum spread rms	σ_p/p_o	4.3%
Longitudinal Emittance	ϵ_z	760 deg keV
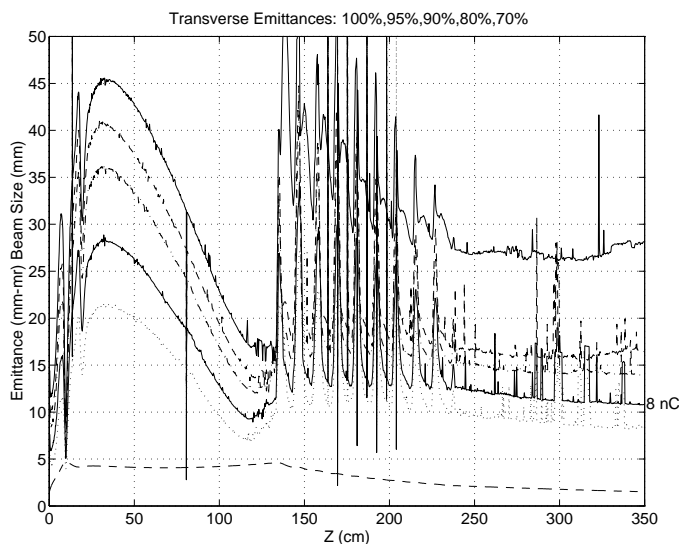
Figure 3.19:   Emittance and envelope evolution for 10 nC operation.

followed by a drift up to $z = 96.2$cm where the beam enters a 9 cell linac extending to $z = 200$. cm, where the beam is again in a drift.

3.2.2   RF Design of the Photoinjector

Simplicity, high shunt impedance, and the ability to accommodate an externally mounted focussing solenoid close to the cathode region motivated the choice of a 1.5 cell TM_{010} π-mode structure. The need to induce a strong on-axis magnetic field made the use of a superconducting cavity problematic, and the need for a high accelerating gradient eliminated the choice of a superconducting gun altogether. The Brookhaven/Grumman [Gun I] S-band photoinjector [8] was taken as a starting point for the design of the TTF injector, the resonant frequency, waveguide coupling, intercavity coupling, and longitudinal exit aperture profile were modified to yield an L-band structure with good shunt impedance and field balance characteristics.

   Widening the iris for improved group velocity lowers the shunt impedance and affects the radial spatial harmonics (flattening the near-axis radial varia-

---

[8]I. S. Lehrman *et al*, *Design of a High-Brightness, High Duty-Factor Photocathode Electron Gun*, NIM **A318**, p.247-53, (1992).
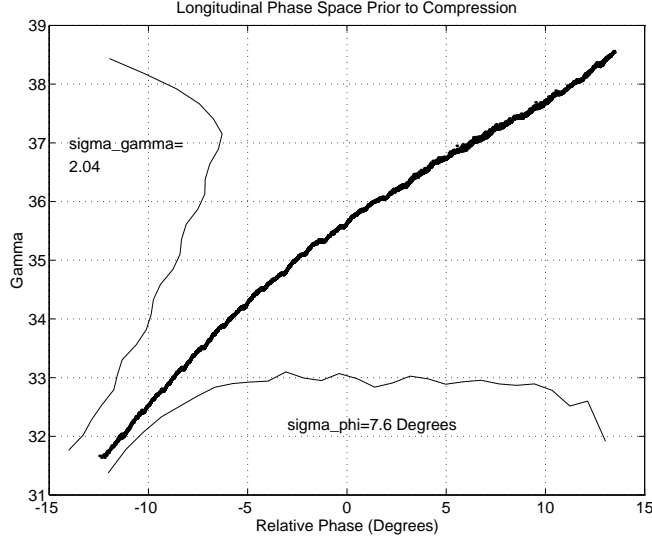
Figure 3.20: Longitudinal phase space at the end of the injector, prior to compression.

tion of E_z as a benefit) and reduces the strength of the higher order longitudinal spatial harmonics. This somewhat unusual coupling scheme has already been employed successfully in a photoinjector for a free electron laser [9] [10].

Although RF power efficiency was of prime concern in designing the photoinjector, the standard shunt-impedance increasing procedure of decreasing the gap length with the addition of "reentrant noses" on the entrance and exit irises was not undertaken. Although such a geometric modification can appreciably improve the power efficiency of an RF structure, it does so at the expense of significantly enhancing the nonlinear components of the accelerating field. As the rms bunch radius for the high-charge case is significant (7 mm at the maximum, 10 cm from the photocathode), nonlinear RF emittance growth in such a cavity would be unacceptably large. Also, the large accelerating gradient (twice the Kilpatrick threshold) makes an RF structure with a low peak-field to accelerating-field ratio especially desirable, making the addition of any geometric disturbances in the high electric field region of

[9] M. Takabe *et al*, NIM **A318**, P. 367-71 (1992)
[10] H. Sakae *et al*, NIM **A331**, p. 349-9, (1993)
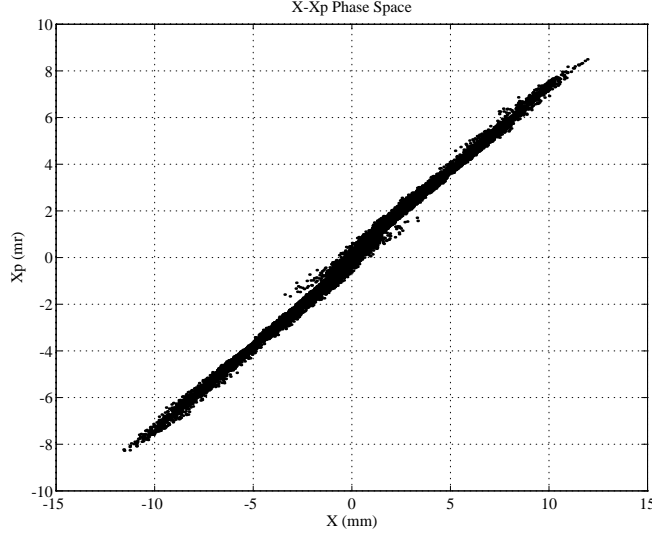
Figure 3.21:   Transverse phase space at the end of the injector, prior to
                compression.

the cavity undesirable.

An elongated half cell was chosen to provide improved beam divergence
control (A small amount of RF focussing occurs in the region right off the
cathode as a result of the lengthening) and additional time to start the
solenoidal focussing kick to initiate the emittance compensation before the
time-dependent kick of the first iris becomes appreciable. After some opti-
mization, a half cell length equal to $\frac{5}{4}\frac{\lambda_{RF}}{4}$ was chosen. To ameliorate further
higher spacial harmonic pollution of the accelerating mode, the full cell has
a length that is exactly $\frac{\lambda_{RF}}{2}$.

The iris diameter between the full cell, where RF power is coupled in, and
the half cell was chosen to yield strong enough coupling that the longitudinal
position of the photocathode could be used as a frequency tuning mechanism
without causing a substantial shift in the field balance between the two cells.
Various field balance options were considered, motivated by the possibility
of using RF focussing at the first iris on the one hand, and by the possibility
of improved longitudinal phase space linearity (and thus compressibility)
on the other. A field imbalance between the half and full cell could be
made to enhance the time dependent focussing kick centered at the first

iris, but was found to significantly interfere with emittance compensation, degrading final beam quality, and was not pursued further. Thus a balanced ($E_{z,max}^{halfcell} = E_{z,max}^{fullcell}$) field profile was chosen. To ensure the field balance, the mode separation was chosen to be approximately 2.5 MHz (40 times the -3dB cavity bandwidth), implying a coupling constant of $\gamma = 0.19\%$. Assuming the half cell field to be $E_1 = 45$ MV/m, the full cell field $E_2 = 35$ MV/m, the stored energy $U = 10.5$J, the iris thickness to be $d = 1.5$cm, and the free space wavelength $\lambda = 23.061$cm,the electrical coupling iris radius needs to be [11]:

$$r_o = \left[\frac{3\gamma U}{2\epsilon_o E_1 E_2 e^{-\alpha d}} \right]^{\frac{1}{3}} \approx 2.0cm \tag{3.4}$$

where $\alpha = k_o\sqrt{(\lambda/\lambda_c)^2 - 1}$ is the inverse of the attenuation length for the TE_{11} mode. Simulation of the cavities using the Superfish code yields $\gamma = 0.189$ for an iris radius of 2.0 cm, in good agreement with prediction. As the hole is not uniform in radius, (rather the edges are rounded to prevent field line concentration) the coupling constant for the simulated and actual photoinjector will be somewhat higher than equation 3.4 predicts.

Beam loading in the half cell is expected to be:

$$P_{beam} = \int E_z dz \cdot \frac{N_b Q_b}{\tau_{RF}} \approx 18.5kW \tag{3.5}$$

which is to be compared with the power dissipation on the walls of the half cell:

$$P_{diss,HC} = \frac{R_s}{2} \int H_\phi^2 d\mathcal{S} \approx \frac{R_s}{2} \frac{\epsilon_o}{\mu_o} \frac{k^2}{k_r^2} E_o^2 J_1^2(k_{01}) 2\pi R \frac{L_z}{2} \approx 0.94MW \tag{3.6}$$

for $E_o = 35MV/m$, or less than 2%. Since the entire cavity fills in $3\tau_{RF} = 8.7\mu sec$, recovery from beam loading will be well within the 1 μsec requirement.

The electrical properties of the accelerating structure are summarized in table 3.7.

Tuning of the photoinjector will be accomplished with the aid of four largely separate controls. Gross frequency tuning of the photoinjector as a whole will be accomplished by regulating the cooling water temperature.

---

[11]J. Gao, NIM **A311**, p. 437-43, (19092)

Table 3.7: Electrical Properties of the Photoinjector Gun

Parameter	Symbol	Value
Operating mode		$TM_{010,\pi}$
Frequency	f	$1300MHz$
Transit time factor	T	0.73127
Structure quality factor	Q	23700
Structure fill time	τ_{RF}	$2.90~\mu$ s
Structure Shunt Impedance	Z_s	$13.82M\Omega$
Effective Shunt Impedance	ZT^2	$27.92M\Omega/m$
Peak-to-accel field ratio	E_{pk}/E_{acc}	1.870
Typical operating gradient	MeV/m	18.1
Power diss at $E_{acc} = 18MV/m$	P_{diss}	$2.2MW$
Average Power diss at $E_{acc} = 18MV/m$	P_{ave}	$22kW$

Thermal analysis of a similar L-band structure dissipating much higher average power (150 kW, versus 45.0 kW for the present case) found no serious difficulties in providing adequate cooling[12]. Indeed, an S-band structure sustaining the same duty cycle (1%) but higher accelerating gradient (by a factor of 2), and thus substantially higher dissipated power density (by a factor of 20), has been designed and successfully operated at Brookhaven National Lab [13].

For an L-band copper structure, the frequency change per degree Kelvin is approximately $\Delta f/\Delta T = -(k_{01} \cdot c \cdot \kappa_T)/(2\pi R) \approx 21.8kHz/K$, with the thermal coefficient of expansion $\kappa_T = 16.92 \times 10^{-6}/K$ for copper. Tuning of the half and full cells is accomplished by means of a paddle-style tuner in each cell, allowing individual frequency control (details of the paddle design may be found in Appendix A). Lastly, the photocathode will be mounted on a micrometer, allowing fine longitudinal positioning of the cathode, and thus the resonant frequency of the half cell. Assuming the cathode and paddle actuators provide a linear positioning precision of 20 microns and an angular positioning precision of 5 degrees (paddles only), the tuning sensitivities

[12]J. B. Rosenzweig *et al*, Proc. IEEE PAC 1993, Washington D.C.

[13]Lehrman *et al, op cit*
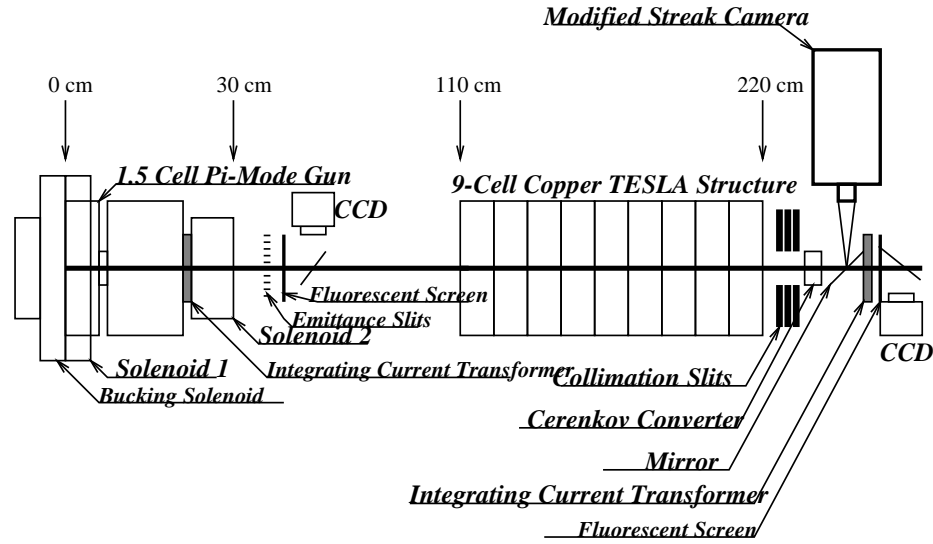
Figure 3.22:   Layout of beamline components for testing the photoinjector
at A.N.L.

will be -17.94 kHz/20 micron, 28.0 kHz/20 micron, and 3.1 kHz/5 degrees,
respectively.

3.2.3   Diagnostics and Instrumentation

The layout of the Argonne National Laboratory Phase I photoinjector test
setup is shown in Figure 3.22. Instrumentation of the beamline has been
chosen to permit exploration both of the injector performance in general,
and to allow direct observation of emittance compensation.

A new approach to emittance measurement has been proposed [14] to ex-
plore the physical basis for emittance compensation. A time-resolved vari-
ation of a slit emittance measurement technique (similar in principle to the
pepper pot) employed at UCLA[15] will be used, providing emittance measure-
ment in one transverse plane as a function of longitudinal position within the
beam. While prior time-resolved measurements of electron beam emittance

---

[14] J. B. Rosenzweig, private communication, December 1993

[15] J. B. Rosenzweig, G. Travish, *Design Considerations for the UCLA PBPL Slit-Based
Phase Space Measurement Systems*, PBPL internal, Feb 22, 1994.

on the nanosecond time scale at Los Alamos [16], and of three-dimensional spacial distribution at LEP [17] have been successfully undertaken, measurements with sufficient resolution (picosecond or better) to observe the emittance compensation process have not. Figure 3.23 provides a schematic of the proposed measurement. A detailed analysis of the apparatus will appear in the near future, but a brief description is included here for completeness. [18].

The space charge dominated beam is brought to a non-ballistic waist (*ie* particles do not cross the axis) and collimated into several emittance dominated beamlets by a slit emittance mask. The beamlets retain the transverse temperature of the original beam, but at such reduced charge that space charge forces within the individual beamlets contribute negligibly to their momentum spread. The beamlets then drift several meters to allow the correlated transverse momentum time to impart a measurable transverse distance offset, and are passed through a Čerenkov radiator to produce an optical signal that can be extracted from the beamline. The light is focussed (optics not shown) onto the photocathode of a streak camera, and the streaked image recorded with a high resolution CCD camera. The spread of the light from each beamlet may be analyzed to unfold the contribution due to the transverse temperature of the beam from the natural spread angle of the Čerenkov radiation. The centroid of the beamlets at the radiator provides the centroid of the transverse momentum spread, while the transverse position centroid is known immediately from the separation of the collimator slits. From these data the transverse phase space of the beam may be reconstructed as a function of longitudinal position within the beam. The slit separations are chosen to ensure that the light from adjacent beamlets does not overlap at the CCD camera.

The measurement will be made at two locations, once at the photoinjector exit, and again at the exit of the linac, allowing comparison of the beam's slice emittances immediately after the focussing kick, and shortly after the emittance compensation minimum has occured.

With this diagnostic, investigation of the effectiveness of emittance compensation will be explored as a function of compensating lens position and strength by adjusting the current sum and the current ratio, respectively, of

[16]T. Kauppile *et al*, Proc. 1992 IEEE NAC Conf., San Francisco, p.2107-9

[17]G. Baribaud *et al*, Proc. XV Int. Conf. on high Energy Accel., p.212-4

[18]J. B. Rosenzweig, private communication, December 1993, *op cit*
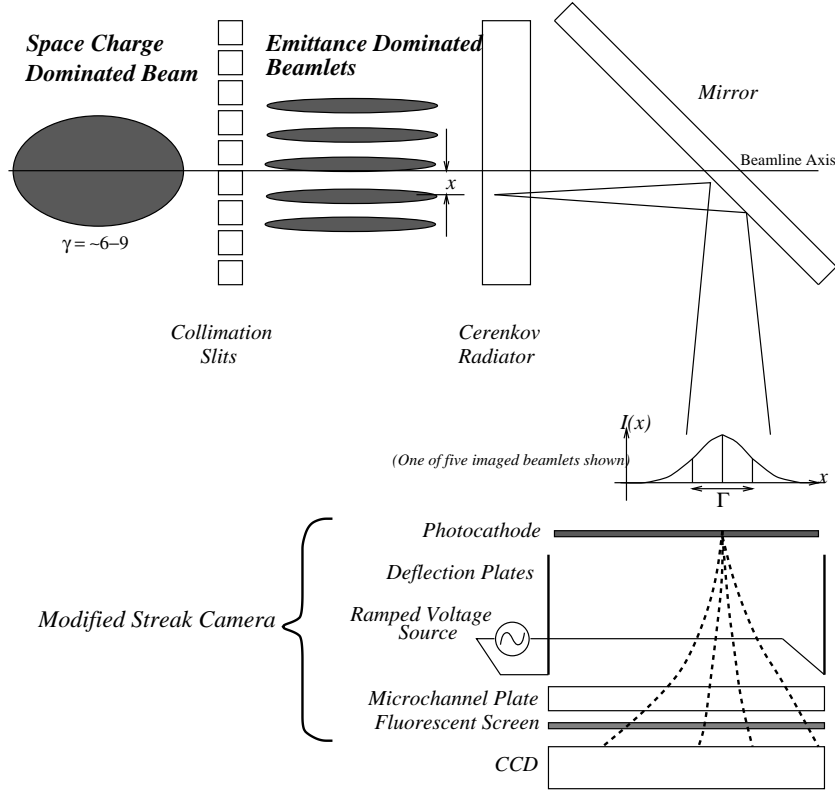
Figure 3.23:   Schematic of time resolving emittance measurement apparatus

the two focussing solenoids depicted in figure 3.16 above. With information about the actual slice emittances (*viz.* the emittance of a subset of the beam electrons between z and $z + \Delta z$) and the orientation of the slice emittance ellipses before and after compensation, detailed study of emittance compensation will be possible for the first time.

In addition, two integrating current transformers will be mounted, one immediately downstream of the photoinjector to non-destructively monitor bunch charge at emission, and another after the collimators downstream of

the first linac section to monitor final beam charge. Ordinary fluorescent screens, fitted with CCD cameras, used with the emittance slit mask, will provide ensemble emittance measurements as a cross check for the time resolving emittance measurement. A dipole spectrometer (not shown) will be mounted at the end of the beamline for beam momentum analysis.

3.2.4   Photocathode Excitation Laser Requirements

Although a number of different methods of producing electrons have been developed and successfully used in electron guns, the highest current densities ($> 1kA/cm^2$) possible with a laser driven photocathode are well matched to the high peak current requirements for the TTF and TESLA 500 linacs. Additionally, some flexibility is available in the shaping of the charge distribution within the laser-generated beam, allowing some control over the nonlinear space charge contributions to the emittance.

The laser system requirements suitable for the TTF and TESLA 500 injectors are summarized in Tab. 3.8. Laser pulse energies are listed for two photocathode materials which roughly represent the two extremes of photocathode performance: a metallic cathode (Yttrium is taken as an example), with low quantum efficiency (QE), and a semiconductor photocathode (Cs_2Te) with excellent QE. Restrictions on the timing jitter arise from the need to launch the bunch at a particular time during the RF cycle to minimize the RF contribution to the emittance growth, while restrictions on the amplitude jitter are needed to ensure consistent charge per bunch, and thus consistent beam loading in the downstream linac sections.

Discussions with industry have led to the conclusion that a laser matching the outlined requirements is technically feasible, although challenging. The conflicting requirements of high gain (for useful output pulse energy) and very long pulse trains (requiring little sag or fluctuation in the gain as subsequent pulses are amplified) will require state-of-the gain media, and potentially some form of closed-loop control system, as suggested by the researchers at the Max Born Institut für Physik.[19]

At this writing, we assume that a Cs_2Te cathode will be used. A bunch charge of 10 nC will be extracted from the cathode and 20% of that will be

---

[19]I. Will, P. Nickles, W. Sandner, *A Laser System for the TESLA Photo-Injector*, Max Born Institut, Berlin, 1994.

Table 3.8:   Laser requirements for the TTF/TESLA500 Photoinjectors

Parameter	*Required Value*	
(Photocathode Material)	Cs_2Te	*Metallic*
(Photocathode QE)	1%	0.05%
Micropulse Energy	$> 5\mu J$	$> 80\mu J$
Wavelength	< 300 nm	
Pulse Length (FWHM)	$13 - -28$ ps	
Micropulse Repetition Rate	1 MHz	
Macropulse Length	$800 - 1000$ pulses	
Macropulse Repetition Rate	10 Hz	
Timing Jitter	< 2 ps	
Amplitude Jitter	$< 5\%$	
Pointing Stability	$< 100\mu$rad	
Pulse Rise Time	5 ps	

scraped to provide the required 8 nC charge and 20π mm-mrad emittance. With this cathode, a 2% quantum efficiency should be realized, but the laser design should be able to provide for as low as 1%. The cathode disk of 1.4 to 3 mm should be uniformly illuminated. Cathode edge masking and pointing stability requirements are still to be worked out.

In this model, a three stage Nd:YLF laser with "standard active mode lock" will be used (Fig. 3.24). The rise time and fall time (10–90%) will be a minimum of 5 ps. The flat top of the pulse will range from a minimum of 5 ps to more than 20 ps. At present, the pulse length needed is expected to lie in the range 13–28 ps. Variations during flat-top are anticipated to be about 20%.

The provision of sufficient laser power is not expected to be a problem as long as the average power is kept at the 1 W or so level. But the atypical macropulse structure implies that further review of the laser power is appropriate. The present sense of the relevant factors is given in Tab. 3.9.

There are constraints on the laser pulse energy stability at the pulse to pulse level and on the approximately 100 μs time scales. Bunch charge variations influence the loading of the RF cavities. Current thoughts on laser

Table 3.9: Summary of factors relating to laser power.

Charge	10 nC (20% scraping)
Minimum QE	1–2 %
Wavelength (harmonic 4)	260 nm
Photon energy	4/66 eV
Energy to cathode (QE 1%)	5 μJ
Laser system loss factors	
Scatter and mirror	times 2
Lenses, spatial filter	times 1.5
Scatter, reflection at gun	times 1.25
Feedback stabilization	times 2
Net of above	times 7.5
Conversion to harmonic	30%
Resultant energy needed	
at fundamental (1.05 μm)	125 μJ/pulse
Power per macropulse	125 watts
Average power (0.8ms, 10 Hz)	1 W

design include a number of feedback loops (2–3) to stabilize the gun charge output. Primary laser stability at the level of $\pm 0.3\%$ in 100 μs and $\pm 1.5\%$ pulse to pulse is assumed. This allows for a factor of 3 jitter amplification on the harmonic conversion to give charge stability of $\pm 1\%$ in 100 μs and $\pm 5\%$ pulse to pulse.

Charge stability of $\pm 10\%$ random from bunch to bunch and $\pm 2\%$ drift of the average over 100 μs should be adequate to limit the energy variation from gun charge to $\pm 10^{-3}$ with the use of feedback systems on the cavities. Further investigation is necessary to confirm this.

For a Nd:YLF laser system satisfying the requirements outlined above, the following arrangement would be appropriate:

- Diode-pumped acoustooptically mode-locked quasi-CW YLF-oscillator for producing the seed pulse length of 5–8 ps duration. This could be an oscillator comparable to the commercial LIGHT WAVE model130. An appropriate modifications of this oscillator will permit the tuning of

pulse length by changing the modulation depth of the the acoustooptical modulator.

- Pockels cell selecting single pulses with 10 Hz repetition rate out of the pulse train.

- Faraday rotator to improve the optical isolation between oscillator and the following amplifiers.

- Injection-seeded pulse-train oscillator (ILPTO) based on Nd:YLF and producing a 1 ms long output pulse train of 50 ns spaced pulses of 5 to 10 μJ each. Two appropriate modelockers have to be used in the resonator to keep the injected pulse at the right length during the 20,000 round trips. Furthermore, active control of the cavity length will be required in order to keep the pulse jitter at an acceptable level. Pulse energy must be controlled by a feedback system. Both semiconductor diodes and common flash lamps should be considered as pump sources for the ILPTO. Diode pumping has the advantage of minimized thermal lensing. Consequently, the micropulse parameters could be kept more stable over the macropulse. This is especially important if lengthening of the pulse train for generation of up to 8000 micropulses is considered. For these reasons, diode pumping is incorporated in the present laser design considerations, even at the expense of an increase in the price of the whole system by about 20%.

- Pockels cell to select single pulses with 1 MHz repetition rate out of the pulse train

- Linear Nd:YLF amplifier.

- Beam shaping aperture cutting off flat-top beam profile out of the Gaussian beam emittance by the injection seeded YLF amplifier. Consequently this aperture reduces losses by 50–70%

- Spatial filter and telescope to smooth the flat-top beam profile and increase the beam diameter to 3–4 mm. After this filter, the remaining pulse energy amounts to about 10μJ.

- Nd:YLF amplifier to enhance the pulses to the energy of 40 μJ. A double-pass symmetry is used to reach a suitable amplification; this

two-stage amplifier is pumped by flash lamps. These are driven by a special pulse-forming network generating nearly rectangularly shaped pulses of a length exceeding 1 ms.

- Frequency conversion stage (one KDP and one BBO crystal) to transform the pulse wavelength to $\lambda = 260$ nm. A telescope will be required to decrease the beam diameter and simultaneously increase the intensity in the beam. The conversion to the higher harmonic leads to a pulse shortening by a factor of 1.5 to 2.

- UV Pockels cell for both cutting the required 800 pulses out of the pulse train and further reducing the energy tolerances of the micropulses.

- Spatial filter and imaging system both to clean the flat-top beam profile and transform it onto the surface of the cathode.

- Feedback system controlling the electrooptical crystal inside the ILPTO, the Pockels cell in the linear amplifier chain, and the UV Pockels cell in order to stabilize the micropulse energy.
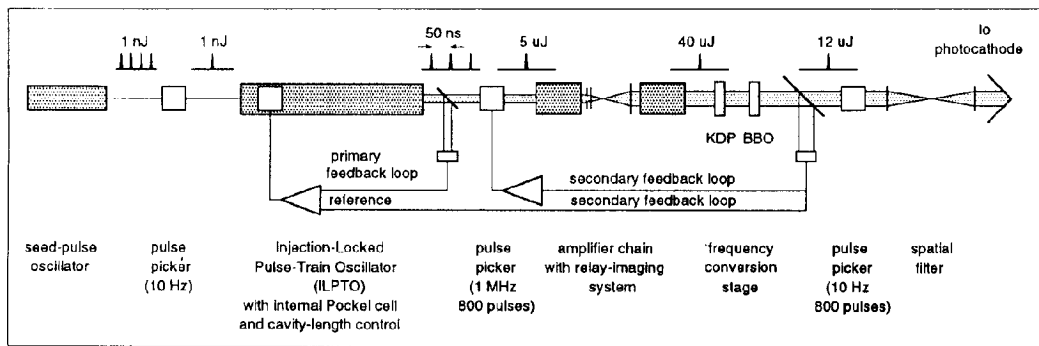
Principle scheme of the proposed laser design. Energy values are given with regard to a single micropulse.
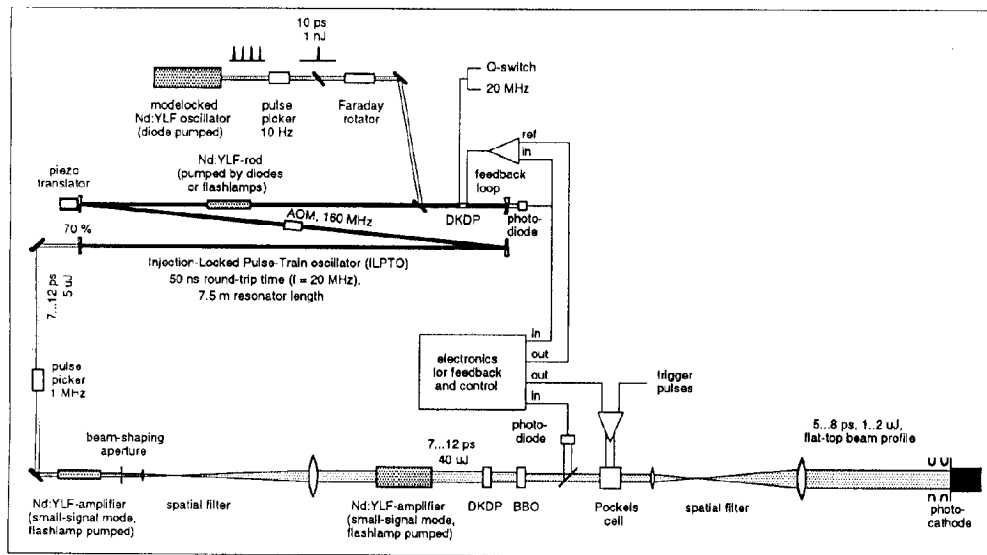
Proposed scheme of the Nd:YLF laser system. Energy values are given with regard to a single micropulse.
The pulse duration (FWHM) can be lengthened by decreasing the modulation depth of the modulator in the ILPTO.

Figure 3.24:   Preliminary design concept of MBI laser, from I. Will, TTF/Hasylab Meeting Proceedings, DESY, May 6, 1994.

3.2.5   Electrical Dimension Specifications and Tolerances

Electrical dimensions and tolerances derived from physical constraints on the resonant frequency, coupling constant, and normalized structure impedance are listed in table 3.10. Engineering drawings of the cold test model components follow on the subsequent pages.

Constraints on the cavity resonant frequency, f_o, set by the available tuning range of the paddle tuners, cathode plunger, and thermal control system, are necessary to have the resonant frequency of the structure fall at the desired frequency, and to avoid field imbalance ($viz.$ the ratio $E_{z,max}^{halfcell}/E_{z,max}^{fullcell}$) problems due to a mismatch in the individual cavity resonant frequencies. As the outer walls of the cavity experience substantial magnetic field, the frequency of the cavity varies rapidly with radius, placing tight tolerances on the radii. Tolerances listed below derive from the frequency constraint $\Delta f \leq 1MHz$.

The coupling constant γ prescribes the frequency separation of the zero and pi modes of the structure, and controls to what extent movement of the photocathode perturbs the field balance. So long as gamma is large enough to provide for well separated zero and pi mode frequencies, ($ie.$ the separation is greater than a half Q-width: $\omega_\pi - \omega_o \geq \frac{\omega_0}{2Q}$, where ω_0 is the resonant frequency of the uncoupled cavity) small changes in γ will not appreciably alter the field balance. Correspondingly, the tolerance on the coupling constant is generous at $\Delta\gamma \leq .05\%$.

The normalized structure impedance, β, determines the behavior of the photoinjector when coupled to an RF source. Optimal power transfer from RF source to accelerating structure occurs when $\beta \equiv \frac{P_{cavities}+P_{beam}}{P_{transmission\ system}} = 1$. Tolerance on the physical dimensions of the coupling hole are tight, owing to the rapid ($\propto$ (slot area)^6) variation of β. Stipulating that the reflected power from the cavity not exceed 1% requires $0.818 < \beta < 1.222$.

Table 3.10:   Key Electrical Dimension Specifications for Photoinjector

Dimension	*Nominal Value*	*Tolerance*	*Main Effect*
radius of half cell	8.904	±0.0068=2.7 mil	f_o^{HC}
radius of full cell	8.884	±0.0068=2.7 mil	f_o^{FC}
radius of iris	2.0	±0.0833=33. mil	γ
thickness of iris	1.5	±0.0142=5.6 mil	γ
length of coupling slot	6.0	±0.0500=19. mil	β
width of coupling slot	2.0	±0.0167=6.6 mil	β
depth of coupling slot	0.5	±0.0548=22. mil	β
All dimensions in centimeters unless specified			

Chapter 4

Cavities and Auxiliary Systems

In the last several years, there have been remarkable strides in the performance and application of superconducting cavities. More than 400 structures are operating in electron accelerators around the world. Key aspects responsible for achieving the design performance for these accelerators are the antimultipactor rounded cell shape, high thermal conductivity niobium (RRR=200–300) to avoid thermal breakdown, and clean surface preparation to avoid field emission.

Among the chief difficulties facing the achievement of the 25 MV/m gradient goal for the linear collider are the phenomena of thermal breakdown and field emission. To overcome thermal breakdown, a technique (called solid state gettering with titanium) is now available to double the thermal conductivity of industrially produced niobium. The purity of industry-supplied niobium also continues to improve steadily. To fight field emission, improved cleanliness techniques have been proven, such as high pressure water rinsing. Finally a technique called high pulsed power processing has been demonstrated to destroy field emitters and substantially improve gradients. By applying the new techniques, the TESLA collaboration has already reached gradients of 26–28 MV/m in three 5-cell, 1.3 GHz cavities. Tests on multicell cavities have also proved that high pulse power processing is able to destroy additional field emitters introduced during vacuum "accidents".

A new infrastructure has been set up at the TTF site that has installed all the needed capabilities, such as automated chemistry, high pressure water rinsing, UHV high temperature furnace, and high pulsed power processing. Already a 9-cell cavity has reached a gradient of 20 MV/m.

4.1   Cavity Design and Characteristics

Parameters like fundamental frequency, number of cells, shape of the cavity and higher order mode damping have to be fixed in designing a superconducting cavity. Some parameters will influence other design values and vice versa. For example a strongly coupled HOM damper allows one to go to a large number of cells per coupler. The coupling strength, on the other hand, can only be determined after elaborate measurement on a model with given number of cells have been made. The conclusion of the measurement might be to increase or to reduce the number of cells. It is not clear whether there is a straight forward process to find the overall design optimum. A summary of the resultant TESLA cavity parameters are given in Table 4.1.

4.1.1   Choice of Frequency

There are distinct arguments for the choice of a high or low fundamental mode frequency (see Table 4.2).

Arguments in favor of higher frequency are:

- The shunt impedance per length increases linearly with frequency. This means that the cryogenic loss decreases if one assumes a constant cavity quality factor Q. If one takes into account the temperature and frequency dependent surface resistance, then an optimum temperature has to be determined for each frequency. The analysis in [1] concludes, that at higher frequencies the cryogenic effort is reduced but the optimum temperature is lowered.

- The surface area of the cavity decreases with increasing frequency. An analysis of the maximum surface fields measured shows, that higher fields can be reached with smaller surfaces. This is explained by a statistical model of defects and field emitters.

- The stored RF energy is lower at higher frequencies. During pulsed operation, this energy must be delivered by the klystron and will be dissipated during decay of the cavity field.

---

[1]C.H. Rode,D. Proch, Proceedings of the 4th Workshop of RF Superconductivity, KEK, 1989, Editor Y. Kojima, p. 751

Table 4.1:   TESLA cavity data. Quantities marked with an asterisk differ slightly from those shown in the Introduction due to alternative calculational techniques.

Parameter	
Fundamental π mode frequency	1300 MHz
Number of cells	9
Coupling cell to cell	1.87%
E_{peak}/E_{acc}	2
H_{peak}/E_{acc}	42 Oe/MV/m
(R/Q) per cavity	1030 Ω^*
HOM loss factor $k_{\parallel}$ for $sigma_z$=1mm	9.24 V/pC*
Effective length L	1036 mm
Cavity length	1384.8 mm
$\Delta f/\Delta L$	404 kHz/mm
$df = f_{\pi} - f_{\pi-1}$	740 KHz
Aperture–diameter	70 mm
Cavity bandwidth $Q_{ext}3 \times 10^6$	433 Hz

Table 4.2: Choice of frequency

high:	high r/Q (low cryogenic load at fundamental)
	small surface area
	low stored energy
	low dark current
low:	small wakes $(K_{\perp}, K_{\parallel})$
	low HOM power
	long cavity module (for fixed # of cells)
	low R_{BCS} (thermally stable at high gradient)

broad minimum of total cryogenic load for 1 ... 3 GHz
low frequency
1.3 GHz, klystrons available

- The threshold for the onset of dark current i.e., captured field emitted current scales linearly with frequency. This has been calculated and was verified by experiments.[2] The threshold value is 25 MV/m at 2.5 GHz.

Arguments in favor of lower frequencies are:

- Wake fields are strongly influenced by the iris diameter. The longitudinal k factor (transverse k factor) scales inverse with the third (fourth) power of the iris diameter. Therefore emittance dilution is strongly reduced at lower frequencies.

- The maximum number of cells per cavity is mainly determined by HOM damping requirements. For a given cavity layout the number of "components" per length (couplers, welds, cryostat penetrations, tuners,...) increases linearly with frequency.

- The superconducting surface resistance R_{BCS} scales with f^2. Therefore a thermal runaway situation due to enhanced RF heating is suppressed at lower frequencies.[3] The key deciding factor for the choice of 1.3 GHz rather than 3 GHz is the global instability (thermal) limit on the maximum achievable magnetic field.

In summary the arguments for low frequencies are more relevant. The total cryogenic load due to fundamental and HOM dissipation shows a broad minimum around 1 to 3 GHz.[4] Pulsed high power klystrons are available at 1.3 and 3 GHz. In addition, lower frequency offers the further advantage of lower wake fields.

4.1.2   Choice of Geometry

Several geometric parameters of the cavity must be determined (see Table 4.3):

- number of cells

---

[2]G. Geschonke, D. Proch, Proceedings of LC92, Garmisch Partenkirchen, 1992, p. 407

[3]H. Padamsee, Proceedings of the 5th Workshop on RF Superconductivity, Ed. D. Proch, p. 903

[4]H. Padamsee, private communication.

Table 4.3: Cavity design choices.

A large number of cells are desirable, but one must worry about limitations of:	trapped modes
	tuning field flatness
	beam power per input coupler
9 cells, 1.04 m active at 1.3 GHz	
Choose cavity shape to optimize:	low E_{peak}/E_{acc} (field emission)
	low H_{peak}/E_{acc} (thermal stability)
	high cell to cell coupling (field flatness)
Parameters to play with:	equator ϕ
	iris ϕ
	iris shape
	transition equator to iris
optimization with URMEL	

- equator diameter,

- iris diameter,

- iris rounding,

- equator rounding,

- transition iris to equator,

- cut off pipe diameter,

- iris distance.

The number of cells should be high to get a large ratio of acceleration length to overall length (filling factor). The danger of trapped modes, field unflatness problems and the beam power per input coupler give an upper limit for this number. The extrapolation of the experience with 4- and 5-cell cavities in storage rings seems to allow a number of cells around 10. No striking arguments are known to propose an even or odd number. A choice of 9 cells was made for the TESLA cavity.

Table 4.4:   Cavity shape parameters, all dimensions in [mm].

cavity shape parameter	midcup	endcup 1	endcup 2
cavity radius Ro	103.3	103.3	103.3
external curv. radius R	42.0	40.34	42
iris radius Ri	35	39	39
horizontal half axis a	12	10	9
vertical half axis b	19	13.5	12.8
length L	57.692	56	57

Equator diameter and iris distance are fixed to first order by choice of frequency and velocity of light condition, respectively. The choice of diameter of the iris has different consequences to figures of merit like: the ratio of the peak electric surface field to the accelerating field, E_{peak}/E_{acc}, the fundamental shunt impedance, R, the cell to cell coupling, k, the ratio of magnetic surface field to the accelerating field, H_{peak}/E_{acc}, and the HOM loss factors, $k_{\parallel}$ and $k_{\perp}$. The chosen iris diameter of 70 mm is a compromise between reducing E_{peak}/E_{acc}, $k_{\parallel}$ and $k_{\perp}$ at an acceptable reduction of R and k and increase of H_{peak}/E_{acc}.

As a next step the iris rounding was varied in order to further decrease the E_{peak} value. URMEL was used to calculate the peak electric field for different shapes. As can be seen in Fig 4.1 a sufficient number of mesh points has to be used for consistent results. Fig. 4.2 shows the contour of three different shapes: a is the scaled HERA shape with a E_{peak}/E_{acc} ratio of 2.5, b and c are improved curvatures. The shape c was selected because of its higher cell to cell coupling value k of 1.87%. Fig. 4.3 and Table 4.4 lists the dimensions of the TESLA cavity.

4.1.3   HOM and HOM Couplers

4.1.3.1   Trapped HOM

Some higher order modes have the tendency to concentrate the stored energy in the middle cells. This results in low field values at the end cells and makes damping by HOM couplers at the beam pipe very inefficient. The TE_{121}
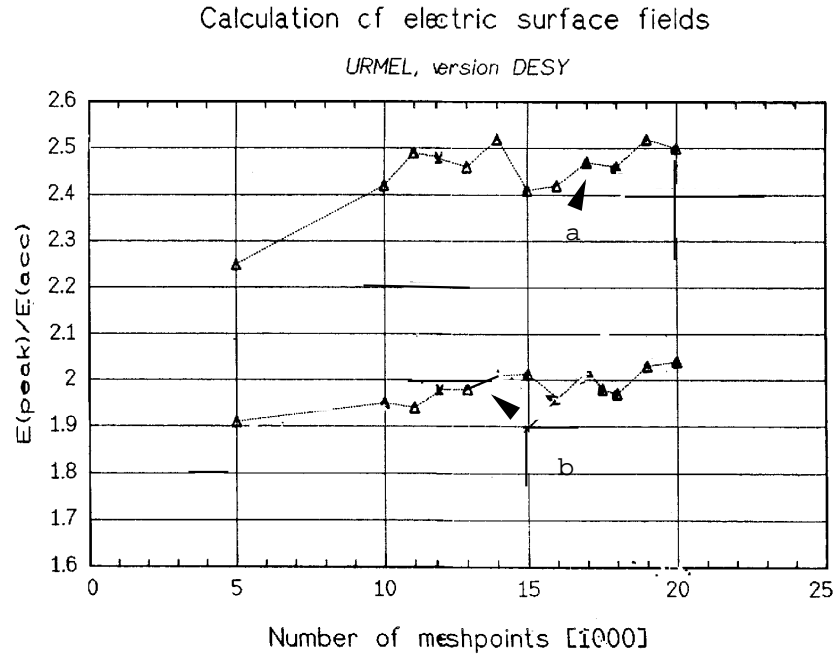
Figure 4.1:   URMEL calculation of E_{peak}/E_{acc} for different number of meshpoints, and two cavity shapes, a and b.

Figure 4.2:   Contour of different cavities for minimizing E_{peak}/E_{acc} (a: scaled HERA shape; b and c: improved cavity shape)
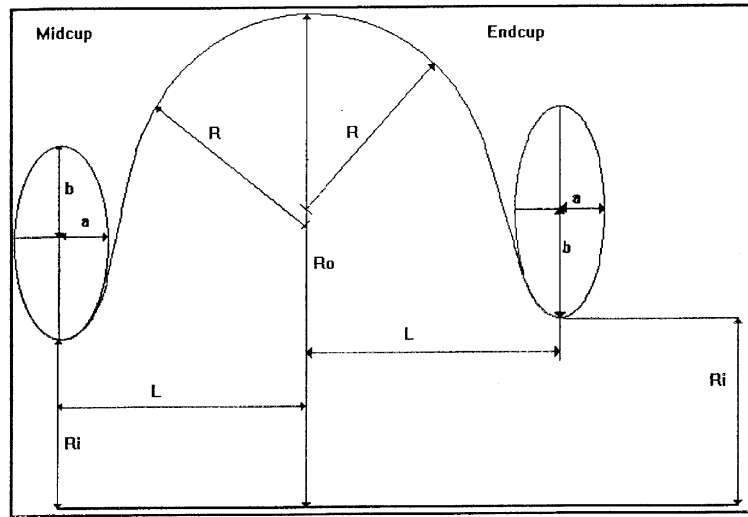
Figure 4.3: Geometric parameters of the TESLA cavity

mode is one of these resonances, which are usually named "trapped modes". The unequal distribution of the stored energy can be explained by different resonance frequencies of the individual cells. Both end cells are distorted by the presence of the beam pipe on either end of the cavity. In the fundamental mode frequency both end cells are compensated in order to produce a flat field profile. This is, of course, not true for the HOMs. Tuning the end cells for the "trapped modes" is is one way to improve the field profile. The fundamental mode should not be influenced by this method. The curvature from equator to iris, the iris ellipsis and the iris distance were modified in order to "untrapp" the TE_{121} but still have the TM_{010} accelerating mode flat and preserve good coupling for the TE_{111}, TM_{110} and TM_{011}. It turned out, that an asymmetric end cell tuning gave the best results.[5] The TE_{121} will have sufficiently high fields at one end of the cavity. Fig. 4.4 shows the field profile of the most dangerous member of the passband of the TE_{121} for non tuned (i.e., trapped modes) and asymmetric tuned end cells. This result will not be changed by errors in fabrication of the individual cells. Fig. 4.5 compares the field profile of the TE_{111} mode as fabricated and with artificial detuning of one cell by 1 MHz. Fig. 4.6 summarizes the effect of asymmetric end cell tuning.

Another method of tuning the end cells for HOM field profile might be to vary the length of the beam pipe between two 9-cell structures.[4] This method also produces sufficient HOM fields at the location of the HOM coupler. The disadvantage is that the cavity to cavity distance is no longer a free parameter.

Cavity Polarization

Dipole modes have two resonant frequencies with orthogonal field patterns. In the worst case a HOM coupler might see only electric fields at one resonance and magnetic fields at the other frequency. Therefore a single cell cavity should be equipped with two HOM couplers, one at each side and a relative angle of 90° between both couplers (see Fig. 4.7, upper graph). For a multi cell cavity, however, two couplers on each side are in principal needed. A sensitive HOM might have, in a nonpredictable manner, a tilt to the field profile due to fabrication tolerances (see Fig. 4.7, lower graph). One

---

[5]J. Sekutowicz, 6th Workshop on RF Superconductivity, Newport News (1993).
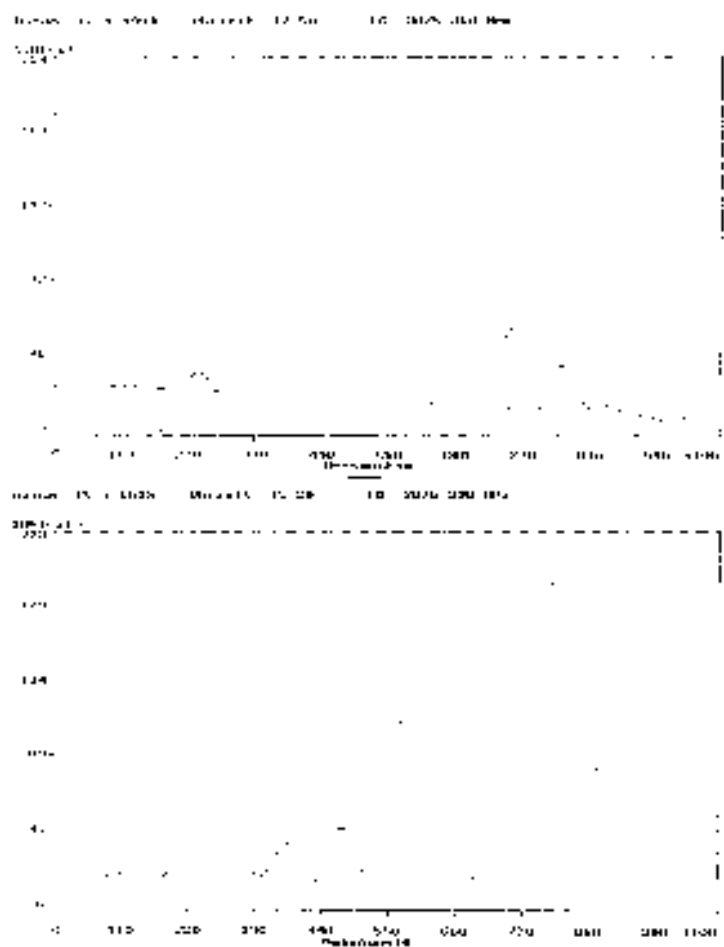
Figure 4.4:   Trapped TE_{121} mode (upper curve) and untrapped TE_{121} mode by use of asymmetric end cells (lower curve). The 9-cell cavity extends from 116 to 960 on the horizontal scale. Vertical scale is proportional to the magnitude of the electric field.
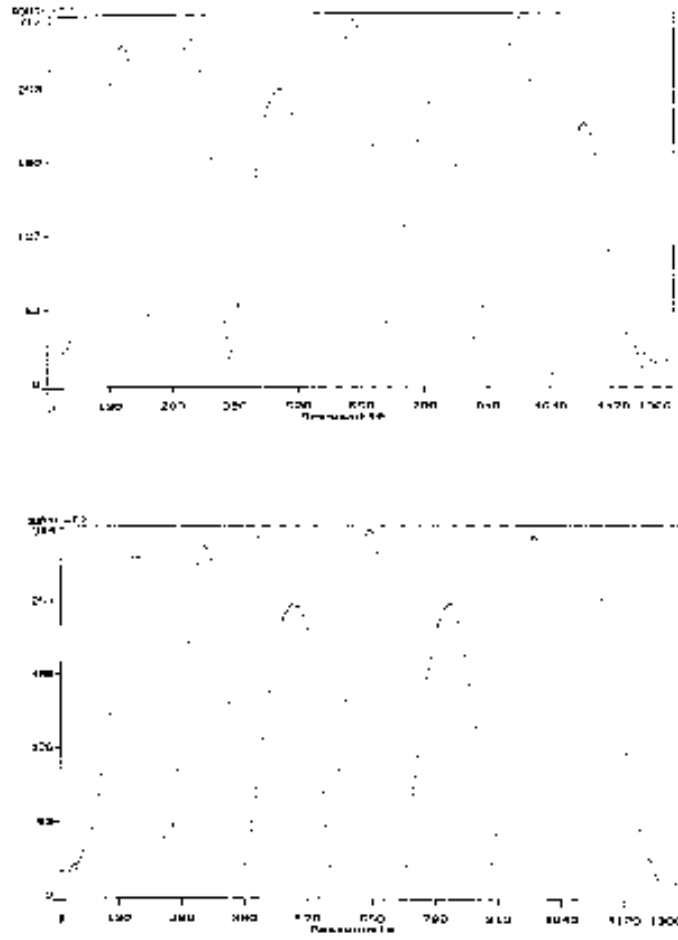
Figure 4.5: Effect of detuning of one cell to the TE_{111} field profile; upper curve as fabricated, lower curve with one cell detuned by 1 MHz.
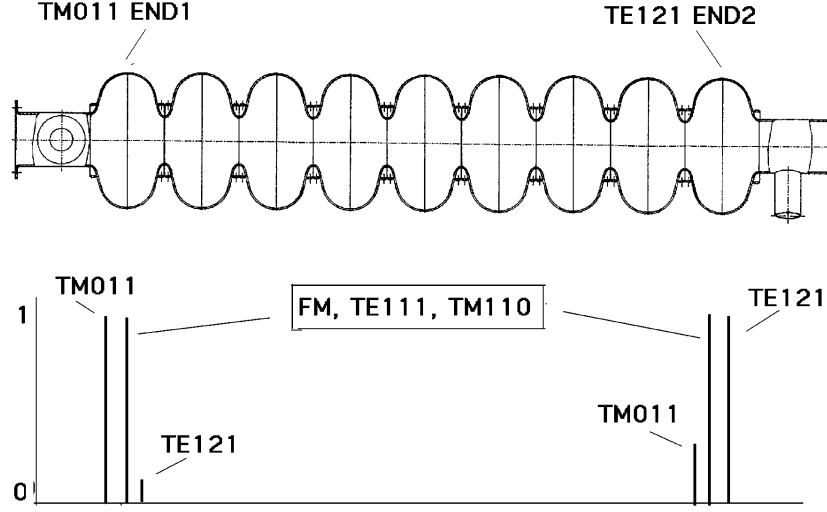
Figure 4.6: Effect of asymmetric end cell tuning. The magnitude of the fields in the end cells are indicated in the lower graph.

way to overcome the need of two HOM couplers on each side of the cavity is to polarize the cavity and thus fix the plane of polarization (see Fig. 4.8). The cavity can be polarized by a distortion of the azimuthal symmetry. This method increases the mechanical complexity of the cavity and will increase the fabrication costs. A closer look to the properties of the relevant dipole HOMs reveals the following conclusion (see Fig. 4.9):

a) Non propagating dipole modes (TE_{111}, TM_{110}): These two modes have a large cell to cell coupling factor. As consequence the field pattern is not very sensitive to fabrication errors. This qualitative statement is verified by the measurement on the 5 Cu 9-cell cavities. In no case was a tilted field profile observed. Therefore the situation is like in a single cell cavity where only one coupler on each side of the cavity is needed.

b) Propagating dipole mode (TE_{121}):
In this case the HOM coupler of the next neighboring cavity acts as the second coupler per cavity end. The relative angle between both couplers on one cavity is 115° (design for the welded HOM coupler).

All modes which are not rotational symmetric have two polarization due to
the perturbation of the symmetry of the cavity

1-cell structure

Very good coupling E
parallel to the antenna tip

Very bad coupling E
vertical to the antenna tip

2 HOM couplers shifted with angle φ Pi/(2m)
provide always coupling.
m=1 for dipoles
m=2 for quadrupoles
m=3 for sextupoles

N-cell structure

Not only polarization but also field unflattness makes damping more difficult

E has high amplitude but coupler is placed
at wrong azimuthal position,no coupling

E has low amplitude, coupler is placed
at good azimuthal position,no coupling

Figure 4.7: Damping of dipole modes. The upper graph demonstrates
that two couplers are needed for a single cell. The lower
graph demonstrates that four couplers are needed for a mul-
ticell cavity, without polarization.

Instead of 4 HOM couplers, one can try polarizing the modes and use only 2 couplers at each prot, but that each one couples to both polarization
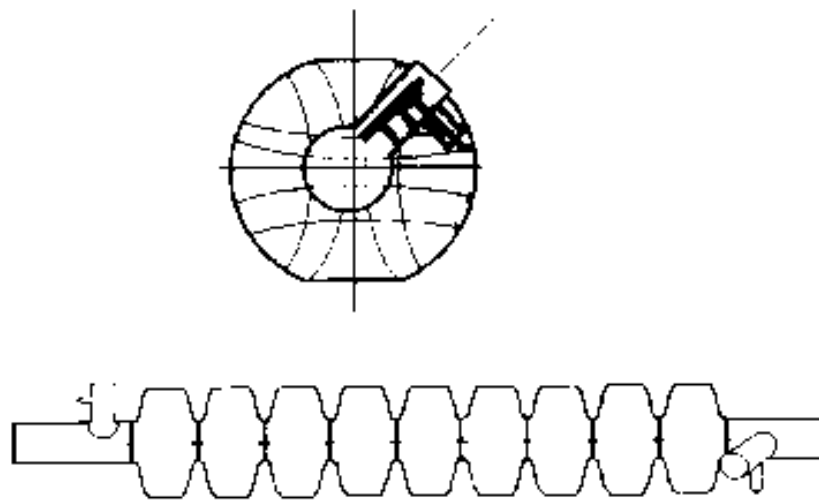
Figure 4.8:   Effect of polarizing the cavity. Only two couplers are needed for a multicell cavity.

Measurements proved, that this arrangement provides sufficient damping to both polarizations and for both types of couplers.

4.1.3.2   HOM Couplers

In order to restrict the multi-bunch phenomena due to wakefields, the higher order modes of the TESLA cavity must be damped down to the Q_{ext} level of $10^4 - 10^5$. For this purpose, special devices, the HOM-couplers, are mounted at both ends of the cavity, with a relative azimuthal angle close to 90° to insure the damping of both polarizations of dipole modes. They must strongly couple to the most dangerous HOMs, while rejecting by means of a filter, the accelerating mode. The coaxial type was chosen, because of their more compact size, but on the other hand the design of the helium vessel prevents liquid cooling of the antenna or loop. Two versions have been developed, one is welded to the cavity and the other one is demountable. Thermal calculations and power tests have been then carried out to study the thermal behavior under high field conditions.

Demountable HOM Coupler   The key component of the demountable type coupler is a loop whose plane is orthogonal to the beam axis (see Fig. 4.10), which couples mainly to magnetic field for the dipole modes and mainly to electrical field for the longitudinal modes. The rejection filter of the fundamental mode is simply formed by the inductance of the loop itself and the capacity between the loop end and the outer conductor. A capacitive coupling links the loop to the external load via a N-connector. The loop is cooled by conduction through an upper stub, which can be connected to the 2°K He bath through a thermal shunt. No stringent mechanical tolerances are necessary and the final tuning of the filter can be performed outside the clean room, once the coupler is mounted and the cavity is closed. This tuning is performed with the help of the small Nb bellow, located above the Helicoflex gasket. Table 4.5 gives the dampings measured with this coupler geometry on a 9-cell asymmetric cavity for the highest impedance modes and are well below the prescribed values. Tab. 4.6 and Tab. 4.7 present the HOM measurements.

Power tests in cw mode with this coupler (which was 5 times more coupled to the fundamental mode than the final TESLA coupler design in the

1) Non propagating dipole modes:
        TE111 and TM110

All 5 copper models did not show
any field unflatness:

- cells are well manufactured
- cell to cell coupling is big :
    k_{TE111} = 10 % and k_{TM110}= 4.8 %

2) Propagating dipole modes: TE121
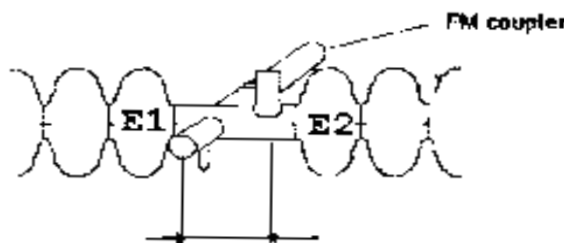
λ_{TE121}=144 mm $2 \lambda_{TE121} - \lambda_{TE121}/4 \cong 256$ mm

Lower frequencies (6 untrapped modes):
    - Qext 3 orders of mag. below
      required values.
Higher frequencies:
    - all propagating modes which have
      stored energy in the beam tubes
      are damped by 4 HOM couplers and
      couplers change polarization of
      the modes.

Figure 4.9:   Strategy to overcome the need of polarizing the cavity.
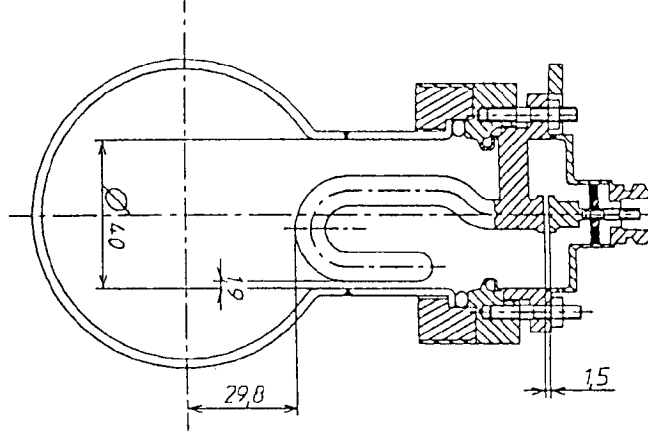
Figure 4.10: Demountable HOM coupler.

Table 4.5: Damping measurements with the demountable coupler.

Mode	Frequency (MHz)	R/Q	Meas. Qex ($\times 10^4$)
TE111	1706.43 1707.57	10.0 Ω/cm^2	0.22 0.45
TE111	1734.11 1734.50	15.4 Ω/cm^2	0.36 0.16
TM110	1874.41 1874.92	8.7Ω/cm^2	7.3 5.4
TM011	2448.29	67.0 Ω	5.8
TM011	2454.03	79.5 Ω	11.0

experiments) and the associated thermal shunt showed no abnormal thermal behavior up to an accelerating field of 21 MV/m, limited by a quench of the cavity. The maximum temperature measured on the stub end is plotted on Fig. 4.11 at different field levels. In pulsed mode, the temperature distribution obviously depends on the duty cycle. For the TESLA RF duty cycle of about 2%, a safety margin of at least 10 is expected for the thermal quench of the coupler. Without thermal shunt, the safety margin would be reduced because of the contact resistances of the gasket-flange assembly (in cw mode,
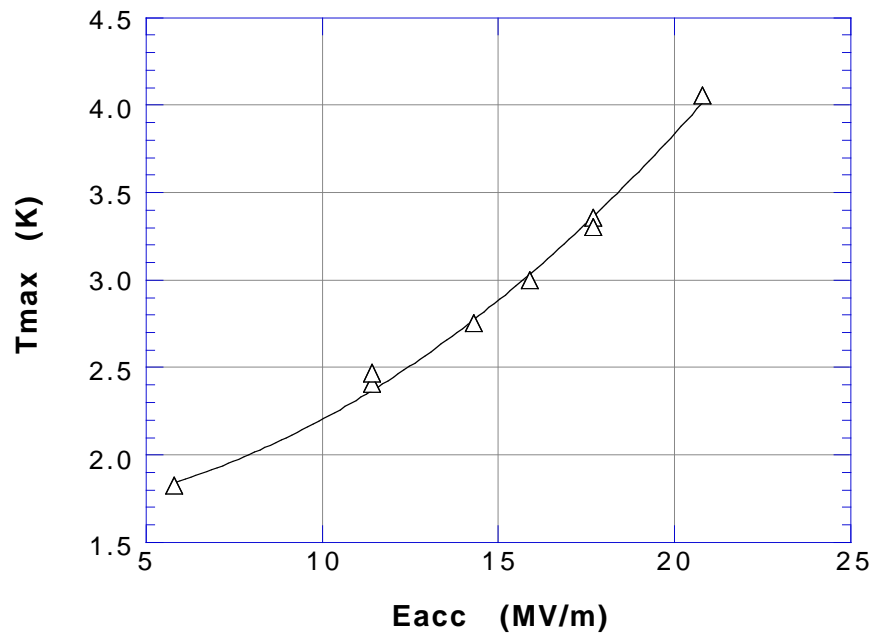
Figure 4.11:   Maximum temperature on the stub end of the coupler vs cw field.

the quench of the coupler occured at a field of 13 MV/m). In addition, tests in pulsed mode, made by detuning the filter, showed that the coupler can withstand the peak power during the pulse (1.75 kW) induced by the HOMs when they are excited resonantly by the beam.

Welded HOM Coupler The welded version (see Fig. 4.12), constructed and partially tested at DESY, is based on the HOM couplers designed for the superconducting 500 MHz, four-cell HERA cavities.[6] Three years of the experience with 48 couplers in the HERA electron ring showed that this type of coupler works stably without quenches in cw operation at 4–5 MV/m and beam current up to 30 mA, even in the presence of strong γ radiation. The good cooling of the inner conductor by two stubs makes the welded coupler less sensitive to the γ and electron bombardment than the demountable coupler. A disadvantage of this version is that the mechanically complicated inner part of the coupler requires more effort in the fabrication and make more difficult the chemical cleaning and the heat treatment. On the other hand, the probability of dust contamination is reduced since only small output flanges must be attached during the final assembly. It seems possible to simplify the fabrication of the inner part to lower the cost of the coupler. The electron beam welded inner part, which consist of the inner conductor and two inductive stubs can be replaced by one part, fabricated as a whole out of the 8 mm thick Nb material. [7]

Measurements Many copper models of both versions have been built to optimize coupler dimensions, the position of the coupler ports, and the orientation and penetration of the coupling elements. Pairs of the welded couplers have been tested on the asymmetric cavity models. Pairs of the demountable couplers have been tested on both symmetric and asymmetric cavities.

Tab. 4.6 and Tab. 4.7 contain Q_{ext} values of dipole and monopole modes, measured for the most recent versions of both HOM couplers. The last column of Tab. 4.6 shows the BBU limit for these calculations of high R/Q dipole modes and of these modes which in the standard cavities, without the

---

[6]J. Sekutowicz, *HOM Couplers at DESY*, Proceedings of 3rd Workshop on RF Superconductivity, ANL Illinois, ANL-PHY-88-1/2, 1987.

[7]H. Kaiser, private communication
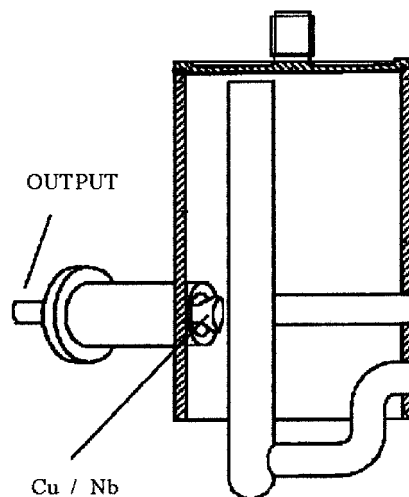
Figure 4.12: Welded version of HOM coupler

endcell modification or the distance adjustment, would be trapped (TE_{121} passband).

In the case of monopole modes, Q_{ext} values were chosen to keep peak power out of the coupler below the specification for the cables used in the TESLA cryomodules and to lower the heat losses due to their attenuation ($\approx$ 1dB per cable, 16 HOM cables in each cryomodule).

The comparison of the measured Q_{ext} values with the BBU limit shows that both of the coupler types provide enough damping of those HOM's which have been taken into account in the emittance growth calculation.

Table 4.6: Damping of dipole modes

MODE	FREQ.	R/Q	2 welded couplers on asymmetric cavity	2 demount. couplers on asymmetric cavity	2 demount. couplers on symmetric cavity	BBU LIMIT
			Qext	**Qext**	**Qext**	**Qext**
	[MHz]	[W/cm2]	[1.0E+3]	[1.0E+3]	[1.0E+3]	[1.0E+3]
TE111 1	1622.2	0.01	193	290	210	
2	1622.3		366	100	540	
3	1629.8	0.14	48	40	60	
4	1629.9		77	40	100	
5	1642.2	0.03	25	16	19	
6	1642.3		37	61	61	
7	1659.1	0.75	42	12	7.6	
8	1660.3		22	8.9	28	
9	1681.2	0.04	11	9.1	5.6	
10	1682.2		23	4	14	
11	1706.7	10	4.8	2.2	2.3	8.1
12	1707.8		5.5	4.5	7.4	8.1
13	1734.0	15.4	3.4	3.6	1.1	7.5
14	1734.3		4.5	1.6	3.2	7.5
15	1762.1	2.23	2.7	4.1	2.2	7.4
16	1762.2		3.2	1.8	3.2	7.4
17	1786.5	1.4	2.1	4	2.8	
18	1789.4		2.8	1.8	2.8	

MODE	FREQ.	R/Q	2 welded couplers on asymmetric cavity	2 demount. couplers on asymmetric cavity	2 demount. couplers on symmetric cavity	BBU LIMIT
			Qext	**Qext**	**Qext**	**Qext**
	[MHz]	[W/cm2]	[1.0E+3]	[1.0E+3]	[1.0E+3]	[1.0E+3]
TM110 1	1799.9	0.71	5.2	4.6	4	
2	1800.9		4.2	2.1	13	
3	1835.7	0.45	19.8	32	21	47
4	1837.0		18.9	16	15	47
5	1852.7	0.33	27.7	38	22	52
6	1853.2		20.9	19	24	52
7	1865.3	6.47	50.6	52	48	76
8	1865.5		26.5	28	30	76
9	1874.4	8.75	50.2	73	43	120
10	1874.8		51.1	54	85	120
11	1880.8	1.83	95.1	126	99	194
12	1881.2		85.5	94	86	194
13	1885.2	0.1	18.1	322	130	330
14	1885.4		75.2	121	190	330
15	1887.4	0.18	633	472	480	670
16	1887.8		251	250	250	670
17	1889.1	0.01	1800	3270	520	
18	1889.4		1500	3270	1400	

MODE	FREQ.	R/Q	2 welded couplers on asymmetric cavity	2 demount. couplers on asymmetric cavity	2 demount. couplers on symmetric cavity	BBU LIMIT
			Qext	Qext	Qext	Qext
	[MHz]	[W/cm2]	[1.0E+3]	[1.0E+3]	[1.0E+3]	[1.0E+3]
TE121 1	3075.7	0.11	171	62	6900	1.0E6
2	3076.0		229	1200	300	1.0E6
3	3076.5	0.01	408	59	650	1.0E6
4	3076.7		121	660	1600	1.0E6
5	3077.5	0.02	569	140	520	800
6	3077.6		79.5	210	2900	800
7	3079.0	0.14	248	39	610	600
8	3079.1		35	230	1400	600
9	3081.9	0.92	94.3	27	11	800
10	3082.1		44.5	41	17	800
11	3087.4	1.27	43.7	10		600
12	3087.7		75.9	52		600
13	3097.0	0.16	33	27		
14	3097.2		102	12		
15	3113.3	0.02	16.8			
16	3113.5		98.9			

Table 4.7: Damping of monopole modes.

MODE		FREQ.	R/Q	2 welded couplers on asymmetric cavity Qext	2 demount. couplers on asymmetric cavity Qext	2 demount. couplers on symmetric cavity Qext	Qext Limit
		[MHz]	[W]	[1.0E+3]	[1.0E+3]	[1.0E+3]	[1.0E+3]
TM011	1	2379.6	0.00	350.0	1150	1600	
	2	2384.4	0.17	72.4	360	460	
	3	2392.3	0.65	49.5	140	220	
	4	2402.0	0.65	84.0	68	110	
	5	2414.4	2.05	32.0	70	97	
	6	2427.1	2.93	29.1	81	59	
	7	2438.7	6.93	20.4	66	49	1000
	8	2448.4	67.04	27.4	58	51	100
	9	2454.1	79.50	58.6	110	100	100
TM012	1	3720.0	1.26	3.0			
	2	3768.9	0.07	5.1			
	3	3792.2	0.75	5.2			
	4	3811.7	1.43	3.9			
	5	3817.5	0.18	15.2			
	6	3829.2	2.33	11.3			
	7	3839.8	0.77	40.0			
	8	3845.3	22.04	240.0			300
	9	3857.3	6.85	6.1			1000

Broadband Characteristics   Preliminary computation and measurement confirm expectation that some of the modes are above cutoff of the beam tube can be trapped between two neighboring structures. Since the interconnection between two cavities is superconducting the only damping of these modes is provided by the HOM and input couplers. To avoid buildup of the parasitic fields one should use couplers with broadband characteristics. The transfer function of the welded coupler, measured up to 10 GHz, shows that in this frequency range can still provide HOM damping.

Fundamental Mode Rejection Filter   The fundamental mode rejection filters of both couplers have been optimized for minimum RF power transferred from the cavity to an external load. The characteristic of the filter of the welded coupler shows that the filter detuning of $\pm$ 20 MHz causes reduction of the Q_{ext} to 5×10^9, which is still save. For $Q_{ext} = 5 \times 10^9$ the mean values of the extracted power from the fundamental mode is only 1 W at $E_{acc} = 25 MV/m$ (100 W peak). Both coupler versions have the possibility

of final filter tuning after the coupler is already attached to the cavity. The adjustment makes the fundamental mode Q_{ext} higher than 1×10^{11}, limiting the coupler power to less than 50 mW at 25 MV/m. During the TESLA operation rejection filter should stay very stable since the couplers are placed in the insulating vacuum, and no change of pressure difference between between the insulating and the beam vacuum is expected. To lower cavity cost one may use the HOM coupler as the pickup probe. For this purpose Q_{ext} in the range from 1×10^{10} to 5×10^{10} should give enough signal to drive all electronic devices for phase and amplitude control.

Cold Test of HOM Couplers   The existing 1.5 GHz infrastructure at Saclay has been used for testing of HOM couplers at 4.2 K and 2 K. Niobium models (RRR≈300) of HOM couplers scaled from 1.3 GHz to 1.5 GHz had been prepared at Saclay[8] and tested on two 1.5 GHz single cell cavities. Couplers have been placed in vacuum as is planned later in the TESLA cryostat. Six temperature sensors were attached to the coupler and the beam tube for temperature mapping during the test. The welded coupler was test twice. For the first test, the output antenna tip was made of low quality copper. The heat produced by the magnetic field at the output location (about 2% of the field at the equator of the cavity) was high and the increase of the temperature was detected by all sensors placed near to the output flange. An additional heater mounted on the output flange has been used to estimate the total heat produced by the magnetic field. To get the same temperature maps as at 5 and 10 MV/m, the power of the heater was driven to 80 mW and 320 mW respectively. For the next experiment, the cavity was once more chemically cleaned (5 μm) and the Cu part was replaced by the Nb part. The measurement of Q_o vs E_{acc} has been continued until indication of the temperature increase of the output flange was detected. At this point, a drop in Q_o from 1.8×10^{10} to 6.5×10^9 was observed. The magnetic field heating of HOM couplers in the cw operation exceeds by far the heating expected for the TESLA operation in the pulse mode with a duty factor of 1.4%. The extrapolations of the measured behavior toward the shorter duty cycle cross the design value line E_{acc} = 25 MV/m at a duty cycle of 30–35 %, which is still 20 times higher than the duty cycle of the TESLA collider. Unfortunately, measurements for the TESLA duty factor could not be made

---

[8]S. Chel, M. Juillard, private communication

due to the quenching of both single cell cavities.

4.1.4 Filling Time

The slope in the Brillouin diagram can be interpreted as group velocity. For the TESLA 9-cell cavity this slope at the π-mode frequency is near to zero. Therefore the question has been raised, as to whether the beam extracted power can be refilled uniformly in the 1 microsec time between bunches. Some measurements were done on a 9-cell copper cavity to investigate the transient behavior of a standing wave structure. The cavity was exited by a fast RF-pulse in cell 1 and the fields in the other cells were monitored. This experiment was simulated by a lumped element circuit. There is good agreement between experiment and model calculation.[9] The main conclusions are:

- The delay of the start of filling depends on the distance from the drive cell.

- The filling curve is modulated by an interference type of distortion.

- At some time intervals the more distant cells have a higher field than the near by cells.

- The filling process does not depend on the drive frequency; it does depend on the rise time of the drive pulse.

Fig. 4.13 shows a comparison of measured and calculated filling behavior. The amplitude modulation of the filling curve is caused by interference between fields of other members of the passband. With the given parameters of the 9-cell cavity ($Q_0 = 5 \times 10^9$, $Q_{ext} = 3 \times 10^6$ and coupling k=1.87%) all nine cells will be refilled within the 1 microsec between bunches. The modulation of the filling curve might degrade the energy resolution of the beam. This effect can be substantially reduced by increasing the rise time of the drive pulse.[10]

---

[9]J. Sekutowicz, to be published in Particle Accelerators.
[10]J. Sekutowicz, to be published in Particle Accelerators.
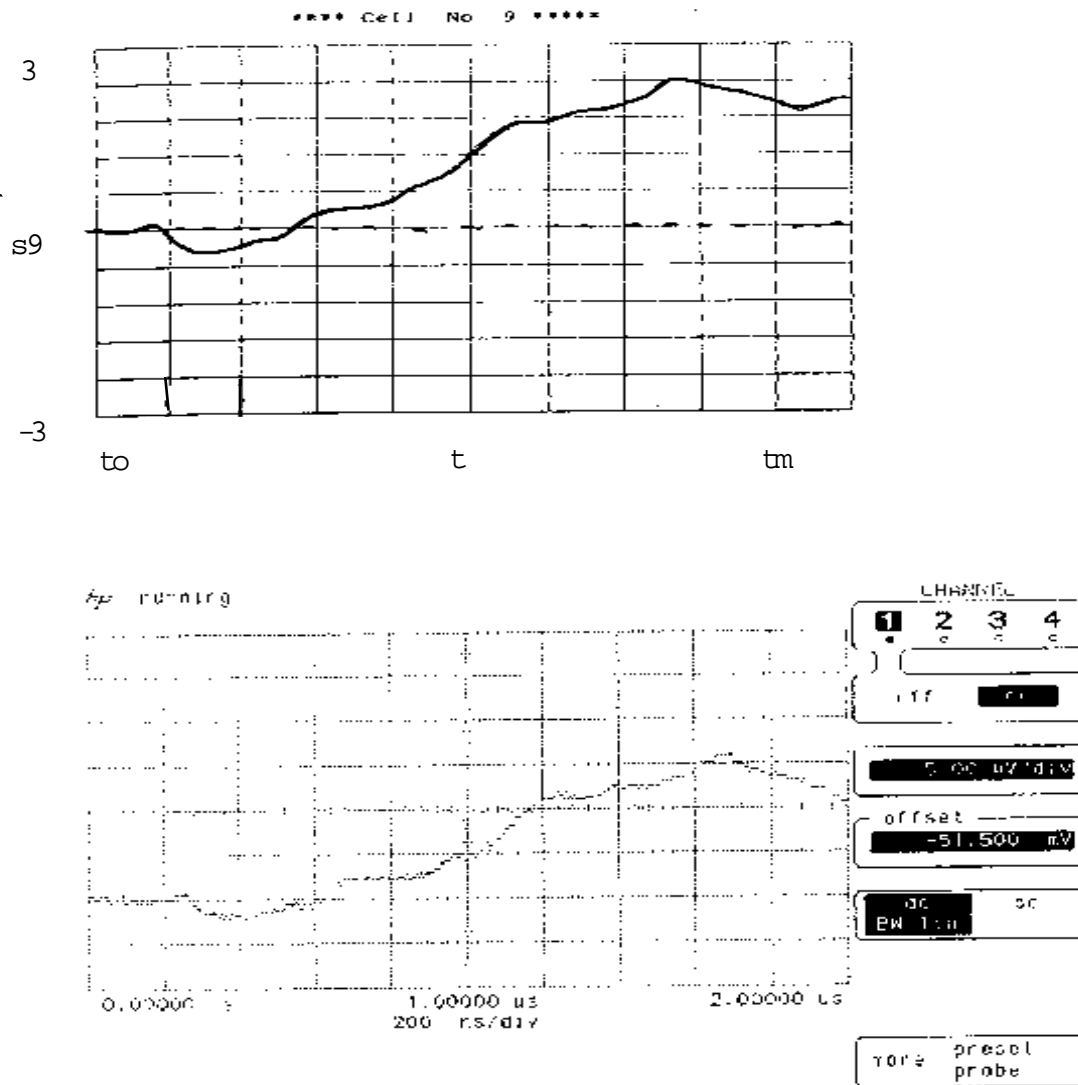
Figure 4.13:   Filling process of a 9-cell cavity; drive pulse in cell 1, field in cell 9: upper curve as calculated, lower curve as measured. Horizontal axis in both cases 200 nsec/div or 2 microsec full scale. The vertical axis is proportional to electric field in cell 9.

4.2 Auxiliary Systems

The bandwidth of the loaded cavity system at a quality factor of 3×10^6 is only about 433 Hz. Thus especial attention must be given to the tuning system and the mechanical rigidity of the cavity, its helium vessel and the tuning system itself. The Lorentz force of the pulsed electromagnetic field in the cavity causes time-dependent mechanical deformations of the cavity and results in changes in resonant frequency. These frequency changes must be minimized and a strategy must be worked out so that the low level RF phase and amplitude control can compensate for remaining changes during the RF filling and beam pulse time. The present design should stabilize the shift of resonant frequency to less than 500 Hz.

The Q value of the cavities and resultant cryogenic load depends on the surface resistance. It has two parts: the theoretical resistance R_{BCS} and the residual resistance R_{res}. At 1.3 GHz and 1.8 K the contribution of the trapped earth's magnetic field to R_{res} dominates the surface resistance. Therefore, a careful design of the magnetic shielding is necessary.

Achieving high gradient in the superconducting cavities is a fundamental goal of TTF. Just as important as the cavity itself is the RF input coupler. Experience has shown that it is difficult to design a reliable, trouble-free, coupler and RF windows. The TTF coupler must transfer 200 kW power at nominal conditions and be capable of HPP processing at higher levels if cavity degradation occurs after installation.

4.2.1 Summary of Lorentz Force Detuning and Cavity Stiffening

The geometry of the stiffened cavity is optimized by first computing the electromagnetic field for the π-mode in the unperturbed cavity[11] at $E_{acc} = 25\,MV/m$. For convenience the quantities $\epsilon_0 E^2$ and $\mu_0 H^2$ at the inner surface are plotted in Fig. 4.14. The pressure on the cell wall is then

$$P = \frac{1}{4}(\mu_0 H^2 - \epsilon_0 E^2) \tag{4.1}$$

---

[11]Calculations performed by M. Marx, Jacek Sekutowicz, DESY; A. Mosnier, Saclay and Massimo Ferrario INFN Frascati
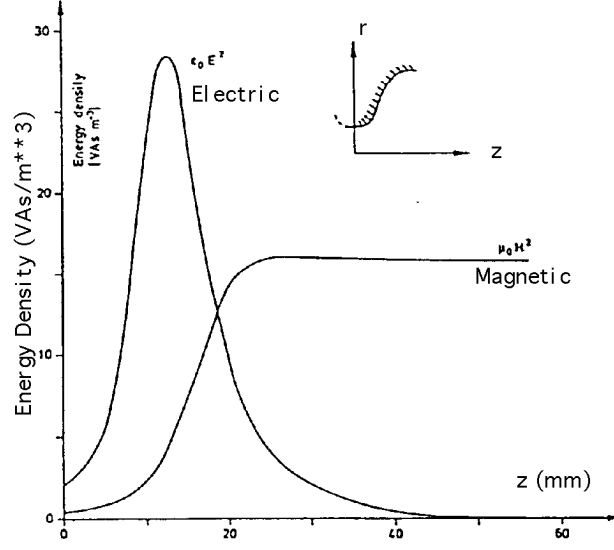
Figure 4.14: Energy density at inner surface of a half=cell.

The resulting change of cell form is computed for a particular geometry of stiffening with the FEM code "IDEAS" and results in a cell volume change ΔV. This causes a frequency shift Δf [12] that is to be minimized:

$$\frac{\Delta f}{f_0} = \frac{1}{4W} \int_{\Delta V} (\epsilon_0 E^2 - \mu_0 H^2)dV \qquad (4.2)$$

where

$$W = \frac{1}{4} \int_v (\epsilon_0 E^2 + \mu_0 H^2)dV \qquad (4.3)$$

and f_0 =resonant frequency of the unperturbed cavity.

The stiffening geometry shown in Fig 4.15 has been chosen for the TTF cavities. The diameter of the stiffening tube has been optimized for minimum frequency shift due to Lorentz-forces. The characteristics of this stiffening scheme are:

- The stiffening tube is loaded in an almost ideal way. It connects the walls of adjacent cells and thus causes compensation of equal and opposite forces. It is under axial tension with only small circumferential stress. Only a relatively small amount of Niobium is needed.

---

[12]Calculation by H.B. Peters, DESY
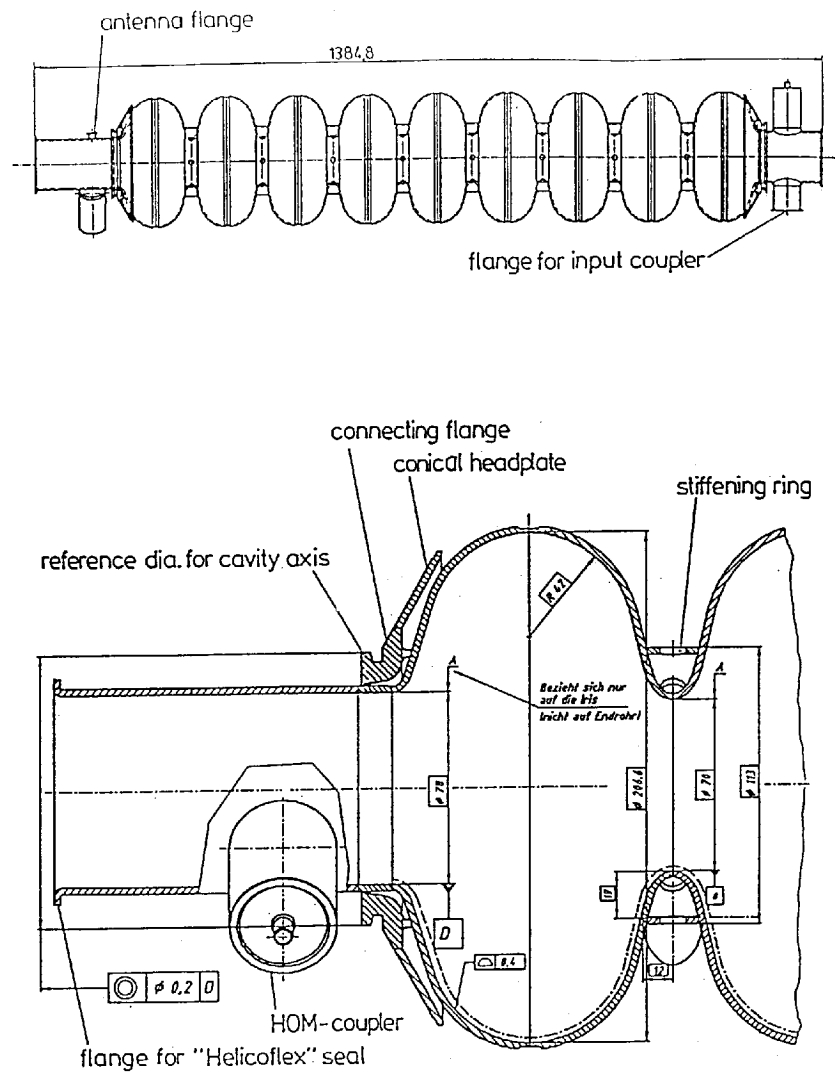
Figure 4.15:   TTF Cavity with conical reinforced head plate and stiffening
ring.
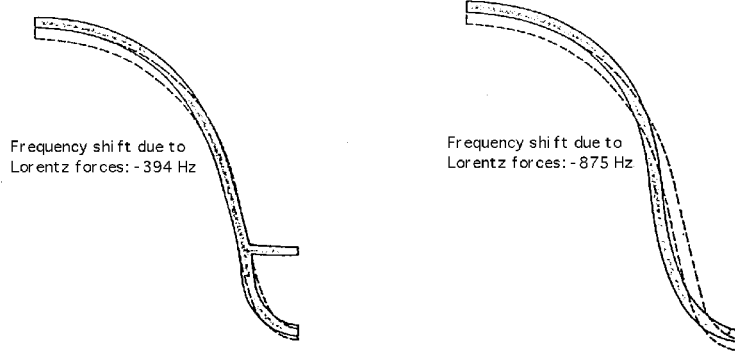
Figure 4.16:   a) Deformation of a 2.5mm thick stiffened cell wall due to
                Lorentz forces of $E_{acc} = 25 MVm^{-1}$ (gray = deformed). b)
                Deformation of a 2.5mm thick unstiffened cell wall due to
                Lorentz forces at $E_{acc} = 25 MVm^{-1}$ (gray = deformed).

- The frequency shift at constant cell length due to Lorentz forces com-
  puted by Eq. 4.2 as described is -394 Hz for a 2.5 mm thick cavity wall.
  Without stiffening it would be -875 Hz. The deformations of cell wall
  for these 2 cases are shown in Fig. 4.16. It is seen that deformation
  of the stiffened cell is negligible for the region where the electric field
  is large (near the iris), but nearly unchanged with respect to the un-
  stiffened cell where the magnetic field dominates near the equator. As
  a result the corresponding contributions to frequency shift are -16 Hz
  and -378 Hz. No elegant scheme exists to reduce the latter contribu-
  tion. Only increasing the wall thickness near the equator could decrease
  stress and deformation here.

- The constraint needed to hold cell length constant experiences at $E_{acc} =$
  25 MV/m a force of 31 N (the cavity wants to become shorter). A *real*
  constraint, consisting for example of a He vessel around the cavity
  and some tuning mechanism, is not ideally rigid and will allow some
  decrease $-\Delta L$ of cavity length causing the aforementioned frequency
  shift of -394 Hz due to change of cell form to be *enhanced* by $-\Delta L[mm]\cdot$
  $530[kHz/mm]$ (c.f. Tab. 4.9). This effect imposes lower limits on the
  rigidity of He-vessel, tuner and He-vessel head at the non-tuner end.
  For instance, the conical plate (Fig. 4.15) connecting the cavity to the

He-vessel at the input-coupler end contributes -59 Hz to detuning at 25 MV/m.

- For plastically increasing the length of a particular cell for tuning purposes the necessary force is introduced just outside the stiffening tube against the neighboring cells leaving them undistorted and therefore undetuned.

  In an unstiffened cavity, plastically lengthening a cell is known to detune its neighbors.

- Flexural rigidity and resonant frequencies are increased[13] with respect to unstiffened cavity (c.f. Table 4.8).

- The stiffening tubes are compatible with external etching requirements where through 2 diametrically opposed slots the acid can drain completely with cavity axis horizontal. The welds to the half cells are continuous and by electron beam, as are all other welds on the resonator.

- The "connecting ring" at the ends of the undulated structure stiffens the end cells in a way characteristic for the inner cells, allows cooling for part of the end tube, serves as a reference for the cavity axis, may be attached to the tuner or handling devices during processing and forms part of the He-containment. The shape of this ring is carefully optimized to keep maximum stress below 29 N/mm^2.[14]

- All 9 cells share equally in cold tuning. The field distribution over the 9 cells is very nearly left unchanged by changing cavity length. Small changes are only possible in case of variation of wall thickness from cell to cell. If in a hypothetical resonator of initially flat field distribution the cells 1 to 5 were at the permitted minimum wall thickness of 2.65 mm, and the cells 6 to 9 at the permitted maximum of 2.95 mm, the field-unflatness produced by a resonant frequency shift of 500 kHz (caused by changing the cavity length) would be 13%.

---

[13]H.A. Schwettmann, Stanford University, Private Communication.
[14]Calculation by H.B. Peters, DESY.
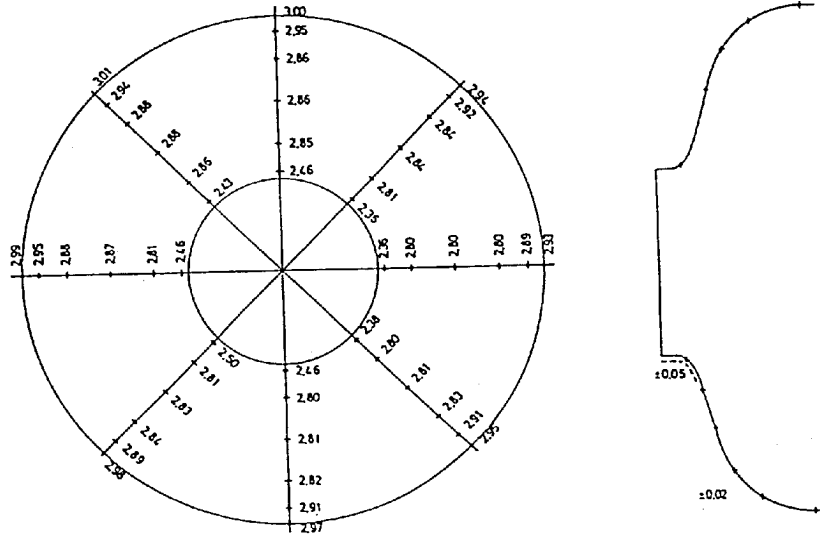
Figure 4.17:   Typical measured thickness variation of cavity cell.

- The cavity, at its end tubes is provided with HOM[15] and input[16] couplers, as shown and has a pick up antenna. The flanges at the end tubes are formed onto the prefabricated tubes and are intended to be sealed with metal gaskets ("Helicoflex").

The properties related to elastic deformation of the stiffened cavity have been checked on Nb 9-cell test cavities with wall thickness variation similar to that of Fig. 4.17 as far as it is possible at RT with low power RF. The results are indicated in Table 4.8 and agree relatively well with the calculated values if one considers that the real cell wall is non-uniform and that its average value is larger than the 2.5 mm wall assumed for the calculations.

As the Young's modulus of Nb changes little with temperature, the values of Table 4.8 will also approximately hold at LHe-temperature.

---

[15] J. Sekutowicz, 6th Workshop on RF Superconductivity, Newport News (1993).

[16] B. Dwersteg, et al., "TESLA Main Coupler Development at DESY", 6th Workshop on RF Superconductivity, Newport News (1993).

Table 4.8:   Selected Properties of TTF-Cavity. Calculated values are for a cell wall 2.5 mm thick; measured values are for a test cavity with thickness of cell wall as in Fig. 4.17.

Characteristics	stiffened		unstiffened		Unit
	calc.	meas.	calc.	meas.	
Effect of Lorentz-forces at Eacc=25 MV/m length held constant					
Frequency shift due to H-field only	-378		64		Hz
Frequency shift due to E-field only	-16		-939		Hz
Total frequency shift	-394		-875		Hz
Tuning					
force to change cavity length by 0.18 mm	517	554	290	282	N
Frequency shift as function of cavity length	530	404	440		kHz/mm
Effect of change of external pressure at const. length					
Frequency shift	+15	10.3 ± 1	-12		Hz/mbar
Max. stress at 3 bar	12		26		N/mm^2
Sag, Vibration					
Deflection. one end supported other end fixed	0.2	0.17			mm
Frequency of lowest transverse vibration mode	50.8		32.8		Hz
Frequency of lowest longitudinal vibration	199		166		Hz

4.2.2 Helium Vessel

The He tank contains the super fluid helium needed for cooling the RF cavity[17] of the TESLA Test Facility. It also supports the cavity, and takes part in tuning it.

The design put forward in this note differs from an earlier one in that it incorporates recent proposals for the TESLA cryogenic system[18] leading to smaller He inventory, reduced cold mass and gentler yet faster cool down and warm up. Further it reduces Lorentz force detuning, and - by being more compact - opens the way for a less costly smaller future cryostat.

The tank is made from titanium rather than the more commonly used stainless steel to reduce problems with joining to niobium, and relative shrinkage with respect to the cavity.

4.2.2.1 Cryogenic features

The earlier design of the He vessel (Fig. 4.19) was with ca. 380 mm substantially larger in outside diameter than the cavity. With the liquid He partially filling the He supply tube, the 2 phase flow in steady state passes through the upper part of the He tank with a rather generous amount of He surrounding the cavity and an unnecessarily large gas-liquid interface.

The present design (Fig. 4.18) has a He vessel diameter slightly larger than that of the cavity, a separate 2 phase tube of 72 mm inner diameter connected to the He vessel by a vertical tube of diameter 60 mm, and a LHe volume of only 22 l as compared to 65 l of the earlier design (both vessels considered filled with liquid to the axis of the 2 phase tube).

Further, while in both designs cool down through the 2 phase tube would present no problems with one cavity after the other filling with liquid, there may during warm up be insufficient heat exchange between hot gas above and cold cavities below with buoyancy preventing the gas to flow downward. This effect would be more pronounced in the present design. To remedy this, a tube of diameter 40 mm feeding He to the *bottom* of the tanks via capillaries of diameter 3 mm has been introduced (Fig. 4.20). The flow is distributed quite evenly over the string of He vessels because the capillary has much greater flow resistance than the 40 mm tube, and heating is therefore

---

[17]D. Proch, 6th Workshop on RF Superconductivity, Newport News (1993).

[18]G. Horlitz, D. Trines, T. Peterson, 15th Int. Cryogenic Eng. Conf., Genova (1994).

much gentler and more effective than in the old design. Cool down can of course also occur via the capillaries.

4.2.2.2 Shift of Resonant Frequency

The He vessel with tuner bounds the environment that is capable of effecting shifts of cavity tune from (in decreasing importance) Lorentz forces, He pressure fluctuations and temperature changes. Only the first 2 effects will be treated, as temperature influence under steady state operation is negligible (below 10K very little, if any, thermal contraction occurs).

Consider the cavity held to constant length by some ideally rigid external constraint. At $E_{acc} = 25 MV/m$ the Lorentz forces would produce a calculated resonant frequency shift of - 347 Hz due to deformation of *cell form*. The cavity, in addition, would exert a force of F = - 31 N on the constraint (the cavity wants to become shorter). Removing the constraint will cause the cavity length L to decrease elastically, and suffer a resonant frequency shift of:

$$\Delta f_{\text{unconstr.}} = -347 + \partial f / \partial L \cdot \partial L / \partial F \cdot F \qquad (4.4)$$

That one may superimpose the 2 contributions has been verified by first computing the cavity form change produced by both effects acting together, and then the corresponding shift of resonant frequency, which equaled that from Eq. 4.4.

$$
\begin{aligned}
\text{With} F &= -31N, \text{ and measured values}^{19} \text{ of} \\
\partial f / \partial L &= 404 kHz/mm, \text{ and} \\
\partial L / \partial F &= 3.25 \cdot 10^{-4} mm/N \text{ there results:} \\
\Delta f_{\text{unconstr.}} &= -4416 Hz.
\end{aligned}
$$

This intolerably large resonant frequency shift demonstrates the need for rigidity in the *real* constraint consisting of tuner, He tank and conical vessel - heads (for the earlier design, also the dome shaped vessel-heads). The calculated Lorentz force induced shift of resonant frequency for each of the above named components as well as the resulting total resonant frequency shift is recorded for the 2 tank versions in Table 4.9. The rather large contributions from the head domes do not exist for the smaller vessel, and favor it by a decrease of resonant frequency shift by 281 Hz.

Table 4.9:   Contributions to resonant frequency shift [Hz] at 25 MV/m
               (see text)

Tank type	tuner	head dome right	tank tube	head dome left	conical head	deform. cell form	total shift
large dia.	-68	-140	-23	-161	-59	-347	-798
small dia.	-68		-43		-59	-347	-517

The shift of resonant frequency produced by a change in He pressure Δp also arises from 2 additive effects: With cavity length held constant, there has been measured[20]:

$$(\partial f/\partial p)_{\text{cell deformation}} = 10.3 Hz/mbar.$$

The effective area of the large bellow near the tuner exceeds that of the cavity which also acts like bellow. Therefore, increasing the He pressure tends to lengthen the cavity. The corresponding resonant frequency shift (ignoring pressure induced tune shift) has been calculated for the cavity constrained by the small He tank and tuner at:

$$(\partial f/\partial p)_{\text{length change}} = 10 Hz/mbar.$$

Adding the 2 contributions results in a total resonant frequency shift of

$$(\partial F/\partial p)_{\text{total}} = 20.3 Hz/mbar.$$

Since 1 mbar is the expected approximate steady state fluctuation of He pressure, the pressure induced shift in resonant frequency is relatively unimportant.

4.2.2.3   The choice of titanium

Titanium competes with the more commonly used stainless steel as material for the He tank, the 2 phase tube and the various bellows. In this application titanium has the following advantages over stainless steel:

---

[20]H. Kaiser, 6th Worksh. on RF Superconductivity, Newport News (1993).

- It is well matched to Nb in thermal expansion. The $(\Delta L/L)_{RT\to 4K}$ is:

$$1.43 \quad\cdot\quad 10^{-3} \text{ for niobium,}$$
$$1.51 \quad\cdot\quad 10^{-3} \text{ for titanium, and}$$
$$3 \quad\cdot\quad 10^{-3} \text{ for stainless steel.}$$

  Shrinkage relative to niobium is seen to be 20 times smaller for titanium than for stainless steel. Cool down produces therefore only negligible stress at the Nb - Ti joint between cavity and tank and merely a maximum stress of 3 N/mm2 in a cavity which was stress free at RT. With a stainless steel tank this value would be 60 N/mm2. As a consequence there is no need for operating the tuner during cool down to limit cavity stress, if titanium is used for the tank.

- Lower mass of cavity He vessel and therefore higher frequencies for modes of resonant vibration of the cavity He tank assembly.

- Direct welding to niobium is possible. Stainless steel may be joined to Nb only via intermediate metals such as copper. Such joints have not been developed for the particular geometry required here and are considered risky by some experts. The increased cost for this type of joint about balances the higher material-cost of the niobium vessel.

4.2.2.4   Selected features of the helium vessel

In the following discussion all pressures will be referred to vacuum. Under certain non stationary states of operation the pressure in the He vessel may reach 2 bar, and so the test pressure has been set at 3 bar. The unalloyed Ti foreseen for the tank will stand the corresponding maximum stress of only $7.2 N/mm^2$ safely, especially since it will not turn brittle at LHe temperature.[21] Ti is not a material formally qualified for use for low temperature pressure vessels. However, personnel safety is formally assured to the satisfaction of the Safety Agency by having the He vessel contained in the vacuum vessel of the cryomodule.

The He tank tube with outside diameter of 240 mm and a wall thickness of 5 mm leaves a radial gap of 9 mm for He flow between it and the cavity,

---

[21]DIN 17869, Entwurf (Mai 1990).

and is thick and stable enough to sustain the machining of weld preparations at the ends. It can accept the forces introduced locally at the tank support stations and the tuner mounting points without appreciable local deformation (Fig. 4.18 and Fig. 4.20). Further, its detuning contribution (Table 4.9) is about equal to that of tuner and conical head.

Assembly of cavity and He tank proceeds in the following sequence: The bellow unit is electron beam welded to the conical head at the tuner end. The cavity is then introduced into the tank and the bellow collar welded to the vacuum vessel. At the input - coupler end the connecting collar is then put in place and welded to conical head (by electron beam) and vacuum tank tube. At the joint between connecting collar and tank, variation in cavity length, due to warm-tuning it, can be taken up such that at the tuner end the dimension 6.1 mm is achieved (Fig. 4.18).

The He tank is fastened with 3 screws each at the 2 support stations to Ti plates with outside diameter eccentric to the tank axis. With these plates the tank - cavity unit may be held and aligned from the support rings that are fixed to the diameter 300 mm He-return tube. There is provision for alignment in the axial direction as well as transversely and azimuthally at the 2 support stations (Fig. 4.18).

The aforementioned capillary with inside diameter of 3 mm and made from stainless steel is connected with a "Conflat" type flange from stainless steel to a mating flange from Ti, welded to the bottom of the tank. This "mixed metals" connection has been tested at 1.8 K and found to be leak tight. The capillary tube is formed into an expansion loop to sustain $\pm 15 mm$ maximum relative longitudinal motion between the diameter 40 mm warm up / cool down tube and the tank (Fig. 4.20).

The 2 phase He tube is rigidly connected via the short 60 mm tube at one end to the He tank. At the other end it is transversely guided, but longitudinally free to accommodate longitudinal expansion relative to the He tank. To connect it to its neighbors each 2 phase tube is fitted with a bellow for accepting tolerances as well as thermal shrinkage and flanges for a machine made fusion TIG weld that may - if necessary - be ground open and redone (Fig. 4.18).

At the tuner end of the He tank there is provision made for attaching two cantilever - shaped fixing brackets to the He tank (Fig. 4.20) such that - during testing the cavity (pressure and leak tests) - there may be no relative longitudinal motion between cavity and tank with possible damage to
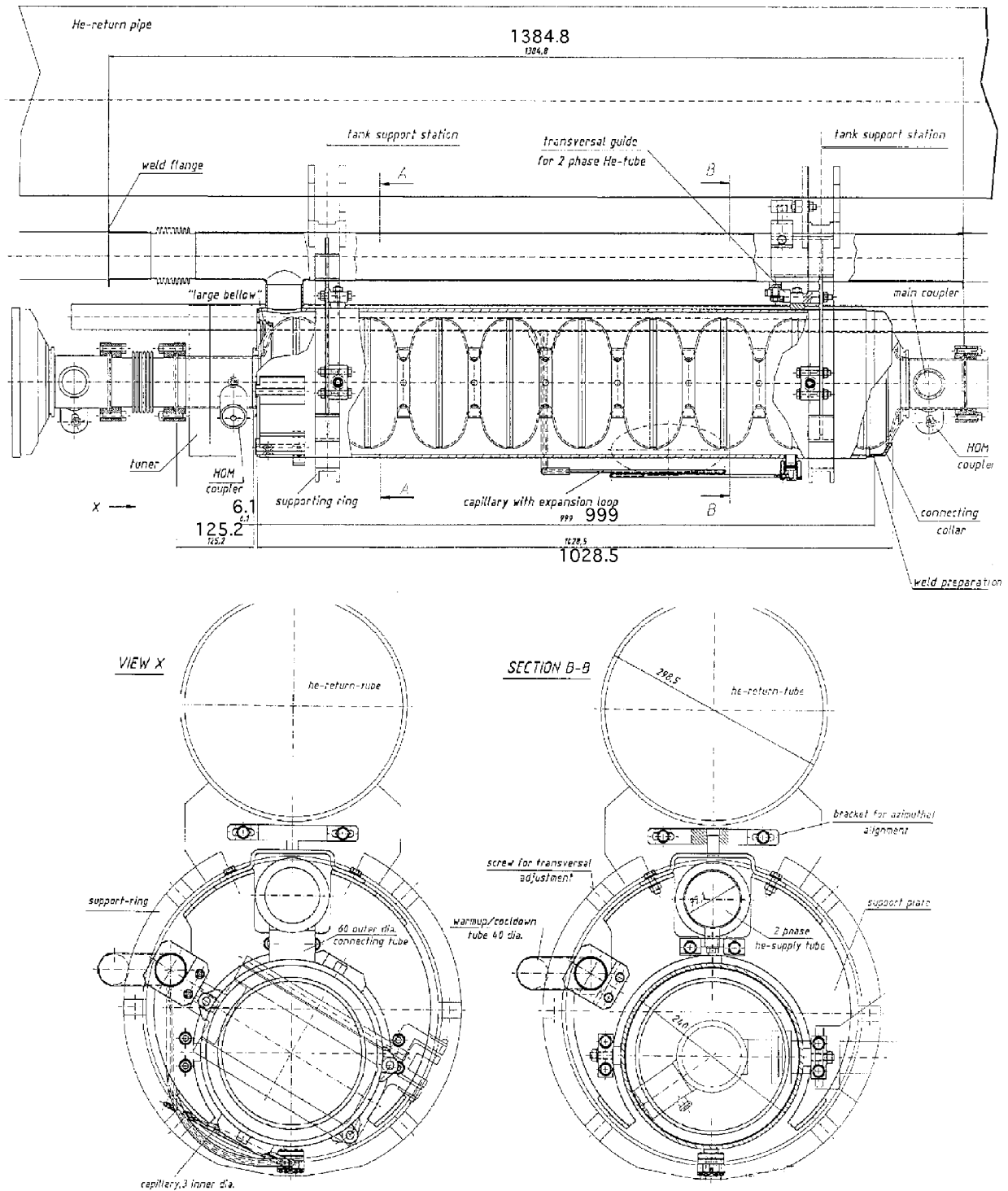
Figure 4.18:   New design of the He-vessel with reduced diameter and cross
section of new vessel.
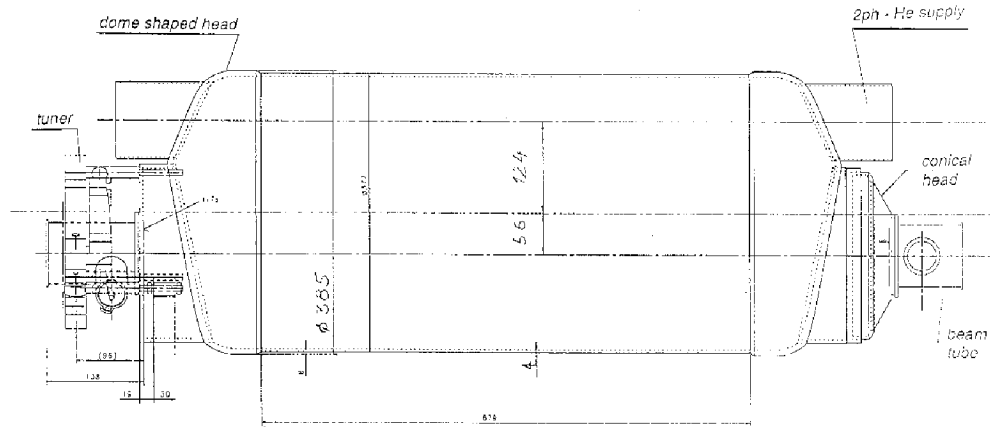
Figure 4.19:   Earlier design of He-vessel with larger diameter.
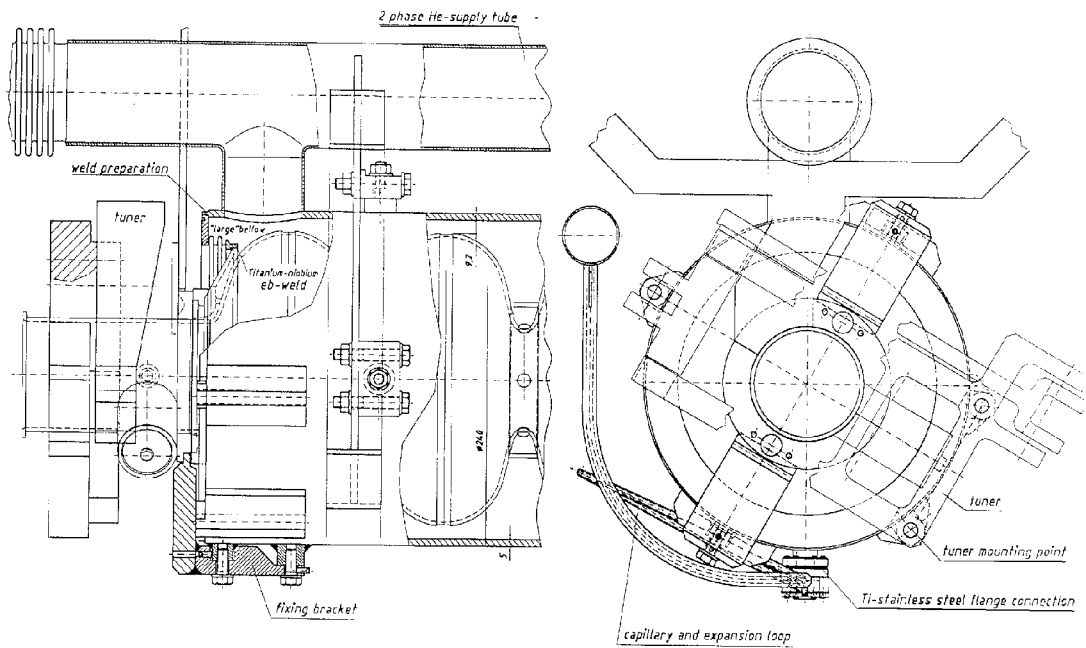
Figure 4.20: Attachments to He-vessel.

the cavity. To this end, the fixing brackets engage into slots of the split connecting ring joining cavity and tuner. The brackets may remain in place during connecting up of cavities at the beam tube and while the tuner is being mounted. After the last named operation they need of course to be removed. The tuner acts on the cavity via short fingers (not shown) that are connected to the split connecting ring with axial and transversal possibility of adjustment. The laterally quite rigid large bellow (Table 4.10) defines the transverse position of the cavity relative to the tank.

Table 4.10: Miscellaneous data of helium vessel.

outside diameter of tank	240	mm
wall thickness	5	mm
material	titanium I (unalloyed)	
mass	21.2	kg
large bellow near tuner:		
transverse spring rate	80000	N/mm
longitud. spring rate	190	N/mm
operating pressure	16 $\cdots$ 2000	mbar
test pressure	3	bar
max. stress at 3 bar	7.2	N/mm^2

4.2.2.5 Outlook

The new design of He vessel is smaller in outside diameter than the earlier design by 140 mm. Thus, the next generation vacuum tank of the TTF cryomodule could be reduced in diameter and its cost be lowered thereby. Moreover, the promising new cryogenic ideas can be tested, and experience be gained regarding fabrication and performance of the titanium parts, and the niobium-titanium welded joints.

4.2.3 Cold Tuning System

The goal of the cold tuning system (CTS) is to adjust the cavity frequency within an accuracy of 1/20 of the width of its resonance curve. Assuming a

loaded quality factor of about 3×10^6, the bandwidth (FWHM) will be about 433 Hz, giving a required resolution of the CTS less than 13 Hz.

Tuning is achieved via the variation of the total length of the cavity, so that the original field flatness is preserved. As each (dressed) cavity is enclosed in its helium vessel, the latter must show some flexibility (see the description of the helium vessel). The length of the cavity is controlled by an electromechanical system acting differentially with respect to the body. See Fig. 4.21.

The CTS is made of a stepping motor, a gear box (harmonic drive), a screw and nut assembly and a double lever arm system with leaf shaped articulations. The latter acts symmetrically on the cavity. Its thrust is transmitted on the same diameter as the stiffening rings. See Fig. 4.22. The CTS operates at 2K in vacuum. So a special surface treatment is required for the moving parts. A qualification procedure has been thoroughly done, leading also to a modification of commercially available gear boxes. No electrical switches are used to tell the limits of the tuning range. Mechanical stops are provided at each end. Tests have shown that these stops support the full torque and full speed of the motor for one hour and allow to go back in the other direction without trouble, and that the stepping motor is not damaged.

Lorentz forces acting on the cavity have been estimated to be about 31 N at 25 MV/m. The cavity harness cannot be infinitely rigid and its flexibility will result in a frequency shift. The flexibility of the CTS has been carefully studied to keep that shift below 600 Hz at 25 MV/m. The following table gives the contributions of the different parts of the harness.

Flexibility Analysis Summary

Item	kN/mm
Niobium conical end piece	278
Titanium e=5 mm helium vessel	388
Tuning system	183
TOTAL	**850**

Total detuning at 25 MV/m	517 Hz
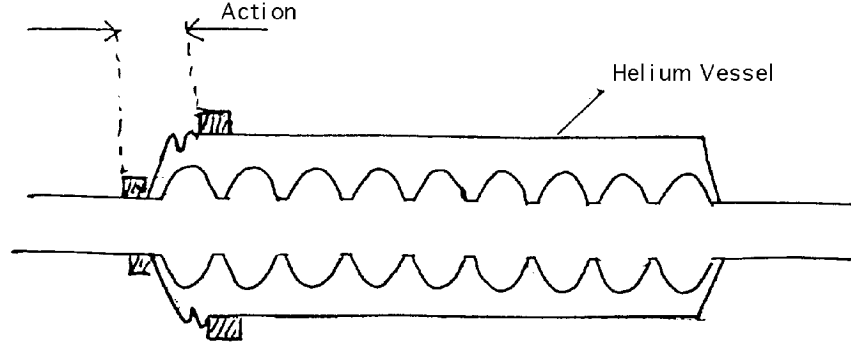
Figure 4.21: How the CTS is acting on the cavity length.

The tuning range is about ± 1.5 mm. The calculated tuning sensitivity being of the order of 500 kHz/mm, the corresponding frequency range is about ± 750 kHz. The resolution given by one step of the stepping motor is 2 nm, i.e. 1 Hz.

Once the tuner is assembled on the dressed cavity, it is set at the center of its range. Extra adjusting screws allow a final room temperature setting of the frequency (± 1 mm, i.e. ± 500 kHz) with a resolution of ≈ 0.25 mm, i.e. ≈ 125 kHz.

It is required that the relation between frequency and motor steps be as linear as possible, for simple programming. This is generally obtained but in one case, when a backlash shows off if the tuning range crosses an equilibrium point between pushing and pulling. This must be avoided. As the helium vessel is made out of titanium, the warm tuning frequency of the cavity must be so that, once harnessed, it is compressed by at least 1.5 mm. Thus the neutral point is out of the range of the cold tuning system.

4.2.4 Magnetic Shielding

In order to reach their nominal performance level, the superconducting cavities of TESLA TTF must be cooled in a magnetic field smaller than ca 20 mGauss. This corresponds to a field 20 to 40 times smaller than the ambient magnetic field in the hall of TESLA TTF. To achieve this shielding level, the use of a mixed scheme, combining a Cryoperm tube around the cavity helium
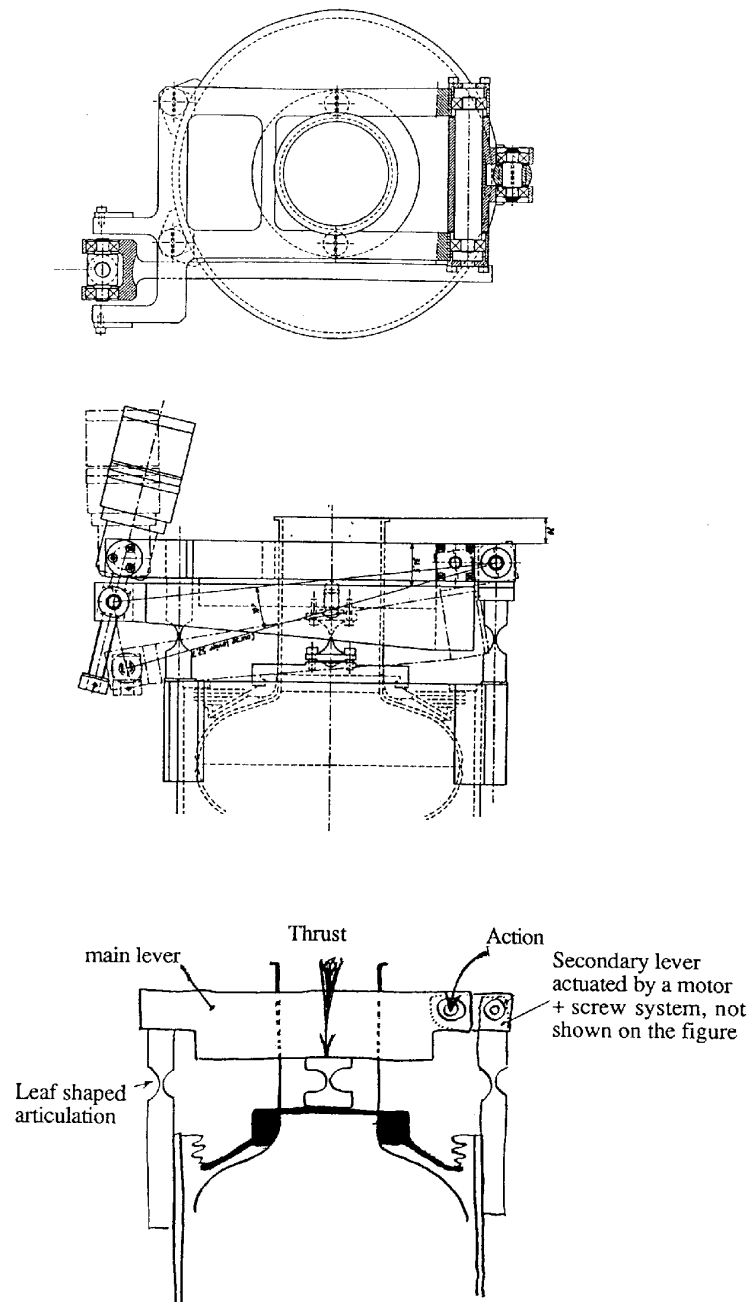
Figure 4.22:   Two lever concept and leaf shaped articulation.

vessel, and a string of Helmholtz coils around the cryomodule vacuum vessel, is proposed.

4.2.4.1 Why should we shield **TESLA** cavities and what is the required shielding level?

In principle, a perfect superconductor cooled in an ambient, static magnetic field smaller than its critical field HC1, should expel the magnetic flux from its volume. However, it has been demonstrated that in the case of a niobium superconducting cavity cooled in an ambient field smaller than about 3 gauss, 100% of the magnetic flux was trapped in the cavity walls.[22] The pinning of the flux lines is thought to be due to the lattice imperfections in the niobium sheet, or to its surface oxidation. This trapping of flux gives rise to an RF dissipation, which can be represented by a local residual surface resistance: $R_S \simeq R_n \frac{H}{H_{c2}} \sin \alpha$, where R_n is the normal state surface resistance of niobium, H the ambient magnetic field during cooldown and α the angle between the field and the surface. When applied to the case of a TESLA cavity (Nb of RRR 300, at a frequency of 1.3 GHz), this corresponds to an average surface resistance of 0.35 $n\Omega$/mGauss, in good agreement with experimental results. In order to get the Q value of 5×10^9 specified for the TESLA TTF cavities, it is desirable to have a residual surface resistance due to trapped flux smaller than 25 $n\Omega$. This corresponds to a remanent field of 70 mGauss or less. This prescription may not seem very stringent, but if one wants to improve slightly the Q-value above this design value, it will be necessary to improve drastically the shielding. For example, in order to get a Q value of 10^{10}, the residual surface resistance due to trapped flux must be smaller than $3n\Omega$, corresponding to a remanent field of 10 mGauss. This level of field is the one achieved in well-shielded vertical test cryostats. This standard value may be difficult to achieve in an actual accelerator environment. For this reason, we propose (with some arbitrariness) a more modest and reasonable objective for the remanent field around TESLA TTF, namely: B=20 mGauss.

4.2.4.2 The ambient magnetic field

At the latitude of Hamburg, the earth magnetic field has a magnitude of 400 mGauss. Its horizontal component (250 mGauss, oriented North-South) is

---

[22]V. Vallet et al. EPAC Conference Berlin (1992).
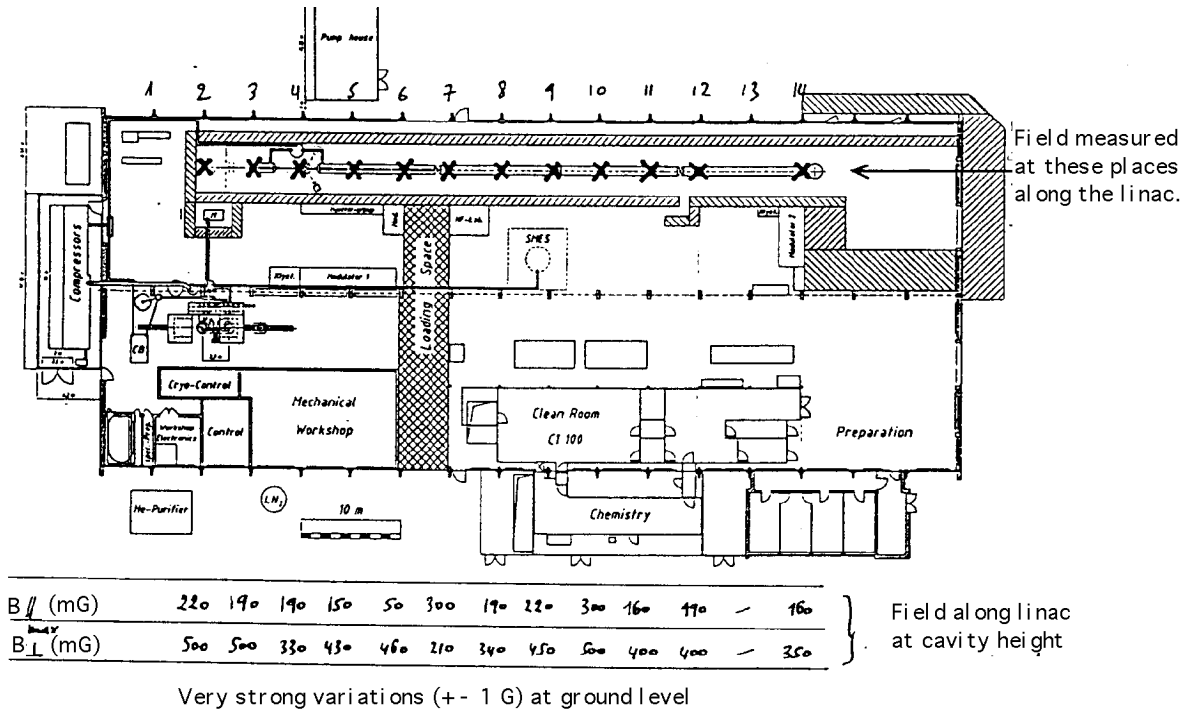
Figure 4.23:   Map of the magnetic field in the hall of TESLA TTF.

roughly equal in magnitude to the vertical component. The experimental hall of TESLA TTF has been used in the past for testing magnets, and has kept a remanent magnetization, mainly from the floor. Measurements at the floor level indicate field levels as high as 2 000 mGauss. Fortunately, the field from the floor is short ranged, and decreases to a typical value of 50 mGauss at the cavity level. This component varies from place to place in magnitude and in orientation along the linac (Fig. 4.23).

4.2.4.3   How to shield TESLA cavities?

Two possibilities will be examined in turn: passive shields, and active cancelation of the ambient field by coils.

Passive shields.   By passive we mean layers of a material with a high magnetic permeability, which concentrate the field lines in their volume, thus
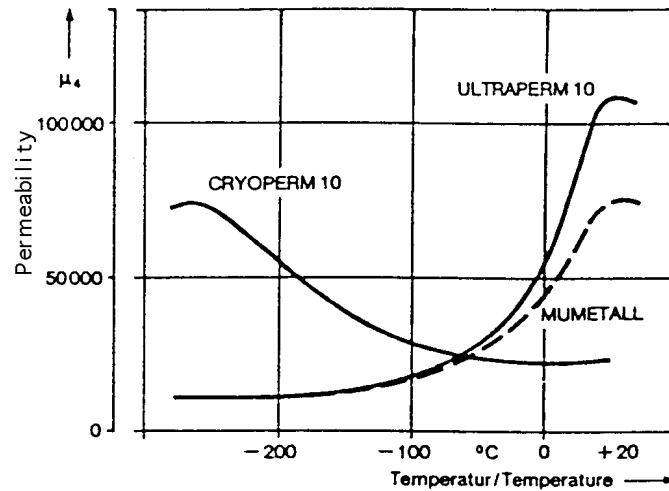
Figure 4.24:   Permeability of some magnetic materials as a function of
                temperature (from VAC catalogue).

producing an attenuation of the field in the vicinity of the cavity. The attenuation depends on the value of the permeability μ. Values as high as 50,000 are reported in the literature or even in catalogs for commercially available material such as Mu metal, Conetic or Cryoperm. However, the permeability of most materials decreases strongly with temperature,[23] with the exception of Cryoperm (Fig. 4.24). On the other hand, to be effective, passive shields must lie reasonably close to the cavity. This implies that the shield will be cooled at cryogenic temperatures. Measurements of μ were made at room temperature (RT) and at 4 K on cylinders of Mumetal and Cryoperm (Table 4.11).

The μ–degradation predicted between RT and 4 K appeared indeed on Mumetal, but the expected opposite behavior for Cryoperrn was hardly observed. Altogether, it should be noted that these magnetic materials are very delicate to handle: proper annealings are required to obtain high permeabilities; moreover, shocks or strains (either thermal or plastic) can reduce μ drastically. Finally, we consider that the choice material for the passive

[23]D. L. Martin and R. L. Snowdon Rev. Sci. Inst. 46 (1975) 523.

Table 4.11:   Permeability μ_1 measured on test cylinders (from M. Bork, VAC, private communication)

	Mumetal	Cryoperrn
RT	54700	10200
4K	7500	13300

shielding of TESLA TTF cavities is still Cryoperm, but that a realistic value for its permeability is only $\mu = 12000$. Specialists from the company VAC confirmed this view.

Shielding factors for one single cylinder.   The shielding factors of a passive shield can be defined as the ratio of the field before and after installation of the shield. Analytical formulae exist for the shielding factors at the center of single cylinders placed parallel or perpendicular to the field.[24] These are:

$$S_\perp \simeq \frac{\mu \cdot d}{D} + 1$$

$$S_\parallel \simeq \frac{4N(S_\perp - 1)}{1 + D/2L} \text{ closed cylinder}$$

$$S_\parallel \simeq 4N S_\perp \text{ open cylinder}$$

In these equations, D is the diameter of the cylinder, L its length, d the wall thickness and N its demagnetizing coefficient, shown in Fig. 4.25.

Orders of magnitude can readily be obtained from the above equations for single tubes of dimensions fitting those of TESLA cavities. For example, for a tube of dimensions L=1300 mm, D=250 mm, d=1 mm, and a permeability of $\mu = 12000$, $S_\perp = 50$ and $S_\parallel = 12$. The former value may be acceptable, but the latter is not sufficient for TESLA TTF purposes.

It can already be seen at this stage that the longitudinal component of the field will be much more difficult to shield than the transverse one.

For very elongated tubes, the demagnetizing coefficient N goes to zero like $(D/L)^2$. These tubes will shield the transverse component of the field, but

---

[24]A. Mager J. Appl. Phys. 39 (1968) 1914.
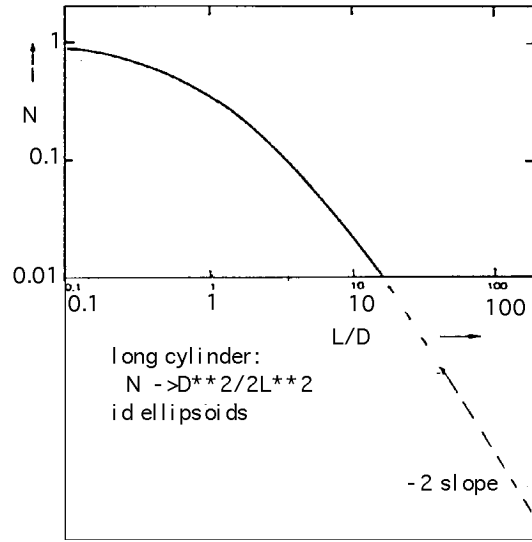
Figure 4.25: The demagnetizing coefficient of a cylinder vs. its Length/-Diameter ratio.

not the longitudinal one. Almost by definition, linear accelerators are very elongated structures, and we shall see that this will cause severe difficulties for a proper shielding of the TESLA TTF cavities with purely passive magnetic shields.

Role of end caps. The above equations neglect end effects. Fringe fields are to be expected at the ends of the tube. Elementary considerations on the conservation of $\int B_\| dl$ along the cylinder axis indicate that the longitudinal component of the field is depleted in the tube, and is enhanced at the ends of the tube. This enhancement extends over a diameter inside the tube (Fig. 4.26). Calculations with a numerical code[25] confirm this point, and indicate that it is possible to reduce the effective diameter of the tube, and thus the range of the fringe fields by adding annular shaped pieces at the end of the tube(s). The field enhancement is then stronger, but extends on a smaller distance, thus permitting an improved shielding of the cavity

---

[25] The finite element code BACCHUS was developed by CISI engineering for the study of charged particle beams in static electromagnetic fields.
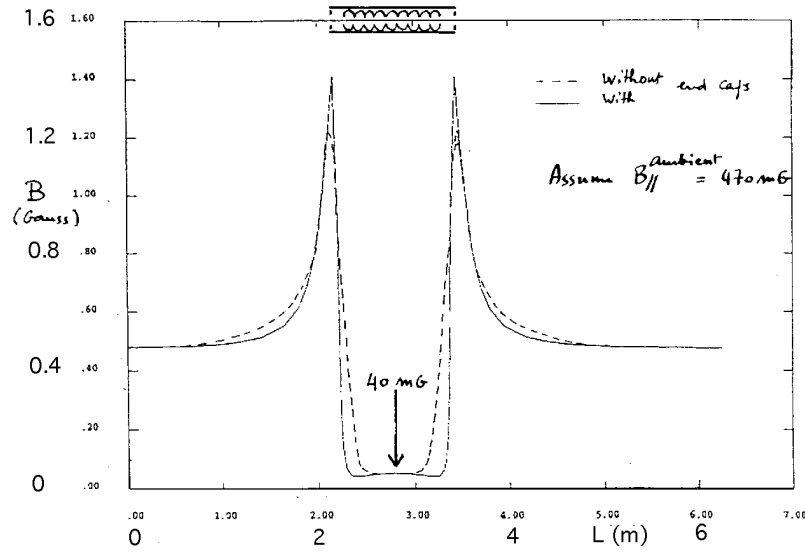
Figure 4.26:   Distribution of $B_{\|}$ along the axis of a cylindrical shield: a) without end cap; b) with end cap. Calculation with the finite element code BACCHUS, assuming a tube of dimensions: L=1300 mm, D=250 mm, d=1 mm, with a permeability $\mu = 12000$.

end cells.

Shielding factor of a string of cylinders.   It should be noted that a given cavity surrounded by its passive shield cannot be considered as magnetically isolated from its neighbors. If the string of cavities of TESLA TTF is to be shielded by a string of tubes, each tube will modify the field seen by other tubes. The situation of the string is in fact close to the case of a continuous tube of the same total length and diameter. Since the aspect ratio of this "global tube" is very long, the corresponding longitudinal shielding factor will probably be rather poor, necessarily less good than the one evaluated for one single cylinder shielding an isolated cavity. Also, fringe fields are to be expected at the ends of the tubes. These complications can hardly be handled analytically, and this motivated the use of a numerical code (BACCHUS[4]) to describe the field geometry.
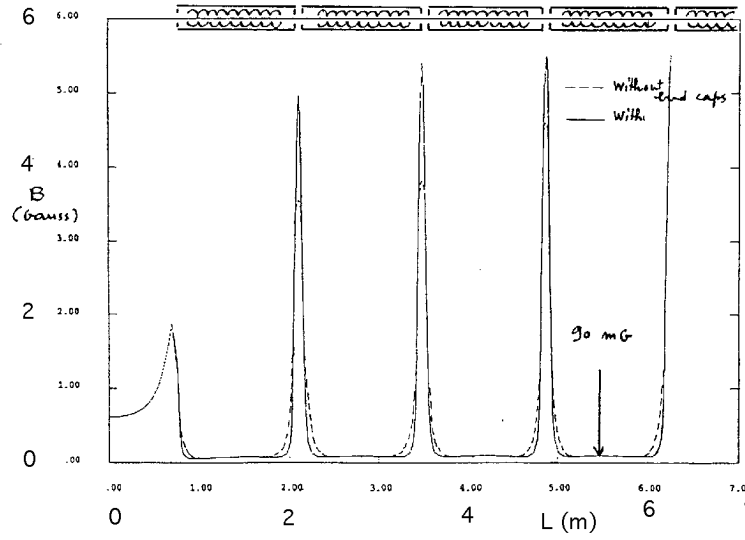
Figure 4.27:   Distribution of $B_\parallel$ along the axis of a string of cylindrical shields of same dimensions and characteristics as in Fig. 4.25: a) without end cap; b) with end cap.

The field profile for a string of tubes corresponding to the TESLA geometry (one magnetic cylinder around the Helium vessel of each cavity) is shown in Fig. 4.27. It can be seen there that the shielding is much poorer in the case of a string as it is for a single tube. Even by using large thicknesses, by optimizing the spacing between tubes and by adding end caps, it is probably very difficult to achieve a shielding level better than 50 mGauss at the end cells of TESLA cavities with a single layered string of magnetic cylinders. Therefore, this solution cannot be recommended in the practical case of TESLA.

Plausible schemes using purely passive shields.   Various concepts of passive shielding with two layers of magnetic material, either inside or outside the helium vessel, were considered. Results from BACCHUS on the best geometry fitting the one for a TESLA TTF cryomodule are shown on Fig. 4.28. Here, the considered geometry was a string of passive shields consisting of two layers of magnetic material, one outside the Helium vessel,
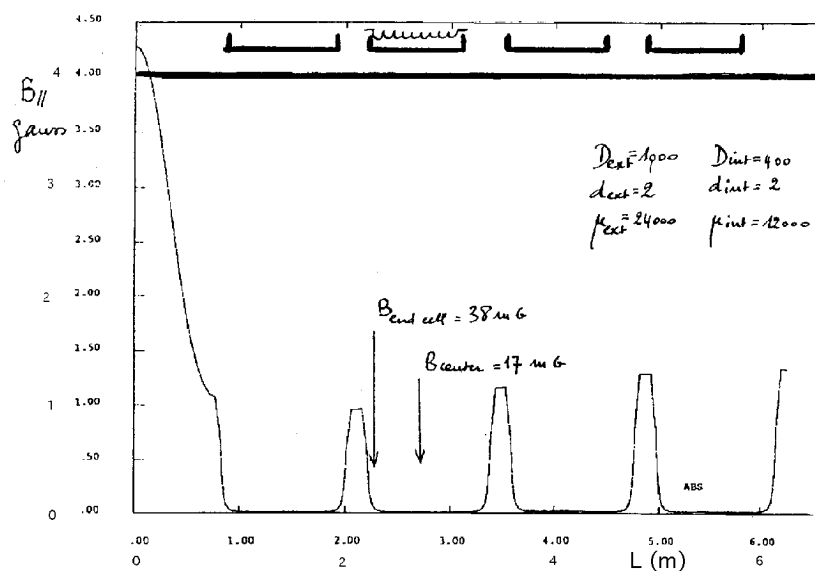
Figure 4.28:   Field profile along the axis of a TESLA TTF cryomodule shielded by two layers of passive shields, as calculated with BACCHUS.

one outside the vacuum vessel. With this double shield and realistic values for μ and for the shield thickness, it is not very difficult to reach acceptable field levels at the center of the shield. The difficult part is to shield the cavity end cells. This is already true for an isolated cavity, and is even more so if one takes into account the deleterious effect of neighboring tubes.

It is possible—but rather difficult—to obtain on a TESLA TTF cryomodule the required shielding of the longitudinal component of the field by means of purely passive shields. Large shield thicknesses, and probably two layers of shielding are necessary. The shield could be a string of tubes containing the string of cavities. The gap between tubes is a crucial parameter: if it is too small, the overall shielding factor of the string becomes small because the geometry of the shield becomes close to the shape of a very elongated cylinder with very small demagnetizing coefficient; if the gap is too large, the shielding tubes are not much longer than the cavities, and the fringe fields at the end of the tubes hamper a proper shielding of the cavity end cells. End caps can cure the problem to some extent, but they complicate the design

and increase the cost of the shields.

4.2.4.4 Active devices

The principle of active devices is to cancel the ambient magnetic field by coils. The advantages of this option lie in its simplicity, and cheapness. Cancelation of the longitudinal component of the field, so difficult with passive shields, can readily be achieved with a very simple solenoid or a string of Helmholtz coils.

A few possible drawbacks remain. Does the ambient field have time dependent variations that may be difficult to track. If changes go unnoticed, the current in the coils will become inadequate for a proper protection of the cavities. In principle, the current in the coils needs to be set only during cooldown of the cavity, since flux trapping occurs only at the superconducting transition. However, during a quench, a macroscopic portion of the cavity becomes normal conducting, and is re-cooled down to the superconducting state immediately afterwards. At the transition, the cavity is again liable to trap flux, and this means that the shields must be properly adjusted at this time. This is not automatically realized with active shields.

4.2.4.5 The recommended solution for TESLA: a mixed scheme

In view of the respective qualities of passive shields and active devices, it is very tempting to combine advantages of both, by canceling the average longitudinal component of the field by a coil, and by taking care of $B_\perp$ and of the fluctuations of $B_\parallel$ by a light passive shield (Fig. 4.29).

In order to qualify completely the above described concept, a 1/4 scale model of a TESLA TTF cryomodule was built at Saclay. The vacuum vessel was simulated by a 2 mm thick steel tube. The passive shield was simulated by tubes of Conetic of adequate length and diameter. The permeability of the Conetic was roughly 30000, and the thickness of the tube was d=0.1 mm, chosen so that $(\mu d)_{Model} \simeq scale \times (\mu d)_{Tesla}$.

The model was oriented North-South, in an ambient magnetic field similar to the one of the TESLA TTF hall. The distribution of the three components of the magnetic field in the model was measured by means of a Förster probe. The field distribution obtained after optimization of the shield geometry and careful degaussing of the "vacuum vessel" is shown in Fig 4.30 and Table 4.12.
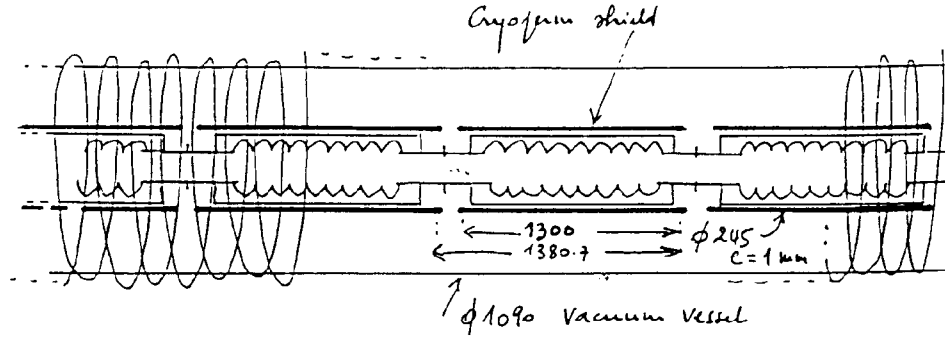
Figure 4.29:   Principle of a mixed shielding scheme, applied to a TESLA
                TTF cryomodule.

The level of field achieved in the model is quite satisfactory, thus giving much
hope that similar results will be obtained with the full scale cryomodule.

The 1/4 scale model enabled us to recommend the design for the TESLA
TTF shielding scheme that is described below.

Table 4.12:   Field level measured on the scale 1/4 model of a TESLA
                TTF cryomodule.

	Cavity center	Cavity end cell
$B_\parallel$	$0 \pm 25mG$	$0 \pm 35mG$
$B_\perp$	$10 \pm 8mG$	$l5 \pm 5mG$
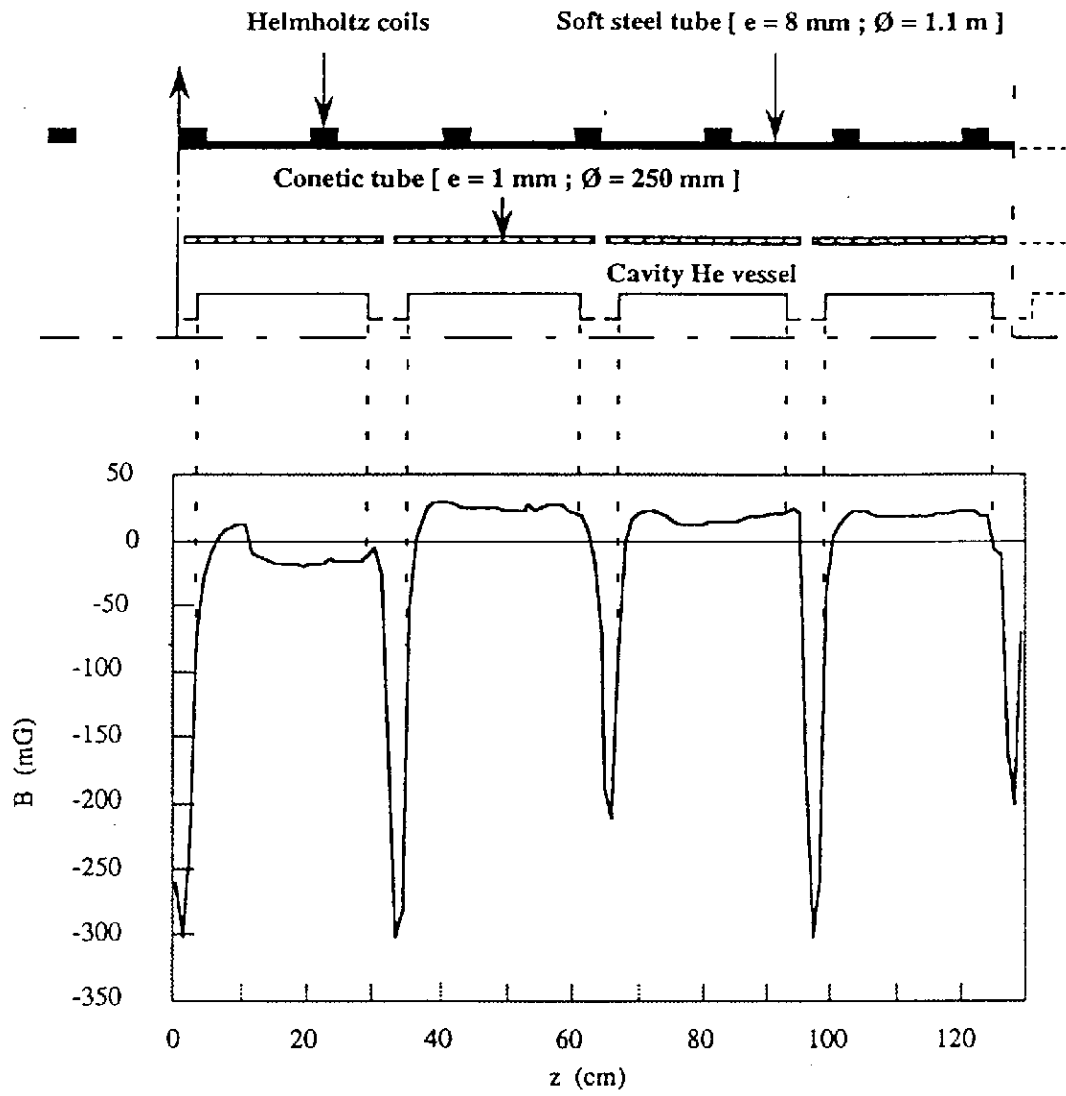
Figure 4.30:   The field profile measured along the axis of the scale 1/4
model of a TESLA TTF cryomodule.
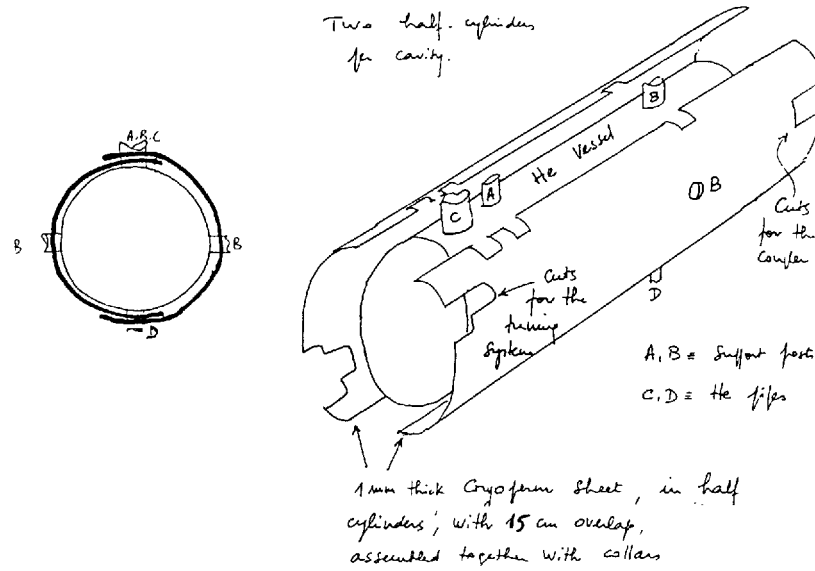
Figure 4.31:   The Cryoperm shield around the helium vessel.

4.2.4.6   The Cryoperm Tube

The passive shield should be of small diameter to minimize the range of fringe fields. For this reason we recommend the use of a single tube around the helium vessel. The thickness of the tube wall should be of 1 mm, to give a transverse shielding factor of 50. To avoid the complication brought by end caps, the tube should extend rather far away on each side of the cavity. As mentioned above, the exact length of the Cryoperm cylinder is a compromise between the average quality of the longitudinal shielding, and the local quality of the longitudinal shielding at the end of the tubes, due to fringe fields. This length has been optimized on the scale 1/4 model. The criterion retained here was to minimize $B_{\parallel}$ at the level of the cavity end cells. The optimal shield length was found to be 1300 mm (full scale). Given the spacing between cavities, this corresponds to a gap between shields of 80.7 mm. Some cuts will be necessary at the tube ends to allow room for the coupling lines and cold tuning system. Being cold, the shield should be made of Cryoperm. We recommend to re-anneal the half cylinders after forming to shape.

4.2.4.7 Design of the coils

The average current necessary to cancel $B_\parallel$ is 25 to 50 Amp. turns/m. A plausible solution might be to use a string of Helmholtz coils instead of a solenoid. The modularity of the coils, and their mechanical independence with respect to the vacuum vessel would be another advantage of this solution. What is the allowable spacing between coils compatible with an homogeneous cancelation of the field? On the TESLA TTF cryomodule, the diameter of the lateral ports in the vacuum vessel is 60 cm. This corresponds to a minimal spacing ratio S/D of 0.6 for the coils, where S is the spacing of the coils, and D their diameter. Such a geometry was tried on the scale 1/4 model and yielded results very similar to the ones obtained with a uniformly wound solenoid. Of course, inhomogeneities grow when the coil spacing increases, but we found that acceptable results, identical to the ones reported in Table 4.12, were still obtained with a spacing ratio of 1.1, corresponding to a coil spacing of 1.2 m on the TESLA TTF cryomodule. We are thus led to recommend a spacing between 0.6 and 1.2 m for the Helmholtz coils of the TESLA TTF shielding scheme.

4.2.4.8 Magnetic properties of the vacuum vessel

The TESLA TTF vacuum vessel is made of steel, and will not be neutral from the magnetic point of view. The vacuum vessel may help to shield the cavity, playing the role of a (poorly controlled) passive shield. However, its ratio $\mu d/D$ will be of the order of 2 to 3, i.e., small as compared to the $\mu d/D = 50$ of the Cryoperm shield. The efficiency of the vacuum vessel as a shield will thus be rather limited.

But the role of the vacuum vessel may also be a harmful one: it will have a remanent magnetization, due to its metallurgical, thermal and magnetic history. This magnetization, especially probable at the welds, risks to perturb the field distribution in the tube. Fortunately, it was demonstrated on the scale 1/4 model that the vacuum vessel can be demagnetized with the coils of the active device. The degaussing procedure consisted of DC pulses of alternating sign and decreasing intensity. Note that the current capability of the coils required by the degaussing procedure (300 Amp. turn/m during a few seconds) differs from the one needed for the cancelation of the earth field (25 to 50 Amp. turn/m, DC). This should be taken into account in the

final engineering of the coils.

4.2.5   RF Input Coupler

A critical component of the TESLA Test Facility is the radiofrequency input coupler, for which designs have been developed by both DESY and Fermilab. The main features of the coupler include two ceramic RF vacuum windows, one cold and one at room temperature, bellows on the inner and outer conductors of the coaxial line, and a waveguide to coaxial transition.

4.2.5.1   Design Requirements

Electrical-RF

Normal operation: Required power transmission of the main coupler is 213 kW at 1.3 GHz, 10 pulses per second of 1.31 msec length which corresponds to 2.8 kW of average power. This power is needed to provide 25 MV/m acceleration gradient at a beam pulse current of 8.25 mA. Pulse time is distributed to 0.51 msec filling time and 0.8 msec beam on time. In addition, after the beam pulse is over, energy is extracted from the cavity.

The coupler also should be capable of up to 1 MW pulse power transmission at reduced pulse length (High Peak Power Processing). This will allow for reprocessing of the superconducting cavity *in situ* if it experiences performance degradation . At power levels of 1 MW, field strengths at the inner conductor near the cavity (where the outer conductor diameter is 40 mm) will reach 1.4 MV/m for the case of total reflection as the cavity begins to fill with energy.

During each RF pulse the cavity input impedance changes dynamically between open circuit, short circuit and matched conditions.

Adjustment of cavity external Q is required by a length change of the capacitive antenna (inner coax) which couples to the electrical beam tube fields of the cavity. The external Q of the coupler is to be 3×10^6, adjustable over the range 1×10^6 to 9×10^6. The variable coupling is required due to variations in the cavities, couplers, RF distribution system, and beam current.

The input coupler should be impedance matched for a return loss of better than 20 dB (1% power reflection).

Ceramic windows   Two ceramic (alumina (Al_2O_3)) vacuum RF windows are necessary for the coupler. One needs a cold window very near the cavity because the cavity vacuum has to be closed at an early assembly stage in the clean room. Thus an additional warm vacuum RF window at room temperature is unavoidable as well. After insertion of the cavity string into the cryostat the warm coupler part has to be mounted via the cryostat flange from outside. The warm coupler part includes the 300 K window and connects to the 70 K flange of the cold coupler part. The cavity side of the 70 K window will be evacuated by the cavity/beamline vacuum system, whereas the region between the two windows will be pumped by a separate vacuum system, complete with pumps and pressure instrumentation.

Cryogenic Design   The input coupler connects room temperature WR650 waveguide to a cavity at 1.8 K, hence minimum heat leak is necessary. This requires a compromise between high electrical and low thermal conductivity over the distance between warm and cold end and is achieved by using copper plated thin-wall stainless steel coaxial transmission line. Thermal budget requires a 70 K heat load of 6 W, a 4 K heat load of 0.5 W, and a 2 K load of 0.06 W. Both coupler designs are calculated to meet this budget.[26]

Mechanical Design   During cool down to 1.8 K the eight cavities shrink toward one fixed point at the center of the cryomodule. The input couplers must accommodate this shrinkage, which is at most 15 mm. Since the waveguide end of the input coupler is fixed, the coupler must be flexible so that the cavity end of the coupler can move with the cavity.

4.2.5.2   The Fermilab Input Coupler

This section describes the Fermilab input coupler, which is shown in Fig. 4.32. The requirement of variable coupling is met by the use of bellows on the inner and outer conductors of the coaxial input coupler. The inner and outer conductors move together toward or away from the beam tube by means of a coupling adjustment mechanism outside the cryomodule. A range of motion of up to 25 mm is possible, which is more than adequate for the required range of external Q.

---

[26] Tom Peterson, TESLA Report 93-??
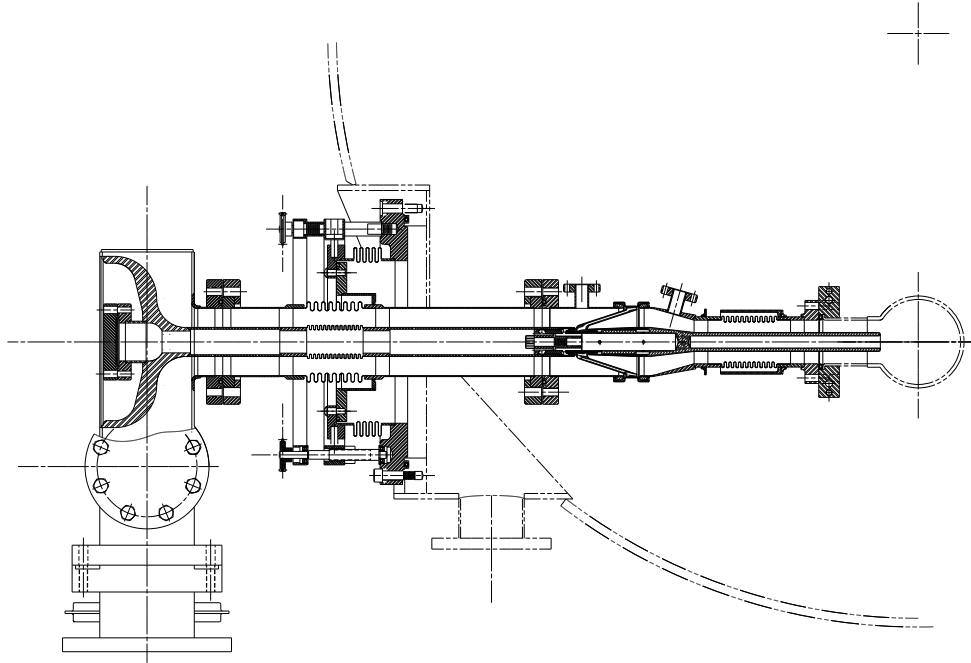
Figure 4.32:   The Fermilab RF input coupler for the TESLA Test Facility.

Flexibility for thermal shrinkage is achieved via the inner and outer conductor bellows. There is a pivot point outside of the cryomodule about which the coupler can rotate as the cavities shrink. When the coupler is mounted at room temperature, the center conductor will be off center at the beam tube. As the cavities shrinks during cool down, the center conductor will pivot into a position concentric to the outer conductor. In opposition to the requirement for flexibility, there is a need to avoid mechanical vibration of the input coupler, which could lead to difficulties in controlling the amplitude and phase of the RF drive to the cavity. It may be necessary to install a damping system to reduce the effects of mechanical resonances.

Two alumina (Al_2O_3) ceramic RF windows will act as vacuum barriers and ensure the cleanliness of the cavity. A conical window is installed at the 70 K intercept in the 62 cm diameter coaxial line. Several possibilities are being considered for the warm window. These include a cylindrical window that is incorporated in the waveguide to coaxial transition, a planar waveguide window upstream of the transition, and a conical coaxial window downstream of the transition.

The cold RF window must stay with the cavity after the cavity has been chemically processed, rinsed, and assembled in the clean room. Hence, the portion of the input coupler which extends out of the cryomodule must be removable. This is accomplished with an outer conductor flange joint sealed with a metal seal and an inner conductor joint fastened with a screw.

4.2.5.3 Component Development

Conical Ceramic   The conical ceramic window is the first level of protection of the cavity interior. The conical shape was conceived of as a good candidate for a broad band impedance-matched window. The angle formed by the cone with respect to the axis of the coaxial line was chosen to be 18.2 degrees, which is the result of setting the angle of incidence equal to the Brewster angle for the vacuum to ceramic interface. The depth of penetration of the ceramic into both the inner and outer conductors was chosen to reduce the field strengths at the braze joints to approximately 50 % of their values at the surfaces of both conductors. Two possibilities were examined for obtaining a good impedance match. One technique is to taper the ceramic thickness so that it is thinner near the inner conductor. The other method is to taper the inner or outer conductors. The tapered ceramic was rejected

in order to simplify the ceramic. The thickness of the ceramic in the conical region is 3.2 mm. We chose to taper the inner conductor due to ease of fabrication. The Hewlett-Packard High Frequency Structure Simulator (HFSS) was used to model the window and to determine the shape of the tapered inner conductor. A return loss of 22 dB was achieved during simulation by iterating on the inner conductor taper. A plot of the S11 magnitude and phase response is shown in Fig. 4.33. Implementation of the design is shown in Fig. 4.34. The ceramic is 99.5% Al_2O_3 from WESGO. The OFHC Copper inner and outer conductor bands were brazed to the ceramic by Alberox using 35/65 Au/Cu braze alloy. Initially, the inner conductor band contained a small plug of ceramic to prevent the band from shrinking away from the cone during the brazing cool down period. However, this plug caused cracking of the cone during brazing. The ceramic is coated on both sides with Titanium Nitride (TiN) by an evaporative process at Fermilab. The thickness goal has been 10 nm on the ceramics coated to date. The inner conductors on each side of the ceramic are attached via electron beam welding at Fermilab. The outer conductors are attached via conventional TIG welding in an Helium/Argon atmosphere.

Bellows The bellows used in the three prototype input couplers are off-the-shelf units purchased from MDC Corp. End pieces that connect the bellows to the inner/outer conductor tubes were fabricated at Fermilab and attached by resistance welding at Flexonics Corp. The attachment by resistance welding resulted in a crevice that may trap copper plating acids, dirt, etc., so an improved design will be used in the future. This new design has no crevices on the surfaces carrying the RF currents. This type of bellows is being procured from Hyspan Corp. The thin wall (0.18 mm) bellows are hydroformed and are rated for a range of travel of 25.4 mm.

Doorknob Transition The doorknob transition is a waveguide to coaxial transition that incorporates a cylindrical knob as the impedance transforming device. Two types of doorknob transitions have been designed for the Fermilab input coupler. The first type incorporates a cylindrical ceramic vacuum window at the doorknob, the second type uses a planar waveguide ceramic window which is mounted a short distance away from the doorknob, and the third type uses a conical ceramic window mounted in the coaxial line
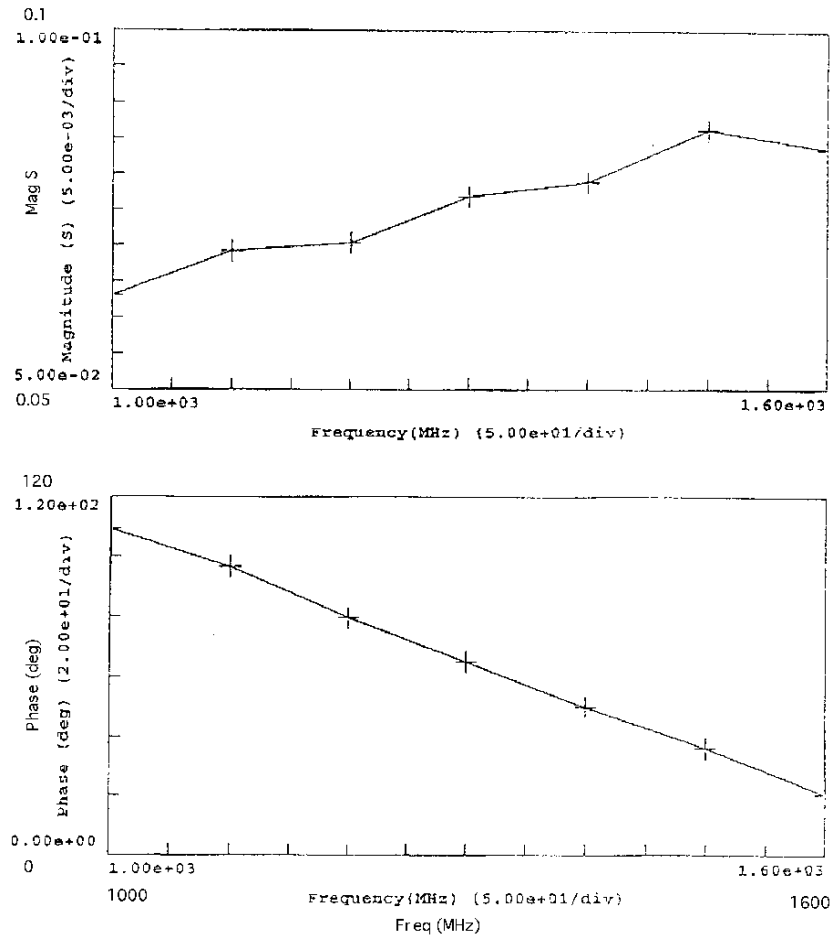
Figure 4.33: Calculated $S_{\parallel}$ magnitude and phase response of the conical coaxial ceramic window.
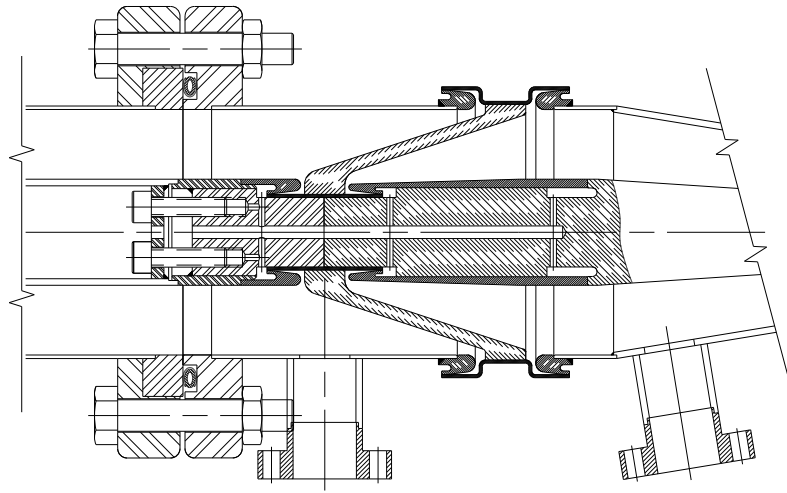
Figure 4.34: Implementation of the coaxial window design.

adjacent to the waveguide-to- coaxial transition.

Cylindrical window transition-   The cylindrical window transition includes a cylindrical ceramic window at the doorknob as shown in Fig. 4.35. Narrowband impedance matching (approximately 1 % of center frequency) is achieved by adjusting the height of the inner doorknob and the length of the waveguide stub. An E-plane capacitive tuner is included at 1/4 wavelength from the stub endplate to provide for adjustment of the electrical length of the stub to compensate for mechanical tolerances. The ceramic is 99.5 % Al_2O_3 from WESGO. Fermilab fabricated the copper and stainless steel rings which were brazed to the ceramic by Alberox. The ceramic is TiN coated on the vacuum side (inner surface). The waveguide side of the ceramic will be exposed to >1 Atm dry air. The addition of a window results in the
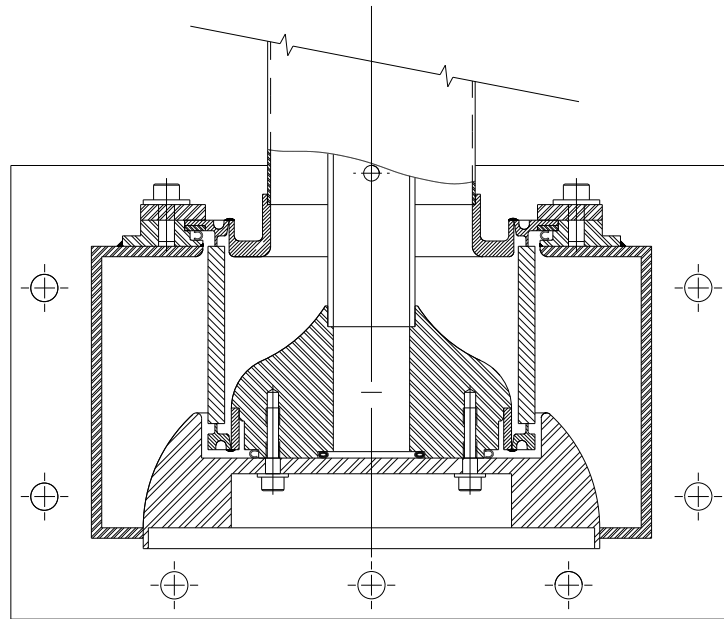
Figure 4.35:   Doorknob transition with cylindrical ceramic window.

use of a two-piece doorknob. The outer piece is welded to the waveguide, whereas the inner piece is welded to the ceramic window. The ceramic and inner knob are bolted into the waveguide assembly, so the ceramic may be replaced if necessary. C-seals are used as RF joints in the bolted assembly. The shape and size of the doorknob determines the impedance characteristics of the transition. These parameters have been determined through bench measurements. The HFSS program was subsequently used to model the design and help understand the field characteristics of the transition.

Planar window transition- The planar window transition separates the ceramic window from the doorknob. A planar waveguide window is mounted upstream of the doorknob transition. The window used to date has been provided by Philips Components. It is the output window used
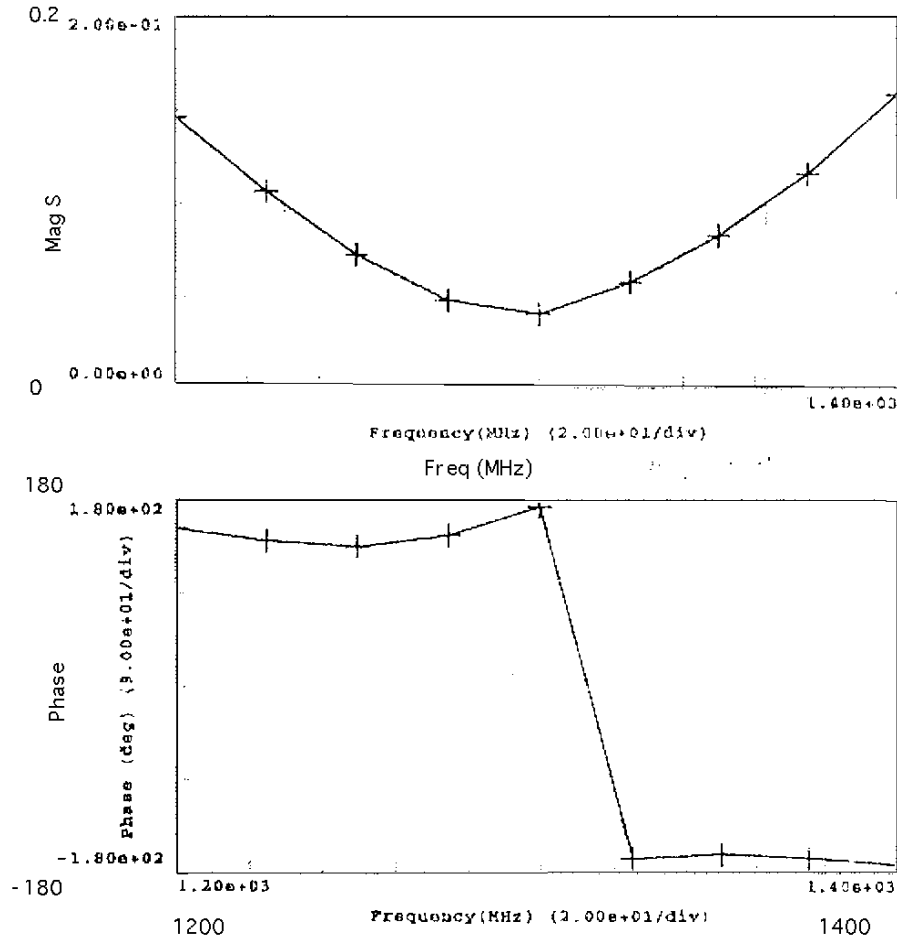
Figure 4.36:   Calculated $S_{\parallel}$ magnitude and phase response of the broad-band doorknob transition without window.

one of their klystrons and is provided with a flange on one side and open waveguide on the other side. A vacuum flange for use with a Helicoflex seal is fabricated and attached to the window at Fermilab. A pair of matching posts is required on the air side of the window to impedance match the window at 1.3 GHz. The doorknob transition was designed using HFSS and is impedance matched over a fairly broad band. The S11 magnitude and phase calculations are shown in Fig. 4.36.
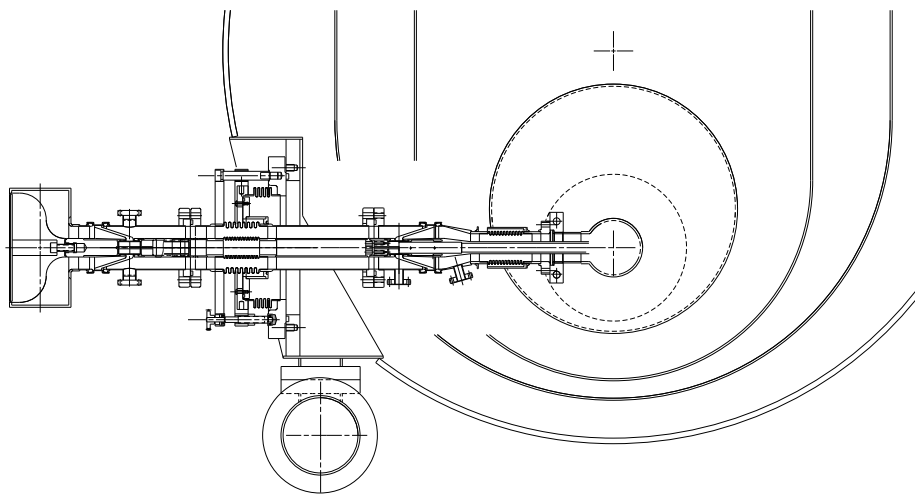
Figure 4.37:   A coupler design featuring two coaxial windows.

Conical Window Transition-   The conical window transition again separates the ceramic window from the doorknob, but in this case the window is a conical window mounted in the coaxial line adjacent to the waveguide as is shown in Fig. 4.37. The window design is identical to that of the 70 K ceramic window described earlier. The only difference is that the warm window will have vacuum on one side and air on the other side. Therefore the doorknob transition also operates in an air atmosphere instead of vacuum.

4.2.5.4   The DESY Coupler

The DESY type main coupler (Fig. 4.38) has two cylindrical ceramic windows, one at 70 K level near the cavity, the second one at 300 K inside the wave guide to coax transition. Both parts of the coupler are coaxial with an outer conductor diameter of 40 mm. Total coupler length inside the cryostat
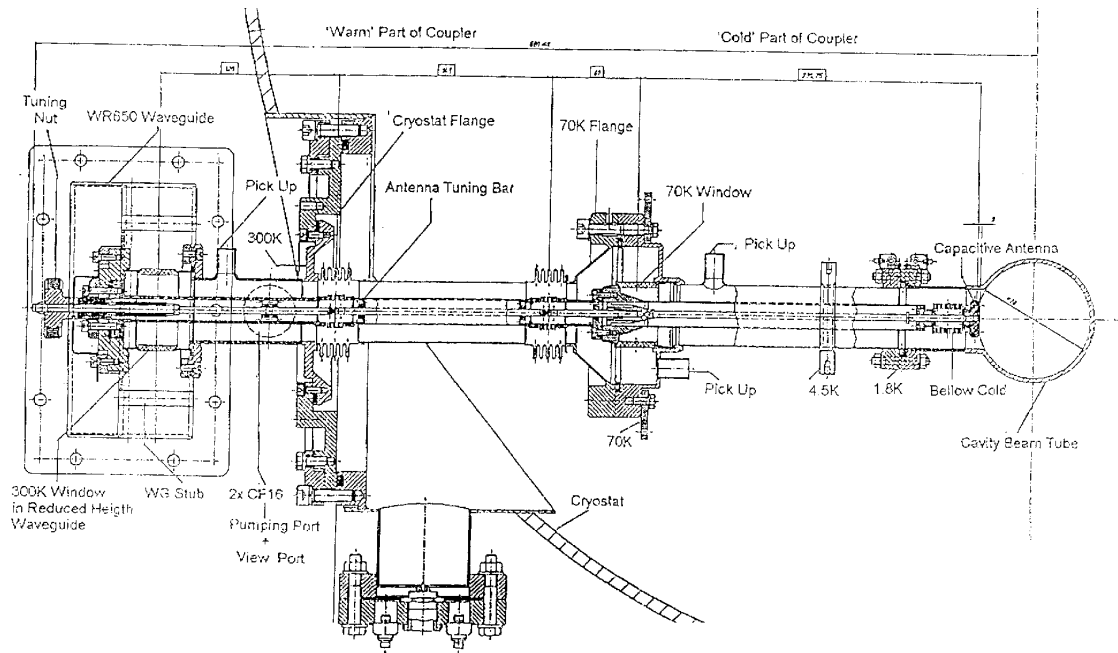
Figure 4.38: DESY type TESLA Main Coupler.

is roughly 40 cm.

A reduced height wave guide matches the WR650 wave guide to the 50 Ohm coax transition under incorporation of the warm window as a UHV barrier towards the wave guide. Two stubs are inserted to the wave guide transition. They mainly compensate the short taper between full and reduced height wave guide. The coupler part outside the cryostat is very rigid and not sensitive against forces from the wave guide system. The warm ceramic window is mechanically decoupled by thin supporting copper collars and a weak area of the wider wave guide wall.

Two bellow sections in the inner and outer conductor of the warm coupler part inside the cryostat provide bends which allow transverse motion of the 1.8 K coupler end by ± 15mm if the cavity flange connection migrates thermally.

Inside the inner conductor there is an antenna tuning bar. Turning the tuning nut at the room temperature end of the bar moves the tuning bar and changes the capacitive antenna position by lengthening or shortening

the cold inner conductor bellow. Thus the cavity external Q change is easily performed.

Combination of low cryogenic losses and low RF losses is realized by 0.5 mm stainless steel walls of the outer conductors with thin high conductivity copper coatings inside (between 10 μm and 20 μm). The inner conductor bellows of the warm part are made of hydroformed thin wall stainless steel. With proper copper coating their thermal impedance is high enough to allow the rest of the inner conductor to be copper. Copper is also used for the cold coupler part inner conductor in order to conduct its RF losses to the 70 K window which has a connection to the outer conductor. The cold bellow has a thick copper plating.

Temperature distribution and thermal power flow of the coupler are determined by the thermal intercept points at room temperature, 70 K, 4.5 K, 1.8 K. The heat losses at the low temperature levels are expected to be 6 W, 0.6 W, 0.06 W at full RF load.

An additional feature of the coupler are ports for diagnostic instrumentation which serves to increase reliability of the device if connected to the interlock system. One vacuum port between wave guide and cryostat flange is thought for multiplier observation of light effects. Three capacitive pick up probes allow measuring of charged particles near the windows. Charged particles can indicate multipacting effects or plasma discharge before light comes up. It is very important for the coupler to prevent RF operation conditions which lead to multipacting or discharges inside the vacuum. The resulting pressure increase will cause material evaporation by RF plasma welding within a few msec and thus lead to damage.

4.2.5.5 Fabrication

The coupler consists of three subassemblies: the cold coupler part including the 70 K window which is only one piece after assembly, the inner conductor of the warm coupler part, and the warm outer conductor including the 300 K window.

These subassemblies will be welded as far as possible with exception of the window connections and most bellow connections. Those will be brazed in an UHV furnace in maximally two steps at two different temperatures with two different braze alloys. One temperature is 820°C using CuAg eutectic braze for the first step. The other temperature is 500°C using AuGe10Cu2

braze. Critical copper coatings especially for the low temperature areas of the coupler will be done after brazing or before the 500°C braze. The ceramic windows will be provided with a Titanium antimultipactor coating on their vacuum side surfaces before brazing because it will be difficult to coat the windows after that. Brazing temperature for the window assemblies will be 820°C. High quality copper plating and final assembly of the manufactured parts by brazing will be done by two experienced industrial companies.

4.2.5.6   Technological Problems

There are still questions under study. One of those is influence of heat treatment on the conductivity of thin copper layers. This question comes up because the aim is first to plate the RF conducting surfaces with copper and afterwards to braze the coupler with eutectic braze. This is easiest to use and needs 820°C. Investigations of different copper platings and heat treatments have shown that very thin copper layers of only a few microns can degrade at this high temperature during brazing to RRR (residual electrical resistance ratio between 300 K and 4 K) values less than 2 which would be to low copper quality. The aim is to achieve a coating quality with a final RRR value of about 30. This is possible at brazing temperatures up to only 550°C with a different braze alloy.

A second question is the influence of heat treatment on the Ti antimultipactor coating which has a thickness of only a few nm. Actually tests of Ti coatings on ceramic surfaces and heat treatment of those are done at DESY. The influence of heat treatment is investigated at Hamburg University by Auger electron spectroscopy and XPS. Actual results say that the Ti stays at the ceramic surface but it is not clear what the chemical changes are. Most probably Ti forms a compound with Oxygen from the ceramic surface and Nitrogen. Both compounds are known to have very low secondary emission coefficients and prevent surface multipacting.

One of the questions which are still open is multipacting behavior due to the coupler geometry. Under this aspect the RF field distributions especially of both windows have been studied under all possible operation conditions with the Hewlett Packard HFSS program (different phases at full reflection and travelling wave). In addition a multipactor research program has been started in summer 1993 at Rolf Nevanlinna Institute, Helsinki.
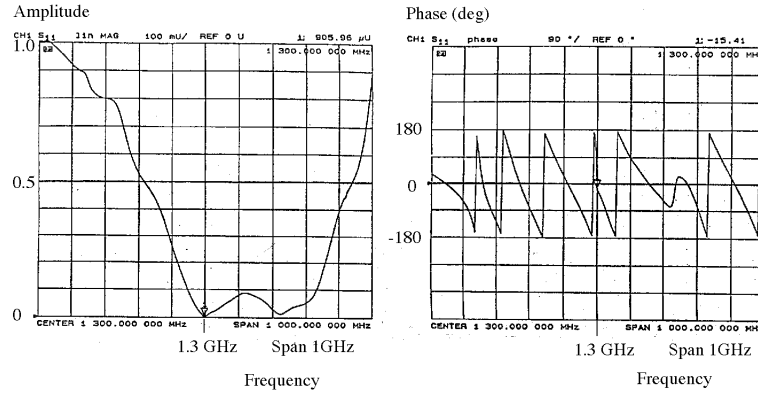
Figure 4.39: Reflection of 300 K window vs. frequency from measurement. a) Amplitude. b) Phase.

4.2.5.7 Window Details

It should be mentioned that the position of the 70 K window is in the voltage standing wave minimum at the end of the RF pulses if there is no beam (high power conditioning). The 300 K window will be near the voltage maximum at that time. This inverts roughly at pulse beginning. Both windows have no enhanced field regions which means that the fields due to compensation techniques are not evidently higher than the unperturbed wave guide and coax fields. This is due to a very broad band design. Thus the window positions seem uncritical.

Also field concentration inside the ceramic is uncritical. The inside peak fields are about 3 MV/m at 1 MW full reflection. The breakdown field of the ceramic is 26 MV/m up to 43 MV/m. Fig. 4.39 and Fig. 4.40 show reflection of the windows vs. frequency. Voltage reflection at 1.3 GHz is less than 1 % in both cases.

The construction of window assembly is the same for both windows. They are connected to their environment by weak copper rings of 1 mm thickness and 1 cm height. The mechanical and thermal behavior of this assembly have been tested thoroughly. Destructive mechanical force is at least 50 N/mm^2 stress at the copper to ceramic connection.
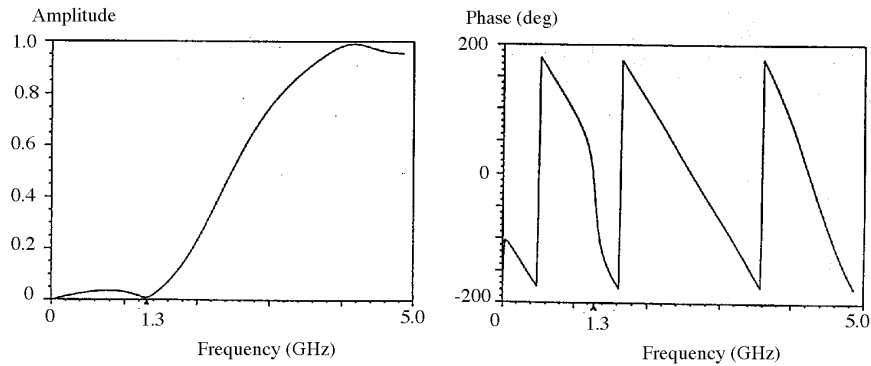
Figure 4.40:   Reflection of 70 K window vs. frequency by computation.
a) Amplitude. b) Phase.

At tests with LN2 the assembly proved to be absolutely thermal shock proof. No leak occurred after many tests.

Also the heat transfer capability of the 70 K window was tested because the inner conductor losses of about 4 W are cooled via this ceramic window. It was possible to transfer about 100 W of thermal power without leak with the outer conductor connection of the ceramic cooled at 70 K.

4.2.5.8   Power Tests of the 70 K Window

A 1.3 GHz coaxial resonator of 3 half wavelengths has been built with the 70 K type window in the voltage standing wave maximum at the middle of the resonator. With two 400 W RF amplifiers it was possible to excite a standing wave corresponding to a fully reflected travelling wave of 100 kW. Hence the achieved voltage at window position corresponds to 400 kW of travelling wave power.

An uncoated 70 K type window was tested up to this power at 2 msec pulses. The observed vacuum-, discharge- and light phenomena were eliminated by conditioning. No limitations were visible up to this power even with an uncoated window.

A test stand for coupler conditioning is planned. It connects two couplers

by a piece of wave guide inside a cryostat at liquid Nitrogen temperature and allows transfer of high RF power via both couplers to an external absorber.

Chapter 5

Cryostat and Cryosystems

5.1 The TTF Cryogenic System

The TTF cooling scheme as of April, 1992, provided for cooling of the vertical test cryostats, the horizontal test cryostat and 50 meter TTF linac, via a large 1.8 K cold box and a large distribution box. Although this allows the most cooling capacity and flexibility in the final system, it would require the acquisition of the large 1.8 K cold box and distribution box at the start, for testing in the first vertical cryostat. This scheme was modified to retain as much capacity at 1.8 K as possible in the final system, but also to allow the startup with the first vertical cryostat with a minimum of auxiliary equipment. This reduced initial costs as much as possible but allows the addition of later components with little disruption of the existing system.

As a result of this design modification, the cryogenic system is assembled in two major stages. The first stage allows only cooling of individual RF cavities in the vertical and horizontal test cryostats, and of a single module. The second stage allows cryogenic operation of the complete TTF linac.

5.1.1 First Stage of Assembly of the System

Since the experiments first of all begin with the tests of single 9-cell cavities, it is enough in the first phase of the test operations to supply one horizontal and two vertical cryostats. Single 9-cell niobium cavities will be tested in a 1.8 K bath in the vertical cryostats. Then, after assembly into its helium vessel, the cavity and its helium vessel are tested at 1.8 K in the horizontal

cryostat. Figure 5.1 shows a block diagram of the cryogenic components for the first stage of the Tesla Test Facility.

For the vertical test cryostats liquid helium at 1.8 K is needed. The horizontal cryostat requires 1.8 K liquid and 4.4 K helium for a thermal radiation shield and intercepts. Cooling of 80 K radiation shields and thermal intercepts in the test cryostats is by means of liquid nitrogen.

An existing 900 W 4.4 K helium plant has been rebuilt and expanded to fulfill the need for 1.8 K and 4.4 K cooling. Supercritical helium (ca. 5 K, 3 bar) is taken from the 900 Watt plant and is carried through an already existing but modified distribution system to the cryostats. In the supply line of each cryostat (see Fig. 5.5) is a low temperature heat exchanger, which precools the incoming helium to about 2.2 K by means of counterflow heat exchange with the pumped vapor. An isenthalpic expansion into the low temperature bath is then carried out via a Joule-Thomson valve, and by regulation of the JT-valve the liquid level in the cryostat is held constant. The returning, low pressure helium vapor is warmed to about 3.5 K in the counterflow heat exchanger, and via an insulated transfer line, a collection box, and a helium heater it is carried to a large room-temperature vacuum pump assembly where it is compressed to 1.2 bar, and in the gas circuit fed to the screw compressors and the 4.4 K cryoplant.

The helium temperature of 1.8 K corresponds to a helium vapor pressure of 16 mbar. The vacuum compressor assembly is sized for a maximum of 10 g/s helium at a suction pressure of 10 mbar. This flow specification corresponds to the requirements of the final stage of the 1.8 K facility. The suction pressure of 10 mbar is necessary in order to compensate for the pressure drop occuring in the heat exchangers and piping. The vacuum compressor assembly, consisting of three stages of roots blowers and one stage of rotary vane pumps, has been manufactured by the Leybold company in Germany.

The cooling capacity available in the test cryostats results from the liquefaction capacity of the 4.4 K cold box and totals a maximum of 100 W at 1.8 K (at a maximum liquefaction mass flow of about 5 g/s). The static losses in the vertical cryostats, including the equipment necessary for the testing of the cavities, are estimated at about 10 W. The remaining cooling capacity is available for the field and quality measurements, as well as the HPP processing. It is possible to reduce the suction pressure of the vacuum compressors further, and thereby to operate the cryostats at temperatures less than 1.8 K with reduced cooling capacity.
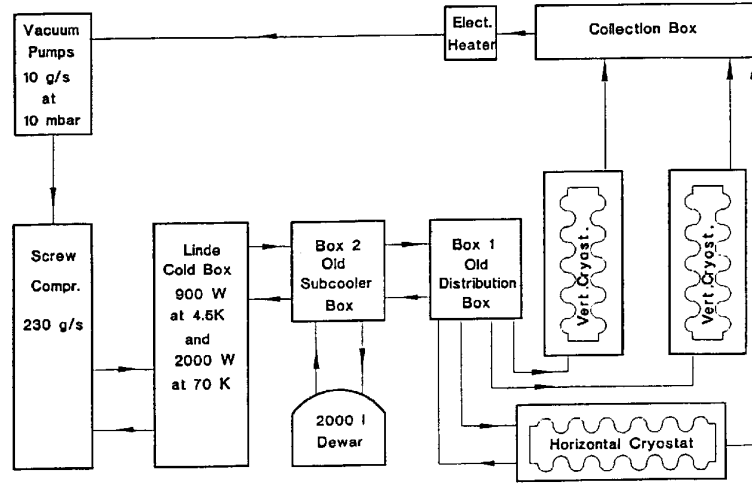
Figure 5.1: The First Stage of the Assembly of the Cryogenic System

In the vertical cryostats the maximum reachable field strength and the cavity quality should be measured with high frequency antennas for single cavities. (The full range of input coupler adjustment allows direct measurement of Q versus E.) To reach higher field strengths the cavities will be treated with high frequency pulses of high power. These may deposit large amounts of heat into the 1.8 K bath. The total heating rate can be controlled via the pulse repetition rate and will be limited by the 100 Watt cooling capacity at 1.8 K.

The limit of achievable field strengths, which in theory should lie at 50 MV/m, is in practice set by field emission of electrons on the inner surface of the cavities. These field emissions are caused by dirt and contaminants in the niobium. Field emission leads to local hot spots on the cavity walls and to the release of gamma rays. With the help of thermometers and photodiodes, temperature maps and gamma emission maps are made.

In the horizontal cryostat further measurements are carried out on the cavity furnished with its own helium tank, before the installation of the cavity in the final crostat module. The high frequency input coupler is tested and the maximum reachable field in the RF cavity, and the cavity quality are measured. Unlike the test in the vertical cryostat, the RF quality mea-

surement here can only be made through the cryogenic measurement of the losses, since the final high frequency input coupler does not have sufficient adjustment range to permit direct electrical measurement.The dynamic load of about 1.5 W should be known with a precision of ± 0.4 W. This measurement will be done by means of a precise measurement of the boiloff gas flow rate and the liquid level.

5.1.2   The Second Stage of the Assembly

Finished 9-cell RF cavities, which have been tested in their helium vessels in the horizontal test cryostat, will be assembled into a 12.2 meter long cryostat module consisting of 8 RF cavities, a superconducting quadrupole, beam position monitors, and various other instrumentation. The second stage of the TESLA Test Facility consists of the additional equipment to cool a string of four of these modules and a capture cavity, which together will form the main part of a test linac (see Fig. 5.2).
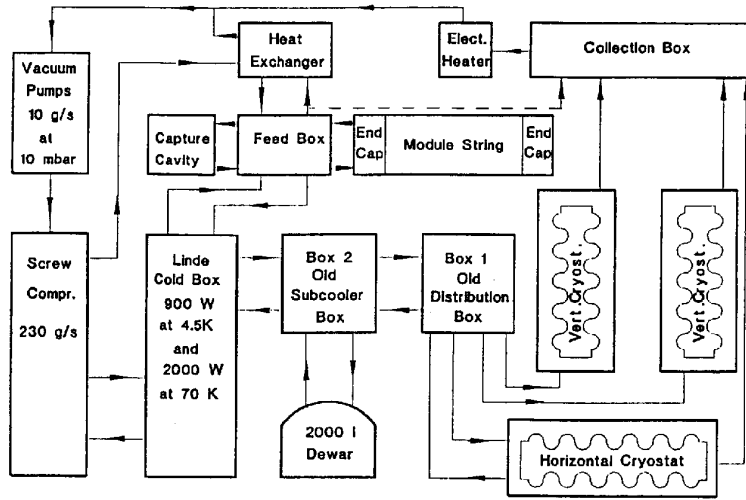
Figure 5.2:   Block Diagram of the Cryogenic System after second stage

The scheme for cooling the TESLA prototype modules in the test linac corresponds to the cooling process which is envisioned for a future TESLA linear accelerator. The cavities will be in a 1.8 K helium bath. Through this

string of 4 modules, between the feed box and end box, an approximately uniform helium level is maintained. The regulation of the JT valve in the entrance of the modules via the measurement of the liquid level in the end box. The vapor returns back to the feed box via a 300 mm diameter return line, which at the same time serves as the mechanical support. The design of this return line and the other process lines is based on the dimensions of TESLA. A cryogenic unit would have a length of 1880 meters in TESLA. Tables in Section 5.7.2 summarize some of the cryogenic parameters for TTF and TESLA.

The cryostat module has two radiation shields. Using the supply of the 4.5 K shield, one superconducting quadrupole per module will operate for beam focussing. The 70 K shield circuit cools an additional high frequency absorber in order to remove parasitic high frequency modes from the cavities (higher order mode losses). For the test of the 50 meter long linac consisting of the four cryostat modules including a beam injection system, the liquid production of the first stage of the cryogenic assembly is no longer sufficient. Cooling must be made available at three temperature levels. The heat loads for the 4 test modules and an injection module total about 80 W in the 1.8 K bath, about 90 W at the 4.4 K shield level, and about 430 W on the 70 K shield. Further losses appear in the transfer lines and supply boxes.

Therefore, with the help of an additional heat exchanger, shown in Figure 5.2, (flow scheme shown in Figure 5.3) the cooling capacity at 1.8 K will be increased to 200 W (10 g/s). About 90 % of the cooling capacity which is carried in the 3.5 K, 16 mbar, return stream is transferred in this heat exchanger to a counterflow stream of 14 bar, the process pressure of the 4.4 K cold box (in the first assembly stage the cooling capacity of the 3.5 K, 16 mbar, stream is lost to the process through the heat added by a heater). After an isenthalpic expansion via feed box to 1.2 bar, this counterflow stream returns to the compressors via the 4.4 K cold box.

Except for the unbalanced mass flow in the supply and return streams of this heat exchanger, required due to the differences in the thermal properties of the two streams, and the cooling of some small current leads, no other liquefier performance of the system is required, whereas the system in the first assembly stage ran as a liquefier. Because of the small permitted pressure drop in the low pressure stream in the heat exchanger, and the therefore small stream velocity required, there are unfavorable conditions for the heat transfer and heat exchange. The above described heat exchanger therefore
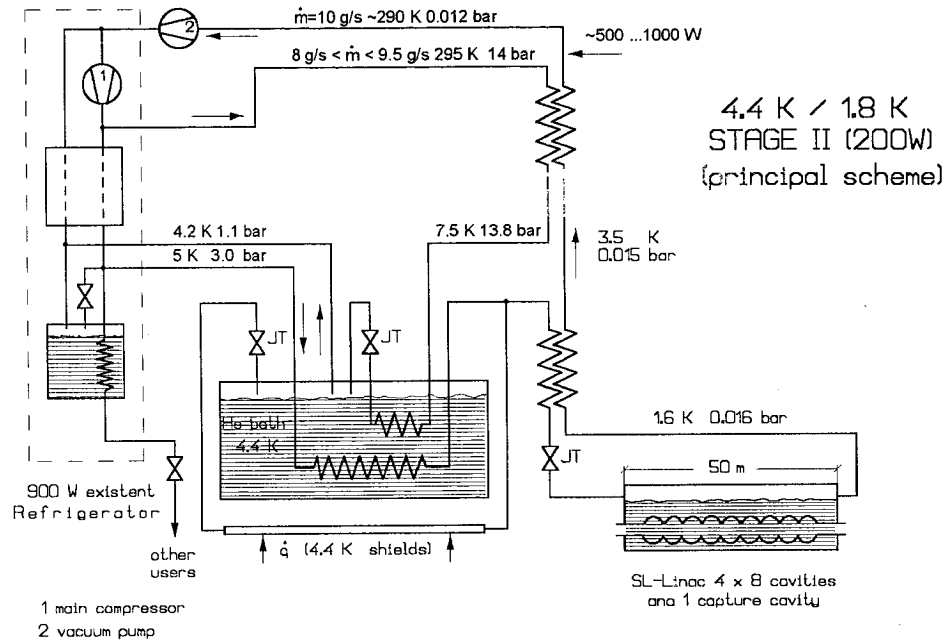
Figure 5.3:   4.4 K/1.8K Stage II (200 W) (principal schema)

requires special engineering.

Table 5.2 summarizes the planned refrigeration and liquefaction capacity for TTF.

Like in the horizontal cryostat tests, heat loads to the 1.8 K bath must be measured in order to quantify the dynamic losses of the RF cavities and understand their performance. It is also desirable to measure the static losses to the 1.8 K bath and the total losses to the 4.5 K and 70 K temperature levels. Therefore, careful flow and temperature measurements are planned at all temperature levels, as well as measurement of the boiloff flow rate from the 1.8 K bath.

5.1.3   The Schedule for the TTF Cryogenic System

At the end of 1993 the first vertical cryostat was brought into operation. The start of operation of the horizontal cryostat took place in October of 1994. In 1996 the second stage of the cold facility with the low pressure heat

exchanger should be finished. The initial operation of the test linac with one module is planned for the end of 1996.

5.2 The Module Cryostat

5.2.1 General Remarks

The TESLA, and TTF cavity production technique has been carefully designed and specified to produce absolutely clean surfaces and to keep them such throughout the whole manufacturing and assembly process. This poses significant constraints on the design and assembly of the cryostat module: eight cavities and the magnetic lens are assembled together in a clean room and have to be inserted in the cryostat as a single UHV tight unit.

5.2.2 Alignment

Another very significant requirement, deriving from beam dynamics considerations is the overall alignment requirements. The axes of the eight cavities must stay aligned to the ideal beam axis to within $\pm$ 0.5 mm and those of quadrupoles to within $\pm$ 0.1 mm over the entire length of the accelerator; in addition, the vertical midplane of the lens assembly must be aligned to the vertical direction to $\leq \pm$ 0.1 mrad. This alignment is to be done warm before assembly into the cryomodule and must stay aligned during operation after cooldown and thermal cycles. (These numbers needs some qualifiers as to the various components of the alignment budget.)

The TESLA design philosophy of very long modules necessarily puts most of the load of keeping such tight alignment tolerances unto the cryostat designer. Cavities and quad package modules, and the cryomodules are therefore equipped with special survey fixtures. Each cavity or quad module carries two pairs of optical target arrays fastened to either side of each cavity neck. Other alignment features are incorporated the module suspension system. For each element, the target arrays define two axes positioned with respect to its mechanical axis so that the axis, and the rotation around it, can be optically surveyed.

All targets must be visible from the outside of the vacuum vessel, through appropriate viewing ports, so that the positions of all elements can be sur-

veyed at any time during handling and thermal cycling.

The internal reference axis is appropriately and permanently reference marked on the outside of the cryostat vacuum vessel so that the various cryomodules can eventually be aligned to each other to $\leq \pm 0.2$ mm.

5.2.3   The Cryostat

The design solution presented here has been chosen for its simplicity and ease of assembly. It has the disadvantage of requiring the cavity input couplers to be flexible (see below); however, preliminary data on flexible couplers designed at FNAL and DESY[1] have not so far evidenced any serious problem in making them perform to specification. Also to minimize costs, we have excluded performing any machining on large items such as the vacuum vessel and the He gas return pipe (see below).

The cryostat outer vacuum vessel, which provides thermal insulation, is of carbon steel and is evacuated to a pressure of 10^{-6} mbar; its design critical external overpressure is 1.25 bar. To minimize the number of warm-cold transitions and avoid external transfer lines, all refrigeration piping runs inside it. The vacuum vessel is supported on two adjustable supports resting on the floor. A schematic view of the cryostat is shown in Fig. 5.5.

The 300 mm diameter helium gas return pipe (HeGRP), required to recover the 16 mbar cold gas evaporated from the 1.8 K He bath, is also used as main support beam for the accelerator module. The overall weight of items (acceleration modules, shields, etc.) hanging from the pipe is approximately 2300 Kg. The HeGRP operating pressure is specified to be 2 ABar, the test pressure 3 ABar. Cross sections of the cryomodule at the locations of the valve at the end of the module, the cavity and the quadrupole are shown in Fig. 5.4, Fig. 4.18 and Fig. 6.2.

The HeGRP beam is supported from above by three support posts that provide the necessary thermal insulation; posts are fastened to large flanges on the upper part of the vacuum vessel, by means of adjustable suspension brackets (ASB). The scope of the adjusting mechanism is to allow for the accelerator module axis to be brought into its proper position, independent of the absolute position of the vacuum vessel flanges on which it rests.

---

[1]M.Champion et al, *Input coupler and windows for TESLA* and B. Dwersteg et al. *Tesla input coupler*, 6th Workshop on Superconducting RF, 1993, CEBAF, Newport News, VA.
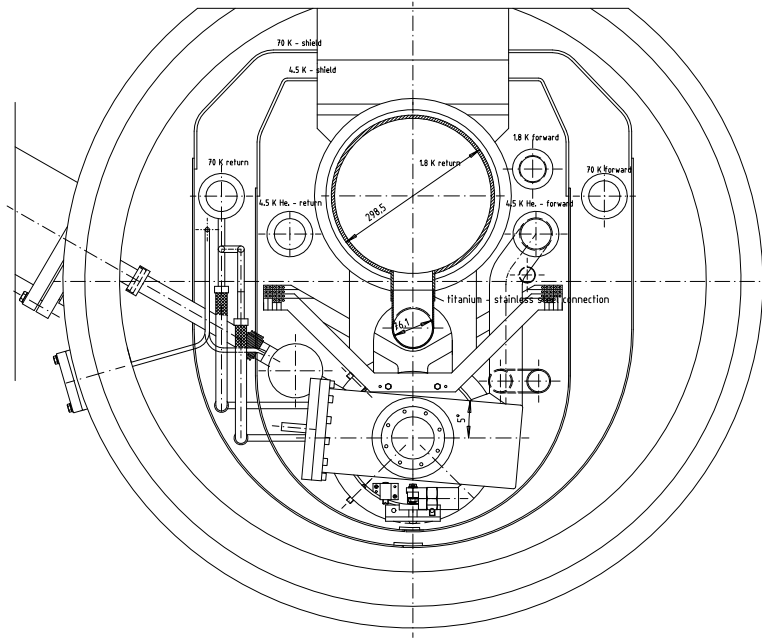
Figure 5.4:   Cryomodule cross section at the location of the gate valve at
the module end.
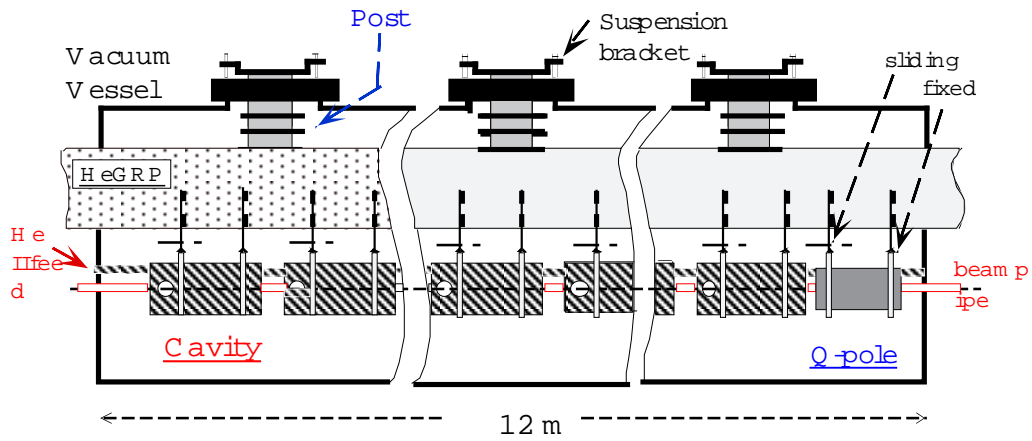
Figure 5.5: Schematic View of the Cryostat

In the longitudinal direction the center post ASB is fixed to the vacuum
vessel while the two end brackets are allowed to move to accommodate dif-

ferential shrinkage during temperature cycling. The posts[2] consist of a fiberglass pipe terminated by two shrink-fit stainless steel flanges (Fig. 5.6). At appropriate intermediate positions, optimized to minimize the heat leak, two additional shrink-fit flanges are provided to allow intermediate heat shield connections to 4.2 K and 70 K. The post diameter has been chosen to push up the assembly main mechanical resonance frequency, corresponding to a pendulum-like motion, to $\approx$ 25 Hz, far enough above the dangerous 10 Hz (rep. rate) frequency.

The accelerator module (8 cavities + quadrupole + auxiliary equipment) is attached to the gas return pipe by means of stainless steel collars (two half-collars, upper and lower, bolted to each other), equipped with adjusting screws for alignment; the screws are spring loaded to prevent them from losing contact during cooldown and warmup. The support system is designed to allow the accelerator module to move with respect to the vacuum vessel during thermal cycling: because the center point of the assembly is fixed to the vessel, the outer ends will be displaced longitudinally by up to 15 mm. The flexible cavity main couplers have to accommodate a displacement of the same magnitude.

The loads on the HeGRP and the pipe computed deflection under load are shown in Fig. 5.7.

Two aluminum radiation shields are provided at intermediate nominal temperatures of 4.2 K and 7 K. Each shield is made in two halves and each half consists of 3 sections for assembly and thermal reasons. The half-shields upper sections are supported by the post intermediate flanges: they are bolted on to the center post but can slide on the end post, to avoid buildup of excessive forces on the posts during thermal cycling, when temperature differences of $\approx$ 100 K can develop between different points of the shield sections. Shields are cooled by means of flexible copper braids connected, at regular intervals, to the centerline of the shield upper section; the braids are directly connected to the cooling pipes, and their cross section is such as to keep the ΔT between shield connection and pipe to $\leq$ 10 K and $\leq$ 2 K for the 70 K and the 4.5 K levels respectively.

The cavity main couplers penetrate both shields and end each at a separate flange on the vacuum vessel side. Special radiation shield 'cones', that also serve as thermal anchoring points for the coupler body, are provided at

---

[2]T. Nicol, FNAL Int.Rep. TM-1794 (Aug.92) and private communications.
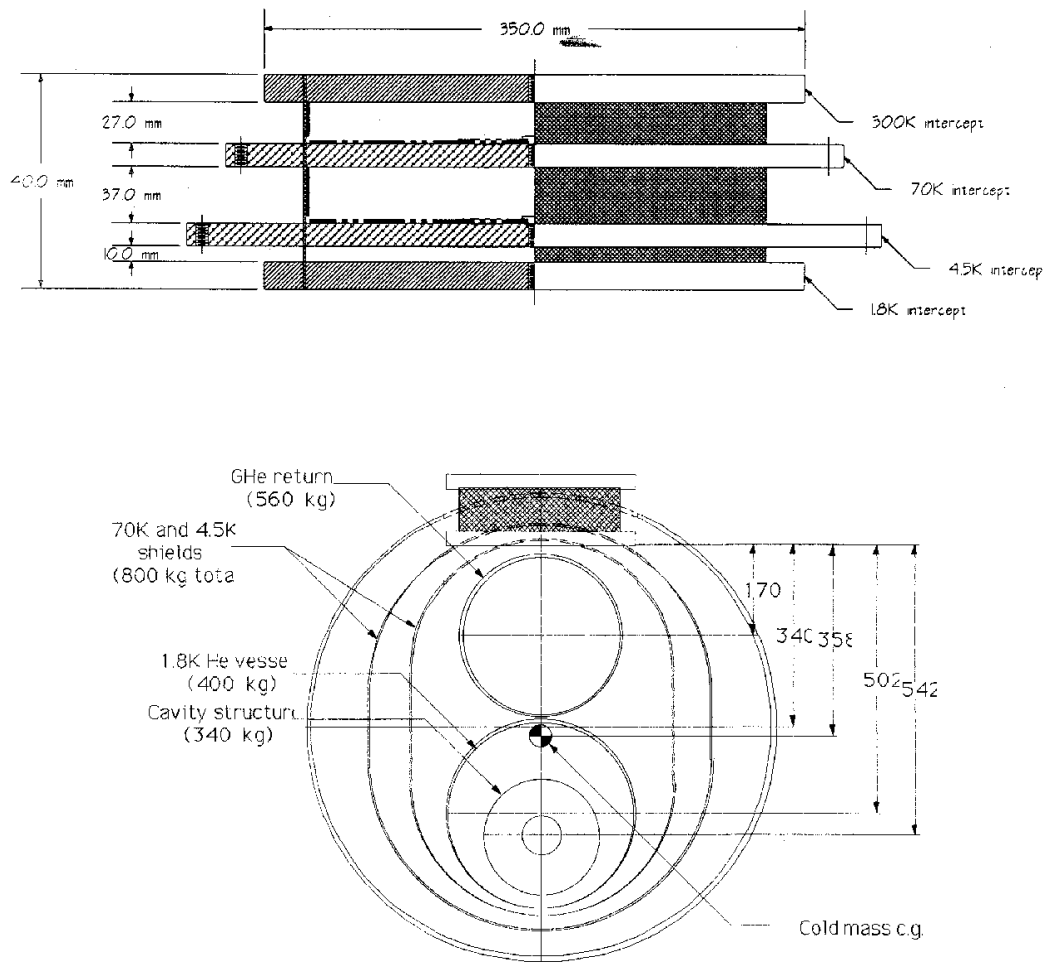
Figure 5.6: Detailed view of cryostat posts

the shield penetration locations.

Seven additional cooling pipes are run through the cryomodules (temperatures are nominal):

- 1.8 K two phase line to supply the cavity baths;

- 2.2 K pressurized He forward, to cool downstream cryomodules;

- 4.5 K pressurized He forward, also used to cool the quadrupole lens windings;

- 4.5 K pressurized He return, also used to cool the 4.5 K shield;

- 70 K He forward, also used to cool the quadrupole beam pipe;

- 70 K He return, also used to cool the 70 K shield;

- a warmup/cooldown line.

A further pipe, running through the vessel is used as shield for the drive wires of the tuner stepping motors.

All pipe connections in between modules are welded; bellows are provided as needed, to mechanically decouple the modules and allow for thermal contraction. Connections to the radiation shields are preformed at regular intervals using flexible copper braid.

All surfaces at 70 K and 4 K, facing surfaces at ambient temperature or at 70 K respectively, are covered with multilayer insulation (MLI). Ten and thirty layers of MLI are provided on the 4 K and 70 K shields respectively . The He vessel, the HeGRP and the quadrupole 4 k feed pipes also have a 5 layer wrap, to reduce heat transmission in case of vacuum failure.

Vacuum vessels are connected to each other by means of a cylindrical sliding sleeve, equipped with O-rings for vacuum tightness; radiation shield connection pieces are also provided. A relief valve on the sleeve and appropriate venting holes on the shields prevent excessive pressure build-up in the vacuum vessel in the event accidental spills of LHe from the accelerator module.

Wires and cables of each module are brought out at the module itself, through flanges equipped with vacuum-tight connectors.

The thermal behaviour of the HeGRP during cooldown shall be studied experimentally to check that no significant stratification occurs, resulting in a nonuniform temperature distribution across its diameter.

Approximately 128 thermosensors and 2 accelerometers shall be installed on the prototype cryomodule to be able to follow temperature distributions during cycling in detail and to measure vibration frequencies and amplitudes.
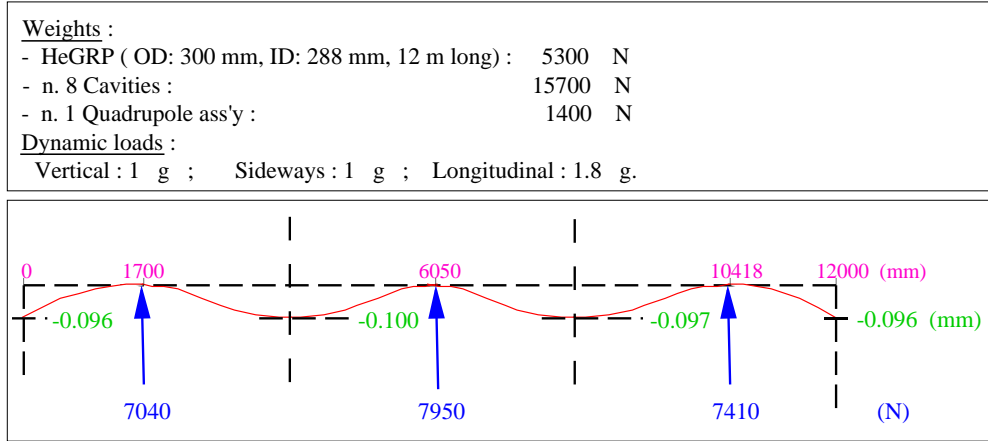
Figure 5.7:   Loads and HeGRP computed deflection under load

The anticipated static heat load budget for the Cryomodule is $\leq$ 3 W @ 1.8 K, $\approx$ 14 W @ 4.5 K, $\approx$ 80 W @ 70 K; except for the last figure it is in good agreement with that in the original design report.

5.2.3.1   Miscellaneous Specifications

An end cap to seal off the quad end of the cryovessel will be supplied with two UHV 100mm diameter glass view ports.

The vacume vessel is carbon steel. All flanges will be stainless to provide good vacuum surfaces.

Vessel shall be leak tested at 1.2 ABar of He gas pressure to 10^{-9} torr l/s individual leak sensitivity, or 10^{-8} overall.

The He GRP material shall be non magnetic at LHe temperature $\mu <$ 1.03.

Piping shall be leak checked at pressure of 20 ABar to sensitivity of 10^{-10} torr l/s after thermal cycleing to 77 K .

5.2.4   Special Assembly Tooling

5.2.4.1   Suspension System Assembly Tooling

Because the assembly shall be subject to thermal cycling over a very large temperature range, and because tight alignment tolerances have to be kept on the hanging mass, buildup of stresses is as much as possible avoided throughout construction and assembly. A sketch of the various assembly phases is shown in Fig. 5.8.

All ribs connecting the three post-supporting flanges and the 18 upper half-collars to the HeGRP are welded to the as-received pipe. The HeGRP is then subjected to an appropriate treatment to prevent permanent deformations in the pipe material, caused by internal stresses having exceeded the material elastic limit or by changes in the structure of the material itself, from taking place after alignment, during subsequent assembly stages and/or during cooldown. The pipe shall also preferably be straightened to better than $\pm$ 3 mm, by a procedure to be determined and depending on the kind of treatment applied. After treatment, the HeGRP is transferred onto a bench on which an ideal beam axis surveyed to $\leq$ 4 mm is defined and put to rest on (adjustable) supports longitudinally positioned in correspondence with the three support-post locations; the reactions on each of the supports are made equal to those computed for the straight pipe.

The HeGRP resting on the supports is adjusted so that the centers of its end sections define the pipe reference axis, to better than $\pm$ 2 mm. Post carrying flanges and upper half-collars are then welded to their respective ribs to within $\pm$ 1 mm of their ideal position. Next, the fiberglass posts and their respective ASBs are be mounted on the post-carrying flanges, also to within the same tolerance. Appropriate pins ensure that the ASBs can be dismounted and remounted to within $\leq \pm$ 0.1 mm. The upper sections of the radiation shields, all supply pipes, cabling anchor plates, etc., shall also be assembled on the HeGRP at this stage. The bracket adjusting screws are finally made to take up the weight of the structure, monitoring displacements and load distributions by means of comparators and dynamometric tools; three spherical optical targets are fastened (but not permanently since readjustment may become necessary during final assembly of the module) to the brackets and positioned with respect to the ideal reference axis to within $\leq$ 0.1 mm; a reference surface, horizontal to within $\leq$ 0.2 mm/m, is also

established on each bracket. Targets and reference surfaces allow the geometry of the pipe to be surveyed precisely throughout the following assembly stages.
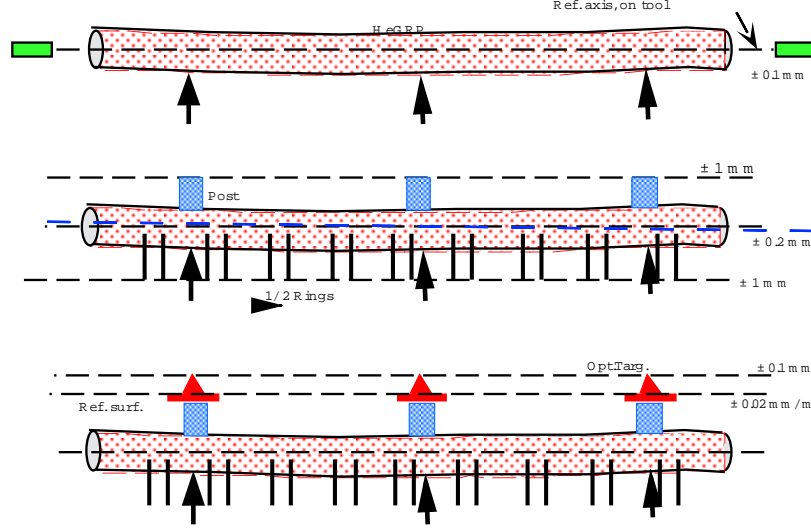
Figure 5.8:   Sketch of the AM Suspension System First Assembly Phases

5.2.4.2   Accelerator module lifting rig

The tooling is used to connect the accelerator module, assembled and aligned to better than ± 0.2 mm and delivered to assembly Station 1 in the assembly hall on a carriage rigidly guided by a rail in the floor, to the HeGRP assembly. The latter is brought to Station 1 directly above the accelerator module carriage and lowered onto a bench. The bench is rigidly fastened to the hall floor. The bench carries three shelves, horizontal and level (under load) to ± 0.1 mm and positioned to match the assembly suspension brackets. A local surveyed ideal AM axis and the optical targets and reference surfaces on the suspension brackets allow the HeGRP to be positioned so that the AM supporting upper half-collars are in place with respect to the AM itself to ≪ ± 1 mm. Finally, the lower half- collars are fastened to the upper ones and the adjustment screws brought in contact with the AM outer vessels so as to block it into position. The whole assembly can be then transported to the final alignment Station 2.

5.2.4.3   Final Alignment and Assembly Bench

The HeGRP and accelerator module assembly is placed on the bench, similar
to that of 5.2.4.2, where final assembly and alignment shall be performed.
It is brought to rest on the bench support shelves horizontal and flat to $\leq$
0.1 mm. Cavities and quadrupole are fine-aligned using the support collars
adjustment screws so as to bring them all on the ideal locally surveyed AM
reference axis, within the specified tolerance. Optical-targets and horizontal
reference surfaces on the suspension brackets are then readjusted to refer
to the AM reference axis to within $\pm$ 0.1 mm and then finally blocked.
The targets allow the AM configuration to be reproduced within tolerance,
using the bracket adjusting screws; when the cold mass is hung in its final
position from the cryostat vacuum vessel upper flanges, independent (within
the adjustment range) of the absolute position of the latter.

5.2.4.4   Cold Mass Insertion into the Vacuum Vessel Tooling

The assembly is completed by adding the lower sections of the radiation
shields, superinsulation, piping and cabling, with the loaded beam assembly
resting on the bench and by rechecking the alignment. The final operation,
sketched in Fig. 5.9, is then to insert the completely assembled cold mass
into the vacuum vessel.

The cold mass is lifted on an outhanging beam that engages the HeGRP
and the ASBs are dismounted. Fig. 5.9 is self explanatory as concerns the
following operations. Once the cold mass has been inserted in the vacuum
vessel, the ASBs are bolted back unto the posts through the vacuum vessel
upper flanges, and pinned into position.

When the adjustment screws are set to reproduce the bracket optical
targets alignment, the AM module alignment is reproduced to the required
tolerance.

5.3   Other Major Cryogenic Components

5.3.1   Vertical Test Cryostat

The vertical dewar is used in the testing of individual superconducting radio
frequency (RF) cavities. Tests are performed in a saturated bath of approxi-
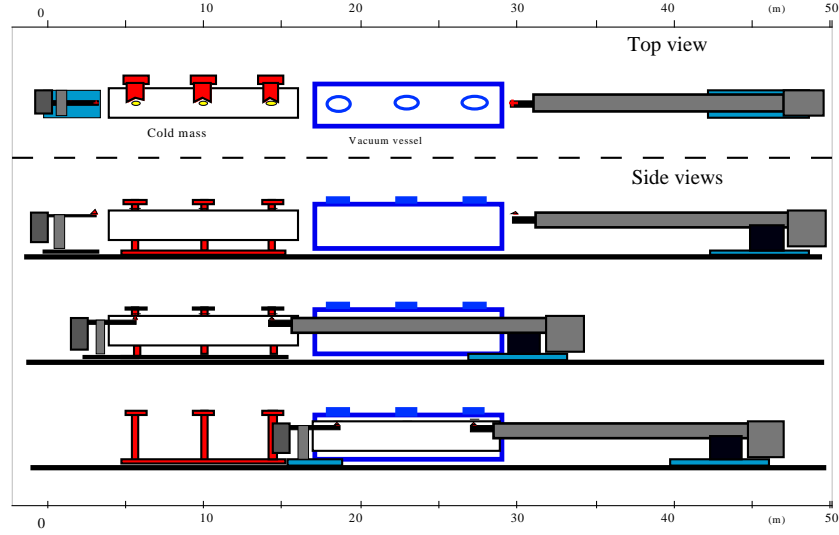
Figure 5.9:   Schematic View of the AM Insertion into the Cryostat Sequence.

mately 700 liters of 1.8 K liquid helium. The dewar assembly is a standalone system comprised of an inner helium vessel, liquid nitrogen (LN_2) shield, and outer vacuum vessel. The dewar assembly is shown in Figure 5.10.

The apparatus under test is suspended from the cover plate. Connections to the electrical, cryogenic, and vacuum systems are via connections located on the top plates of the inner and outer vessels.

To simplify the design of this distribution system, the heat exchangers and J-T valves for subcooling 4.5 K helium to 1.8 K were moved to the individual downstream devices. As such the design of the vertical test dewar involves more than a helium vessel, LN_2 shield, and insulating vacuum vessel. Figure 5.11 illustrates the cryogenic system in the vertical dewar. Helium at 4.5 K is supplied through a warmup and cooldown valve to the bottom of the inner vessel for initial filling. After the vessel is full, this valve is closed and flow passes through the tube side of a heat exchanger which provides counterflow exchange with gas being pumped from the liquid volume. The subcooled inlet flow, initially at 4.5 K, enters the inner helium vessel and is controlled by a J-T valve. The gas flow on the shell side of the heat exchanger is pumped by warm vacuum compressors and is controlled by a 60
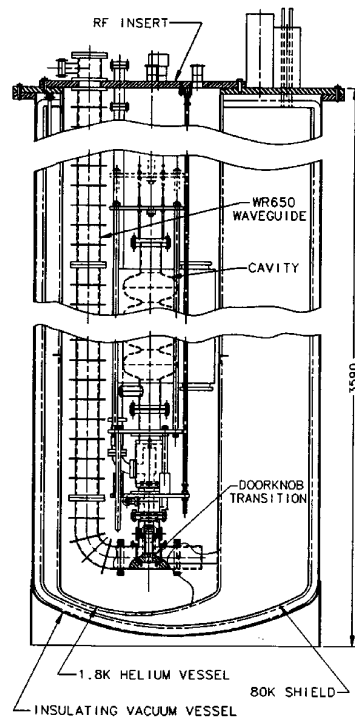
Figure 5.10: Vertical test cryostat

mm isolation valve. The design flow in all the piping circuits is 5 grams/sec helium, which would allow 100 W of cooling at 1.8 K. The heat exchanger and all of the valves are located in the annular space between the inner helium vessel and the LN_2 shield.

5.3.2   Horizontal Test Cryostat

An horizontal test cryostat: C.H.E.C.H.I.A.

(**C**ryostat **H**orizontal d'**E**ssai de **C**avités **H**abillées et de l'**I**nstrumentation **A**ssociée: Horizontal test cryostat for dressed cavities and associated instrumentation)

A test cryostat (C.H.E.C.H.I.A.) shown in Fig. 5.12 has been designed and built for testing horizontally positioned single cavities. It will not only allow one to compare cavity performance measured in vertical and horizontal
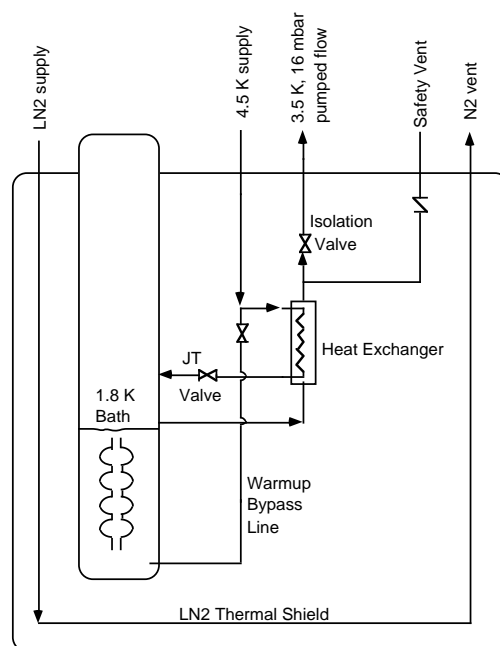
Figure 5.11: Vertical test cryostat schematic

position, but will offer the possibility of testing 9 cell cavities fully equipped with their welded helium vessel, HOM couplers, cold tuner and main coupler before the final assembly of 8 cavities together in the main TTF cryomodule. In particular, it will allow checkout for the first time of:

- the tightness at cold of the helium vessel,

- the tuning range, accuracy and speed of the cold tuner,

- the detuning of a stiffened cavity due to bath pressure variations as well as radiation pressure.

5.3.2.1   Cavity performance measurements:

One aim is to measure a few points of the curve Q versus accelerating field. As the input coupler will not have the right coupling coefficient, cryogenic
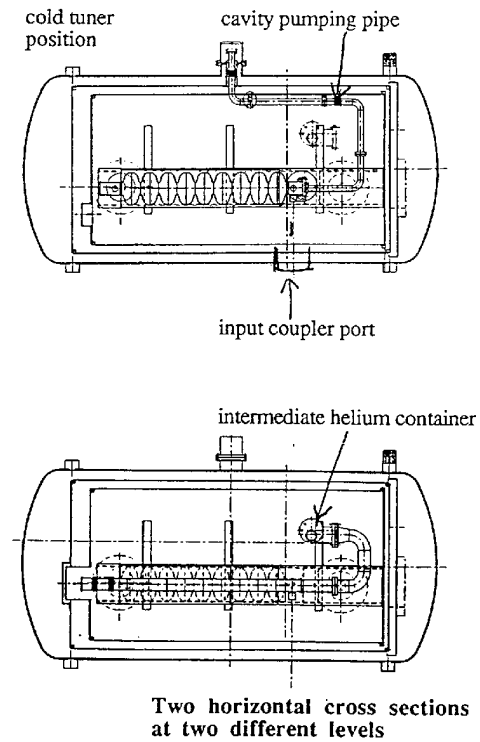
Figure 5.12: Horizontal Test Cryostat CHECHIA

measurements have to be done to determine the heat load to 2 K with and
without RF. The goal is to reach an accuracy of 0.4 W, which means that
the static head load has to be at most about 4 W.
Two methods are possible:

1. For a steady liquid level, one measures the flow rate out of the cryostat.
   A good accuracy is expected in measuring the pumped helium gas flow,
   provided one does it during several hours (the longer the measurement
   lasts, the better is the accuracy).

2. With no helium flow in, one measures the liquid helium change. To
   improve the accuracy, the level probe is installed in an intermediate
   container. This container is built higher than the helium vessel so that
   the latter can be kept full during the measurement. Its cross section is

small to amplify level variations.

HPP treatment: It is necessary to be able to do some HPP treatment. The helium consumption at 2 K will then be higher than under normal RF conditions, and the pipes and valves have to be sized large enough. This is somewhat in contradiction with the mentioned above required sensitivity (0.4 W) for heat load measurements. A compromise has been set at 2 g/s for the maximum helium flow at 2 K (corresponding to 40 W). The duty cycle of HPP treatment will have to be adjusted to stay below this allowed maximum.

5.3.2.2   Main features of the cryostat:

- A vacuum vessel, made of carbon steel, and equipped with a large hinged cover. Once a cavity is in, all connections to be made in place are near the door (input coupler, cavity vacuum pipe and cabling).

- Two aluminum shields, one cooled at 70 K with liquid nitrogen, the second to 4.5 K with liquid helium. Permanent tubing connections are at the back of the cryostat.

- Two insulating posts, with intermediate connections to the shields, for supporting the cavity.

5.3.2.3   Magnet shielding:

Each cavity will be installed within a 1300 mm long permanent shield, around the helium vessel. Measurements have shown that, under these conditions, at Saclay, with a south-north orientation of the cryostat, the field values around the cavity stay at a reasonable level: the values are below 10 mG, excepted along the few last centimeters on the end-cells, where it reaches up to about 35 mG.

5.3.3   Capture Cavity

The capture cavity is a standard TESLA cavity (9 cell, 1.3 GHz), identical to the 32 other cavities in the TTF linac. It incorporates all of the new concepts developed for the TESLA project, i.e. the helium vessel inte grated
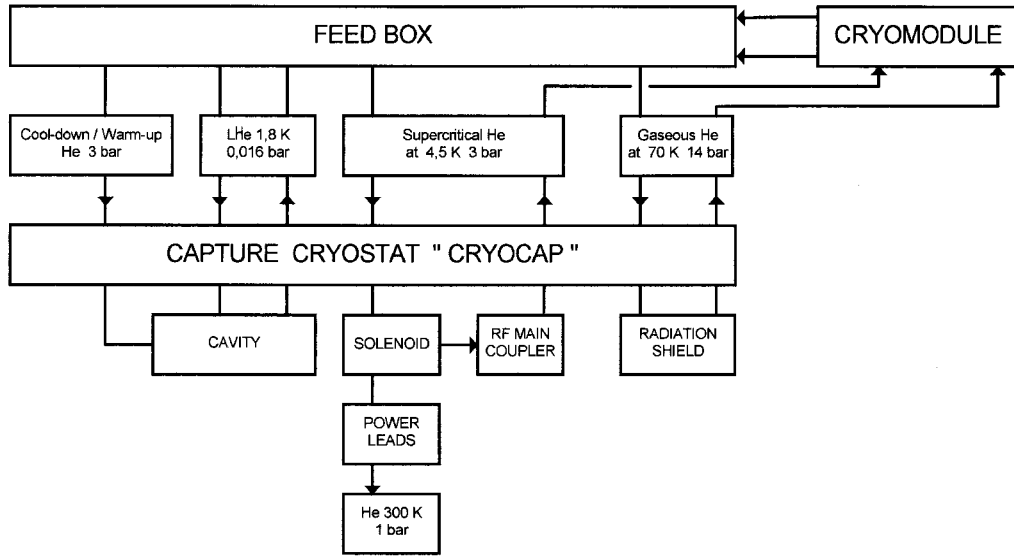
Figure 5.13:   Functional diagram of the capture cavity cryostat.

to the body of the cavity with a reduced LHe volume (25 liters) and with both the main and HOM couplers located in the cryostat vacuum.

The role of the capture cavity is to :

- terminate the bunching initiated upstream. The bunches will have a duration of $\leq$100 ps at the entrance to the cavity and will be compressed by a further factor of 10,

- provide the necessary energy (7 - 14 MeV) for injection into the first cryomodule, the energy depending on the field at which the structure in operated.

5.3.3.1   Refrigeration

The capture cavity is installed in a separate cryostat (CRYOCAP) at the end of the injector. A common cryogenic feed box supplies the cooling for Cryocap and for the cryomodules connected partly in parallel, partly in series as shown, in the block diagram of Fig. 5.13.

Refrigeration is produced with He only circulating in three loops at different temperature levels :

- a supply of two phases He at 1.8 K and 16 mbar maintains a constant LHe level of the cooling bath around the cavity,

- a second loop fed with supercritical He at 3 bar successively refrigerates a superconducting focu sing solenoid and a heat sink on the main RF coupler. A small fraction of the mass flow is diverted to cool the solenoid power leads and is allowed to warm up to ambient temperature,

- a third loop with He gas in forced convection at 14 bar and 60 K cools a radiation heat shield at 80 K.

For initial cool down or final warm up of the cavity another small ancillary feed line is connected to the bottom of the LHe tank.

5.3.3.2 Cryostat Description

Fig. 5.14 shows the composition of Cryocap in an isometric presentation.

Vacuum tank The vacuum tank is made from stainless steel. Its essential dimensions are the following:

- external diameter 800 mm (over flanges : 870 mm),

- length 2165 mm (end connection flanges included : 2620 mm),

- volume (tank empty) : 1.00 m^3

It is considered as a containment volume for any hazard which may occur to the fragile cavity vessel containing some 25 liters of LHe. A safety valve set at 1.2 bar absolute limits any overpressure.

The cylindrical vacuum tank has precisely machined end flanges, equipped with removable end caps which perfectly define the cavity axis by means of two sight lines through the cryostat. These are necessary for the initial cavity alignment but might be useful for an occasional control of its position even in the cold state.
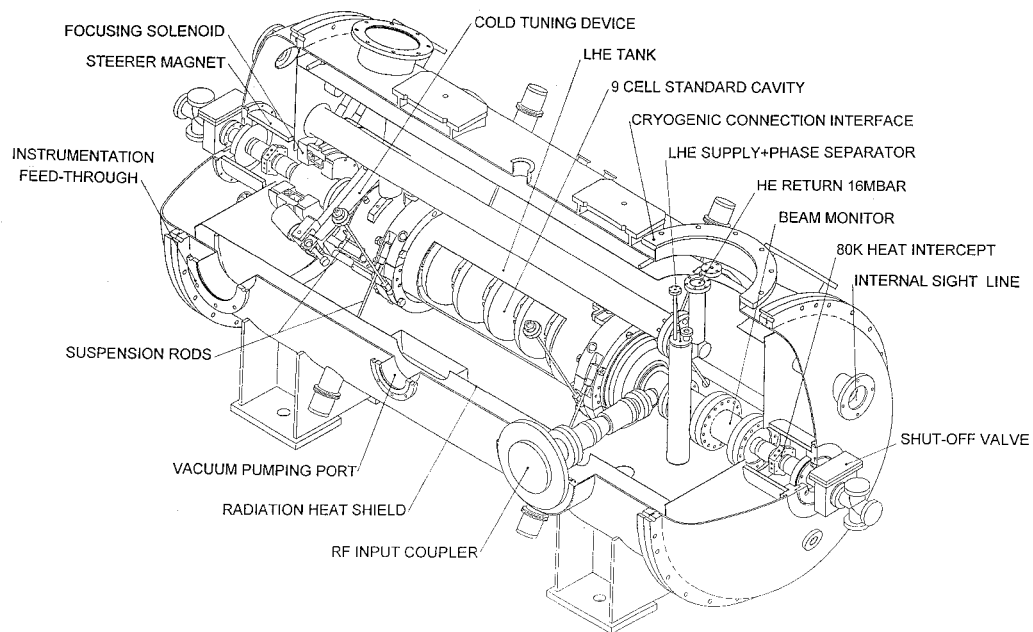
Figure 5.14:   Isometric representation of the capture cavity cryostat.

The insulating vacuum of Cryocap is autonomous; a specially devised barrier, located in the cryogenic connection line, separates it from the feed box vacuum space.

A residual pressure of $\leq 10^{-5}$ mbar is achieved with a turbomolecular pump during start up, with cryopumping from the LHe tank later on in steady state conditions.

Radiation heat shield The thermal radiation from ambient temperature to the cold cavity vessel is intercepted with a copper radia tion shield cooled to 80 K with forced flow He circulation on its cylindrical part which is integrated in the vacuum tank where it stands on 4 nylon bases. Both removable end covers are conduction cooled.

A blanket of 40 layers of superinsulation is applied on the outside of the shield and substantially reduces the incoming heat flux.

A direct passage through the radiation shield, equipped with a baffle to prevent radiation penetrating, allows an efficient evacuation of the core of the cryostat.

Its basic function apart, the radiation shield also serves other purposes :

- it provides a heat sink for different thermal intercepts with flexible copper braids linked to the main coupler, the beam tubes, the instrumentation wiring, etc...

- it supports a solenoid coil for active magnetic shielding during cool down,

- it may be used to warm up the cryostat with an electric heater (with a thermocoax cable soldered onto the copper cylinder).

LHe tank with cavity For reasons of standardisation the LHe tank with its 9 cell cavity, the cold tuning device, the RF input coupler and the HOM couplers are strictly identical to the elements used in the cryomodule as desribed in Chapter 4.

Magnetic shielding)

- Passive magnetic shielding for the cavity is provided with a sheet of Cryoperm wrapped on the LHe tank.

- Active magnetic shielding is produced during cool down by a solenoid coil (10A, spaced 20cm) wound on the 80 K heat shield.

Suspension system   Since for Cryocap no large He return tube is needed its suspension system differs completely from the concept of the cryomodule.

Two split suspension rings are clamped onto the LHe vessel at each end. A radial suspension device with 2 sets of 4 epoxy-fiberglass rods permanently maintains the cavity in its initial position, an arrangement which blocks any thermal shrinkage of the suspension rods. This is acceptable since the low Young's modulus of these composites induces only moderate thermal stresses.

In axial direction the LHe tank and also the 80 K radiation shield are blocked with a finger device mounted on the vacuum tank which maintains one of the suspension rings.

Aligment procedure   The alignment of Cryocap on the TTF linac beam axis is essentially accomplished in two steps:

- an internal aligment of the cavity on the geometric axis of the vacuum tank. With an individual adjustment of the suspension rods the cavity is precisely positioned on the cryostat axis, this is checked by bringing two precision survey marks, fixed on each end collar of the cavity, on two known sight lines through the vacuum tank,

- an external alignment which adjusts the whole cryostat until its external survey marks fit onto an external sight line.

Beam tubes   The beam tube connects the cold niobium cavity to the beam line at ambient temperature. It requires :

- some flexibility to compensate the thermal contraction of the cavity and to tolerate minor adjust ments of its position,

- a very low heat leak for thermal conduction and radiation,

- a cryopump section for hydrogen trapping to protect the cavity itself.

Therefore each beam tube consists of :

- a 2 K cold section, a externally copper plated stainless steel tube flanged on the end of the cavity,

- a metallic bellows from 2 K to 80 K, and a heat intercept section at 80 K,

- a metallic bellows from 80 K to ambient temperature,

- an end plate with a tubular feed-through for the vacuum tank,

- a provisional shut off valve to keep the operational cavity under vacuum during assembly.

In order to avoid a bulky end plate and to facilitate final assembly, a special gate valve from CETEC is provided which can be temporarily removed, leaving a simple tap, maintained by vacuum only, on a standard CF - 35 flange.

Focusing solenoid   For beam corrections at the cavity entrance a focusing solenoid is necessary. A superconducting solenoid with its iron yoke is supported from the LHe vessel suspension ring. The magnet and its shielding are conduction cooled from the 4.5 K loop.

Beam monitor   Space is provided at the cavity exit for a beam monitor still to be defined.

Steering coils   Two steering magnets are necessary in proximity to the cavity. A set of coil at ambient temperature is fixed on the inner side of each and cap in the vacuum tank.

5.3.4   Helium Collection Box and Heater

When one of the vertical cryostats or the horizontal cryostat is operating at 1.8 K, the pumped helium vapor emerging from the small JT heat exchanger associated with the test vessel is at a temperature of about 3.8 K and a pressure of about 15 mbar. This low temperature, low pressure helium must be warmed to near room temperature (at least 253 K) before entering the large vacuum pumping system (see 5.3.5).

Warming up to 5 g/s of this low pressure helium is not easy. At 5 g/s one must add about 7.5 KW of heat to the helium stream without significantly impeding its flow. For this purpose an electric heater was designed and built. The heating element consists of a bundle of 648 stainless steel tubes, each 1 cm diameter and about 1 m long. Electric current passing through the tubes warms them, and heat is transfered to the helium flowing through and around the tubes. The heating element is assembled into a 60 cm diameter vessel which is vacuum insulated.

Since the heater is a rather large and costly device, instead of providing separate heaters for each of the two vertical cryostats and the one horizontal cryostat, a vacuum insulated valve manifold, called the helium collection box, was built which can direct the 3.8 K, 15 mbar flow from any one of these devices to the single heater. The collection box contains a fourth input line, so that pumped flow from the TTF linac may also be brought through the same helium heater. This is an optional method of warming the pumped helium vapor from the TTF linac without the large, low pressure heat exchanger (see 5.3.6). However, the system would be limited to 100 W total cooling capacity without that heat exchanger.

5.3.5   Vacuum Compressor Pumping System

During stage I operation of the TTF cryoplant a flexible helium pumping system is needed to meet the demands of the experiments. With a maximum mass flow of 5 g/s at stationary conditions temperatures down to 1.8 K are achievable. Also lower temperatures can be reached at lower mass flows.

The stage II cooling capacity of 200 W at 1.8 K for the operation of the complete test linac corresponds to a maximum helium mass flow of 10 g/s at 16 mbar.

The vacuum pumping assembly is designed to meet the demands of stage I as well as of stage II: for helium mass flows in the range of 0.2 to 10 g/s the pressure can be regulated from 10 mbar to 30 mbar with a relative stability better than 1 %. For mass flows lower than 10 g/s the pressure can be lowered to about 1 mbar.

Although cold compressor systems for this pressure range and mass flows up to 10 g/s are available, warm vacuum compressors where chosen for the TTF because of their flexibility and simplicity of operation. After crossing low temperature heat exchangers and a gas heater in stage I or a large low

pressure heat exchanger in stage II the helium gas should have a temperature of more than 253 K before entering the vacuum compressors.

The vacuum compressor assembly consists of four stages. At the low pressure end the gas is compressed by two roots blowers (LEYBOLD RA 16000) in parallel followed by two stages of single roots blowers (RA 13000/RA9000). All roots blowers are dry pumps, only the bearings are oil lubricated. In the last stage four rotary vane pumps (LEYBOLD SOGEVAC 1200) in parallel feed the gas back to the main gas circuit of the helium refrigerator at a pressure of 1.05 to 1.3 bar, corresponding to the suction pressure of the screw compressors.

Under full stationary load the maximal electrical power consumption does not exceed 150 kW (with 340 kW power installed).

All pump stages are separated by gas coolers. The rotary vane pumps are cooled in addition by oil/water heat exchangers . The oil contamination of the gas is lower than 60 ppm at the outlet of the rotary vane pumps and is further reduced to < 1 ppm by additional filter elements to avoid any risk of oil condensation in the cold parts of the refrigerator. Breox B 35 oil is used in all vacuum compressors as well as in the screw compressors of the refrigerator.

The suction pressure of the vacuum compressor assembly is regulated by two bypass valves in parallel to the rotary vane pumps and the roots blowers respectively.

The whole machinery is operated by an internal process control system (SIEMENS SIMATIC S5) which communicates with the process computer of the refrigerator. In automatic mode the internal process control can be set to local or remote. With the wanted suction pressure set, the system reacts to changes of mass flow and pressure by operating the bypass valves and switching pumps on and off.

The vacuum compressors are housed in an extra building attached to the TTF-experimental hall but separated by its own foundation with a distance of about 20 m to the test linac. The frame of the vacuum compressors is separated from the floor by special damping elements (BARRYMOUNT SLM), resulting in more than 90 % damping of the vibrations. (The RMS oscillation velocity of 2 mm/s at the frame is reduced to less than 0.1 mm/s at the floor.) The outer shell of the compressor building is designed for a noise reduction of more than 30 dB(A), to meet the demands of environmental protection laws.

The complete vacuum compressor assembly was designed and constructed by the LEYBOLD AG in Germany and delivered to the TTF-collaboration in time and on schedule.

5.3.6   Large, Low Pressure Heat Exchanger

During stage I operation of the TTF-cryoplant all cooling capacity at the 1.8 K temperature level results from the pure helium liquefaction capacity of the 4.5 K Cold-Box, which is limited to about 5 g/s of liquid helium in stationary operation. The cooling capacity of the pumped gas is used only in part by precooling the 4.5 K helium in the supply of the JT's of the test cryostats, most of the cooling capacity is "wasted" by heating the gas to room temperature in the gas heater of stage I. (The delivery of liquid from the plant in stage I can be enhanced temporary and buffered by means of a 2000 l helium storage tank which is connected to the helium distribution system of the two vertical cryostats and the horizontal cryostat).

For a long term operation of the test linac more than 100 W cooling capacity at 1.8 K (corresponding to more than 5 g/s mass flow) under stationary conditions is needed. Therefore the cooling capacity of the pumped gas has to be fed back to the cryoplant turning the liquefaction operation mode into refrigerator mode.

The enthalpy of the low pressure gas has to be transformed to a pressure and temperature level which can be used in the cryoplant by means of a Large Low Pressure Heat Exchanger.

In this heat exchanger incoming warm 14 bar helium gas is cooled to a temperature lower than 7.5 K by the low pressure gas which enters the heat exchanger at a temperature of about 3.5 K.

At a maximum mass flow of 10 g/s of the low pressure gas the high pressure mass flow has to be tuned to the performance of the heat exchanger resulting in a mass flow of about 9 g/s. The high pressure gas is expanded via a JT valve into the precooler of the TTF-feedbox. The high pressure gas flow rate is controlled by the gas temperature in the supply of this JT valve.

The design of the heat exchanger has to accept some challenges: At a low pressure mass flow of 10 g/s a pressure drop of only 3 mbar can be allowed. Large thermal stress due to a high temperature gradient is expected. The performance of the heat exchanger will be seriously affected by internal heat flow along the tubes.(A small gas heater of 1.5 kW at the warm outlet of

the low pressure flow is added to give more flexibility).

The Large Low Pressure Heat Exchanger is installed into a vacuum isolated box, separated from the 4.5 K Cold-Box and from the feedbox of the test linac.

5.4 Cryogenics of the Module Helium Vessel

Cool-down, operation, and warm-up of a string of RF cavities in their helium vessels must be considered during the design of the helium vessel as well as during the design of the cryogenic system. Operation of strings of pool-boiling RF cavities in superfluid will be different from the operation of strings of superconducting magnets to which some of us have become accustomed.

Figure 5.15 shows the module crystat. The concept is to supply 1.8 K liquid to the helium vessels via the "1.8 K forward" pipe above the helium vessels. The saturated bath surrounds the RF cavity, heat is absorbed by the latent heat of vaporization of helium, and the vapor is pumped away through the "He gas return pipe". Thermal shields at 4.5 K and 70 K are also included. The following describes some of the considerations for cryogenic operations.
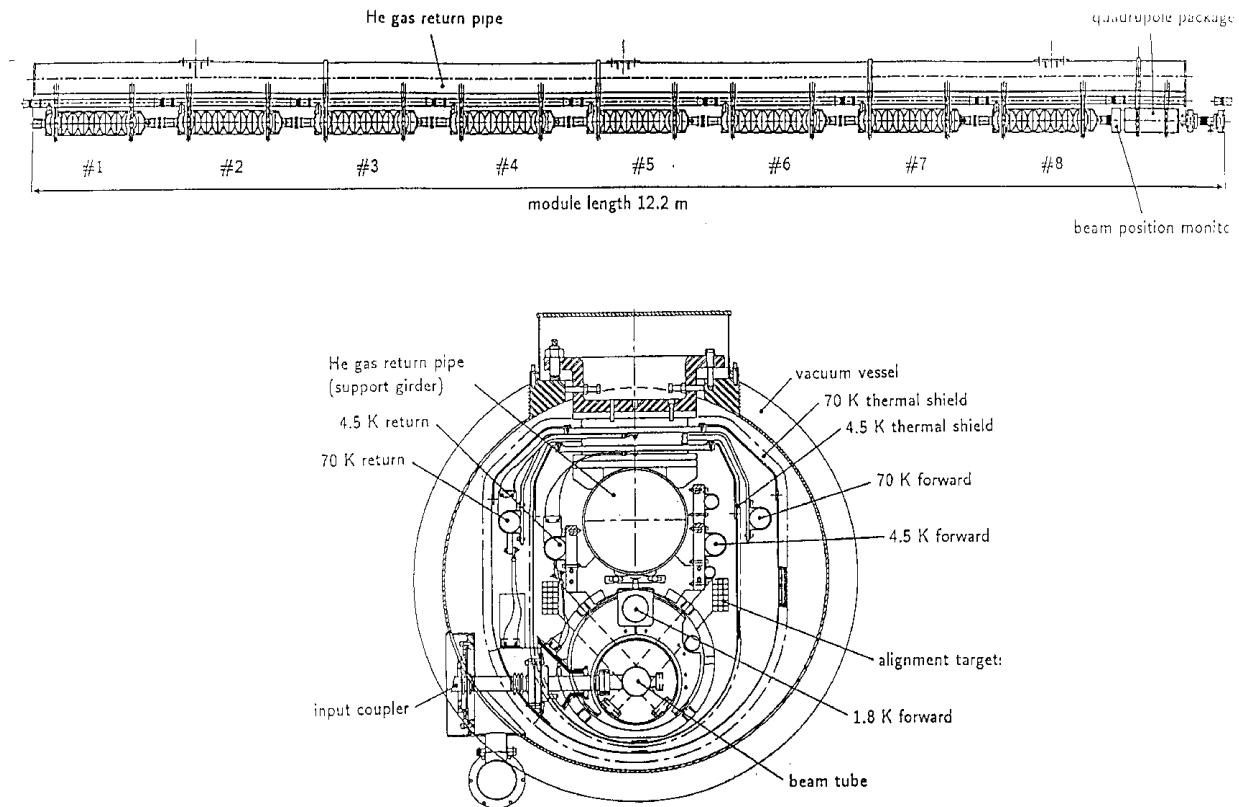
Figure 5.15: Module cryostat

5.4.1   Cool-down from 300 K to 5 K.

For the cool down of the module cavities, the cooldown/warmup tube is used which supplies all helium vessels of the module string in parallel. The cavities can be cooled to 5 K in this way. However, it will also be possible to cool the helium vessels from the 76 mm liquid supply line.

Each niobium cavity is 14.6 Kg. In cooling that mass of niobium from 300 K to 5 K one must remove 759 KJ of energy. The titanium helium vessel iis about another 20 Kg. With magnetic shielding and other 2 K material, not including the 300 mm header, there are about another 3313 KJ of energy per cavity to remove. This totals 130 MJ of thermal energy to remove from

4 modules from the 2 K mass in cooling from 300 K to 5 K, which would require 695 liters of liquid helium if one cooled directly from 300 K. The TTF cryogenic system can provide this in 5 hours; so a 5 hour cool-down of the 4 modules in TTF looks feasible.

5.4.2 Filling with liquid.

Flow in the 76 mm tube is completely stratified. Liquid runs along the bottom of the tube and vapor above the liquid, so liquid runs into the helium vessels sequentially, filling one and then the next. The cavity helium vessels can also be filled by means of the cool-down tube with liquid at about 4.5 K. It will also be possible to fill the helium vessel by flow through the 76 mm tube as well with 4.5 K or 1.8 K liquid, depending on the vapor pressure in the helium vessels. The liquid volume in the 230 mm diameter helium vessel is about 23 liters. Four modules of eight helium vessels each will hold about $4 \times 8 \times 23 = 736$ liters. In TTF, based on the steady-state capacity of the helium liquefier (5 g/s, or 144 l/h), fill time for a four-module string will be about 5 hours.

5.4.3 Steady-state operation

The concept of the warm-up header for parallel forced-flow warm-up of the vessels allows frequent open (no check valve) connections from the 76 mm tube to the 300 mm tube, greatly reducing potential steady-state pressure drop problems in the 76 mm tube; large pressure drops could lead to liquid level instabilities.

Pressure stability due to the pulsed nature of the accelerator requires that only a small amount of liquid be present to avoid excessive pressure changes with each pulse. Calculations have been done regarding the pressure and temperature response of the string of 32 helium vessels in TTF to a step change in heat load. For a single RF pulse of 8 ms duration, 10 times the present 0.8 ms design, the pressure change is 0.015 mbar, or 0.23 mK temperature change. The volume of liquid necessary to have no more than a 0.1 mbar pressure pulse is 3.4 liters of liquid helium per cavity, which is to be compared to our present 23 liters per cavity with the smaller, concentric helium vessels.

Turning on or off the power to the four modules in the string test results in a 0.47 mbar/min decrease or increase in pressure. If we want to keep pressure steady within $\pm$ 0.1 mbar, the pumped flow rate has to be adjusted within 12 seconds. This amount of time is proportional to the amount of liquid helium. If the liquid inventory were cut in half, for example, the response time available for the controls would be cut in half. A heater in the end can could be used to provide a more nearly constant vaporization rate, reducing the requirement for flow control. Only about 12 W per module would compensate for dynamic loads during these tests.

Liquid level will tend to be very stable. The initial effect of a heat load change will be for the system to cool down or warm up, with liquid level depending only on the ratio of pumped flow and supply flow.

Studies of heat transport in saturated baths of superfluid indicate that a heat flux of at least 1 W/cm^2 can be carried vertically to the bath surface without vapor formation in the liquid. For the reduced volume helium vessel with a 70 mm OD connection, this means about 30 Watts. This is less than the amount of heat that could be removed in the old design, with its more wide-open bath, but should still be more than sufficient since we expect at most a few Watts per cavity.

5.4.4   Liquid removal.

Liquid can be removed from the cavity helium vessels by parallel supply of warm gas through the cooldown/warmup tube.

5.4.5   Warm-up from 5 K to 300 K.

Warm-up flow is provided by a warm-up header and "capillary" tubes to the helium vessels, allowing a forced convection warm-up. The amount of mass to be warmed is relatively small compared to the superconducting magnet systems with which many of us are more familiar. Therefore, warm-up heat transfer can be relatively inefficient and warm-up time still acceptably short, even for TESLA. This fact can be illustrated by working backwards from the requirement of a 24 hour warm-up of a 145 meter TESLA string to 290 K from around 50 K. (After liquid removal the experience at CEBAF is that, due to the low heat capacity of the low temperature material, the cavities and helium vessels are at 40 to 50 K.) The mass of niobium is about 15

Kg per cavity, and the mass of titanium for titanium vessels is about 12 Kg per vessel. Call it 20 Kg niobium and 20 Kg titanium per vessel to allow for magnetic shielding, interconnecting pipes, etc. This means the energy required to warm one helium vessel and cavity is 1150 KJ (niobium) + 2000 KJ (titanium) = 3150 KJ. With 96 of these in series in a 145 meter string one needs 302 MJ. To add this in 24 hours means adding heat at an average rate of 3500 W, or just 36.5 W per cavity. When providing 36.5 W of warming, the 15 g/s of warm helium flow supplied by the JT valve would be cooled by just 0.5 K per cavity. Thus, only poor heat transfer from the helium to the cavity and vessel is required.

Since the TTF string is only 50 meters, a 24 hour warmup means adding about 1200 W to the cold mass of 4 modules to get the 36.5 W per cavity.

5.5   Safety and Venting for the Helium and Vacuum Vessels

5.5.1   Emergency Venting of the Helium Vessel

Venting of the rapidly boiling helium from a string of helium vessels following the loss of insulating vacuum or cavity vacuum to air is a significant consideration in the design of the system. The condensation of air on the cold metal surfaces can result in heat fluxes of 2 W/cm² to the liquid helium, and the very rapid internal pressurization of the helium vessels and external pressurization of the RF cavities. Preventing pressures of more than 2 or 3 bars absolute requires venting about 0.8 Kg/s of helium from the helium vessels. Since the vessels vent in series via the 76 mm tube to a connection to the 300 mm header, frequent connections to the 300 mm header are required. With a liquid supply tube of approximately 100 mm in diameter, 8 vessels can safely vent in series, but 16 vessels in series is too much. Therefore, with flow from both directions through the vessels and 100 mm tubes to a vent to the 300 mm header, a two bar limit implies one vent to the 300 mm header for every 2 modules.

The reduced volume cryostat has the advantage for emergency venting that the total volume of liquid which can boil off is less than in the present design. The surface area for air condensation in a loss of insulating vacuum accident is less, so the venting rate in that accident would be less, but the loss

of cavity vacuum accident is the worst and results in the same flow for any helium vessel design. Therefore, the number of connections required from the nominally 100 mm tube (presently 76 mm) to the 300 mm tube is the same for the reduced volume design as in the present design. One must have at least one connection for every two modules. The present design includes one connection to the 300 mm header at each interconnect, one per module.

The port from the helium vessel to the 76 mm tube need not be very large for emergency venting. One 50 mm diameter port between the helium vessel and 76 mm tube is sufficient to vent vapor from the helium vessel into the 76 mm tube at a low pressure in a loss of vacuum accident.

5.5.2   Helium Spill in a TTF Module or Module String

Assumptions and starting data.   The TTF module presently includes: 23 liters of liquid helium per helium vessel, 8 helium vessels per module, one vacuum vessel relief per module, and a net insulating vacuum volume of 9200 liters per module.

Suppose liquid from one helium vessel "instantaneously" dumps into the vacuum vessel. It evaporates, fills the insulating vacuum space with cold helium gas, continues to warm by free convection, and causes the helium in 8 vessels to rapidly boil and vent helium into the vacuum space via the ruptured vessel. (Venting from only 8 vessels needs to be considered even in a long string of modules since there is one relief for every module.) This helium is mostly confined within the two cylindrical shields as it flows to the vacuum relief on the stainless steel sleeve at the interconnect. The helium in the vacuum space vents out the vacuum vessel relief at the interconnect. Figure 5.16 is a sketch illustrating a module cryostat with the vacuum vessel vents at the interconnects.

Calculations.   (23 liters liquid helium) × (125 g/liter) = 2875 g helium in the insulating vacuum space initially. Consider just one module since this gives the most rapid initial pressurization. Density is (2875 g)/(9200 l) = 0.31 g/l. At 1.2 bar absolute pressure this corresponds to 188 K. Therefore, if no other helium were added to this initial spill, the vacuum relief would open when the gas in the vacuum space reached an average temperature of 188 K.
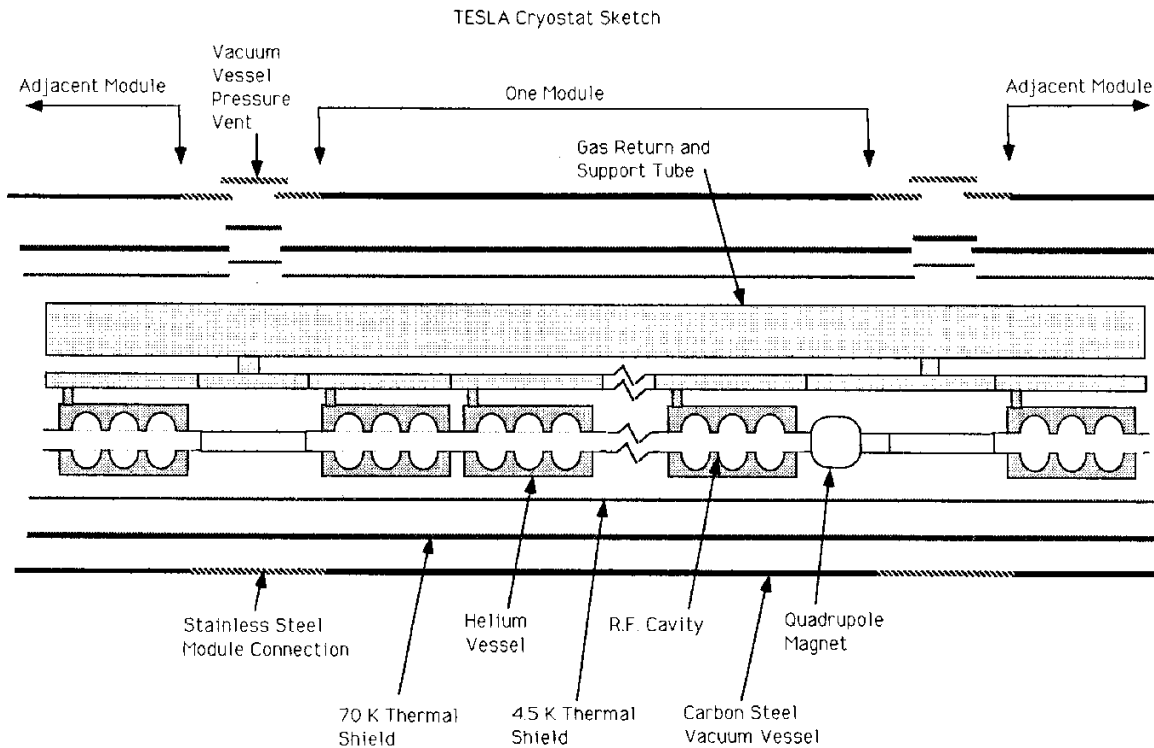
Figure 5.16: TESLA cryostat sketch

Check the rate of warm-up of the helium in the vacuum space. Assume the helium outside the shields is warmed by free convection from a 300 K vacuum vessel wall. The heat flux from the vacuum vessel wall ranges from 0.8 W/cm^2 for 8.5 K gas to 0.08 W/cm^2 for 200 K gas. From 8 K to 188 K the heat flux averages about 0.2 W/cm^2, so the initial 2875 g of helium would take 30 seconds to warm to 188 K and begin venting from the vacuum relief.

Check the rate of heat transfer to the helium vessels. Assume the heat flow is limited by conduction through helium gas in the MLI, and is from a 300 K outside temperature to a 4 K vessel temperature. Thus, neglect the limitation of the free or forced convection outside the MLI, and consider only the limit due to conduction through the MLI. This results in 783 W/vessel. The $8 \times 783 = 6263$ W/module to liquid helium at 1 bar produces a flow

rate of 327 g/s.

If this flow is warmed by a heat flux of 0.2 W/cm^2 from the vacuum vessel walls via the helium around the outer shield, it is warmed by about 100 kW per module, which results in a temperature at the vent of 64 K.

Suppose the vent temperature is 80 K, and 327 g/s flows out of it at 1.0 bar. The vent is a 10 cm diameter port. The pressure drop through this port is then 0.034 bar. Thus, the maximum pressure in the vacuum vessels is 0.034 bar over atmospheric pressure.

Calculate the rate of cooling of the vacuum vessel walls. They are 8 mm thick carbon steel. With the density of steel = 7.8 g/cc, we have 6.24 g/cm^2 of vessel wall. The heat capacity at 300 K is 0.45 J/gK, so the walls hold (0.45 J/gK) $\times$ (6.24 g/cm^2) = 2.81 J/cm^{2}K. With a heat flux of approximately 0.2 W/cm^2, cooling is initially at a rate of 0.07 K/sec, or 4 K/min.

Check the ultimate equilibrium temperature of the vacuum vessel walls versus the amount of helium warmed by the vacuum vessel. Assume the heat stored in the vacuum vessel steel is the only source of heat for the helium (i.e., neglect warming of the vessel by convection from are and condensation of water vapor, and neglect the 80 K shield) and that all the helium is warmed to the equilibrium temperature (i.e., neglect the fact that most of the helium vents at a temperature lower than the equilibrium temperature). Equilibrium temperature versus amount of helium warmed is plotted in the attached figure.

Conclusions.

1. Warm-up and venting of the helium are quite gentle compared to the capacity of the vacuum relief. The predicted maximum pressure reached is 0.034 bar over atmosphere.

2. The two layers of MLI-covered cylindrical shields conduct the venting helium to the vacuum vent at the sliding sleeve. Cooling of the carbon steel vacuum vessel shell is primarily by free convection to the initial load of cold helium and occurs initially at a rate of about 4 K per minute.

3. The ultimate temperature reached by the carbon steel vacuum vessel depends on the amount of helium warmed. Even if the helium from all 8 helium vessels comes to an equilibrium temperature with the carbon steel vacuum vessel walls, the ultimate temperature is -10 °C.

4. The metal around the vent is cooled significantly by the exit flow, but the sliding sleeve is stainless steel. The O-rings may be cooled to the point of leaking, an insignificant problem compared to what else has happened.

5. The only way to get severe cooling of the carbon steel is to have locally concentrated cooling by the spilled helium. We claim that this is very unlikely due to the intervening double-cylinder of thermal shields. However, if this did occur there should be no danger since the overpressure above atmosphere is so small.

5.6   Measurements and Instrumentation

The primary cryogenic measurement of interest in TTF is the heat load to the 2 K liquid helium. Finding the component of this heat attributable to dynamic losses in the RF cavities allows us to calculate the Q of the cavity or cavities. The quantities of interest for measurement, the single module heat loads that are anticipated, and the associated instrumentation are summarized in Tab. 5.1, Tab. 5.2, and Tab. 5.3 respectively.

5.6.1 Summary Table of Cryogenic Measurements

Table 5.1: Summary Table, based on 25 February 1993 TTF Design Workshop at DESY, revised in April and December, 1993, by T. Peterson

Measurement	Est. meas (W)	Back- ground + meas.(W)	Method (see comments below)	Estimated error (W)	Notes
Static heat load to 2K in 1 module	4	9	1,2,3	± 1	Calib. with electric heater in liquid
2 modules	8	13	1,2,3	± 1	" " "
3 modules	13	18	1,2,3	± 1	" " "
4 modules	17	22	1,2,3	± 1	" " "
0 modules	5	5	1,2,3	± 1	" " "
Static heat loads vs vacuum and vs shield conditions	4 - 30	9 - 35	1,2,3 4,5	± 1 ± 5	" " "
Total load with RF for 1 module	21	26	1,2,3	± 1	1.3% duty factor, 15 MeV/m, Q=3E9
2 modules	42	47	3 4,5	± 1 ± 5	" " "
3 modules	63	68	3 4,5	± 1 ± 5	" " "
4 modules	84	89	3 4,5	± 1 ± 5	" " "
Heat load with one cavity powered **Q meas.** 1 module	1.4	10	1,2,3	± 5	Measure difference of power on vs off, not absolute value
2 modules	1.4	14	1,2,3	± 0.5	" " "
3 modules	1.4	19	1,2,3	± 0.5	" " "
4 modules	1.4	23	1,2,3	± 0.5	

Measurement	Est. meas (W)	Back-ground + meas.(W)	Method (see comments) below)	Estimated error (W)	Notes
Static, dynamic, and beam-loaded **capture cavity**	6	up to 95	3 4,5	± 1 ± 0.5	Can do much better when measuring differences
Whole system with electron beam	∼ 10	100	3 4,5	± 1 ± 5	
4.5 k heat load for 1 module	23	33	flow rate	± 3	Calib. with heater in pipe
2 modules	46	56	” ” ”	± 5	” ” ”
3 modules	69	79	” ” ”	± 1	” ” ”
4 modules	92	102	” ” ”	± 1	” ” ”
70 k heat load for 1 module	135	155	flow rate and ΔT	± 10 to ± 30	Again need heater for Calibration
2 modules	270	290	” ” ”	”	” ” ”
3 modules	405	425	” ” ”	”	” ” ”
4 modules	540	560	” ” ”	”	” ” ”
HOM absorber	0.2-20	0.2-20	Separate flow via ”2 k supply tube”	?	Measure cold Δ T, measure flow at room temperature

Measurement methods.

1. Integrated measurement of pumped gas volume at vacuum pump discharge. Hold steady liquid level (lfashed vapor from JT adds to "noise" in measurement)

2. Pumped gas heater power plus temperatures into and out of heater. Hold steady liquid level or liquid supply closed,

3. Measure change of 2 K helium vapaor pressure with both the supply valve and the cold exit valve closed.

4. Cold venturi flow meters upstream of parallel large and small JT valves. Must have steady liquid level, error is in liquid level changes, so method is only as good as liquid level measurement.

5. Measure change of liquid level with liquid supply closed. Large liquid surface area makes it a "course" measurement of heat load.

Heat loads.   Heat loads for the various test conditions which are summarized above in Tab. 5.1 are based on the following numbers plus the assumption of 5 W, 10 W, and 20 W, respectively, to 1.8 K, 4.5 K, and 70 K in the feed can. (Tab. 5.2

Assume for the TTF linac static loads of 1.5 times our latest estimates of 2.8, 13.8, and 76.8 W per module to 2 K, 4.5 K, and 70 K, respectively. This means use here: 4.2 , 21, and 115 W static loads. An estimate of total loads (with 15 MV/m at $Q=3 \cdot 10^9$) is 14.3, 15.2, and 91.2 W (did not include HOM absorber loads at 70 K since they are on a separate stream for TTF), at 2 K, 4.5 K and 70 K, respectively. Again, use 1.5 times these estimates for design purposes. This means use here: 21, 23, and 135 W total loads.

5.6.2   Comments on measurements at 2 K

Three methods of heat measurement could be sufficiently sensitive. These are:

1. Measurement of pumped gas volume at the pump discharge.

   Check one hour of operation. (23 J/s) × (3600 s/hr) × (1 hr) / (23.2 J/g) = 3569 g (averaging 0.905 g/s). At 1 atm, 300 K, this is (3.57 Kg)

Table 5.2:   Summary Table of TTF Heat Loads for One Module

	2 K Watts	4.5 K Watts	70 K Watts
Estimate of static load	2.8	13.8	76.8
Estimate of total load	14.3	15.2	115.2 (- 24 W HOM = 91.2)
Static load x 1.5 (for design)	4.2	21	115
Total load x 1.5 (for design)	21	23	135

$\times$ (5.9 m^3/Kg) = 21 std m^3/h. This mass of helium corresponds to a mass of helium in the 70 mm liquid supply pipe 12 meters long, when it is about half full of liquid. So one hour time without any liquid supply is possible. The gas meter should be sized for about 20 standard cubic meters total helium gas per hour.

The main source of error may be assessing the average temperature and pressure of the metered flow.

2. Pumped gas heater power with temperatures into and out of the heater.

Again suppose 23 total Watts, so (23 W)/(23 J/g) = 1.0 g/s. Suppose our thermometry says the heater warms this gas from 4.0 K to 290.0 K. This would correspond to 1488 Watts of heat to the helium. If we make a 1 % error in the power measurement we would have a 1error in the heat load estimate. If we measured the correct 1488 W but measured temperature out as 291 K, a 1 K error, we would estimate mass flow as (1488 W)/(1493 J/g) = 0.997 g/s, a 0.3 % error, or 0.07 W error in the heat load estimate. So this method is potentially very accurate. (It was suggested by R. Duthil of Saclay in our February, 1993 meeting.)

The main source of error may be unsteady conditions and latent heat effects in the heater, so one will have to maintain conditions as steady

as possible for a period of time before the temperatures and current are recorded.

3. Pressure rise in the closed system.

   With the liquid supply valve and the cold shutoff valve to the 16 mbar pumping line closed, as the liquid evaporates the vapor pressurizes the vapor space. If we measure pressure to 0.1 mbar, we could sense the addition of 200 Joules of energy per module to this closed system. Over a period of 24 minutes for the measurement of 21 Watts, we would measure 200 J out of 30 KJ, for an accuracy of 0.7 %, or 0.14 W. So this method is potentially very accurate. CEBAF uses it.

   A source of error could be the warming of the vapor in the upper part of the vapor space. This would also absorb heat and contribute to the pressure rise, but at a different rate from the system with just saturated vapor. This method also has the disadvantage for testing with RF power that the temperature and pressure are slowly rising during the test. One could limit the effect by stopping the test after some smaller pressure change, sacrificing some sensitivity for more constant conditions.

   The next two methods are less promising. Estimating heat load from liquid level or supply flow will probably not be as sensitive as the above three methods.

4. Liquid level measurement.

   Suppose our liquid supply pipe is 70 mm OD, so 64 mm ID. We will not go smaller than this, and a larger pipe will give less sensitivity of the liquid level, so this is the best case. Suppose the tube is half full of liquid. The liquid surface area in one module is then 6.4 cm × 1220 cm = 7808 cm^2. This implies a rate of change of liquid level of 7.808 l/cm height. (0.7808 l/mm) × (145 g/l) x (23.2 J/g) = 2630 J/mm, initially. At 23 Watts we have (23 J/s)/(2630 J/mm) = 0.0088 mm/s, or 0.5 mm/min level change, very slow. With a sensitivity of 1 mm, it would take 2 minutes to notice a change due to 23 Watts of heat!

5. Supply flow measurement.

Cold flow meters (orifice plate or venturi) upstream of the JT valves will be included in the module transfer line. These measure the liquid supply flow rate. Although we can measure the liquid supply rate to within 5 % (based on experience elsewhere with venturis and orifice plates), the measurement also depends strongly on whether liquid level is steady. If our control system can hold a steady liquid level to $\pm$ 5 mm, this is a range of 1 cm height, or about $\pm$ 13100 J, a large error. But its effect can be reduced by time-averaging. For a one hour measurement this is an uncertainty of $(13100 \text{ J})/(3600 \text{ sec}) = 4$ Watts. The error is more than this in the middle of a tube larger than 70 mm and less near the top or bottom. In February, 1993, we estimated $\pm$ 5 W for this method, which still seems reasonable, so that number remains in the table.

This method may work best for high heat loads (above 30 W total) over periods of several hours.

5.6.3   Measurement of heat loads to 4.5 K and 70 K.

At both of these levels we plan to measure the flow rate and a temperature difference. Our experience with this method at Fermilab in magnet systems is that the results are good to about 10 %, for example, 2 Watts out of 20 Watts. The uncertainties are result of temperature sensing errors, flow measurement errors, and unsteady conditions. If a heater can be used to calibrate the measurement, one can do much better than this. The 10 % error is conservatively listed as the estimate in Tab. 5.1.

5.6.4   HOM cooling and heat measurement.

We plan to run a single-pass flow of nominally 4.5 K, 3 bar helium through the "2 K supply line" (which is not used in TTF since we supply liquid to the 70 mm tube at the feed can) and back through a separate HOM cooling tube. The flow comes out the feed can and is warmed to room temperature, after which the flow rate is measured. A temperature difference around the HOM absorber is measured.

Early tests will be at low power. Say we want to measure about 1 Watt. A ΔT from 4.5 K to 4.8 K would be nice for our temperature measurements.

This is a change in 3 bar helium enthalpy of 1.53 J/g. For one Watt this means 0.65 g/s flow, about like the flow for cooling a 6000 amp current lead. At the feed can we need a 1 KW heater to warm this flow to 300 K.

Say we keep this same flow rate and have 10 Watts at the HOM absorber. This warms the helium to 5.77 K, still reasonable to measure. For low heat loads like 0.2 W, 0.1 g/s would provide a 0.4 K rise. Therefore, for HOM cooling tests design the lines and flow measurement for 0.1 to 0.5 g/s nominal, 1.0 g/s maximum, and plan on a heater capable of 1.5 KW maximum at the exit. The flow can be both measured and controlled at room temperature, like current lead flow at Fermilab.

Table 5.3:   Instrumentation Summary for TTF Heat Load Measurements

Temp level	Device	Location	Range	Accuracy	Notes
2 K	flow orifice	feed box	0.4-2.0 g/s	±0.1 g/s	In the 2 K supply to the small JT
2 K	flow orifice	feed box	2.0-10 g/s	±0.5 g/s	In the 2 K supply to the small JT
4.4 K	flow orifice	feed box	2.0-10 g/s	±0.2 g/s	In the 4.4 K supply to the capture cavity
70 K	flow orifice	feed box	4-20 g/s	±0.5 g/s	In the 70 K supply to the capture cavity
2 K	s.c.liquid level probe	linac end cap	g/s	± 1 mm	Also is input for control of JT valve
300 K	gas meter	pump discharge	20 std m^3/hr	± 1 m^3/hr	Sized only for loads up to about 23 Watts
300 K	thermo-meter	low press. disch. out gas heater	250 - 300 K	± 1 K	Not the same as the sensors on the heater
4.4 K	thermo-meter	feed box and end of module	4-10 K	± 0.002 K	Want at least one per module in helium
70 K	thermo-meter	feed box and end of module	60-150 K	± 0.5 K	Need not be in the helium pipes
300 K	flow-level	feed box	0-1 g/s	± 0.05 g/s	Warm meas. of 4.5 K HOM cooling flow

5.7   Cryogenic Tables

5.7.1   Heat Load Budget and Losses

Table 5.4: Heat Load Budget for Test Module

2 K Load·Watts per meter (*8/12 of load per cavity for cavity associated loads)			
Losses Grad Q (10^9)	static Losses	Total Losses 15 MV/m 3	Total 25 MV/m 5
RF Load*	·	0.73	1.22
Radiation	·	·	·
Supports	0.01	0.01	0.01
Input Coupler*	0.02	0.031	0.04
HOM Load*	·	0.31	0.31
HOM Absorber	·	·	·
Power Lead	·	·	·
Cables	0.2	0.2	0.2
Sum 2 K Load·Watts/m	0.23	1.28	1.78
Losses/ 12m Module containing 8 Cav	2.8	15.4	21.4
Losses for 4 modules	11.2	61.6	85.6
4.5 K Load·Watts per meter (*8/12 of load per cavity for cavity associated loads)			
RF Load*	·	·	·
Radiation	0.35	0.35	0.35
Supports	0.2	0.2	0.2
Input Coupler*	0.21	0.27	0.33
HOM Load*	·	·	·
HOM Absorber	0.1	0.1	0.1
Power Lead	0.1	0.15	0.15
Cables	0.2	0.2	0.2
Sum 4.5 K Load·Watts/m	1.16	1.27	1.33
Losses/ 12m Module containing 8 Cav	13.9	15.2	16.0
Losses for 4 modules	55.6	60.8	64

70 K Load-Watts per meter (*8/12 of load per cavity for cavity associated loads)			
RF Load*	-	-	-
Radiation	2.0	2.0	2.0
Supports	2.3	2.3	2.3
Input Coupler*	1.5	2.7	3.6
HOM Load*	-	2.8	2.8
HOM Absorber	-	-	-
Power Lead	-	-	-
Cables	0.6	0.6	0.6
Sum 70 K Load-Watts/m	6.4	10.4	11.3
Losses/ 12m Module containing 8 Cav	76.8	125	136
Losses for 4 modules	307	500	544

Table 5.5: Input data for preceding table.

R/Q	973	ohm/m
Eff pulse length	1.40	ms
Charge/bunch	5.14	$\cdot 10^{10}$ (8.22 nC/bunch)
k long @sigma z= 1 mm	8.5	V/pC/m
$\Rightarrow$ HOM power	4.6	W/cav (k$\cdot$Charge$^2 \cdot$f)
10 % 2/3 HOM power	0.31	W/m effective
k long	11.5	V/pC/m
For sigma z = 1/2 mm		
Assume 10 % HOM @ 2K		
And 90 % HOM @ 70K		

Table 5.6: Summary Cryogenic Losses

Losses Grad Q (10^9)	static Losses	Total Losses 15 MV/m 3	Total 25 MV/m 5
Summary 2 K			
Sum 2 K Load-Watts/m	0.23	1.28	1.78
Losses/ 12m Module containing 8 Cav	2.8	15.4	21.4
Losses for 4 modules	11.2	61.8	85.6
Losses/ 12 Modules (96 Cav. 148 m)	33.6	-	230
Losses/ 1.75 km 2760	403		
(12x12x8=1152 Cavities, ∼1/ 16-1/ 18 of Tesla 500 two linacs)			
Summary 4.5 K			
Sum 4.5 K Load-Watts/m	1.16	1.27	1.33
Losses/ 12m Module containing 8 Cav	13.9	15.2	16
Losses for 4 modules	55.6	60.8	64
Losses/ 12 Modules (96 Cav. 148 m)	167	-	192
Losses/ 1.75 km 2304	2000		
(12x12x8=1152 Cavities, ∼1/ 16-1/ 18 of Tesla 500 two linacs)			

Table 5.7: Summary Cryogenic Losses

Losses Grad Q (10^9)	static Losses	Total Losses 15 MV/m 3	Total 25 MV/m 5
Summary 70 K			
Sum 70 K Load-Watts/m	6.4	10.4	11.3
Losses/ 12m Module containing 8 Cav	76.8	125	136
Losses for 4 modules	307	500	544
Losses/ 12 Modules 1632 (96 Cav. 148 m)	922		
Losses/ 1.75 km 19584	10064		
(12x12x8=1152 Cavities, ~1/ 16-1/ 18 of Tesla 500 two linacs)			

Table 5.8:   Summary Table of TTF Heat Loads for One Module @15 MV/m

	2 K Watts	4.5 K Watts	70 K Watts
Estimate of static load	2.8	13.8	76.8
Estimate of total load	14.3(15.4)	15.2	115.2 (125)
(without HOM - 24 W			= 91.2)
Static load x 1.5			
(for design)/module	4.2	21	115
Total load x 1.5			
(for design)	21	23	135(w/o-HOM)
Total load x1.5x5@15MV/m	105	115	675(w/o HOM)
Total load x1.5x5@25MV/m	160	120	1020(with HOM)
Efficiency conversion - Watts @ 273 K/ Watt @ * K			
Watts	1.8/2 K*	4.5 K*	40–70 K*
Watts/Watt	800/720	250	25

Table 5.9:   TTF linac heat loss budget, assuming 25 MV/m field gradient, 100 m transfer line from coldbox to TTF-feedbox, and stage II cryogenic heat exchanger. The * marked values of the 16 mbar return tube reduce the performance of the big heat exchanger and increase the 14 bar precooling heat load ** indirectly. For comparison, the "900 W" refrigerator has a capacity of 600 W (4.5 K) at a liquefaction rate of 2.5 g/s and a 70 K load of 2000 W.

	70 K	4.5 K	1.8 K bath	1.8 K return	4.5 K liquefaction
CRYOCAP	65 W	17.8 W	1.78 W		
one TTF module	136 W	17.8 W	21.4 W		0.1 g/s
big transfer return	250 W	30 W		(20 W*)	
big transfer supply	20 W	30 W			
module transfers	59 W	9 W	5 W	(7 W*)	
valves		3 W	7 W	(10 W*)	
14 bar tube precooling		110 W**			
big HEX mismatch					1 g/s
Sum=	938 W	271 W	100 W		1.5 g/s
Total estimates :					
1.5 x Sum=	1403 W	406 W	150 W		2.5 g/s
resulting					
coldbox load	1403 W	556 W	(adds to 4.5K)		2.5 g/s

5.7.1.1   Fermilab Input Coupler Heat Calculations

A FORTRAN program originally written for the analysis of current leads for magnets was modified to calculate the heat generated and conducted through copper-coated stainless steel carrying a 1.3 GHz oscillating electric current. The program divides the conductor into segments and performs an energy balance on each segment. Given a heat leak"guess" for the cold end, a temperature at the warm end is calculated. By iterating until the specified warm end temperature is obtained, heat flow to the cold end is found.

Skin depth in the copper coating, electrical resistivity of the copper, and thermal conductivity of the copper and stainless steel are found for each segment as a function of temperature. The "nomalous skin effect" in the copper at low temperature is approximated by treating the copper as if it had a RRR = 20 for the purpose of calculating the surface resistance.

The following assumptions were used: copper RRR = 40, coax impedance

Table 5.10:   Coupler Heat Summary Table for 2.0 K, 4.5 K and 70 K
               Temperature Levels

No power, and 208000 Watts peak power (25 MV/m)			
	2.0 K Watts	4.5 K Watts	70 K Watts
2 K to 5 K	0.03	-0.03	0
outer	**0.06**	0	0
conductor			
5 K to 70 K	0	0.35	0
outer	0	**0.49**	**-0.1**
conductor			
70 K to 300 K	0	0	2.0
outer	0	0	**2.4**
conductor			
70 K lower,	0	0	0
inner	0	0	**1.1**
antenna			
70 K to 300 K	0	0	0.6
inner	0	0	**2.0**
conductor			
SUM	0.03	0.32	2.2
	0.06	**0.49**	**5.4**
Room	24	80	31
temperature	**48**	**123**	**76**
cooling power			

= 50 Ohms, RF frequency = 1.3 GHz, peak RF power = 208 KW, pulse
length = 0.0016 sec, rep. rate = 10 Hz.

For more information, see M. Champion[3] and T. Peterson[4].

The calculated heat loads are summarized in the following table.

Room temperature cooling power is calculated as 800 W/W times 2.0 K

---

[3]M.Champion, et. al., "TESLA Input Coupler Development", presented at the 1993
PAC and part of TESLA Report #93-33

[4]"Fermilab Input Coupler Heat Calculations", TESLA Report #93-37

Watts, 250 W/W times 4.5 K Watts, 25 W/W times 40 K Watts, and 14 W/W times 70 K Watts. Total room temperature power required per coupler is 135 Watts with no power and 247 Watts under full power.

5.7.2 Cryostat Diagnostics

Table 5.11: Diagnostics in Cryostat.

Cavity Diag	#items cavity	#wires item	tot#w	coax
Main Coupler				
TSC 4.5	1	4	4	
PT 1000	1	4	4	
e- pick up	2			2
{Main Coupler (perhaps more for CHECHIA, 1st module }				
{ TSC 4.5	2	4	8 }	
{ PT 1000	2	4	8 }	
HOM Coupler				
TSC 4.5	2	4	8	
RF pick up	2			2
(term resist)				
Cavity He Ves				
TSC 4.5	2	4	8	
Cavity				
RF pic up	1			1
Cavity end pipes ?				
Accel-vib	2			2
Tuner System				
(all run in conduit from end)				
Motor drive	1	5	5	
Warm Main Coupler				
e- pick up	1			1
photo MP	1			1

Table 5.12: Diagnostics in Cryostat.

Quad Package Diagnostics	#items	#wires item	tot#w	coax
Quadrupole Diag				
Voltage tap	1	1	2	
TSC 4.5	2	4	8	
Accel-vib	2			2
PT 1000	2	4	8	
Quad Package Magnets			8 tot	@ 100 A
Quads	2	3/2	2+1	@ 60 A
H,V Steering	4	3/2	6	@ 100 A,/ 3 A
BPM				
BPM pic up	4			4
Cryostat Diagnostics				
Gas Stream Temp Monitors				
2K ves 100mm pipe				
TSC 4.5	1	4	4	
2K frw pipe				
TSC 4.5		4	4	
4.5K frw pipe				
TSC 4.5	1	4	4	
4.5K ret pipe				
TSC 4.5	1	4	4	
Pipe Monitors				
Beam pipe				
TSC 4.5	1	4	4	
He Gas Return Pipe				
TSC 4.5	6	4	24	
70 K foward pipe				
PT 1000	1	4	4	
70 K return pipe				
PT 1000	1	4	4	
Shield Monitors				
4K shield				
TSC 4.5	14x2	4	112	
70 K shield				
PT 1000	14x2	4	112	
Support posts				
TSC 4.5	1x3	4	12	
PT 1000	1x3	4	12	

Table 5.13: Diagnostic Summary

Classification of types of devices			
	#/cryostat module		
PT 1000	1x8+4+28+3=	43	Platinum resist
TSC 4.5	5x8+7+6+28+3=	84	carbon resistor
Accel-vib	2x8+2=	18	coax Typ 4379
Motor Drive	1x8=	8	
RF pic up	5x8=	40	coax
(2 e-,2 term res, 1 rf)			
Voltage tap	1=	1	diagnostic
BPM pic up	4x1=	4	coax
Magnets	2Q, 4B	6	
Prehaps additional (at least in the Horiz test cryo)			
PT 1000	2x8=	16	
TSC 4.5	2x8=	16	
Warm Monitors for Main Coupler			
e- pickup	1x8=	8	coax
photo Mult	1x8=	8	coax

5.7.3   Pipe Sizes for Supply and Return Lines

Based on estimated heat loads from a module and other cryogenic compo-
nents of TTF, with those heat loads then multiplied by a 1.5 safety factor,
mass flow rates for the various circuits were calculated. In some cases the
maximum possible supply mass flow was simply used in order that the sys-
tem piping not limit the flow. From these mass flow rates, allowable pressure
drops, and estimated lengths of pipe runs, pipe sizes were calculated for the
TTF cryogenic supply and return lines. These are summarized in Tab. 5.14.

A similar list for valves in the TTF feed box and adjacent transfer lines
has been developed, and is shown in Tab. 5.15.

Table 5.14:   TTF Module Test Cryogenic Pipe Parameter List

Location	Design mass flow	Maximum ΔP	Pipe cross-section
Module 70 K shield circuit	22 g/s	0.1 bar	30 mm
Module 4.5 K shield circuit	40 g/s	0.5 bar	20 mm
Module 1.8 K supply	10 g/s (2 g/s for cryocap)	0.1 bar	10 mm (5 mm to cryocap)
Module warm-up and cool-down bypass lines	50 g/s	2 bar	25 mm
Module 16 mbar, 1.8 K, vapor return	10 g/s	0.1 mbar	100 mm (50 mm from cryocap)
Cold box to feed box transfer line, 5 K supply tube	80 g/s	0.1 bar	30 mm
Cold box to feed box transfer line, 4.4 K vapor return tube	80 g/s	0.05 bar	40 mm
Big ht exch to feed box transfer line, 14 bar, 7.8 K supply tube	9 g/s	0.1 bar	15 mm
Big ht exch to feed box transfer line, 16 mbar, 3.8K return tube	10 g/s	0.1 mbar	150 mm

TTF Module Test Cryogenic Valve List

location	feed box	feed box	feed box	feed box	feed box	feed box	feed box	t-line to modules	t-line to modules	t-line to modules	t-line to Cryocap	t-line to Cryocap
function	liquid level	cooldown	4.5K return	7.5 K line cooldown	7.5 K to subcooler	2 K cooldown	2 K isolation	He vessel warmup	2 K liquid level	2 K liquid level	2 K warmup	2 K liquid level
valve name	VL2V1	VD2R2	VF2R3	VD2R4	VT2V5	VD1R6	VP1R7	VP1V26	VL1V27	VL1V28	VP1V44	VP1V45
operating P (bara)	3.0	2.0	3	12	12	2	0.015	3	3	3	3	3
delta-P (bar)	1.8	1.0	1.8	11	10.8	1	0.0005	0.5	2.985	2.985	0.1	2.985
max mass flow (g/s)	40	50	40	40	25	50	10	44	20	2	2	2
max inlet temp (K)	6.5	300	6.5	300	8.0	300	3.5	300	2.2	2.2	300	2.2
Full-open Cv	1.5	20	1.5	2.5	0.17	20	150	13	0.22	0.022	1.5	0.022
normal flow (g/s)	7	--	20	--	9.0	--	10	--	5	1	--	0.5
normal inlet T (K)	5.4	--	5.4	--	5.0	--	3.1	--	2.2	2.2	--	2.2
normal position	30% open	closed	60% open	closed	65% open	closed	100% open	closed	65% open	80% open	closed	65% open
DN valve body	10	25	10	15	6	25	150					
pipe size	17.2 mm x 1.6 mm	33.7 mm x 2.6 mm	17.2 mm x 1.6 mm	21.3 mm x 2.0 mm	13.0 mm x 1.5 mm	33.7 mm x 2.6 mm						
regulation or digital	level regulation	digital	temp. regulation	digital	temp. regulation	digital	pressure regulation	pressure regulation	level regulation	level regulation	pressure regulation	level regulation

Notes for all valves:

Equal percentage regulation characteristic (except perhaps DN100 and DN150 valves).
Right angle valve bodies.
Normally closed without control air pressure.
Butt-welded connections.

Table 5.15: Cryogenic Valve List.

Chapter 6

Quadrupole Package

The quadrupole package is shown in Fig. 6.1. It consists of

- a superferric quadrupole doublet powered in series enclosed in a stainless steel vessel and cooled by 4 K LHe;

- two pairs of dipole steering windings that fit inside the quadrupole yoke bore, and provide a horizontal and a vertical correction dipole field;

- an RF beam position monitor (BPM) consisting of a pill box RF cavity, rigidly connected to the quadrupole yoke. The BPM's are described in Chapter 9.

- a stainless steel beam pipe through the magnet bore, evacuated to UHV, rigidly connected to the BPM and the quadrupole doublet and, through a bellow, to the nearest cavity. The pipe also serves to absorb unwanted electromagnetic energy (HOM) leaking out from the cavities: a cooling sleeve is therefore provided around it in which 70 K gas is circulated;

- 8 main current leads powering the quadrupole doublet and the dipole steering coils, enclosed in a special pipe that runs from the LHe vessel to a flange on the cryostat vacuum vessel, and cooled by cold He gas fed into the pipe. At the end nearest to the quadrupole the pipe terminates in a connection box. The current leads are inserted into the pipe from the outside and then connected to the windings in the connection box.
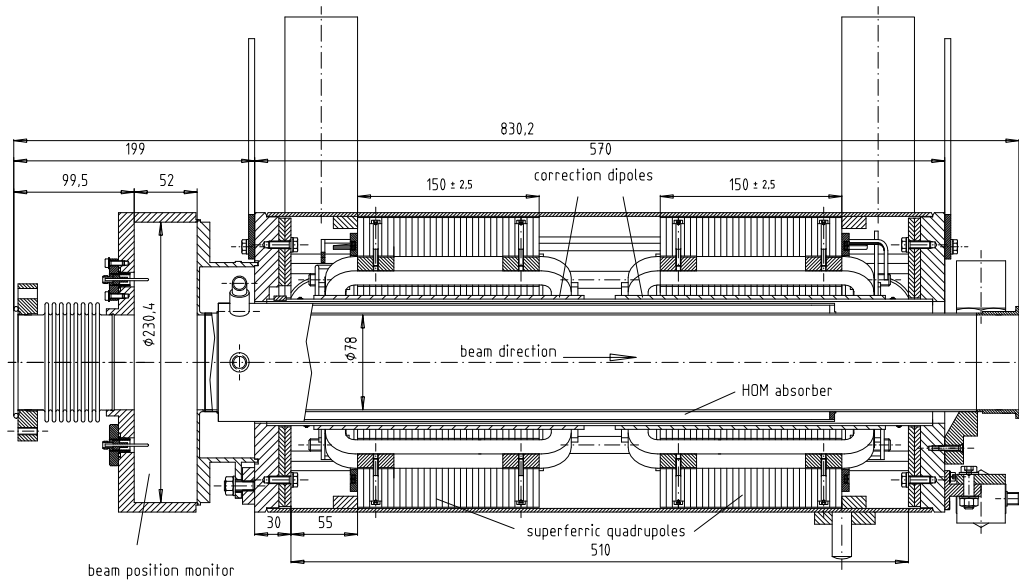
Figure 6.1: Quadrupole Package

A cross section through the cryomodule at the position of the quadrupole is shown is Fig. 6.2.

The quadrupole coil is equipped with temperature monitoring thermoresistors. Their wiring is run together with one voltage tap wire through a separate uncooled pipe also running from the He vessel to a flange on the cryostat vacuum vessel. Two thermoresistors on the beam pipe and two accelerometers attached to the helium vessel of the quadrupole doublet are also part of the instrumentation.

6.1   Quadrupole Module

At the end of each cryomodule a 0.8302 m long magnet module is connected to the cavity string. It consists of the components described below.

Helium Vessel   The helium vessel, shown in Fig. 6.3, houses a quadrupole doublet (horizontally focusing and defocusing quadrupole) for beam focusing and two pairs of dipole correction coils used for two purposes, for correcting the quadrupole field axis and for steering the beam (see Fig. 6.1).
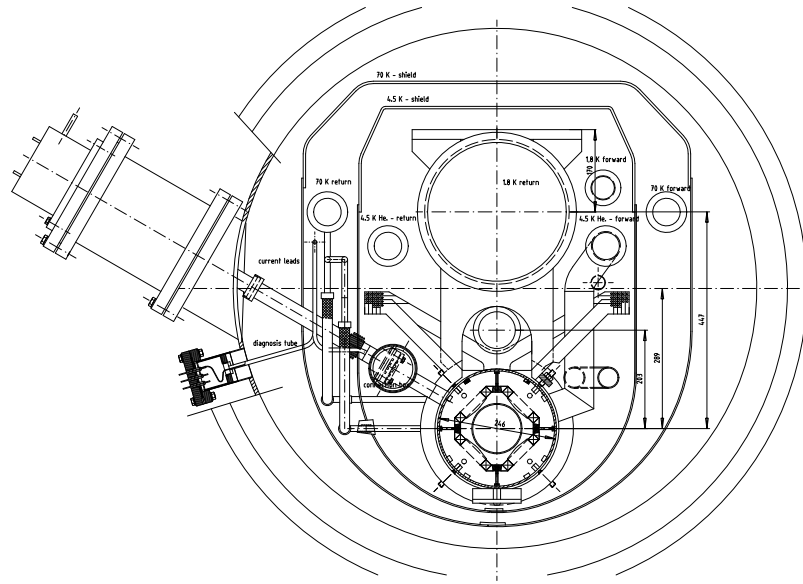
Figure 6.2: Cross Section of Quadrupole inside Cryomodule
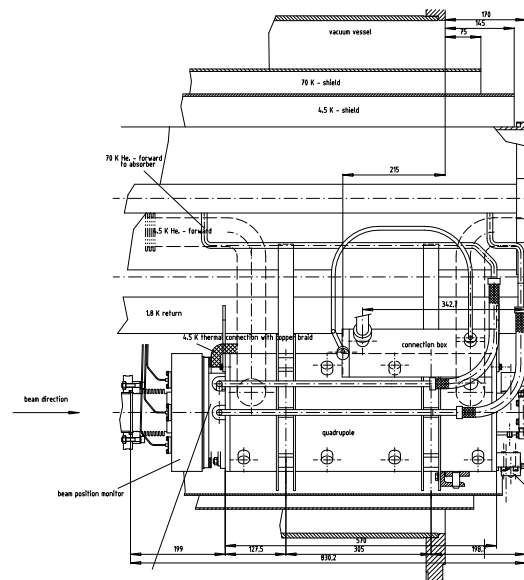
Figure 6.3: Side View of Helium Vessel in Cryomodule

The vessel consists of stainless steel inner and outer tube and end plates welded together after assembly.

The quadrupoles are superferric ones with a maximum gradient of 20 T/m and maximum integrated gradient of $\sim$ 3 T at 55.7 A. The yoke (and field) length is 0.15 m. The field gradient along the quadrupole axis is shown in fig 6.4, the integral gradient as a function of current in Fig. 6.5 and the multipole coefficients b_6/b_2 and b_{10}/b_2 in Fig 6.6.

The yoke, shown in Fig. 6.7 is made from 5 mm thick punched laminations assembled on a tool and locked through keys which give the required position accuracy (0.02 mm). The keys are connected through pins and bolts to the outer helium vessel tube and to the end plates of the vessel.

The end plates carry frames with two arms each holding reference targets for alignment (see Fig. 6.8).

The superconducting single layer dipole correction coils are placed around the inner tube of the helium vessel (see Fig. 6.9). They have the same length as the quadrupoles. An epoxy unidirectional glass fiber bandage tightens and secures the coils on the tube.

The quadrupole and correction coils are powered through 8 current leads capable of carrying 100 A. The leads are running from the helium vessel to a cold connection box and through a $\sim 0.7m$ long tube to the warm outside of the vacuum vessel (see Fig. 6.10). At full current a helium gas stream of 0.1 g/s has to run through this tube for cooling resulting in an additional heat load of 1.8 W at 4.2 K. The head of the current lead tube will be heated electrically to avoid icing.

A voltage tap wire between the quadrupoles allows to locate quenches or shorts. The wire is fed through a thin tube to the warm outside of the vacuum vessel together with 8 wires of two carbon sensors placed in the liquid helium. The electrical connections inside the helium vessel are shown in Fig. 6.11.

Accelerometers for measurement of vertical and horizontal motion are bolted to the end plate of the helium vessel at the beam exit end.

The superconducting magnets are cooled with the 4.2 K forward flow helium used also to cool the inner shield of the cryomodule.

Beam Tube   The beam tube is equipped with a high order mode absorber and a beam position monitor (see Fig. 6.12).
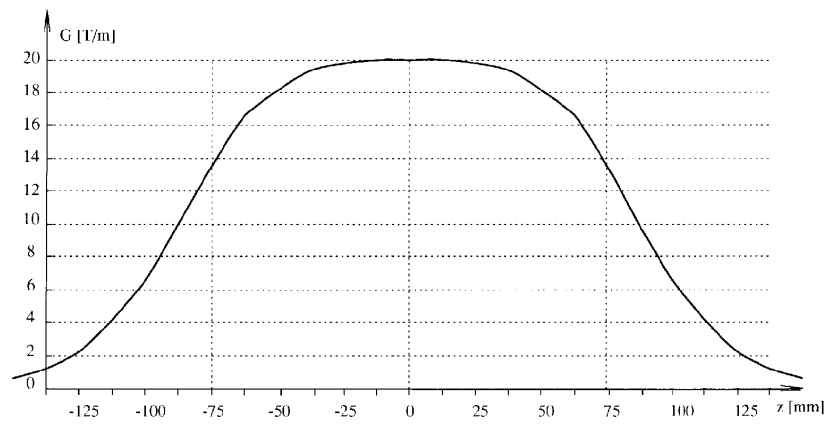
Figure 6.4: Field Gradient along Quadrupole Axis
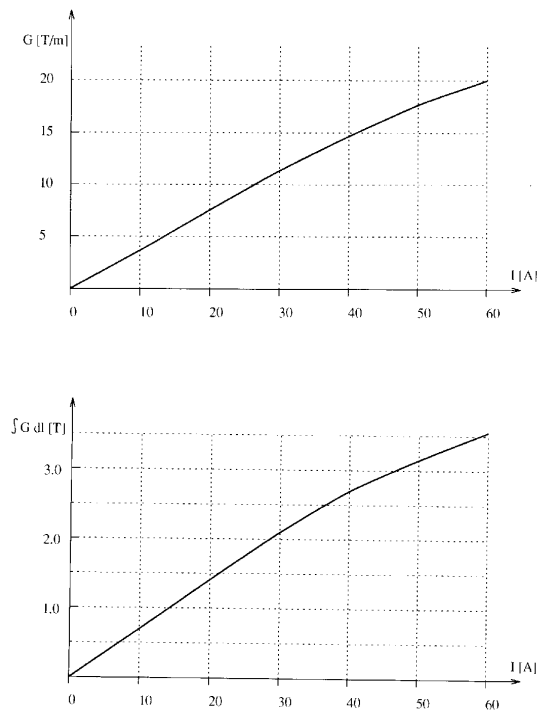
Figure 6.5: Integral Gradient as a Function of Current
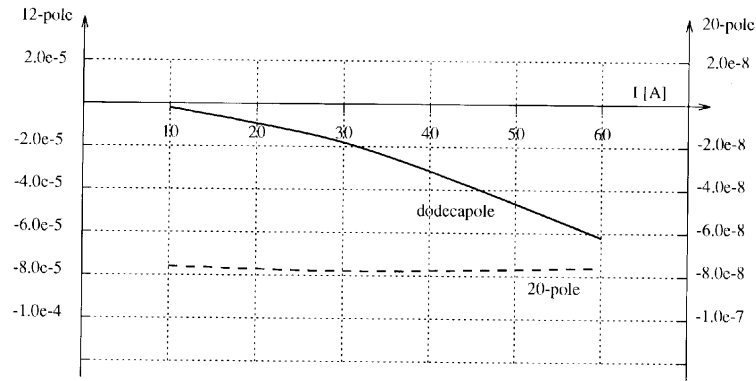
Figure 6.6:   Integral Dodecapole and 20-Pole of Quadrupoles at 10 mm
                Radius
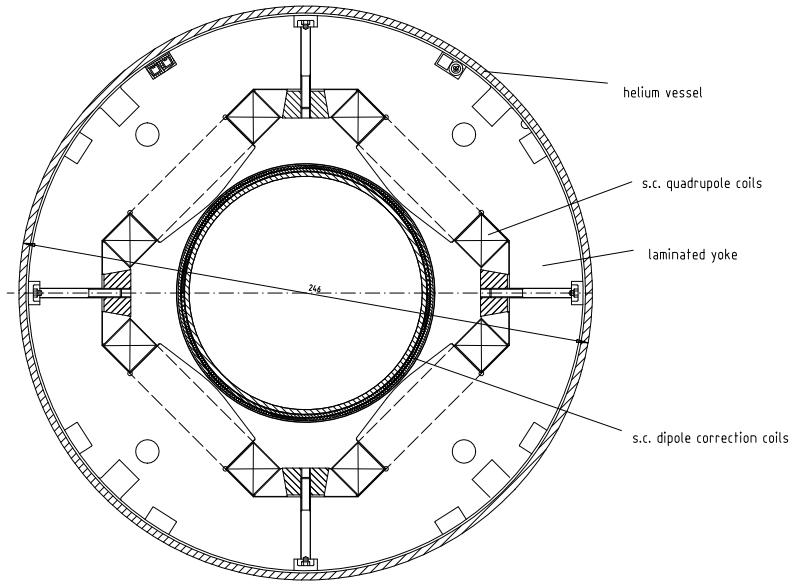
Figure 6.7:   Quadrupole Cross Section showing Yoke and Coils
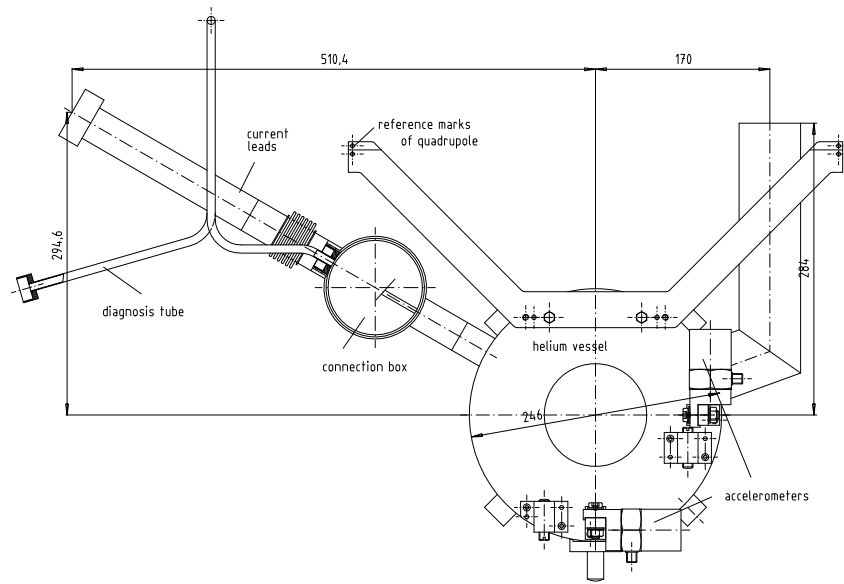
Figure 6.8: Helium Vessel End Plate with Reference Arms
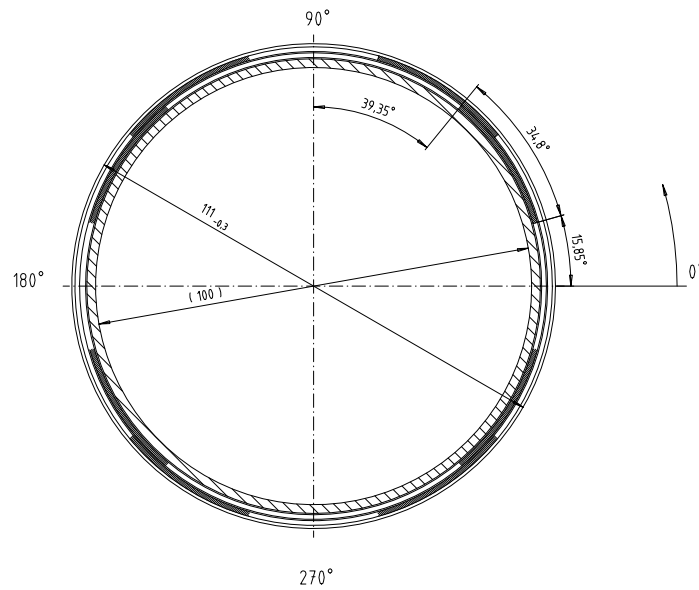
Figure 6.9: Cross Section of Dipole Correction Coils
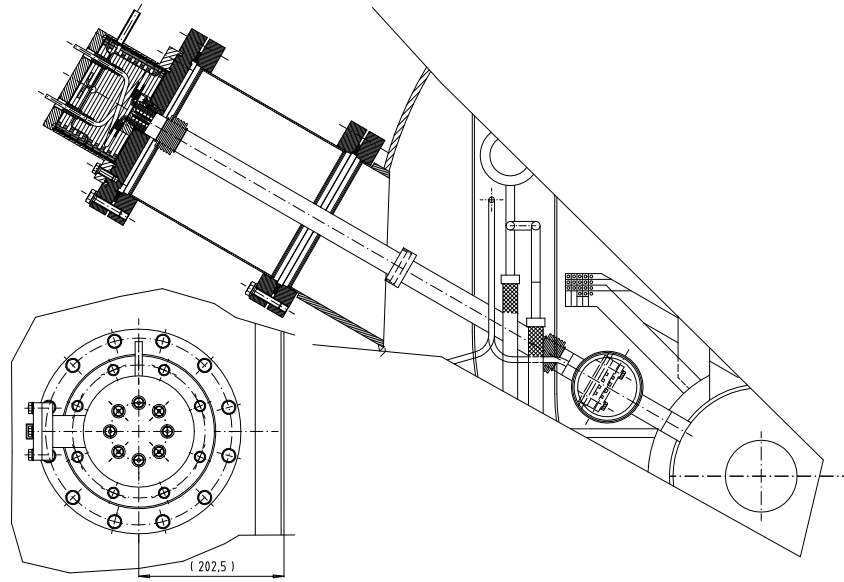
Figure 6.10: Current Leads

The stainless steel beam tube vacuum isolated with respect to the quadrupole helium vessel will be copper plated at both ends in order to avoid heating. In the central part inside the quadrupole helium vessel the copper plating is left off over a length of 0.5 m. This results in heating by image currents of the higher order modes of the beam. The heat ($\sim$ 20 W) is removed at a temperature of $\sim 70K$ (the temperature of the second shield of the cryomodule) by running helium gas through an annular space around the tube. For removing 20 W a helium flow rate of $\sim 0.4g/s$ is necessary at a temperature difference of 10 K.

The temperature of the high order mode absorber is monitored through two platinum temperature sensors.

The beam position monitor being designed by Technische Universität Berlin is a cavity of the pill box type (see Fig. 6.13) with two antennas for each direction (x and y). The position measuring accuracy aimed at is $10\mu m$ (see Chapter 9).

The beam pipe part between the beam position monitor and the cavity string is equipped with a copper coated stainless steel bellows (0.2 mm wall) to compensate for misalignments and cooldown motions.
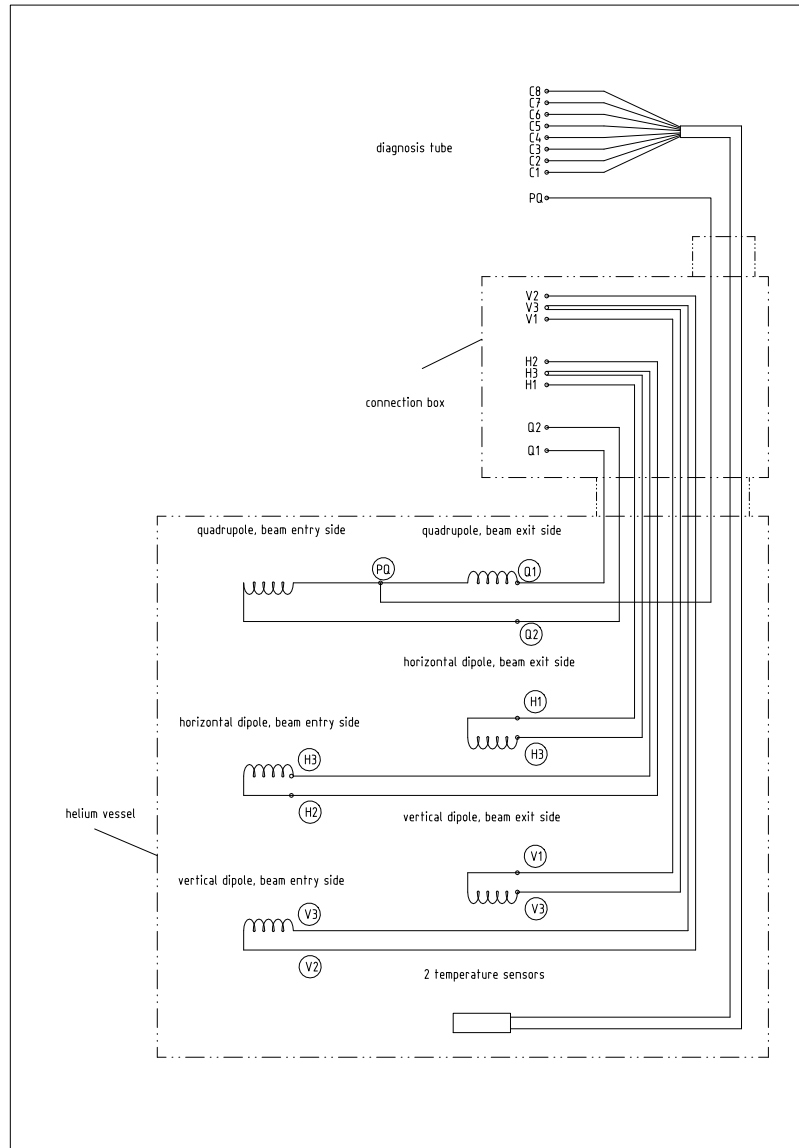
Figure 6.11: Electrical connections inside Helium VesseL
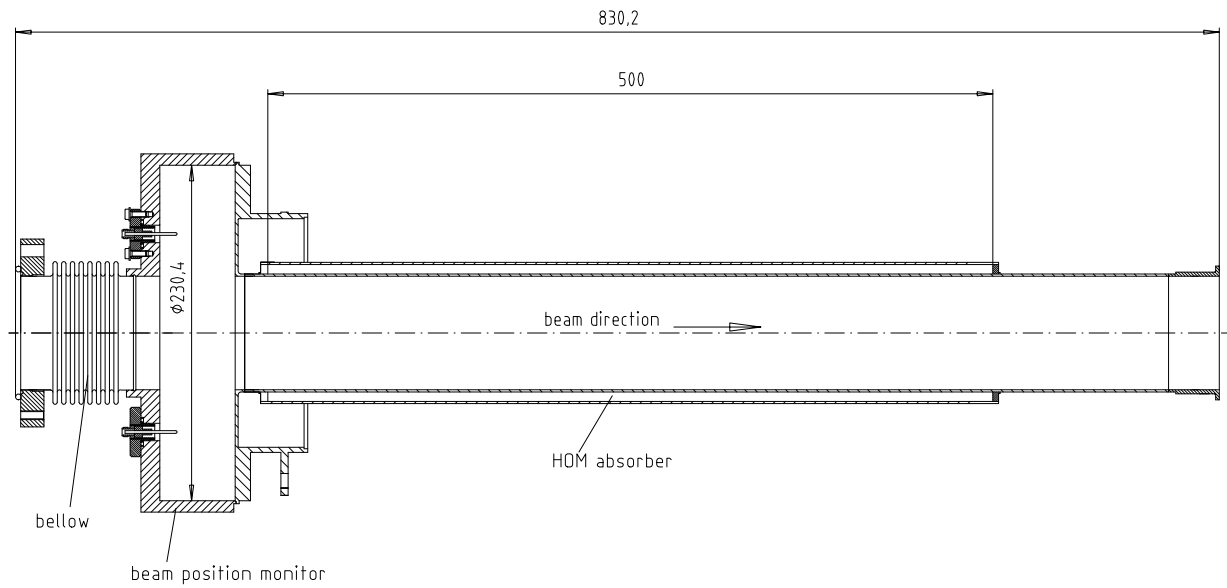
Figure 6.12: Beam Tube at Quadrupole Package
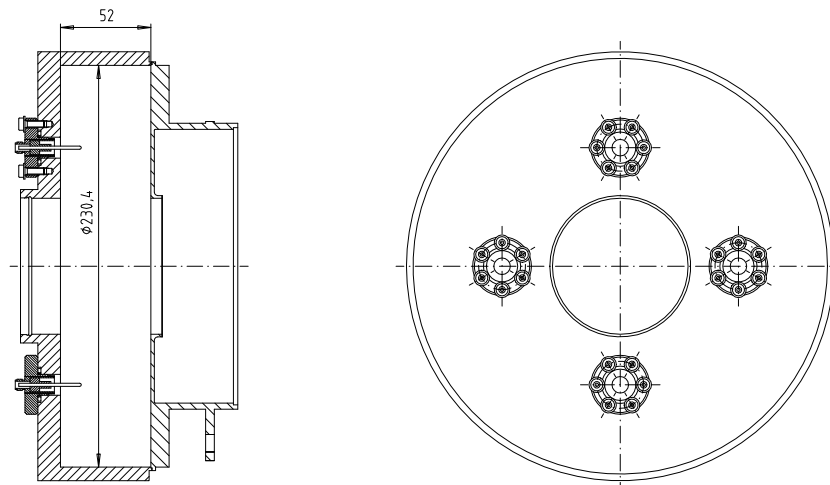
Figure 6.13: Beam Position Monitor

The beam position monitor is connected rigidly to the quadrupole helium vessel through a structure with relatively low heat conduction.

Support System The support system connects the quadrupole helium vessel with the 300 mm diameter helium gas return pipe (see Fig. 6.2).

The system consists of two rings (one at each end of the helium vessel) split in halves for easy mounting similar to the ones used to support the cavities. It allows to adjust the quadrupole unit with the aid of reference targets on extension arms attached to each helium vessel end plate.

6.2 Alignment and Survey

Alignment and survey play an important role because of the given tolerances (rms values):

cavity	0.5 mm
quadrupole	0.1 mm
beam position monitor	0.05 mm (with respect to quadrupole axis)

The alignment of the quadrupole is the most critical one.
In order to achieve the required tolerances we have chosen

- a superferric quadrupole where the accuracy of the field is mainly given by the accuracy of the yoke;

- a laminated yoke where the contours are most accurate due to punching keys locating the yoke lamination precisely;

- a helium vessel with pins to locate the keys and yoke inside the vessel;

- grooves in the end plates accurately machined to take over the position of the keys;

- frames with arms for targets machined in one set-up together with the endplates;

- accurate machining of the structure to hold the beam position monitor.
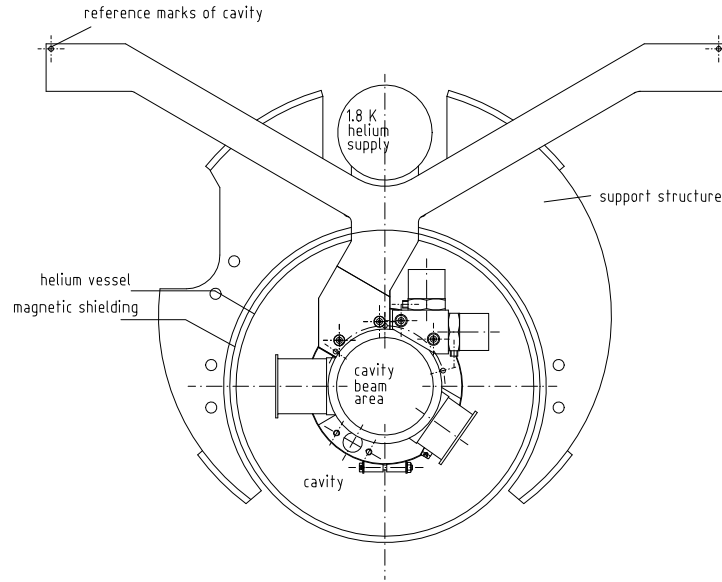
Figure 6.14: Arms with Reference Targets at Cavities

For the alignment an optical system is foreseen in which a theodolite is used to look at optical targets on arms on each end and on each side of each helium vessel (cavity or magnet). The arms with reference targets at the cavities are shown in Fig. 6.14. For the quadrupole module the position in x and y direction is important whereas for the cavities the radial position only is sufficient due to their rotational symmetry. The rotational position is given by the angle of the main coupler and its tolerances.

A string of 8 cavities and one quadrupole module are assembled and prealigned on a rail in the class 10 clean room. The precision of the rail is ±0.3 mm horizontally and vertically and ±0.2 mrad azimuthally (rms values) over its entire length (~ 40 m). During this assembly the beam tube connections between the individual helium vessels are made. The string is then moved out of the clean room for further assembly with the 300 mm diameter helium gas return tube and for insertion into the vacuum vessel of the cryomodule. This requires a final alignment of the components using a theodolite and the above mentioned optical targets. The theodolite will look at the targets from the quadrupole end of the string. In order to see all targets from this end the targets must be staggered in an appropriate

manner. The alignment inside the vacuum vessel is performed with respect to two reference marks on the outside of the vacuum vessel. The survey of the four cryomodules of the TTF makes use of these outer reference marks. A cross section of 300mm × 500mm over the whole length of the linac must be kept free on top of the cryomodules.

It is planned to check the alignment of the inner components after complete assembly of the testlinac, during cool down, at helium temperature and during warm up. Therefore several inner targets must stay in place and must be visible from the linac beam exit end through windows in the endcap. At the first cryomodule all inner targets (in 18 planes) will stay in place. At cryomodules 2-4 the targets in three planes (with one at the quadrupole at least) will stay in place. The others will be removed before inserting the cold parts into the vacuum vessel.

As the optical targets are sitting in the dark when the vacuum vessel is closed they have to be illuminated when the measurements are performed. The illumination is done by red LEDs of type MV5053 which have been tested to work at liquid helium temperature under vacuum (for instance at 2 V at 5 mA).

Investigations are under way to use a wire system to monitor continuously the alignment of components inside the cryomodule when it is operated cryogenically. This system similar to the one used for the final focus at SLAC consists of 2 about 0.5 mm thick stainless steel wires spanned from the feed box through the vacuum of the first cryomodule to the end box — one wire on each side of the cavities and quadrupole. For a given wire tension set at the wire ends outside the end box the position of the wire is well known over its entire length of approximately 13 m. A maximum sag of 2mm seems to be achievable.

Monitors consisting of two orthogonal pairs of metal plates (one pair for x-, one for y- direction) forming an open square of 8 mm by 8 mm will be placed at each end of each cavity and of the quadrupole. The first cryomodule will therefore contain a total of 18 monitors. A suitable place inside the cross section of the cryomodule must be found where the sight line is not interfered by other components. The most reasonable place is underneath the optical reference marks. The wire must run close to the center of the opening square of the monitors for better measuring accuracy. Different from the system at SLAC the monitors have to operate at liquid helium temperature under vacuum. The wires will run in tubes between the monitors and the end boxes.

These tubes are necessary to form a coaxial cable for the RF with which the wire is operated. The connection of the tubes to the monitors must be flexible and is therefore done with bellows in order to avoid interconnecting forces between the components.

The operation frequency will be around 140 MHz allowing a measuring accuracy of 10^{-4}. The required positional resolution is $10\mu m$, about a factor 100 larger than achieved at SLAC.

For measuring purpose each monitor has 4 coaxial cables connected to feedthroughs at the vacuum vessel close to the position of the input couplers. An elaborate control system is required to run the measurements on line.

6.3 Vibration

Mechanical vibration may influence the performance of the linac. They are driven for instance by pumps, motors, traffic or by beam forces in the cavities. The analysis of the mechanical structure indicates lowest resonance frequencies at about 19 Hz in vertical direction.

In order to measure vibrations in x and y direction accelerometers will be attached to the cold mass of quadrupoles and cavities (see Fig. 6.8 and 6.14). Accelerometers of the piezo quartz type from Bruel & Kjaer have been used successfully at a superconducting HERA quadrupole [1] The same accelerometers will be used for the cavities. More accurate ones (type 8381) will be used for the quadrupoles. The measuring sensitivity at 2Hz will be about 20 nm and is mainly determined by the noise of the amplifier.

The output of the accelerometers may be used to control power supplies of the dipole correction coils in such a way that the displacement of the quadrupole axis is compensated.

6.4 Power Supplies and Regulation

Tab. 6.1 lists the power supply requirements of the linac (exclusive of the injector) for initial operation with one cryo module. Tab. 6.2 gives the requirements for final operation with 4 cryomodules and a drift space between modules one and two.

---

[1]J. Roßbach and K. Flöttmann, private communication.

The data of the superconducting magnets in TTFL relevant for the power supplies are:

number of quadrupole doublets:	4
nominal current of quadrupoles:	60 A
number of correction coils:	2×8 (divided)
nominal correction coils current DC:	100 A
nominal correction coils current AC:	3 A
maximum correction coils AC frequency:	50 Hz
appr. inductance of the quadrupole:	360 mH (room temperature)
appr. inductance of correction coil:	15 mH

At 100 A one correction dipole is capable of bending a 800 MeV beam by 3.75 mrad. Only 52 % of this value are required to maintain a beam offset of 10mm throughout the TTF to measure higher order mode excitations. An AC current of 1 A in the second correction dipole could correct a vibration with an amplitude of 100 μm.

6.4.1 Types of Power Supplies needed for TTFL

Superconducting Quadrupoles The quadrupole doublets will operate at a steady state DC current with a maximum value of 60A. This current limit is determined by the cryomodule current leads. A switched mode power supply of the HERA type will be used as the current source. The nominal current of the choppers will be 120 A. This is in order to use for the most part the same units in the TTF. The choppers will be equipped with mechanical polarity switchers. The output voltage is 30 V.

Superconducting Steering Magnets Each steering magnet is divided into two coils. One coil will have a steady state DC current of 100 A maximum. Since this is a steering coil, polarity switchers are foreseen. Mechanical polarity switcher are sufficient as no dynamic zero crossing is required.. The nominal current of the power supplies is 120 A, the voltage is 30 V.

AC Excitation coil The second coil can be used to investigate or eliminate the influence of motion or vibration of the quadrupoles on the beam. Current in the steering coil effectively changes the position of the magnetic center of

the quadrupole and can compensate for quadrupole motion. An AC supply will be available with a current of up to 1 A at up to 150 Hz.

Normal conducting magnets in the High Energy Experimental Area
In the experimental area the following magnets are installed:
spectrometer magnet
2 quadrupole doublets 120 A for the final focus
2 quadrupoles 270 A for defocusing
2 dipole correction coil.

Due to the high voltage needed for the spectrometer magnet, a SCR rectifier has to be used. The two quads having 120 A will be fed with the same type of chopper as the superconducting coils. The other two quads will have a 270 A chopper. The dipole correction coils require a current of 3 A. The power supply for this magnet is also of a HERA type. It is a 3.5 A/120 V supply.

6.4.2   Description of the Power Supplies

Switched mode power supplies   For HERA switched mode power supplies, so called choppers, have been developed. This type of choppers will also be installed in the TTF. The choppers are buck converters. Via semiconductor switches, here MOSFETs, the magnet load is periodically connected to a primary DC voltage. This is done with a pulse width modulation (PWM) that is switching at a frequency of 16 kHz. The primary voltage is decreased according to the ratio of turn on and turn off time. The buck converter acts like a variable step down transformer. The input DC voltage is delivered by a diode rectifier. All choppers will be fed by one diode supply.

Power supply modules   The power supplies are constructed in modules. These are: power part with MOSFETs and filter regulation electronic mechanical polarity switchers 2 DCCTs (DC current transformers) programmable logic controller (PLC), one PLC for two choppers

The modules are bought separately and assembled at DESY and can be easily replaced. The choppers are mounted into electronic racks. For each four choppers three racks are needed. One rack having just the electronics
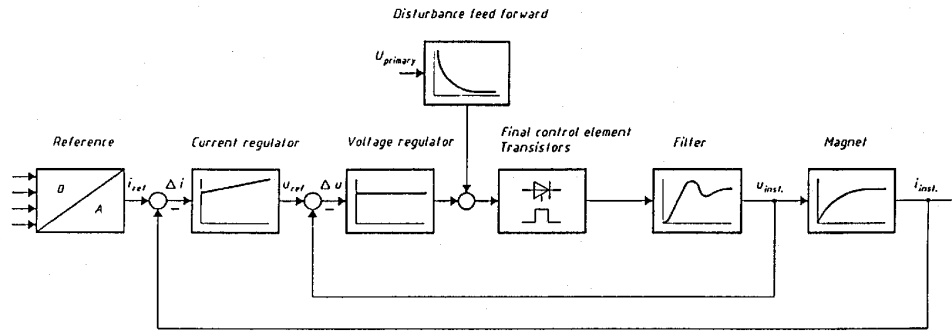
Figure 6.15: Power supply regulation schematic.

and PLCs, the second containing the power parts and the third is for the polarity switchers.

Regulation The regulation is in two loops. The outer loop is for the current regulation and the inner is for the voltage regulation. It has to compensate the power supply ripple and disturbances from the grid. An additional disturbance feed forward signal decreases the ripple of the 6-pulse diode rectifier. The reference value for the supply is a parallel 16 bit digital value. The DAC is part of the regulation electronic. Fig. 6.15 shows the regulation schematic.

Diode rectifier To feed the switched mode power supplies a pre-rectifier is required. This will be a 6-pulse diode rectifier. There will be only one supply for all 16 choppers in the TTF. The nominal data is:

max. current	800 A
output voltage	30 V
rated power	24 kW

The control is done with a programmable logic controller. When one chopper is turned on, the diode rectifier is turned on automatically. When all choppers are turned off, this will turn it off as well.

SCR power supply   Since the spectrometer magnets needs a higher voltage than given by the diode rectifier a SCR rectifier will be used. It is a 6-pulse unit rectifier. The rectifier has a nominal current of 500 A, 100 V. Since the magnet has nearly 600 m ohm resistance only 166 A can be driven by this supply. The required current is 109A at 800 MeV. The regulation is the same as for the choppers. The regulation electronic, pulse firing sets, PLC and DCCT electronic are assembled in an separate electronic rack for thermal de coupling.

Space for the power supplies and distribution   All power supplies will be placed in a separate room beside the experimental area. Here a space of $\approx 4.1\text{m} \times 15\text{m}$ is reserved. This room will house:

1 diode rectifier	$80 \times 80 \times 200$ cm
+ electronic rack	$55 \times 55 \times 200$ cm
1 SCR supply + electronic rack	$100 \times 100 \times 200$ cm
15 electronic racks containing choppers	$15 \times 55 \times 55 \times 200$ cm
2 electronic racks containing spare parts	$110 \times 55 \times 200$ cm
24 V power supply for PLCs	$60 \times 60 \times 200$ cm
power panel for 400V, 230V, 24V	

AC Vibration Compensation Power Supplies   As mentioned above these supplies compensate for low frequency motion of the quadrupoles by feeding an AC current into the steering coils. For this purpose a power supply was developed at DESY. The nominal data is ± 1 A and ± 7 V. The maximum frequency will be 150 Hz. The power supply has an analog input of ± 10 V. Here the signal representing the amplitude of the vibration have to be fed into. Each supply will be mounted on a separate board. The eight boards will fit into one frame.

Table 6.1:   Power supplies for the TTFL. One cryo module, temporary warm beam line, and high energy EAA.

Position	Number of Supplies	Max. Magnet Current [A]	Max. Supply Current [A]	Max. Supply Voltage [V]	Voltage Req. [V]	Resistance Mag + Cable [mΩ]	Power Req. [W]
Module 1							
quadrupole	1	60	120	30	0.6	10	36
steering coil							
vert DC	1	100	120	30	1	10	100
horiz DC	1	100	120	30	1	10	100
vert AC	1	100	120	30	1	10	100
horiz AC	1	100	120	30	1	10	100
Warm beam line							
quadrupole							
2 - 5	4	120	120	30	15.6	130	5616
steering coil							
vert DC	4	3.5	120	120	45.5	13000	637
horiz DC	4	3.5	120	120	45.5	13000	637
Experimental area							
quadrupole 1a	1	270	270	30	13.5	50	3645
quadrupole 1b	1	270	270	30	13.5	50	3645
spectrometer							
magnet	1	170	500	100	102	600	17340
quadrupole 2a	1	120	120	30	6	50	720
quadrupole 2b	1	120	120	30	6	50	720
correction CV	1	3.5	3.5	120	45.5	13000	159
correction CH	1	3.5	3.5	120	45.5	13000	159

Table 6.2: Power supplies for the TTFL. Final configuration with 4 cryo modules, one section warm beam line, and high energy EAA.

Position	Number of Supplies	Max. Magnet Current [A]	Max. Supply Current [A]	Max. Supply Voltage [V]	Voltage Req. [V]	Resistance Mag + Cable [mΩ]	Power Req. [W]
Module 1 - 4							
quadrupole steering coil	4	60	120	30	0.6	10	144
vert DC	4	100	120	30	1	10	400
horiz DC	4	100	120	30	1	10	400
vert AC	4	100	120	30	1	10	400
horiz. AC	4	100	120	30	1	10	400
Warm beam line							
quadrupole 2 steering coil	1	120	120	30	15.6	130	1872
vert DC	1	3.5	120	120	45.5	13000	159
horiz DC	1	3.5	120	120	45.5	13000	159
Experimental area	same as above						

6.5 Parameters of the Quadrupole Module

Table 6.3: Parameters of the quadrupole lens

quadrupole lens		
quadrupole type	superferric	
pole radius	56 mm	
yoke outer diameter	238 mm	
yoke length	150 mm	
distance of quad centers	250 mm	
no. of turns/pole	464	
inductivity of coil in air	0.36 H	
resistivity of coil at 20° C	Ohm	
field gradient	14 T/m	37.5 A
	17 T/m	46.1 A
	20 T/m	55.7 A
max. integrated gradient	~ 3 T	55.7 A
max. field at conductor	~ 2.23 T	55.7 A
integrated b6 at r=10 mm	-0.6×10^{-4}	55.7 A
integrated b10 at r=10 mm	-0.8×10^{-8}	55.7 A
field at cavity flange, without mirror	7.3×10^{-4} T	
field at cavity flange with mirror plate	5×10^{-5} T	
superconduction wire	0.95 mm$\times$ 0.5 mm	
I_{SS}	112 A at 4.6 T and 4.6 K	

Table 6.4: Parameters of the dipole correction coil

dipole correction coil		
dipole type	single layer	
inner coil radius	52.5 mm	
outer coil radius	54.2 mm	
inner coil angle	15.85°	
outer coil angle	50.65°	
field strength	0.0639 T	100 A
integrated field strength	~ 0.00959 Tm	100 A
integrated b3 at r = 10 mm	2.4×10^{-4}	
integrated b5 at r = 10 mm	12.4×10^{-4}	
superconducting wire diameter	0.7 mm	
I_{SS}	> 250 A	at 5.5 T, 4.6 K

Table 6.5: Parameters of miscellaneous components

beam position monitor	
type	pill box cavity
material	stainless steel
inner diameter	230 mm
inner width	52 mm
high order mode absorber	
type	ann. space cooled with 70 K He
assumed heat load	20 W
helium cooling	$\sim 0.4g/s$ 60 K, dT=10 K
heat input	
at 4 K	~ 1.5 W
at 2 K	~ 0.2 W
material	stainless steel
current leads	
type	gas-cooled copper wires
no. of pairs	4
optimized current	100 A
cooling	~ 1.8 W at 4 K + 0.1 g/s
support system	
type	rings att. to helium return tube
no. of support planes	2
accuracy of adjustment	0.1 mm in x- and y- dir.
instrumentation	
T-sensors at quadrupole	2, carbon, TSC
T-sensor at HOM absorber	2, platinum, PT1000
accelerometers	2, helium vessel

Chapter 7

Vacuum and Vacuum Isolation

The requirements on the quality of the cavity vacuum do not come from beam gas interactions, but from the lifetime of the gun in the injector region and the performance of the superconducting cavities in the rest of the linac. The flow of gas molecules into the cold part of the linac must be kept small to avoid accumulation of gas layers on the surface of the cavities, eventually giving rise to field emission. Due to the smaller surface area the capture cavity is most critical. Without special precautions like vacuum firing of adjacent vacuum parts and differential pumping 1 monolayer of hydrogen would be accumulated in the capture cavity after 10 days [1], which seems to be the regime where field emission gets enhanced [2] [3] [4]. We therefore have vacuum parts close to the cold linac vacuum fired and install sufficient pumping speed close to the beginning of the cold section.

7.1 Requirements on Vacuum Parts

Metallic dust within the superconducting cavities must be avoided as it leads to field emission. For the cavities themselves great care is being taken to clean them and to prevent dust from entering the cavities. Comparable care has to

---

[1] D. Trines, Tesla 93-20

[2] R. W. Röth et al., Universität Wuppertal, Proceedings of the 5th Workshop on RF Superconductivity, p. 559

[3] T. Tazuma et al., KEK IBID, p. 766

[4] H. Padamsee et al., *New Results of RF and DC Field Emission*, 4th Workshop of RF Superconductivity, Tsukuba, Japan 1989

be taken for the adjacent vacuum components as dust within these chambers can migrate into the cavity after successive pump downs and venting. Venting and pump down must be done such that the gas flow is directed away from the cavities. This is however not possible everywhere and is a problem for the section between capture cavity and main linac.

In addition all vacuum parts have to be treated in the clean room area to get them dustfree. During installation similar care as for the cavities has to be taken to avoid dust entering the system.

We know for example from the e-ring of HERA that ion getter pumps are a source of dust particles, which may eventually enter the beam tube. For the test facility there is no inexpensive alternative to the use of ion pumps. The production of dust particles is however dependent on the gas load that has to be pumped. It is thus appropriate to operate at low base pressure. Therefore all vacuum chambers will be vacuum fired. Pumps will only be switched on when a good base pressure is achieved by oil-free pump stations.

7.2   General Layout of the Beam Vacuum System

The linac vacuum is separated into several sections by gate valves. This permits successive setup and testing and also adherence to the philosophy of venting and pumping with the gas flow away from the cavities as much as possible (see Fig. 7.1).
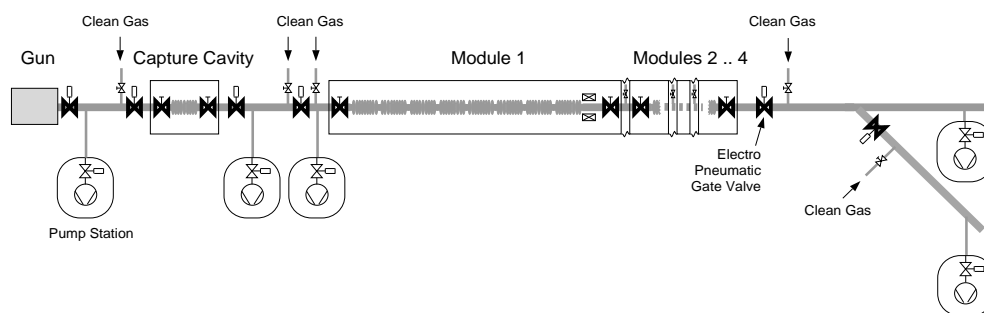
Figure 7.1: Layout for the Beam Pipe Venting

Each module of 8 cavities has manual gate valves at either end, which are mounted in the cleanroom to maintain the cleanliness of the cavities during installation (see Fig. 7.2). It is planned to use local cleanrooms at all installation work on the open vacuum system. The type of valves to be used is controversial. All-metal valves may produce metallic dust by friction, valves with organic seals may also have rub-off from the seal and they are sources of gas from or through the organic material. Valves with organic seals are mainly used in the injector, all-metal valves are used in the rest of the linac.

The cavities are connected by short bellow sections of about 10 cm length to allow for length variations of the cavity and thermal contraction during cooldown.

Schieberventil   Schieberventil
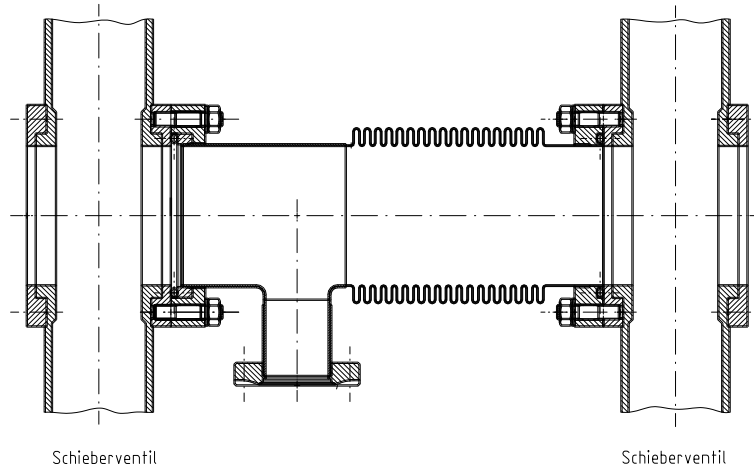
Figure 7.2: Gate valves at module interface

Consideration has been given to the installation of an RF shield to avoid higher order mode losses in the bellows which add to the cryogenic load at 1.8 K. However, all designs thought of, bared the danger of producing metallic dust by friction. Therefore it was decided not to install an RF shield. The bellows material is under discussion. It is necessary that the higher order modes propagate to the 70 K absorber to reduce resistive losses at 2 K. It is not clear at this time whether copper coated stainless bellows are adequate or if they must be superconducting.

The values of the loss factor (V/pC) as a function of the number of waves

of the bellow for two values of the gap between two successive waves are
shown in Fig. 7.3. This loss factor must be compared to that of a Tesla
cavity =8.5V/pC.

Beyond 10 mm, the height of the bellow waves does not modify the value
of the loss factor whereas the gap plays an important role: it must be kept as
small as possible. So, if we take a 7 wave bellow (acceptable for a flexibility
range of ±6.5 mm) with a 3 mm gap, the loss factor is 1.05V/pC. It represents
an increase in the HOM losses of 1.05/8.5 = 12%, which is acceptable [5]. An
example of the bellow connection is shown in Fig 7.4.
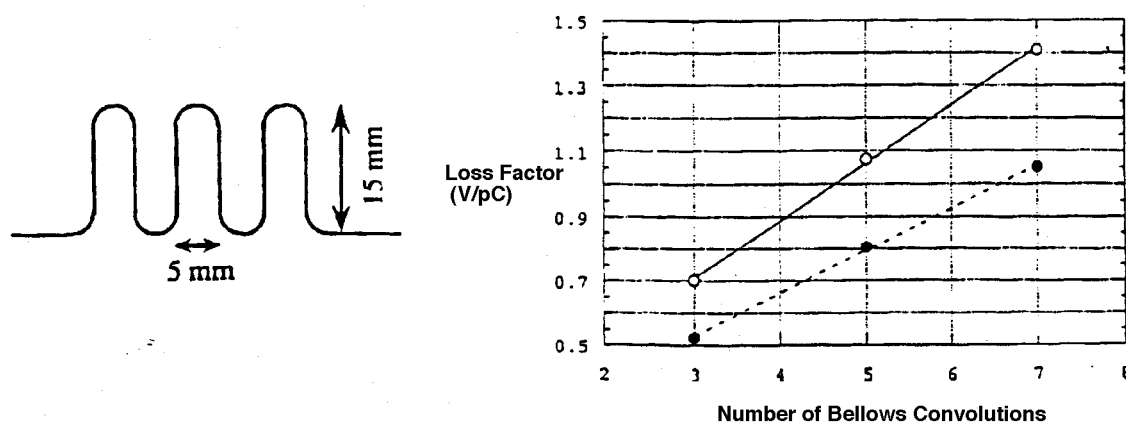
Figure 7.3: Loss factor (V/pC)

Travelling higher order modes which are not coupled out of the cavities
by the HOM couplers will be absorbed in a short section of the beam pipe
inside the quadrupole at the end of each module. The beam tube connecting
the last cavity of one module to the first cavity of the next module will be
made from stainless steel. A detailed view of the interconnection between
modules is shown in Fig 7.5. Except for a section of about 60 cm it will
be copper-coated from the inside. The uncoated section is in good thermal

[5] Ph. Leconte, A. Mosnier, M. Maurier, D. Trines, A. Matheisen, *Connections between TESLA Cavities*, Tesla 93-28

contact with helium gas at 70 K, so the power of the travelling HOM is deposited at a higher temperature level.
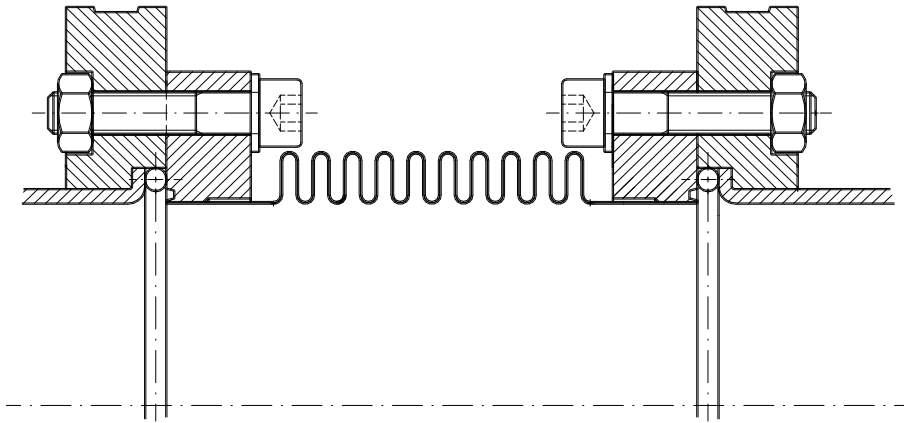
Figure 7.4: Layout of the bellow section between cavities
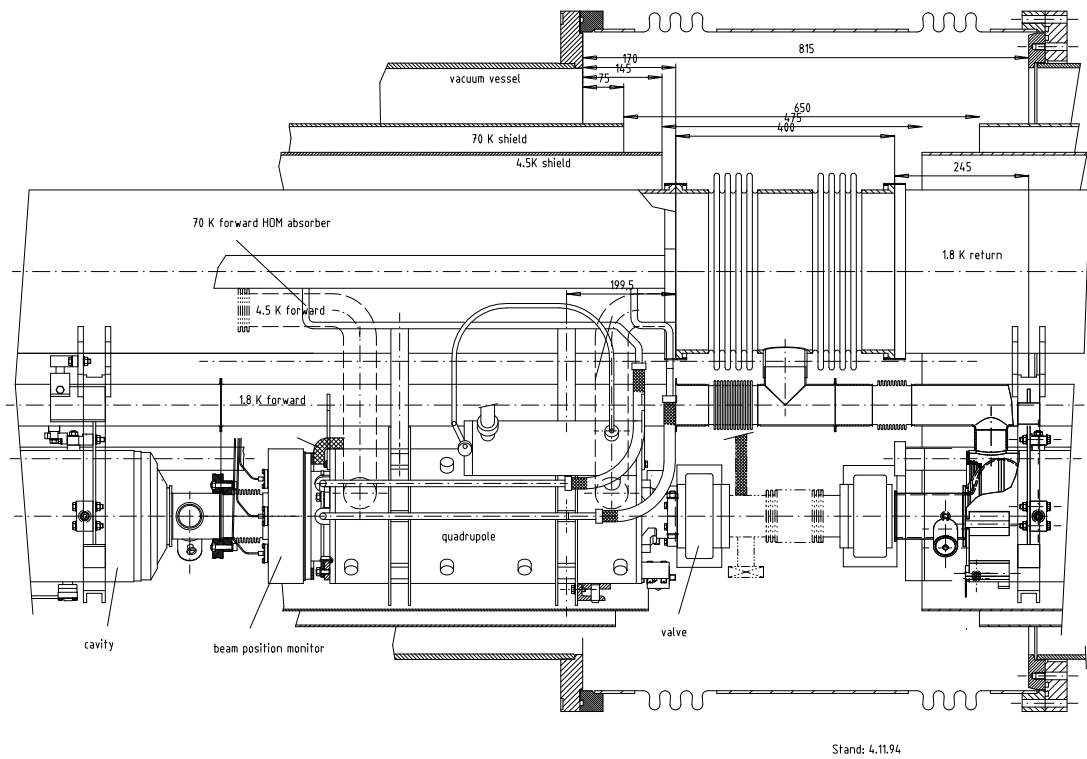
Figure 7.5: Interconnect of modules

Between modules and between the valves at the ends of the cavity string a beam pipe section of about 20 cm length will be inserted. It contains a copper-coated bellow and a pumping port with an additional manual valve to pump and purge. The manual valves to the pumped cavity strings will only be opened when the intermediate piece is clean and pumped to UHV.

7.3 Vacuum System for the Input Coupler

The part of the input coupler between the cold ceramic window at 70 k and the room temperature ceramic window is pumped separately. At each input coupler there is a small all metal valve (NW16) which allows the connection of the couplers to a pipe of 100 mm diameter which runs along the module (see Fig. 7.6). The pipe is pumped by one ion getter pump with 100 ℓ/sec pumping speed. The header can be pumped down via an additional manual valve by a turbomolecular pump station.
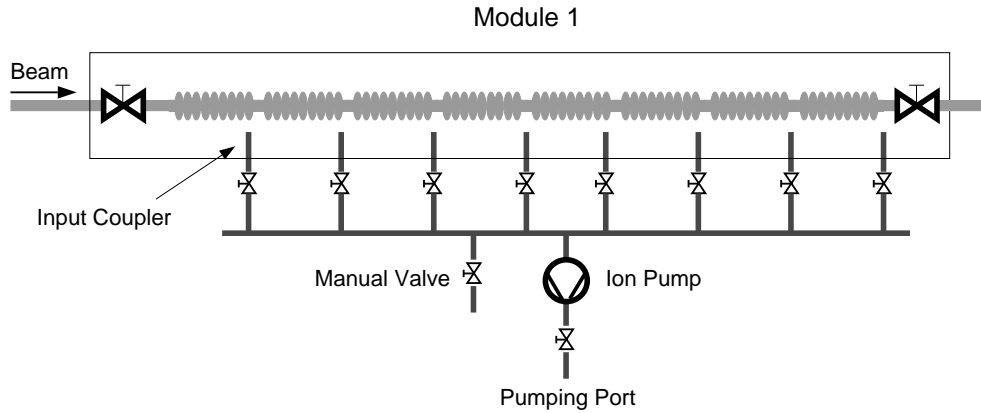
Figure 7.6:   Input Coupler Vacuum System for the TTF Modules

7.4 Oil-Free Turbomolecular Pump Stations

To avoid pollution of the cavity surfaces by hydrocarbons we built pump stations containing turbomolecular pumps without oil lubrication and oil-free roughing pumps (see Fig. 7.7).
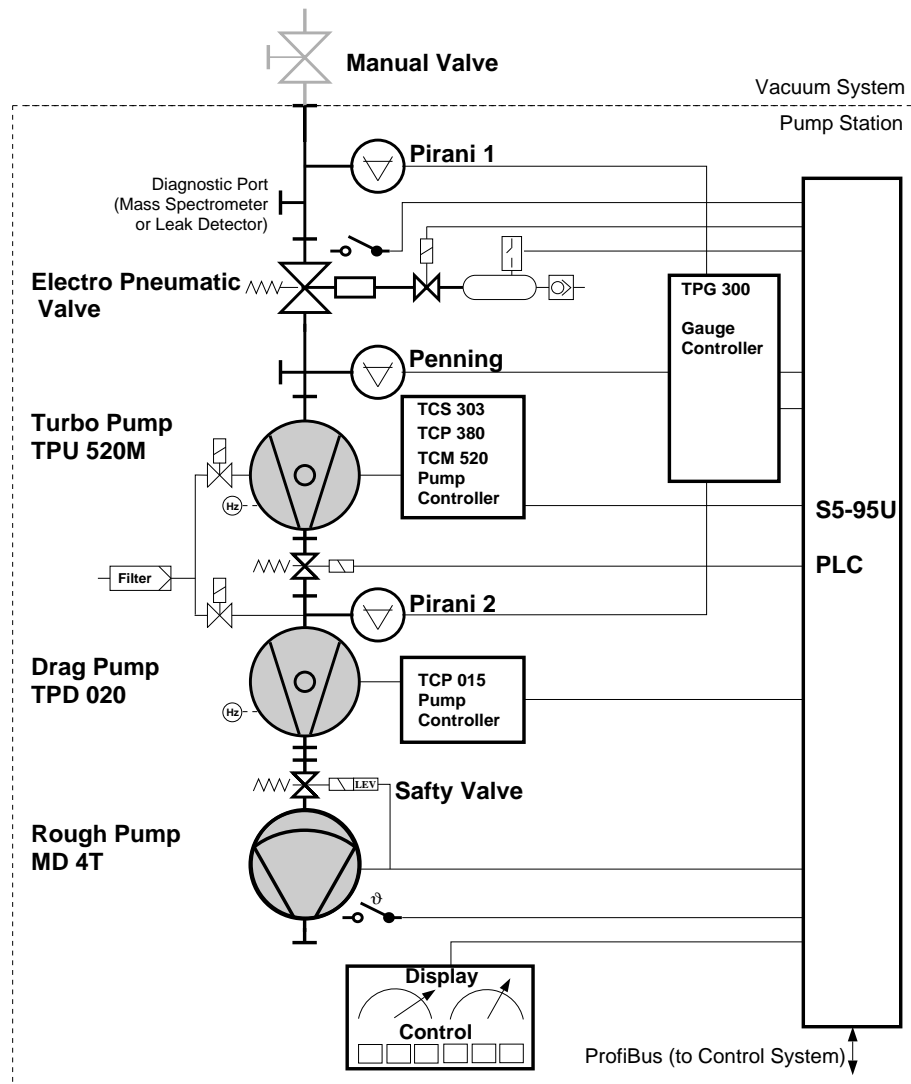
Figure 7.7: Oil-Free Pump Station.

We ordered different types from different companies to find out which type will fit our requirements best at adequate cost. The logic of all pump stations is similar. There is a electropneumatic valve at the pumping port of each pump station. It can only be opened if certain conditions are fulfilled.

Before the valve can be opened, the pump station must have demon-

strated that it is fully operational: all pumps must be running properly and a pressure below 10^{-5} mbar at the valve must be achieved.

In front of the valve there is a pirani gauge to measure the pressure in front of the valve. If the pressure is below 10^{-2} mbar and the turbomolecular pump is operated at full rotational speed the pneumatic valve can be opened.

If the valve is requested to open at pressures larger than 10^{-2} mbar, the turbomolecular pump will be switched off and the valve will open when the rotational speed of the pump with magnetic ball bearing is below a critical limit. When the pressure has been reduced by the roughing pump below 10^{-2} mbar the turbomolecular pump will be switched on automatically. If the pressure at the turbopump will exceed 10^{-1} mbar due to a sudden gas load for example, the pump will switch off automatically and only switch back on again if a pressure below 10^{-2} mbar is reached.

7.5   The Insulating Vacuum

The insulating vacuum of the four cryostat modules will be maintained by one turbomolecular pump station of the type used at the superconducting magnets of HERA. The pumping speed of $150\ell/\text{sec}$ is sufficient to maintain a pressure below 10^{-4} mbar with the module string at room temperature. The total gas load due to desorbing surfaces and permeation through O-rings is comparable to the HERA magnet system. If there are no larger leaks from the helium circuits into the insulating vacuum the pumps can in principle be turned off once the string is cooled down to operating temperatures.

This may be possible for the short string of four modules in the TTF. However for the large system in the 500 GeV collider one has to be able to cope with a certain number of helium leaks, as we have learned form HERA. Thus one has to assume that some turbomolecular pumps have to run all the time. This may cause problems with vibrations transferred from the pump station to the cavities. This problem and ways to get rid of it can be studied at the TTF.

The insulating vacuum of the feedbox and the transferline will be separated from the module vacuum by vacuum barrieres. Also the capture cavity is separated from the modules.

There will be bypass tubes with valves, however, which allow to couple the various systems, thus minimizing the number of pump stations needed

during operation.

For pump-down and commissioning all systems can be pumped separately. On the module string there is a pumping port at each interconnect between modules. In case of a leak they can be used to help localize the leak within the string.

All seals at the insulating vacuum systems will be O-rings. The sealing of the vacuum vessel at the interconnects between modules is done in a similar way to the sliding sleeve layout used at the superconducting magnets in HERA.

The ends of the string are a concern due to the large forces (order 10^4 kg) acting on the endplates. The bellows in the sliding sleeves needed to make up for tolerances can be bridged by rigid bars before pump-down. However, to avoid motion of the endplates in case the rods have not been installed properly and to provide anchor points for internal piping the preferred solution appears to be to fix the end plates to the floor by rigid supports.

Chapter 8

The RF System

The RF needs for the TTF are threefold:

A The main demand comes from the four cryomodules. In each cryomodule there are eight cavities. The peak RF power needed for one nine cell cavity at full gradient and maximum beam current, i.e. 25 MV/m and 8.22 mA during the pulse, is 208 kW.

The beam pulse consists of 800 micropulses with a spacing of 1 μs and 470 μs are needed to fill the cavity with RF, hence the minimum RF pulse length has to be 1.27 ms. The repetition rate is 10 Hz.

For more flexibility, we have specified a minimum RF pulse length of 2 ms. This will also allow us to double the beam pulse length in order to reduce the loss of electrical energy due to cavity filling.

So, the total peak and average RF powers needed for the four cryomodules are 6.65 MW and 140 kW respectively.

B The injector, which consists of a gun, a subharmonic prebuncher and a preacceleration cavity identical to one of the the nine-cell cavities installed in the cryomodules, also needs about 208 kW of RF power.

C Finally, 1-2 MW of RF power are needed for high peak power processing (HPP) of the cavities in the vertical dewar or elsewhere as required.

For all these cases fully reflected power during some fraction of the RF pulse must be expected and circulators will be used to limit the reflected power seen by the klystrons to 1.2 : 1 VSWR or better.

In order to have a sufficiently fast response of the amplitude and phase regulation loops, a Klystron bandwidth of 3 MHz (or more) should be more than adequate.

In addition, a power reserve of about 30 % for amplitude and phase regulation is required. A maximum pulse power close to 10 MW is therefore needed.

In the spectrum of the commercially available L-band klystrons there are several tubes which can deliver about 5 MW peak power at a pulse length of 2 ms. For 10 MW peak power the pulse lengths lie rather in the 100 μs range. We have decided to power the four TTF cryomodules by two 5 MW klystrons TH 2104 C from Thomson. These are conventionally pulsed cathode klystrons without modulating anode. One of these klystrons will also alternatively deliver the power for HPP of the cavities.

For more flexibility, the RF for the injector cavity will be supplied by an extra 300 kW pulsed klystron. We had the opportunity to purchase several of these tubes and also high power circulators as second hand devices, which were formerly used in plasma physics in Munich.

In the following we will discuss possible klystron-modulator schemes, the wave guide RF distribution system, phase and amplitude control, beam loading,and a scheme to cope with the detuning of the cavities due to Lorentz-forces. We will also sketch some perspectives for the development of new RF sources for TESLA.

8.1   Klystron-Modulator Schemes

8.1.1   Modulator/Klystron choices

The commercially available klystrons, which correspond to our needs, can be divided in two categories. These are diode klystrons without a modulating anode and devices with a modulating anode. They are schematically shown in Fig. 8.1.

Pulsed diode klystrons need a pulsed cathode voltage of the order of 130 kV with a current of about 100 A in our case whereas a klystron equipped with a modulating anode usually is subjected to a CW cathode voltage, and the electron beam current in the tube is controlled by the potential of the modulating anode. Such a modulator is indicated in Fig. 8.2. The
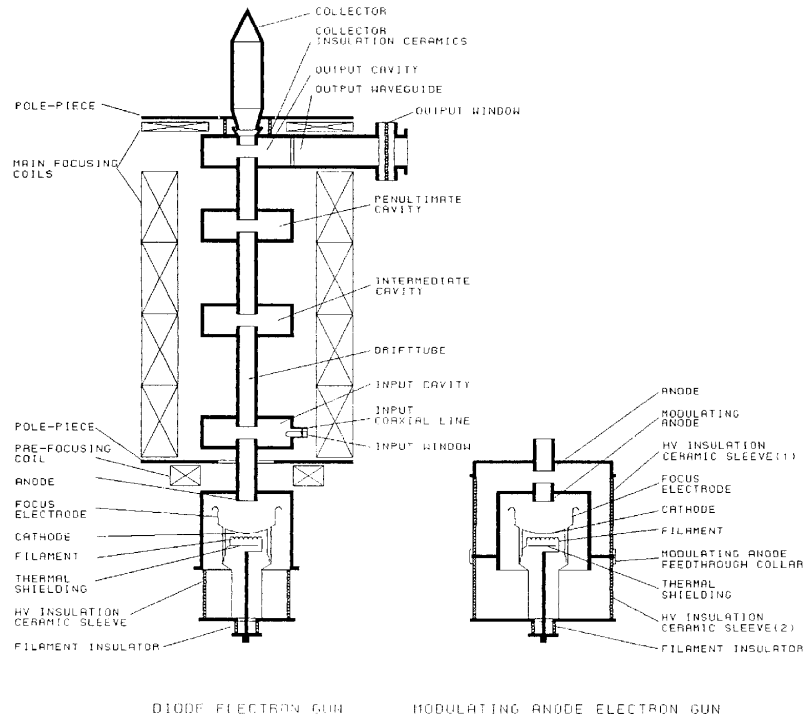
Figure 8.1: Klystron with and without modulating anode.

advantage of this latter scheme is that the current that has to be handled by the switching tube is only of the order of an ampere, and no pulse transformer (see below) is needed. So there is flexibility with respect to pulse length.

At cathode voltages well below 100 kV this scheme works very well. For cathode voltages well above 100 kV, however, some tube manufacturers hesitate to recommend modulating anode klystrons because the additional ceramic insulator necessitated by the modulating anode is a critical element and likely to cause sparking.

Note that the klystron beam current is suppressed for modulating anode potentials close to the cathode potential, hence the ceramic cylinder between modulating anode and ground potential anode sees the full cathode voltage during the long intervals between RF pulses (98 ms in our case). The distances cannot be arbitrarily increased because of electron optics. The other ceramic cylinder sees only high voltage during the duration of the RF pulse. For pulses as long as 2 ms this is feasible but at the limit of today's state of
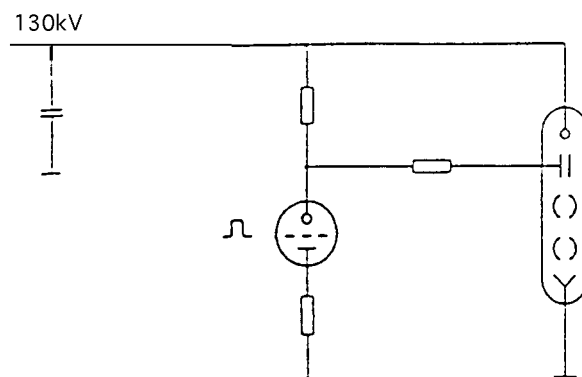
Figure 8.2:   Hard tube modulator for a klystron with modulating anode.
The beam current in the klystron is controlled by the poten-
tial of the modulating anode.

the art.

Nevertheless, there are manufacturers who claim to be able to solve or
to have solved these problems. We are, however, not aware of an existing
modulating anode klystron that can deliver 5 MW pulses of 2 ms length. On
the other hand, many examples of newly built diode klystrons suitable for
the TTF exist.

The procurement of a suitable hard tube for the modulator would be
difficult and expensive since this tube has to endure the full cathode voltage,
as is apparent from Fig. 8.2. Above 120 kV there is only a very limited choice
for these tubes.

Other disadvantages of the modulating anode klystron are that the ca-
pacitor bank has to be charged up to the full cathode voltage rather than to
some 10 kV, as is the case for the alternatives discussed below. This implies
considerable increase of crow bar cost. Furthermore, the electromagnetic
focusing solenoid of the klystron has to be bigger and will consume more
power. Finally, these tubes are more expensive than diode tubes.

These arguments and others concerning gain and efficiency led to our
decision for the Thomson TH 2104 C diode klystron. The main parameters
of this tube, which were measured during commissioning in July 1993, are
given in Tab. 8.1.

Table 8.1:   Measured Parameters of the TH 2104 C Thomson Klystrons

Frequency:	1300 MHz	
Pulse length:	547 μs	
Repetition rate:	40 Hz	
Beam Voltage:	130 kV	
Beam Current:	89 A	
Perveance:	$1.94 \cdot 10^{-6}$	
Drive Power:	45 W peak	
Output Power:	5.1 MW peak	102 kW average
Body Dissipation:	3.2 kW max.	
Efficiency:	44.7 %	
Gain:	50.5 dB	
Bandwidth:	7 MHz	

8.1.2   Modulator choices

Next we were confronted with the task of designing a cathode modulator which produces 130 kV pulses with a current of almost 100 A. The solution of a switch tube in series with the klystron as depicted in Fig. 8.3 does not seem attractive. To our knowledge, at most one tube exists which could switch currents of about 100 A for intervals like 2 ms. We fear that this solution, if feasible at all, would be very expensive and unreliable.

More exotic solutions like Superconducting Magnetic Energy Storage[1] as shown in Fig. 8.4 and discussed more fully in Sec. 8.5.2 merit consideration, but are certainly too far from maturity to be used for the TTF at the outset. Serious R&D effort in this area is ongoing.

A proven solution consists of a Pulse Forming Network (PFN) in conjunction with a pulse transformer. It is shown in Fig. 8.5. This technique has been successfully used at SLAC, FNAL and at other places, but only with pulse lengths up to some hundred μs. Evaluation of the costs of a 2 ms PFN stimulated search for other solutions.

---

[1]H. Steinhart, K. P. Jüngst, *Einsatz von SMES für die Versorgung von Hochleistungsklystrons*, Primärbericht, 1992, Kernforshungszentrum Karlsruhe GmbH.
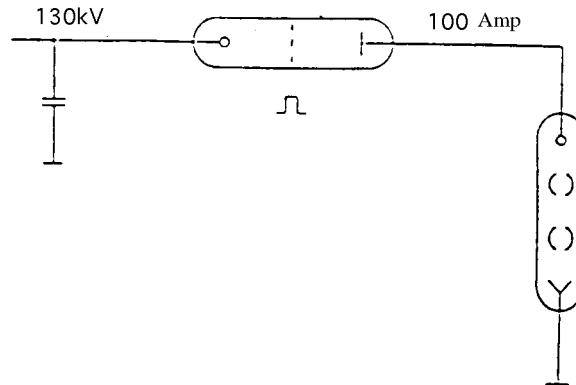
Figure 8.3: Klystron modulator with a series switch tube.
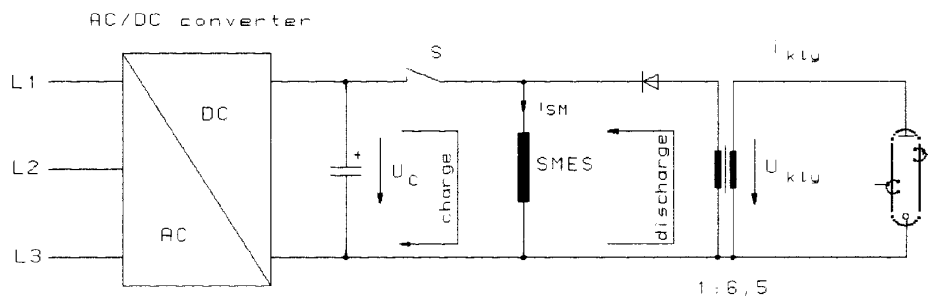
Figure 8.4:   Schematic electrical circuit of the Superconducting Magnetic
              Energy Storage (SMES) coil circuit coupled to a klystron
              through a pulse transformer. Transfer of a part of the electri-
              cal energy stored in the superconducting coil requires switch-
              ing of the high current in the coil at a 10 Hz rate.
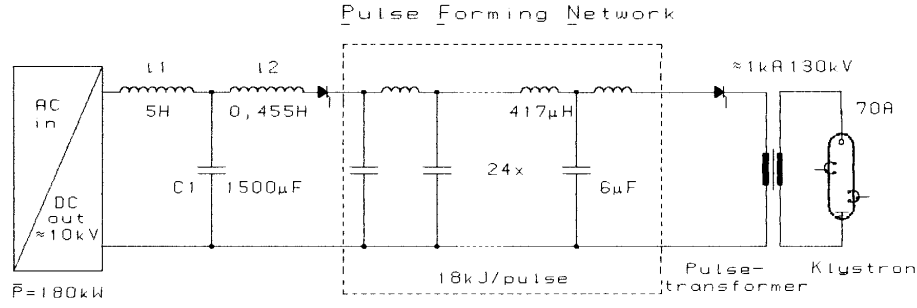
Figure 8.5:   Principle of a Pulse Forming Network (PFN) or Line Type
Modulator. At the voltage level of 10 kV the network L1, C1
reduces fluctuations of the charging current of the subsequent
PFN below the 5 % level. By discharging the PFN into the
pulse transformer, a 2 ms 130 kV pulse is generated every
98 ms. The energy stored in the PFN is comparable to the
total amount of energy needed per pulse, i.e. about 18 kJ.

The very elegant solution which has been adopted was executed at FNAL[2]
and is described in detail in Sec. 8.6.

8.1.3   RF System Efficiency

The overall modulator efficiency has been measured to be 86 %. The mea-
sured electronic efficiency of the klystron is close to 45 %. Since we need
about 30 % peak power reserve for amplitude and phase regulation (see be-
low) we cannot operate the klystron in saturation, and the effective klystron
efficiency reduces to 30 %.

The assumed power loss in the circulators is 4 %, and the klystron focusing
solenoid needs a continuous power of 3.8 kW. Hence, for a duty cycle of 2.07
% the wall-plug power to RF power efficiency for a 5 MW source is about 25
%.

It should be noted here that we are triggering developments for future
klystrons with the efficiency goal of 75 %, (see last section), and it seems

---

[2] *The TESLA Modulator*, H. Pfeffer, C. Jensen, S. Hays, L. Bartelson, TESLA Report
93-30

also possible to develop circulators with an insertion loss of 0.1 to 0.15 dB, i.e. about 3 % , so that ultimately an overall efficiency around 42 % should be reached.

8.2   The RF Distribution System

There are four cryounits in the TTF and the RF distribution system is based on one klystron for two cryounits. Each unit contains eight 9-cell cavities. The distance between adjacent cavities is $3/2$ λ. Therefore the phases are identical at each feed point. In principle, a tree-like RF distribution can be used, but a linear system branching off identical amounts of power from each cavity from a single line by means of directional couplers matches the linear tunnel geometry better and will be installed for the TTF. Such a system is already in use for the HERA superconducting RF system and all required components are readily available. One might object that unlike the case of the tree-like system, where all paths have the same electrical length, thermal expansion could be a problem for the linear distribution system. Fortunately the effect is only 0.05° of RF phase per degree centigrade and per meter and is therefore not too critical. The total power of 5 MW (including a safety margin of 30 % for eventual overcoupling or to compensate for tuning errors) is symmetrically divided by a 3 dB power splitter and feeds the two cryomodules, see Fig. 8.6 and 8.7. Individual three stub wave guide tuners for impedance and phase matching of each cavity are planned. They provide the possibility of ± 30° phase adjustment and to correct for VSWR up to 2 : 1.

Circulators are indispensable. They have to protect the klystrons against reflected power and, in conjunction with load resistors and the power input coupler, they define the loaded cavity impedance as seen by the beam. The circulator will be located between the klystron and the 3 dB power splitter.
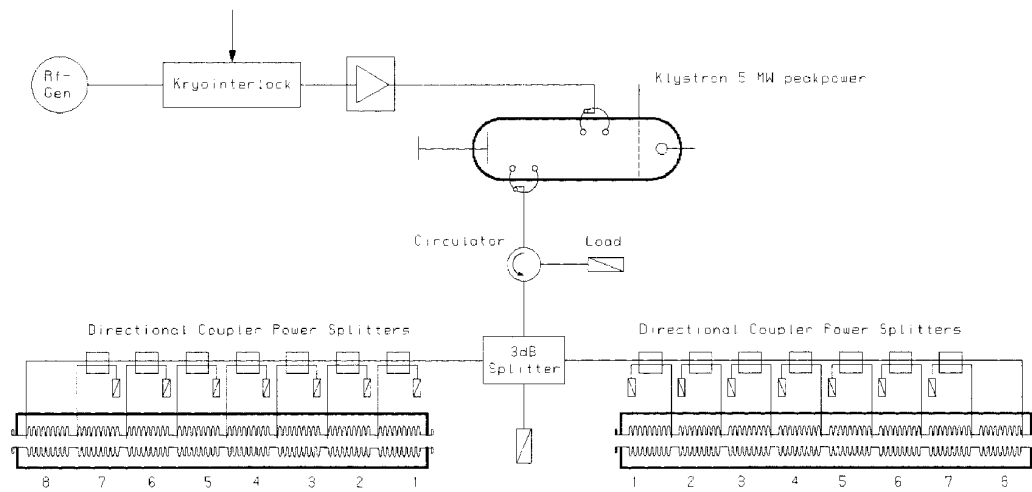
Figure 8.6: Layout of the RF distribution scheme. One 5 MW klystron feeds two cryounits. The coupler hybrids branch off equal amounts of power into the individual cavities.
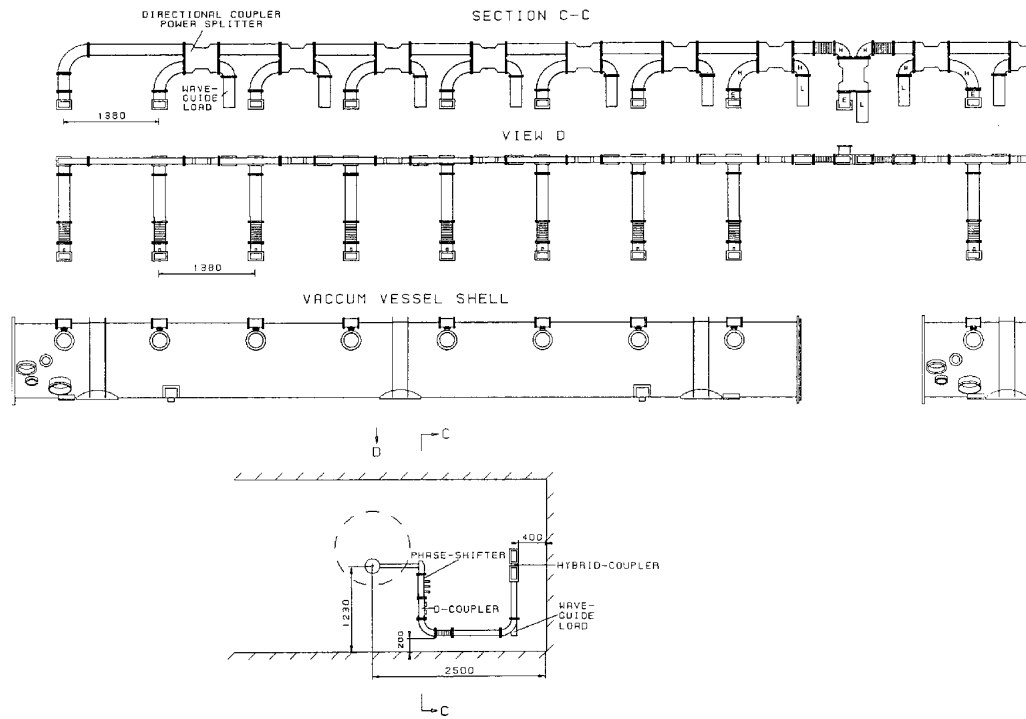
Figure 8.7: Detail layout of RF distribution scheme.

Since, due to cavity filling, there is almost total reflection of the RF power at the beginning of the pulse, the standing wave RF voltage which occurs in the circulator and in some parts of the wave guide system may double. In other words, with respect to sparking protection, the equivalent power to be considered is 4 times the real power entering into the circulator, i.e. almost 20 MW. Assuming a breakdown field of 30 kV/cm, the recommended power rating for WR 650 wave guide is 14.8 MW for straight wave guide under ideal conditions, which means dry and clean. It is, however, not *a priori* clear by how much this value will reduce in wave guide sections other than straight ones like in the coupler hybrids, and if some dust or other impurities are present.

Of course, the wave guide lengths will be arranged so that the reflected powers from each cryomodule will add up constructively in the load associated with the 3 dB power splitter rather than propagating to the circulator.

This can work perfectly only if both power signals arrive with equal amplitude and proper phase at the power splitter. Clearly it is unrealistic to hope that this will always be the case. Therefore we will fill the wave guide section between the klystron and the power splitter with the protective gas SF_6 of normal pressure, which can increase the power handling capability by up to 8 times. The disadvantage of SF_6 is that, if sparking occurs, aggressive radicals are formed, and one may have to change the gas in order to avoid wave guide corrosion. Other gases would require an overpressure of several bars to get the same relative power capability as SF_6 at normal pressure.

Presently we are investigating experimentally whether the long wave guide sections after the power splitter can be operated with normal air. In these sections of the RF distribution the equivalent power corresponding to the worst case standing wave voltage should stay below 8 MW.
Specification of circulator parameters, directional coupler power splitters and associated wave guide loads are given in Tab. 8.2, Tab. 8.3 and Tab. 8.4.

Table 8.2:   Specification of WR 650 Directional Coupler Power Splitters

Frequency:	1300 MHz ± 10 MHz
Power:	9 MW peak during 2 ms, 50 kW average
Directivity	20 dB
VSWR:	1.1 : 1 max. for all ports
Flange:	CPR 650 F
Waveguide:	WR 650, normal wall thickness

All aluminum components shall be fabricated using 6061-T6 alloy.
Finish MIL C5541 class 1A.

We need seven different types of power splitters with coupling ratio:

    1.   9.03 dB ± 0.1 dB
    2.   8.45 dB   ”
    3.   7.78 dB   ”
    4.   6.98 dB   ”
    5.   6.02 dB   ”
    6.   4.77 dB   ”
    7.   3.00 dB   ”

All couplers shall have the same electrical length.

Table 8.3: Specification of WR 650 Wave Guide Load

Power:	1MW peak during 2 ms, 12 kW average
VSWR:	1.05 : 1 by full power
RF leakage:	-95 dB
Cooling liquid:	35 % glycol-65 % water
Physical length:	< 500 mm
Flange:	CPR 650 F

Table 8.4: Specification of Circulator

Frequency:	1300 MHz $\pm$ 5 MHz
Peak power:	5 MW Due to total reflection of the RF signal during an important fraction of the pulse duration the maximum standing wave voltage will correspond to 20 MW!
Average power:	120 kW
Insertion loss:	0.1 dB
VSWR:	better than 1.2 : 1 for total reflection
Isolation:	30 dB, min. 26 dB
RF pulse length:	2.2 ms
Repetition rate:	10 Hz

In principle one can imagine how to simplify this proposed RF distribution scheme and reduce cost by replacing the directional couplers (and their loads), which split off of the main wave guide identical amounts of power for each cavity, by doorknob or crossbar couplers, and make sure that the distance between all these couplers is an integral multiple of $\lambda/2$. Then, electrically, all cavities are in parallel. However, a detailed study investigating the effects of reflected power and crosstalk between cavities under all possible circumstances in this case needs yet to be performed.

Very recently another very promising variant has been proposed. Here, each cavity would have its own individual circulator which would be located between the directional coupler power splitter and the power input coupler to the cavity. Then the maximum standing wave voltage seen by the circulator would be equivalent to less than 1 MW of RF power. The amount of reflected power seen by the directional coupler power splitters and the rest of the RF distribution system would be reduced by 30 dB, the isolation of the circulator, and become negligible. Cost estimations of this solution involving 16 small circulators per klystron rather than a single big one are presently being made.

8.3 Interlocks

In addition to the interlocks associated with the modulator which are described in Sec. 8.6.8 there are other interlock conditions which result from sparks in the RF distribution system, wave guide pressurization, reflected power, RF leaks, power couplers and from cryogenics.

Sparks in the RF distribution system will be monitored by photodiodes which are mounted at the klystron window and at critical regions of the wave guide system like the circulator and the coupler hybrids. The VSWR between the klystron and the circulator should never be worse than 1.2 : 1. This is monitored by a directional coupler, and in case of too high reflected power in this place, an interlock will be activated. The SF_6, wherever present in the wave guides, will be at an overpressure of some 10 mbars which would disappear in case of a leak and which is monitored. Since RF leaking out of the wave guides is of considerable potential danger to people working in the area two independent interlock systems, which would be triggered by several RF receivers distributed along the wave guides, have been installed. Finally, all the interlock conditions resulting from cryogenics and x-ray protection

have to be fulfilled before Rf can be sent from the klystron into the cavities.

8.4   Phase and Amplitude Control

RF control overview

The beam energy spread at the exit of the TESLA linac must be below the energy acceptance of the final focus but also small enough to limit the emittance dilution due to chromatic and dispersive effects. The intra-bunch energy spread, resulting from the RF sinusoidal wave and the induced bunch wake potential, can be reduced to about $5 \cdot 10^{-4}$, by running properly the bunch off the crest of the accelerating wave[3]. Any cavity field fluctuation, in phase and in amplitude, during the beam pulse will generate some bunch-to-bunch energy spread. It would be desirable to keep this energy spread below the intra-bunch energy spread in order to assure that the bunch-to-bunch chromatic effects will be no worse than the single bunch ones.

Phase and amplitude stability of the accelerating RF are controlled by the circuits depicted schematically in Fig. 8.8. Some of the limiting factors, which are reviewed in the following, were extensively discussed and derived during the workshop on RF Superconductivity[4] held at DESY in 1991. Possible sources of phase or amplitude errors are:

Errors in Cavity Tuning

Each cavity has an individual tuner, and it has been estimated that the tuning angle could be adjusted to within $10°$, giving $\Delta E/E = 3 \cdot 10^{-2}/\sqrt{N_{cav}}$ for uncorrelated tuning errors. N_{cav} is the number of cavities.

The tuner input signals are derived from an individual cavity voltage pick up in each cavity and from a common forward power signal, which comes from the directional coupler between the klystron and the circulator. Due to the finite directivity of the directional couplers it would be difficult or even impossible to get such a signal behind the circulator given the large amount

---

[3]A. Mosnier and O. Napoly, *Energy spread Induced in the TESLA Linac*, TESLA Report 93 - 07

[4]Summary of RF working group, compiled by S. Noguchi and G. Geschonke, Proceedings of the 5th workshop on RF superconductivity held at DESY, VOL.2, pp 1031-1043, August 19-23. 1991
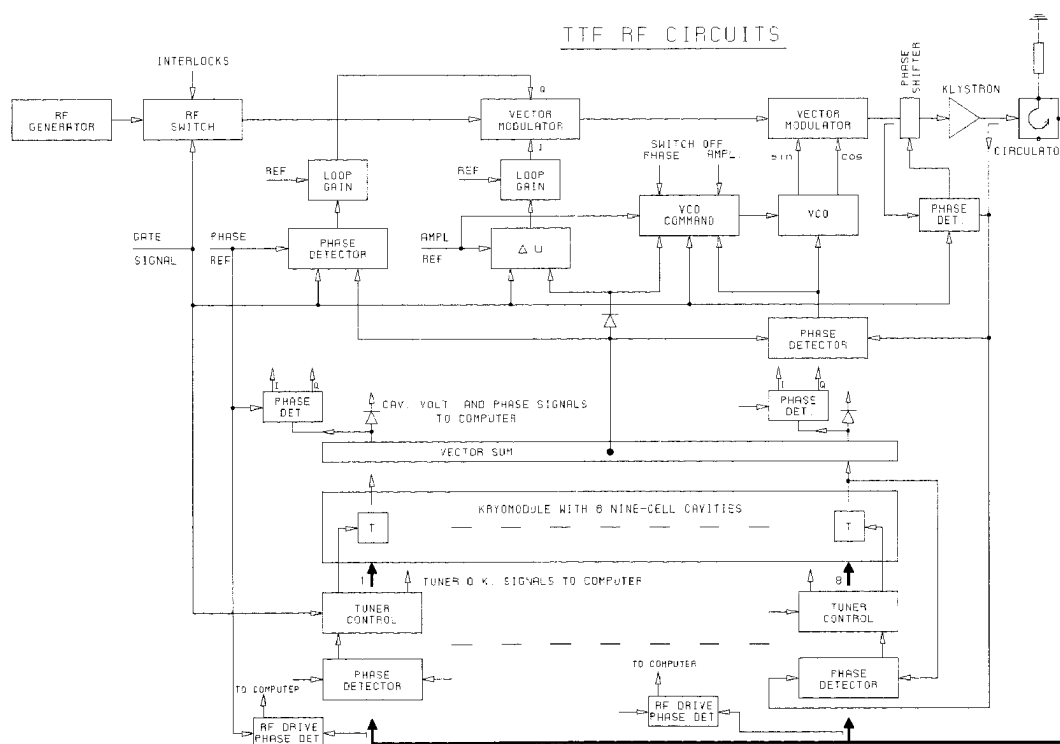
Figure 8.8:   Schematic of the phase, amplitude and tuner control circuits.

of reflected power during cavity filling, and whenever one operates without beam. This is usually the case when initial tuner adjustments are made.The thermal effect on the wave guides can be minimized by adjusting the tuner offset only after thermal equilibrium has been reached.

Error in Phase of RF Drive

It is also assumed to be kept below $\pm$ 1° either by optical transmission or by a resonant drive line.

Fluctuations of Generator Power and Phase

According to experience they can be kept below ± 0.2 % short term sta-

bility, leading to $\Delta E/E = \pm 2 \cdot 10^{-3}/\sqrt{N_{power}}$ sources .

As is apparent from Fig. 8.8 we plan to have a common feedback loop, which stabilizes for each klystron the vector sum of all cavity voltages. We believe that phase stability of $\pm$ 1° can be reached.

Errors in Relative Phase between Beam and Cavity RF Voltage

The proper timing of the cavity RF voltage relative to the beam can be defined by first tuning the beam loaded cavity to maximum RF voltage. Subsequently the phase of the klystron induced voltage is tuned until a minimum in total cavity voltage is achieved. Ideally, for this adjustment, the magnitudes of klystron induced cavity voltage and beam induced one should be equal. Then, the total cavity voltage is zero at the correct phase which, therefore, can be detected with a precision of better than a degree. A slow phase loop (not shown in Fig. 8.8) must stabilize the klystron drive RF phase to the beam signal to a similar precision over longer periods of time. The input signals to this loop can be the RF voltage signal from one cavity and a filtered beam monitor signal. Assuming a maximum phase error of ± 5 degrees on crest for an individual klystron, the total energy spread is $\Delta E/E = -3.8 \cdot 10^{-3} / \sqrt{N_{power}}$ sources.

Errors in the Injection Phase

An error in injection time is more critical since its effect on the energy spread is not reduced by statistics. An error of $\pm$ 1° in injection phase (corresponding to a time jitter of 2 ps) gives already an energy deviation of 0.03 %.

It should be noted here that errors in the injection time on the microsecond scale will cause energy fluctuations too, even if the injection phase angle is correct. This is due to the exponential time dependence of cavity filling. Injection prior to the moment where the cavity voltage without beam has reached the nominal value will result in an RF voltage which is still rising during acceleration whereas too late injection will have the opposite effect. An error in timing $\Delta T / T_{fill}$ of 1 % ($\approx$ 5 μs) yields a $\Delta E / E = 1$ %.

Stability of Total Bunch Charge in a Batch of 800 Bunches

Here, an error of 0.1 % results in ΔE / E = 0.1 % for critical coupling. If, in practice, fluctuations of a few per cent of the total bunch charge occur, the resulting energy variations can, of course, be reduced by the amplitude feedbackloop. The price for this will be a loss of effective klystron efficiency, which is proportional to the power reserve required for regulation (see below).

Charge errors of individual bunches are much less critical (see below).

8.4.1 Beam Loading

In order to get a better feeling for the influence of errors in coupling ratio and fluctuations of individual or total bunch charge on the time dependent cavity voltage, beamloading calculations simulating these effects were performed.

In Fig. 8.9a through Fig. 8.9g several cases are displayed. First we show the nominal case, where everything is matched. The rising cavity voltage is given by

$$U_{cav} = ((R/Q_o) \cdot Q_L \cdot P_G \cdot 4 \cdot \beta/(1+\beta))^{1/2} \cdot \left(1 - e^{-\frac{t}{\tau}}\right)$$

Here R, Q_o and Q_L are cavity shunt impedance, unloaded and loaded Q respectively. The generator power is P_G and β is the coupling factor. The time constant τ is given by $\tau = 2 \cdot Q_L/\omega$.

Once the cavity voltage has reached the nominal voltage of 25 MV in our case, the beam is injected and the voltage, which would rise up to 50 MV otherwise, stays constant as one can see in Fig. 8.9a. The immediate voltage drop ΔU of cavity voltage caused by the passage of a bunch of charge q is given by ΔU = q/C, if the bunch arrives at the crest of the RF voltage. C is the capacity of the cavity. After the bunch passage, the cavity voltage rises again with the time constant τ. This microscopic behavior is shown in Fig 8.9b.
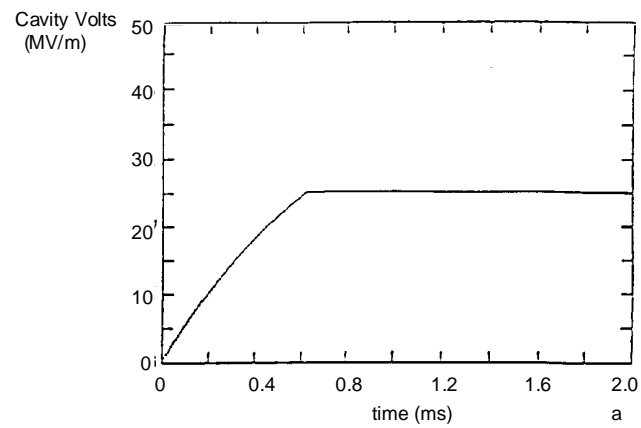
Figure 8.9a: Matched case. Once the cavity voltage has reached the nom-
                inal voltage of 25 MV in our case, the beam is injected and
                the voltage, which would rise up to 50 MV otherwise, stays
                constant.
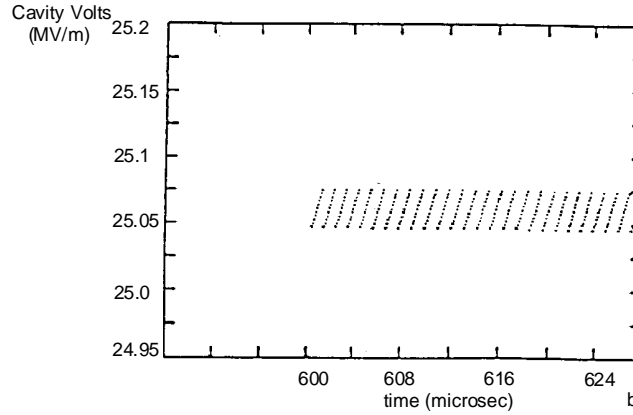
Figure 8.9b: Microscopic behaviour. The immediate voltage drop ΔU of cavity voltage caused by the passage of a bunch of charge q is given by $\Delta U = q/C$ if the bunch arrives at the crest of the RF voltage. C is the capacity of the cavity. After the bunch passage, the cavity voltage rises again with the time constant τ. The time spacing between individual bunches is $1\mu s$. Note the zoomed vertical scale. Here we neglect the effect of the finite propagation velocity of the RF power in the 9 cell cavity structure. It has been shown to be a small effect (see footnotes in text).

The effect of random fluctuations of individual bunch charge of 30 % and 100 % is well below 1 % as Fig. 8.9c and 8.9d show. This is not unexpected since the energy stored in the cavity is about 400 times the nominal energy carried away by one bunch. In these calculations the finite group velocity of propagation of generator power in the multicell cavity has not been taken into account. Sekutowicz[5] and Henke[6] have shown that the effect is small.

---

[5] *Transient State in Standing Wave Accelerating Structures*, J. Sekutowicz, Particle Accelerators, 1994, vol. 45, pp 47 - 58

[6] *Envelope Equations for Transients in Linear Chains of Resonators*, H Henke, M Filtz, TU Berlin, DESY Print TESLA 93-26
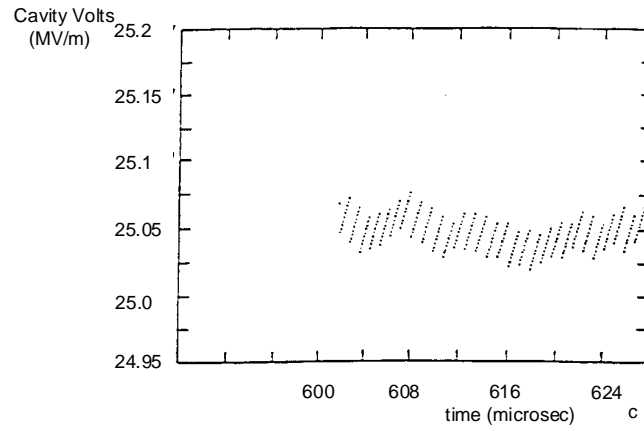
Figure 8.9c: The effect of random fluctuations of individual bunch charge
of 30 % is well below 1 %. This is not unexpected since the
energy stored in the cavity is about 400 times the nominal
energy carried away by one bunch. Note the zoomed vertical
scale.
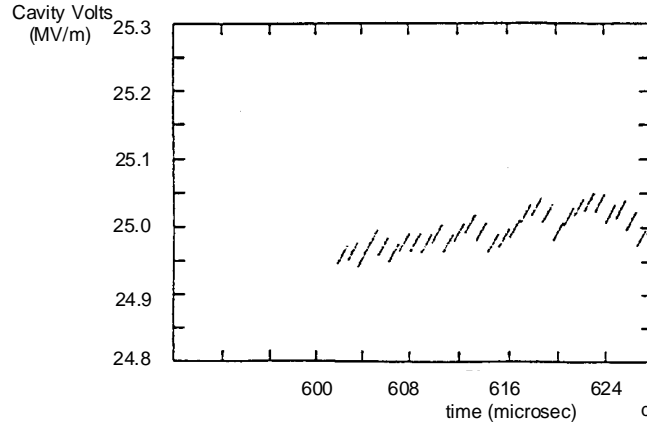
Figure 8.9d: The effect of random fluctuations of individual bunch charge of 100 % is well below 1 %. This is not unexpected since the energy stored in the cavity is about 400 times the nominal energy carried away by one bunch. Note the zoomed vertical scale.

Fig. 8.9e shows that an error of 20 % in β causes a maximum deviation of 3 % from nominal voltage.

A 5 % change in total bunch charge or beam current changes the cavity voltage by 3 % during the duration of the pulse as is apparent from Fig. 8.9f.

In Fig. 8.9g the sum of 10 cavity voltages with coupling ratio β ranging from 0.4 β_0 to 1.3 β_0 is displayed. For some coupling ratios the voltage variation may be of the order of 3 % as is shown in Fig. 8.9e. Due to the changing slope of the cavity voltage as a function of β the variation of the sum is well below 1 %. Naturally, the absolute value of the voltage sum is somewhat reduced in this case, i.e. 235 MV rather than 250 MV.
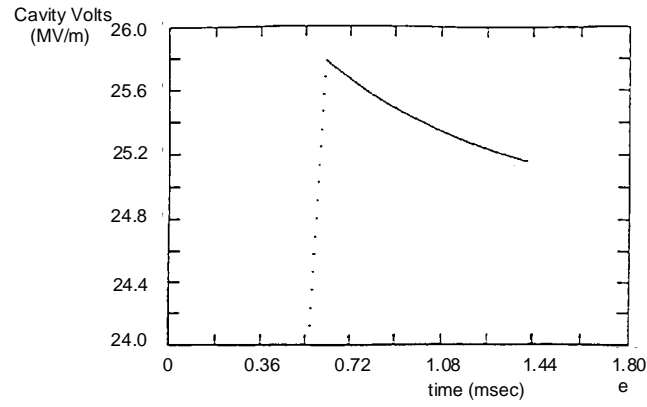
Figure 8.9e: An error of 20 % in β causes a maximum deviation of 3 %
from nominal voltage.
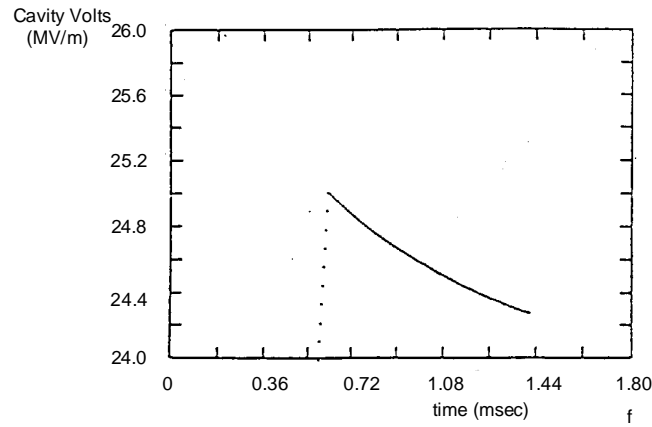
Figure 8.9f: A change of 5 % in total bunch charge or beam current
changes the cavity voltage by 3 % during the duration of
the pulse.
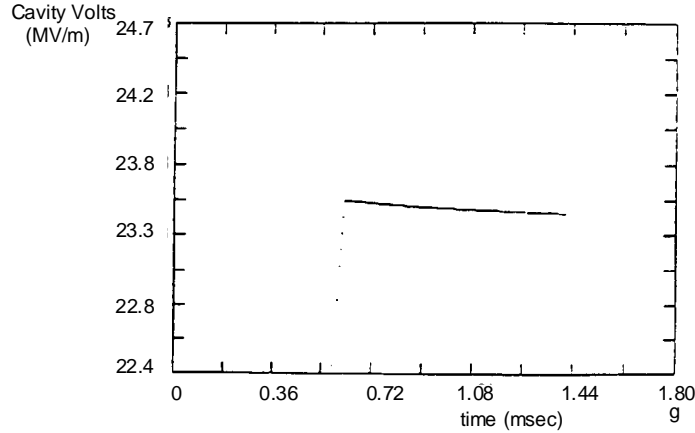
Figure 8.9g: Sum of 10 cavity voltages with coupling ratio β ranging from 0.4 β_0 to 1.3 β_0. For some coupling ratios the voltage variation may be of the order of 3 % as is shown in Fig. 9e. Due to the changing slope of the cavity voltage as a function of β the variation of the sum is well below 1 %. Naturally, the absolute value of the voltage sum is somewhat reduced in this case, i.e. 235 MV rather than 250 MV.

8.4.2   Lorentz Force Detuning of the Cavities

The Lorentz forces (also called "radiation pressure") and microphonics, by shifting the cavity frequency, are the main bunch-to-bunch energy spread sources. With superconducting cavities operating in pulsed mode, the Lorentz Forces problem arises from the wall deformation response time. The cavity frequency goes on to shift after the field rise time, while the beam is passing through the cavity. Two methods, one based upon a jump in the drive frequency and one using the self exciting loop, have been proposed to cope with the Lorentz forces detuning. The former will be realized for the 8-cavity modules while the latter will be realized for the injector cavity.

Without stiffening system, the static Lorentz forces detuning has been estimated[7] to be slightly higher then 1000 Hz for a field gradient of 25 MV/m.

---

[7] *Mechanical Characteristics of the RF Cavity for the TESLA Test Facility*, H. Kaiser, Tesla Report 94 - 19

With the stiffening system, the detuning reduces to 400 or 600 Hz according to the rigidity of the tuning system. A detuning parameter of $1 \text{ Hz}/(\text{MV/m})^2$ has been conservatively retained. The mechanical time constant, which parameterizes the dynamic wall deformation response, has been measured on a 5-cell cavity at 1.5 GHz, and is assumed to be of the same order of magnitude as the RF pulse length.

Since the bandwidth of the loaded cavity is 465 Hz ($QL = 2.8 \cdot 10^6$) a tuning error of 400 Hz corresponds to the detuning angle 60°. The voltage seen by the beam is then reduced by the intolerable factor of $\cos^2(\pi/)3 = 0.25$.

Therefore, a fast tuning mechanism, which is effective on the millisecond time scale, where the detuning occurs, is needed. The solution, which we propose and which has been realized at DESY, is also indicated in Fig. 8.8. A phase detector delivers a signal proportional to the detuning to the VCO where it is converted into a frequency signal. Combining this signal with the one from the reference frequency source in the vector modulator yields a signal of frequency f_{ref} - $f_{vco} = f_{cav}$.

In this mode the detuning angle is always near zero because the cavity is driven at its proper resonance frequency, which depends on the square the RF fields.

Prior to injection of the beam, once the nominal RF voltage in cavity has been reached, one has to synchronize to the reference frequency signal. This can be done either by means of an amplitude or a phase criterion.

If the cavity is mechanically tuned so that its resonance frequency at full RF gradient equals the reference frequency, this synchronization happens automatically since then, the output from the VCO is zero. Measurements from A. Mosnier[8] have shown, however, that, due to mechanical properties of the cavity its resonance frequency still changes after the nominal field has been reached. The resulting tuning errors can be minimized to about 6° by introducing a frequency jump of the order of 200 Hz prior to injection of the beam as was shown by Henke and Littmann[9] (see Fig. 8.10. In practice, this means that the cavity is tuned so that its resonance frequency at the time when the full gradient is reached deviates by 200 Hz from the reference

---

[8]*Dynamic Measurements of the Lorentz Forces on a MACSE Cavity*, A. Mosnier, TESLA Report 93-09

[9]*Mechanical Parameter Influence on the TESLA Cavity Tune under Lorentz Forces*, H. Henke, B. Littmann, TESLA Report 93-12
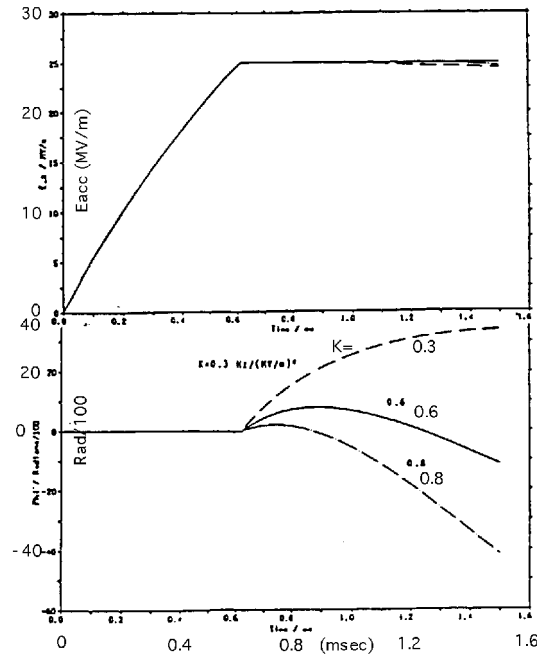
Figure 8.10: Due to mechanical properties of the cavity its resonance frequency still changes after the nominal field has been reached. The resulting tuning errors can be minimized to about 6° by introducing a frequency jump of the order of 200 Hz prior to injection of the beam. During filling of the cavity the generator frequency is locked to the cavity resonance frequency and there is no phase error.

frequency. Forcing then the value of the VCO input signal to zero within some μs results in a frequency jump of the drive frequency. With this method one minimizes an a priori known tuning error by predetuning.

A second method uses the self-exciting loop principle during the field rise time and during the beam pulse, without any frequency jump[10][11]. To minimize the phase shift for both methods during the beam traversal, the cavity frequency must be higher at the beginning (positive phase slope) and

---

[10] A. Mosnier, *Field Stabilization with Lorentz Forces*, DAPNIA/SEA Note 93 -03

[11] A. Mosnier and J. -M. Tessier, *Field Stabilization Study for TESLA*, DAPNIA/SEA 94 - 07

lower (negative phase slope) at the end than the reference frequency. Fig. 8.11 gives the cavity frequency shifts (relative to the reference frequency) and the phase error evolutions for the TESLA cavity parameters when the initial phase and the initial cavity frequency have been adjusted to cancel the phase deviation when the beam is injected and to minimize the phase error during the beam pulse.
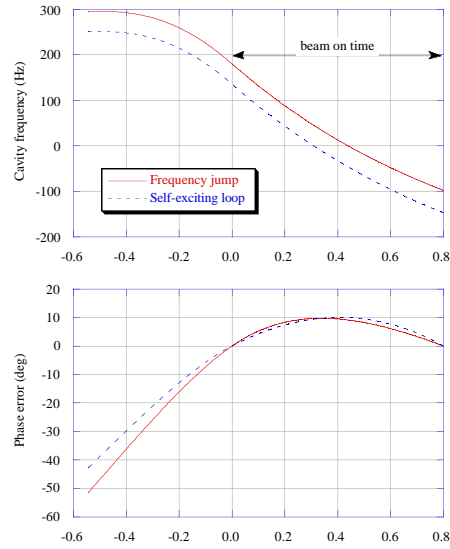
Figure 8.11:   Relative cavity frequency and phase errors for both methods.

The TESLA and TTF parameters and the resulting amplitude and phase errors, assuming one cavity driven by one generator, are listed in the Tab. 8.5 for comparison.

Since ultimately one klystron will drive 16 cavities we must demonstrate that the resonance frequencies of individual cavities do not differ by more than 40 Hz to keep the tuning errors below 10°.

Table 8.5: Compensation of Lorentz force detuning in TESLA 500 and in TTF

	TESLA	TTF
Accelerating Gradient	25 MV/m	15 MV/m
Beam current	8 mA	8 mA
electric time constant τ_e	0.78 ms	0.78 ms
mechanical time constantτ_m	1 ms	1 ms
beam injection time τ_e ln2	0.54 ms	0.54 ms
beam pulse duration	0.8 ms	0.8 ms
detuning parameter K	1 Hz/(MV/m)²	1 Hz/(MV/m)²
Amplitude error	5-6 10⁻3	0.7 10⁻3
Phase error	10 deg	3.5 deg

8.4.3   Measurements on a 1.5 GHz cavity

In order to prove the validity of the methods, they were tested on existing 5-cell cavities at Saclay. Since the Lorentz forces detuning is much stronger on these non-stiffened cavities (a factor 3.6 higher), the same static detuning of about 230 Hz was obtained with a lower accelerating gradient (8 MV/m instead of 15 MV/m). In addition, the beam current was simulated by injecting an RF signal in phase with the beam. Fig. 8.12 show the amplitude and phase errors for the self- exciting loop arrangement during the field rise time and the beam pulse with different initial tunings of the cavity. The phase error was set to zero at the beginning of the beam pulse by readjusting the initial phase for each tuning value. For optimal initial tuning (200 Hz higher than the reference frequency), the amplitude and phase fluctuations are min-

imum, whereas the amplitude is growing with the time when the cavity is not correctly tuned and the phase slope is positive (negative) just after the field rise time when the tuning frequency is too high (low).
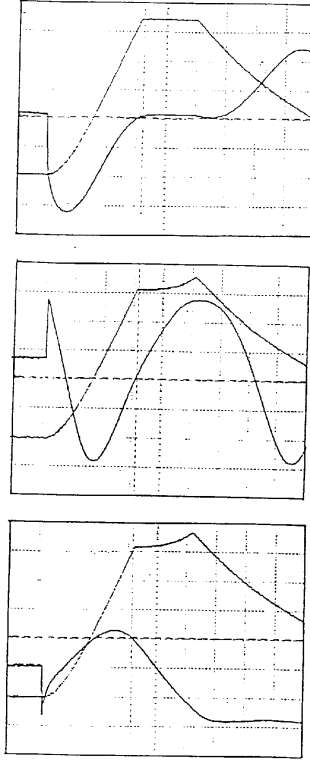
Figure 8.12:   Measured amplitude and phase error for optimal (top), too high (center) and too low (bottom) tunings for the self-exciting loop

8.4.4   Effects of parameter spreads

In the aim to reduce the cost of the power sources, two 8-cavity modules are powered by one 5 MW klystron. Since the RF and mechanical parameters of the cavities are expected to be not identical, the effects of a spread in the different parameters have been studied. During the field rise time, the generator frequency has to be locked on the varying cavity frequency. Since

the cavities cannot be initially perfectly tuned, the frequency tracking must be carried out by using the phase signal from the vectorial sum of all cavity voltages and not from a single cavity voltage. With this arrangement, there is no dramatic performance degradation when a spread in the initial cavity tuning or a spread in the detuning parameter K and mechanical time constant are introduced. Fig. 8.13 shows the histograms of the errors for a gradient of 15 MV/m and with 1000 different simulations, where the initial tuning of the 16 cavities has been randomly varied between ± 40 Hz (corresponding to a tuning angle error of 10°).
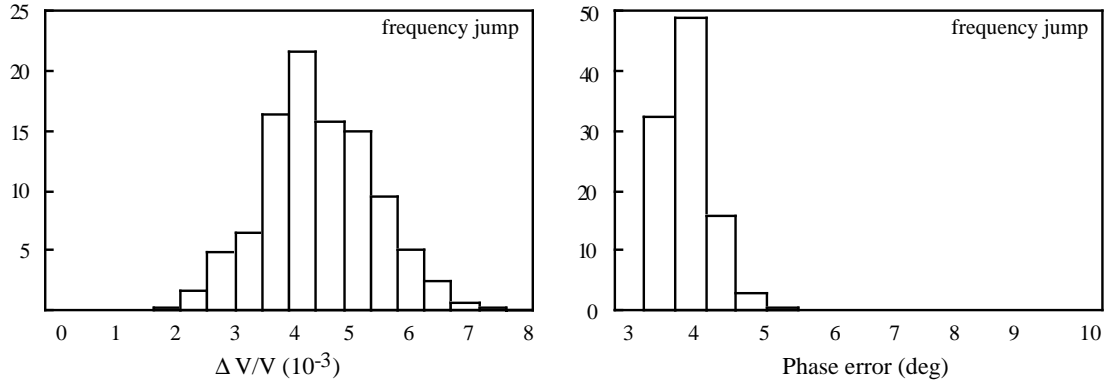
Figure 8.13:   Amplitude and phase histograms for static cavity tuning errors

In the same way, the histograms of the errors for a simultaneous spread of 20 % in the detuning parameter K and the mechanical time constant, are shown on the Fig. 8.14, for 1000 simulations. Fig. 8.15 gives the histograms for a spread in cavity Q_{ex} of $\pm 20\%$.

8.4.5   Feedback loops

Feedback loops have to stabilize the field fluctuations, which are induced mainly either by Lorentz forces or by microphonics detunings, while keeping the needed extra RF power (peak and average) within a reasonable level. In order to reduce the coupling between amplitude and phase feedback, the feedback loops must use a vectorial modulator, in which an in phase signal, proportional to the amplitude error and an out of phase signal, proportional
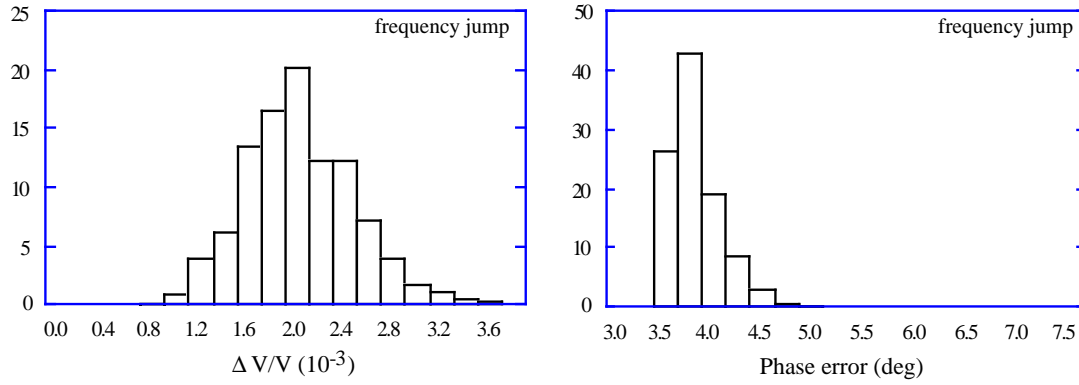
Figure 8.14:   Amplitude and phase histograms for K and τ_m spreads
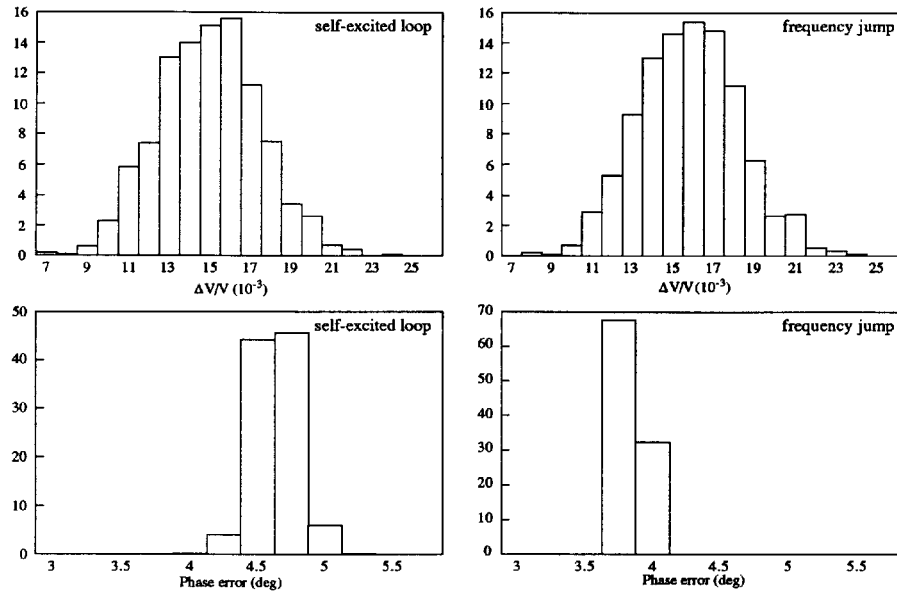
Figure 8.15:   Amplitude and phase histograms for a external Q spread with both methods

to the phase error are added to the main drive signal. Loop gains of 50 for the phase and 100 for the amplitude are a good compromise between the extra needed RF power and the resulting amplitude and phase errors. Taking into

account the perturbation due to the Lorentz forces only, the resulting energy spread is of the order of 10^{-5} for an increase of the RF powers of about 10 % peak and 4 % average.

8.4.6 Q-spread effects

In order to make the best possible use of the SC gradient capability, it would be advantageous to operate each cavity at its maximum field. Since the cavity tuning is not allowed to play with (see previous study), the easiest way of varying the cavity gradients in a chain fed by one klystron, is to change the external Qs from cavity to cavity. Even without Lorentz forces detuning however, a spread in external Qs, resulting from coupler tolerances or on purpose for having different cavity fields, will affect dramatically the amplitude error of the total voltage, because the source is not any more matched to the beam loads. This error must therefore be minimized first by means of the incident power (P_g) and of the beam injection time (t_0), before attempting to close the feedback loops, which would result to a huge extra RF power. Assuming for example a uniform spread in accelerating field around 25 MV/m of a string of 16 cavities, the Fig. 8.16 gives the required source power in kW as a function of the total voltage fluctuation for different widths of the gradient spread (10, 15 and 20 %). About 230 kW per cavity (instead of 200 kW) are needed to reach amplitude errors of the order of 10^{-4} for a gradient spread of $\pm$ 20 %.

If the Lorentz forces effects are included, the final energy spread is of the order of $2 \cdot 10^{-4}$ with the gains of 100 and 50 for the amplitude and phase loops. The net additional powers to be delivered by the source are finally 30 % peak and and 20 % average with a Q-spread of $\pm$ 20 %.

8.4.7 Microphonic effects

The main effect of microphonics, because they change the cavity frequency, is to displace the RF phase with respect to the beam, assuming that the initial phase is fixed. The demand of RF power from the feedback loops would then be huge. Instead of having a fixed initial phase, we could think of a feedback system acting on this initial phase to recover a vanishing phase shift when the beam is coming. Unfortunately the frequencies of mechanical vibrations are expected to be around and above the TESLA repetition rate
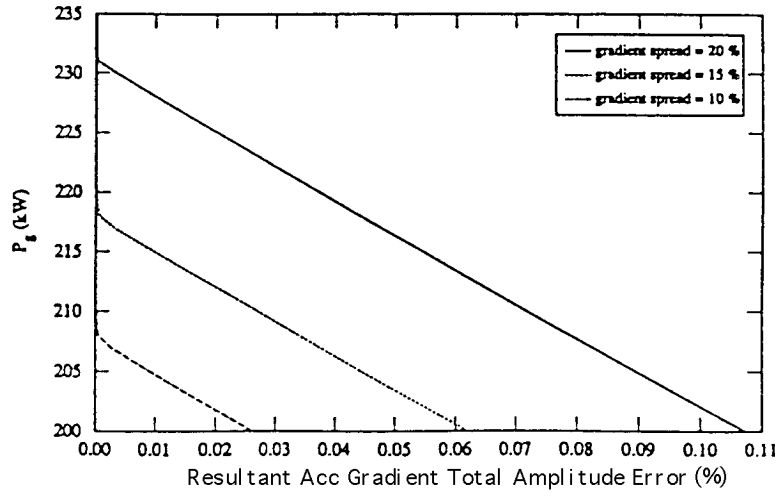
Figure 8.16:   Needed source power (in kW) vs. the fluctuation level of the total voltage

of 10 Hz, making a direct feedback inefficient. Instead of having fixed phase and amplitude references of the feedback loops, floating references following the actual phase and amplitude at the beginning of the beam pulse (by means of a tracking-and-hold circuits), can solve the microphonics problem in case of too large mechanical vibrations. The beam energy is then constant within a beam pulse but could slightly fluctuate from pulse to pulse. This is not harmful for a long machine like TESLA because the errors coming from the Lorentz forces detuning are correlated whereas the errors coming from the microphonics detuning (jitter) are essentially uncorrelated. The Fig. 8.17 shows for example the phase error curves during the beam pulse for 3 cavity tunings, including the Lorentz forces effects : the optimal one and with a shift of ± 50 Hz due to microphonics, giving moderate extra powers (20 % peak and 6 % average), with amplitude and phase loop gains of 100 and 50.
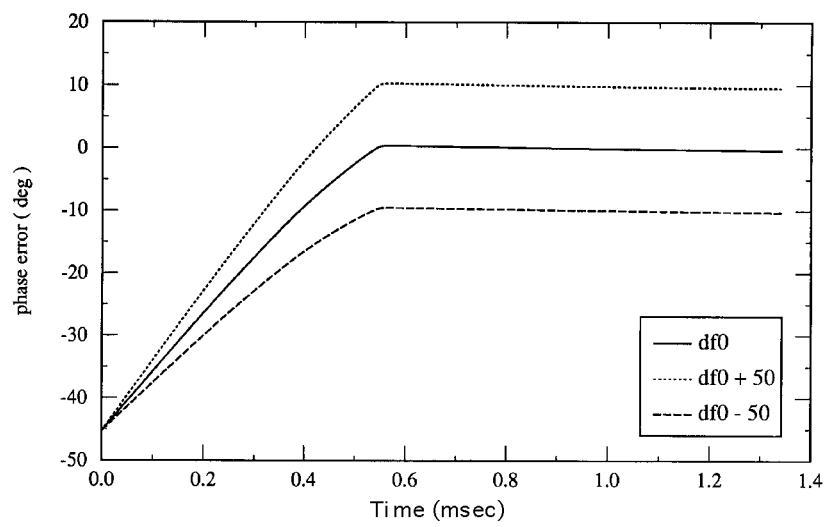
Figure 8.17:   Phase profiles for the optimal initial tuning and $\pm$ 50 Hz variation due to microphonics.

8.4.8   Hardware: the RF control circuits
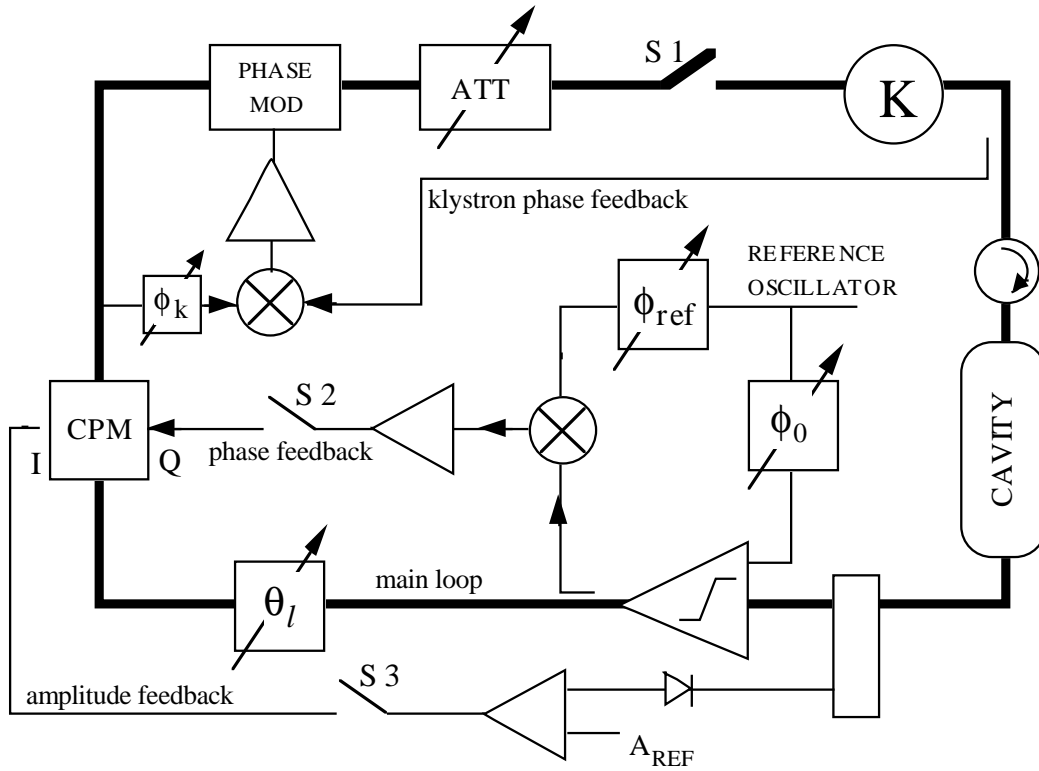
Figure 8.18: RF control module for the capture cavity.

Figure 8.18 gives a simplified sketch of the RF control module realized for the capture cavity. The main self-excited loop (thick line) contains the klystron, the resonator, the limiter-amplifier (nonlinear component setting the amplitude of the loop oscillations), the loop phase shifter (compensates the unwanted constant phase shifts in the loop) and the attenuator (provides the cavity field level). Since the phase shift across the klystron varies with the RF power, a secondary feedback loop, compensates the klystron phase variation during the field rise time. The amplitude and the phase of the cavity field are controlled by the main two feedback loops. Both error signals are combined through a vectorial modulator, which eliminates the coupling between phase and amplitude feedback. Except the phase modulator of the klystron phase feedback, built from varicap diodes, all phase shifter components, including

the vectorial modulator are realized with the same circuit, using a splitter, a 90°-hybrid and two mixers, operating at the RF frequency.

8.5 Potential Further Developments

8.5.1 Possible new RF sources for TESLA

With the present RF structure 1250 klystrons would be needed for the TESLA 250 GeV + 250 GeV linac. In order to reduce RF capital investment and running cost we have investigated the possibilities to halve the number of klystrons by doubling the output power to 10 MW and to increase the electronic efficiency from the presently available 45 % into the 70 % region. The presently considered pulse length and repetition rate remain unchanged, i.e. 2 ms and 10 Hz. Another goal is to increase the tube reliability so that a lifetime of the order of 70000 hrs is obtained. We see the following possibilities to achieve this goal:

A means of increasing efficiency is the depressed collector. Here, the collector is divided into several parts, which are subjected to different potentials, such that the residual electron beam is decelerated and the extracted electrical energy can be reinjected into the cathode voltage power supply. A gain of 20 % in efficiency due to the depressed collector has been reported for TV klystrons. There is, however, no convincing scheme of applying this principle to our case, where pulsed RF is needed.

Improvement of standard klystrons by increasing the cathode voltage to values around or above 200 kV. In this case, with the microperveance of 0.75, an efficiency of 70 % might be expected. The microperveance P is defined as $P = (I \ / \ U^{3/2}) \cdot 10^6$, where I and U are the klystron beam current and voltage. The relation between efficiency and microperveance [12] [13] is shown in Fig. 8.19. The increase in efficiency for small P is due to the reduction of space charge, which tends to blow up the beam bunches in the klystron. The inconvenience of this method is the high cathode voltage, which the klystron has to endure during the long pulses of 2 ms. For pulse lengths in the μs range, operation at much higher voltages is possible.

---

[12]G. Faillon, C. Bearzatto, Int. J. Electronics, 579,**65**, No. 3 (1988)

[13]C. Bearzatto, M. Bres, G. Faillon, *Advantages of Multiple Beam Klystrons*, ITG 92, Garmisch Partenkirchen 4–5 May 1992.
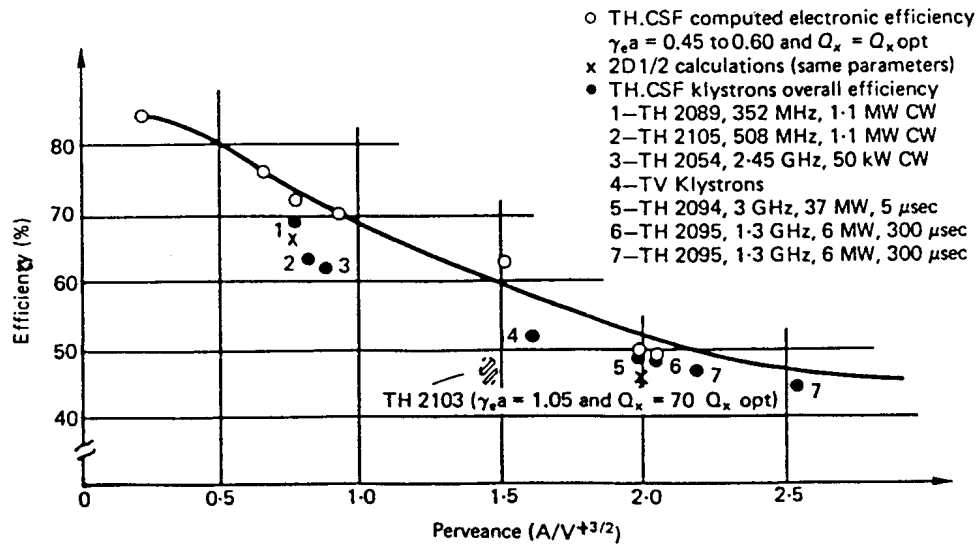
Figure 8.19:   Influence of perveance on klystron efficiency. From G. Faillon et al.

A very attractive low perveance tube is the Multibeam Klystron (MBK), where the total beam current is carried by several separated electron beams rather than by a single one. The perveance per beam is thus reduced correspondingly. Such a tube[12] [13] is schematically shown in Fig. 8.20. The main advantage of MBKs is the relatively low operating voltage, which simplifies HV power supplies and X-ray protection. Furthermore, the overall tube length may be reduced by up to 50 % and the power output is 1.8 W/g klystron weight as opposed to 0.6 W / g for a normal klystron.

THOMSON TUBES ELECTRONIQUES
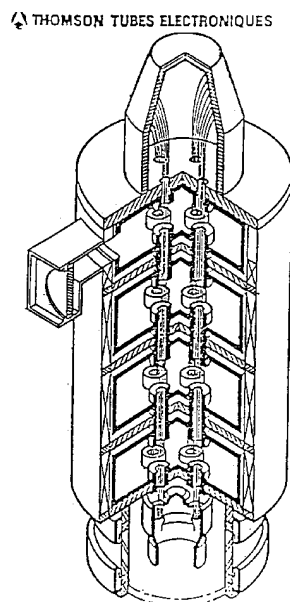
Figure 8.20:   Structure of Multibeam Klystron. From G. Faillon et al

A prototype of a 64 kW 4 beam klystron operating at 425 MHz has demonstrated[14] [15] an efficiency of 44 %. The cathode voltage was only 18 kV. A proof of existence and feasibility of 5 MW L-band MBKs operating at ms pulse lengths comes from the Moscow Meson Factory, where 33 MBKs are running. These tubes have 6 beams and the operating voltage is only 75 kV. The microperveance of 1.4 per beam should allow for a higher efficiency than the 40 % of the actual tubes.

More recent designs of MBKs promise efficiencies between 60 %and 70 %.

Last, but not least, we would like to mention a new RF source, the magnicon, which was invented by Oleg Nezhevenko from Budker Institute in Novosibirsk[16].

---

[14]G. Faillon and C. Bearzatto, op cit

[15]C. Bearzatto, M. Bres, G. Faillon, op cit

[16] *The Magnicon: A New RF Power Source for Accelerators*, Oleg A. Nezhevenko, IEEE Particle Accelerator Conference Vol. 5, May 6-9, 1991, San Francisco, Ca, USA
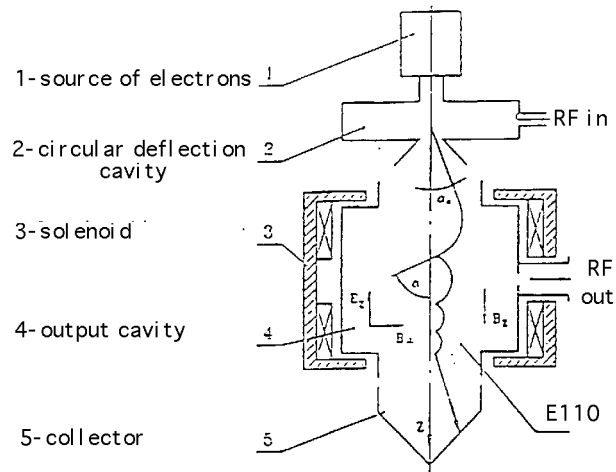
Figure 8.21:   Schematic of the magnicon. From O. Nezhevenko et al
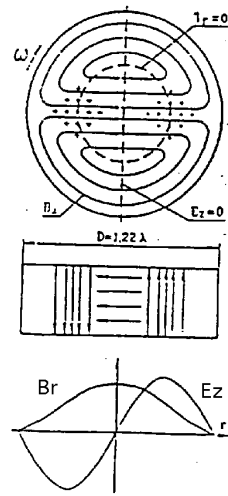
Figure 8.22:   Distribution of electromagnetic fields in magnicon cavities.
                 From O. Nezhevenko et al

The principle of operation can be understood from Fig. 8.21. A continuous electron beam from the electron source 1 reaches the circular deflection cavity 2 to be deflected there at an angle α_0 by an RF magnetic field rotating with deflection frequency ω. The field distribution in the cavity is shown in Fig. 8.22. It is generated by the excitation of two degenerate TM_{110} modes. The maximum magnetic field from one mode coincides with the maximum electric field from the second one. In the drift space electrons deviate from the device axis and get into a stationary magnetic field B_z of the solenoid 3. While entering the magnetic field the longitudinal velocity of the electrons is transformed into a rotational transverse one, and the degree of transformation is characterized by the pitch angle α. Further on, travelling along a helical trajectory and steadily changing their entering point in the output cavity 4, the electrons excite a wave in the cavity travelling along the azimuth (TM_{110}) oscillation mode and transfer their energy to this wave. If the cyclotron frequency Ω is equal to the ω, then the interaction can remain effective during many periods of RF oscillation. The particle energy is transferred to the electromagnetic field in the magnicon output cavity due to the decrease in the transverse component in its velocity at a practically constant longitudinal one. Feasibility of the magnicon has been demonstrated by two prototypes. One has delivered 2.6 MW RF pulses of 30 ms length at 915 MHz, the other has demonstrated 25 MW output power at 7 GHz for 2 ms pulses. The reported efficiencies of these two magnicons are 73 % and 60 %. It is claimed that a 10 MW magnicon for TESLA could be built with an efficiency in excess of 78 %[17]. The disadvantage of the magnicon is its high operating voltage. For the TESLA magnicon it would be 250 kV.

Summarizing we can state that there are several promising alternatives for the development of high efficiency and high power L-band RF sources for TESLA. The decision which way(s) to go will be made within the next few months.

---

[17]O. A. Nezhevenko, op cit.

8.5.2   Superconducting Magnetic Energy Storage (SMES) based Modulator

The energy that is necessary to supply a certain number of TESLA klystrons can be stored in a superconducting magnet energy storage. There are several possible modulator concepts using a SMES based power supply. These concepts differ in the amount of totally stored energy and the complexity of the circuit. A circuit design for supplying two klystrons for the TTF will be introduced in this paper.

Nevertheless an appropriately sized SMES for TESLA should be able to provide groups of about five to ten klystrons. On the base of the high current carrying capability of superconducting cables, currents in the range of 10 kA are easy to achieve.

The elementary SMES based modulator uses only one energy storage and a fast acting power switch. The basic circuit is shown in Fig. 8.23.
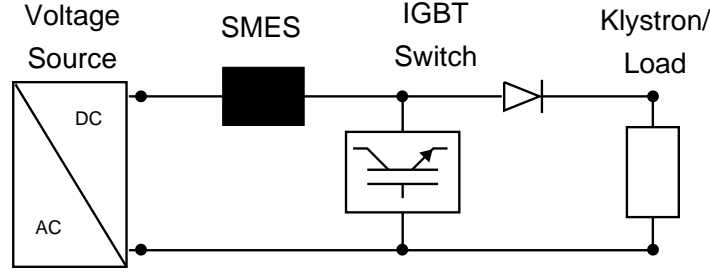
Figure 8.23: Basic Circuit Diagram

The operation of this system can be divided into two modes. During the conduction time of the IGBT switch the voltage source charges the SMES. The SMES current increases to the required value. Then the switch will be opened and the current has to commutate into the klystrons. Across the load the voltage $V_p(t)$ will be generated.

$$V_p(t) = V_{source} + R_{KL}I_{SM}(0)e^{-\frac{R}{L}t}$$

The shape of a pulse depends only on the turn on/off times of the switch and the ratio of L_{SMES} to $R_{KLYSTRON}$. The decay of V_p during a pulse will

depend only on the time constant L/R of the circuit, if we neglect the supply voltage. Since the width of a pulse and the repetition rate are only depending on the switch operation this device can generate varying pulse sequences. A model of a TTF modulator based on this concept is being developed[18]. It was designed to generate 2 ms long 3 kV / 300 A pulses with a repetition rate of 10 Hz. First successful tests have demonstrated the proof of principle.

A device for providing two klystrons should meet the following requirements for the case that the primary voltage of the pulse transformer were 10 kV and the primary current were 1100 A for each klystron. The maximum voltage drop during a pulse should not exceed about 2%.

$$
\begin{aligned}
R_{LOAD} &= 10kV/2.2kA = 4.54\Omega \\
I_{SMES} &= 2.2kA \\
L_{SMES} &= 0.45H \quad \text{(for 2\% voltage drop)} \\
V_{SOURCE} &= 200V \\
E_{SMES} &= 1MJ \quad \text{(for 2\% voltage drop)}
\end{aligned}
$$

The semiconductor switch will be built of IGBT's because of the high switching speed and easy control of this device. To reach the 2.2 kA SMES current that is required for TTF a parallel connection of three IGBT's (1.2 kA types) or the use of a 3 kA type is possible. Parallel operation of IGBT's is not problematic if there will be a sufficient thermal coupling between the elements. The results of our model device show an equal current sharing between paralleled IGBT's.

Our model switch that is build of parallel and serial connected IGBT's shows that a serial operation of groups of IGBT's is not problematic. For a blocking voltage of 10 kV a series connection of ten 1600 V devices seems to be reasonable.

At present other concepts for SMES based power modulators that allow an evident reduction of the stored energy in the SMES are being verified. A decrease of the SMES size by a factor of about eight seems possible.

---

[18]H. Salbert, K. P. Jüngst, *Generation of High Power Pulses Using a SMES*, Twenty First International Power Modulator Symposium, June 1994, Costa Mesa, CA, USA

8.6   The Long Pulse Modulator Design

This section is a description of the TESLA 5 MW modulator built at Fermilab[19] for use at a test stand at DESY. We examined several different modulator techniques and chose a new design suited to a long (2 ms) output pulse. The requirements for the modulator are:

Pulse Width (99 % to 99 %)	Output Voltage	Output Current	Repetition Rate	Operating Lifetime
2 ms	130 kV	95 A	10 pps	> 10 years

8.6.1   Design Approach

Our initial approach to the modulator design was a PFN type unit with a step-up transformer, although we realized the 2 ms. pulse length was rather long for this technique, a 24 section, 8.3 Ω PFN was designed to meet the specifications. Iron core inductors were used because of the long pulse length and the need to reduce physical size. The PFN that we designed was 2 m x 4 m x 2 m high and had a component cost of approximately 225 k$. The total modulator component cost estimate was 535 k$.

A modulating anode supply was then investigated. The estimated cost of this system is less than the PFN approach. However , no switch tube was available that would meet performance requirements. Additionally, the efficiency of a modulated anode approach is significantly lower than a PFN approach.

We next looked into a switched-capacitor design. Our main concern about this approach was the large amount of stored energy (1 MJ) that would be required.

The classic text by Lebacqz and Glasoe shows how the output of hard tube modulator may be flattened by the use of a parallel L R circuit in series with the load[20]. This circuit has power loss; however the reduction in stored energy is impressive. The stored energy is reduced by adding low loss passive components to the modulator. A switched capacitor bank is used.

---

[19]Fermilab is operated by Universities Research Association under contract with the U.S. Department of Energy.

[20]Glasoe, G. N., Lebacqz, J.V., *Pulse Generators*, pp. 165 - 172, McGraw Hill, 1948, First Edition

However, it is allowed to discharge approximately 20 % during the pulse. This large droop is then compensated for by the use of a low impedance resonant LC ("bouncer") circuit. This greatly reduces the loss over the L R circuit but retains the benefit of lower stored energy. The estimated cost of this "bouncer" circuit was 20 k$, and its size was approximately 2m by 1m by 2m. The component cost estimate for this modulator was under 400 k$, and we decided to pursue this design.

8.6.2   Principles of Operation

The modulator topology is shown in Fig. 8.24. The main capacitor bank, C1, is charged to approximately 10 % higher than required output voltage, while the bouncer, L3 & C2, is charged to 10 % of the required output voltage. To produce an output pulse, the bouncer resonant circuit switch, S4, is closed, and the capacitor starts to ring with the inductor. At the appropriate time, the GTO switch, S1, connecting the main capacitor bank to the pulse transformer is closed. After the 2 ms output pulse length, the GTO switch is opened. The bouncer circuit continues to ring through its full cycle. Figure 8.25 shows the bouncer voltage and main capacitor bank voltage. The bouncer waveform is subtracted from the main cap bank waveform, and Fig. 8.26 shows the resultant output voltage in full size and expanded versions. The specifications are clearly met.
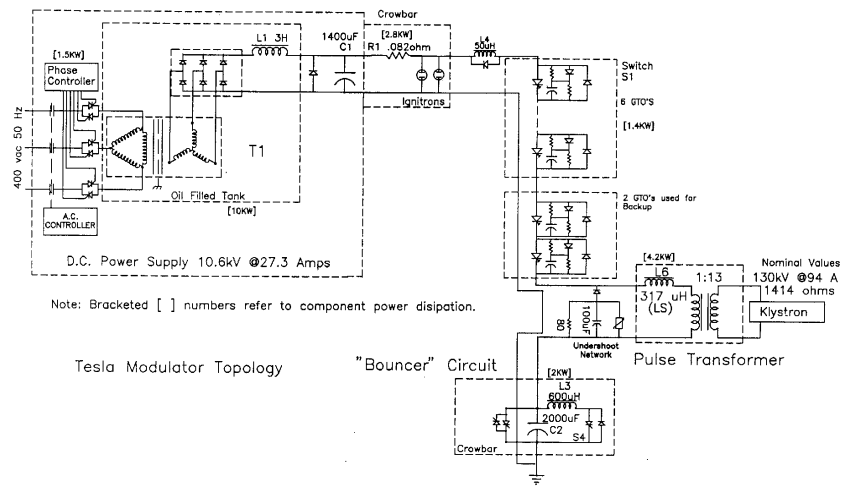
Figure 8.24: Tesla Modulator Topology
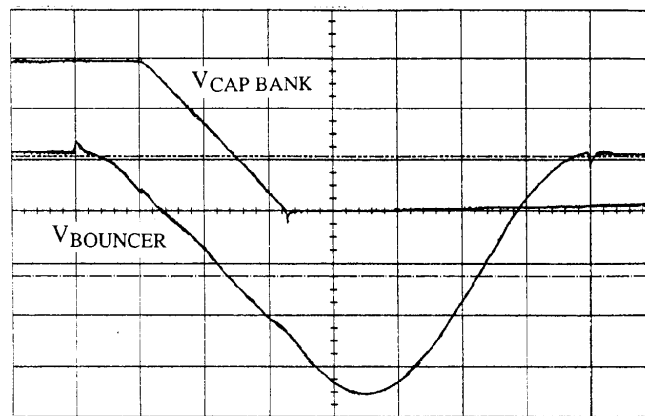
Figure 8.25:   Main Capacitor Bank Voltage (Top) and Bouncer Voltage (500V/div, 1 ms/div, Main Capacitor Bank Zero Suppressed)
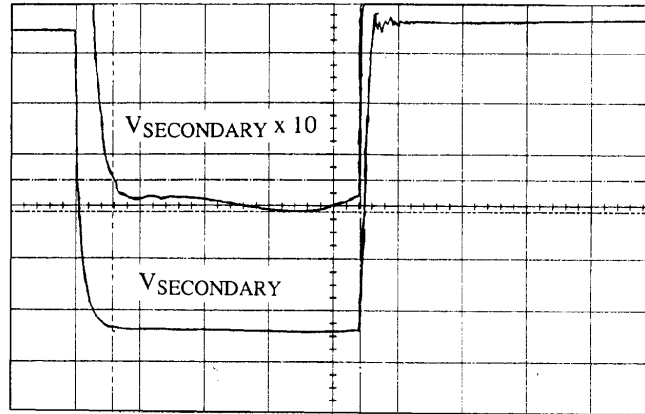
Figure 8.26: Expanded Secondary Voltage (Top) and Secondary Voltage (2 kV/div, 20 kV/div, 0.5 ms/div,Expanded Zero Suppressed)

8.6.3 Key Modulator Components

Several components are unique to this modulator. A reliable and robust closing and opening switch is required, so a series stack of six GTOs (Gate Turn Off thyristors) is used. The bouncer circuit must be designed for a minimum load impedance with low loss. The main capacitor bank must be designed for crowbar operation and capacitor fault conditions. The bus bar must have low inductance between all major components and must be designed to tolerate the crow bar current between the main capacitor bank and the crowbar switch. The pulse transformer must have a very large volt second rating with a relatively low leakage inductance. Mechanical vibration from the system must be kept to a minimum because the RF superconducting cavities are nearby.

8.6.4 The GTO Switch

The switch element in the transformer primary circuit must be rated to operate at 12 kV and switch 1200 Amps both on and off. We seriously considered the use of a series SCR switch with a forced commutation circuit to turn it off. The design effort releaved that the forced commutation circuitry

was costly, dissipative and complex. A series GTO switch seemed like a natural choice for this application. We were hesitant to proceed due to the scarcity of documented series GTO applications. We decided to use the GTOs after studying their manuals and talking to the designer of a successful commercial application[21].

The switch is a series string of six devices as shown in Fig. 8.27. Two more series GTOs are controlled independently and constitute a backup switch that operates in conjunction with the capacitor bank crowbar if the main switch fails to open properly. The GTOs we have used are GEC type DG758BX45. The key ratings are a maximum controllable current of 3.0 kA, maximum repetitive off state voltage of 4.5 kV and maximum turn off storage time 25.0 μs.
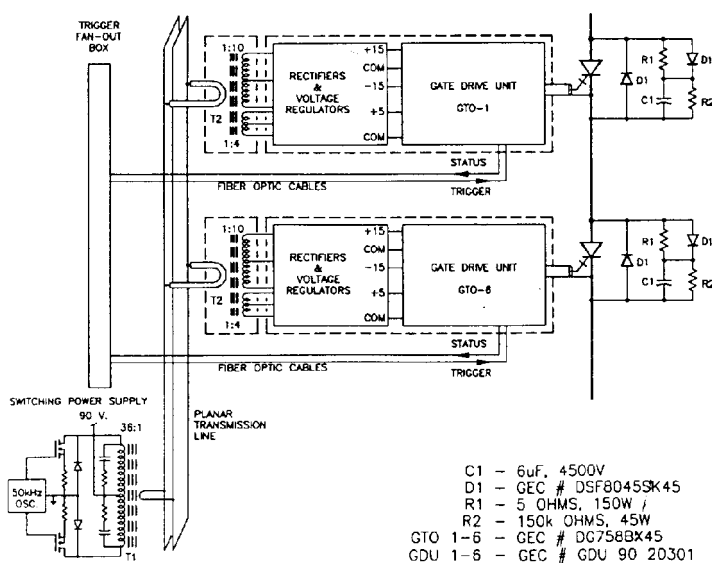
Figure 8.27: GTO Switch Schematic

The snubber circuits are those recommended by the vendor. The gate drive units are purchased from GEC/Plessey. They are controlled by fiber optic cables, but require isolated power.

We designed a high current, low voltage 50 kHz switcher supply capable

---

[21]Espelage, Paul M., *Symmetrical GTO Current Source Inverter*, IAS 1988, Vol. 1 pp. 302 - 306, 1988 IEEE Industry Applications Annual Meeting.

of delivering 10 W of isolated power to each of the eight gate drive units. Power from the switcher supply is distributed using a planar transmission line connected to the secondary terminals of a ferrite (MN100) stepdown transformer (T1, Fig. 8.27). Eight one turn loops of the center conductor of RG17 cable are connected in parallel across the planar transmission line. These are the primary windings of stepup transformers (T2) located at each gate drive unit. The RG17 cable provides the voltage isolation between the switcher supply and the GTO gate-drive units. At the step-up transformers, power is converted to $\pm$ 15 V and + 5 V and used by the gate drive units. The stepup transformers are driven in parallel rather than in series. The series configuration suffers from unequal drive voltage sharing due to variations in loading of the individual gate drive units. The unequal sharing is exacerbated by the use of voltage regulators in the secondary circuits.

Although the nominal primary current is 1200 A, a klystron gun spark causes the current to rise to 1800 A. The extra current is generated because of the 20 μs storage time (Tgs) of high current GTOs. When a gun spark is detected, the switch is immediately gated off. During the storage time the switch current rises at a rate of 27 A/μs, as limited by the pulse transformer leakage inductance (320H) and the inductance of a 50 μH coil in the primary circuit. We chose 3 kA GTOs in order to have sufficient margin to be able to reliably turn off at 1800 A. Figure 8.28 shows the primary current rising to 1800 A before turning off in an actual gun spark.

The switch turn-off transients have been controlled in two ways. First, the turn-off voltage sharing has been balanced through the matching of device storage times to within 2.5 μs. Second, the turn-off voltage overshoot has been limited by the use of planar transmission line buswork to limit stray primary circuit inductance to less than 2 μH. In addition, the snubber network inductance has been limited to 140 nH.

In order to protect the switch from catastrophic failure, we added control circuits to monitor and react to such situations as lack of cooling water flow, excess heat sink temperature, malfunctioning gate drive units, or the failure of a single GTO.

8.6.5 Bouncer Circuit

The bouncer circuit is a resonant LC circuit that is placed in series with the pulse transformer primary. The bouncer is triggered to ring through its single
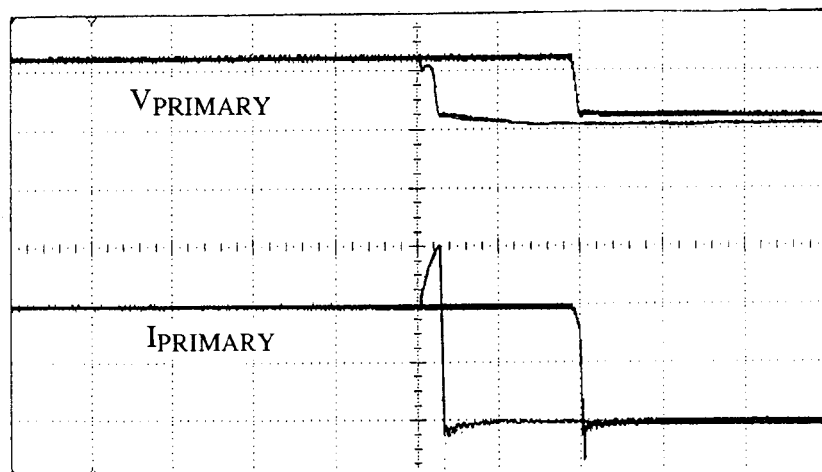
Figure 8.28:   Primary Voltage (Top) and Current During a Gun Spark (
               10 kV/div, 600 A/div, 100 μs/div)

cycle sine wave just before the main pulse is started. As shown in Fig. 8.29,
the bouncer is in the linear part of its waveform as the output pulse goes
through the bouncer circuit. The linear voltage is subtracted from the main
capacitor bank voltage, and compensates for the capacitor bank 20 % droop.
The resultant output pulse is flat to within 1 %.

Two ideas have been key for us in understanding the operation of the
bouncer. The first concerns the bouncer impedance. If the bouncer were
designed at an infinitesimally low impedance level, the presence of the pulse
current going through it would make a negligible distortion of its sine wave,
and the subtraction of the capacitor droop would be straightforward. Un-
fortunately, such a circuit would be infinitely large and expensive. On the
other hand, the sine wave of a high impedance version would be drastically
distorted if the pulse current were much larger than the bouncer resonant
current. We started with a design in which the peak bouncer current was
twice the pulse current. Our SPICE model showed that although the bouncer
waveform was somewhat flattened during the current pulse, the droop com-
pensation still worked at the 1voltage was raised to adjust for the flattening
effect. If we doubled the impedance of the bouncer components, the model

no longer worked at the 1 % level. We therefore used our initial impedance choice.

The second key idea concerns the power flow into the bouncer circuit. Figure 8.29 shows that the bouncer capacitor voltage has equal positive and negative parts during the current pulse. During the first half of the pulse, the pulse current adds energy to the capacitor, and during the second half of the pulse it subtracts an equal amount. The only losses in the bouncer circuit are due to the dissipation factors of the bouncer components. The components were specified to dissipate less than 2 kW at full power operation.
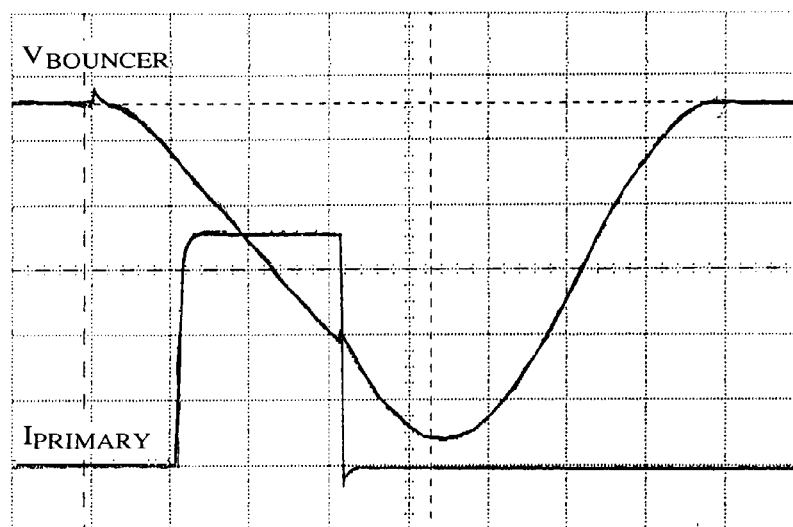
Figure 8.29:   Bouncer Voltage (Top) and Modulator Primary Current (500 V/div, 300 A/div, 1 ms/div)

It is interesting to note that if the pulse is shifted earlier in the bouncer waveform, a net positive energy is deposited in the bouncer capacitor. We make use of this feature by adjusting the relative timing of the bouncer and output pulse so that the bouncer is charged to the desired level. No bouncer capacitor charging supply is required! A closer look at Fig. 8.29 reveals that the bouncer voltage zero crossing is slightly later than the midpoint of the current pulse since we were using this feature at that time.

We were surprised to find how stable this charging system turned out to be. For any timing relationship the bouncer voltage is stable. If the

pulse timing is set too late, the bouncer capacitor charges to a lower stable operating voltage, and the output pulse has a negative slope. If the pulse timing is set too early, the bouncer capacitor charges to a higher stable operating voltage, and the output pulse has a positive slope. It is stable because as the bouncer charges to a higher voltage, the output pulse voltage and current are reduced. The linear portion of the sine wave therefore has a larger slope (less flattening), and the average bouncer capacitor voltage during the pulse is made more negative. The net power delivered to the bouncer capacitor is thus decreased until a stable balance point is reached.

8.6.6   Main Capacitor Bank and Crowbar

The main capacitor bank has the standard concerns of a large stored energy application, and the additional concerns related to its high-speed crowbar. The crowbar circuit must remove the GTO switch input voltage within microseconds in order to protect the klystron from a switch failure. The crowbar resistive dump is in the main circuit path of the GTO switch. This enables the crowbar to remove the GTO switch input voltage in 4 s while the capacitor bank is undergoing a 100 μs discharge. However, the resistance must be minimized to avoid excessive dissipation during normal operation. This minimal resistance causes large crowbar currents but has been chosen to critically damp the crowbar circuit.

The capacitor bank was divided into eight sections of 175 μF at 10 kJ each. Each section is connected to the main bus with a 0.1 Ω resistor to absorb the energy during a capacitor fault. Since a crowbar is a recoverable event and crowbar current and capacitor fault current are comparable, commercially available fuses could not be used. The crowbar of the main capacitor bank is a back-up protection measure for the klystron, so we have made it redundant. The crowbar consists of two independent NL8900 Hg ignitron switches, each capable of the full discharge current (70 kA). Each ignitron is fired by an independent trigger circuit from independent fault detection logic. The buswork between the main capacitor bank and the crowbar was designed as planar transmission line to minimize the inductance in the GTO circuit. This bus must also handle the forces during a crowbar, and be corona free at the 12 kV operating level. Lexan ©(polycarbonate) was selected, because of its mechanical and electrical properties, both to insulate the bus conductors and to clamp them together. Extensive AC and DC

hipotting of the buswork was done to insure a low partial discharge. Lexan's ©corona threshold level was higher than either glass reinforced epoxy or fiber reinforced paper.

8.6.7   Pulse Transformer

The pulse transformer was also a challenging component . The primary leakage inductance was required to be less than 500 μH, and the primary magnetization was to be less than 12 A with at least 25 Vs before saturation. The transformer as delivered is large, approximately 1 m by 2 m by 1 m, with 320 μH of leakage inductance and 7 A magnetizing current at 27 Vs. The output voltage divider met specifications, however it had to be rebuilt to avoid excessive pickup during gun spark transients. There is very little acoustic noise from the transformer; the stiff core clamps and vibration isolation mounting of the core worked very effectively.

8.6.8   Klystron Protection

Klystron and modulator availability is a critical element of reliable linac operation. Protection of the klystron during gun sparks is an important element of the modulator design. The use of a pulse transformer makes possible an all solid state, and therefore more reliable and lower maintenance, modulator. However this same pulse transformer complicates the problem of protecting the klystron during a gun spark.

The klystron manufacturer has put a limit of 20 J on the amount of energy deposited into the klystron during a gun spark. During a normal pulse, 270 J is stored in the transformer leakage inductance. This energy must be removed from the transformer before it can be deposited into the sparking klystron. Crowbarring the primary circuit is not sufficient to remove this energy; the GTO switch must be opened so that the primary voltage can be inverted to at least 400 volts to rapidly reduce the leakage current.

The voltage inversion is controlled by an undershoot network installed across the transformer primary. The network is a parallel combination of a resistor, a capacitor, and a ZOV transient suppressor. The resistor absorbs the transformer magnetizing current and resets the core during normal operation. The capacitor absorbs the leakage inductance current during normal pulse turn-off, and limits the undershoot to 700 V. The ZOV clamps the

undershoot to 1600 V following a gun spark. The capacitor would otherwise overcharge since the klystron does not share in absorbing the leakage inductance energy following a gun spark.

For the undershoot network to work at all, the GTO switch must first be opened. There is an alternate mechanism for opening the primary circuit if the GTO switch fails. If the primary current reaches a threshold indicating that the GTO has not turned off, the backup system is used. The backup system crowbars the main capacitor bank and opens a pair of single GTOs in series with the main switch. Redundant control systems are used to monitor the current and control the crowbar and GTO switches to insure reliability.

Figure 8.30 shows the secondary current and voltage during an actual gun spark. Gun spark energy for this event is less than 4 J. The spark protection circuitry has functioned well through 40 gun sparks to date.
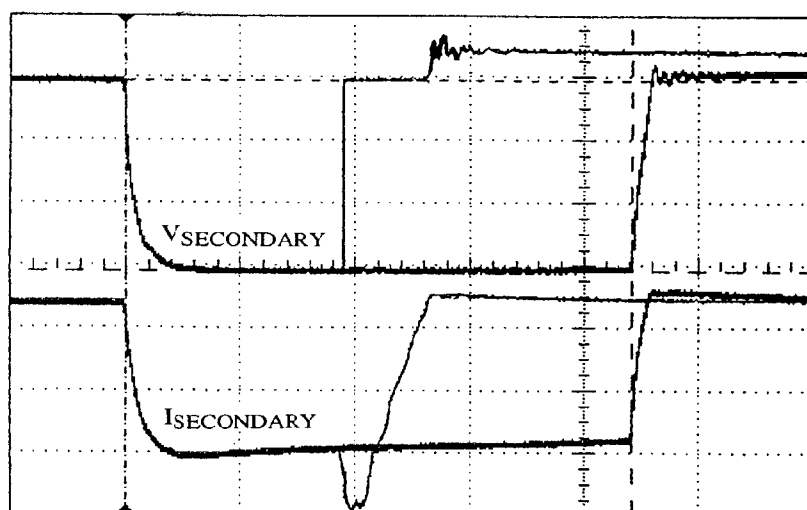
Figure 8.30:   Secondary Voltage (Top) and Current During a Gun Spark
(40 kV/div, 40 A/div, 0.5 ms/div)

8.6.9   Modulator Controls

The controls system used for this modulator is an in-house design rather than commercial equipment. Most of the electronics modules are copies or

modifications of equipment designed for the recent Fermi LINAC upgrade. The controls consist of three functional blocks:

1. Signal transmission modules consisting of current drivers and receivers for transmission of analog signals from the high power section to the controls section, and fiber optic modules for the transmission of digital control signals to the high power section.

2. Analog circuit modules to generate the required signals for modulator operation and to compare the signals to references and generate error signals.

3. Digital modules which latch error signals and perform system control and timing correlation of the modulator switches.

There are two independent systems that monitor gun sparks. The first system monitors secondary voltage and current and responds to the rapid collapse of the gun voltage. The second system monitors the primary current with two independent current transformers. This system detects both gun sparks and failure of the system to respond to gun sparks. If the normal protection malfunctions, it initiates the backup protection system. In addition, all control circuits related to gun sparks have parallel redundancy.

8.6.10 Operational Results

The primary result is that the modulator works well and meets specifications. Operation at required voltage, pulse width and duty cycle were achieved. In addition, the complete modulator and klystron system has been installed at DESY in Hamburg Germany after commissioning at Fermilab. Recommissioning at DESY took only five weeks from unpacking to full RF power. A number of interesting problems occurred during the initial commissioning phase at Fermilab.

Various changes to the pulse transformer auxiliary circuits were made as a result of studies of spark related transients. These studies were done by using a triggered spark gap across a dummy load on the transformer secondary. The capacitor divider circuit needed modification to handle secondary transients, and high frequency bypass capacitors were added to suppress voltage transients on the transformer primary.

There was one GTO device failure during the commissioning phase. This occurred when the capacitor bank was crowbarred just as the GTO switch opened. The controls system also suffered a transient that caused erroneous status and the failure of a logic chip. We dont fully understand what happened, but we changed a crowbar threshold to prevent a recurrence and more carefully shielded some of the status monitoring cables in the modulator cabinet. No similar failure has happened since.

We have experienced some problems with the pulse transformer. On three occasions the waveforms associated with gun sparks looked strange, indicative of a turntoturn transformer short initiating after the gun spark. Upon turning the modulator back on after these events we experienced low voltage turn-to-turn transformer shorts which cleared up after two pulses. Inspection of the transformer was inconclusive and we decided to run at 115 kV rather than 122 kV in order to minimize gun sparks. The subsequent three gun sparks that we experienced at this new level showed no signs of turn-to-turn shorting. Since the klystron generates sufficient power for test stand operation at the 115 kV level, our operational approach for now is to run at this level and investigate transformer replacements.

The ability to vary the pulse length easily has been very useful, especially in conditioning the klystron. The klystron came to Fermilab conditioned with a 500s pulse. We lengthened the pulse over several days completing the conditioning process.

8.6.11   Power Efficiency

The power efficiency of this modulator is an important criterion. We measured the efficiency while running at 122 kV with a 2.2 ms pulse length and 10 pps. The 480 VAC power was 274 kW as measured by a Yokagawa power meter. The usable pulse power as defined by the output voltage between +1.0 % and -5 % of the nominal, was 236 kW, and the efficiency is 86 %. Our calculated efficiency is 89 % and Fig. 8.24 shows the calculated dissipation in various modulator components. For future systems, tradeoffs between component cost and power efficiencies can be explored.

8.6.12 TESLA Modulator Controls Hardware

The control system for the TESLA modulator is a general purpose data acquisition system based on the Motorola MVME- 162, a single board VMEbus computer. In this system, four MVME-162 are included; one in a VMEbus crate, one in a VXI crate, and two mounted in Internet Rack Monitors (IRM). An IRM is an intelligent data acquisition system that combines the processor, network connection and the analog and digital I/O, all within the same chassis. As its name suggests, this device is a node on the world-wide Internet. A local database within each IRM allows it to function as a stand-alone control system for equipment it controls.

8.6.12.1 Overview of the Internet Rack Monitor

The overall arrangement of I/O of the IRM is patterned after the Fermilab DZero Rack Monitor and the Smart Rack Monitor (SRM) used in the Fermilab Linac Upgrade. Characteristics of the Internet Rack Monitor are:

- Runs Local Station Software

- Operates as an Internet node

- Ethernet LAN Interface

- 64 Channel Multiplexed 16-bit A-D

- 8 Bytes of digital I/O

- 8 Channel 12-bit D-A

- I/O expansion via IndustryPack Modules

Earlier version rack monitors functioned as I/O chassis connected to a VMEbus crate. The IRM differs architecturally in that no external VMEbus crate is required unless special VMEbus-based I/O cards are needed in a particular application. In that case, the MVME-162 card is installed in the VMEbus crate rather than the IRM 2U chassis. The software is identical for the two cases.

8.6.12.2   The MVME-162 Single Board Computer

A Motorola MVME162 single board computer includes the usual serial ports
and memory along with an Ethernet adapter and four IndustryPack daugh-
terboard sockets for I/O interface. The MVME162 can be configured as a
VMEbus cpu or as an embedded controller. Both configurations execute the
Fermilab Local Station software that performs data acquisition, control loops,
alarm scanning, and TCP/IP communication on Internet. The MVME-162
computer includes the following onboard resources:

- Motorola 25 Mhz MC68040 Processor

- Ethernet Network Interface

- Optional SCSI interface

- 4 MBytes of dynamic RAM

- 512 KBytes Static RAM with Battery Backup

- 1 MByte of Flash Non-volatile memory

- 8 KByte NVRAM with time-of-day clock

- 1 PROM Socket

- 6 32-bit programmable 1 MHz timers

- 2 Watchdog timers

- 4 IndustryPack I/O sockets

IndustryPack sockets can contain custom designed modules, such as TClk
processors, or any of several dozen commercially available modules.

8.6.12.3   Analog I/O

Four connectors on the rear panel of the IRM are used to connect the analog
inputs to eight 8-channel differential input multiplexers. Outputs from these
multiplexers are combined by a ninth multiplexer that drives an instrumen-
tation amplifier fol-lowed by the digitizer. The AD converter is an Analog
Devices 676 16-bit, 10 s digitizer that uses a successive approximation charge
redistribution digitizing technique and includes an onboard microcontroller
to recalibrate the device at power-on time or by external command. An input
signal sample-and-hold function is inherent in the design of these converters.

A custom IndustryPack (IP) module connects the MVME-162 to the
analog I/O board. The main component of this analog control card is the
Actel 1240 field programmable gate array that provides the following features:

- Operates offboard A-D and D-A interface modules

- Repetitive 64 channel scan mode

- 1000 Hz or External scan rate

- Stores A-D results sequentially in RAM

- Arbitrates IP and A-D access to 64kB RAM

An octal D-A chip is included on the analog interface board. The eight
analog output signals are available via two 9-pin D connectors located on the
rear panel of the IRM.

8.6.12.4   Digital I/O

An interface board containing eight bytes of TTL-compatible digital signals
provides the digital I/O for the IRM. Each byte can be selected as input or
output. Four D connectors, each with two bytes of digital signals, are located
on the rear panel of the IRM chassis.

The digital I/O interface board is controlled by an IndustryPack mounted
on the MVME-162 computer board. This IP module is similar to the analog
IP controller but includes a 64-byte FIFO and a different Actel chip providing
the following capabilities:

- Controls 8 bytes of offboard I-O

- TClk interface

- Delay timer for P start time

- Supports 1 byte of sense switch input

- Provides 1 byte of LED indicators

- Interface for clock event recording in FIFO memory

8.6.12.5   Network Interface

An Ethernet adapter is included on the MVME-162 cpu card. Ethernet sig-
nals from the VMEbus P2 connector are cabled to a standard 15-pin D con-
nector compatible with the Ethernet transceiver specification. To interface
with Thin Ethernet, a small commercially available transceiver-to- thin-net
module is installed internal to the chassis. The Ethernet interface is then a
single BNC connector.

8.6.12.6   I/O Daughterboard

Because only two of the four available IndustryPack sockets are required to
interface the analog and digital I/O boards, other IPs can be added to the
system. A variety of commercially available IndustryPacks can be used as
well as custom designed modules. Space is provided on the back panel for
additional interface connectors. Accelerator clock processors that generate
delay triggers from events decoded from the accelerator clock can be installed
in spare IP sockets.

8.6.12.7   Packaging

The IRM is packaged in a self-powered 2U (3.5 in.) rack mount chassis and all
I/O is attached using socket type "D" connectors mounted to the rear panel.
The MVME162 module is housed in a two-slot VMEbus crate. Within the
constraints of the power supply, an additional VMEbus card can be added
in the 2U chassis.

8.6.12.8 VMEbus and VXI Support

The low Level RF system is implemented using a VXI crate, a Motorola MVME133 single board computer and a selection of commercial and custom VXI modules. Control system support for the LLRF system is by way of an MVME162 cpu board running the same software used in the IRM. Readings and settings in the LLRF system are available via shared memory on the backplane of the VXI crate.

The timing system and Quick digitizers for snapshot recording of modulator waveforms are located in a VMEbus crate. Again, the processor in this crate is an MVME162 executing the same software as the IRMs and the VXI crate processors.

8.6.12.9 Software

After several years of development, the Fermilab Local Station software provides much of the capability needed by several types of accelerators. Each Local Station is a stand-alone control system containing a local database for the equipment it controls. Remote hosts can request repetitive readings of and make settings to hardware devices over the network. Each analog channel and each bit of digital I/O can be monitored for alarm conditions. Alarm messages are sent to host computers over the network. Because the local station contains descriptors and calibrations for the data channels, data can be requested by channel name, and alarm messages describe out of tolerance conditions using the names of the data channels. New features can be added by installing separately compiled local application programs in selected stations. The local database, hardware settings and configuration tables describing what data to acquire are all kept in non-volatile memory so that each rack monitor can power up fully operational without needing to be downloaded from a host. At reset time, the system software is normally downloaded over the network from a server using TFTP protocol.

8.6.13 IRM Software Overview

Internet Rack Monitor software is an evolution of that used in several front end control systems at Fermilab and elsewhere. This latest version runs on the MVME162-22 cpu board with MC68040 cpu, 4MB dynamic ram, 0.5MB

static ram, 1MB flash memory, ethernet interface, and support for up to four
IndustryPack daughter boards. The latter allows connection to I/O signals
via ribbon cables to digital and analog interface boards mounted inside the
IRM chassis. The ethernet interface allows network connection and supports
widely-used Internet protocols that allow data request and setting access as
well as alarm reporting, all based upon the UDP (User Datagram Protocol)
transport layer.

8.6.13.1   Local database

The nonvolatile memory houses a number of configuration tables that char-
acterize each stations installation. Included in these tables is a local database
for analog channels and digital bits. It includes text and scale factors used
by local control applications for scaling as well as alarms reporting. It also
houses down- loaded code for local and page applications in a memory-
resident file system. Local applications are used for closed loop support
and for system extensions such as TFTP protocol server support. Page ap-
plications support a virtual console access to the system for local control,
configuration and diagnostics use. The system code is acquired from a server
station by the prom-based 162 bug via the TFTP protocol at boot time.

8.6.13.2   Cyclic data pool activities

IRM software is a collection of tasks that use the pSOS operating system
kernel. The primary activities of the system are synchronized by an external
timing signal, which may be an external trigger input, or it may be decoded
from a Tevatron clock signal. (In the absence of a synchronizing signal at
10Hz or 15Hz, the system operates asynchronously at 12.5Hz.) At the be-
ginning of each cycle, the data pool is refreshed according to instructions in
the nonvolatile Data Access Table that are interpreted at the start of each
cycle. Also, all active local applications are run to operate on the fresh data
for closed loop jobs or more complex data pool updates. (A local application
is compiled and downloaded separately from the system code itself.) After
the data pool is refreshed, all active data requests having replies that are due
on the present cycle are fulfilled and delivered to network requesters. Alarm
scanning is performed on all analog channels and binary status bits that are
enabled for such monitoring. Finally, the currently active page application

is run. So, the data pool is accessed by local application activities, replies to data requests, alarm scanning, and the current page application.

8.6.13.3 Synchronization

The Tevatron clock signal can carry up to 256 events. The IndustryPack digital board decodes each event and interrupts the cpu, allowing time-stamping of each event. Status bits derived from this event activity are part of the data pool and can be used to synchronize data pool updating and local application activities. The time stamps can be applied to data points returned in response to data requests for up-to-1000 Hz data available from the IndustryPack analog board; i.e., one can plot 300 Hz data, say, with time stamps measured from a selected clock event.

8.6.13.4 Data request protocols

Due to the evolution of this front end system, three different data request protocols are supported. The original request protocol is called Classic; it is used by stations that communicate among themselves as well as by the Macintosh-based parameter page application developed by Bob Peters. A second protocol was designed by the Fermilab D0 detector people to fulfill their specific needs. The third is that used by the Acnet control system at Fermilab.

Data server logic is included for both Classic and Acnet request protocols. This allows one station (the server) to be targeted by a requesting host with a request for data from other stations, in which the server station forwards the request via multicasting to the other stations and compiles their individual responses into the single reply it delivers to the requesting host. The purpose of this logic is to reduce the number of replies a host might have to endure, in response to a request for data from many different stations. The server station can do this efficiently because of the built-in logic in each station that combines multiple repliesdue on the same cycle to the same destinationinto a single network datagram. For example, suppose three hosts make requests for data from the same 10 stations at 10 Hz, and each host uses the same server node. The server node will receive 10 composite replies each 10Hz cycle, and it will send 3 replies to the three hosts, for a total of 130 frames/second, thus requiring each host to receive only 10 frames/sec. Without the server

station, each host would have to receive 100 frames/sec.

8.6.13.5   Alarm handling

Alarm scanning is performed on all selected analog channels and digital bits each operating cycle, as mentioned above. When a change in alarm state (good-bad or bad-good) is detected, an alarm message is queued to the network to share this news with the outside world. Such alarm messages can be multicast, so that multiple interested hosts can learn of them. A local application can also sample such alarm messages and reformat them to target a designated host alarm server, as is required in the Acnet system. As a local diagnostic, such alarm messages can be encoded for display or printout via the stations serial port, including both locally-generated ones as well as those received by that station listening to the alarm multicast address.

8.6.13.6   Diagnostics

Several diagnostic features are included in the IRM design. The digital IndustryPack board provides test signals that are driven by interrupt and task activities. The interrupt signals are also displayed on 8 LEDs. These signals can be connected to a logic analyzer to capture timing and related program activities of the stations operation.

A suite of page applications is available to perform various diagnostic displays via the virtual console support.

1: Display areas of memory from any station(s), with 10 Hz updating. Clear blocks of memory, or copy them from one station to another.

2: Display Tevatron clock events with 10 Hz updating. Capture and display network frame activity, providing a kind of built-in poor mans sniffer, in which the timing of frame reception or transmission processing is shown to 1 ms resolution within the time-of-day-specified operating cycle.

3: A network client page allows exercising the standard IP ping and UDP echo tests, as well as Network Time Protocol and Domain Name Service queries.

4: A list of kernel-allocated blocks of dynamic memory in the local station can be displayed and updated continuously.

5: All three data request protocols can be exercised in a test mode to verify particular cases and measure response times.

6: A station survey page allows listing several characteristics of a list of stations, including system code version, amount of free dynamic memory, time since last reset, number of allocated channels and bits, number of active data requests, and operating cycle time.

7: A log of recent settings performed in a given station can be displayed in a similar fashion to that of recent network frame activity.

8.6.13.7 Software development

Program preparation is done on a Macintosh using the MPW (Macintosh Programmers Workshop) development system. The system code and application codes are both developed under MPW. The system code provides a core level of support that can be enhanced by the addition of local applications (LAs) to support the specific needs of a given installation. Such LAs may be written by a user in C or Pascal and, using the MPW tools, compiled and linked with the help of a small library of glue routines that invoke system code services. The resulting linker output is downloaded to any local station using the TFTP client also running as an MPW tool. The code received by the stations TFTP server is copied into the non-volatile memory resident file system. Using a page application for the purpose, a set of parameters are specified to be passed to the LA upon each invocation. These parameters are constant data that are often Channel#s or Bit#s, whose present readings determine the course of action of the LA. The first parameter is always an enable Bit# for the LA. When the enable bit is set, the system finds the code for the LA in the resident file system and copies it into allocated dynamic memory for subsequent execution. Every operating cycle, during Data Access Table processing, each enabled LA is called with the set of specified parameters. It can perform any short-term activity it needs to according to its context. The first time it is called, it allocates memory to maintain its own execution context. A pointer to this context memory is also passed to the LA each time it is called. An LA that is written to be a network server

can also be invoked upon reception of a network message intended for it. If the enable bit is turned off, thus disabling the LA, a final call is made to the LA to allow it to release any resources. An LA can be edited, compiled, linked and downloaded to a target station without requiring a reset of the station. In the case that such an LA is already enabled and active at the time of downloading, the switch to the new version is automatic. Minor program changes can thus be accomplished in seconds.

8.6.13.8   Data Acquisition and Display

There are three fundamental mechanisms for acquiring data from and controlling devices via the remote control system computers:

(1) a general-purpose Macintosh application;

(2) LabVIEW virtual instruments;

(3) special application provided by the user.

The Macintosh application (usually named paramPage) provides the user with a means of accessing and displaying various characteristics of the accelerator hardware devices known to the low level, distributed, VME systems. The display windows can be digital or graphical in nature and can span more than one local screen. Any device known to a VME system can be read and, if applicable, controlled through these displays once the user enters the device identifier (a device name, the node number of the controlling VME system and the device channel number, or the node number of the controlling VME system and the memory address) into the appropriate field of the display. Data are obtained via raw token ring or any interface accessible to the MacTCP Control Panel (UDP/IP).

The basic digital display consists of a window containing at most a single device on each line. The displayed characteristic (reading, setting, nominal, tolerance) can be viewed in engineering units (volts, amperes, etc.), raw analog-to-digital/digital-to-analog converter volts, or hexadecimal, on a line-by-line basis. This is the display format used to control a device. A sample window showing a few of the Fermilab preaccelerator parameters is shown in Fig 8.31. The leftmost field of the display contains the name of the device. The remaining fields show the descriptive text, alarm state, reading (or some

other characteristic), the units associated with the numerical field, and any digital control/status fields. Note that device HEXTV (the H- extraction voltage) is attached to a scrollbar which provides the functionality of a control knob. Once a page has been created it can be saved to disk for later use without additional input from the operator. Note, however, that the device occupying any line can be changed at will by simply typing different new device identifier into the name field and pressing the RETURN or ENTER key.

Figure 8.31:   Sample Parameter Page display of FNAL preaccelerator parameters. Devices may be adjusted by typing new values or using scroll bar

The graphical display consists of a window containing up to four (4) dependent variables on the vertical plotting axis and a single independent variable on the horizontal axis. The displayed characteristic (reading, setting) can be presented in engineering units (volts, amperes, etc.) or raw analog-to-digital/digital-to-analog converter volts on a device by device basis. Three different window variations are provided for graphical display depending upon the origin of the data to be plotted: standard scatter plots, raw data obtained from a known memory address (such as a "quick digitizer"
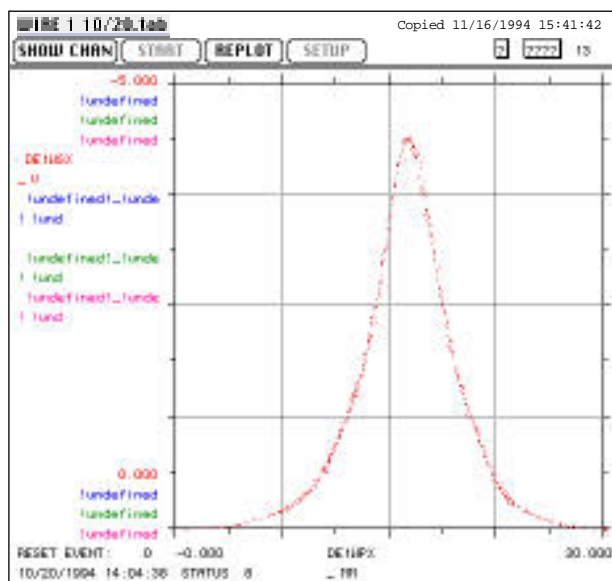
Figure 8.32:   Standard plot display. In this case, beam profile measured
with a wire scanner is displayed. Plots vs time with sample
rates up to 1kHz are displayed in this mode.

or am embedded transient recorder), or fast time plots (up to 1 kHz sample
rate). Fig. 8.32 illustrates a standard scatter plot of the Fermilab linac beam
profile (a motor-driven wire scanner). Fig. 8.33 on the other hand is from
four memory blocks (such as a "quick digitizer") which contain various wave
forms from klystron station number 3 of the Fermilab 400 MeV linear accel-
erator. In this particular case, each trace contains 3328 values 800 of which
are displayed in this figure. At the present time this type of plot is limited
to 10000 samples per channel but could within a few days be increased to
many times that value if the need arose.

Additional diagnostic displays allow the user to view and control the
screen image of any remote VME system (even in the absence of a physical
screen on that system), display and modify the memory contents of a VME
system, and transfer large blocks of memory from one system to another.

LabVIEW is an iconic programming "language" developed by National
Instruments which does not require much programming expertise and is avail-
able for Macintosh, Sun, and MSDOS computers. With it, the user designs a
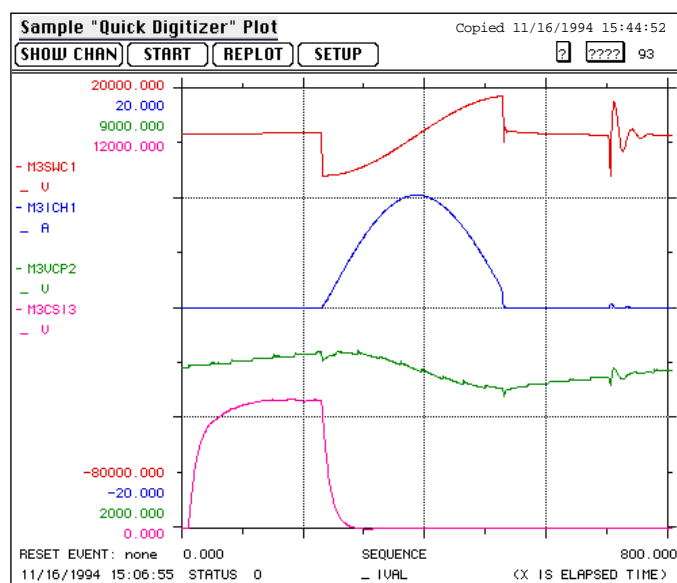
Figure 8.33:   "Quick Digitizer" plot of FNAL modulator. Sample rate is
1MHz and 800 μs are displayed for various modulator voltage
and current signals. From top to bottom: resonant charging
voltage and current, dc supply voltage, and pfn pulse.

virtual instrument by graphically connecting supplied components (meters,
graphs, analysis sub-units, I/O interfaces, etc.) until the desired function-
ality is obtained. If the desired functionality cannot be provided by the
standard LabVIEW product, special code modules (*Code Interface Nodes*
in LabVIEW terminology) can be created to provide the services required.
These modules can then be used in the same way as any of the standard
LabVIEW units.

Special needs which cannot be met by the Macintosh parameter page
application or LabVIEW can be fulfilled by creating a stand-alone program.
Within that program the user creates a short message listing the specific
devices of interest, the device characteristic(s) desired, and the desired rate
at which data are to be returned. The message is then sent (by invoking a
library routine) to the network interface application which handles the details
of communicating with the remote VME systems. As the responses arrive
from the remote VME system they are returned to the application that made

the original request.

8.6.14   Development Environment

The development environment presently used for the Macintosh application
(and the VME system code) is the Macintosh Programmer's Workshop from
Apple Computer. This system consists of a command-line window, numerous
tools, source code editor, code compilers (C++, C, Pascal, to name a few),
assemblers, libraries, and object code linkers which support code generation
for computers using Motorola MC680x0 processors as well as those which use
the Power PC RISC processor.

Chapter 9

High Energy Analysis Area

The TTF linac with its up to four modules, each containing 8 superconducting cavities, will be followed by a warm beam transport section as well as an experimental beam analysis area. Experiments carried out with beam have to show the stability of beam position, energy and emittance. With the high beam charge injector (see section 3.2) the same parameters have to be measured. In addition to this, the measurement of HOM losses, wake field effects, and the observation of cavity misalignment by mode excitation is planned. For some studies the beam will be injected off-axis and might exit the TTF linac with a larger emittance (longitudinal and vertical). This beam has to be analyzed as well and has also to be transportable to the beam dump.

The present chapter therefore deals with the warm beam transport sections. An overall layout is given for the temporary beam line installed prior to the cryomodules #2 − 4 as well as for the high energy analysis area. The following sections of this chapter describe the elements to be installed in the beam line. Detailed information about the diagnostic devices is also included. A final section lists the requirements for the shielding and contains considerations on the beam dump.

9.1 Beam Experiments and Experimental Details

A variety of experiments with beam will be performed at TTFL, first with the low bunch charge Injector I, then with the high bunch charge Injector II.

The HOM power dissipated at helium temperature is a key measurement. This requires careful calorimetric measurements and the full charge injector. Bunch wake fields can be estimated with bunch charges of at least 1 to 2 nC. Multibeam measurements require a few hundred bunches per pulse. The beam will be injected either on-axis or off-axis by as much as 10 mm in order to carry out some experiments. RF steering due to couplers will be observed. Measurements of accelerated dark current will be made and its attenuation compared with results of simulations.

9.1.1   RF to Beam Power Transfer

Bean energy stability bunch to bunch during a beam pulse, and pulse to pulse will be carefully studied in TTFL. The bunch to bunch chromatic effects in the TESLA linac are expected to be much less important than the single bunch ones. Lorentz force detuning and microphonics are the main sources of energy spread along the bunch train. The RF feedback system must be developed to provide constant acceleration during the 800 microsecond beam pulse. Monitoring of energy and energy spread during the pulse at 1 microsecond time intervals will be performed using a BPM and profile monitor in the analysis area. All this information can be collected with the low charge injector and the spectrometer of the end station. The energy vs time and the energy spread versus time should be measured for the full pulse length and at time intervals of 1 microsecond or less.

9.1.2   Beam Power Deposition at 2K

Through wakefield excitation, some energy will be left by the bunches passing through the cavities. It is extremely important to make sure most of this energy is not absorbed in the low temperature helium system.

The loss factor due to the longitudinal higher order modes has been calculated to be about 8.5 V/pC/cavity for a bunchlength of σ_z=1mm. For the TESLA bunch charge of 8 nC and the bunch rep rate of 8 kHz, the HOM power deposited by the beam is then 4.35 W per cavity. The low frequency part (up to 5 GHz) of this HOM power will be mainly extracted by the HOM couplers and has been estimated at about 30%. In order to limit the cryogenic load, the amount of HOM power deposited on the 2K parts must be as small as possible. Special HOM absorbers (at 70 K) are located at the end

Table 9.1:   Amount of HOM power deposited at various places. Most of the HOM coupler power is extracted to room temperature. For comparison the 2K static the load is estimated at 2.8 W/8 cavity-module, and the load from the fundamental RF mode at 25MV/m is 1.8W/cavity. This table differs from those in Chapter 5 which assumes 10% HOM power to 2K (not 7%). Under that assumption, HOM power is about 17% of the total estimated load at 25MV/m.

	percent	W/cavity
HOM-couplers	30	1.3
70K absorbers	63	2.75
2 K parts	7	0.3
Total	100	4.35

of each module installed inside the quadrupoles. Assuming 90% of the high frequency part is absorbed by these special HOM-absorbers, the percentage of deposited power in the different parts is given in Tab. 9.1.

Under these assumptions, the extra power deposited by the beam at 2K will be 2.4 Watts for one module of 8 cavities and for the full TESLA beam pulse. A resolution of a few tenths of watt in the cryogenic heat measurement will allow for the measurement of the beam power deposition with a hundred of bunches of the high charge injector.

9.1.3   Cavity Offset Measurement from HOM Power

The alignment tolerances on the quadrupoles (about one tenth of a millimeter) and cavities (about one half of a millimeter) in TESLA are not very tight in comparison with other room-temperature linear collider proposals, but the final component displacements in the real cryostat environment must be carefully checked in the TTF linac. It is planned to monitor the motion of the inner components during cool-down, operation and warm-up by means of optical targets. In addition, the individual cavity offsets of one module will be measured by detecting with a spectrum analyzer the dipole HOM power coming from the HOM couplers, excited by the beam which is assumed on-

axis of the module. With the high charge injector and due to the large bunch spacing, a harmonic of the beam spectrum is always close to a dipole mode frequency giving rise to resonant build-up of fields. Taking the TM_{110} mode (1875 MHz) of highest impedance and assuming the beam can be steered close enough to the centerline, cavity offset measurements with resolution lower than 10 micron will be possible. According to the performance of the available spectrum analyzer, the required number of bunches from the high charge injector could be lowered to a hundred or so. On the other hand, we checked that the power induced by the longitudinal modes, including the fundamental mode, will be harmless. Concerning the low charge injector, the beam current is the same but the bunch spacing is much smaller, giving practically no chance to have a harmonic in coincidence with a mode frequency.

9.1.4   Bunch Wake Potentials Measurement

The knowledge of short-range wakefields is of outstanding importance for the estimation of the emittance growth in the TESLA linac. These quantities are however not easily computable for such short bunches and will be carefully studied with the high charge injector.

The beam will be observed either after the first module, with its 8 cavities unpowered, or after the entire TTF linac operating at a low gradient (about 5 MV/m). The beam will be injected about 1 cm off- axis. In this way, the wakefields effects will be stronger with the low energy beam. For the observations at the end of one cryomodule more clear-cut measurements can be obtained if the focusing quadrupoles are not excited and measurements are made directly behind the module.

When the beam is observed at the exit of the entire linac, a 30 degree per module focusing scheme (weaker than the nominal 90 degree per module) is much more convenient as it does not cancel out the wakefield effects so much.

Fig. 9.1 shows a simulation of the correlated energy profile at the end of the first module for a 8 nC bunch of length 1 mm. The rms energy spread is 2.5% and the mean exit energy is 5% lower than the input energy. By varying the bunch charge, the longitudinal wakefield will be inferred from the measurement of the mean energy of the bunch. An energy spread of 0.5% rms would result from a charge of 1.6 nC.

Fig. 9.2 shows the correlated energy profile for acceleration through the
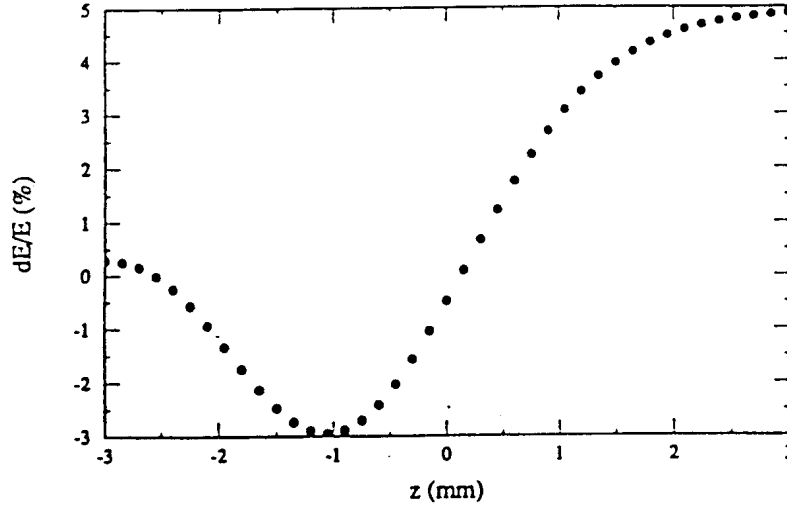
Figure 9.1:   Correlated energy profile at the 8 cavity module exit (8 nC bunch charge, idle cavities)

linac at 5 MV/m and a 8 nC bunch. The resultant rms energy spread is 0.7%.

Fig. 9.3 shows the head (dotted line) and the tail (solid line) of a N= 10^{10} bunch as it proceeds down the linac set at 5 MV/m gradient. The trajectory of the head is kept constant by means of steerers located at the quadrupoles. Owing to the weak focusing, the two trajectories clearly diverge and are almost 5 mm apart at the exit of the linac. The focusing effect of the standing wave cavities can be seen in the low energy end.

Fig. 9.4 shows the corresponding transverse profile of the bunch. A simulation after traversal of the first module with idle cavities is shown in Fig. 9.5. A head-tail displacement of 15 mm and a bunch centroid displacement of 5 mm is predicted for N=5×10^{10}. (For N= 10^{10} the corresponding numbers are 5 mm and 1.5 mm.)

The beam centroid can be measured by the BPM system. The energy and transverse profiles of the bunch might best be measured by a streak camera if it were fast enough. Total spot size and energy spread of a bunch can be measured by OTR or other beam profile devices in the straight ahead or
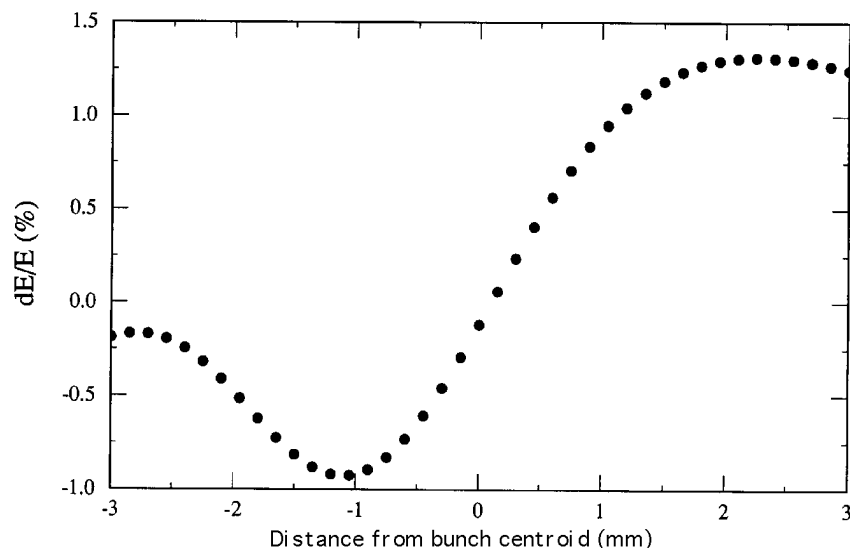
Figure 9.2:   Correlated energy profile at the exit of the linac (1.6 nC
bunch charge, 5 MV/m gradient)

spectrometer lines.

9.1.5   Transverse Multi-bunch Beam Breakup

The beam breakup phenomenon, caused by the long-range wakefields, is con-
trolled in the TESLA linac through mode damping combined with a large
bunch spacing on the one hand and the natural cavity-to-cavity mode de-
tuning on the other hand.   The multi-bunch effects in the TTF linac will
be however very weak, even with a beam travelling through all the cavities
operating at low field level. As in the shortrange wakefields measurements
however, the beam will be injected 1 cm off-axis into the first non-powered
8-cavity module and the position of the bunches will be observed at the
BPM located at the end of the module. The bottom curve of Fig. 9.6 shows
a weak bunch displacement, once the steady-state is achieved. Ten dipole
modes were used with the natural mode frequencies. An RMS frequency
spread of 1 MHz, and an RMS cavity offset of 0.5 mm were assumed in this
simulation. Each mode can be studied individually by tuning the cavities
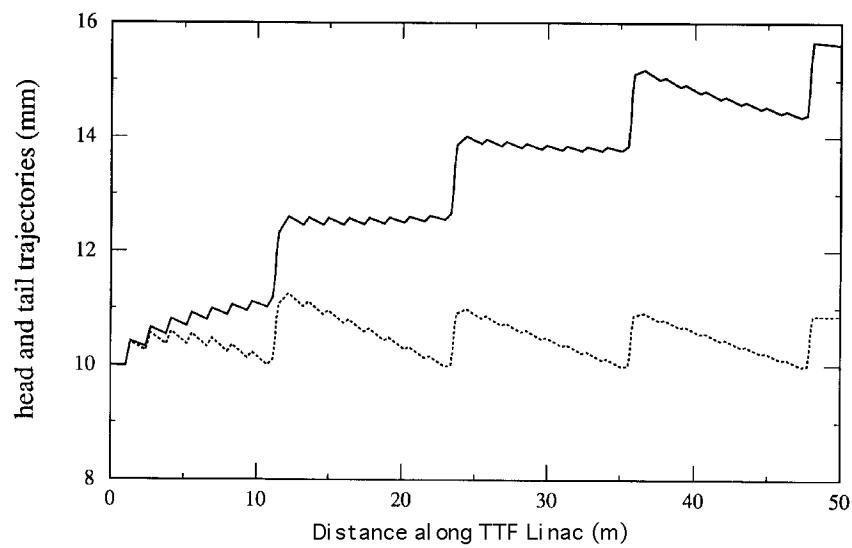
Figure 9.3:   Head and tail trajectories down the TTFL with 10 mm beam offset and weak focusing (1.6 nC bunch charge, 5 MV/m gradient)
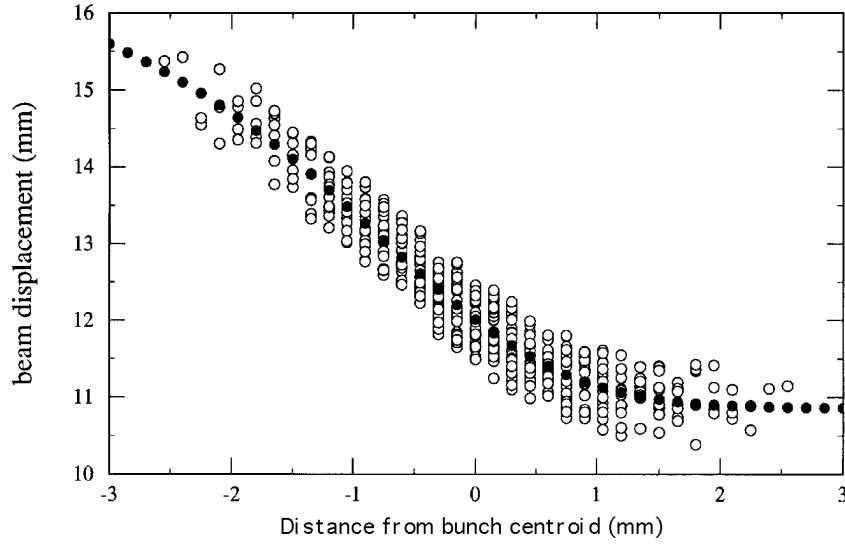
Figure 9.4:   Transverse profile at the end of the TTFL with 10 mm beam
                 offset (1.6 nC bunch charge, 5 MV/m gradient)
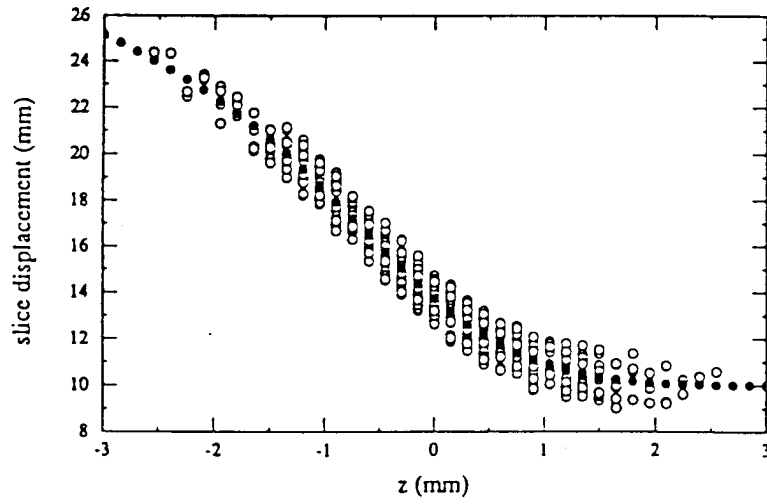
Figure 9.5:   Transverse profile with 10 mm offset at the 8-cavity module
                 exit (8 nC bunch charge, idle cavities)
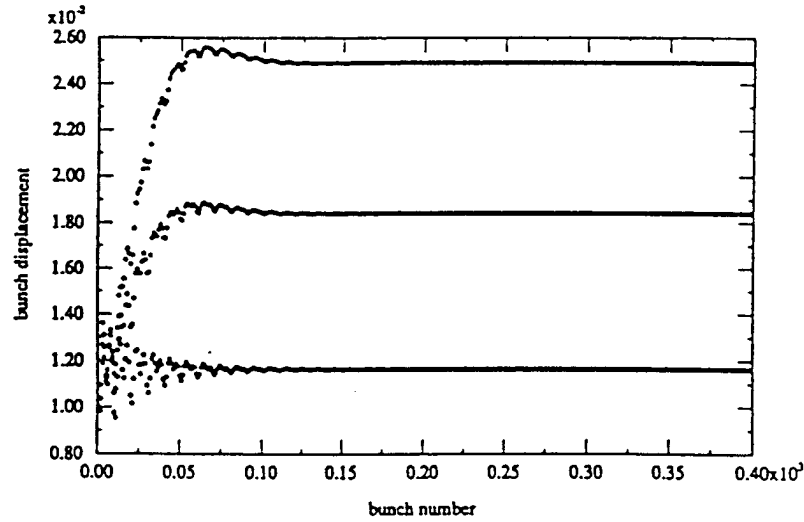
Figure 9.6: Bunch displacement with 10 mm offset at the 8-cavity module exit. Zero, one, or two cavities tuned to resonant condition (8 nC bunch charge, cavities unpowered)

to the resonant excitation The tuning system can be actuated because the cavities are not powered. The middle and the upper curves show the bunch displacements when the first and the first two cavities, respectively, are tuned to the resonant condition for a TM_{110} mode, giving final relative displacements of 8 and 15 mm for 8 nC bunches. Results at a bunch population of $N=10^{10}$ when two or four cavities are tuned to resonance are shown in Fig. ??. Displacements of 2.5 and 5 mm result.

Due to the rapid build up of the steady-state, a beam of about two hundred bunches per pulse with the high charge injector is sufficient for this experiment.

9.1.6   RF Steering

Radial asymmetries in the RF fields in the accelerating structures deflect the beam transversely. The static deflections of the beam centroid and the variations in the deflections due to field jitters from pulse to pulse can be compensated by the dipole magnets and the fast kickers in the TESLA linac.
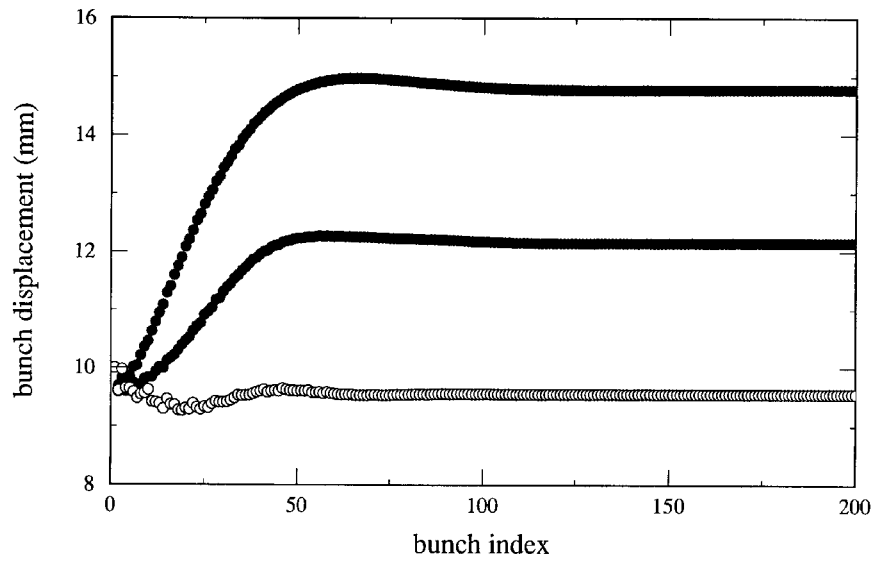
Figure 9.7:   Bunch displacement with 10 mm offset at the 8-cavity module exit. Zero, one, or two cavities tuned to resonant condition. (8 nC bunch charge, cavities unpowered)
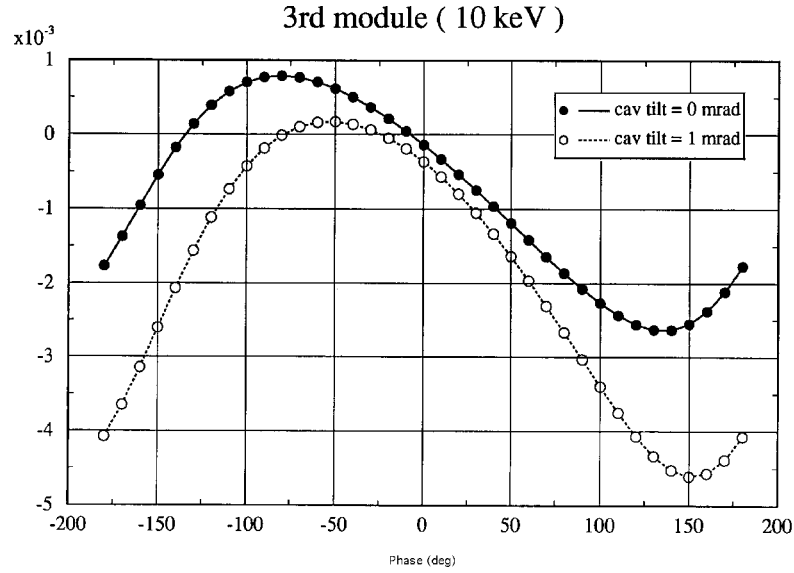
Figure 9.8:   Beam displacement (mm) for a RF phase variation (deg) of the 3rd module.

Their contributions to emittance dilution through wakefield and chromatic effects will be small. Due to the finite bunch length, however, the RF kicks vary during the passage of a bunch, causing a tilt to the beam, driven by the out-of-phase RF component. The main sources of RF deflections in TESLA are the input and HOM couplers. The tolerance on the allowable RF kick angle has been estimated to 0.1 mrad per cavity and five times more if we alternate the couplers orientation every module.

By varying the RF phase of one TTF module at a time and monitoring the change in the beam position with the BPM located before the focusing magnets at the module end, the strength and the phase of the RF deflection can be inferred with a resolution below 100 mrad. These experiments can be carried out with the low charge injector and will be more sensitive at the low energy end of the TTF linac, but the RF focusing effects of the accelerating structures are stronger and must be taken into account. The Fig. 9.8 shows the expected BPM reading when the RF phase of the third module is varied, assuming a RF kick of 10 keV/c per cavity, without (solid circles) and with (empty circles) the effect of a random cavity tilt of 1 mrad.
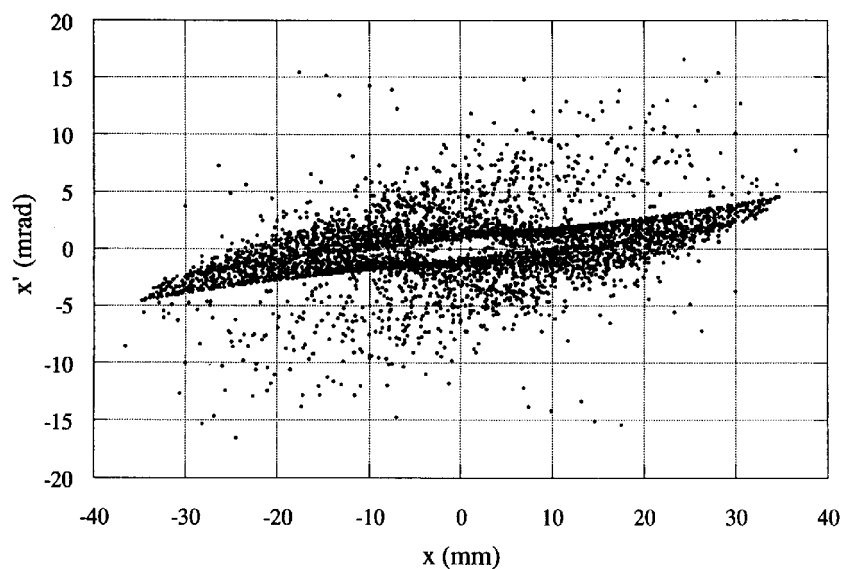
Figure 9.9:   Field emission beam in transverse phase space after a 2nd
cavity

9.1.7   Dark Current

Field emission currents can be easily captured by the accelerating wave in
the TESLA L-band cavity operating at 25 MV/m, because at low frequency,
the electrons have time enough during one RF period to be accelerated.
The potential emission sites are located near the irises of the cavity and the
electrons are transported out of the cavity when emitted at a proper phase.
This dark current emerging from one cavity can then be transmitted and
accelerated through the downstream cavities. The field emitted currents,
instead of being accelerated the full length of the linac, forming a halo to the
beam and finally causing a significant background problem to the interaction
region, will be fortunately intercepted along the machine by the low energy
acceptance of the focusing optics.

Fig. 9.9 plots the field emitted beam in transverse phase space after ac-
celeration through a second cavity. The potential emitters were disclosed by
sweeping of the first cavity surface and of the RF phase.

This dark current has then been tracked in simulation through the TESLA
linac, with usual components misalignments, the one-to-one correction, and
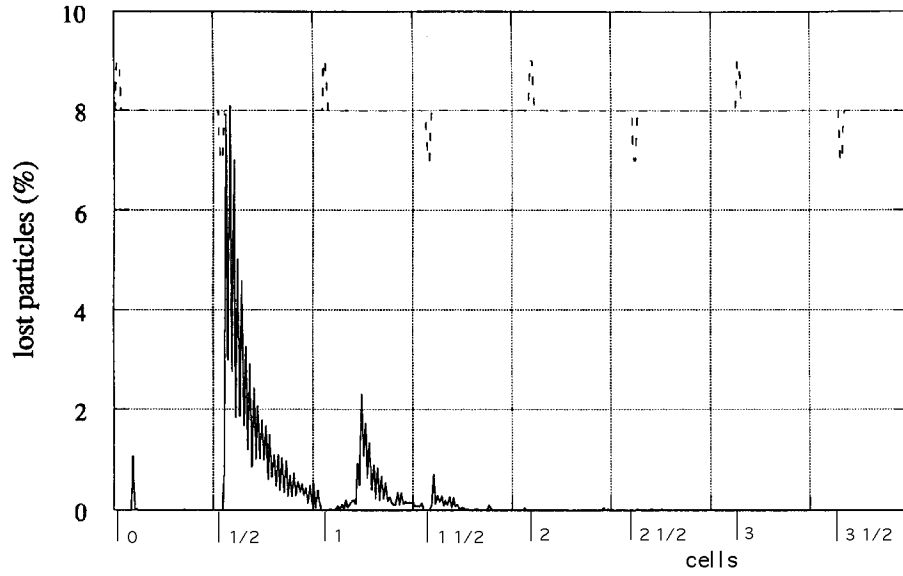
Figure 9.10:   Amount of particles in % lost along the TESLA linac.

induced wakes from the main bunches have been taken into account. Fig. 9.10 shows the amount of particles lost along the machine, assuming the current, formed by 10000 particles, was emitted from the first cavity of the linac after the damping ring(worst case). Most of the particles are lost in the first quadrupoles and the last particle after five FODO cells. In the TTF linac, since the injection energy is much lower, about 70% of the dark current issuing from the first cavities is expected to be transmitted for the design quadrupole settings and about 40% when the quadrupole strengths are increased by 20%. The transmitted field emission currents will be carefully measured at the end-station and scintillation counters will be placed at the critical points to measure the expelled current.

9.2   Warm Beam Line (prior to Cryo Modules 2,3,4)

The four modules of the TTF linac will be assembled one after another. With the first installed module, containing eight superconducting cavities

as well as a beam position monitor followed by a quadrupole doublet, and being the first cell of an optics lattice, cryogenic and RF tests are planned. As soon as they are carried out successfully the operation with beam has to be performed. The resulting beam parameters should give the information which is needed to optimize the RF control system and the matching between the injector and the main linac. Therefore, the beam has to be transported to some experimental area which should provide the necessary diagnostic stations in a straight section as well as in a dispersive section. Since moving downstream such an area with each newly installed module is ineffective, a temporary warm beam line is planned. With respect to the optics lattice this beam line will be a replication of the cold situation. The fact that it will be a warm system allows for some additional diagnostics. This clearly supports the commissioning of the TTFL.

9.2.1   Components of the Temporary Beam Line

The temporary beam line will be modular with a unit length equal to the linac modules. Thus, the standard length will be 12.2 m and the optics can be a replication of the cold situation. Pure FIDO cells will be used with the geometry and focal strengths as given in Sec. 2.3. Nevertheless, while the drift of the standard cell can be a simple beam tube, the drift of the first cell has to include the terminating end cap of the linac cryostat and the last cell of the temporary beam line has to be followed by some warm beam tube with the length of this end cap.

Each module in this temporary beam line will have the quadrupole doublet at the same position as the superconducting quadrupoles in the linac module. Instead of the cavity beam position monitor of the linac module, a diagnostic station equipped with view or OTR screens and standard TV cameras will be used as well as stripline beam position monitors. In contrast to the superconducting quadrupoles, the envisaged warm magnets have no correction coils and since the operation with a separate power supply for each coil is more expensive, we will use additional trim magnets (one horizontal and one vertical) placed just at the beginning of each module of this temporary beamline. The quadrupole strength and the gradient have been listed in Sec. 2.3. A maximum gradient of 10 T/m is adequate and could handle beam energies corresponding to accelerating gradients well above 25 MV/m. The trim magnets should be able to produce a 1 cm offset per module length

which corresponds to a deflection angle of about 1 mrad. At an accelerating gradient of 25 MV/m the energy behind the third installed module will be 600 MeV which gives a magnetic rigidity of $B\rho = 2$ Tm. Thus, a 10 cm long trim magnet with a field of 0.2 T or a strength of 2000 Gcm would deflect the beam by 1 mrad.

In addition to the use of the view screens as simple beam position monitors, they can also act as a kind of oscilloscope screen. The long distance between the end of the first installed linac module and the experimental area permits the installation of transverse deflecting devices like steerers or RF cavities which only have to produce small deflection angles in the order of 1 mrad. For the measurements of the beam parameters as a function of time, two different time scales are of interest. A steering magnet, ramped with a repetition rate of 10 Hz and a velocity of 1 mrad / 800 μs would convert the macropulse length of 800 μs into a screen trace of 12 mm behind one or even 24 mm behind two modules of the temporary beam line. An L-band, 1.3 GHz TM_{110} cavity could be used for average bunch length measurements in the picosecond scale. This transverse deflecting cavity will be discussed in Sect. 9.3.

9.2.2   Dog Leg for Offsets

Some experiments are planned to study the behavior of an electron beam which is injected at an offset of 1 cm with respect to the cavities' axis. Although injector I does not deliver a high enough bunch charge and therefore can not really excite high order modes (HOMs) in the cavities, some tests might be done with just one installed linac module. Thus, the beam offset of one 1 cm has to be canceled behind this module. Doing this over a length of one cell in the optics lattice, this requirement is consistent with the trim magnet strength. Figure 9.11 shows the chosen beam axis for this kind of measurements together with a schematic layout of the temporary beamline.

9.3   EAA Component Layout and Rationale

The TTFL is followed by the High Energy Experimental Beam Analysis Area (EAA). This area has to fulfill three purposes:
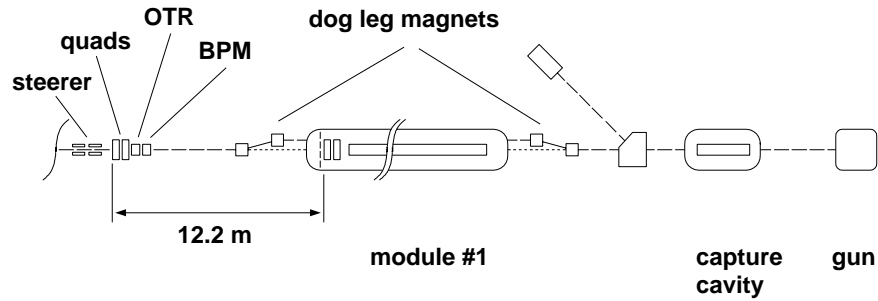
Figure 9.11:   Schematic layout of the temporary beam line with the dog
                leg included. At the end of each warm module diagnostics
                and focusing is provided.

- It serves as a room to measure the relevant beam parameters such
  as beam position, beam size and emittance, beam energy and energy
  spread, beam current and transmission through the linac, bunch length
  and shape, RF beam phase, and dark current from the cavities.

- It houses the beam dumps which are covered in all directions with a
  3.2 m thick shielding made of heavy concrete.

- It provides space for testing new diagnostic tools developed for TESLA/TTF,
  e.g. cold beam position monitors, special shaped warm stripline detec-
  tors and bunch length measurement for ultrashort bunches based on
  coherent radiation.

The Analysis Area consists of a straight section (Experimental Area 1, EXP1)
followed by another straight section (Experimental Area 2, EXP2) and a 20
degree spectrometer bend (Experimental Area 3, EXP3). Figure 9.12 shows
the schematic layout of the area.

- A possible off-axis beam position at the entrance of Experimental Area
  1 of 10 mm at maximum is corrected in a dog leg section consisting
  of a horizontal and a vertical steering magnet. Two diagnostic sta-
  tions verify the result. They house a retractable fluorescent screen
  and an OTR-foil as well as a beam position monitor to measure the

beam position and a current monitor used in combination with a similar detector in front of the linac to measure the beam transmission through the cavities. The following measurement section consists of a quadrupole doublet that is powered in series and a diagnostic station. An off-line measurement based on the multiple-gradient method (see Sec. 2.4 can be performed. The diagnostic station consists of a vacuum chamber housing a retractable fluorescent screen with a TV-camera port, a retractable OTR-foil viewed by another port, a slow and a fast wire scanner to measure the beam profile, and a position monitor. The emittance measurement section is terminated by a matching section (series-powered quadrupole doublet) to minimize the non-dispersive contribution of the beam size at the diagnostic station of the spectrometer. A diagnostic station (fluorescent screen, beam position and current monitor) in front of the spectrometer dipole helps to control the beam.

- The straight section (Experimental Area 2) behind the spectrometer is not used under normal operation conditions. A specially shaped vacuum chamber in the spectrometer dipole gap allows the bremsstrahlung photons coming from the wires of the scanners and the synchrotron light emerging from the dipole to exit the beam pipe by windows. The γ-quanta from the scanners will be detected by a retractable scintillation counter. The synchrotron light must be guided by an optical system to the camera. Otherwise it would hit the first quadrupole of Experimental Area 3. Some meters behind the dipole a beam dump will be placed which has to stop the beam in the case of spectrometer magnet failure.

- The 20 degree spectrometer (Experimental Area 3) provides on the one hand a large energy aperture (dE/E $\leq$ 5 % at 800 MeV, RMS value) and on the other hand enough dispersion to perform a good measurement of energy and energy spread under TTF design conditions (dE/E $\leq 10^{-3}$ at 800 MeV, RMS value). A beam with a small energy spread can drift downstream to the diagnostic station where it is analyzed. A worse quality beam would blow up too much in the horizontal plane if the large-bore dispersion suppression quadrupole between the spectrometer dipole and the diagnostic station is not powered. This magnet

focuses the fan of particles with different momenta in order to transport the beam through the limited aperture of the diagnostic station. This station consists of a fluorescent screen as well as an OTR screen and a secondary-emission grid (SEM - grid) to measure the beam profile, a beam position monitor to measure the beam energy, and a current monitor. The diagnostic section is followed by a second large-bore quadrupole which has to blow up the beam under TTF design conditions, i.e. small emittance and small energy spread, to produce a tolerable large beam spot at the beam dump as well as to refocus the beam in the case of a large momentum spread to keep the electrons inside the vacuum tube. The area is terminated by the beam dump.

It turns out that the beam in the spectrometer arm is not very sensitive to the optical beam parameters (size, divergence) behind the linac as well as to changes of the magnet settings in Experimental Area 1 if the energy spread is not too small, i.e. $\ll 10^{-3}$. This means that the beam size in the spectrometer arm is dominated by the dispersion. The optics calculations show that the design TTFL beam as well as a beam with ten times larger initial size and divergence can be handled. An energy spread up to 1.0 % can be accepted by the spectrometer without powering the large dispersion suppression quadrupole. The dispersion at the diagnostic station of Experimental Area 3 amounts to 1.20 m corresponding to a beam offset of 1.4 mm per 1 MeV energy deviation. At 800 MeV the beam spot at the beam dump must be kept larger than $\sigma_x \sigma_y = 2.25$ mm^2 (RMS values). Fig. 9.13 through Fig. 9.16 show the beam envelopes (RMS-values) for different beam conditions as a function of the position in the Analysis Area (E = 800 MeV). Table 9.2 lists the corresponding quadrupole settings.
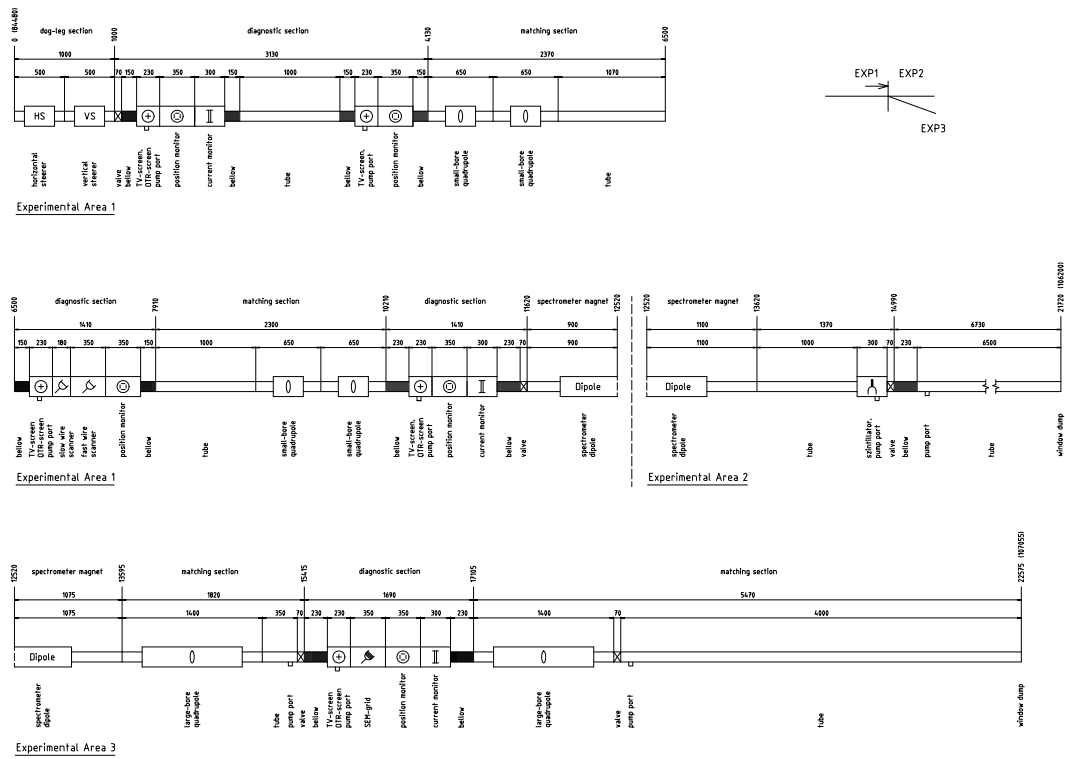
Figure 9.12: Layout of the Experimental Beam Analysis Area

- Fig. 9.13 shows a standard TTF-beam (ϵ_{xnorm} = 3.9 mm mrad, x_{max} = 0.18 mm, x'_{max} = 0.020 mrad, ϵ_{ynorm} = 3.8 mm mrad, y_{max} = 0.15 mm, y'_{max} = 0.017 mrad, E = 800 MeV) with an energy spread of 10^{-3}. The beam is well guided towards the dump.

- In the case of a 5 % energy spread (Fig. 9.14) large beam sizes result in the spectrometer arm, inside the first quadrupole due to the dispersion and inside the second quadrupole because the beam width must be kept small in the diagnostic station.

- A ten times increased initial beam size and divergence produce a large beam at the second quadrupole doublet of the straight section and in the gap of the spectrometer dipole. The beam size may reach the aperture limit if the beam waist is moved across the scanner during the emittance measurement. This is shown in Fig. 9.15 for an energy spread of 10^{-3}.

- If the spread amounts to 5 % the complete beam pipe of the large-bore quadrupoles is filled (Fig 9.16).
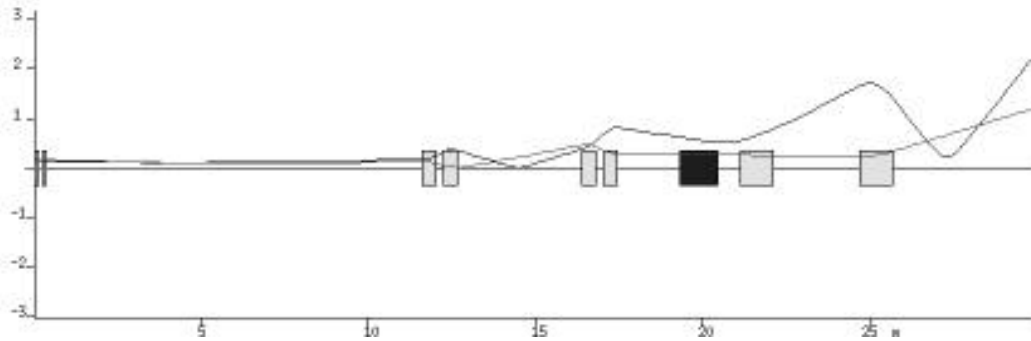
Figure 9.13:   Horizontal (black) and vertical (grey) beam envelopes (RMS-values in mm) along the Beam Analysis Area for a standard TTF-beam with an energy spread of 10^{-3}.(The calculation starts with the last cold quadrupole doublet.
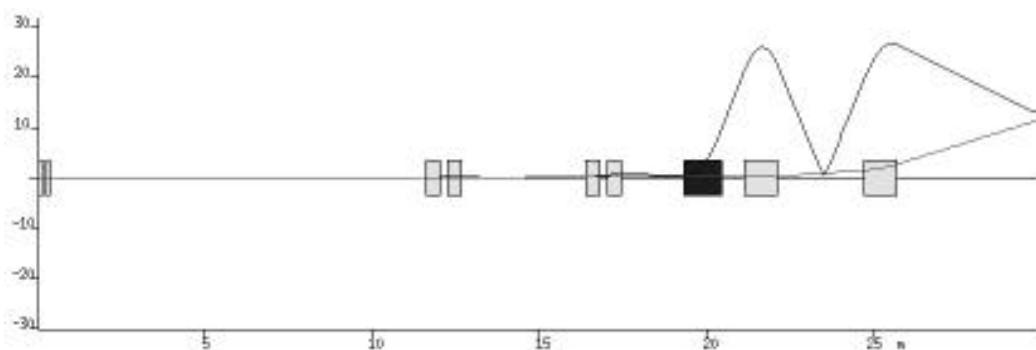
Figure 9.14: Horizontal (black) and vertical (grey) beam envelopes (RMS-values in mm) along the Beam Analysis Area for a standard TTF-beam with an energy spread of 5 %. (The calculation starts with the last cold quadrupole doublet.
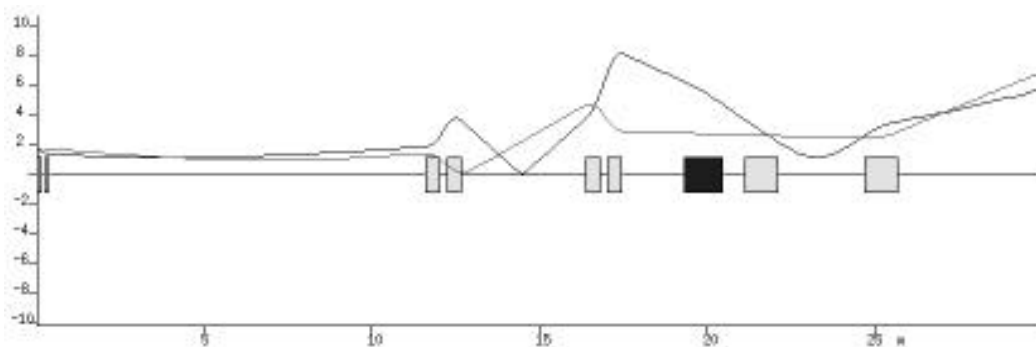
Figure 9.15: Horizontal (black) and vertical (grey) beam envelopes (RMS-values in mm) along the Beam Analysis Area for a non-standard beam with ten times increased beam size and divergence as well as an energy spread of 10^{-3}. (The calculation starts with the last cold quadrupole doublet.
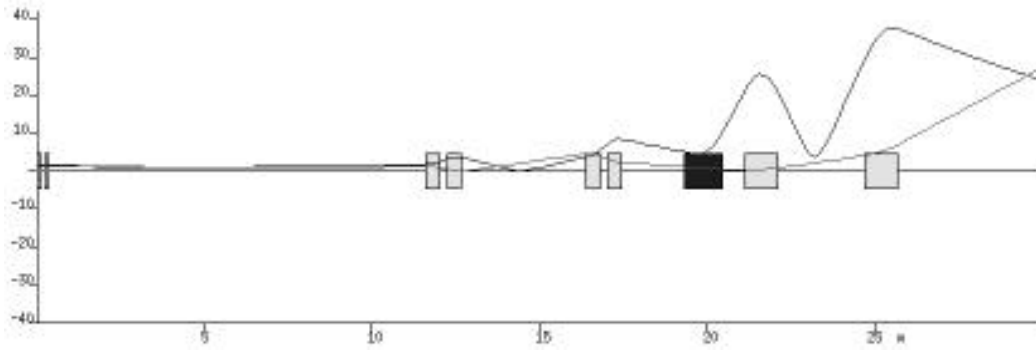
Figure 9.16:   Horizontal (black) and vertical (grey) beam envelopes (RMS
                 - values in mm) along the Beam Analysis Area for a non -
                 standard beam with ten times increased beam size and di-
                 vergence as well as an energy spread of 5 %. (The calculation
                 starts with the last cold quadrupole doublet.

Table 9.2:   Integrated gradients of the quadrupoles of the Experimental
                 Beam Analysis Area for different beam parameters at the end
                 of the linac (standard TTF - beam: $\epsilon_{xnorm} = 3.9$ mm mrad,
                 $x_{max} = 0.18$ mm, $x'_{max} = 0.020$ mrad, $\epsilon_{ynorm} = 3.8$ mm mrad,
                 $y_{max} = 0.15$ mm, $y'_{max} = 0.017$ mrad, E = 800 MeV). The
                 gradient of a doublet is positive if the gradient of the first
                 magnet of the doublet is positive.

	standard TTF - beam		ten times larger beam size and divergence	
energy spread (RMS) at 800 MeV	0.1 %	5 %	0.1 %	5 %
integrated gradient (1. quadrupole doublet) / T	-3.87	-3.87	-3.87	-3.87
integrated gradient (2. quadrupole doublet) / T	-2.51	-2.51	-2.51	-2.88
integrated gradient (1. single quadrupole) / T	0.00	3.6	0.00	4.00
integrated gradient (2. single quadrupole) / T	2.00	2.10	1.0	1.75

9.4 Warm Beam Transport Sections

The warm beam transport sections have to be built in UHV technique. Standard flanges should be of the CFxx type. Pumping is planned at most of the diagnostic stations. The whole system will be divided into sections in order to allow for an easy replacement of e.g. wires and screens. The present section describes the beam transport system in terms of slot lengths; a detailed discussion of the beam transport elements being planned is also included. The beam height in all sections is 1230 mm.

9.4.1 Components: Slot Lengths / Aperture / Flanges

Table 9.3 lists all components of the Beam Analysis Area with their corresponding slot lengths, apertures and beam pipe shapes as well as flanges according to the schematic layout shown in Fig. 9.12.

Table 9.3:   Components of the Beam Analysis Area (slot length, aperture, beam pipe shape,flanges)

Experimental Area 1			
Component	**Slot Length / mm**	**Aperture (maximum extension / mm, shape)**	**Flanges (in, out)**
laser light port	210	± 30, special design	CF63, CF63
tube (horizontal steerer)	500	± 30, round	CF63, CF63
tube (vertical steerer)	500	± 30, round	CF63, CF63
valve	70	± 30	CF63, CF63
bellow	150	± 30	CF63, CF63
fluorescent screen, OTR - foil, pump port	230	±30, special design	CF63, CF63
position monitor	350	± 30, special design	CF63, CF63
current monitor	300	± 30, special design	CF63, CF63
bellow	150	± 30	CF63, CF63
tube	1000	± 30, round	CF63, CF63
bellow	150	± 30	CF63, CF63
fluorescent screen, pump port	230	± 30, special design	CF63, CF63
position monitor	350	± 30, special design	CF63, CF63
bellow	150	± 30	CF63, CF63
tube (quadrupole)	650	± 30	CF63, CF63
tube (quadrupole)	650	± 30, round	CF63, CF63
tube	1070	± 30, round	CF63, CF63
bellow	150	± 30	CF63, CF63
fluorescent screen, OTR - foil, pump port	230	± 30, special design	CF63, CF63
wire scanner (slow)	180	± 30, special design	CF63, CF63
wire scanner (fast)	350	± 30, special design	CF63, CF63
position monitor	350	± 30, special design	CF63, CF63
bellow	150	± 30	CF63, CF63
tube	1000	± 30, round	CF63, CF100
tube (quadrupole)	650	± 50, clover-leaf	CF100, CF100
tube (quadrupole)	650	± 50, clover-leaf	CF100, CF100
bellow	230	± 50	CF100, CF100
fluorescent screen, OTR - foil, pump port	230	± 50, special design	CF100, CF100
position monitor	350	± 50, special design	CF100, CF100
current monitor	300	± 50, special design	CF100, CF100
bellow	230	± 50	CF100, CF100
valve	70	± 50	CF100, CF100
tube (spectrometer dipole)	900	± 33 (vertical), special design	CF100

Experimental Area 2			
Component	Slot Length / mm	Aperture (maximum extension / mm, shape)	Flanges (in, out)
tube	1000	± 50, round	CF 100, CF 100
szintillator box, pump port	300	± 50, special design	CF 100, CF 100
valve	70	± 50	CF 100, CF 100
bellow	230	± 50	CF 100, CF 100
tube, pump port	6500	± 75, round	CF 100, CF 150

Experimental Area 3			
Component	Slot Length / mm	Aperture (maximum extension / mm, shape)	Flanges (in, out)
tube (spectrometer dipole, 20°)	1075	± 33 (vertical), special design	CF 150
tube (quadrupole)	1400	± 75, clover-leaf	CF 150, CF 150
tube, pump port	350	± 75, round	CF 150, CF 100
valve	70	± 50	CF 100, CF 100
bellow	230	± 50	CF 100, CF 100
fluorescent screen, OTR - foil, pump port	230	± 50, special design	CF 100, CF 100
SEM - grid	350	± 50, special design	CF 100, CF 100
position monitor	350	± 50, special design	CF 100, CF 100
current monitor	300	± 50, special design	CF 100, CF 100
bellow	230	± 50	CF 100, CF 100
tube (quadrupole)	1400	± 75, clover-leaf	CF 100, CF 150
valve	70	± 75	CF 150, CF 150
tube, pump port	4000	± 75, round	CF 150, CF 150

9.4.2   Quadrupoles, Steering Magnets, Spectrometer Dipole Magnet in the EAA

Two types of quadrupoles are planned, four small-bore magnets (QMN, DESY-design) installed in the Experimental Area 1 and two large-bore magnets (HERA QC, DESY-design). The gradients listed in Table 9.4 are sufficient to perform an emittance measurement at 800 MeV based on the multiple-gradient method as well as to transport safely a non-standard beam (ten times larger beam size and divergence, 5 % energy spread) to the dump.

Table 9.4: Parameters of the quadrupoles, steering magnets, spectrometer dipole and corresponding power supplies installed in the Beam Analysis Area (800 MeV).

QMN	bore diameter / mm	70
	maximum integrated gradient / T	6.08
	iron length / mm	300
	total length / mm	420
	maximum current / A	270
	resistance / mΩ	31.4
	integrated gradient needed / T	5
	current needed / A	222
	voltage needed / V	7
	# of magnets needed	4
	type of power supply	DC, bipolar
	stability	$< 10^{-3}$
	resolution of ADC	16
	# of power supplies needed	2
HERA QC	bore diameter / mm	100
	maximum integrated gradient / T	16
	iron length / mm	1000
	total length / mm	1170
	maximum current / A	380
	resistance / mΩ	145.5
	integrated gradient needed / T	5
	current needed / A	119
	voltage needed / V	17
	# of magnets needed	2
	type of power supply	DC, bipolar
	stability	$< 10^{-3}$
	resolution of ADC	16
	# of power supplies needed	2

HERA CV	gap width / mm	90
	maximum integrated field / Tm	0.03
	iron length / mm	300
	total length / mm	300
	maximum current / A	3
	resistance / Ω	13
	integrated field needed / Tm	0.03
	current needed / A	3
	voltage needed / V	39
	# of magnets needed	4
	type of power supply	DC, bipolar
	stability	$< 10^{-3}$
	resolution of ADC	12
	# of power supplies needed	4
spectrometer dipole	gap height / mm	66.3
	iron length / mm	1130
	maximum field / T	1.67
	maximum current / A	220
	resistance / mΩ	590
	field needed / T	0.83
	current needed / A	110
	voltage needed / V	65
	type of power supply	DC, bipolar
	stability	$< 10^{-4}$
	resolution of ADC	16
	# of power supplies needed	1
	deflection angle / Ω	20
	bending radius / mm	3233

The two steering magnets (HERA CV) are able to correct an beam off-set of 10 mm at the end of the linac.

The spectrometer magnet already exists (B4, Saclay-design). The deflection angle will be reduced to 20°. The old magnet stand has to be adapted to the TTF beam line height.

The high energy bending magnet gets a new vacuum pipe which will have three ports for the electron beam and one additional port for the observation of synchrotron light (SR). The bending angle is 20°. Since the pole gap height is 66.3 mm the beam tube planned so far is non-standard but should have CF100 flanges. The injected electron beam as well as the bent beam does not see any edge focusing.
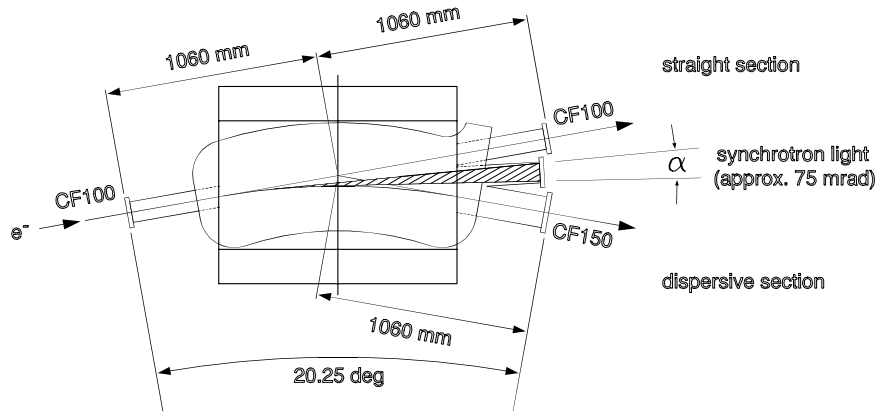
Figure 9.17:   The geometry of the vacuum beam pipe for the high energy analyzing magnet. The maximum output angle for the synchrotron radiation is ≈ 50 mrad.

In order to maximize the angle α under which SR can be observed, the window flange has to be as close as possible to the magnet coils. At the minimum distance of ≈ 1000 mm a slightly tapered beam tube would allow for a 100 mm diameter flange. This corresponds to an angle $\alpha \approx 50$ mrad (≈ 2.8°). At the output flange towards the dispersive section, an extremely flat vacuum chamber will be constructed. Thus, a possibly large energy spread on the order of a few percent can be accommodated.

9.4.3   Quadrupole Magnets and Steering Along the Temporary Beamline

Quadrupole magnets for the temporary beam line have to have a focal strength of 6.115 m^{-1} (see Sect. 2.1.2) which corresponds with a gradient of up to 10 T/m at the highest achievable energy. The parameters of a quadrupole designed and built for Dafne/INFN (Italy) would fulfill all requirements as they are first of all the gradient, the aperture, the good field region, and the magnetic length. These parameters are shown in Tab. 9.5. The electric properties allow us to use the same power supplies that are going to be installed for the superconducting quadrupoles in the cryomodules. Modules of two quadrupoles preceded by one standard diagnostic station (view screen) are to be built by INFN. Each of the four modules will have its own support stand.

Table 9.5: Quadrupole Parameters

Magnet Designation	temporary beam line	
Quantity	8	
Gradient	10	T/m
Magnet Bore Diameter	60	mm
Good Field Region	± 25	mm
Field Quality	$\pm 2.5 \times 10^{-3}$	
Magnetic Length	200 ± 1	mm
Ampere Turns per Pole	3.633	
Current	86.5	A
Turns per Pole	42	
Conductor Size	5×5	mm
Coolant Hole Diameter	3	mm
Current Density	4.82	A/mm^2
Resistance at 50°C	0.12	Ω
Voltage	10	V
Power	0.9	kW
Water Circuits per Magnet	2	
Total Flow Rate	0.013	l/s
Pressure Drop per Circ.	2.7	ATM
Water Initial Temp.	32	°C
Water Temperature Rise	20	°C

The trim magnets along the temporary beam line have to handle an electron beam with a maximum magnetic rigidity of $B\rho = 2$ Tm. The deflection angle that is needed is 1 mrad, so the integrated field amounts to 2×10^{-3} Tm (2000 Gcm).

The trim coils mentioned above of the HERA-CV type (see Table 9.4, Sect. 9.3.2) meet the requirements although they clearly have been built for higher energies, and therefore have an integrated field of $30 \cdot 10^{-3}$ Tm. Their gap of 90 mm is more than sufficient for the CF63 beam line. The length of 300 mm is adequate.

9.5 Diagnostics and Instrumentation Details

This section deals with the diagnostic elements of the warm beam transport system. In addition, the RF cavity beam position monitor, to be installed in the cold modules, is described. The elements in the warm beam line are toroids as intensity monitors, wire scanners and SEM grids as profile monitors, their scintillation detectors, view screens as well as OTR screens, a synchrotron light monitor, bunch length measurement setups using coherent radiation, streak cameras or a deflecting cavity, and diodes for beam losses detection.

9.5.1 Intensity Monitors

As one type of intensity monitor, the TTFL will be equipped with beam charge monitors (BCMs) in the form of integrated current transformers. Such a current transformer sums up the charge of current pulses having risetime in the range of less than picoseconds to longer than a microsecond. It has to be specially adopted to the time structure of the electron beam and needs enough sensitivity if used for a charge transmission control, i.e. as a beam loss monitor.

The basic principle of the integrated current monitor is the propagation of some fraction of the wakefield energy of the traversing electron bunch through a capacitive gap in a ceramic beam pipe section into a surrounding cavity. Spectral components of the so trapped electromagnetic field induce corresponding signals at the output of transformers. These transformers are realized as small loops winded around toroidal magnetic cores with the traversing electron beam being on axis. The wall currents are bypassed around the beam current sensor.

For the TTF linac four BCMs are planned, exclusive of the injector area in which similar devices but developed by Saclay will be used. Two of the BCMs, one at each end of the linac, and will be used to detect losses in the charge transmission through the machine. The others are placed in front of and behind the spectrometer dipole, in order to check for beam losses in the experimental area.

- A pair of BCMs should detect differences in the integrated charge larger than 10^{-3} (permanent losses); the same system has to be able to detect a complete beam loss within 1 μs; this is one bunch for the TESLA time structure or an average over 216 bunches for the TTFL Injector I.

- One single bunch has a length of 1 mm ($\hat{=}$ 3.3 ps) and a bunch charge of 5×10^{10} e (TESLA) or 2.3×10^8 e (TTFL Injector I); so 10^{-3} of the over 1 μs integrated charge is 8 pC.

- The system of BCMs consist of the four integrating current transformers, as sensors, and the signal processor; this signal processor should output the integrated charge as well as two different trigger signals in case of permanent beam losses (10^{-3}) and complete beam losses (trigger within 1 μs) respectively.

- The overall length of one integrating current monitor is 300 mm flange to flange; the two monitors in front and behind the linac will be placed on CF63 beam tubes while the two placed in front of the spectrometer magnet and the beam dump need a CF100 vacuum pipe.

- Since the measurement is based on the excitation of electromagnetic fields via wakefields, some high frequency component might disturb other sensors situated close to the current transformer; special magnetic shielding might be necessary.

- The magnetic material (toroids) should have sufficient radiation hardness; external magnetic fields from neighboring dipoles or quadrupoles could principally drive the material into saturation. Some distance (remaining field ≤ 1 gauss) or shielding is needed.

9.5.2   Beam Position Monitors

The transverse position of the beam in the TTF will be measured using two different types of monitors. Both systems have to work for two different injectors.

For the alignment of the quadrupoles a circular cavity was designed because of the limited longitudinal space and the desired resolution (about 10 μm within 500 μm from the center). A single cavity will be attached to each quadrupole within 50 μm mechanical alignment precision. The amplitude

of the TM_{110}-mode will be measured in a synchronous detector, using a 216 MHz - signal from the timing system as a reference.

Strip-line BPMs will be installed in the experimental area, having a resolution of about 100 μm. For injector #1 the averaged position of the whole bunch train will be measured in a narrowband receiver (amplitude-to-phase conversion).

9.5.2.1 TM_{110}-Cavity

The amplitude of the TM_{110}-mode excited in the cavity by an off-center beam yields a signal proportional to the beam displacement and the bunch charge. This signal is much stronger than the signal given by other monitors and is a linear function of the beam displacement. The phase relative to an external reference yields the sign of the displacement. Both polarizations of this mode have to be measured to get the displacement in x and y, respectively. For injector #1 this system can measure only an average over the bunch train.

Prototype Design The cavity parameters given in Table 9.6 were calculated with URMEL, and the measurements were performed on a stainless steel prototype (Fig. 9.18) at room temperature. To avoid interferences from the accelerating cavities, the cavity was designed for a resonant frequency of $f_{110} = 1.517$ GHz.

One of the main mechanical problems was to reduce asymmetries caused by welding. CrNi was chosen as the cavity material to measure individual bunches spaced 1 μs and to have a good thermal isolation between an accelerating cavity and a quadrupole.
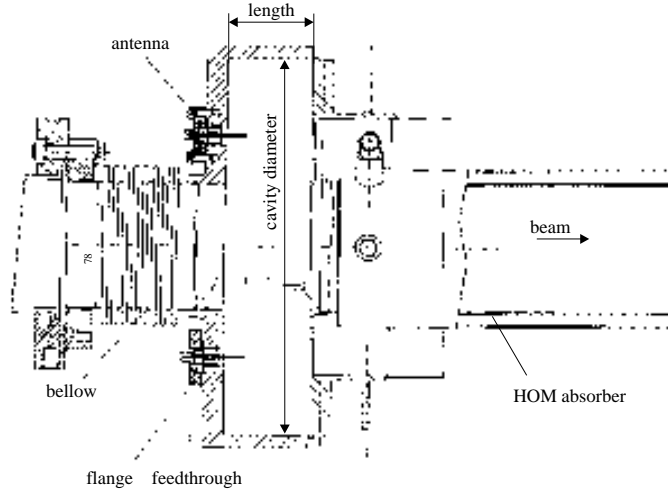
Figure 9.18: Design of the Prototype-Cavity

Table 9.6: Cavity design and measured parameters

parameter, dimension	at 290 K	target	sensitivity $\pm.1$ mm $\triangle$
radius R_0	115.2 mm	114.77 mm	∓ 1247 kHz
length l	52.0 mm	51.80 mm	± 79 kHz
beam pipe diameter	78.0 mm	77.70 mm	∓ 610 kHz
theoretical loss factor $[\frac{V}{pC}]$		$k_{110} = 0.242,$	$k_{010} = 0.179$
theoretical unloaded Q		$Q_{110} = 2965$	
measured frequency [GHz]		$f_{110} = 1.5133,$	$f_{010} = 1.04$
measured coupling		$\beta_{110} = 1.31,$	$\beta_{010} = 0.1$

After cooling down the structure, the seventh harmonic of 216.7 MHz has to be within the cavity bandwidth to avoid an active tuning system inside the cryostat. This requires a pre-tuning, which will be done by adjusting

the coupling after welding. Therefore, the antennas consisting of Kyocera-feedthroughs welded into a special flange, are replaceable.

Estimated Signals The resolution near the electrical center of the cavity is limited by the thermal noise of the electronics and the excitation of common modes. For a cavity without beam pipes, the voltage in the TM_{110} excited by a beam at a position δ_x can be estimated as

$$V_{110}(\delta_x) = V_{110}^{max} \frac{\delta_x \cdot a_{11}}{2 J_1^{max} R_0} = \delta_x \frac{k'_{110} a_{11} q}{J_1^{max} R_0} \approx 0.417 \cdot \delta_x \frac{\text{mV}}{\mu\text{m}}$$

where a_{11} is the first root of the Bessel function J_1 and $k'_{110} = 0.228$ V/pC is the longitudinal lossfactor of the geometry in Tab. 9.6 (but without a beam pipe).

Assuming a noise figure of NF = 6 dB, the S/N-ratio in a bandwidth $B = 100$ MHz at room temperature is given by

$$\frac{V_{signal}}{V_{noise}} = \frac{0.417 \text{ mV}}{\text{NF} \cdot \sqrt{Z_0 \cdot k_0 \cdot T \cdot B}} \frac{\delta_x}{\mu\text{m}} \approx 47 \cdot \frac{\delta_x}{\mu\text{m}}$$

Since the field maximum of the common modes is on the cavity axis, they will be excited much stronger than the TM_{110} by a beam near the axis. The voltage of the TM_{010} with respect to the TM_{110} and the ratio of the spectral densities at ω_{110}[1] can be estimated as

$$S_1 = \frac{V_{010}(\omega_{010})}{V_{110}(\omega_{110})} = \frac{1}{\delta_x} \frac{\lambda_{110}}{5.4} \frac{k_{010}}{k_{110}} \approx \frac{0.027}{\delta_x}$$

$$S_2 = \frac{v_{110}(\omega_{110})}{v_{010}(\omega_{110})} \approx \delta_x \frac{1}{S_1} \frac{Q_{110}}{1 + 2\beta_{110}} \left(1 - \frac{\omega_{010}^2}{\omega_{110}^2}\right) \approx 16000 \cdot \delta_x$$

S_1 gives the required frequency sensitive common-mode rejection - about 69 dB for a displacement of $\delta_x = 10\mu$m (for the parameters in Tab. 9.6). But the minimum detectable signal is still limited by residual signals at ω_{110}. For a single antenna, this can be estimated using $S_2 = 1$, which yields $\delta_x^{min} \approx 62$ μm. With a combination of two antennas in a hybrid one gets a field selective

---

[1] W. Schnell, *Common-mode rejection in resonant microwave position monitors for linear colliders*, CLIC note 70, CERN-LEP-RF/88-41

filter, which gives a rejection of unwanted common field components at ω_{110} of more than 20 dB. Hence, the theoretical resolution near the electrical center of the cavity is ≤ 6 μm. The common mode rejection is limited only by the finite isolation of the hybrid between the Σ- and the Δ-port.

The amount of power extracted from the beam and stored in all modes of the cavity depends on the total loss factor k_{loss}, the averaged repetition frequency f_{rep} and the charge per bunch, Q_b. For the injector II, the averaged P_{loss} for a max. beam displacement ($\delta_x = 39$mm) will be

$$P_{loss} = k_{loss} \cdot f_{rep} \cdot Q_b^2 = 1.1 \frac{V}{pC} \cdot 8KHz \cdot (8nC)^2 \approx 0.56W$$

Signal Processing   For signal processing, we adopted a synchronous detector scheme (Fig. 9.19), where the amplitude of the TM_{110} and a reference are mixed down to DC. The reference-signal will be generated by mixing a 217 MHz-signal from the timing system and amplifying seventh harmonic. When the beam is to the right, the system can be set up to give positive video polarity. The signal changes the phase by 180^0 when the beam moves to the left, and for a centered beam it becomes zero. The reference phase can be remotely adjusted to maximize the mixer output.

Due to the limited space, the combination of two opposite antennas has to be realized outside the cryostat. The isolation of standard (broadband) hybrids is about 25 dB, which limits the resolution. The tubular bandpass filter has a bandwidth of 100 MHz and a stopband attenuation of more than 80 dB, up to 8 GHz. Together with the hybrid and the different coupling factors this gives a common mode rejection of more than 100 dB (frequency sensitive).

Because of the finite isolation of the hybrid and between both polarizations (due to asymmetries in the cavity), the full aperture was divided into two measurement ranges:

$0 \cdots 300$ μm, normalization from the hybrid sum

$0.3 \cdots 39$ mm, normalization from current monitors

The LO-RF-isolation of the double-balanced mixer (DBM) determines the dynamic range of the electronics. About 45 dB are required, due to the displacement and differences in the bunch population. An isolator was inserted between the filter and the mixer to reduce reflections and error signals due to second-time mixing. We are planning to test a Quadrature IF Mixer instead
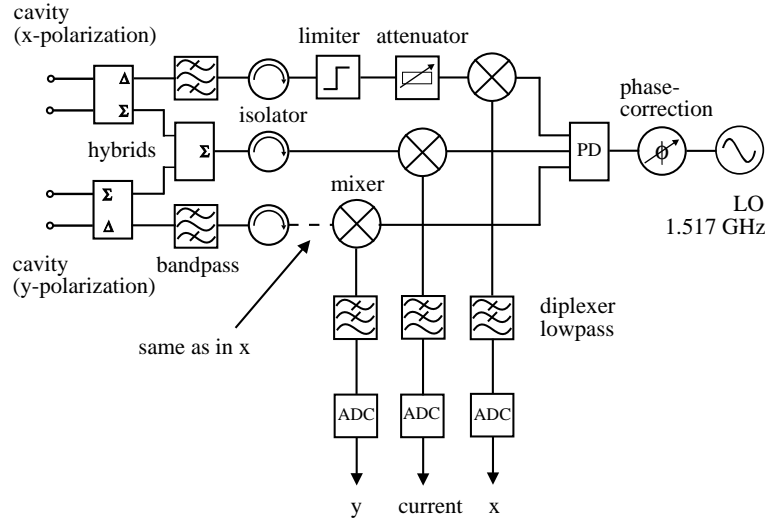
Figure 9.19: Signal processing scheme for the cavity BPMs

of the DBM, too. Such a system does not need an additional phase shifter for the reference signal. A low-pass filter removes the residual LO-signal and the sum-signal of both mixer inputs.

After passing a bipolar video amplifier, the signal may be either viewed directly on an oscilloscope for adjustment, or digitized and used for the quadrupole alignment. The trigger will be generated by the sum-signal of the hybrid. Using a 12-bit ADC-board, four samples will be taken spaced 50 ns. All data can be read out between two bunch trains and the normalization will be done in a computer.

Bench tests were carried out on a stainless steel prototype to determine the resolution near the center and to test the electronics. Therefore, the cavity was excited by an antenna, fed by a network analyzer or a pulser, and a resolution of about 5 μm was measured by moving the cavity[2]. In addition, a prototype was tested at the CLIC Test Facility at CERN to demonstrate the principle single bunch response of the monitor. Unfortunately, due to the measurement position, the mechanical setup and some machine parameters it

---

[2]R. Lorenz, K. Yezza, *Test results on a Beam Position Monitor Prototype for the TTF*, presented at the EPAC 94, London, July 1994.

was impossible to measure the minimum detectable signal near the monitor
center.

9.5.2.2   Stripline Monitors

Stripline monitors were selected for the position measurement in the experi-
mental area because of the relaxed requirements - 100 μm resolution around
the center - and the warm location. The four monitors in the straight section
will consist of four 175 mm long, 50 Ohm coaxial striplines, positioned 90
degrees apart in azimuth in a 60 mm beam pipe. The housing for the one in
the dipole arm will be slightly modified due to the elliptical beam pipe.
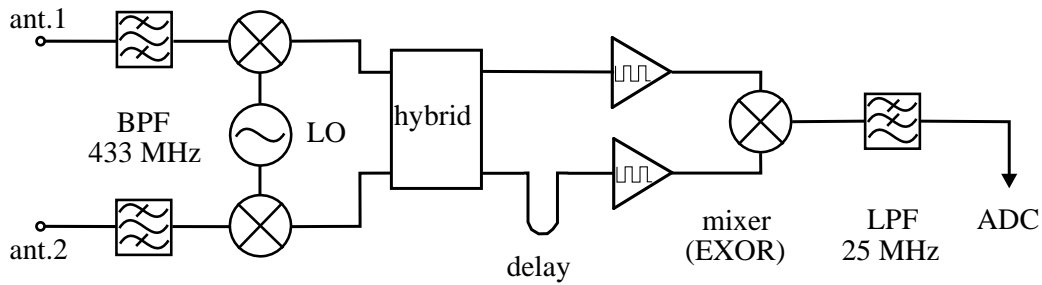
Figure 9.20:   Signal processing scheme - AM/PM-conversion

The signal processing electronics have to measure the Δ-signal and the
Σ-signal of two opposite electrodes to calculate the position in one direc-
tion. Because of the small charge per bunch and the multibunching, an
amplitude-to-phase conversion scheme was adopted. Its basic component is
a device which transforms the amplitude ratio of two input signals into a
phase difference. Usually, this device is a $\frac{\pi}{2}$-hybrid. The generation of a nor-
malized output (position versus current) over a wide dynamic range is the
main advantage of this system.

The signal of each electrode will be fed into a 433 ± 10 MHz bandpass filter. After passing the $\frac{\pi}{2}$-hybrid, the signals will be clipped to a constant amplitude in a hard-limiter circuit and their phase difference will be detected in an exclusive OR. Again, the signal coming out of the phase detector may be either viewed directly on an oscilloscope or digitized using the standard 12-bit ADC-board.

Usually, hard-limiters restrict the system performance the most and they work best at frequencies below 20 MHz[3].

Therefore, the 433 MHz output of the bandpass filters will be down-converted to about 18 MHz. The real-time bandwidth is about 10 % of the processing frequency. Phase matching of the cables from the BPM to the electronics is required to keep the relative phase at the hybrid within $\pm 5^0$. This system will be able to measure individual bunches spaced one μs for injector II, too. Another alternative is to adopt the SLAC-broadband system, where the signals of each electrode are individually stretched, amplified, hold at their peak value and than digitized. Proceedings 212, 1989

9.5.3 RF - Beam Phase Detection

The RF beam stability is important to observe, especially in correlation with many other measurements, like energy, energy spread, signals from the RF control circuits, and even position monitors. Therefore a non-destructive method should be chosen which could be either a pickup or a very high frequency RF cavity. In cases in which a correlation with signals from the phase and amplitude controller of the superconducting cavities is of interest, one surely could also use OTR signals with fast optical detectors. The time scale for such measurements should vary from 1μs (the bunch spacing) to seconds.

A simple button pickup together with a 1.3 GHz band pass filter can be used to select the frequency component. Multiplying this component with the 1.3 GHz reference signal of the TTFL, this using a 2π phase detector, would allow the direct observation of the RF phase stability on an oscilloscope operated in polar plot mode, or digitizing of the resulting sine and cosine signals.

---

[3]R. Shafer, *Beam Position Monitoring*, pp.26-58, AIP Conference Proceedings 212, 1989.

In order to gain resolution, a much higher frequency component can be measured. For this purpose a simple TM_{010} like coaxial cavity can be used which has its lowest mode frequency in a region where the Fourier spectrum of the bunch length starts decreasing (typ. above 30 GHz). The design of such a cavity is simple, it could be coaxial with the beam on axis (small aperture!) or any other design with some coupling to a ceramic gap in the beam line. The more difficult thing here is the RF measurement technique at such high frequencies.

9.5.4 Beam Profile Monitors

As explained in Sec. 2.4, the emittance measurement proposed is based on the measurements of beam profiles. The beam sizes measured could vary from $O(1\ mm)$ to $O(10\ \mu m)$. In the dispersive section of the Beam Analysis Area the horizontal beam size mainly reflects the energy spread of the beam. The RMS value might be in the range from $O(0.1\ mm)$ to $O(1\ mm)$.

The emittance will not be measured bunch-to-bunch. However, according to the experimental program listed in Sec. ?? a measurement of the time dependence of the energy spread along the macropulse is anticipated. To detect the influence of short-range wake fields the energy as well as the transverse profile at the head and the tail of a bunch should be measured.

Standard devices to measure a beam profile are secondary emission grids (SEM-grids), wire scanners and view screens.

SEM grids consist of a couple of parallel strips or wires placed in the beam path. The incident beam releases secondary electrons from the grid. This mechanism provides a signal proportional to the beam current. Thus, a histogram-like plot of the beam profile will be available.

Wire scanners are widely used in present storage rings and linear accelerators. A thin wire is moved through the beam. The wire thickness as well as the minimum stepsize determine the resolution of the measurement. Analogous to a SEM grid, the current in the wire produced by the secondary electron emission can be measured. Another alternative is to detect scattered beam particles, secondary emitted electrons or bremsstrahlung γ - quanta in a scintillation counter placed somewhere downstream. For TTFL we can distinguish between three different operation modes:

- Slow scan: A fork holding the wire moves perpendicular through the

beam on a straight line driven by a stepping motor. The speed of the
scanner is less than 1 mm/s so that the signal from each macropulse
gives one data point of the profile histogram. A start trigger is not
necessary.

- Fast scan: A fork holding the wire moves perpendicular through the
beam on a straight line driven by a pneumatic actuator or a DC motor.
The speed of the scanner is some meter per second, so that the signal
from each bunch of one macropulse gives one data point of the profile
histogram. The triggering of the motion and a precise position decoding
is difficult. A speed of 2 m/s is maximum at present.

- Synchronous scan: A fork holding the wire rotates permanently through
the beam. As in the case of the fast scan, the **signal from each bunch
of one macropulse** gives one data point of the profile histogram. How-
ever, the requirements for the trigger are relaxed because the revolution
frequency and phase can be locked to the time structure of the beam.
A scan speed of 100 - 200 m/s should be achievable.

View screens are helpful tools to set-up the optics. In combination with
a camera they provide fast, but more qualitative informations.

Recently the observation of optical transition radiation is used to measure
beam profiles. This with regard to other beam parameters powerful technique
is described in detail in the Sec. **??** of this chapter.

9.5.4.1 SEM Grid and Wire Scanners

A SEM grid will be used to measure the energy spread with good resolution.
The dispersion two meters behind the spectrometer dipole is 1.2 mm per
10^{-3} energy spread (at 800 MeV). The SEM grid will be composed of 40
wires of tungsten, 0.1 mm in diameter and 0.75 mm apart. This will allow
a measurement of a total energy spread in the range of some tenths of a
percent with 10^{-4} resolution. The grid should be retractable. Larger energy
spreads can be measured with OTR screens but with reduced resolution.

Wire scanners will measure the horizontal as well the vertical beam profile
in the non-dispersive section of the beam analysis area. The scanners must
cover a total excursion of some centimeters to have a safe parking position
far from the beam axis. The thickness of the carbon wire will be 10 μm to

get a resolution of the same size. The relative position of the wire must be known to better than 10 μm.

- Slow scan: To avoid too large scan times a dual speed scheme is proposed, either slower when crossing the beam or faster when approaching or withdrawing from the beam. The slower speed should be adapted to the beam size expected to get a reasonable number of samples; 50 samples within the FWHM is equivalent to 0.01 mm/s for a 10 μm spot (RMS value) and 1 mm/s for a 1 mm spot (RMS value), respectively. The Fermilab wire scanner redesigned for the linac upgrade might fulfill the requirements listed above.

- Fast scan: Flying wires are not fast enough to scan a large beam size. At present, a speed of 2 m/s can be realized corresponding to a maximum beam size (RMS value) to be scanned much smaller than 1 mm. Measuring with 2 m/s gets 12 samples per FWHM for a 10 μm spot (RMS value). The trigger jitter should be smaller than 10 % of the macropulse length. The features[4] of the LEP wire scanner might fulfill the requirements listed above.

- Synchronous scan: A rotating wire can move much faster than a flying wire. Such a device might be compared to a turbomolecular pump rotating with maximum 50000 cycles/min or more. It must be synchronizable with the repetition rate of the linac. The revolution frequency of the scanner must be adapted to the beam size expected. To scan a 10 μm spot (RMS value) 6 Hz (20 samples/FWHM) is sufficient. This calculation assumes a rotating disk with a radius of 10 cm. A lower frequency would cause problems with the heating of the wire. A higher frequency lowers the number of samples. For a 1 mm spot (RMS value) the frequency must be increased to at least 15 Hz (350 samples/FWHM) in order not to exceed the macropulse length. The use of a rotating device for slow scans is not recommended because the revolution frequency is very small ($< 10^{-3}$ Hz) implying a dual speed scheme as explained above but a much more complicated mechanism compared to a slow moving linear scanner driven by a stepping motor.

---

[4]K. Wittenburg, H. Schultz, TESLA report 94 - 15

All the techniques mentioned above might suffer from the heating by the beam.

A wire of a SEM grid is hit only by a small fraction of the beam. Only about 3.3 % of the particles passing the grid deposit energy in a 0.1 mm thick wire placed in the center of the beam profile. This calculation assumes that the grid is used to measure an energy spread of 10^{-3} at 800 MeV corresponding to a RMS beam size of 1.2 mm. The instantaneous heating of a tungsten wire by one macropulse is about 300 °C.

Analogous to the argument above, about at maximum 38 % of the particles of a macropulse during a slow scan hit the wire (beam size assumed: 10 μm (RMS value), wire thickness assumed: 10 μm). The resulting temperature rise per macropulse in a carbon wire would be more than 10^6 °C. Therefore, to measure small beam sizes the number of bunches per macropulse (injector II) should be lowered to one or two.

During a fast scan with a speed of 2 m/s about five bunches (injector II) hit a 10 μm thick wire while it moves a distance equal to its thickness, so that approximately $2.5 \cdot 10^{11}$ electrons will produce heat in the wire during one scan. The bunch charge is $5 \cdot 10^{10}$ electrons. The temperature of a carbon wire would increase to 16500 °C for a 10 μm beam spot (RMS value) which is much above the melting point (3500 °C). However, this is a conservative estimate because about half the energy lost is not deposited in the wire but carried off by knock-on electrons. The situation in the case of a rotating wire is similar.

Optionally, the OTR screens can be used to measure the beam profile but with worse resolution. In combination with a fast-gated camera bunch-by-bunch profiles could be recorded.

9.5.4.2   Scintillation Detectors

Above the critical energy of about $800/(Z + 1.2)$ MeV where Z is the atomic number of the target material, an electron loses energy in matter mainly by the emission of bremsstrahlung. The photons have an energy up to the beam energy and are emitted into a very narrow cone around the beam with an opening angle of about $1/\gamma$ with γ the Lorentz factor. The path of the photons and the electrons must be separated by a downstream bending magnet.

The cross section[5] for the emission of a 300 keV photon at a beam energy of 800 MeV for carbon is 2.65 barn/atom. For a 10 μm thick carbon wire the probability for an electron to emit a 300 keV photon is $2.92 \cdot 10^{-4}$. With a bunch of $5 \cdot 10^{10}$ electrons and a beam width of 10 μm (RMS value) about $5.6 \cdot 10^6$ photons will be emitted during one bunch passage with the wire centered on the bunch. For a 1 mm thick beam (RMS value) the corresponding number of photons is $5.8 \cdot 10^4$.

The photons emitted will be detected in a scintillation detector. The detection efficiency for 300 keV photons of a 1 cm thick plastic scintillator is about 10 %. About 3 - 5 % of the photon energy is converted to visible light producing about 6 secondary photons per absorbed photon. About half of these are lost or do not release a photoelectron from the cathode of the photomultiplier. This results in about 1 photoelectron per 3 incident bremsstrahlung photons. The number of photoelectrons is drastically increased by the photomultiplier (gain: 10^5 - 10^9) resulting in a reasonable signal.

9.5.5   View Screens and OTR Screens

A commonly used technique to visualize the beam are view screens in combination with a TV camera. The screens are placed in the beam path at 45 degrees to the beam axis. The luminous signals obtained from the screens when the beam passes them and viewed by the camera provides fast qualitative information on the beam profile and position. It is a very helpful tool during the set up of the optical elements.

A more recent technique uses the Optical Transition Radiation (OTR) generated when a beam passes the interface of media with different dielectric constants, e.g. a foil in the vacuum. There are both forward and backward lobes of radiation with an opening angle of $\pm 1/\gamma$, where γ is the Lorentz factor. The backward lobe angular distribution depends on the Fresnel reflection coefficients so that light exits at 90 degrees to the beam for a 45 degree orientation of the foil. The mechanism of the OTR generation might be viewed as the instantaneous collapse of an electric dipole when the electron in vacuum reaches the surface image charge in the medium. Since it is a

---

[5]A. Burns, J. Camas, E. D. Amico, G. Ferioli, Q. King, K. H. Kissler, J. Mann, R. Schmidt, 1989 IEEE Particle Accelerator Conference, Chicago, Il, USA

surface or transition boundary phenomenon, the effective spatial resolution given by the extension of the formation zone is excellent and the mechanism's vacuum formation time should be in the sub-picosecond domain. The photon yield per incident electron in the optical domain for particles in the range $\gamma \leq 1000$ is approximately 1 % and the spectrum is flat. Using an optical system with a variable focus either the beam profile (focus at the object, image plane) or the beam energy, the beam divergence and the energy spread (focus at infinity, focal plane) can be measured. The OTR pattern in the focal plane (angular distribution pattern) shows a doughnut structure. The opening angle is inversely proportional to γ and the width of the lobes is determined by the beam divergence and the energy spread. In combination with a fast-gated camera snapshots of the parameters mentioned above along the macropulse can be recorded.

The multiple scattering produced by either a view screen or an OTR foil impacts the beam quality. The resulting RMS angle behind a 0.5 mm thick aluminum screen at 500 MeV is about 2 mrad and 0.8 mrad for a 25 μm thick Kapton foil so that a simultaneous measurement at different screens along the beam line is impossible. For this reason, the screens or foils must be retractable.

Another problem is the heating by the beam. The instantaneous temperature rise per minimum ionizing electron is $2.7 \cdot 10^{-13}/F$ °C cm^2 for Kapton and $2.9 \cdot 10^{-13}/F$ °C cm^2 for aluminum where F denotes the target area. In the case of a 10 μm beam spot (RMS value) the bunch population has to be decreased to less than 1 % to avoid the destruction by the macropulse. A large spot of 1 mm (RMS value) allows to measure at full bunch charge.

9.5.5.1 Optical Diagnostic Stations: General Description

Two types of optical beam diagnostic stations are placed both in the experimental area and along the warm transport line: a complete one, allowing precise measurements of beam parameters, and a simpler and cheaper one, giving only visual information of beam position and dimension, to be used mainly in the commissioning phase.

Each complete diagnostic station is equipped with a stepping motor driven vacuum actuator carrying a fluorescent screen (Chromium doped ceramic target Cromex) and an Optical Transition Radiation (OTR) emitting screen.

The Cromex targets allow very sensitive and easy to use visual diagnos-

tics. They prove to be a valuable tool in the first stage of the commissioning, however they can easily give a non linear response at the linac full current, and the fluorescence decay time, ~ 10 ms, makes them useless when time resolved beam study is of concern. Moreover, survival of these screens when hit by a intense, well focused beam, is not assured.

The OTR screens are composed of a thin metallic layer deposited on a Kapton foil. The light intensity is much less than that from Cromex, but emission is instantaneous allowing time resolution in the range of picoseconds. In order to simplify the alignment of all optical elements and to check correct replacement of the OTR screens a laser beam will track the SC linac axis giving a reference line.

The schematic drawing of a diagnostic station is shown in Fig. 9.21. The target holder moves along a vertical axis; the screens are mounted one above the other, and their surfaces slides over a fixed plane at 45 degrees with respect to the beam line, so that the intersection point with the beam line is fixed in space. A horizontal window at right angle to the beam axis allows observation of the radiation.

During measurements the screens can be moved after each macropulse, in order to reduce cumulative surface damage due the beam power.

The emitted radiation is measured by means of a high linearity CCD camera. The measurements that can be performed and the required optics will be described later.

The simpler stations have a shorter fixed movement allowing only one screen to be inserted, normally a fluorescent Cromex target. The camera used to observe these screens are also of lesser quality, enough to assure a clear observation of the radiation, but unable to give very precise measurements.

A completely different geometry is required for the optical station at the focal point of the high energy spectrometer. Indeed, at this location the beam dispersion function is of the order of 1.2 m, so that, for an energy spread of 0.5 %, not a too large number in the initial phase, the beam will be spread over almost 3 cm in the horizontal plane.

This requires a larger screen, tilted around a horizontal axis and seen by a camera along the normal to the screen surface. On the other hand OTR will be emitted following the reflection law. To cope with these requirements, together with space constraints to allow also the presence of a wire scanner or a SEM grid, the station will be as in Fig. 9.22. Two different viewports are needed for fluorescent radiation and OTR.
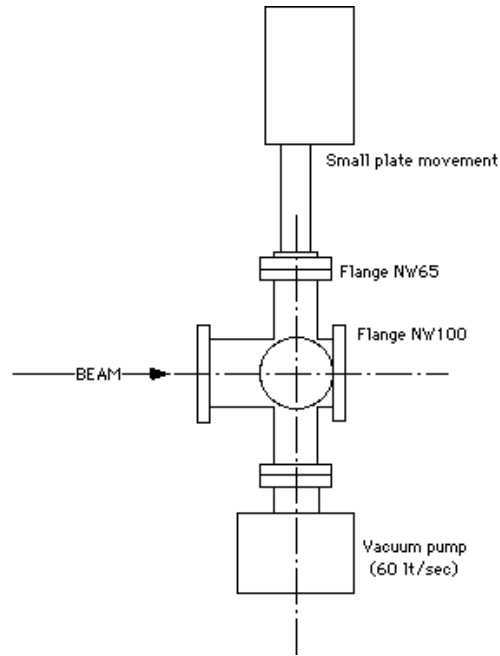
Figure 9.21:   Schematic drawing of a diagnostic station used in the temporary beam line and in the straight section of the Beam Analysis Area

All stations will carry ion pumps (of larger pump speed than the one near the cryostat exit) and, where required, ports for roughing pumps.

9.5.5.2   Beam Parameter Measurements

Measurements integrating the whole macrobunch

For this kind of measurements a free running CCD camera, locked to the main 50 Hz, with standard video output is used. The video signal is sent to a frame grabber which digitizes each image as a $512{\times}512$ 8 bit matrix. Simple analysis can be performed on line, and selected images are stored for off line study. The storing time (few seconds) does not allow a continuous recording, for this reason a standard video tape recorder will be also used.

Beam position and profiles can be easily measured both with fluorescent screens (at low current) and OTR radiators. The result of these measurements can be presented on-line on the console either in a graphical form or as
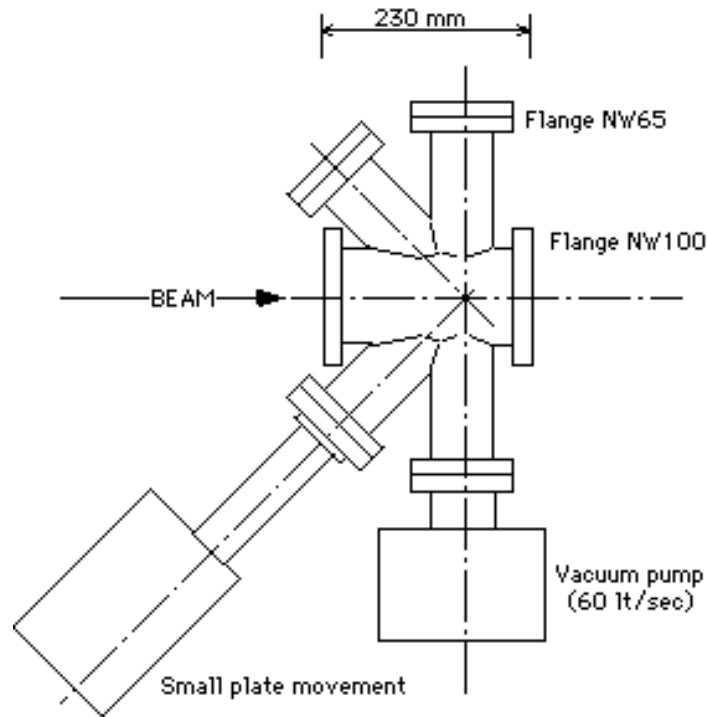
Figure 9.22:   Schematic drawing of a diagnostic station used in the spectrometer of the Beam Analysis Area

numbers for every pulse at a linac repetition frequency of 1 Hz or for sampled pulses at higher frequency.

Obtainable resolution is difficult to estimate; it depends on many parameters which are not well known, as optical transmission and conversion efficiency of the CCD on the whole radiation spectrum. But some remarks can be made, based on previous experience on similar devices.

Resolution is limited by many causes, but for fluorescent ceramic screens it is ultimately limited by non linear emission, granularity and thickness of the screen, to about 0.05 - 0.1 mm. For OTR radiators, if problems due to the formation zone width at high energy will not arise, the main limitation derives from the size of the spot image on the CCD sensor; that is, how many pixels it covers. For a 0.2 mm beam spot size, with a $\times 10$ magnification, a resolution of 1 micron on beam position and 10 microns on profiles should

be possible. Systematic errors, as wrong scaling, chromatic aberrations etc., can easily be larger, but, at least in principle, they could be compensated.

Larger spot size may require a smaller magnification factor, and this cannot be easily performed automatically. This means that the best resolution cannot be obtained for every measurement in a sequence in which beam spot size is greatly changed.

The same measurement, performed along the spectrometer arm, allows the evaluation of beam energy and energy spread. Due to the large dispersion, in this case a reduction of the image size is required, and the match between the spot width and the sensor size determines the resolution. A rough estimate says that, without particular optimization, a profile corresponding to an energy spread of 1 % can be measured with a resolution better than 10 %. The same resolution can be maintained, by changing the optics, down to an energy spread of 0.01 %. The corresponding energy spread resolution depends on the natural width (spot size of a monochromatic beam) at the measuring position.

Beam spot size measurements allow the evaluation of emittance and Twiss functions as described in Sec. 2.4.

A different set of measurements can be performed by looking at the angular distribution pattern of OTR. This can be achieved by positioning the CCD sensor in the focal plane of an optical system aimed at matching the angular aperture of the radiation, which depends on the energy, with the CCD dimension. Due to the polarization of OTR, filtering the radiation with a horizontal or vertical polarizer results in an effective separation of beam parameters in the two planes.

The OTR computed angular pattern from a 500 MeV electron filtered by a horizontal polarizer is shown in Fig. 9.23, while the projection on the horizontal axis is in Fig. 9.24. The distance between the two peaks, knowing the focal length of the optical system and the CCD dimension, gives directly the energy of the beam. From preliminary simulations it seems that with a good match of the optics a resolution of 1 % can be reached by a simplified fit to the intensity distribution. Some experimental work is needed, and systematic errors must also be analyzed.

From the same distribution, which for a real beam will be a convolution over particle phase space, by means of a more elaborate fit, it is possible to evaluate also energy and angular spreads. Although energy spread can be measured better in the spectrometer, this is the only way to measure the
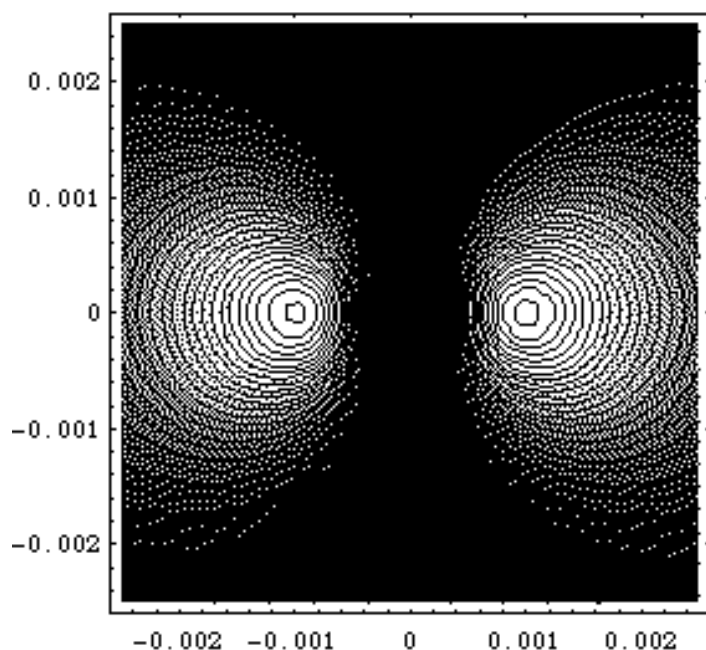
Figure 9.23:   Calculated angular OTR pattern emitted from a 500 MeV
                 beam filtered by a horizontal polarizer

beam angular spread. Spreads of the order of 15 - 20 % of the radiation
angular aperture can be measured, so it is convenient to have a beam waist,
at least in the plane in which the measurement is performed, on the screen.
With a simultaneous measurement of the spot size (by means of the same
camera for a different pulse or by a second one for the same pulse) emittance
can be evaluated in an almost on-line way.

Time resolved measurements

Measurements of beam parameter variations along the macropulse can
only be performed by use of OTR. Taking into account the micropulse time
structure of injector 2, it has been decided to consider 1 microsecond the
minimum required resolution, so that we can integrate the radiation in such
a time span.

An optical gate of this speed can be obtained by the use of an intensi-
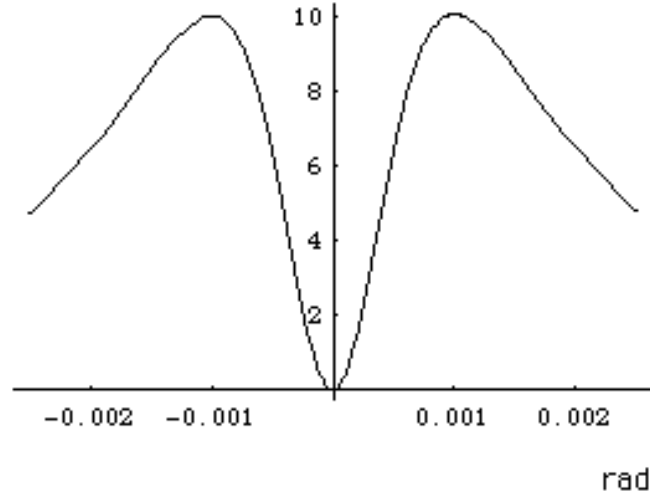
Figure 9.24:   Calculated angular OTR pattern emitted from a 500 MeV beam filtered by a horizontal polarizer and projected on the horizontal axis

fied CCD camera. The multichannel plate intensifier (MCP) allows an easy electronic gate with a very high rejection rate.

A single image for each macrobunch can be acquired, so that a time scanning along successive macrobunches must be performed, assuming that beam parameters can be kept stable for the measuring time.

All the measurements previously described can be carried out with this camera. It is thus possible to follow the evolution of beam position, profiles, energy and energy spread.

Resolution in this case is not limited by the CCD, but by the intensifier, and become worse at higher gain. For this reason the amplification factor must be kept as low as possible compatible with a good signal-to-noise ratio.

With a gate length covering the whole macrobunch it is also possible to

make OTR measurements at very low current.

Beam position and profiles variation along the same macrobunch will be measured by means of a different instrument. OTR beam spot will be imaged on the cathode of a multianode PMT (Hamamatsu H4140-20 whose anode is segmented in a 16×16 matrix) with parallel readout. A 40 kHz image recording is possible, giving up to 32 images for a single macrobunch. Simple, but accurate, simulations show that the resolution on beam relative position can be 1 % of beam dimension, and that the spot size can be measured with a 10 % resolution. To obtain these results a well matched optics is required.

These resolutions are worse than that obtainable from an intensified camera, but in this way beam loading or RF effects can be measured even in presence of slight bunch-to-bunch instabilities.

A high resolution single line CCD camera (Thomson TH7804 with 1000 pixels in 1.5 cm) will also be used to record at 20 kHz energy and energy spread evolution in the spectrometer. In this case resolution is limited by the signal to noise ratio that can be obtained integrating 50 microseconds of OTR radiation on a standard CCD line.

9.5.6   Synchrotron Light Monitor with the Bending Magnet

In addition to the OTR beam profile monitors described in Sect. 9.4.4, a measurement using optical detectors together with the synchrotron radiation (SR) from a bending magnet is possible. Such a measurement includes the determination of the beam profiles as well as the beam divergence although the resolution in divergence is clearly limited by the natural opening angle of the photon beam ($\sim 1/\gamma$).

Investigating the SR from a dipole magnet the first aspect to consider is the power of the photon beam as a function of the electron beam energy and the magnet bending radius. The spectral power $P(\lambda)$ [W/Å mA mrad] is given by[6]

$$P(\lambda) = 3.92 \cdot 10^{-30} \cdot \gamma^{-8} \cdot \left(\frac{\lambda_c}{\lambda}\right)^4 \cdot K_{2/3} \cdot \left(\frac{\lambda_c}{2\lambda}\right) \cdot \frac{1}{r^2} \cdot \frac{1}{\gamma}$$

---

[6] H. Winick, Properties of Synchrotron Radiation, in: Synchrotron Radiation Research, eds. H. Winick and S. Domiach (Plenum Press., 1980) p.11.

with the critical wavelength

$$\lambda_c = 4\pi r/3\gamma^3$$

γ being the electron beam Lorentz factor, the Bessel function $K_{2/3}$, and the bending radius r. This spectral power relates to an 1 mrad acceptance angle of the optical detector. So, in Fig. 9.25 the integrated spectral power for three different wavelength regions is shown as a function of the electron beam energy; the bending radius was chosen to be 3.2 m, this corresponding to the above described dipole magnet. Figure 9.26 gives the same integral, but now as a function of the bending radius and for a constant electron beam energy ($\gamma = 1000$). Both figures emphasize that the photon beam power, emitted in a part of the visible wavelength region, easily exceeds a few μW, considering a macro pulse current of some mA and acceptance angles in the order of 10 mrad. Assuming a constant sensitivity in the 555 nm region, a 1 l×1/2 inch^2 CCD camera detects 0.185 μW.

In precise optical imaging of SR it is necessary to more or less monochromate the light. Typically a band pass filter with a 500 nm center wavelength and 30-40 nm bandwidth is used. However, going to slightly shorter wavelengths would be of advantage since here the spectral power increases; the critical wavelength λ_c is usually in the UV.

The resolution of profile measurements using SR is strictly limited by fundamental effects. One has to consider the depth of field error, the diffraction error, and the curvature error. The influence of the error terms on the resolution differs between the horizontal and vertical plane[7]

The depth of field error is a consequence of the bunch length and occurs from the imaging of the SR. It depends upon the acceptance angle of the optical detector. The depth of field error is given by

$$\Delta_{df} \approx \frac{L}{2}\theta$$

where $L \approx 2r \cdot (\theta + \psi_{SR})$ is the source length, i.e. the apparent bunch length. The angle θ is half the acceptance angle of the detector, r is the magnet bending radius or electron orbit radius, and

[7]J. A. Clarke, A Review of Optical Diagnostics Techniques for Beam Profile Measurements, EPAC 94, London, to be published.
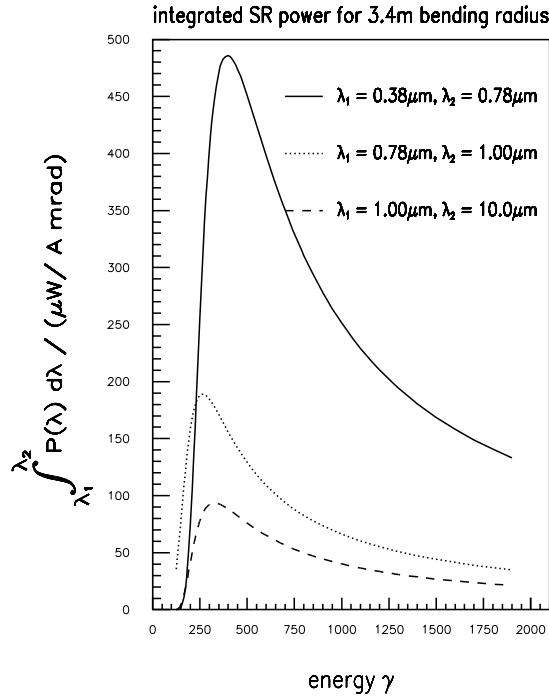
Figure 9.25:   The integrated spectral power for three different wavelength
                regions as a function of the energy. The magnet bending
                radius is 3.4 m.

$$\psi_{SR} = \left(\frac{3\lambda}{4\pi r}\right)^{\frac{1}{3}}, \lambda \gg \lambda_c$$

is the natural opening angle of the photon beam.

Since the imaging of the SR involves apertures, a diffraction error has
to be taken into account. Depending on the selected aperture type, the
diffraction resolution for a circular iris is given[8] as

---

[8]A. Hoffmann and F. Meot, Optical Resolution of Beam Cross- Section Measurements
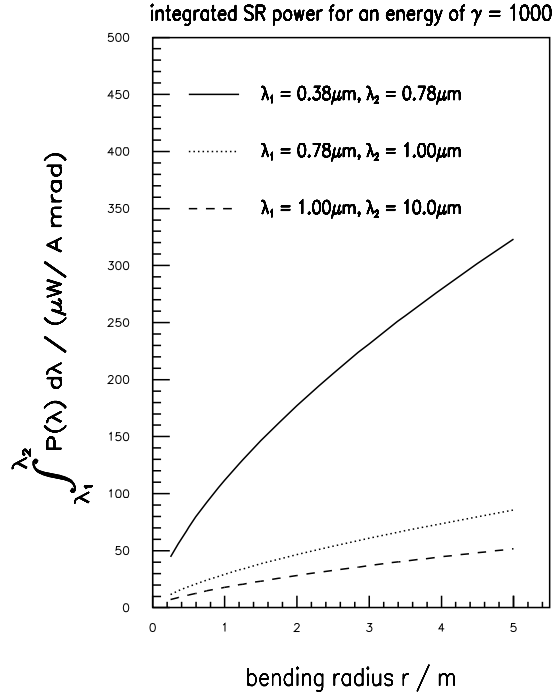
Figure 9.26:   The integrated spectral power for three different wavelength regions as a function of the bending radius. The electron beam energy is $\gamma = 1000$.

$$\Delta_{diff,iris} = 0.61\frac{\lambda}{\theta},$$

and for a vertical slit as

$$\Delta_{diff,slit} = 0.5\frac{\lambda}{\theta}.$$

by Means of Synchrotron Radiation, Nucl. Instr. Meth., 203 (1982), pp. 483 - 493.

The vertical slit clearly gives the better resolution.

In addition to the just mentioned errors, limiting the resolution of measurements in both, the horizontal and vertical plane, the curvature of the electron bunch along the orbit also contributes an error term. But as it will be shown below, only in the horizontal plane. The apparent width of the source, i.e. the electron bunch, is straight forward to derive (see also Fig. 9.27):

$$\Delta_{curv} \approx \frac{r\theta^2}{2}$$

where again r is the electron orbit radius and θ half of the acceptance angle.
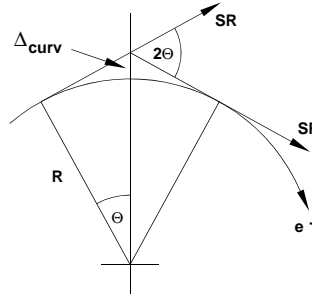
Figure 9.27: Curvature error sketch

So, for a particular wavelength λ, the best resolution is found by minimizing the sum of the square of the three error terms. Figure 9.28 shows the resulting imaging resolution as a function of the half acceptance angle θ, here for a certain bending radius of $r = 3.4$ m, at a wavelength of $\lambda = 500$ nm,

and using a vertical slit for measurements in the horizontal plane. The best imaging resolution (≤ 100 μm) can be achieved with a half acceptance angle $\theta \approx 3.9$ mrad. Figure 9.29 emphasizes the imaging resolution as a function of the bending radius and optimized with respect to the angle θ.

r = 3.4 m, λ = 500 nm, Ψ$_{SR}$ = 3.27 mrad
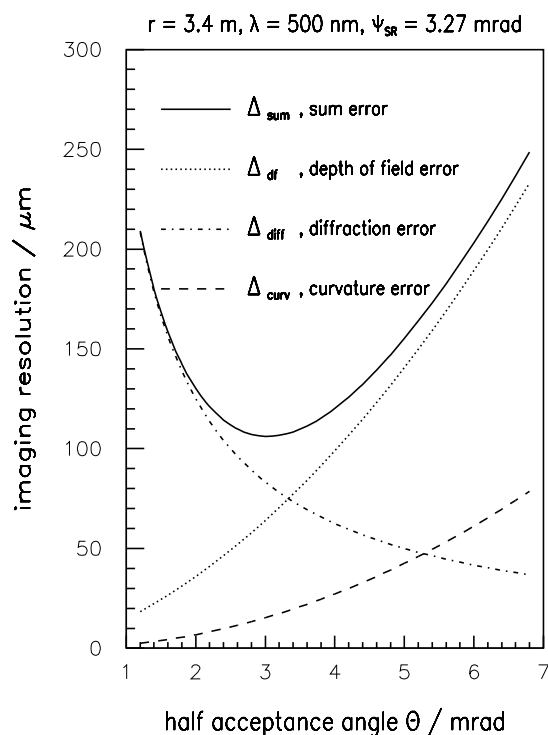
Figure 9.28:   The imaging resolution as a function of the half acceptance angle θ. The different error contributions are shown as well as the sum error. The magnet bending radius was chosen to be r = 3.4 m, the wavelength as λ = 500 nm.

In order to minimize the effect of diffraction, one can choose a defined polarization of the SR. The polarization properties of SR can be described with two components: one parallel to the deflection plane (δ or $\parallel$ component); one perpendicular to the deflection plane (π or $\perp$ component)[9]. The perpendicular component should be suppressed by using polarizers[10] in order to get a sharper image.

---

[9] A. A. Sokolov, I. M. Ternov, *Synchrotron Radiation*

[10] C. Bovet, M. Placidi, *A dedicated Synchrotron Radiation source for LEP beam diagnostics*, LEP Note 532 (1985).
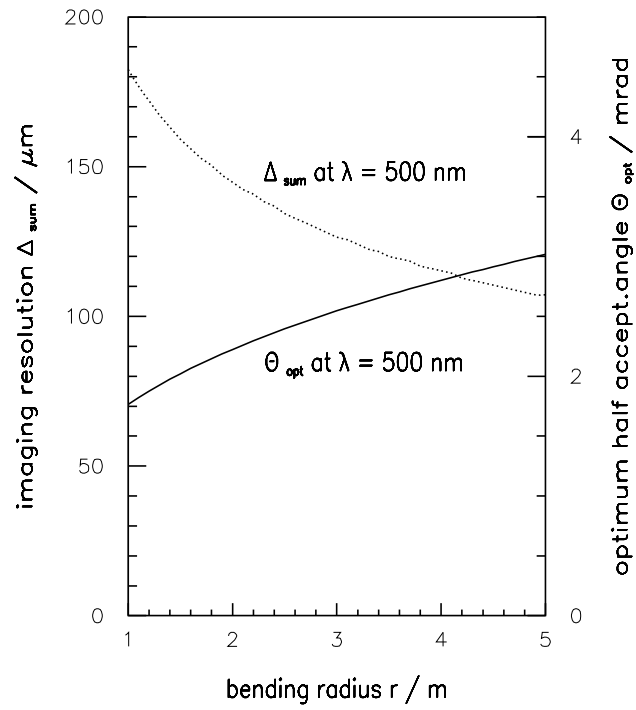
Figure 9.29: The imaging resolution (dotted line) as well as the optimum half acceptance angle as a function of the bending radius.

In the vertical case the depth of field error and the diffraction effects are no longer in the same plane. Beside limiting the depth of field, there is no reason to introduce apertures into the system. Any vertical acceptance limit would introduce unnecessary broadening due to diffraction. Therefore, in the vertical plane, it is most advantageous to use a vertical slit instead of the circular iris. The minimum diffraction error is then determined by the natural opening angle of the source. But anyhow, since the half acceptance angle θ in Fig. 9.28 is close to the natural opening angle ψ_{SR}, there is only a slight improve in the imaging resolution when going from the horizontal to the vertical plane.

In order to summarize the discussion about measurements of beam profiles using SR, the following parameters for a setup could be envisaged. At an energy of $\gamma = 1000$, and a bending radius of $r = 3.4$ m, the integrated power in a 50 nm wide wavelength region centered at 500 nm would be approximately 30 μW/A mrad. The best imaging resolution (≈ 90 μm) would be achieved with a full acceptance angle of 2$\times$3 mrad. So, the photon beam power of an 8 mA average current electron beam would be 1.44 μW. Assuming some losses in the optics system, the above mentioned sensitivity of a CCD camera seems to be sufficient. But in order to examine lower bunch charges as well, a higher sensitivity should be chosen.

In comparison with OTR , SR provides an important tool to get information about beam properties without interference with the machine operation. SR will be produced parasitically. Its broad spectral range allows the use of various instruments for beam monitoring. Since the maximum of the power spectrum is located at short wavelengths, the impact of diffraction can minimized.

9.5.7   Bunch Length Measurements

9.5.7.1   Streak Cameras

Streak cameras offer the unique feature to resolve the time structure of very short light pulses. A streak camera consists of a photocathode, a high speed sweeping device deflecting the photoelectrons released from the cathode, a microchannel plate based image intensifier, a phosphor screen and a high resolution CCD camera.

At TTF the design electron pulse length is 3.3 ps (RMS value). This

Table 9.7:   Parameters of sub - picosecond streak cameras available

	Hamamatsu FESCA-500	**Hadland Photonics FS 300**
temporal resolution / fs	600	300
streak time (full screen) / ps	60 - 1200	70 - 700
trigger jitter / ps	$< \pm 30$	$< \pm 15$
maximum repetition rate / kHz	1	5
estimated costs / kDM	380	250

pulses irradiate light of the same pulse length as OTR at the surface of foils or as synchrotron light from the spectrometer magnet. For this report a comparison of streak cameras presently existing was performed. Two vendors, Hamamatsu (Japan) and Hadland Photonics (United Kingdom), are able to provide a streak camera with a temporal resolution of some 100 femtoseconds. The temporal resolution is defined as the FWHM of the response curve of the streak camera to a infinitesimally short light pulse. Table 9.7 lists the technical specifications of the two cameras as specified in the corresponding data sheets.

9.5.7.2   Bunch Length and Longitudinal Shape Measurement

Measurement of the bunch distribution will be critical in assessing the operation of the linac injector. Control of the final focus and beamstrahlung will ultimately require good control and knowledge of the bunch distribution function. Fortunately a method for making the needed measurements has recently been developed[11] [12] [13]. The method relies on the excitation of some form of coherent radiation by the bunch, be it synchrotron, transition or Čerenkov radiation, and the fact that the spectrum of that radiation is sensitive to the bunch distribution function. The measurement consists in

---

[11]R. Lai and A. J. Sievers, *Determination of a charged particle bunch shape from the coherent far IR spectrum*, to be published.

[12]E. Blum, U. Happek and A. J. Sievers, Nuclear Inst. and Methods Phys. Res. Sect. A 307, 568 (1991).

[13]U. Happek, E. Blum and A. J. Sievers, PRL 67, 2962 (1991).

taking the spectral distribution by means of a scanned Michelson interferometer and applying a mathematical deconvolution procedure to extract the shape. Figure 9.30 shows the results from two scans of the Cornell linac beam under different conditions[14].

---

[14]R. Lai, U. Happek and A. J. Sievers, *Measurements of the longitudinal electron bunch shape using coherent synchrotron and transition radiation*, to be published

Synchrotron–08129404(b2)

Synchrotron–08129408(b2)
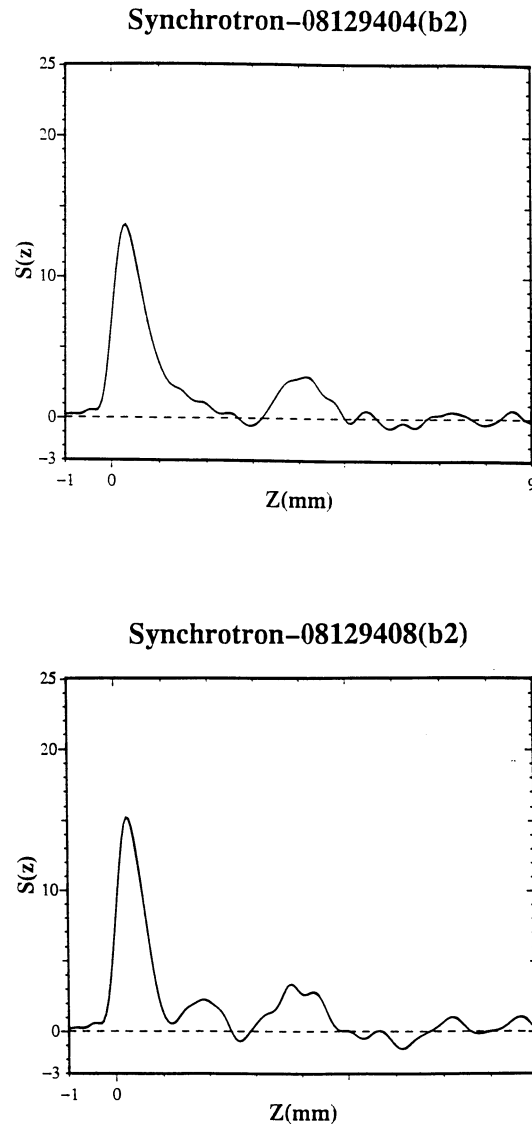
Figure 9.30: Spectral distribution from two scans of the Cornell linac beam under different conditions

Since the intensity of the radiation is only logarithmically dependent on the electron kinetic energy the method can be applied to beams of energy from a few hundred keV up through full linac energy. Bunch lengths (rms) from about 2 mm down to the micron region can be accommodated, the resolution improving as bunch length decreases.

Coherent synchrotron radiation from the injector or high energy analyzer magnets could be used for the measurements or it might be more convenient to use the transition radiation from a foil that can be inserted into the beam at the location of the phosphorescent flags. The foil of conducting material should be angled at 45 ° to the beam with a window of, preferably, crystalline quartz to pass the far infrared radiation out from the beam vacuum envelope. The axis of the window should be perpendicular to the beam line and pierce the foil at the point where the passes through.

A portable apparatus including the interferometer, detector and control/analysis computer exists at Cornell and should be used for initial measurements of the injector performance at Saclay/Orsay and again at DESY. It should be also used as a model from which to construct a permanent apparatus for the TTF should that be deemed desirable after demonstration in situ. The portable unit occupies an area of about one meter on a side. If placed in a horizontal plane the apparatus occupies about one half meter in the vertical direction. If the envelope of the apparatus is thought of as a parallel piped, the coherent radiation beam line passes through the geometric center of the figure, parallel to one edge. Figure 9.31 is a schematic diagram of the instrument.
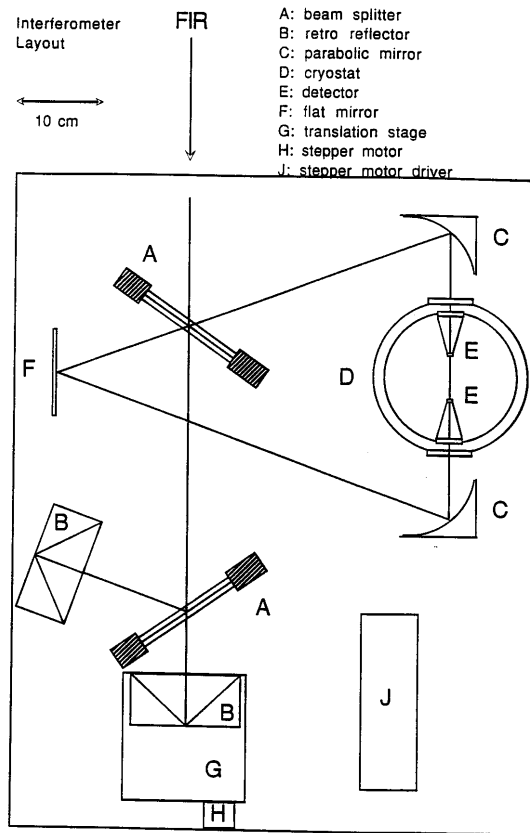
Figure 9.31: Schematic diagram of the Michelson Interferometer

9.5.7.3 Transverse Deflecting Cavity

Bunch length measurements using a transverse deflecting cavity need the RF cavity itself and a long drift followed by an imaging screen. Having installed only the first out of the four cryomodules one could think about carrying out such a measurement. Therefore we describe the technique as well as we will give the parameter for such a setup.

With an interest in measuring pico second long electron pulses, there is the demand for a GHz-oscilloscope. Since the bunch repetition rate is a sub-harmonic of the linac operating frequency (1.3 GHz) but at the same time still a high frequency (in our case either 1 MHz or even 217 MHz), a transverse deflecting field at 1.3 GHz would be suitable for an average bunch length measurement. Assuming a cavity to screen distance of 15 m and aiming for a projection length of 1 mm per 1 ps, an angle velocity of 1/15 mrad is needed. A time periodic magnetic dipole field $B = B_0 \sin(\omega t)$ causes a deflection $\alpha(t) = \alpha_0 \sin(\omega t)$, so that the angle velocity $\omega \alpha_0 = 1/15$ mrad gives an amplitude $\alpha_0 = 8.16$ mrad. From the magnetic rigidity $\overline{B}\rho(200 \text{ MeV}) = 667$ kG cm and with the magnetic field averaged over half the RF period, $\overline{B} = 2B_0/\pi$, one calculates the need for 1048 kG cm per 10^3 mrad deflection angle. Therefore, the amplitude B_0 amounts to $B_0 = 0.073$ T.

For the TM_{110} mode cavity, the electric field amplitude and the above magnetic field are connected by $E_0 = (\omega/3.83 \text{ m}^{-1})B_0$ from which we calculate $E_0 = 156$ MV/m. With a typical shunt impedance $R_S = 5$ MΩ and the cavity length $\lambda/2 = 0.115$ m one finally gets the average RF power for for a 1% duty cycle operation $\overline{P} = 162$ kW. This power scales with the beam energy squared,

$$\overline{P} \approx 160\text{kW} \left(\frac{\text{E[MeV]}}{200} \right)^2,$$

so depending on the efforts for the construction of the needed cavity, a bunch length measurement behind the first module at moderate energies seems to be possible only at very moderate energies. The energy of 200 MeV chosen above is clearly too high. At an average power of a few 10 kW the construction of deflecting cavity starts to become difficult.

Although going to a multicell cavity reduces the needed RF power, the construction of a deflecting cavity is not planned so far. The use of OTR seems to be more applicable for bunch length measurements at higher energies.

9.5.8   Beam Loss Detection

Besides posing a radiation safety problem, beam loss provides an additional heat load to the cryogenic system, e. g. a permanent loss of about 0.1 % along

the linac already saturates the capacity of the He refrigerator. Therefore, to protect the linac itself as well as the environment a beam loss detection system is a necessity.

A wealth of different beam loss detection systems exists. Most of them are based on ionization chambers (standard-type or Panofsky-type chambers). Others detect the scintillation or Čerenkov light emitted from the glass tubes of photomultipliers or secondary electrons emitted from special photocathodes. All these systems need a high-voltage supply. At TTF three types of low-voltage detection systems are planned:

- Measurement of the global transmission through the linac by two identical current transformers in front and behind the linac. These monitors are described in the Sec. 9.5.1

- Measurement of beam losses at the collimators of the injector beam transport line by arrays of four photodiodes sensitive to X-rays produced by electrons of some MeV. This system is described in Chapter 3.

- Measurement of local beam losses by a distributed detection system based on the HERA beam loss monitors.[15]

A HERA beam loss monitor is formed by two reverse biased PIN photodiodes (Siemens BPW 34) mounted face-to-face and operated in coincidence technique. Charged particles crossing both diodes produce coincident signals with a high efficiency. However, detected photons produce signals only in one of the two diodes. In this case, the coincidence rate is proportional to the photon counting rates in both diodes and the length of the coincidence time gate. An additional suppression of the synchrotron light background with lead shielding is possible. The signal of each diode is individually two-fold amplified by a low-noise amplifier and a following video amplifier. To suppress the noise a threshold can be specified. Table 9.8 summarizes the parameters of a HERA beam loss monitor.

---

[15] K. Wittenburg, NIM A 345 (1994) 226-229 and references therein.

Table 9.8: Parameters of a HERA beam loss monitor

active size / mm^2	2.75×2.75
total volume / cm^3	$5 \times 5 \times 5$
radiation hardness level of diodes / rad	5×10^5
bias voltage / V	24
detection efficiency of charged particles	0.3
decay time of low noise amplifier / ns	< 100
dark current counting rate / Hz	< 0.01
maximum counting rate / MHz	10
output signal	TTL

Example:

- 1 % permanent beam loss, losses equally distributed along the linac

- every lost particle leaves the cryostat, no absorption, no beam spray

- detector placed in a distance of 2 m from the beam axis

counting rate:

- injector I: 1 count every 280 ns (per 62 bunches)

- injector II: 5 counts every 1 μs (per bunch)

9.6   Radiation Shielding and Beam Dumps

9.6.1   Shielding along the TTF Linac

Based on the TTFL parameter list, the shielding for the linac with its 500-800 MeV maximum electron beam energy has to be calculated according to the German safety regulations[16]. Two comprehensive[17] [18] publications

---

[16]Strahlenschutzverordnung 1989, Bundesanzeiger Verlags-Ges. mbH, Köln.

[17]H. Dinter et al., Calculations of Doses due to Electron-Photon Stray Radiation from a High Energy Electron Beam behind Lateral Shielding, Rad. Prot. Dosimetry Vol. 25 No. 2, pp. 107 – 116, (1988).

[18]K. Tesch, Shielding Against High Energy Neutrons from Electron Accelerators - A Review, Rad. Prot. Dosimetry, Vol. 22 No. 1, pp. 27 - 32, (1988).

emphasize the requirements for scattered radiation.
Considering the following operating parameters

$$
\begin{aligned}
\text{E} &= 800 \text{ MeV} \\
\text{N}_e \text{ / macro pulse} &= 4\times 10^{13} \text{ e}^- \text{ / pulse} \\
\text{f}_{rep} &= 10 \text{ Hz} \\
\text{N}_e \text{ / second} &= 4\times 10^{14} \text{ e}^- \text{ / second} \\
\\
\Rightarrow \quad \overline{I} &= 6.4\times 10^{-5} \text{ A} \\
\text{P} &= 51.2 \text{ kW}
\end{aligned}
$$

one can calculate the dose per lost electron behind some shielding material. Important for this calculation is the fact that detailed calculation prove the independence of the dose behind various thicknesses of the absorber material. This is valid up to a thickness $X_a \times \rho = 75$ g/cm^2 at which the exponential decay starts.
The dose per electron H/e$^-$ gives the dose per macro pulse H/m.p.

$$
\text{H/e}^- \times 4\times 10^{13} \text{ e}^- \text{ / pulse} \longrightarrow \text{H/m.p. [Sv]}.
$$

The dose per macro pulse H/m.p. gives the total dose H/m.p. per time

$$
\text{H/m.p.} \times 10 \text{ s}^{-1} \times 3600 \text{ s/h} \longrightarrow \dot{\text{H}}_{tot}[\text{Sv/h}].
$$

So, the results of the calculation can be written down for different shielding material (OC: ordinary concrete, HC: heavy concrete) and thickness. Table 9.9 gives the dose per electron H/e$^-$, the dose per macro pulse H/m.p., and the number of macropulses which result in a total dose of 15 mSv. The last two columns give the total dose per time for a point like loss of 1 % of the electron beam current and for a 1 % loss equally distributed along the TTF linac. All values are calculated for the maximum beam energy of 800 MeV.

According to the safety regulations, the one year (2000 working hours) integrated dose must be less than the above mentioned 15 mSv ('Betrieblicher Überwachungsbereich'). Thus the dose per hour must not reach the level of $\dot{\text{H}}$ $\approx 10^{-5}$ Sv/h assuming that the TTF Linac will not be operated at maximum energy for the whole 2000 hours of the working year.

In order to draw conclusions for the results given in Tab. 9.9 , one has to investigate three different cases. Case 1 is the loss of the complete macro pulse at some certain point. Case 2 is the permanent loss of 1 % of the beam

Table 9.9:

shielding		1 e⁻	1 macro pulse		1 % spot	1 % eq. distr.
mat.	d	H/e^-	$H/\text{m.p.}$	$N_{m.p.}/$	$\dot{H}$	$\dot{H}$
	cm	Sv	Sv	15 mSv	Sv/h	Sv/h
OC	80	4.1×10^{-19}	1.6×10^{-5}	900	5.7×10^{-3}	5.7×10^{-4}
	120	5.4×10^{-20}	2.2×10^{-6}	7000	7.6×10^{-4}	7.6×10^{-5}
	160	1.1×10^{-20}	4.4×10^{-7}	30000	1.5×10^{-4}	1.5×10^{-5}
	240	8.7×10^{-22}	3.5×10^{-8}	30000	1.2×10^{-5}	1.2×10^{-6}
HC	80	1.0×10^{-19}	4.0×10^{-6}	4000	1.4×10^{-3}	1.4×10^{-4}
	120	1.3×10^{-20}	5.2×10^{-7}	30000	1.8×10^{-4}	1.8×10^{-5}
	160	2.2×10^{-21}	8.8×10^{-8}	30000	3.1×10^{-5}	3.1×10^{-6}
	240	8.6×10^{-23}	3.4×10^{-9}	30000	1.2×10^{-6}	1.2×10^{-7}

current or beam power at some point and Case 3 the permanent loss of again 1 % of the beam current equally distributed along the linac.

Case 1 Considering the injection of a full macropulse (800 μs) at maximum bunch charge (Q = 5 · 10^{10} e⁻/bunch), i.e. an average current in the macropulse of $\overline{I}_{m.p.} = 8$ mA or an overall average current of $\overline{I} = 64$ μA, and assuming e.g. a power supply break down, then no beam will exit the linac. A 100 % loss will occur. In this situation two integrating current transformers of the above described toroidal type, one placed at each end of the linac, will detect the total beam loss within 1 μs. After signal processing and transport to the gun high voltage terminal, the gun bias voltage can be switched in order to inhibit further emission. Since there are involved only small capacitors (current transformer, relatively simple analog electronics, and a few nF for the bias controller) the time between the actual beam loss and the end of electron emission should be less than 10 μs which is equal to approximately 1 % of the macro pulse length. For heavy concrete shielding this corresponds to going from 80 cm shielding thickness to almost 2 m (see Tab. 9.9), and therefore one could in principle accept a huge number of sudden beam loss events until 15 mSv are reached.

Case 2 The assumption of permanently losing 1 % of the beam at one point

somewhere along the linac (see Tab. 9.9) is not realistic. This would be a beam loss power of a few hundred Watts (see below, case 3) at one spot which one anyhow cannot accept for the linac operation. One certainly has to take care of this situation by using the beam loss monitors described earlier, i.e. a set of detectors distributed along the TTF linac.

Case 3 The last but most important point to consider is the equally distributed loss of the beam. Any of such a loss in the cryostat has consequences for the cavity cooling. Additional refrigeration power is needed.

For electron beam energies of a few 100 MeV the energy loss ΔE per material thickness x can be estimated as

$$dE/d(\rho \text{ x}) = 2 \text{ MeV/g cm}^{-2} \text{ with } \rho_{Nb} = 8.6 \text{ g cm}^{-3}.$$

Assuming a beam loss in a cavity one easily gets a niobium thickness of 1 cm, e.g. at the iris or when passing through several cell walls. Thus, losing the total bunch charge (average beam current of $\overline{I} = 64$ μA) at one certain point would cause a power deposition of P $\geq$ 1 kW/cm with $\Delta E \approx 17$ MW/cm. A transmission of less than a part per thousand would be non-negligible since these 0.1 % losses would require several Watts of additional refrigeration power at 2 K as well as at higher temperatures.

On the other hand a beam loss of less than 0.1 % gives a dose per unit time of less than 1.4×10^{-5} Sv/h for a HC shielding of 80 cm thickness. This is the above mentioned and by the safety regulations required level.

The conclusion to be drawn from these three cases is that starting at the gun area and all along the TTF linac a 80 cm HC shielding is sufficient. This is of course not valid for the beam dump area; this will be discussed in Sect. 9.6.2. The resulting layout of the shielding is shown in Fig. 9.32.

tunnel width		6500	5200	1200	5000	5800	6400
tunnel height		2000	2500	1600	2500	3300	3300
wall thickness	3200	1600	800	800	800	800	800
roof thickness	> 3200	1600	800	800	800	800	800
[mm]							
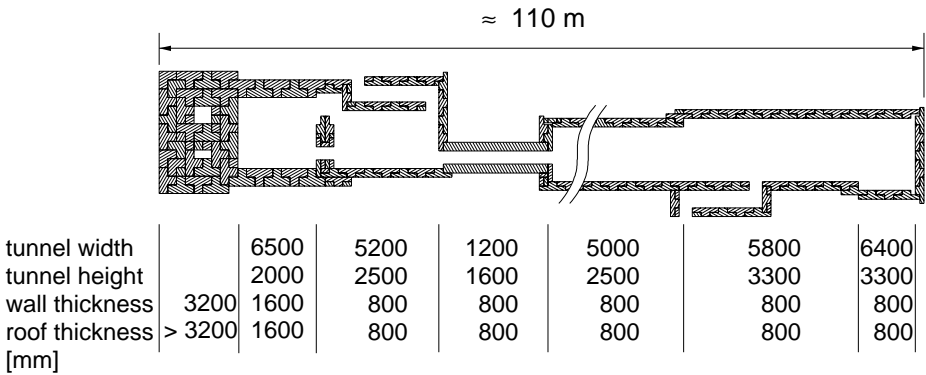
Figure 9.32:   The resulting layout of the shielding. A second exit in the
                5 m wide section is not shown here.

9.6.2 Beam Dumps

The beam dump of the test facility must be capable of absorbing an average beam power of 51 kW at a beam energy of 800 MeV. The average power is comparable to existing beam dumps (Tab. 9.10). However, the low duty factor of the TTF (10 bunch trains per second with a length of 800 μs each) leads to a strong temperature rise in a narrow beam cone inside the absorber material. The high beam energy per bunch train presents at least a lower limit for the beam dimensions at the surface of the dump block (or at the surface of a possible spoiler). Two different dump designs have been under discussion — the so called sphere dump[19][20] and the classical scheme of a solid dump block with optional spoiler [21][22][23].

Table 9.10: Beam parameters of several machines (E_{mac} is the beam energy per macro pulse).

machine	E_{beam} [GeV]	N_{mac}	P_{avg} [kW]	E_{mac} [kJ]	type of dump
SLAC	18	10^{12} (180 Hz)	500	2.8	sphere ($Al + H_2O$)
MAMI	0.84	CW	84	–	sphere ($Al + H_2O$)
SLAC	50	$5 \cdot 10^{10}$ (180 Hz)	72	0.4	solid ($Al + Fe$)
CEBAF	0.6	CW	96	–	solid ($Al + Cu$)
LEP	100	$7 \cdot 10^{12}(1\times)$	–	106	solid ($Al\,Cu$ alloy)
TTF	0.8	$4 \cdot 10^{13}$ (10 Hz)	52	5.1	solid

The sphere dump consists of a hollow cylinder which is filled with a closely packed bed of aluminum spheres. The bed of spheres is continuously cooled by circulating water. The advantage of this design is the very efficient cooling of the spheres due to the high surface to volume ratio. The sphere dump is therefore well suited for very high average beam powers. Furthermore the solution is relatively easy to manufacture and cheap. The most impor-

---

[19]D. R. Walz, L. R. Lucas, *The Sphere Dump — A New Low Cost High-Power Beam Dump Concept*, SLAC-Pub. 555 (1969)

[20]G. Dimmer, *Entwurf der Strahlfänger für MAMI B*, diploma thesis (1988)

[21]D. R. Walz, A. McFarlane, E. Lewandowski, *Beam Dumps, Stoppers and Faraday Cups at the SLC*, LAC-Pub

[22]C. Sinclair, private communication on the CEBAF beam dump (1994)

[23]E. Carlier, et al, *The LEP Beam Dumping System*, CERN SL/94-49 (1994)

tant disadvantage, however, is the large amount of direct power deposition in water. This leads to radiolysis and production of a considerable amount of hydrogen which must be removed by catalytic recombiners (production rate $3 \cdot 10^{-4}\,l\,H_2$ per kJ of in water deposited power. An even more unpleasant problem arises from the production of radioactive isotopes in the water cooling system. Among short living isotopes as O^{15} are some with longer lifetimes as Be^7 which could steadily built up and make the servicing of the system very complicated. On the other hand the moderate average power of the TTF beam does not demand the usage of a sphere dump under any circumstances. An edge cooled solid dump block seems to be a better solution. Such a solid dump is usually made of a low Z material like aluminum in order to achieve a moderate energy loss per unit length. The end of the dump should be backed up with a short copper section in order to absorb the residual radiation. The outer surface of the cylinder is cooled by circulating water. The amount of direct beam power, deposited in the water, is therefore reduced by several orders of magnitude, compared to the sphere dump. The extraction of the average power will present no problem and the parameters of the SLAC design with respect to the water cooling requirements can probably be overtaken. This dump is cooled by a helical water flow channel on the radial surface with a water flow of 1.25 l/s. For a good cooling efficiency it is important to have a highly turbulent flow.

However, in case of the TTF a special problem is presented by the large temperature rise and unacceptable high stresses in the small volume of the beam cone during the passage of a bunch train.

9.6.2.1   Estimate of Dump Heating and Stresses

We consider a solid aluminum cylinder of radius b. The incident beam initiates an electromagnetic shower in the material which leads to a certain distribution of deposited power $Q(\vec{r}, t)$ in space and time. The resulting temperature distribution in the absorber block is obtained as a solution of the heat equation:

$$\frac{\partial}{\partial t} T(\vec{r}, t) = \frac{\lambda}{\rho c} \nabla^2 T(\vec{r}, t) + \frac{1}{\rho c} Q(\vec{r}, t) \, . \qquad (9.1)$$

where ρ is the density of the material,

c is the specific heat and

λ the heat conductivity.

Furthermore one has the boundary condition:

$$T\left(\sqrt{x^2 + y^2} = b, t\right) \equiv T_{edge} \, .$$

A complete solution of Eq. 9.1 is possible only numerically. However, with some simplifying assumptions one can estimate the peak temperature distribution in the material for a certain power distribution. During the passage time τ of a bunch train the temperature distribution broadens up transversally by a typical diffusion length of

$$< d >= \sqrt{D\tau} = \sqrt{\frac{\lambda\tau}{\rho c}} \approx 0.3\,\text{mm} \, .$$

This distance is small compared to the beam size and therefore we can assume that the instantaneous temperature rise is directly proportional to the distribution of deposited energy. After the bunch train passage the temperature distribution spreads and the temperature on the axis decays with time till the next passage. From these considerations we expect a qualitative behavior of the temperature on the beam axis as shown in Fig. 9.33.

In the case of a CW beam with an assumed average power of the real beam we would expect an equilibrium temperature of $T_{edge} + \Delta T_{eq}$. The passage of a bunch train on the other hand will cause a sudden temperature rise of ΔT_{inst}. A conservative estimate of the maximum temperature is therefore $T_{max} \leq T_{edge} + \Delta T_{inst}(r = 0) + \Delta T_{eq}(r = 0)$. The value of ΔT_{inst} is simply given by the assumption that the whole beam energy is deposited in the volume of the beam cone:

$$\Delta T_{inst}(r) = \frac{q(r) \cdot n_{mac}}{\rho \cdot c} \, , \tag{9.2}$$

where $q(r)$ is the transversal distribution of deposited energy per incident particle and n_{mac} the number of particles per macro pulse. For the calculation of ΔT_{eq} we have to solve Eq. 9.1 in the stationary case $\partial T/\partial t \equiv 0$. We neglect the longitudinal dependence of q and assume a round beam which allows the
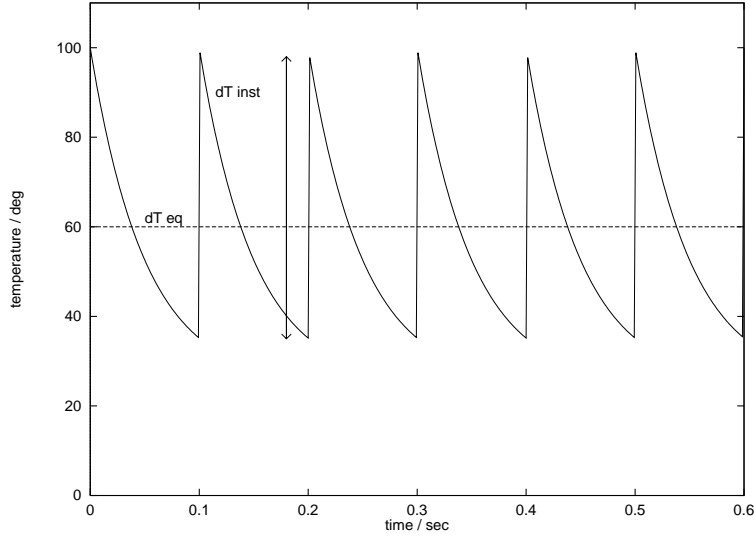
Figure 9.33:   Qualitative time dependence of the temperature on the beam
                 axis.

use of cylindrical coordinates. Then we obtain from Eq. 9.1:

$$n_{mac} \, \nu_{mac} \, q(r) = -\lambda \frac{1}{r} \frac{\partial}{\partial r} r \frac{\partial}{\partial r} \Delta T_{eq}(r) \,, \tag{9.3}$$

where ν_{mac} is the bunch repetition rate in s^{-1}. Eq. 9.3 can be solved by twice
integration, yielding the solution

$$\Delta T_{eq}(r) = \frac{\nu_{mac} n_{mac}}{\lambda} \int_{s=r}^{b} \frac{ds}{s} \int_{u=0}^{s} q(u) u \, du \tag{9.4}$$

with b the outer radius of the dump block.

For the radial distribution $q(r)$ of deposited energy per particle and per
volume we use the parameterization of Grindhammer[24]:

$$q(r) = \left(\frac{dE}{dz} \right) \frac{R^2}{\pi \left(r^2 + R^2 \right)^2} \,, \tag{9.5}$$

[24]G. Grindhammer, M. Rudowicz, S. Peters, *The Fast Simulation of Electromagnetic
and Hadronic Showers*, Nucl. Instr. & Methods, A290 (1990) 469 - 488
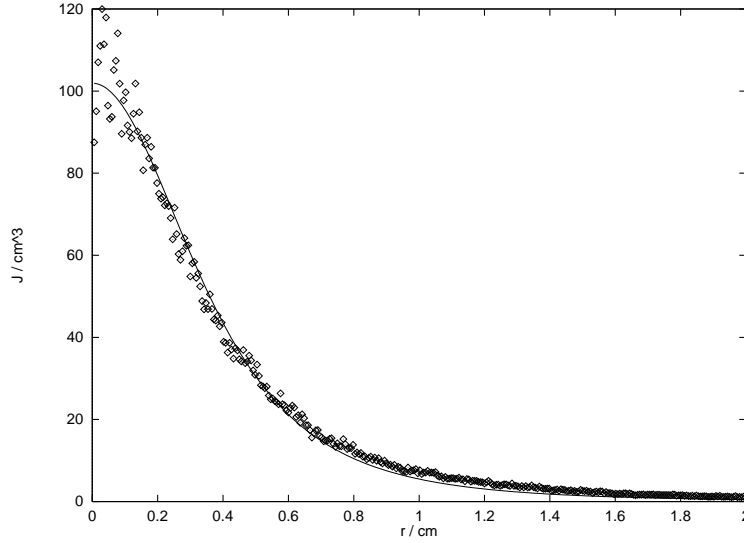
Figure 9.34:   Example of a fit to the transversal distribution of energy deposition per volume and per bunch train at the shower maximum.

where $\left(\frac{dE}{dz}\right)$ is the energy loss in the shower per unit length, per incident particle and R gives a typical transverse shower width. If we consider a Gaussian beam with rms-width σ then it holds at the entrance of the dump approximately $R(z = 0) \approx \sqrt{2}\sigma$. As the shower develops inside the material the values of R and $\left(\frac{dE}{dz}\right)$ have to be determined from the results of a shower code. In Fig. 9.34 an example for a fit of Eq. ?? to a radial shower distribution, obtained from a GEANT simulation, is shown.

Inserting Eq. ?? in Eq. 9.4 yields for the equilibrium temperature distribution:

$$\Delta T_{eq}(r) = \left(\frac{dE}{dz}\right) \frac{n_{mac}\nu_{mac}}{4\pi\lambda} \ln\left(\frac{R^2 + b^2}{R^2 + r^2}\right) . \qquad (9.6)$$

So we obtain in a conservative approach for the maximum temperature on the beam axis (note that $\left(\frac{dE}{dz}\right)$ and R depend on z):

$$T_{max} \leq T_{edge} + \left(\frac{dE}{dz}\right) \frac{n_{mac}}{\pi} \left(\frac{1}{\rho c R^2} + \frac{\nu_{mac}}{4\lambda} \ln\left(1 + \frac{b^2}{R^2}\right)\right) . \qquad (9.7)$$

This temperature should stay well below the melting point of the absorber

material. Furthermore one has to consider stresses which are induced due to the raised temperatures and which may deform or even destroy the material and are therefore limiting factors for beam power and beam size. In case of a cylindrical geometry the stresses can be calculated with analytical formulae[25].

A stress is a force per unit area in a certain direction. In cylindrical coordinates the stress field is given by three components in the directions of the unit vectors $\vec{e_r}, \vec{e_\phi}, \vec{e_z}$. The following formulae hold for a cylinder with not prevented expansion in longitudinal and transversal direction.

$$
\begin{aligned}
\sigma_r &= \frac{\alpha E}{1 - \nu} \left(\xi(b) - \xi(r) \right) \\
\sigma_\phi &= \frac{\alpha E}{1 - \nu} \left(\xi(b) + \xi(r) - T(r) \right) \\
\sigma_z &= \frac{\alpha E}{1 - \nu} \left(2\xi(b) - T(r) \right),
\end{aligned}
\tag{9.8}
$$

where α = coefficient of linear expansion,
    ν = poissons ratio (≈ 0.33 in case of aluminum),
    E = elastic modulus,
    $\xi(x) = \frac{1}{x^2} \int_0^x T(r) r \, dr$.

For estimating allowed stresses the maximum difference between the three components is important. If one wants to avoid plastic deformations it should not exceed the so called 0.2% yield strength $\sigma_{0.2}$:

$$
\sigma_{0.2} > \Delta\sigma = \max(|\sigma_r - \sigma_\phi|, |\sigma_r - \sigma_z|, |\sigma_z - \sigma_\phi|).
\tag{9.9}
$$

9.6.2.2   Simulations and Results

Simulations have been performed with different geometries and beam parameters in order to answer two questions:

1.) Which beam parameters can be handled with an aluminum dump?

2.) What are the required dimensions of this dump to avoid an unacceptable large leakage of radiation?

---

[25] P. Sievers, *Elastic Stress Waves in Matter due to Rapid Heating by an Intense High-Energy Particle Beam*, CERN BT/74-2 (1974)
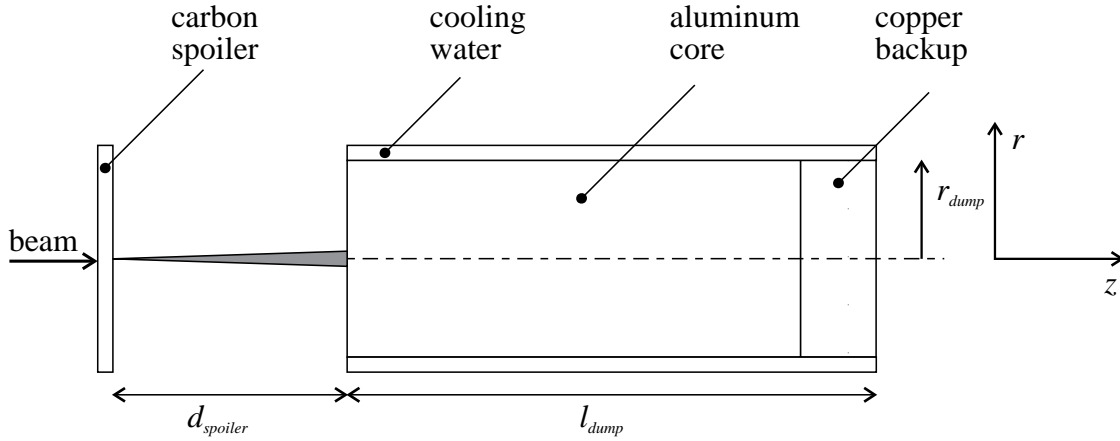
Figure 9.35: Arrangement used for GEANT simulations.

Although the design energy of the TTF linac is 500 MeV we consider here also a possible upgrade to 800 MeV energy with the same beam current. For the calculation of temperatures and stresses the radius of the absorber block was assumed to be 20 cm. All simulations were done with GEANT, using a sample of 20000 electrons, radially gaussianly distributed with rms-widths of 1 and 2 mm. It turned out very soon that these beam dimensions are not acceptable for the dump absorber. Therefore a spoiler with a thickness of $0.4X_0$, made of copper (as in the CEBAF design) or graphite, was introduced in order to spread the beam on the surface of the absorber (see Fig. 9.35).

The GEANT-code delivers a 2-dimensional field of energy deposition per volume - bin as function of r and z. The function Eq. 9.5 is then fitted to each slice of this field in order to obtain $R(z)$. Furthermore the radially integrated value of $\left(\frac{dE}{dz}\right)$ is calculated for each slice. These numbers are then used as input parameters for temperature and stress calculations according to the Eq. 9.7 and Eq. 9.8. The most important results of these simulations are given in Tab. 9.11. Fig. 9.36 and Fig. 9.37 show longitudinal temperature distributions on the beam axis. In Fig. 9.38 an example for the radial distribution of stresses is depicted.

From the results in table 9.11 one can conclude that the introduction
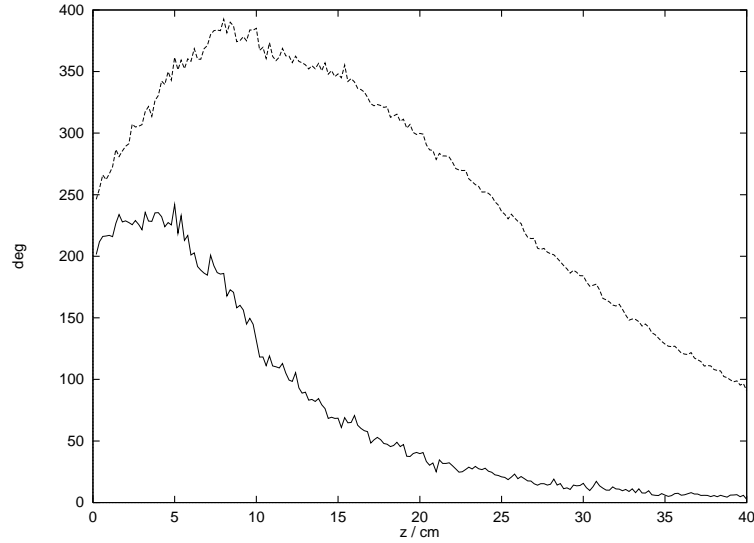
Figure 9.36:   Longitudinal temperature distribution for the case of run 4, i.e. without spoiler. The lower curve shows the instantaneous temperature whereas the upper curve is the sum of instantaneous and equilibrium temperature.

Table 9.11:   Temperatures and stresses for several parameters and arrangements.

run	E_{beam} [MeV]	σ_{beam} [mm]	ΔT_{max} [^{o}C]	ΔT_{inst} [^{o}C]	$z(\Delta T_{max})$ [cm]	$\Delta\sigma$ [N/cm^2]	spoiler
1	500	2	190	35	14	21000	no spoiler
2	500	1	300	170	5	37000	no spoiler
3	800	2	290	45	15	33500	no spoiler
4	800	1	380	160	9	47000	no spoiler
5	800	1	240	25	12	27000	sp. at -30 cm
6	800	1	225	12	14	25000	sp. at -60 cm
7	500	1	120	2.5	11	12000	sp. at -100 cm
8	800	1	190	6	13	20500	sp. at -100 cm
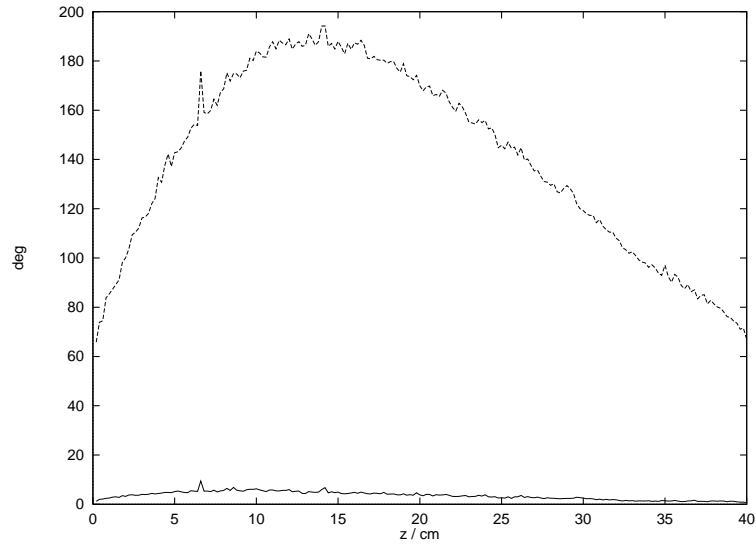
Figure 9.37: Temperature distributions in the case of run 8, i.e. with spoiler.

Table 9.12: Properties of some materials. The pyrolytic graphite exhibits very anisotropic properties. It can be produced in plates of some mm thickness and up to 10...20 cm diameter. The high value of thermal conductivity holds only in radial direction of these plates (which would be excellent for our purposes because it is perpendicular to the beam direction).

material	ρ [g/cm^3]	c [J/gK]	λ [W/cmK]	E [N/cm^2]	α [K^{-1}]
Al	2.7	0.9	2.4	$6 \cdot 10^6$	$25 \cdot 10^{-6}$
Cu	9.0	0.4	3.9	$12 \cdot 10^6$	$16 \cdot 10^{-6}$
C (ordinary)	1.6...1.9	0.75	0.6...1.0	$9 \cdot 10^5$	$3...4 \cdot 10^{-6}$
C (pyrolytic)	2.1...2.2	0.75	(2.0...3.0)		(10^{-7})
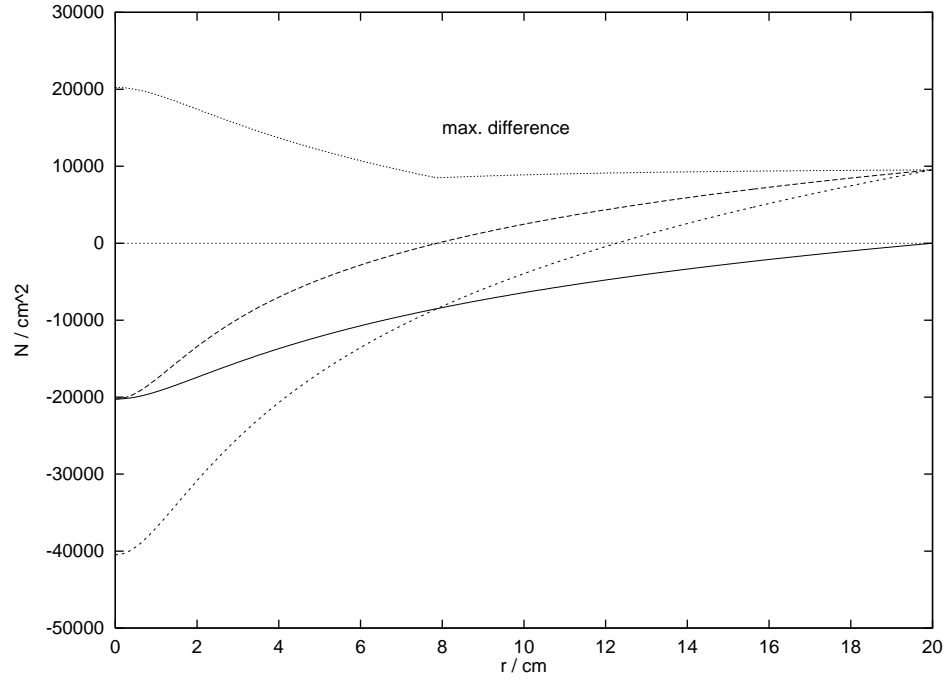
Figure 9.38:   Stresses in the dump cylinder as a function of radius in the case of run 8. The lower three curves belong to the three components in cylinder coordinates (extreme values in σ_z) and the upper curve gives the maximum absolute difference between the individual components. Note that negative values denote compressive forces.

of a spoiler is absolutely necessary to avoid high temperatures and stresses, especially in the case of 800 MeV. The spoiler lowers the instantaneous temperature rise during the passage of a bunch train considerably whereas the equilibrium temperature depends only logarithmically on the shower radius (compare equation 9.6). An increase of the distance between spoiler and absorber above 1 m will therefore not result in a further improvement. The internal stress in this case (see run 8) is acceptable for several Al- alloys at room temperature. However, at 250^oC the yield strength of these materials is already exceeded by a factor of $2 \ldots 4$ which could result in plastic deformations. On the other hand the elastic modulus E decreases towards higher temperatures (numbers are difficult to find in the literature) which will reduce the stresses. If this is acceptable or not and which alloy should be used has to be explored in further investigations. However, the dump designs of CEBAF and SLAC will certainly have similar parameters and they work without problems.

The effect of shock waves has not been considered so far because we expect from experiences at the SPS (where the energy deposition per "shot" is much higher) that these play no important role in our case.

The second of the above listed questions concerns the leakage of radiation out of the dump and the amount of deposited power in water and in the copper section. In the simulation the length of the copper section is assumed to be 18 cm and the thickness of the cooling water layer is 1 cm. In order to find out the optimum dump dimensions several GEANT simulation runs were performed with varying length and radius of the absorber block. The results are given in Tab. 9.13. If one wants to lose not more than 1 % transversally the block radius should be 25 cm. For a goal of less than 1 % power deposition in copper the length of the aluminum section should be ~ 110 cm. With these dimensions one expects a production rate for Hydrogen of 0.5 l per day which presents no need for a catalytic recombiner.

An alternative way of handling the stress problem could be the usage of a graphite core insight the aluminum block. One advantage of graphite is the small coefficient of linear expansion which is one order of magnitude lower than that of aluminum (table 9.12). This results in much lower mechanical stresses. Furthermore commercial graphite is able to stand temperatures of more than $2000\,^o$C. A dump with a graphite core could be designed as depicted in Fig. 9.39. The dump consists of a graphite core insight an aluminum tube, followed by a solid aluminum and a copper section. Due to

Table 9.13:   Power deposition for different geometries (t = transverse lost, w = deposited in water, c = deposited in copper). Longitudinal losses are in all cases negligible. All runs were performed at 800 MeV beam energy.

	$r = 20$ cm	$r = 25$ cm	$r = 30$ cm
l=100 cm	t=1.9 %	t=1.1 %	t=0.64 %
	w=0.08%	w=0.04 %	w=0.02 %
	c=1.1 %	c=1.1 %	c=1.2 %
l=120 cm	t=2.0 %	t=1.1 %	t=0.55 %
	w=0.07%	w=0.04 %	w=0.02 %
	c=0.35%	c=0.33 %	c=0.44 %
l=140 cm	t=1.93%	t=1.1 %	t=0.74 %
	w=0.09%	w=0.04 %	w=0.02 %
	c=0.10%	c=0.16 %	c=0.18 %

the larger radiation length of carbon the length of the hole dump block must be increased to about 1.4 m. The diameter of the graphite core is chosen to be 15 cm which guarantees also in case of extreme mis-steering of the beam (energy deviation) that only graphite and not the outer aluminum tube is hit by beam particles. For the graphite core a composite material from a Russian producer (see Tab. 9.12) could be used. Due to the extreme temperature and stress resistivity of this material the use of a beam spoiler wouldn't be necessary anymore. Furthermore the maximum temperature in the aluminum section is reduced from $\sim 200^{o}C$ to $\sim 100^{o}C$. A temperature simulation for the graphite dump is shown in Fig. 9.40. The temperature peak at a depth of 90 cm is due to the change of the absorber material from graphite to aluminum. The copper section is not included in the simulation. With the dimensions shown in Fig. 9.39 one expects a radiation power loss of 0.6% transversally and 0.3% longitudinally.

9.6.2.3   Neutron Dose Shielding

During operation the beam dump becomes a rather intense source of neutrons. Therefore the dump block has to be shielded with concrete in order to
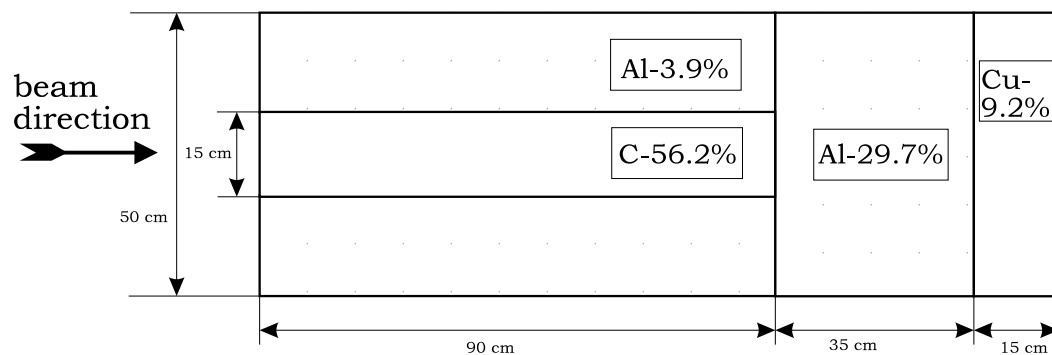
Figure 9.39: Arrangement of materials in a beam dump with graphite core. The relative values of power deposition are given for each section.
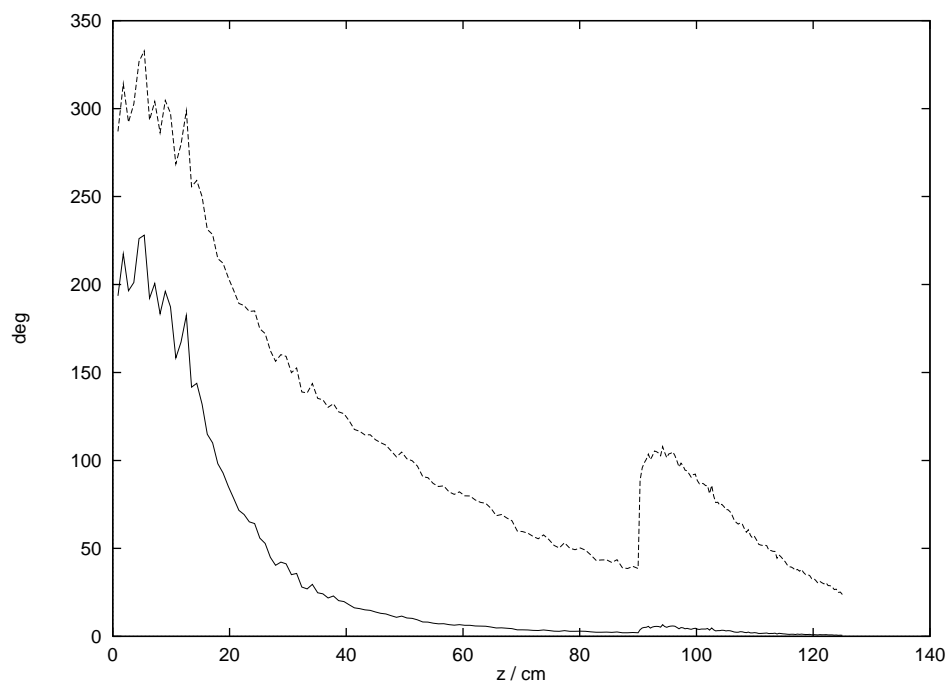
Figure 9.40: Temperature distributions for a dump with graphite core (compare with simulations for the aluminum dump in Figs. 9.36, 9.37).
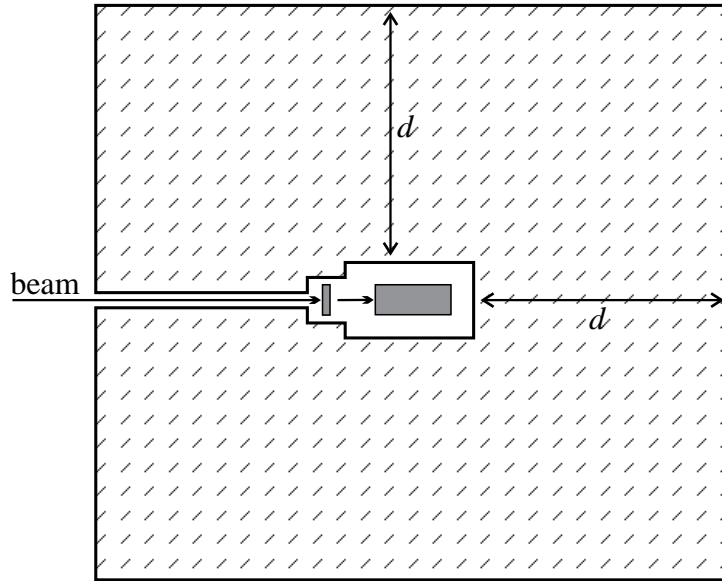
Figure 9.41:   Principle arrangement of spoiler, absorber and shielding.

reduce the radiation to an acceptable level. The goal should be a reduction below $1..2 \cdot 10^{-5}$ Sv/h in all directions around the dump (Fig. 9.41). In that case there is no need for a so called control area.
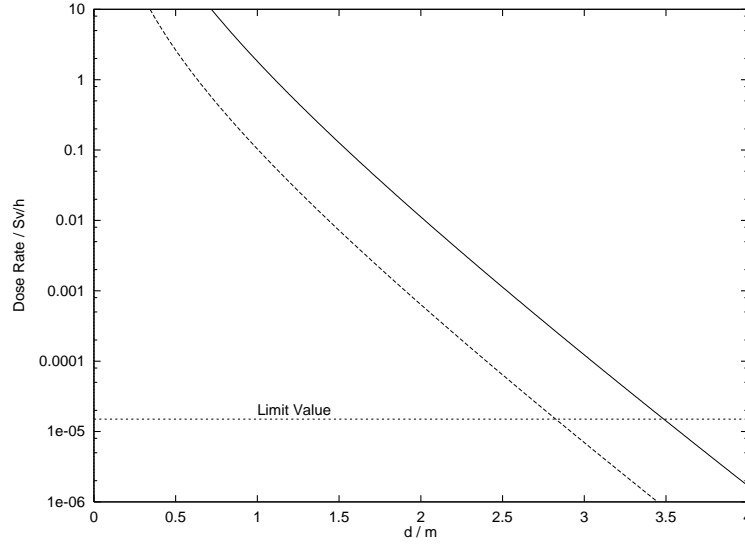
Figure 9.42:   Dose rate behind shielding by heavy concrete for absorber and spoiler as a function of shielding thickness.

The dose rate behind a concrete shielding can be estimated using a parameterization of Tesch[26]:

$$H = \dot{N} \frac{H_0 E_0}{d^2} \exp\left(-\frac{d}{\lambda}\right), \qquad (9.10)$$

where $\dot{N}$ = beam current in particles per sec,
   d = thickness of shielding,
   H_0 = an empirical constant
   $(\approx 1.2 \cdot 10^{-16}$ Sv for graphite, $6.4 \cdot 10^{-17}$ Sv for aluminum),
   $\lambda = 0.42$ m for ordinary concrete, 0.27 m for heavy concrete.

The beam spoiler is positioned 1 m upstream of the absorber and must be shielded as well. Following Tesch, the spoiler can be considered as a so called thin absorber and can be described with equation (9.10) as well, but

[26] K. Tesch, *Shielding Against High Energy Neutrons from Electron Accelerators — a Review*, Radiation Protection Dosimetry, Vol. 22/1 (1988) 27 - 32

H_0 has to be multiplied by a factor:

$$H_0' = \left(\frac{x}{X_0}\right)^2 \frac{\ln(E_0/K_1)}{E_0/K_1} H_0, \tag{9.11}$$

where x is the thickness of the spoiler,

X_0 the radiation length,

$K_1 = 50$ MeV a constant.

In Fig. 9.42 the residual dose rates of dump absorber and spoiler are plotted as functions of shielding thickness. We can conclude that one needs 3.5 m of heavy concrete for the absorber and 2.8 m for the spoiler.

9.6.2.4 Conclusions

An aluminum dump of cylindrical form with 50 cm diameter, 110 cm length, backed up with a 18 cm long copper section is able to absorb 99 % of the beam power. In order to reduce the peak temperatures and stresses the beam should be spread by a spoiler of 0.4 radiation length thickness, installed ~ 1 m upstream of the absorber. The material of the spoiler could be graphite, but this should be investigated in more detail. With this arrangement one expects a peak temperature in the absorber material of $\sim 230^\circ$C (30°C temperature of cooling water assumed). Although the melting point of aluminum with 640°C is far above this value the induced stresses lead already to plasticity in the material. The consequences of this have to be investigated in more detail as well. However, comparable dumps at CEBAF and SLAC are operated under similar conditions and work without problems. A possible solution to avoid the stress problem could be the usage of graphite as primary absorber material insight an aluminum tube. In this case the total length of the dump block will amount to 140 cm.

The absorber block should be edge cooled on the radial surface with a helical water flow channel in order to avoid too much direct power deposition in water.

For a sufficient shielding of the beam induced neutron flux one needs at least 3.5 m of heavy concrete around the absorber.

Chapter 10

Controls and Applications

This chapter is a combination of an outline of the control system with associated systems that we plan to develop for TTFL and an enumeration of the devices it will be necessary to control or get data from in order to operate the linac. Emphasis is focused on the near term needs when Injector I and one cryomodule will be put into operation along with the warm beam line and the high energy analysis area. The discussion on controls for Injector I is the result of well developed plans where implementation is advanced. However, other sections of this chapter relating to the linac after the injector should be thought of as reflecting only initial ideas, which will doubtless undergo changes and mature over the next few months.

Sections of this chapter contain the following:

- A description of the controls hardware and software is given.
- The nomenclature that will be used is defined.
- Closely related global systems are discussed. These are:
    - the clock and timing system
    - the low level RF distribution system
    - the quick digitizer system
    - the gun inhibit protection system
- The devices and subsystems to control and monitor are listed and applications discussed
- A description of the Personnel Safety system is included.

The control system which is being put together is a combination of a variety of different approaches. We must be careful that integration at the

operator interface will occur. We do not want to see one part of the system on one console and have to walk across the room to get the rest of the picture. The achievement of this goal in the R&D environment of the TTFL is a challenge.

An attempt has been made to identify just what sort of dumb or smart (digital, A/D or D/A interface , or microprocessor) interface will be required Also consideration has been made to the desired time response either in control or monitoring.

Little is said about specific special purpose application programs. Some specific devices have applications under development (e.g. the cavity tuning system), other self contained systems have their internal software and need only be interfaced in a reasonable way to the general control system. However general purpose controls applications ("utility applications") must be provided which are reasonably easy to use even during initial operation. The klystron modulator was delivered with a control system, and that system is discussed in Sec. 8.6.

10.1   Control system overview

The control system for TTFL must accommodate and integrate as much as possible control subsystems developed by and familiar to the different collaborators who are supplying the various hardware/software systems and control interfaces. In addition, there are two very different DESY approaches, each of which has strong points. The TTFL may provide an opportunity to investigate their relative strengths and to merge the strong features of both.

However, an operator of the linac should not be asked to worry about differences of representation of components depending on which controls approach a particular subsystem is implemented in. We need application programs that can read and control all subsystems, no matter what the internal controls routing is.

10.1.1   Client - Server Configuration

Although control subsystems for TTF are produced in different countries they all follow the same client-server configuration. It is often called the "standard model" of control systems.

10.1.1.1   Server

Sensors and actors (devices) of the accelerator connect to a server program by a variety of electronics. This program provides a service to the network. All requests to a device have to pass to the appropriate server program. In general the server resides in VME and communicates to the device via a "field bus". Several independent server processes provide support to the various devices of the linac. The services vary from simple reads of device data, automatic controls of device functions and error handling up to complex calculations of data from several devices. Information from these services is available on the common TTF Ethernet.

10.1.1.2   Client

To display the status and to control the machine, client programs make use of these services. The client programs provide the screen graphical interactive display applications and screen drivers. A simple Client-Server configuration with two paths to the monitor is illustrated in Fig. 10.1a. A configuration using "gateways" between one type of server and a different type client is shown in (b). The Application Program Interface (see below) which integrates the approaches is illustrated in (c).

10.1.2   Communication Protocols

At the TTF linac we will use three different system types each with its own communication protocol. These are:

- Experimental Physics and Industrial Control System (EPICS) from Los Alamos with the Channel Access (CA) protocol between clients and servers.
- The Distributed Object Oriented Control System (DOOCS) from DESY with a Remote Procedure Call (RPC) based communication.
- A system based on the commercial PSoS real-time kernel with the so-called "Classic protocol" on top of UDP from Fermilab (for control of the modulators).

All three protocols use the same Ethernet and the TCP/IP family for the communication.

Work Station or
X Terminal

Ethernet

Client
Computer

Server
Computer
(VME)

Field Bus

Device

Application

A.P.I.
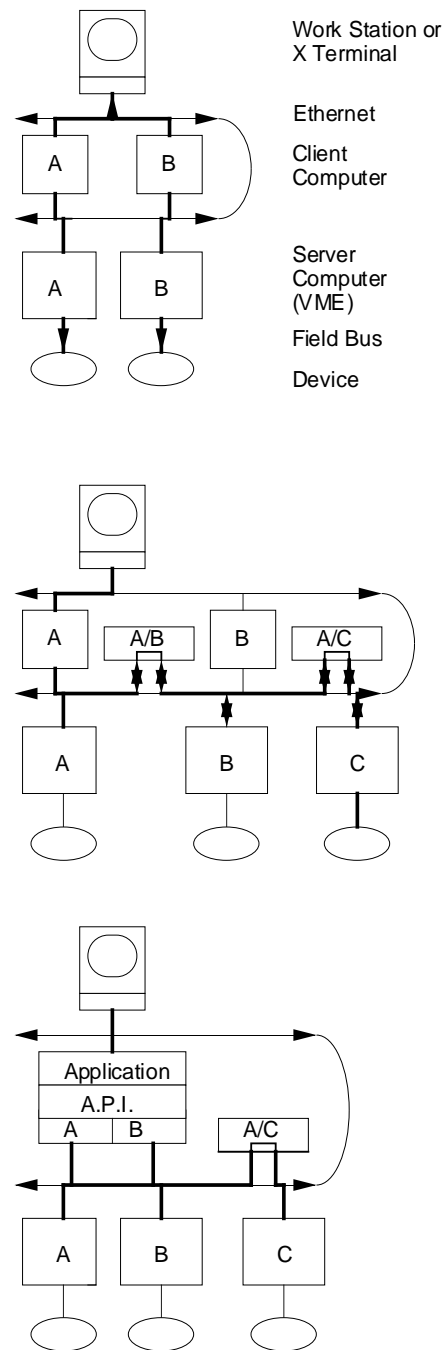
Figure 10.1:   The Client Server Configuration and its planned evolution.
(a) Initial configuration with two parallel paths. (b) The
gateway which allows communication from one type server
to different client. (c) The final integrated configuration with
common applications programs and Applications Programs
Interface.

10.1.3 Gateways and Application Program Interface

Our first solution for integration of these protocols is to add, what we call "gateways" for communication between the systems. The gateways are processes that talk two protocols and can translate between the two. In addition a gateway may add functions to one side like archiving and it then becomes more like a middle layer in the control system. The disadvantage of a gateway is the increase of network traffic, because it needs two network calls to get one piece of information.

In a later step a common Application Program Interface (API) will be implemented. The API solution avoids some of the disadvantages of the gateways. The API defines a set of standard calls with a set of arguments. From the arguments the API library detects which protocol to use. All the complexities of the network protocols are hidden from the client (application) programs.

The definition and implementation of a common API needs some time to develop. Therefore, we are providing the faster to implement gateway solution. Because of the added functionality and the fact that some programs can operate without the complexity of different protocols, the gateways effort is not a waste of time.

10.1.4 Features of the Different Protocols (systems)

The different systems follow different control's models. To make full use of the advantages of each of the systems, it is worth while discussing the differences in the server, communication and client layer.
Channels and Objects:

- In general, DOOCS handles objects rather than channels. A pump station with several analog signals and state handling or a beam monitor are examples of objects. All functions of such an object are handled within a single C or C++ program.
- EPICS deals with channels and allows connections between them by a database configuration. To add the readings of two channels it is necessary to configure the database to link the two outputs to the inputs of a calculation record with an "add" function.

Real Time or Not:

- EPICS and the Fermilab system are based on real-time kernels. The first one uses VxWorks, the latter one PSoS.
- The DOOCS runs under a UNIX operating system (SunOS, Solaris or LINUX) with some limited real-time capabilities.

Fast front-end systems with several real-time tasks are better to implement on a real-time kernel. Complex algorithms are easier to develop under the UNIX operating system and programs of other programming languages may be linked to a server. The calculation for the helium losses in the cryogenic system was a good example of integrating an existent big FORTRAN program into a DOOCS server.

Sequencing:

- An EPICS task can set up a front-end sequencer by a State Notation Language processor.
- The other two systems accomplish this task by a user written C or C++ program.

Configuration Management:

- EPICS uses a distributed database that is downloaded at start time to the front-end. Modifications in the front-end are not transferred back into the local host but can be stored locally in SRAM.
- DOOCS uses a configuration file per server. The file reflects the actual status of the server and after a restart of the server it can continue with the previous states of the devices.

Server Process:

- The Fermilab system is a dedicated program written for the application.
- EPICS uses a set of predefined records extensible by user records to compose a server. The composition is done with a database configuration tool. Since EPICS is used in other HEP labs a rich set of drivers for I/O boards are available.
- DOOCS has a collection of C++ library functions for all standard tasks as a template. The functions are glued together by a small dedicated program.

Archiving Functions:

- The PSoS system has no standard way of archiving. It has to be done in the client.
- EPICS has an archive server that receives buffered data from the front-ends via the Ethernet. Archiving to disk as well as deadband tuning is activated by the user.
- DOOCS archives all data in a local file with on-line adjustable filters. Servers with high archiving loads create mo additional network traffic.

Network Communication:

- EPICS has a highly optimized network layer. It allows polling and monitors in the client programs. Polling is used for single request of a client to a server to get a data item. Monitors indicate the interest of a client for a data update by the server. The server updates the client automatically on changes of the according value.
- DOOCS on the other hand comes with a rich set of network self-describing data types. This includes archived data with time stamps and actual readings of all devices of a certain type in one network call. And DOOCS translates the data into a computer independent format for the network transfer (XDR format). Therefore it is more easily portable between CPU architectures. Part of the network definition in DOOCS is the on-line discovery of names. A client program may ask for a list of all defined devices, instances of these devices and their properties.

In an accelerator some equipment is not fixed to a location or may vary in the number. The control system has to detect the actual positions automatically. Pump stations are an example for moving devices. DOOCS implements this functionality.

10.1.5 The Client Side - Operator Interface

For the operator interface many programs and tools already exist for TTF, others will need to be written. This is only a short overview of them.

- Synoptic status displays:
  These programs display the actual status of the devices in a synoptic

diagram like a circuit diagram. EPICS has two such programs (DM and MEDM) to edit and display device data. DOOCS has one that interprets a display list with macros. LabVIEW has the additional function editing capability.

– Plot tools:
  Plot tools are used to display archived and actual data of devices. Some of these tools are useful in off-line applications only, i.e. PV-Wave and GNU-Plot.
  EPICS, DOOCS, the Fermilab system and LabVIEW display the actual data as well. But, the capabilities are quite different and often also limited. Therefore, we are developing a new plot tool for TTF.

– Knob manager:
  A knob manager connects channels to control on a device with eight radio buttons to set analog values. EPICS only comes with such a tool.

– Parameter Page:
  A parameter page is a display of one device per line. It shows the actual reading, settings, and on/off status, and allows modification of set points. The operator may define groups of devices on a page and create an archive of pages in files. The Fermilab system makes much use of parameter pages. A parameter page for EPICS is under development in Saclay for EPICS. It is based on the Orsay OnX program.

– Alarms and error display:
  This program informs the operator if an error or alarm is detected in the system. Each of the different systems have their own error display program.

– Sequencers:
  A sequencer on the client side allows the control of groups of devices and ordered sequences of procedures. This program steps through complex check and set operations to free the operator from these tasks. LabVIEW provides a graphical programming of sequences.

10.1.6   Concluding Comments

There are many different features in the programs we are going to use for TTFL. Some considerations are necessary to select the right tool for a certain application. To benefit from these features a good implementation of the gateways and API is an important task.

On the other hand it is necessary to limit the complexity of the overall system. No further protocols should be added and a specific device type should be implemented by one system only. For example because of the injector magnets use EPICS all magnet power supplies in the linac should be controlled by it.

Fig. 10.2 illustrates the over all client server software protocol and network configuration planned for TTFL. It shows the three systems (EPICS with Channel Access, DOOCS with RPC, and Classic Protocol with UDP. Both the Gateway and the Applications Program Interface are shown. Prior to the implementation of API, either EPICS or DOOCS will communicate directly with the display terminal.

The Fermilab modulator interfaces to a Mac via Internet and can be operated from any location. However a gate way will be provided so that the operator can access it through work station or X windows displays. The OnX display program is an interface display program for screen interaction.

Fig. 10.3 illustrates the same configuration in hardware. Note that though the clean room, furnace, and cavity processing/measurement equipment are not part of the TTF Linac per se, they are in fact part of the same network. Controls of certain utilities like the cryo plant and the vacuum system serve both the cavity testing and the linac.

10.2   Controls Hardware and Software

10.2.1   Front-ends

VME / VXI Hardware   According to the C-S (Client-Server) model which we define to be the basis of TTFL controls, the front-end systems have to collect and compute the signals from the process. Resulting from this definition nearly all front-end systems will be based on VME. VME has developed from a mainly European to a common system for front end computing. From here the field busses as well as the fast readout system are connected.

Since VME is an industry standard many different types of I/O are available. This enables us to choose from a variety of models and vendors and to pick the one that fits best - as for the fast readout.

If special requirements to the noise/signal ratio are necessary and/or the
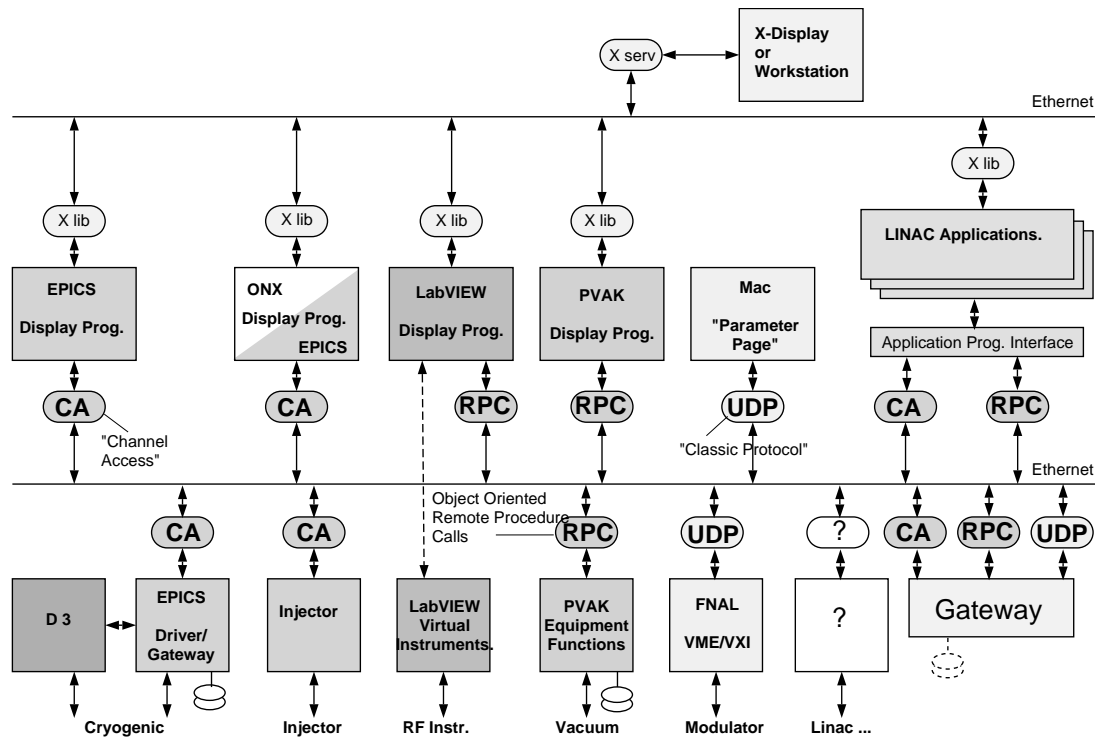
Figure 10.2: TTFL Controls Software Configuration
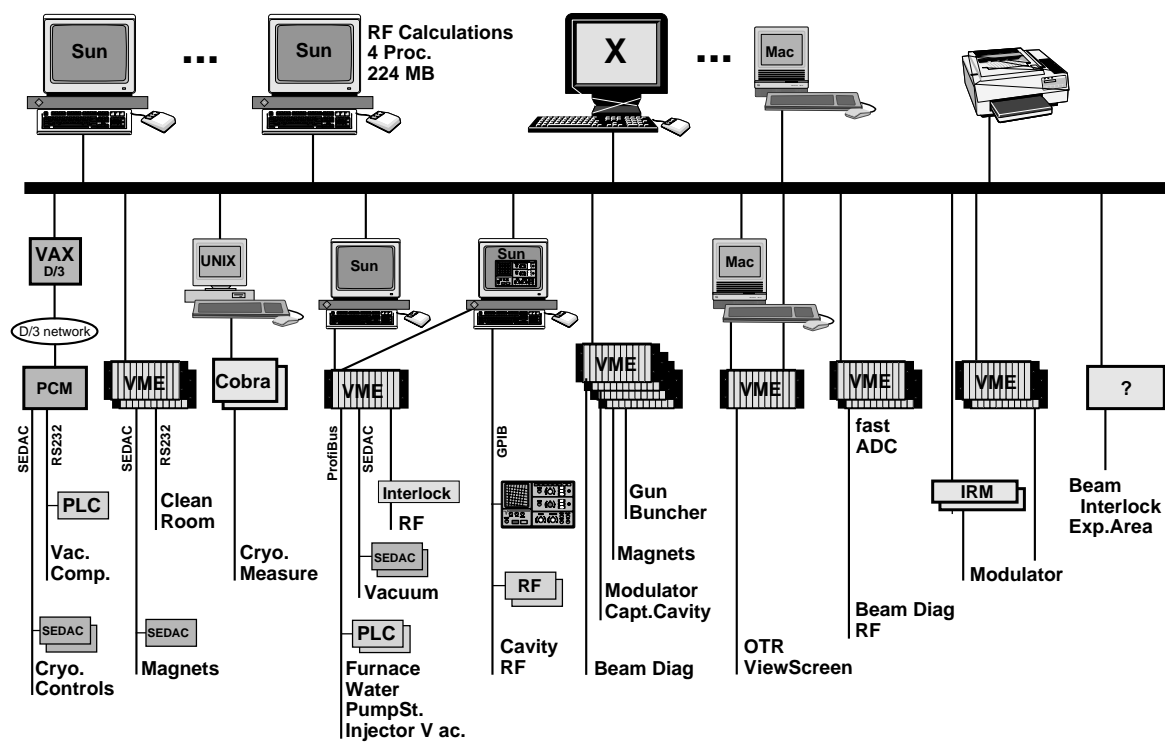
Figure 10.3: TTFL Controls Hardware Configuration

space on the VME-size boards is not sufficient, VXI is an excellent addition
to the VME system. VXI is an extension to VME which includes bigger
boards in length and width and includes auto-configuration of the boards.
For TTFL VXI will be used for the LLRF-module in the modulator. It is also
possible to install scopes directly in the VXI crate which might be reasonable
for permanent precise measurements.

Motorola 680x0   One family of processors which is heavily used in VME
are the Motorola 68000 CPUs. The current generation for this processor type
are the 68040's. Several control subsystems for TTFL will use this processor.
The difference for this subsystems will not only be the application but also
the operating system and the application environment as there are PSoS+
for the modulator and the Fermilab control system and VxWorks for several
other systems with the EPICS application toolbox.

The PSoS+ System   (see Sec. 8.6))

The EPICS System   The main difference between the EPICS approach -
which is a toolbox approach- and other control architecture's is, that a tool-
box leaves a lot of freedom to the one using it to create his own environment,
according to his needs. While complete control systems dedicated to machine
control or process control inhibit a smooth adaptation to the actual control
problem. As soon as the bits and pieces are put together from the toolbox,
there's not much left to program. What does this mean for a 'real' system?
There are three levels of development:

- Device and driver development:
  Once the measuring problem is defined, the necessary software support
  has to be provided. This translates into first a search through the
  EPICS toolbox to find out whether the support for the device is already
  available. This is true in many cases. If not, the device support must
  be written (in *C*).
- Database Support:
  Once the device is defined the database can be filled with definitions for
  all the points. This is performed by means of interactive tools. If the
  database is created from another source (i.e. a relational database) the

output of this source can be directly converted into an EPICS-database by the Database Creation Tool (DCT). There's no programming necessary to define points and actions. At this level - at least - the experimenter can start to define his I/O points and define the actions he wants.

– Application/Graphic Support:
Once the database is defined and downloaded to the front-end, the data are available on the network by means of the Channel- Access (CA) protocol. Graphics/ Alarms / Save-Restore and Trends do not need any additional programming. There are interactive editors available which only need the channel name as an input to display a value, a chart or a bar-graph. The same is true for all other tools available.

Additional programs can be written in 'C' or in a specific language based on the system states. This program can directly call the CA interface to read and write data as desired. At TTF we will want to define an additional software layer on top of CA and the DOOCS communication protocol to enable the physicist to write code on a homogeneous software platform.

10.2.2   Field Bus

SEDAC   SEDAC (Serial Data Acquisition) is a proprietary field bus used at DESY. The origin of this bus is a stripped serial CAMAC. Recently this bus had a renewal when it was adopted to the needs for the 6.4 km long HERA ring at DESY. This bus is the basic backbone for all signals, of the various linacs, boosters and storage rings at DESY. The advantage of SEDAC is the reliable transport of data over distances of more than 3 km. The disadvantage is the low speed of about 15 kByte/s (500 kBits/s) and the trivial protocol which only supports a single master polling mode.

SEDAC will be used at TTF for all components which are already available and adequate for the requirements in the TTF installations. Some examples are the first cryogenic installations (up to 1994) and the first installations for the vacuum system. Other subsystems like the power-supply controllers (except the injector) will use SEDAC to avoid unnecessary developments.

Future (new) developments will be based on new field busses mentioned hereafter.

CAN   One of the candidates to replace SEDAC at DESY is the CAN bus (Controller Area Network). Since the physical connection and the network layer are available on silicon this bus has turned out to be an ideal basis for fast and reliable applications. In addition single chip solutions for the CAN connection including a CPU and even on chip ADC's are available. Because of its origin in car and truck automation these chips are produced in high volumes and thus reasonable cheap.

In cryogenic control systems generally more than 60 percent is standard I/O like 4 to 20 mA or relays output. The CAN bus is designed for transferring short messages between several masters. Collisions on the bus are resolved without destroying data (CSMA/CA). This leads to a maximum performance until the bus load reaches 100 %. Besides the ease of use CAN has the advantage of a multi master communication. The problem of a multi master system being multiple talkers at the same time has been overcome by a fancy arbitration mechanism which guarantees that high priority messages are recognized and passed through within the one bit duration. This forces reliability but also limits the ratio between the bus speed and its length. I.e. at a length of 40m the speed reaches 1 MBit/s.

For network management and vendor-independent data transfer an application layer for CAN has been defined by the manufacturer- and users-group CiA (CAN in Automation). The name of this package is CAL (CAN Application Layer). Implementations are available for different platforms (micro controllers as well as hosts).

CAN-developments   Besides commercially available I/O subsystems several special developments have started at DESY. One of them is a fast response bus for the HERA quench protection systems, the other is a specialized front-end for high precision low temperature read-out (1 mK @ 1.6 K). At TTFL CAN will be used for the cryogenic controls of the components in the linac. In addition, it is under discussion for the power supply controls and the gun inhibit interlock system.

Profibus   Profibus is a well defined industrial field bus. It is standardized by the German DIN (DIN 19245 part 1 and 2). The physical layer is RS 485 based and this defines the speed/length ratio. Since Profibus is a token passing multi-master system the traffic is deterministic and only depends on the

number of connected nodes. To achieve a fast recovery if the token should get lost all nodes have to know the number and address of the connected nodes. Profibus is well established in the PLC domain. Many vendors support this bus. At TTFL this bus will be used as such, i.e. for the PLC controllers of the vacuum and for the PLCs controlling the water supply.

SIEMENS-H1 The H1 bus is running on 802.3 Ethernet standard media like coax, fiber and twisted pair. It is devoted to perform as a backbone connection for distributed PLC systems. At TTFL this bus will be used to integrate large PLC's into the control system. It is a proprietary product of the company Siemens. This limits the usage to PLCs of this flavor.

GPIB GPIB does not fall under the category of 'field-busses' but it should be mentioned here since it is currently heavily used for the initial cavity measurements and has proved to be a very useful bus system specially in conjunction with the software package LabVIEW.

Since GPIB is expandable over Ethernet it has reached the functionality of a quasi field bus. This functionality will help to integrate remote scopes and similar instruments into the control system.

10.2.3 Client/Server Network

Ethernet/Fiber Distributed Data Interface (FDDI) According to the model which has been defined for TTFL controls all control systems need to be connected together to be able to exchange the information about the measured data and their definitions.

The most common communication path used in the computer environment is Ethernet. In principle all systems can be connected together on the same Ethernet segment. This will work until measurements start which might require large amounts of data to be transferred between each individual node. As a first step the data and the display traffic might be separated. Second special segments may be necessary to separate the traffic from dedicated I/O devices (like GPIB) from others.

Eventually if there are large data rates, the whole Ethernet installation of the TTFL test hall could be connected to the FDDI (Fiber Data Distribution Interface) ring which directly connects to the DESY computer center. This

way the data as well as the graphics can be transported with a high band-
width to people outside the experimental hall on the DESY LAN as well as
the collaboration members outside DESY. Having the FDDI infrastructure
available in the test hall will also enable the direct connection of high speed
workstations to this ring.

It may also be desirable to have some fiber optics networks within the
hall in order to isolate systems electrically. These networks probably would
not need to be ultra high speed.

10.2.4 LabVIEW Usage in Present and Future TTF Control

LabVIEW is a graphical programming environment developed by National
Instruments Corporation. LabVIEW runs on the Macintosh, Windows, Sun,
and HPUX environments, with programs being essentially transportable from
one platform to another.

LabVIEW works under the paradigm of the Virtual Instrument (VI),
wherein a program consists of two distinct parts:
(1) the Front Panel, which (like the front panel of a standard instrument)
presents the interface to an operator, and
(2) the diagram which contains the (graphical) programming which controls
the behavior of the instrument. A built in set of displays and controls for the
control panel makes creation of an intuitive, user-friendly interface program
relatively easy. Furthermore, an extensive library of sub-programs (sub-
VI's), makes the programming equally comfortable. These libraries include
interface programs (e.g. GPIB functions), and analysis programs (e.g. curve
fitting or advanced mathematic functions such as integration).

LabVIEW has been a constantly evolving and improving environment,
currently on version 3.1, and there is every reason to believe that National
Instruments will continue to support and improve the product for the imme-
diately foreseeable future.
LabVIEW's strengths include the following:

- a very fast initial learning curve, allowing beginning programmers to
  do real work with a short lead time.
- graphics (such as plots, waveforms, etc.) are built in to the language,
  eliminating the need for a programmer to spend time with this level of

programming.
- built in GPIB interface controls.
- a large built in library of data acquisition and analysis sub-programs.
- built in TCP/IP capabilities.
- the ability to link in specialized code as needed.
- the ability to create stand-alone programs for the working platform (negating the need to run the LabVIEW shell program to execute a completed program.
- very good product support from National Instruments, and a growing consortium of associated third party products.

The primary disadvantages to LabVIEW are:

- it is not a real-time environment.
- it requires a relatively hefty computer configuration for comfortable working conditions. (Memory requirements are 8MB minimum on Mac and Windows, but 12–16 MB is a much better guess for acceptable performance. Floating point processors are required. As a graphical system, a relatively large monitor is also very useful. Compiled programs can grow as large as several MegaBytes.)

At DESY (specifically in the TTFL project), LabVIEW is currently being used for control and data acquisition for the RF cold tests of the 9-cell test cavities for the TTFL on a Sun Sparcstation. Execution of these experiments is accomplished primarily through a series of RF electronic devices which are remotely controllable via GPIB bus. In addition, however, communications are maintained (data transferral) with vacuum and cryogenics computer systems through specialized codes developed by the PVAK group, based on the Sun RPC model.

LabVIEW is being further used for control and data acquisition of the thermometry diagnostic systems for the superconducting cavities associated with the TTFL cavity tests. This includes a rotating frame of 200 thermometers and X-ray detectors for the 9-cell cavities, and a fixed frame of 780 thermometers for 1-cell cavities. Data acquisition is performed through and SCXI module, which is controlled via data acquisition sub-programs (or sub-VI's) which are built in to LabVIEW. Finally LabVIEW is also being used for studies of the thermal conductivity of cryogenic niobium.

LabVIEW is the ideal system for fast development of relatively small, self-contained systems, where real-time reactions are not necessary. Through the use of the RPC subprograms from the PVAK group at DESY (or any similar communications standard), measurements made with programs developed in this environment can easily be integrated into a more complete control environment developed for the TTFL.

10.3 Controls - Nomenclature

A TTFL name is an ASCII string which consists of four parts: a facility name, a device name, a location descriptor and the name of a property. It has the form "FACILITY/DEVICE/LOCATION/PROPERTY". An example for the location along linac of a beam position monitor could read like "TTF.DIAG/BPM/ACC1/X". It is a hierarchical structure as is familiar from computer file systems. And as in a file system, the nomenclature of this form yields to a good structure of names. The TTF control system will have several thousand names. An example which makes use of this structure is the DOOCS online plot tool shown in Fig. 10.4. A step by step selection of the four fields of a TTF name is used to select devices. After selecting a facility all device names known in this facility are shown. A selection of a device shows all locations and in the next step the available properties are displayed. This tree type of selection is well known from file managers.

A further reason for this form of a nomenclature is the ability to specify groups of devices with wild card characters. To be able to read all devices of the penning type one can use an asterisk in the location field and gets a list of pressure readings from all penning gauges in the system, i.e. "TTF.VAC/PENNING/*/P".

FACILITY names   The facility part is important for our API (Application Program Interface). An application programmer should not care about underlaying protocols. From the facility name the API library decides which protocol to use. This facility field is also used to run and debug a server with all device, location and property names identical except the facility field. The server under test could run in parallel without interference with the linac operation. Some of our programs we use for HERA also. These programs run on the same network and are preceded by a facility field of "HERA.VA"C
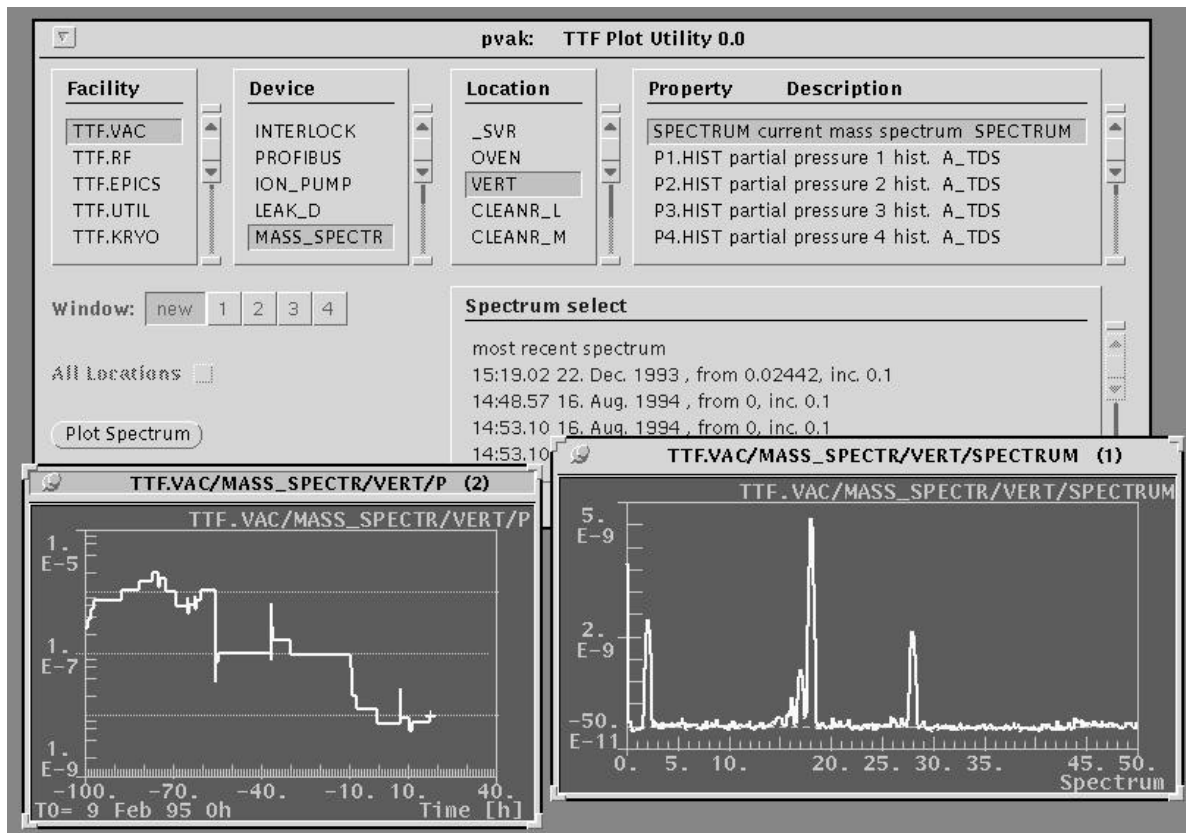
Figure 10.4:   Screen representation of the 'Plot Tool' application illustrating the four fields of the TTF naming convention. Also shown are plots of vacuum pressure as a function of time and mass spectrometer analysis.

for instance.

Examples of facility names are :

TTF.VAC	vacuum
TTF.MAG	magnets
TTF.DIAG	beam diagnostics
TTF.RF	high frequency
TTF.KRYO	cryogenic measurement
TTF.UTIL	utilities e.g. water, power

The following list shows the device names we want to use:

Magnets:	DIPOLE
	QUAD
	STEERER

Beam Monitors:	SCANNER	
	PICKUP	
	BPM	
	LOSS	
	BCM or TOROID	
	OTR	
	VIEW	view screen
	SYNCLIGHT	synchrotron light
	SZINT	scintillator

Vacuum:	ION_PUMP
	PIRANI_VALVE
	VALVE
	MASS_SPECTR
	LEAK_D
	PUMP_STATION
	PENNING

RF: TUNER
  VIBRATION
  CAVITY
  KLYSTRON
  INTERLOCK

Cryo: LEVEL
  TEMPERATURE
  FLOW
  PRESSURE
  CALCULATOR He power loss calculations etc.

Misc.: DUMP
  PARTICLE Particle Counter
  WATER

LOCATION names For the location names we decided to use a system based on section names rather than on meters from the gun. Naming of locations by section names allows one to insert some centimeters in the beam line without changing all of the following names. Also for devices outside the linac a system not based on meters is more convenient, e.g. cryogenics, test stands and klystrons. The general form for devices on the beam line is: "$< number >< section >$". The number field is used if more than one device of the same type is located in one section. The section names are "ACC1" for instance. The location name of the second steerer in a section would be called "2ACC1". For steerer and triplets an additional H or V is necessary in front of the number field, e.g. "H1INJ2" to differentiate between the horizontal and vertical device. Fig. 10.5 shows the areas which go with specific location names.
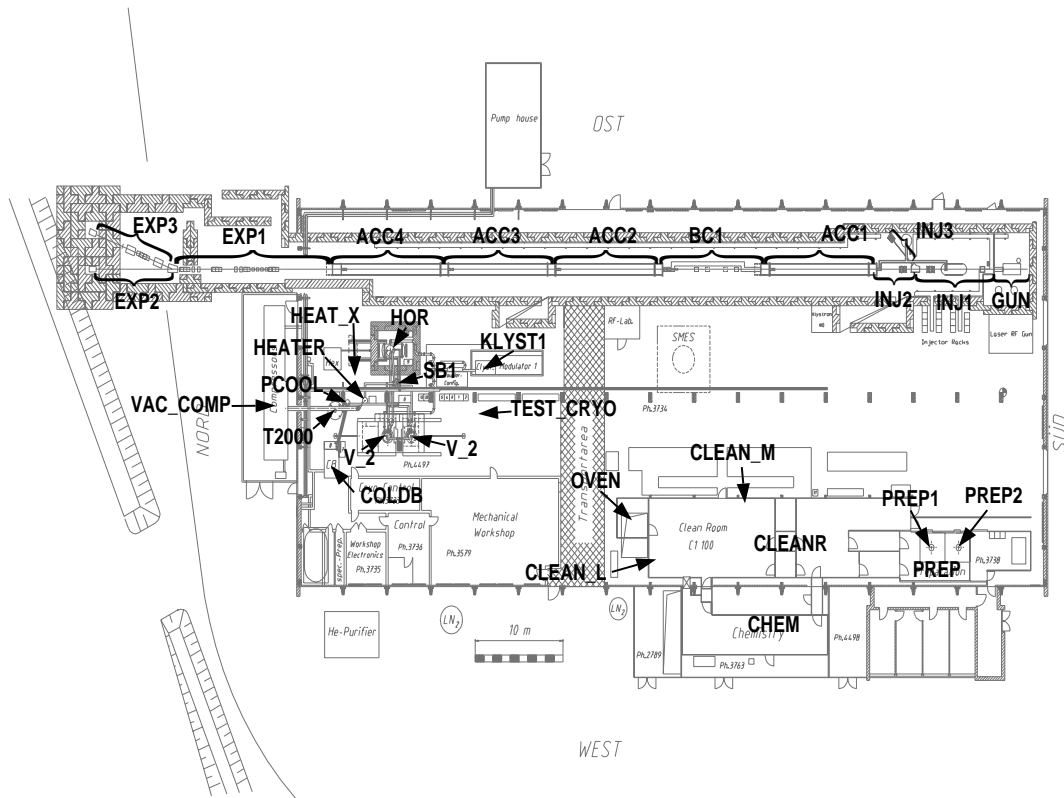
Figure 10.5: Halle 3 with Location names indicated.

Section names for the linac:

GUN	
INJ1	after Gun .. dipole
INJ2	dipole .. end of injector
INJ3	dipole .. dump
ACC1	first cryo module
BC1	first bunch compressor
ACC2	second acceleration module
ACC3	
ACC4	
EXP1	first experimental line up to the dipole
EXP2	dipole .. straight line dump
EXP3	dipole .. bended line dump

For location names outside the beam line of the linac we use
"$< section >< extension >$". The cryo measurement system has several
sensors of the same type at one location. A simple system with numbers
only is not helpful here. We use short mnemonic abbreviations as extensions
to the section name. Examples for temperature sensors in the first cryo mod-
ule are (forward, reverse, shield, high order mode coupler, vacuum vessel):
"ACC1.70K.F", "ACC1.70K.R", "ACC1.4K.S", "ACC1.HOM", "ACC1.VESSEL".

PROPERTY names In simple devices the property naming is straight-forward. In complex devices it is necessary to use hierarchical names with a "." character as a separator. If a device has two heaters for instance one temperature property could be named as "HEAT_TOP.TEMP" and the other one "HEAT_BOT.TEMP" and the status of the heater as "HEAT_TOP.ON". Naming examples for properties:

TEMP	temperature
P	pressure
FLOW	flow
CURRENT	current or
I	current
IPEAK	peak current
VOLT	voltage
COUNT	particle counts
MM	size (in mm)
X	x position
T	time
ON	on status/control

In EPICS devices an optional AI,AO,BI or BO field may be appended to the property. This describes the EPICS record type. A property like a pressure reading may have additional sub-fields as well. Property "P" could give the actual pressure reading and "P.HIST" gives an array with the historical readings. We must use a standard convention for these types of property sub-fields in order to be able to use generic plot programs which simply extend the device name by a ".HIST" field for instance.
Here is a list of proposed sub-fields (the last names are taken from EPICS):

no sub-field	actual reading
.VAL	actual reading (EPICS)
.HIST	historical reading
.DESC	ASCII string with a short description of the channel
.INFO	information of physical unit, max ranges etc. in one record
.EGU	EnGeneering Units as n ASCII string
.HOPR	High OPerating Range i.e. display range
.LOPR	Low OPeration Range, lowest value in displays

Maximum length for EPICS names is 28 characters (not including the sub-field in the property, the total length is 32 characters). Non EPICS devices are allowed to have up to 16 characters per field (4 times 16 characters). Because of the different naming conventions in the protocols used in TTFL, we have to translate the names. This is a very simple process done inside the API and not visible to the user. We cut the facility part and replace the "/" character by an underscore "_". It yields to an EPICS channel name of "DEVICE_LOCATION_PROPERTY". A backward translation is also possible. An example for the current reading of the first dipole in the injector section 3 is: "TTF.INJ/DIPOLE/1INJ3/IAI" and channel name = "DIPOLE_1INJ3_IAI". The setpoint of the same dipole is "TTF.INJ/DIPOLE/1INJ3/IAO" and channel name = "DIPOLE_1INJ3_IAO".

10.4 Controls Related Systems

10.4.1 Timing and Clock

Timing and clock configuration The clock/timing system consists of four component types:

- RF master oscillator operating at 9 MHz.
- The rep rate generator for 10 Hz, reduced rate and single shot resets.
- Clock Generator and Event encoder.
- Timer modules for delayed pulses and width pulse pairs. These modules can be used for individual delayed triggers or in conjunction with the clock generator to produce delayed events.

The timing system clock will be derived from and locked with the RF master oscillator so that it should remain locked relative to the 1.3 GHz to within a couple of nanoseconds. Two clock systems will need to be assembled: one for the Injector I tests at Saclay and the other for use at DESY. When Injector I is set up at DESY then the two systems will be integrated. This should be straight forward to do. A count down of the 9 MHz signal by 9 will provide the 1 MHz bunch spacing of injector II and the reference sample timing for the quick digitizer system.
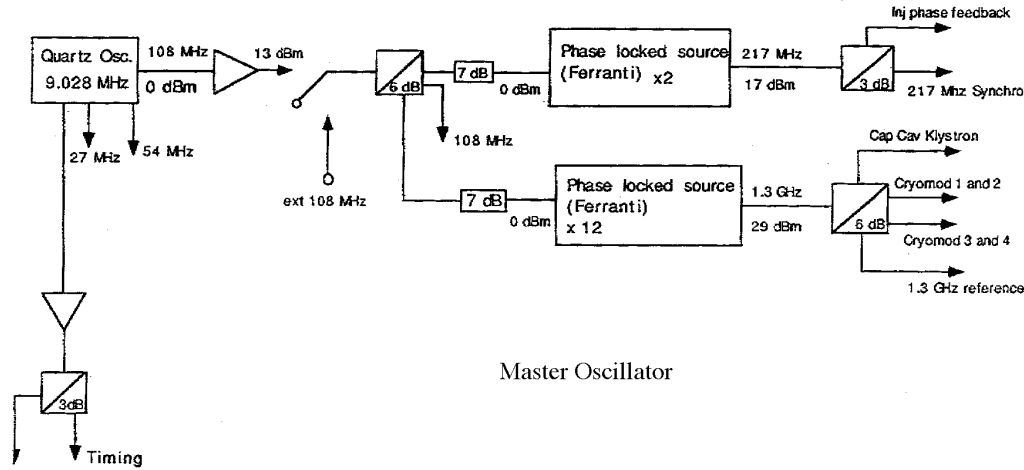
Master Oscillator

Figure 10.6:   Injector I Master Oscillator with outputs at (approximately)
                1.3GHz, 216 MHz, 108 MHz, 54 MHz, 27 MHz, and 9 MHz

RF Master Oscillator   The low level RF distribution system has been
described in Chapter 3. A quartz oscillator at 9.027775 MHz provides out-
puts at the frequencies given in Tab. 10.1. Fig. 10.6 shows the oscillator
outputs. A clock count down of 1/9 will be used extensively to generate the
approximately 1 MHz associated with sampling rates and Injector II.

For those systems which require precise phasing relative to the master
RF signal, separate phase stable low level RF signals will be distributed.
At present there are needs for distribution of the 1.3 GHz for the main RF
system, 216 MHz for the injector I and the cavity BPMs, and 27 MHz for
the laser of injector II. Fig. 10.7 illustrates distribution of the phase stable
low level RF signals. A fiber optic system is under consideration for this
distribution.

Repetition Rate Generator   The repetition rate generator provides the
master "Events" or resets to the clock system. It is designed to operate with
50 or 60 Hz ac and generate a pulse train from the ac zero crossing. With
a divide by 5 or 6 it provides a 10 Hz pulse train. This pulse train may be
further counted down to 5 Hz, 2 Hz, 1 Hz, 1/2 Hz, 1/5 Hz, 1/10 Hz, or off.
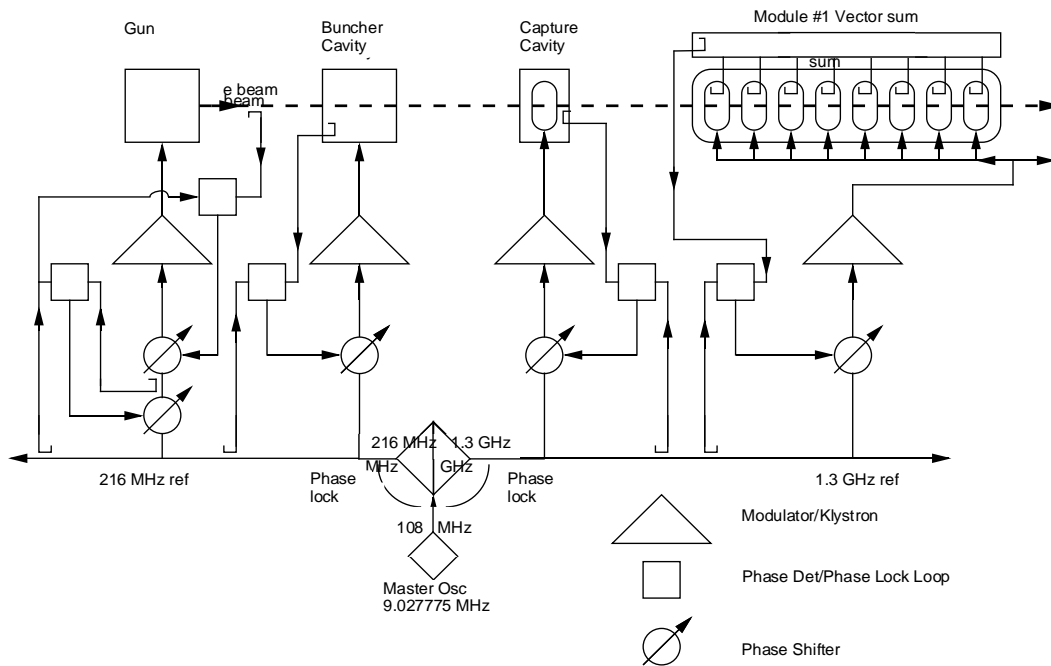
Figure 10.7: Illustration of the phase stable low level RF reference signals at 1.3 GHz and 216 MHz

Table 10.1: Clock Timing, and RF Frequency Harmonics

	MHz	sub har of 1300	sub har of 216.7 MHz
Master oscillator outputs	9.027775	144	24
×12	108.3333	12	2
×3	27.083325	48	8
×6	54.16665	24	4
×24	216.6666	6	1
×144	1299.9996	1	1/6
Clock	9.027775	144	24
Possible count downs of clock			
×1/2	4.513887	288	48
×1/4	2.2569	576	96
×1/9	1.003086	1296	216
×1/10	0.9027775	1440	240

Line driver pulse outputs of 1 microsecond from both 10 Hz and variable rep rate are available.

Clock Generator and Event Encoder The clock generator/event encoder imbeds 8 bit events in the 9 MHz clock signal. It receives the clock from the master oscillator (or other source) and has a backup oscillator on board. It also receives 10 Hz (or other) pulse trains for event encoding and has provision for a 10 Hz backup input.

It can decode events from the incoming clock and re-issue them or not as desired. It accepts up to 8 event input triggers and computer generated triggers for further event generation.

It outputs the encoded clock, the 9 MHz clock un-encoded, the event triggers, and status bits to indicate when the clock or 10 Hz signal inputs are no longer present.

The clock generator in conjunction with Timer Modules can be used to create delayed events.

The configuration of clock generator, rep rate generator and timer modules for delayed events is schematically shown in Fig. 10.8.

Fig. 10.9 shows how the clock and timing components might be configured for the operation of the injector and linac, first separately, then together. It should be very easy to make the transformation.

Timer Module Each timer module board can provide for 8 delay trigger outputs or 4 trigger pairs for start and stop pulse width control. The delayed pulses are referenced to up to 3 selectable clock events or an external trigger.

The timer module receives the encoded clock and outputs up to 8 detected events and copies of the incoming clock. The reference strobes that triggered the timer delays are also available.

Up to 4 timer modules can be assembled on one VME card or in one Internet Rack Monitor. The Internet Rack Monitor (IRM) is discussed in Sec. 8.6.

One half of a timer module is represented in Fig. 10.10. It consists of a combination of 2 control registers, 3 clock counters, and 4 comparators which output the delayed trigger.
The control register functions include:

- Enabling the delay timer outputs.

Clock 9 MHz

AC

Clock
Gen
Encoder

Clock Events Out

Rep Rate Gen

10 Hz
reduced rate

10 Hz

10/n Hz

8
Inputs

Delay

Timer Modules
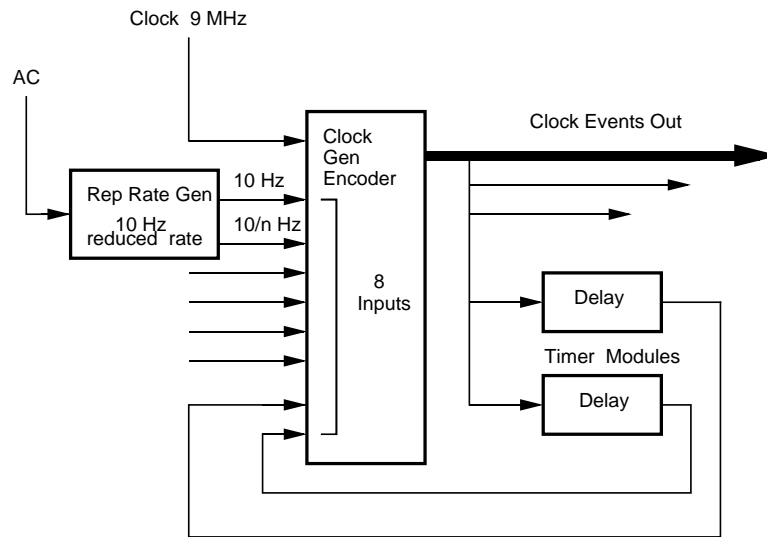
Delay

CLOCK GENERATOR and EVENT ENCODER

Figure 10.8:   Schematic of the Clock Generator with encoded Events on
the output clock. Delayed Events from a master reset can be
created by using the clock generator encoder in conjunction
with timer modules.
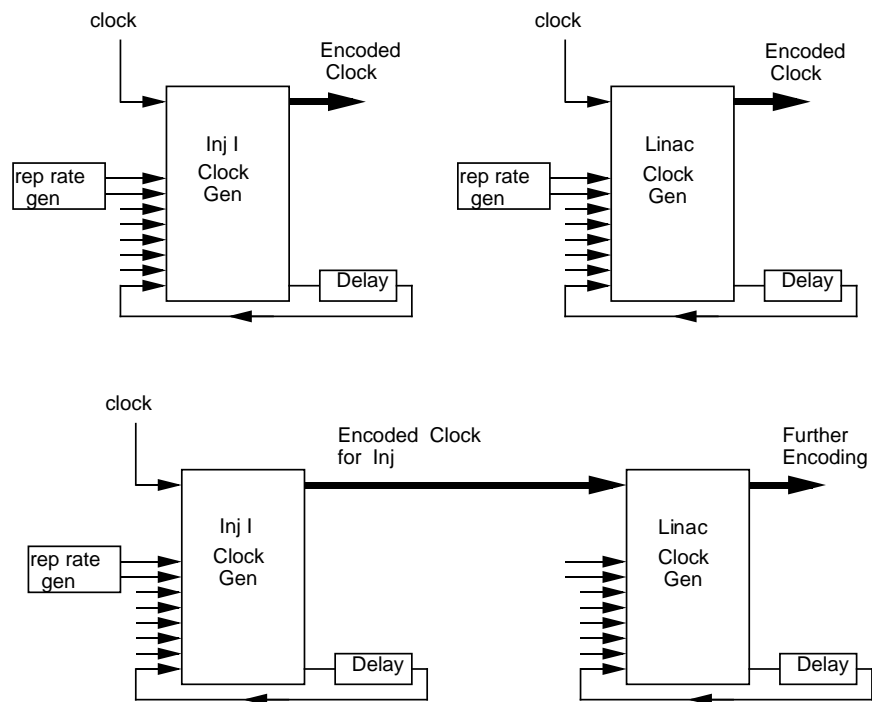
Figure 10.9: The clock system configuration for operation of the injector and linac separately during component commissioning (above), and then combined (below) for linac operation.
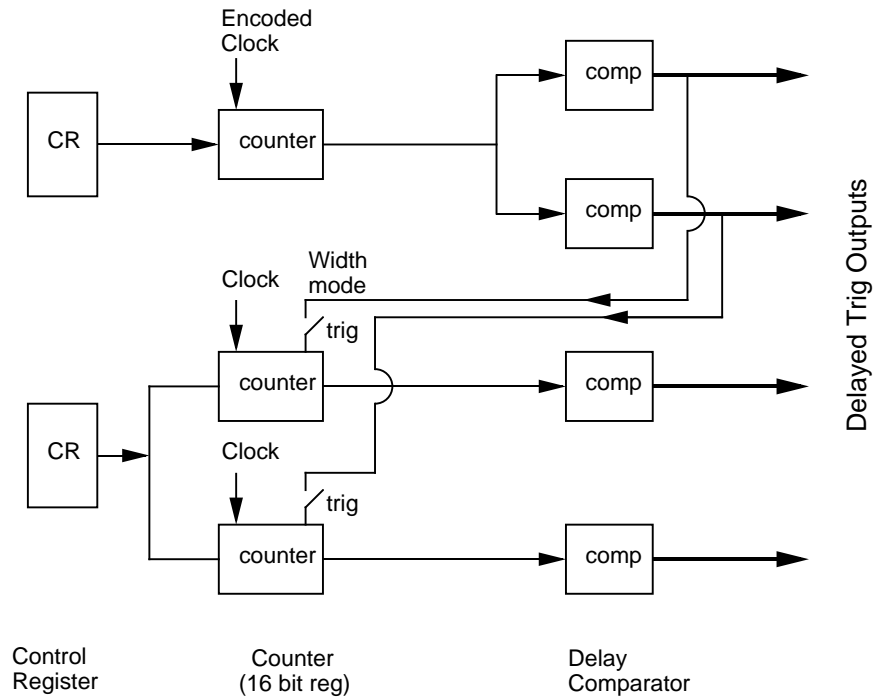
Figure 10.10:   Half of the Timer Module that provides delayed triggers

- Pre-scaling the clock by a divide by 10.
- Selecting: external clock, Event trigger, Off board trigger, On board programmed trigger, pulse length, and daisy chain mode.

The 16 bit delay counter accepts the clock and counts from the programmed event trigger.

The delay registers or comparators compare against the counter. As the counter increments and a match is found the delayed pulse is generated.

In pulse pair (or daisy chain) mode the output of channels 0, 1 can be used to trigger the delays 2, 3. In this way the width of a pulse will not change when the start is changed, and it is impossible for "off" pulses to precede "on" pulses.

Timing duration and resolution The 16 bit delay modules provide for over 7 ms of delay at 9 MHz which should be adequate for most information. They provide 70 ms with the divide by 10 clock scaling. (We will need to find out if this scaling can be changed to divide by 9 to make it more useful for our 1 MHz timing.) The resolution is one clock pulse (0.11 microsecond), or 10 pulses with the pre-scaling.

Events The use of a clock with embedded events allows for ease in coordination of the timing throughout the linac. As events are broadcast on the clock and can be turned off and on easily. they can be used for global coordination on many different devices simultaneously. Individual delays for special devices can then be set up from appropriate overall events.
Typical events might be:

- To at 10 Hz.
- Reduced rate trigger.
- Modulator HV pulse start.
- RF on start.
- Beam on start.
- Data Sample time triggers.

Most of the useful operations and information need to be carried out in the one to two msec of the pulsed RF and beam time. (See Fig. 2.1)

An encoded event (8 bits)takes about a microsecond of clock time so a number can be implemented within the beam pulse time.

The Injector I timing   As planed Inj I will need about 10 timing pulses and 10 start/stop widths. These can be provided on 5 predet (i.e. countdown) IP boards on one VME board.

The linac modulators timing   The linac modulators have about 25 timing channels. The Bouncer trigger must precede the firing of the GTO switch for the HV pulse by 1.09 ms. RF enable is delayed 100 microsecond from GTO on. Actual RF on follows another 300 microsecond after that.

Injector II   Injector II will operate with a bunch spacing of about 1 microsecond. This bunch spacing frequency will be derived by a count down of the 9 MHz clock and will be either 1.003 MHz (9 th sub harmonic).

10.4.2   Quick Digitizer

The pulsed mode of operation of the TTF Linac, about 1.3 ms of RF and 0.8 ms of beam every 100 ms, makes it highly desirable to have a standard analog to digital monitoring system which is capable of recording many parallel channels during the pulse time. The system which has been chosen (Quick Digitizer System) allows each channel to record at a 1 MHz rate during the pulse time. It is planned that the digitizers will be triggered by a count down of the clock to the 1 MHz frequency consistent with that planned for Inj. II. As this could result in a tremendous amount of data if say 100 channels each recorded 1000 data points (1000 microseconds) at 10 Hz (10^6 words/ sec), the digitizers must have local buffer and only that data which is specifically needed at a particular time will be collected into the main control computers. Of course, because of the buffer, substantial amounts of data recorded during one pulse can be transferred over the network during the 98-99% of the time the beam or RF pulse is off.

This general purpose system must have sufficient channels to record numerous transient data: beam intensity, position, loss; cavity voltage, phase and diagnostic signals; low and high level RF signals; mechanical motions and vibrations; etc.

Fig. 10.11 depicts the digitizer, its connection to the timing system, and the controls front end interface (processor board). In some cases timing

relative to the bunch structure will be critical, especially for Inj. II with its 1 microsecond bunch spacing, and for the cavity BPMs.

We expect that of the order of 100 channels might be implemented for the initial operation with one cryomodule. Based upon experience gained there, we will decide just how many channels to have in the final four module linac.

The software for the system data gathering should allow for:

- standard operations mode, i.e. recording of representative data (like the typical or average cavity voltage during a pulse) and display of that data to the operator either by updated values or real time plots. Data rates from individual channels to be adjustable as needed up to 10 Hz. Information to be used for both normal display and data logging.
- replay of transient events i.e. correlated data transient recorder at 1 MHz of all channels. Data to be gathered from the A/D buffers and displayed to the operator on demand. Such a mode would allow correlated diagnostics (snap shot) in the case of an unusual event (such as a quench) or when complete analysis of a beam bunch train is desired.
- repetitive display of a number of channels (like 4-8) "quick plot mode" updated on each beam pulse, showing the data during the digitizing time (e.g. 2000 data points over 2 ms/ channel / beam pulse). Such a mode would aid in understanding just how well the RF feed back was compensating for the bunch charge variations for instance.
- historical mode. This mode records over long time periods mean and or peak values computed from quick digitizes samples and allows correlation's of slower systems.

The Quick Digitizer Board   Because we plan to base most of our general purpose data collection around the quick digitizer, a short description of the proposed A/D board is given below.

We plan to use the Omnibyte Comet VMEbus I/O Multi-Channel Analog Digitizer. This board has the following properties:

- four digitizer-memory channels
- programmable trigger and digitizer clock logic
- VMEbus interface
- 12-bit digitizers with 2 or 5 MHz sampling rates
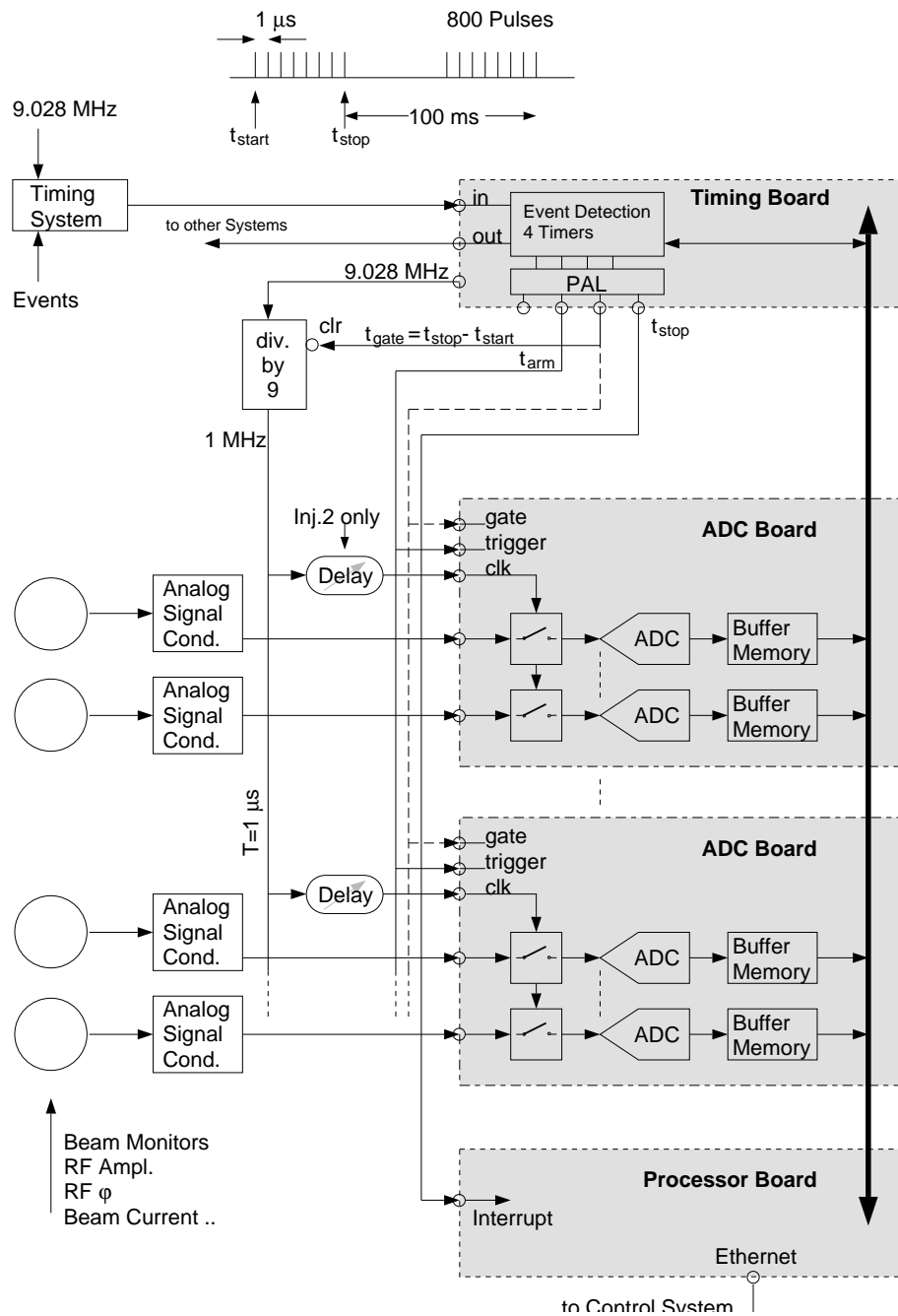
Figure 10.11: The Quich Digitizer fast ADC with signal and timing inputs, and output to the computer processor.

– Analog Inputs for the 2 MHz board are either 0-10V or $\pm$5V. Jumpers provide 50 ohm termination if desired. (5 MHz board has $\pm$1V input.)

– 128 k Bytes (64k samples) of memory for each channel (512k Bytes memory space per board)

– Either internal or external triggers, digitizer clocks and gate signals may be used.

The board is "dumb" and does not require programming of a microprocessor. It is controlled by seven 8 bit R/W parameter registers. Operational modes include:

– Normal mode- Digitizing begins at the external or selected rate following a trigger, and continues up to a preset number of readings.

– Circular Buffer- The digitizer continuously fills memory and is stopped by a trigger. The number of readings after the trigger is preset as above, and allows data capture before and after trigger.

– Oneshot mode- The first trigger starts the channels digitizing. Subsequent triggers are ignored.

– Delays of the different channels can be skewed by amounts given by the delay line on the board.

10.4.3   Beam Inhibit System

The Beam Inhibit System (BIS) is intended to prevent damage to the linac hardware in the case of any anomalies such as equipment faults, operator errors or unexpected beam loss. This means that the "fast" beam- inhibit signal has to be triggered quickly if any problem is detected. It is desired to trigger the inhibit within the time period of a beam pulse train or a few microseconds. A "slow inhibit" should stop the linac operation if fault conditions like: no water, power supply error, bad vacuum, personnel interlock not ready, etc, are detected prior to or during operation.

Reliability and speed of the interlock system and ease of connection of to the various input signals define the requirements for the design. The shutoff conditions, either of analog- or digital signals, must be handled by a local hardware unit, while the status of the individual signals and thresholds must be readable by the control system. In addition the actual values which have triggered any shutoff should be stored in a buffer for later processing. This

leads to a hardware which handles and triggers the Beam Inhibit, while a local processor handles the readout of settings and thresholds and records the cause of the inhibit.

The new HERA quench protection system is proposed as the prototype for this system Communication takes place by the CAN field bus.

In addition to providing the BIS we must provide the input signals and also the interface to the injector gun.

10.5   Applications

10.5.1   Applications Overview

In our controls system environment we understand an application to be a tool – or at least part of a tool – to support the physicist in the commissioning and operation of the accelerator. It can be a means of presenting control points and read backs at the console or client end, or it can be a specific program to interface to a piece of hardware at the "front end" or server hardware interface. Thus an application can vary from a graphic to a program which calculates the emittance, or adjusts a cavity resonant frequency. By this definition it is not the server process or network to collect the data.

The very first applications needed are those to commission the linac. Basic functionality will be required to access any data point in the system and to adjust any device. An application like a parameter page will help to do this job. Specialized tools to interact with complex devices like stepping motors, BPMs, modulator controls, RF control, image processing and power supplies will also be necessary at this stage. Many of these tasks will be running in their native (server) environment and be accessible over the network.

Utility Applications   Specialized applications with general utility could be called "utility applications". Under this category falls:

- Set/Read Value
- On/Off/Reset, Status
- Knob or Trackball Controller
- Time Plotting (Trending)— Time plots, XY plots, and read information- Information must be gathered by: read on request, read at specific

event or time, repetitive read on event or at given frequency (e.g. 10 Hz, 1/60 Hz, etc.) Data must be time stamped. Time plots have three basic time interval structures:

- Slow— plot information gathered over hours from data logger or from read at long time interval.
- Real-time— plot presents requested information at 1 Hz, 3 Hz etc.
- Quick time— plots information requested, gathered from quick digitizer channels during RF or beam pulse at information rates of up to 1 MHz.

In addition, snapshot information should be available by recording information in buffers which can be frozen on event and the last n slots of information leading up to the event displayed. The quick digitizer lends itself to this application.

With the utility applications above goes the parameter page application which provides those utilities for a number of devices at once.
Other tools:

– Alarming
– Save/Compare and Restore
– Archiving (Data logging)

These (three) applications, though important, should take second priority to the more basis control needs outlined above and to necessary special purpose applications.

Needless to say, tools mentioned above which collect information from a server process will also need appropriate interfaces to the operator.

High Level Applications   At a later stage of the project complex applications may be desirable. These programs could calculate and analyze the data from the diagnostic elements of the linac. This implies an easy and common access to the data - which shall be achieved by the API, and an easy way to display the results. The latter could be implemented in several ways depending on the preference of the implementer. SLGMS, LabVIEW and MEDM (and IDL, PVWave) are possible programs for display of sizable quantities of data.

Sequencing Though there is always a desire to implement sequence routines early on in order to facilitate turn on operations, this sort of programming must take second priority to having the basic standard controls tools in hand.

Once the control system reaches a state of maturity which permits standard control operations and the linac is operated with a more or less standard set of procedures, the desire to automate routine work can be undertaken with the development of sequence programs. There are different levels on which the sequencers run: device orientated programs belonging to the servers or front ends, and global sequence programs runing on the workstations or client side.

10.5.2   Injector I

10.5.2.1   Overview of Hardware

The system will consist of an integrated data acquisition and control system for all elements necessary to provide a beam from the injector. The implementation of the control system follows the so-called "Standard Model" which became in the beginning of the 90's a de facto standard for the control of particle accelerators. This model is a distributed system consisting of operator consoles, a network and interfaces to equipments.

In our system, the operator interface is a UNIX-based workstation: namely an entry level Sun workstation with a color screen and, optionally, a knobs panel.

An Ethernet network establishes the necessary link between the operator workstations and the crates containing the interfaces to equipments.

The typical interface crate is based on the VME standard with a 68040 CPU and a variable number of VME modules for the connection to the injector equipments.

10.5.2.2   VME Systems

Four VME crates will be used in order to control the different subsystems:

1. one VME crate for the gun, the high voltage system, the subharmonic buncher and the 216MHz RF source

2. one VME crate for the beam guidance components

3. one VME crate for the modulator and the capture cavity RF system

4. one VME crate for beam diagnostics

They will use mainly commercial interface boards. We foresee using the following types and quantities of boards:

A/D boards:	4	ADAS ICV150 32 differential or 64 single end inputs, 12 or 14 bit resolution, 40 Ksample/sec
Fast A/D board	1	COMET8 4 independent channels, 2 Msample/sec (beam currents acqu.)
D/A boards:	5	ADAS ICV712 8 or 16 analog isolated outputs, 12 bits resolution, states known at power up
Bin. I/O boards:	3	ADAS ICV196 96 digital inputs/outputs, TTL, 12x8 channels, 16 IT sources
Step. Motor boards:	3	ADAS ICV914 intelligent controller for 4 stepping or DC motors (cold tuning system)
Image Proc board:	1	Eltec V-IPP (frame grabber for a video signal coming from the optical transition radiation system).

All the ADAS modules have already been extensively used at Saclay and CERN for several installations and experiments.

Some custom boards are needed also for specialized applications:

Timing system:		VME and mezzanine board from FNAL (triggering of beam diagnostics)
SEM-grids acqu. board:	2	64 channels ADC 8bit + sample + hold for beam profiles + energy spread
BPM acq. board :	1	16 channels ADC 12bit 1.2 μs acqu time + sample + hold.

Although the total number of VME board will be roughly 30 and will occupy only 60 % of the space available in the 12 slots VME crates, this distribution among 4 crates has been chosen to add flexibility and independence of the different hardware components of the system.

Gun

Type	Parameters	Channels
HV 250 kV	Reference	1 DAC
	U,I readbacks	2 ADCs
	Interlocks	2 bin I/O
HV 40 kV	U,I readbacks	2 ADCs
	Interlocks	2 bin I/O
Steering, Enzel Lens	I, rising time references	6 DACs
	U,I readbacks	6 ADCs
	Interlocks	6 bin I/O
Heating	U,I readbacks	2 ADCs
Polarization	U readback	1 ADC
HV Macro Pulse	Amplitude, slope, length references	3 DACs
	Amplitude, length readbacks	2 ADCs
Micro pulse	Repetition rate	1 DAC
	Frequency readback	1 ADC

Subharmonic Buncher

Type	Parameters	Channels
References	Inj., gun, cav. phases, cav. ampl, cav. tuning, cav. temperature	6 DACs
Readbacks	Inj., gun, cav. phases, cav. ampl, cav. tuning, cav. offset, cav. temperature	7 ADCs
Remote / Local Control	Inj., gun, cav. phases, cav. ampl, cav. tuning, cav. temperature	6 bin outputs

BEAM - LINES Power Supplies

Type	Number of P.S.	Channels ADCs+DACs +binary IO
Steering Coils	7 (2 p.s. H/V)	14
Solenoids	4	4
Triplets	2 (2 p.s. /triplet)	4
Dipole	1 (E analysis)	1
H trim coil	1 (in dipole)	1
V trim coil	1 (E analysis beam-line)	1
Supercond. Solenoid	1 (in capture cavity)	1
Chicane dipoles	1 (before linac, 1 p.s.)	1

Requirements for the control of power supplies
  1 reference voltage
  1 shunt voltage readback
  1 fault status binary input (OK / ERROR)
  1 on / off binary output

Capture Cavity Instrumentation

Type	Number	Channels ADC (0 - 10 Volts)
Temperatures	4 (HOM couplers)	5
	1 (stepping motor)	
RF pick-ups	2 (e- pick-ups)	2
Vacuum	1 (main coupler)	1

Beam Diagnostics

Type	Number	Channels
Current monitors	3	3 high-speed ADCs
Faraday cups	3	3 high-speed ADCs
Isolated Collimator	1	1 high-speed ADC
Beam position monitors	4 (electrode buttons)	4 Orsay
OTR monitor	1 system for 2 stations	1 image proc.
SEM-grids	2	2 Orsay

Modulator

Type	Number	Channels
Interlocks	40	40 bin inputs
On / Off controls	20	20 bin outputs + relays board
References	8 (0 - 10 Volts)	8 DACs
Acquisitions	17 (0 - 10 Volts)	17 ADCs

Capture Cavity

Type	Number	Channels
Trigger	1	1 bin input
On / Off Loops	6	6 bin outputs + relays board
References (PHI_K, PHI_ZERO, PHI_REF, PHI_LOOP, AMP_REF, ATT_PINC)	6 (0 - 10 Volts, ± 5 Volts)	10 DACs (incl. 1 16bits)
Acquisitions (ERR_PHIK, ERR_PHI1, ERR_PHI2, ERR_AMP1, ERR_AMP2, DIF_PHI, V_PHI; ACAV_DET1, ACAV_DET2, AKLY_DET, V_PHIK, V_AMP, PDIR_DET, PREV_DET)	13 (0 - 10 Volts, ± 5 Volts)	14 ADCs (12 — 14 bits)

10.5.2.3   Workstations

For the preliminary tests of the injector, 3 workstations will be necessary. One will be devoted to the demanding operation of the capture cavity, the two others will be shared between beam lines control, beam diagnostics, database configuration and software management. Two of them will be equipped with 2 x 8 software assignable knobs. In the final stage, only 2 workstations will be sufficient.

10.5.2.4   Software Architecture

At an early stage of discussion, it was decided to use EPICS in order to control the injector. One of the main advantages of EPICS is to provide a very solid basis to build a control system. In effect, all the basic elements needed for controlling an accelerator are present:

> a distributed database with powerful capabilities in term of types of acquisition, processing, attributes.

> A communication software bus, the so-called Channel Access, used to access the database anywhere in the network.

> A set of tools which constitute the man-machine interface (display manager, archiver, save/restore facility, alarm handler...)

> A sequencer for programming of sequential operations.

The database resides in the different VME crates which act as data servers. The operator tools are run from the workstations and are clients of the data servers. The client/server communication is made through Channel Access requests.

Due to the clear organization of the software, it is very easy to develop one's own application programs and to interface them with the rest of the system.

10.5.2.5   Applications Programs for the Injector

Gun / Subharmonic Buncher / Beam-Lines / Modulator   These controls look rather simple: we will provide synthetic synoptic representations of these different elements. From these pages the operator will control the parameters (reference voltage, on/off, remote/local) and will supervise them (readback value, high/low warning/alarm limits). Besides these graphical pages, a text-based parameter page, easily configurable by the operator, will be used to display a variable number of parameters. Each line will represent all the information concerning a parameter: the readback value, the alarms, the status, the reference value and interactive objects to modify it (keyboard entry, slider, up down buttons, assignment to hardware knobs). It will be also possible to generate a strip chart representation for each readback value present in the parameter page.

Capture Cavity   This complex subsystem needs a meaningful graphical representation to be able to catch easily its overall status. For example, a synoptic representation will give on a single screen all the parameters to control the RF closed loops and will be the main tool of interaction for the RF specialists. Furthermore, specially designed procedures will be used for the tuning of the cavity, for the optimization of parameters and for the achievement of software closed loops. Implementation of these procedures will be done with the State Notation Language of EPICS. Accelerator physicists will be able to easily modify these procedures. In the same way, it is foreseen to start the modulator automatically with a procedure written in SNL.

Beam Current Monitors (Toroids)   Two methods of measurements will be used:

- Acquisition of a DC signal suitable for a standard EPICS processing (check of limits, archiving, display with conventional methods by the display manager). The DC signal will be delivered by a suitable electronics circuit to a A/D board ICV150 and it will be processed like all the others DC signals.

- Acquisition of the whole beam pulse: the fast A/D module will feed a program drawing the pulse on the operator workstation. Additional functionalities will be implemented like superposition and memorization. The A/D module will be externally triggered by the timing system.

SEM-Grids and BPMs Acquisition   The data coming from these 2 diagnostic subsystems will be made available to applications through standard EPICS records. Beam profiles, emittance values, energy spread will be calculated from these raw data. The acquisitions will be triggered by the FNAL timing system. The EPICS display manager is suitable to visualize these data.

OTR Image Acquisition   The pixel map generated by the VME frame grabber module will be delivered to UNIX workstations in a file using the NFS protocol. The off-line digital image processing will be made with OnX, a MOTIF-based tool developed at LAL Orsay to generate pseudo-colors representation, image enhancement and profiles plot.

10.5.2.6   Cold Tuning System Control

The goal of the Cold Tuning System (CTS) is to set the cavity at the frequency of the accelerator in changing its total length with an accuracy of 10^{-8} (13 Hz at 1.3 GHz).The CTS is composed of a stepping motor, a gear box, a screw and nut system and a lever system. There are not electrical limiting switches but only a mechanical stop at each end of the tuning range. The tuning range is fixed at $\pm$ 750 KHz in 4 Hz steps.

Hardware   The hardware to control the CTS for 9 cavities will consist of:

- 3 ADAS ICV914 VME boards (intelligent 4 motor controller)

- 9 ADAS TRL914 translator modules to provide electrical power to the motors

- 3 ADAS RTL914 crates and power supplies for the TRL914.

Software   A MEDM display task controls up to 4 motors. Three buttons are provided to enter the frequency, to reset the motor and to stop a move in progress. A readback value is displayed. The motor features have to be given in the Stepping Motor (SM) Record fields of the EPICS database. It was necessary to design the specific part related to the ICV914 board: namely a SM Device Support and a SM Driver Support. The driver receives the commands (MOVE or RESET or STOP), sets the commands in a message queue and a readback task actually processes the commands. That allows the driver to hand quickly the control back to the database scanning tasks. The readback task updates the motor data in the database thanks to a callback mechanism. When a motor is stopped during 2 seconds it is inhibited. The number of moves and of steps per day will be recorded.

10.5.3   The TTF Linac starting with Cryomodule 1

10.5.3.1   Power Supply Systems

A standard DESY type power supply arrangement will be used for both warm and superconducting magnets: quads, steerers, and analyzing magnet. (See Sec. 6.4) These power supplies and their mode of control, though not an ideal match to the needs of TTFL will be used because of their compatibility with many DESY systems and therefore their ease of maintenance and replaceability. In particular, control features of these supplies seem overly complex relative to the demands of TTFL.

In the cryomodule (see Sec. 6.1) there is a quad doublet, and a pair of horizontal (2) and a pair of vertical (2) steerers. One set is used for H and V steering;, the other will be used for fast excitation and/or vibration compensation.

The warm beam line will have four quad doublets (each pair powered in series) and four pairs of H,V steering magnets. (see Chap. 9)

The high energy analysis area will have an analysis magnet, a pair of H,V steering magnets and two doublets of small bore quadrupoles, and two large bore quadrupoles. The small doublets will have each pair powered in series, while the large quads will be individually powered.

A summary of the number of power supplies is given below. (See also Sec. 6.4)

Module			
Cold quad doublet	1	H,V Cold Steerers	2
		Ripple excitation	2
Warm Beam line			
Quad doublets	4	H, V steerers	8
HE EAA			
Quad doublets	2	H,V steerers	2
Quad singlets	2		
Analysis magnet	1	AM compensation coil	1

The ripple excitation supplies are not needed initially and their control interface will be left till later. The analyzing magnet requires high regulation ripple control and read back resolution at the level of 10^{-4} and 16 bit. For all other supplies, regulation and read back at 10^{-3} and 12 bit would be sufficient however because standard supplies and regulators are being used 16 bit D/A, A/D will be used.

The capability for A/D read backs synchronized and phased to the 10 Hz pulse rate (or some slower synchronized rate) should be provided. Higher frequency monitoring or sampling if necessary (e.g. to investigate ripple) can be done with a scope or by special connection to the Quick digitizing system.

Displays and control of settings and read back of the magnetic devices should be provided in conjunction with beam position information from the BPM system, SEM, wire scanners, and OTR/View screen systems.

Ganged control of multiple devices should be provided with adjustable scale factors in order to easily adjust for changes in beam energy, or allow for localized orbit distortion (like the dog leg adjustment).

Standard controls support of status (on/off, reset), save, compare, restore, data logging, and time plots of set points and read back will need to be supported.

Power Supply Control   Power supply control will be managed as follows. There are two microprocessors associated with power supply control in VME. One, the main CPU handles the Ethernet communication, the VxWorks operating system, EPICS application software, and the local database. The other — the microprocessor that is of interest in this context — handles the communication to the power supply controller. In turn, the power supply controller inputs to the programmable logic unit and to the feedback electronics.

These elements are depicted in Fig. 10.12, Fig. 10.13 and Fig. 10.14. Fig. 10.12 shows the controls software configuration to be used in the linac with the DESY PSCs. Figure 10.13 is the corresponding hardware view. Fig. 10.14 indicates the power supply, and the local PLC, PSC interface with it. The approach used in the injector is conventional with the power supplies directly controlled by analog and digital I/O boards housed in a VME crate.

Programmable logic controller (PLC)   This unit (Siemens type 100 U) provides control and protection for the power supply against failures like over current, over temperature etc.
The PLC:

- monitors the power supply interlocks, protects the supply, and turns it off in case a fault is detected.
- showing the actual status: local via LEDs, and remote as a 16 bit parallel connection.
- receiving commands from the power supply controller (e.g. ON, OFF, RESET, POL. SWITCH) and handling them.
- allowing local turn on/off via push buttons.

Power supply controller (PSC)   This unit interfaces between the power supply and the control system through a serial SEDAC bus connection. The controller is built around a CPU of the 680X0 family. Via the remote control the power supply can be turned on/off, the status can be read, and the
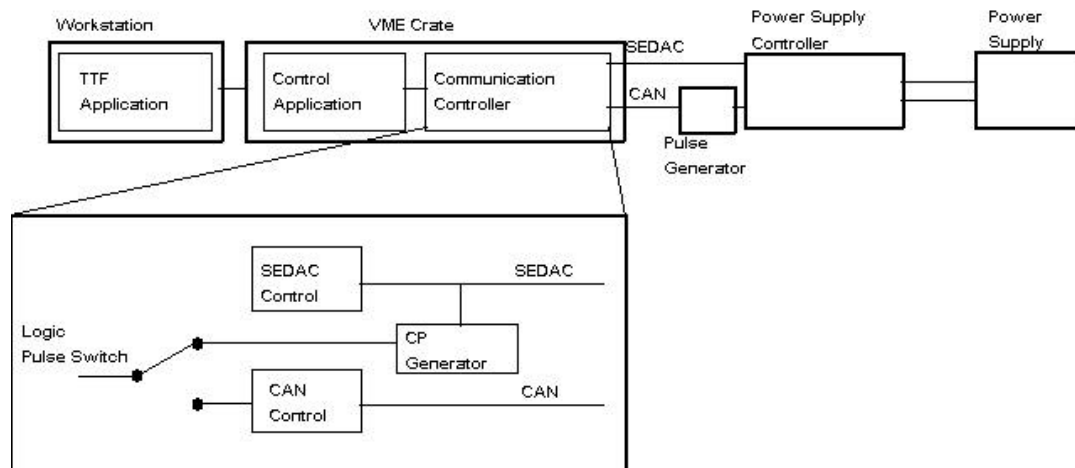
Figure 10.12:   Controls software configuration from the operator workstation to the power supply

current value can be set. (The power supply controller also provides for local control with a hand terminal.)
The power supply controller:

- transmits binary commands (6 bit parallel) to the power supply (ON, OFF, POLARITY SWITCHING)
- transmits the digital reference (16 bit parallel) to the electronics
- reads the status of the power supply (16 bit parallel)
- reads the analog monitored current

Special Signals   For personnel and equipment safety some more signals have to be given as input to the power supply. The signals shall be given as potential free contacts.
These signals are:

- PERMIT— This is the permit to turn on the power supply. The door

Power Supply Control
DESY - Type
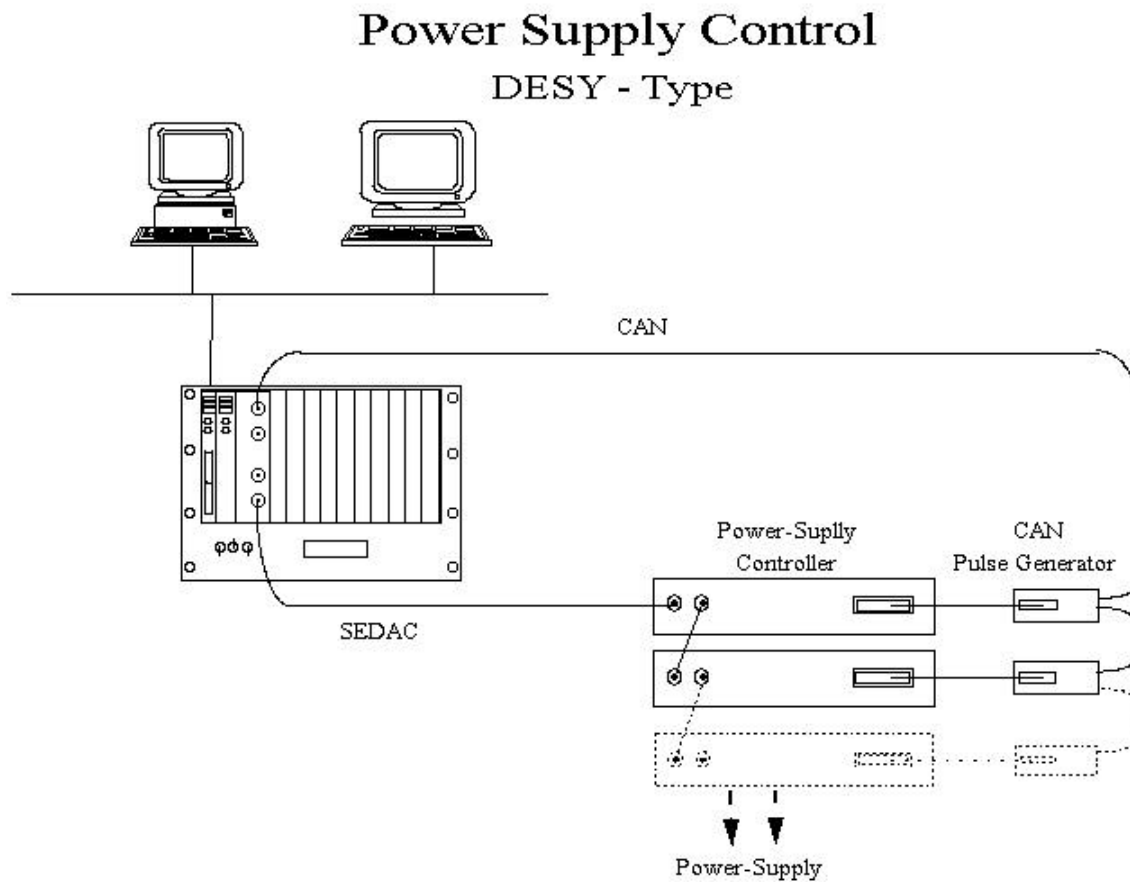
Figure 10.13: Power supply control hardware

interlock and the emergency shut off buttons have to be combined.
– MAGNET INTERLOCK— Protection of the magnet. Here signals like over temperature and quench detection are linked.
– GROUNDING— During shut down or work at the magnets the power supplies will be grounded.

In addition a hardware interlock will be installed that can be connected into the Beam Inhibit System. If the power supply does not work properly a failure signal will inhibit beam and protect the linac from potential beam damage.
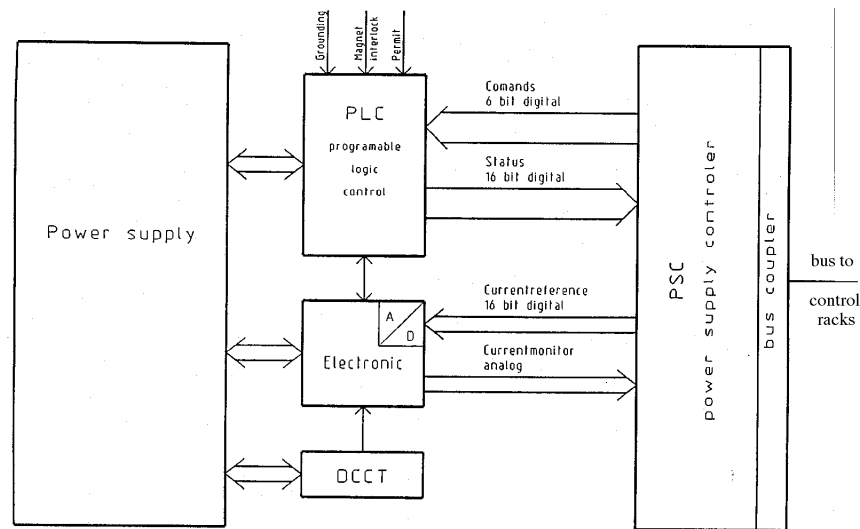
Figure 10.14:   A DESY power supply unit with programmable logic control and power supply controller.

Commands to the Power Supply Controller   The changing of the settings in the controller is done by sending the value of an incremental current to the controller. In addition the controller will receive the bit to define the direction of incremental/decremental changes. The changes themselves are triggered by pulses. The origin of the pulses can be defined to be a common pulse (CP) bit in the SEDAC messages or an external hardware pulse directly at the front panel of the controller. (In fact the real differential value is a binary value which increments or decrements a register which overflows into the register for the set point for the power supply.)

Setting of new set points has to run through the SEDAC field bus. The rate, time and number of pulses have to be calculated. A CP generator is necessary to create test messages to be able to send the necessary CPs to the controllers while read/write telegrams are not available.

(Direct setting of set points to the PSC is also possible. In this case the rate of change has to be carefully adjusted to the maximum rate the power supply can execute, otherwise the power supply may trip. Because of the risk, this mode is not recommended.)

VME Control Processors   Individual PSCs are connected via SEDAC to a VME crate. All the power supplies are controlled by two microprocessors (CPUs) in the crate. Both CPUs communicate over the VME back plane.

The main CPU will supply the Ethernet communication and will have adequate memory to store the VxWorks operating system as well as the EPICS application software and the local database. In addition space for diagnostic tools should be available. The main CPU acts as the gateway between the high-level applications on workstations connected to Ethernet, and the communication path to the controllers. See Fig. 10.12.

A second CPU will hold the SEDAC communication controller designed as an industry-pack (IP) module. The second CPU will handle two tasks: generating SEDAC telegrams for 'standard' SEDAC read/write requests, and generating test telegrams (with the CP-bit set) necessary to change the set point(s) in the controller(s). The second task can be running independently of the first CPU and therefore will not put any load on it. The maximum repetition rate of test-CP telegrams which can be created by the second CPU is about 400 telegrams per 100 msec. This should provide for at least two reads and a set of all the supplies. Further investigation of the communication limitations will be undertaken, but the capability appears sufficient at present.

Possible future option   In case there is a limitation in the CP-repetition rate, a second option under development is possible. Since the controller accepts an external CP trigger this feature can be used to run higher CP-repetition rates from an external source. This can be achieved by an external VCO which itself is controlled by an intelligent device. This device could be a simple CPU with an embedded field bus controller like the ones available for the CAN bus.

This bus has the advantage that it supports broadcasts and would allow one supply to inform the rest when it has reached a limit. This feature might be useful in coordinated control of multiple devices. Since the CAN controller for the VME system is an IP module, it could reside on the second CPU along with SEDAC controller. A single command to the second CPU could switch the CP generation from SEDAC to the CAN controller and set the appropriate control bit in the PS controller to accept external triggering.

Software   A common software interface will be defined for all power supplies installed at the TTF, both in the injector and rest of the linac. This approach will lead to a common set of parameters and commands necessary to run all power supplies installed. The definitions available from CERN will be used as a guideline. They lead to a very general approach of defining a power supply as a device with special properties.

10.5.3.2   Beam Monitor Devices

In general, beam diagnostics will interface to the controls system via VME.

Beam Display Applications Program   It is worthwhile to consider what we might like as a general beam display program which we would try to have available at the beginning of beam commissioning of the linac. As we consider the control of individual devices we should keep in mind this sort of general display.

The BPMs, toroids, loss monitors, and the SEM or screen behind the analysis magnet all provide beam information which can be obtained without destroying the beam quality as is the case for view screens. (The beam after the SEM is no longer used for analysis.) Thus it will be desirable to have the capability of continuous readout and display on a pulse to pulse basis the values, averaged over the beam pulse, from these devices. This the facility often referred to as a "comfort display".

An application program (or programs) which displays this information in an easily understood manner while providing control of steering and quadrupole supplies should be given high priority so that it is (they are) functional when the linac first turns on. Such a program might also analyze SEM data to provide a beam energy measurement and display over all RF gradient and relative RF beam phase.

Beam Position Monitors (BPM)

   Cavity BPM (see Chapter 9)   The first cryomodule will have a cavity BPM. Also a cavity BPM will be mounted either in the injector line just before the cryomodule or just after it. This BPM will be for test in a warm location where it is more easily accessible than the one in the cryostat. These

BPMs need a 216 MHz reference signal phase locked to the RF. The cavity BPM produces X,Y signals proportional to the product of position and intensity. Thus three A/D read out channels are required per detector. For beam with large displacements (>0.3 mm) normalization must be made using the current monitor signals whenever a quantitative measurement is necessary.

At present it is envisaged that each channel will be digitized four times at 50 ns intervals for each position reading. The multiple readings may be necessary to get the 10 μm resolution desired and use of the quick digitizers is planned. Just how the data will be processed for the final TTFL installation will depend on early experience and is part of the evaluation plan for these detectors. One hopes that less complicated processing will be adequate.

Stripline BPMs (see Chapter 9)   These will be the standard warm BPMs. Four will be needed in the warm beam line at the locations of the quads. In the high energy analysis area, five are planned, with one located after the analysis magnet for energy measurement. In addition two more may be located in the injector beam line just prior to the cryomodule so that they can be tested at an early stage. These BPMs produce signals proportional to position (i.e. normalized) and can be read by the quick digitizer boards (or slower A/Ds if the fast resolution is not needed).

Stability of the BPM digitizer sampling time relative to the beam bunch may be critical in order to get accurate information. This may be especially true with injector II and its 1 μsec bunch spacing.

The Quick Digitizer readout system should be capable of gathering the BPM information at a 1 MHz rate during the beam pulse. Under most conditions only a small part of this information will be read back into the control system for display of average or typical position and intensity on successive pulses.

Displays of updated simultaneous position on all detectors should be available in conjunction with the control and display of the magnetic elements as discussed above. Time plots (slow, real, and quick time snapshot,...) derived from that system would be available.

A minimal amount of digital control and status information will be required for the BPMs. For instance, digital control will be necessary for gain selection depending on intensity or position offset.

Cryomodule wire alignment system The wire alignment system planned for inside the first cryo module will have electronics similar to the stripline BPMs and should be supported in the control system by similar control and read back features. This system will be capable of continuous readout (unlike the pulse structure of the beam) and it will be capable of 1000 readings per sec per channel.

The system will have 4 detectors per cavity, and 4 detectors on the quad package, making for a total of 36 detectors each with 4 cables for the H,V plates. Position resolution is expected to be of the order of $\pm 10\mu$m. Data logging of these detectors will provide continuous position information of the cavities and quad package during cooldown, warmup, and operation.

Beam Phase Detection and Standard Beam Display An independent system which continuously monitors and displays the beam phase relative to the LLRF distributed signal will be necessary. Display of this information could be combined in the beam display applications program.

SEM (see Chapter 9) There is one SEM grid planned. It is located behind the analyzing magnet and provides information on beam energy and energy spread. As this is the last device in the beam line it can be treated as a continuously available detector.

This system will be modeled on the one for the injector (see the Injector I material earlier in this chapter and in Chapter 3). The SEM has 40 channels of readout. Time resolution can be less than 1 μs, or over a whole beam pulse. Continuous display of the SEM channels on each macropulse will be needed. We hope this can be provided by an acquisition system like that for the Injector I. Readout to the controls system from the SEM subsystem of the 40 channels and data analysis will be necessary as will setup and control of that system.

Information about the energy of each beam bunch in a pulse (or each microsec) will be wanted. At present we expect to get this information from the BPM system. It is not clear whether the SEM system could provide multiple records per beam pulse and at present we do not plan for such data acquisition.

Toroid Current Monitors, BCMs (see Chapter 3)   These monitors will serve as the primary indication that beam is indeed being transported to the beam dump and not lost along the linac. In the linac, warm beam line and high energy analysis area, four monitors are planned. These are located before and after the cryomodule and before and after the analysis magnet.

Though the requirements given in Chapter 9 may not be obtainable, it seems likely that a dedicated processor should keep track of the beam current in each device and differences in current from device to device. Such differences or missing beam could then be used to provide a signal to inhibit the gun pulse (see Beam Inhibit System). The dedicated processor could make use of Quick Digitizer A/D boards to sample beam current at 1 MHz rate.

The control system should be able to acquire similar 1 MHz data either from the dedicated processor or from parallel Quick Digitizer boards. This data would be read into the control system at a slower rate between beam pulses, and only when needed. As in the case with BPMs most of the data would not be needed most of the time, however readings of total charge per pulse might well be needed every pulse.

The toroids themselves will probably have a minimal amount of control and status information to be provided by the controls system. A dedicated processor might need a number of parameters to be down loaded, and might provide a number of computed read backs.

Loss monitors   Loss monitors will be located along the linac and in the HE EAA. Typically as many as 20 of the pin diode type may be installed initially. (Consideration is also being given to installing some in the cryomodule in order to detect losses and dark current.)

Loss monitors which provide signals associated with beam loss (as distinct from wire scanner data— see below) should be configured to provide alarm or inhibit inputs to the Beam Inhibit System if signals above some threshold are observed. Such protection should be provided by a dedicated system distinct from but interfacing to the overall control system. We plan to use the HERA quench alarm system here. This system integrates the loss monitor readout function and the beam inhibit function.

The outputs of these monitors are TTL pulses. For the control system it will be necessary to monitor the scalar output of these pulses and provide

information as a function of time during the pulse.

Wire Scanner   The wire scanner is nondestructive in the sense it interacts only with a small fraction of the beam at any one time, and can be used while other measurements are going on. One slow and one fast scanner are planned for emittance measurement in the high energy analysis area.

Wire scanner read outs of beam profiles are provided by scintillation photo tube detectors. Signals from these phototubes could be read by the quick digitizer system. If other phototubes or ion chambers are needed they could be read similarly.

The wire scanner system that will first be used will be the slow scanner. Stepping motor control and position readout will be necessary for the scanner. A program should be provided which allows for easy control of steps per beam pulse , or step rate and also for step so many counts, etc. The ability to make displays of loss monitor position vs. wire position should be standard to the plot routines (XY plot).

OTR/View Screens   The OTR/View screen system is a package contained in a single vacuum box. Either type screen must be retractable as beam scattering in the screen destroys the quality of the down stream beam. For this reason a system which provides easy insertion and removal of the screens is important.

Two types of Optical Diagnostic stations will be used. They are characterized as "complete" and "simple" in Chapter 9. The complete one will be provided at four locations in the high energy analysis area (all except the second one of the five in the area). The simple one will be installed at four locations along the warm beam line and in the second location in the high energy analysis area.

Read outs of the beam profiles are obtained by CCD cameras. The screen control, camera control, and data acquisition system is an integrated, dedicated system. It is described below. The system will interface to the main control system via an interfacing processor and appear as a virtual VME module.

Acquisition and Control System   The Optical Diagnostic Control System (ODCS) for the OTR and View screens diagnostic, will be an inde-

pendent component of the accelerator control system. It has been thought as a single device, though complex, connected to the main control system.

This solution will have two main advantages. The first is that the system can be developed and almost fully tested before to be installed at DESY. The second is that the network of the main control system will not be loaded by the heavy traffic due to frequent images transfer from the frame grabber to the processor where images will be analyzed. Digitized images will be transferred to the consoles in the control room only if needed, while typically only the result of the measurements (beam size and position for instance) will be returned.

The ODCS will have two main processors unit. A Local Console will have the control of a VME crate where I/O modules (frame grabber, stepper motor controllers, digital I/O, etc.) will be placed. A dedicated Main Console in the control room will be used to access all the functionality of the ODCS and for the off-line data analysis. Both the consoles will be linked to the VME crate. For the Main Console will be used a memory mapping system based on fiber optic link in order to allow longer distance and electrical noise immunity. For the Local Console close to the VME crate a similar solution, based on parallel bus, can be used. It is worth to mention that in this environment a digitized image don't need to be transferred to the consoles as they can access them directly even in the shared memory of the frame buffer. The two consoles will then communicate via mailboxes defined in the memory area of the VME crate that will be addressable from both.

The connection to the main control system can be realized in several different ways. The most straightforward and simpler one may be the definition of mailboxes for the communication between the Local Console and a processor of the main control system placed in the VME crate. The interfacing processor will communicate with the others of the main control system using one of the standard implemented through the system itself (RPC or EPICS). In this way the ODCS could be really seen as a single extension, a virtual VME module placed at the memory locations where the mailboxes have been defined (extra memory locations can be reserved for large blocks of data to be transferred to the main control system).

The ODCS will have the control over all the devices related to the optical diagnostic stations along the beamline, i.e. cameras, lenses and targets movements, video signal multiplexer for the frame grabber and others, allowing the ODCS to execute its task independently. For some special measurements,

emittance for instance, will be necessary to access other elements that are not directly controlled by the ODCS, i.e. quadrupoles. In this cases the ODCS will ask to the main control system (via same mailboxes and the interface application running on the interfacing processor) to set properly those elements until the procedure will be completed.

Timing signal for acquisition triggers will be locally generated derived from the machine trigger signal and events.

Digitized images and other data will be stored into the console's hard disk or in a external data storage unit for later analysis and archiving. One or both the consoles can be configured as a FTP server to accesses the archived files via Ethernet.

The Main and Local Consoles will be PowerMac from Apple. LabVIEW will be mainly used for the control routines and the graphic user interface. Other specific Macintosh programs will be linked to LabVIEW for automated analysis or available for off-line data processing.

Extra VME CPUs can be added to the ODCS to perform specific tasks as, for example, image analysis or the implementation of the communication protocol with the main control system. Those processors will exchange information using mailbox as well.

A schematics of ODCS is shown in Fig. 10.15.

Other diagnostics (Synchrotron Light, Bunch length, etc.) Many of the diagnostics discussed in Chapter 9 are developmental or exploratory in nature. They need not be integrated in any more than the simplest way into the control system for initial operation. Just what controls interface will be desirable in the long term can best be determined after we have had some experience with them.

Beam Dump The beam dump will be instrumented with thermal monitors and possibly shock wave detectors as well as the standard cooling system monitors. The control system should be able to time plot and data log the temperature and shock wave monitors. Sample rates at 10 to 50 Hz on demand should be sufficient.
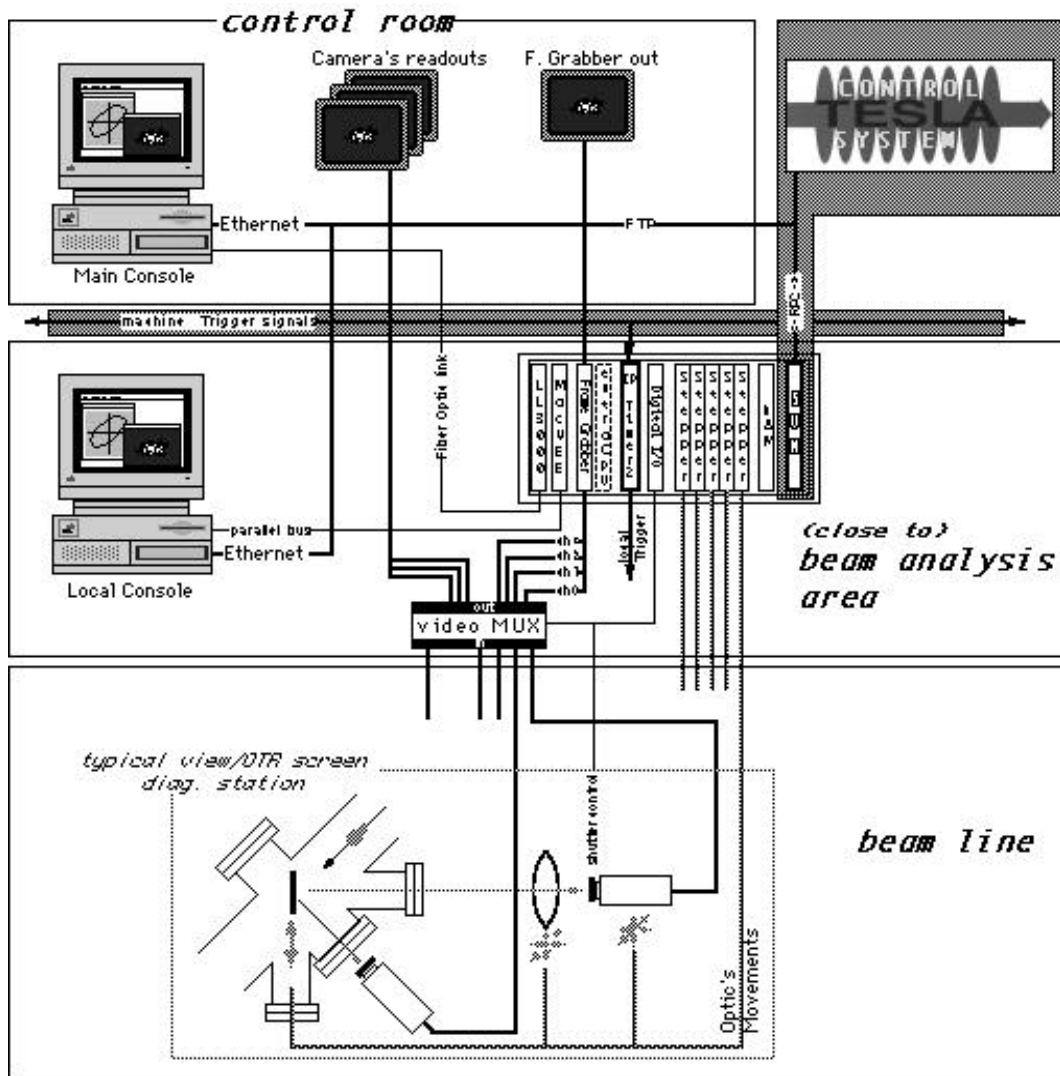
Figure 10.15: Schematic drawing of the Optical Diagnostic Control System for the OTR and View Screen diagnostic

10.5.3.3 Cryosystem Controls and Temperature Monitor System

The standard DESY Cryo-plant control system EMCON (a commercial process control system) will be used to operate the TTFL cryosystem. The

system includes not only the linac and injector capture cavity but also the vertical and horizontal test dewars and the cryo-plant. The control system is being upgraded to operate with EPICS. In addition a temperature monitoring system using Cobra will be used to read out the temperature resistors in the cryomodule.

Cryogenic System Control During the first installation phase of the cryogenic control system it was expedient to choose the same hardware and software already in use for the HERA controls at DESY. Since the requirements are different for HERA, an operating accelerator for high energy physics, and TTFL, a test bench for the TESLA linac, it is planned to add more flexibility to the TTFL cryogenic controls. This will be achieved by using the latest developments available for process controls. Here the EPICS control system will play the major role. This will help to get the required flexibility in data acquisition and graphic display. As a first step a VME system running EPICS will be installed for data acquisition. This is planned for early '95.

The cryogenic control functions for the linac finally will be based purely on EPICS. In addition all the I/O will be hooked up to the CAN field-bus which will replace the SEDAC bus used so far. Because of the improved functionality using the CAN bus it will be possible to add intelligent devices to the I/O system.

Cryomodule Temperature Monitors The list of diagnostics and leads in the cryomodule have been summarized in Chapter 5.

A separate Temperature Monitor System will be used to monitor the many temperature sensors planned for the cryomodule. This dedicated temperature monitor system, which allows for easy programming of changes in instrumentation or new calibration data, is described below.

The first cryomodule will be instrumented with over 43 platinum resistors for temperature measurements at 70 K and above, and over 84 carbon resistors for measurements at 2 to 4 K. These resistors will be read into the Temperature Monitor System.

The first module will have :

Carbon Resistors (Cr)	Platinum Resistors (Pr)
on each cavity- 2 Cr on the helium vessel 1 Cr on the main coupler 2 Cr on the HOM couplers	1 Pr on the main coupler
on the quad package- 2 Cr on the quad package	
on the cryostat piping- 10 Cr	2 Pr
on the beam pipe, HOM absorber- 1 Cr	2 Pr
on the shield - 28 Cr	28 Pr
on the support posts- 3 Cr	3 Pr

In addition to the standard one carbon and one platinum resistor planned for the main couplers, the couplers may have 2 more carbon resistors and 2 more platinum resistors each at least for the first module (for a total of 16 carbon and 16 platinum resistors additional).

Temperature Monitor System (TMS) for the Cryomodule The temperature monitor system for the cryo modules has to be suited for general heat loss measurements with and without RF, measurements of temperature distribution on the 4.5K and 70 K shields, supports and main couplers, HOM heat loss monitoring, analysis of RF pulse heating and cryogenic QRF measurements. For the first module 127 temperature sensors at different locations are foreseen. The type of sensor depends on the temperature range:

temperature / K	accuracy / K	sensor type
1.8 - 5	$\pm$ 0.03	Cernox CX-1030-SD
5-70	$\pm$ 0.05	Cernox CX-1030-SD
70-300	$\pm$ 1	Pt 1000 / Cernox

Cernox as well as Pt 1000 resistors operate in the range 27–1400 ohms. Four wire cabling is used for all sensors. (Time resolution for fast heat pulse

measurements is not yet defined. Thermo-elements could be chosen for this purpose.)

In parallel to the cryogenic EMCON control system for the operation of the cryo-plant a special cryogenic measurement system is installed for the temperature measurements at the cryo modules: the electrical signals from the different sensors are recorded by an integrating data acquisition system "COBRA" at a rate of 250 channels per minute for the standard temperature measurements. The "COBRA" system runs under the LINUX operating system. Data transfer to the other computers of the TTF laboratory is accomplished by remote procedure call servers and Ethernet. A special server combines the recorded data on line with user defined calculations (e.g. cryogenic process calculations). Access to the data is possible via the vacuum control system as well as via the Lab View RF control system. The "COBRA" system gives high flexibility to react on new aspects during the experiments, changes in instrumentation and recalibration of the temperature sensors. In addition the "COBRA" system can handle all 4 - 20 mA signals from pressure, flow and level sensors and can be equipped also for fast temperature measurements up to a repetition rate of 250 measurements per second. For measurements at the complete TESLA-Test-Facility consisting of CRYOCAP, four cryo modules and different sensors in the feed boxes and transfer lines the "COBRA" system can be easily upgraded to 1000 channels.

10.5.3.4 Other diagnostics in the cold cryomodule

The magnet power supply control and beam detector have been discussed above, as has the cryomodule wire alignment system. Loss monitors may also be installed in the cryomodule and their possible readout has been discussed above as well.

Vibration monitors Two vibration monitors are planned for each cavity and for the quad package. These detectors will have special amplifiers. Output signals will initially be observed with scope of spectrum analyzer. Interface to the computer will be made if it appears to be useful. Such information might be time plots of amplifier output at up to a few kHz sample rate and read outs of spectrum analyzer results. At least one channel will be connected to the quick digitizer to provide correlation with other data. The vibration monitors are capable of response to 4 kHz. Noise levels from the

detectors are about 1200 nm at 1 Hz, and about 60 nm at 5 Hz. The room
temperature amplifiers may produce additional noise.

10.5.3.5 RF System Monitor and Control

A major fraction of the data that will need to be observed in TTFL will be
associated with the cavity RF system. Monitoring of numerous RF amplitude
and phase signals at high rates ($\approx$1 MHz) during the RF pulse will probably
be valuable in order to understand the over all system operation, understand
cavity behavior, and resultant impact on the beam, especially properties like
beam energy, energy spread and time variation, and possibly dark current.

The LLRF system will be an interesting and challenging system to build
and must provide for over all RF phase and amplitude control of the RF
under various beam loading conditions. This system needs a control loop
with rates up to one MHz. The relevant parameters must be adjusted and
many signals must be monitored by the control system in order to efficiently
analyze the operation of the LLRF system. Of the order of 64 channels will
be monitored at 1 MHz during the RF pulse by the quick digitizer system
and read back to the controls computers as required.

Cavity tuning   At the beginning of the RF pulse it will be essential to
monitor the amount of cavity detuning by looking at the sin and cos inputs to
the vector modulator. These signals are generated from the phase difference
between the Klystron RF output signal and the vector sum signal from all
cavity voltages.

As we pointed out in chapter 8 predetuning of the order of 200 Hz is
required for each cavity in order to cope with the Lorentz force detuning.
During the RF filling time the tuning of individual cavities can be monitored
by looking at the individual IQ (i.e. phase and amplitude) detector signals.

Ideally the mechanical tuners are adjusted so that all cavities start with
the same phase and they are still in phase when the nominal cavity voltage
has been reached. Depending on differences in mechanical rigidity of the
cavities phase differences indicating cavity tuning errors may arise during
the filling process. The measurement of these phase differences is therefore
of crucial importance.

The tuner input signals are derived from the RF drive and the cavity
voltage signals which are sampled during each RF pulse and held. When the

tuner has reached the correct position a status bit is sent to the computer. Apart from this it will be possible to change the tuner position manually, i.e. by computer remote control.

Once the nominal cavity voltage has been reached one can synchronize to the generator frequency by disactivating the VCO. The VCO command box compares the amplitude (or phase) of the vector sum signal to the amplitude (or phase) reference and disactivates the VCO once the phase and/or amplitude criterion is fulfilled. Practical experience will show which of these methods is the better one.

Phase and amplitude control The error signals resulting from comparison of the vector sum signal with the phase and amplitude reference signals are fed into a vector modulator. Since all these signals can be displayed by the computer together with the individual cavity voltage vectors, cavities which cause problems should be readily identified. Individual gain control for phase and amplitude is foreseen.

Furthermore, envelope signals of forward and reflected power between Klystron and circulator, circulator and cryomodules and of RF power going to individual cavities will be monitored.

An additional independent phase loop is closed around the Klystron in order to reduce phase fluctuations generated by the Klystron itself.

RF sparking in the wave guides There are some 40 photodetectors foreseen to monitor critical points in the RF wave guides. In case of sparking a bit indicating the location of the spark will be sent to the computer.

RF Monitor points and control interface All the signals which will be monitored are listed in Tab. 10.2. This table gives the number of signals for all four cryomodule. The number of A/D channels needed for the first cryomodule is about 64 (or about 242 for 4 modules). The number of D/A set points is initially about 17 and the number of status bits about 19. All D/A outputs and status bits are slow. They need to be refreshed at most at the 10 Hz rate.

We are interested in the time dependence of all the analog signals. Though a 1 MHz sample rate might be overkill and about 100 kHz sufficient, it is

still reasonable to start with a complete set of quick digitizer A/D channels for the first module.

After some experience with the first module one can decide whether or not all channels should go to the quick digitizer or whether some could be monitored at a slower rate or multiplexed on demand to the quick digitizer system.

Coupler diagnostics In addition to measuring the RF signals from the cavities, it will be necessary to carefully monitor the input couplers. A hard wire interlock system will protect the couplers. Signals should be monitored by the controls system as well.

The interlock system will interface to the controls via ProfiBus and data will be logged at 1 kHz. A local buffer will act as a snapshot memory which is frozen by the interlock system itself. Threshold setting and read out capability must be provided by the controls system. Ten channels per cavity are planned.

The HOM couplers will be monitored; both the power they pick up and their heating should be observed. A signal cable with termination will monitor the power and RF spectrum of the HOM couplers. The two HOM signals will be looked at with scope or spectrum analyzer and do not need interface to the control system initially. Each coupler will have a Carbon resistor for temperature measurement.

The input couplers will have 1 to 3 of both carbon and platinum resistors on each coupler. The temperature resistors can be monitored through the TMS discussed above.

The main coupler will have 3 electron pickups (either side of the cold window and at the warm window). There will also be a photomultiplier on the warm window. These four input coupler protection signals should be available on the quick digitizer system in order to have fast playback of potential problems. This follows the experience with a similar system installed in the superconducting cavity system in HERA. Here a PC based 8 channel fast data logger reads data in a ring memory at a (parallel) sample rate of 200 kHz. All signals are stored for a time of ± 5 msec around an interlock event. The system has proved to be essential and sufficient for tracing down the history of effects from beam induced behavior or false component signals.

The cavity field monitor which detects the gradient and phase of the indi-

Table 10.2: RF monitor points for the four cryomodules

	No. of signals to ADC	Signal name
1.	2×1	Lorentz-force-detuning phase detector output (i.e. vector sum phase minus RF drive phase)
2.	2×2	Sine and cosine input to vector modulator.
3.	4×8	Phase of RF drive signal for each cavity
4.	4×16	Individual Cavity voltage and phase from IQ detector
5.	4×8	Individual cavity voltage from diode
6.	2×1	Rectified vector sum versus amplitude and phase reference
7.	4×8	Output of individual tuner phase detector
8.	2×1	Klystron phase detector output
9.	2×2	Envelope of RF forward and reflected power between circulator and Klystron
10.	2×2	Same between circulator and module
11.	4×16	Same for each cavity
	No. of DAC signals	
12.	2×2	Phase and amplitude setpoint for VCO control
13.	2×1	Amplitude setpoint
14.	2×1	Amplitude loop gain
15.	2×1	Phase setpoint
16.	2×1	Phase loop gain
17.	4×8	Tuner control (i.e. tuner setpoint)
18.	2×1	Klystron phase reference
19.	2×1	Klystron phase loop gain
20.	2×1	VCO switch off phase
	No. of digital signals	
21.	2×1	VCO active-passive bit
22.	4×8	Tuner ok (status bit)
23.	4×10	Wave guide light detector bits

vidual cavities has been discussed above as part of the RF system monitoring.

The diagnostics and interlock signals at the input coupler are shown in Tab. 10.3.

Table 10.3:   Diagnostics and interlock signals at the input coupler.

Signal	Hardware interlock	Data log by computer	Fast event recording
e^- pickup at 300K window	yes		on request
e^- pickup at 70K window,1	yes		on request
e^- pickup at 70K window,2	yes		on request
spark detector at 300K window	yes		on request
IR detector at 300K window	yes		on request
vacuum in coupler	yes	yes	on request
temperature at 70K window,1		yes	on request
temperature at 70K window,2		yes	on request
temperature at 1.8K flange,1		yes	on request
temperature at 1.8K flange,2		yes	on request

Cold Tuning System Control   Each cavity has a mechanical tuner. This tuner is adjusted by a stepping motor. Mechanical position is not monitored, rather the resonant frequency is adjusted. These tuners will be controlled by the same system as used on the injector capture cavity and discussed in the material on injector controls.

RF Modulator The RF Modulator is controlled by a dedicated system from Fermilab with complete stand alone functionality including console operation from a Mac. The system operates under "Classic Protocol" and UDPs. It interfaces to the TTFL controls via a gateway. It has time-plotting and parameter page capability and interfaces to Internet.

The number of digital control points is about 85, and read back display points is about 150. The quick digitizers can be used with this system and can be connected to channels of interest.

10.5.3.6 Vacuum Controls

The TTF vacuum system consists of three independent systems. It is described in Chapter 7. The first system is the beam pipe ultra high vacuum with pressures in the order of 10^{-10} mbar. It has to be very clean to protect the inside of the cavities from any contamination. The first pumping will be done by oil-free pump stations. At a certain level of pressure the ion getter pumps and titanium sublimation pumps take over.

The insulating vacuum system has to provide the thermal isolation of the cryo modules and the transfer lines. Permanent installed pump stations are used here. The pressures are measured by Pirani and penning gauges. Electropneumatic valves are used to separate vacuum sections.

The wave guide vacuum is pumped by ion pumps only. These pumps are used to measure the pressure as well. All three systems are controlled by the following devices.

Oil-free Pump Stations These pumps stations are a new design for TTF. The heart is a turbo molecular pump with magnetic bearings. The two or three pumps, valves and gauges of the station are controlled by a PLC. This PLC allows to operate a pump station stand-alone or via the build-in ProfiBus communication from the control system. 125 parameters or values of the pump station are readable/controllable. Five of the analog readings are stored in the archiver. For the linac and the cavity manufacturing eight or more of these pump stations are needed. The connection to the control system is made by little boxes with ProfiBus connectors distributed along the linac. An automatic detection of a new or moved pump station by the control system is implemented.

Pump Stations for the Insulating Vacuum   The development of these pump stations was done for HERA and we take some spares of them for TTF. The pump stations consists of a turbo pump, a roughing pump, two controllable valves, a Pirani and a penning gauge and a SEDAC based controller. Again, these pump stations are stand-alone and remote controllable. From the operator point of view these stations are displayed and controlled in the same way as the other pump stations.

Pirani and Penning Gauges and Valve Controller   The two controllers are SEDAC modules with two channels each. The Pirani module is a combined gauge and valve controller. Depending on the relation of the pressure from the Pirani reading of the left and right side of a valve, the valve is closed automatically by the module. Several units, i.e. Pirani and valves may be chained for an automatic separation of vacuum systems. The whole insulating vacuum system will contain about 25 Piranis, pennings and valves each. One vacuum reading per gauge has to be archived and more than 20 pieces of control information are available for each of the devices.

Ion Pumps   One SEDAC module can control up to eight high voltage power supplies. Each ion pump has it's own power supply. The current and voltage of the pumps are measured. The pressure reading is proportional to the current and corrected according the different pump and power supply types. A protection of the pumps is provided by the control system. Pumps are switched off in case of a very high pressure increase. The pressure reading of all pumps are archived.

Titanium Sublimation Pumps   A SEDAC module to control up to 12 titanium sublimation pumps is available. The module drives a high current power supply, which is mounted closed to the pumps. From the SEDAC module the current in the pump can be set to four different values. The actual current of the pump is recorded and archived by the control system.

Mass Spectrometer and Leak Detectors   These are microprocessor based devices. A link to the control system is accomplished by a SEDAC interface. For the mass spectrometers the current spectrum, the total pressure and seven partial pressures are archived. Historical trending of the total

pressure and the leak rate is available on the leak detectors. In addition the two units have a lot of parameters which are readable and controllable from the control system.

Injector The injector vacuum is designed and build by LAL, Orsay. It consists of ion pumps and four gate valves in the beam line. All instruments are controlled by a PLC. The PLC prevents the valves from opening under bad vacuum conditions and closes the valves if the pressure raises above are certain level. These on and off levels are set by the control system. All pressure readings and status informations are provided to the control system via a ProfiBus link. The PLC checks a lot of error conditions and outside informations to protect the capture cavity and the linac cavities. It also gives an okay signal to permit the linac operation.

The whole vacuum system is controlled by a Sun workstation and DOOCS. Independent server processes with a SEDAC and ProfiBus link in a VME crate maintain all devices. Little connection boxes, distributed in the hall and along the linac, are used as ports to connect SEDAC, ProfiBus and Ethernet based devices. Moveable units like pump stations, mass spectrometer and leak detectors can be flexible connected to the control system. The client programs provide an easy Point and Click interface to the operators. This includes a simple access to archived data by a mouse click on the actual reading.

10.5.3.7   Utilities – Water, Power, Air

The water supply comes from a central location nearby the test-hall. A PLC controls the pumps and valves in this substation. Process data from this PLC are available to TTF-controls by a field-bus (ProfiBus) connection. Data including historical trending (data logging) are available using DOOCS.

Information about the status of the power system and the air supply are desirable but not yet available.

10.6   Personnel Safety Interlock

In addition to the local interlock logic for each component of TTFL there will be two global interlock systems. One of these is the Beam Inhibit System. It

provides a fast turnoff of the beam to protect the linac equipment (cavities, etc.) from damage due to beam miss loss. The other is the Personnel Safety Interlock System that assures there can be no beam operation if there are people in the radiation area.

Safety systems for the protection of personnel in technical equipment areas is based on the "DESY Radiation Protection Rules". Moreover, the application of certain technology is done according to the DIN 31004 regulations. Such a technically protected area will subsequently be called an interlock area.

The interlock area is constructed in a way that access is only possible through specially secured doors. Before releasing the area for the start of accelerator, a safety patrol must search the area. Accelerator operations, search, and the normally controlled access need special technical equipment which is listed below:

Search confirmation switches mounted in the interlock area to enforce following the search path and search start switches at the doors. The last switch is a search complete switch, outside the last door declared as the exit point door of the search area.

Emergency-off switches in the area which interrupt the beam release. There should only be these, clearly labeled emergency-off switches (for this purpose) in this area.

The beam warning starts with yellow warning beacons (WB) illuminating the area. To increase the warning effect the normal illumination of the area is automatically reduced to 1/7 (partial illumination). At the same time there is a recorded voice warning.

There are plans to increase the warning effect during the recorded voice warning by switching on and off in one-second-periods an additional illumination of fluorescent lamps in the interlock area.

The purpose of all this is to warn anyone who might have remained in the area by mistake. The recorded voice warning is normally given for a time which is sufficient for somebody to reach the nearest emergency-off switch or door. Taking into consideration all possibilities, it is concluded that this warning time should be between 30 and 90 seconds. Shortly after that the warning beacons may go out, with partial illumination still remaining. Only the access doors must have warning beacons which are still working (not visible from outside). The situation at present is that all warning beacons are working during the time that beam operation is permitted.

There are sign boards at the access doors reading "No entrance - radiation - prohibited area" and which become visible when the beam warning is started.

Moreover, each door is equipped with a key-box (with 6 keys), a (handsfree) telephone, a color TV for remote control of the access and corresponding illumination as well as a door warning sign board, reading in illuminated letters "stop - don't open the door". The new door warning sign board substitutes for the former door warning lamp and its task is to reduce the possibility of an accidental door opening without door release.

The door is barred with a magnet when the door is locked. In case the door is released for controlled access or in case the area is not set, the magnet is out of circuit and the door opens and closes freely (roller spring-bolts).In case of emergency the door can be unlocked with an emergency-off switch at the door which causes a simultaneous break of the interlock. (This solution is supposed to substitute the electric door spring-bolt now in use.)

The connections of the door-information to the area-interlock have relay circuits. Any information from the door interlock and the emergency-off switch as well as other possible interlock conditions are sent to an interlock control box which enables the start of the warning (including feedback whether warning is audible in the area) and - after warning is over - allows beam operation.

All interlock circuits (e.g. two circuits per door as a standard) operate in two independent systems, using parallel chains for the circuits. The use of relays is reduced to a minimum and in future (in new facilities) only "forced operating contact" safety-relays will be used. (If one contact of a relay doesn't work, all other contacts of the relay won't work either.)

Monitoring and status display in the new system will be done only by computers. They will also monitor the interlock status of the doors.

Chapter 11

Potential Applications

The construction of the TTFL is itself a project of considerable magnitude, offering unique beam physics features, quite aside from its possible linear collider prospects. Thus, it is natural to identify applications in experimental physics for the TTFL. Two examples are presented below; the use of the TTFL as an electon source for a SASE FEL and as a facility for investigations with slow positrons.

11.1 A Self-Amplified-Spontaneous-Emission Free-Electron Laser at 200 eV

The workshop on Fourth Generation Light Sources held at SLAC in 1992 focussed on X-ray lasers[1], and with the recent development of low emittance electron guns the construction of X-ray lasers at 1 Å wavelength at high energy linacs comes in reach. The scientific applications of such coherent X-rays have been discussed at SLAC in February 1994.[2]

The Brookhaven National Laboratory suggested a Free-Electron Laser in the deep UV region, called DUV.[3] The DUV-FEL operates as a combination of a harmonic generator and single pass amplifier. The concept involves coupling of the coherent radiation provided by a "conventional" pulsed laser with a high current electron bunch inside a magnetic wiggler designed to be

---

[1] SSRL Report 92/02
[2] SLAC-Report-437
[3] BNL-Report-49713

resonant at the seed laser wavelength. This scheme imparts the coherence and relative bandwidth of the seed laser on the radiation produced by the FEL. The DUV-FEL will provide intense pulses of coherent ultraviolet radiation with wavelengths ranging from 300 to 75 nm. The pulse width will be variable from about 7 ps to under 200 fs. The DUV-FEL concept cannot be extended to realize a FEL in the X-ray regime.

11.1.1   The TESLA Option

At DESY the construction of a Self-Amplified-Spontaneous-Emission(SASE) FEL at the TESLA Test Facility (TTF) is under discussion. Due to its exceptional capability to maintain high electron beam quality during acceleration, a superconducting linac is the optimum choice to drive a SASE FEL at high energies. The goal is to produce coherent radiation tunable in the photon energy range up to 200 eV (6 nm).

In atomic, molecular and solid state physics the intensity, collimation, polarization, coherence, flexibility, and time structure of the VUV laser radiation allow novel studies of structure and dynamics. Exiting new research opportunities in imaging by coherent radiation, in time resolved pump and probe experiments and in nonlinear laser-matter interaction are expected.

Applications in biology comprise investigations of radiation damage, time resolved phosphorescence and fluorescence studies and Raman spectroscopy providing structural information on biologically important macromolecules in solution. In addition, attempts could be made to directly image the topology of large molecular assemblies.

Possible applications of such a laser in many different fields of sciences have been discussed in some detail within the scientific case of the Brookhaven DUV-FEL proposal proposal.[4] Examples are given for

- photofragmentation spectroscopy

- photoelectron spectroscopy of radicals, complexes, and clusters

- photoionization of vibrationally excited states

- state selective detection of dilute species

---

[4] *op cit*

- photodesorption and photodissociation from surfaces

- crossed beam radical-molecule reactions

- excited state spectroscopy

- microprobe experiments

Construction of this 200 eV laser might pave the way towards an even more challenging FEL in the Ångström range.

With the goal of a 1 Å X-ray laser in mind, experiments with X-ray beams of a degree of coherence typical for 3rd generation synchrotron radiation sources will be carried out at DESY. To this end, the undulator beam under construction at the PETRA storage ring will be used. PETRA will be operated at 12 GeV with a possible emittance of 15 nm at that electron energy.These experiments will supply experience indispensable to handle the enormous X-ray brilliance of a future X-ray FEL.

Besides direct applications of FEL radiation, FEL radiation sources will be needed for the $\gamma - \gamma$ collider option of linear colliders. This represents another link between linear collider R&D and FEL development.

The technical concept

a) basics

The radiated power P of a relativistic charge q in a transverse magnetic field B is given by[5]

$$P = \frac{q^2}{6\pi\varepsilon_0 m_0^2 c} q^2 B^2 \gamma^2$$

Thus, for a point-like electron bunch, P depends *quadratically* on the number of electrons. This is, however, only true as long as the bunch length is shorter than the radiated wavelength. Otherwise, the radiation contributions add up incoherently, yielding a linear dependence only. The generation of (say) nanometer long, intense bunches from an electron gun is impossible, but it can be accomplished by self-bunching of a longer bunch in its own radiation field generated in an undulator. After the self-bunching has been

---

[5]see e.g. Jackson: Classical Electrodynamics

developed within a characteristic distance called gain length L_g, the radiation exponentially increases up to saturation due to nonlinear effects.[6]

The gain in power, compared to spontaneous radiation without microbunching, might be as high as six orders of magnitude. Although stimulated emission is also involved, the essential effect is increasing the spontaneous emission, similar to the optical klystron.[7] This explains the name *Self-Amplified Spontaneous Emission* = SASE. Since SASE is a single pass effect, it is especially interesting in the VUV and X-ray region, where optical resonators are not available due to lack of mirrors.

The basic concept of SASE was first demonstrated experimentally in the microwave region at LLNL.[8]

b) RF gun

Both small emittance values and high phase space densities in all three dimensions are mandatory for achieving microbunching and saturation within reasonable undulator length. To achieve a photon wavelength λ, the transverse beam emittance ε (or the normalized emittance ε_n, respectively) must not exceed a critical value given by

$$\varepsilon = \frac{\varepsilon_n}{\beta\gamma} \leq \frac{\lambda}{4\pi}$$

Thermionic guns are not able to supply the required phase-space densities. The essential break-through was the development of the RF gun by Fraser and Sheffield[9] and the emittance compensation scheme devised by Carlsten[10]. Meanwhile a number of RF guns have been built and operated yielding 1 nC charge at 3π mm mrad normalized emittance and an rms bunch length σ_s in the few mm range.[11]

We aim at a normalized emittance of 1π mm mrad at 1 nC and $\sigma_s = 1$ mm. A key component will be the laser system which has to deliver ultra-short pulses at 1 MHz repetition rate. This is currently under investigation at the Max-Born-Institut in Berlin.

---

[6] R. Bonifacio, C. Pellegrini, L. M. Narducci, Opt. Commun. 50 (1984) 373

[7] N. A. Vinokurov, A. N. Skrinsky, INP/Novosibirsk Preprint 1977

[8] T. J. Orzechowski et al., Phys. Rev. Lett. 54 (1985) 889

[9] J. Fraser and R. Sheffield, Nucl. Instr. Meth. A250(1986) 71

[10] B. Carlsten (Nucl. Instr. Meth. A285(1989) 313

[11] see e.g. C. Travier: Review of Electron Guns, Proc. EPAC, 1994

It should be noted that a low emittance electron gun serving the TESLA pulse train pattern would be extremely useful for the TESLA Linear Collider, because eventually the electron damping ring could be saved. The phase space density required for TESLA500 is very close to what is needed for the SASE FEL.

c) bunch compression and acceleration

The peak electron beam current needed to achieve a reasonably short gain length is in the few thousand Ampere range. Even when starting at 1 mm rms bunch length, further bunch compression is required to reach that value. It cannot be done at very low energy because Coulomb forces would increase the beam size and energy width. On the other hand, it should not be done at too high energy for two reasons:

1. The cosine-like time dependence of the accelerating voltage introduces some correlated energy spread which scales quadratically with the bunch length. To avoid phase space filamentation during bunch compression, the nonlinear part of this energy spread should not get much larger than the initial, uncorrelated energy spread of the beam.

2. At each bunch compression by a factor C, the uncorrelated energy spread increases by at least the same factor C (Liouville Theoreme). The longitudinal wakefield, however, only scales with sqrt(bunchlength). Thus, to make optimum use of adiabatic damping, one should compress before the wakefield dominates the energy width. It is an essential advantage of the low RF frequency of TESLA, that wakefield effects are very small. Consequently, extremely small bunch length and small energy width do not exclude each other.

As indicated in Fig. 11.1, a first compression stage of a factor 4 is foreseen after the first superconducting RF module, i.e. at about 130 MeV beam energy. It still has to be checked if it could be done right after the RF gun preaccelerator, which would be favourable for technical reasons. The second stage brings the bunch length down to 50 mm. This is done after the 4th module at some 500 MeV.

To reach the final energy of 1 GeV required for the FEL, four more RF modules will be necessary.
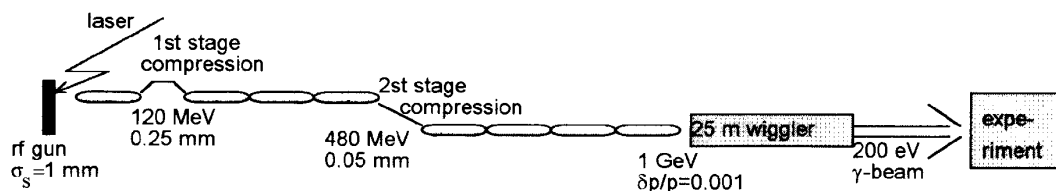
Figure 11.1:   Schematic layout of a 1 GeV SASE FEL facility based on the
                TESLA Test Facility. The bunch length is reduced from 1mm
                to $50\mu m$ within two steps of bunch compression, the first of
                which is after the first superconducting RF module. Whether
                the first stage of bunch compression can, alternatively, be
                placed just after the RF gun, is not yet clear. The over-all
                length is some 160 meters.

We assume the RF gun to deliver a beam of 20 keV rms energy width at
10 MeV beam energy. This means, at $\sigma_s = 1$ mm, a longitudinal emittance of
20 keV mm. As we need a relative energy width of 0.001 at 1 GeV, Liouville
Theoreme would allow a bunch compression down to 20 μm. Thus, we allow
for a factor of 2.5 of phase space dilution due to wakefield effects and phase
jitter. A more detailed analysis will show if less than 50 μm bunch length
can be achieved.

d) undulator

After having prepared an electron beam of high brilliance, the key component
of the FEL will be the undulator. The peak field of 0.5 T at period length of
27.3 mm and a gap of 12 mm (maybe even 8 mm gap would be tolerable) does
not seem to be the problem. However, the considerable length of about 25 m
requires careful investigation of field tolerances, means of periodic focussing
and cost minimization.

A tentative layout of the TTF SASE FEL is sketched in Fig. 11.1. Ta-
ble 11.1 shows a preliminary parameter list.

---

[12]K. J. Kim and M. Xie (Nucl. Instr. Meth. A, 331 (1993), 359)

Table 11.1: Preliminary parameter list of a TESLA SASE FEL. The insertion device is assumed to be a planar hybrid undulator. The values[12] quoted should be considered a guideline only since neither optimization is finished yet nor any experimental experience is available in this wavelength regime. Therefore, a first test is envisaged at a wavelength larger by some factor of ten.

VARIABLE	UNITS	VALUE
beam energy	GeV	1.000
λ (radiation wavelength)	nm	6.4 (200 eV)
λ_W (wiggler period)	mm	27.3
wiggler gap	mm	12
B (wiggler peak field)	T	0.497
β (beam optics beta function)	m	5
rms beam size	mm	0.05
ε^n (normalized emittance)	π mrad mm	1.0
peak electron beam current	A	2490
electrons per Gaussian bunch		6.24×10^9
photons per Gaussian bunch		6.2×10^{13}
peak electron beam power	GW	2490
energy spread σ_ν/γ	10^{-3}	1.00
bunch length	μm	48.
L_g (power gain length)	m	1.00
L_s (saturation length)	m	18.2
P_{sat} (saturated power)	MW	2780
peak brilliance	photons/s/mm^2/mr^2/0.1%	8.73×10^{27}

11.2   A Source of Slow-Positrons for Applied Physics

Slow-positrons, i.e. monoenergetic positrons with an energy of a few eV up to some keV, provide a unique probe for solid state physics[13], but are also widely used for observations of quantum chemistry associated with light-mass particles[14], atomic physics[15], astrophysical applications[16] and tests of the quantum electrodynamics.

The experimental study of the interaction of positrons with matter is a relatively young field which has received a big boost in the late seventies on developments of highly efficient moderator materials[17] with a negative work function for positrons. Positrons which penetrate into these materials are thermalized and reemitted into the vacuum, normal to the moderator surface with an energy of a few eV and an energy width of less than 0.1 eV. This is the basic process for the production of slow-positrons.

The same physical principle – reemission due to a negative work function - can be used to decrease the emittance of the beam by orders of magnitude by means of a re-moderation of the beam.[18] [19]

The improved performance of slow positron sources and experimental possibilities is reflected in a rapidly growing number of publications and increasing interest in workshops and conferences relating slow-positron beam applications.[13]

---

[13]P. J. Schultz, K. G. Lyn, *Interaction of positron beams with surfaces, thin films, and interface*, Rev. Mod. Phys. 60, p. 701 (1988).

[14]H. Arche, Proceedings of the 5th Intern. Conf. on Positron Annihilation, Lake Yamanaka, Japan, p. 31 (1979).

[15]A. Dupasquier, A. Zecca, Riv. Nuovo Cimento 8, p. 3 (1985).

[16]*Positron Scattering in Gases*, Proceeding of the 2nd NATO Advanced Research Workshop 1983, Ed.: J. W. Humberston, M. R. C. McDowell, Plenum New York.

[17]M. Leventhal, C. J. MacCallum, Proceedings of the 7th International Conference on Positron Annihilation, p. 1003, New Dehli (1985)

[18]K. F. Canter, P. G. Coleman, T. C. Giffith, G. R. Heyland, J. Phys. B5, L167 (1972). S. Pendyala, P. W. Zitzewitz, J. W. McGowan, P. H. R. Orth, Phys Lett. A43, p. 293 (1973).
S. Pendyala, D. Bartell, F. E. Giouard, J. W. McGowan, *Energy Distribution of Slow Positrons Diffusing from Incomplete d-Shell Transition Metals*, Phys. Rev. Let. 33, 17, p. 1031 (1974).

[19]A. P. Mills Jr., Appl. Phys. 23, p. 189 (1980).

New kinds of experiments like positron microscopy and studies of exotic antimatter systems like a two-component Fermigas require further developments of the sources with respect to

- emittance,

- intensity and

- time structure.

While sources with modest intensity ($\sim 10^6 \, e^+/s$)based on the moderation of positrons from radioactive materials can be realized with acceptable expenditure in small-scale laboratories, high-intensity sources require the operation in proximity of a high flux reactor or a particle accelerator and, in addition, the organization of a 'service facility' with a large, open user community.

In order to characterize the relevance of the different source parameters, we will consider experiments with slow positrons in a most general form, concentrating on applications in solid state physics and hereby following closely the presentation in the review article of P. J. Schultz and K. G. Lynn.[13]

After a brief discussion of the layout of a slow positron source, we will estimate the performance of a source based on the TESLA Test Facility (TTF) and compare it with existing and planned sources.

11.2.1 Experiments with slow positrons

While the positron is stable in vacuum, it annihilates under the emission of two 511 keV photons in ordinary matter. If the electron-positron-system is at rest, the photons are emitted in exactly opposite directions. Deviations in the collinearity as well as fluctuations of the photon energy (doppler-broadening) are hence direct measurements of the momentum of the electron-positron-system (see Fig. 11.2). When a positron enters a solid, it rapidly loses its kinetic energy until it is thermalized. Since, on the average, only one positron is in the solid at one time, it resides near the bottom of its own energy-band. Hence, when the positron annihilates, it does not contribute to the momentum of the system and the deviation of the collinearity of the two photons is a direct measurement of the electron momentum in the solid. The measurement of the Angular Correlation of the Annihilation Radiation
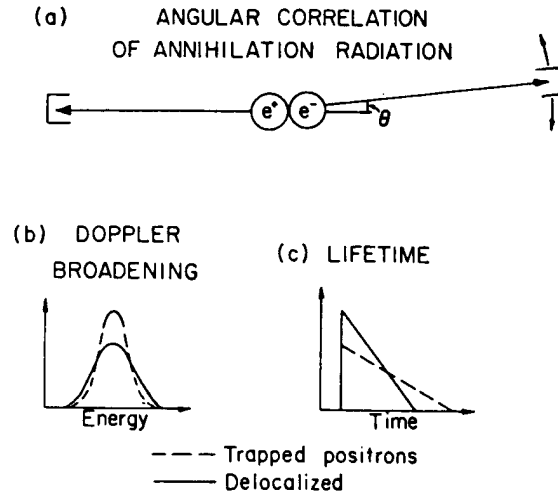
Figure 11.2:   Electron momentum reflected in the deviation of γ-ray
collinearity in ACRA measurements (a), or in the width
of the γ- ray annihilation line shape (b). When positrons
trap in defects there is a reduced overlap with energetic core
electrons, leading to narrow momentum (or γ-ray energy)
spectra, and there is a general decrease in the electron con-
centration, leading to longer positron lifetimes (c).[13]

(ACAR) is therefore a sensitive and widely used technique to measure the
Fermi surfaces of metals and alloys. However, positrons can also be trapped
in lattice defects like vacancies, voids and dislocations. A trapped positron
has a reduced overlap with energetic core electrons which leads to a smaller
doppler-broadening and the general decrease in electron concentration near
traps is reflected in an increased positron lifetime (Fig. 11.2).

Vacancy concentrations of $\sim 10^{-7}$ show a significant effect on the positron
annihilation characteristics and by means of variation of the positron energy
from some eV up to some keV even depths profiles can be measured.[20] The
formation of a positronium atom (Ps), the lightest hydrogenic system, was
predicted in 1934 by Mohorovicic and observed 1951 by Deutsch. While the
formation of positronium in the bulk of defect free metals or semiconductors is

[20]W. Triftshaeuser, G. Koegel, Phys. Rev. Lett. 48, p. 1741 (1982).

forbidden for energetic reasons, a high probability for positronium formation on the surface of a solid is found, due to the opposite signed work functions of positrons and electrons.[21]

These positronium atoms can be thermally desorbed, leading to the formation of a positronium beam.[22]

On the other hand positrons can also be trapped on the surface or be re-emitted as free, slow positrons depending on the (local) surface characteristics. Hence they provide a sensitive probe for surface effects, useful for investigations of thin surface layers, surface defects and contaminations.[23] Since positrons have the same mass as electrons, they will exhibit similar diffraction effects when scattering from a crystal surface. Thus positron diffraction may become a useful surface analysis technique, complementing methods of Low Energy Electron Diffraction (LEED). The absence of exchange forces for positrons allows a more simpler interpretation of LEPD patterns[23] it requires, however, sources with high intensity and small emittance for LEPD to become a practicable technique. Thus brightness enhancement techniques are used to increase the brightness of the beam for LEPD and other applications.[21]

Time structured beams

The time scale for positrons shown in Table 11.2 indicates the relevance of the observable time for slow positron experiments. Hence, bunched slow positron beams seem to have a promising future, even though they require more sophisticated detectors to handle the high intensity in the pulse.

Efforts to bunch a continuous slow positron beam[24] [25] have led to time resolutions of $8 \times 10^{-9} - 2 \times 10^{-10}s$. (The disadvantage of these technique is the necessarily increased energy width which, however, can be offset by a re-moderation stage.)

---

[21] A. P. Mills Jr., Phys. Rev. Lett. 41, p. 1828 (1978).

[22] A. P. Mills Jr., W. S. Crane, Phys. Rev. A31, p. 593 (1985).

[23] A. P. Mills Jr., *Surface Analysis and Atomic Physics with Slow Positron Beams*, Science 218, p. 335 (1982).

[24] A. P. Mills Jr., L. Pfeifer, P. M. Platzman, Phys. Rev. Lett. 51, p. 1085 (1983).

[25] D. Schoedlbauer, G. Koegel, W. Triftshaeuser, Phys. Status Solidi A102, p. 549 (1987). D. Schoedlbauer, P. Speer, G. Koegel, W. Triftshaeuser, in Proceedings of the 7th International Conference on Positron Annihilation, p. 957, New Dehli (1985)

Table 11.2: Time scales for Positrons.

	Time
Lifetime in vacuum	$\sim 2 \times 10^{22}$ yr
Scattering or diffraction	$\sim 10^{-15}$ sec
Thermalization (to $\sim$Fermi energy)	$\sim 10^{-13}$ sec
Thermalization (to $\sim \frac{3}{2}kT$)	$\sim 10^{-12}$ sec
Trapping (after thermalization)	$\sim 10^{-15}$ sec
e^+ lifetime	
Freely diffusing	$\sim 1 \times 10^{-10}$ sec
Monovacancy trapped	$\sim 2 \times 10^{-10}$ sec
Multivacancy/void trapped	$\sim 4 \times 10^{-10}$ sec
Surface state	$\sim 4 - 6 \times 10^{-10}$ sec
Annihilation time	$\sim 10^{-21}$ sec
Ps lifetime	
Singlet, vacuum	$\sim 1.25 \times 10^{-10}$ sec
Triplet, vacuum	$\sim 1.42 \times 10^{-7}$ sec
Triplet, in solids	$\leq 10^{-9}$ sec
(molecular crystals and insulators)	
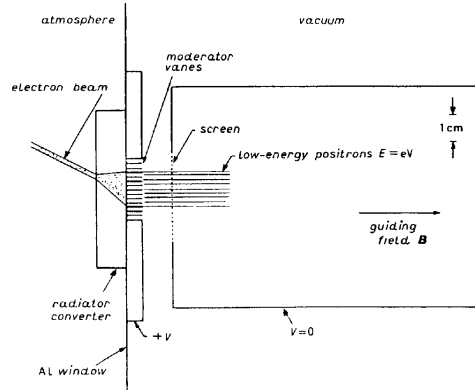
Figure 11.3:   The front-end of the LLNL high intensity slow-positron beam.[15]

The pulsed structure of linac based slow positron beams seems to be an obvious advantage, compared to sources based on radioactive materials, if time tagged experiments are considered.

On the other hand, also devices to stretch a pulsed positron beam to a more or less continuous beam have been developed (penning trap[26]) which are useful for studies like gas scattering experiments and the formation of anti-hydrogen.

11.2.2   Layout of a slow positron source

Figure 11.3 shows the front-end of the LLNL high intensity slow-positron beam. The positrons generated in the conversion target by the high energy primary electron beam are moderated in a vane moderator of vacuum annealed tungsten vanes.

Here the positrons lose their kinetic energy and are re-emitted into the vacuum, preferentially normal to the surface, due to the negative work function of the moderator material. Typically 10^{-6} positrons are re-emitted in this way to form a positron beam with an energy width of only $< 0.1eV$ at $\sim 1eV$. (The moderator efficiency of low energy positrons ($\sim$ keV) from

---

[26]L. D. Hulett Jr., T. A. Lewis, R. G. Alsmiller Jr., R. Peele, S. Pendyala, J. M. Dale, T. M. Rosseel, Oake Ridge National Laboratory, CONF-861114–21 (1987).
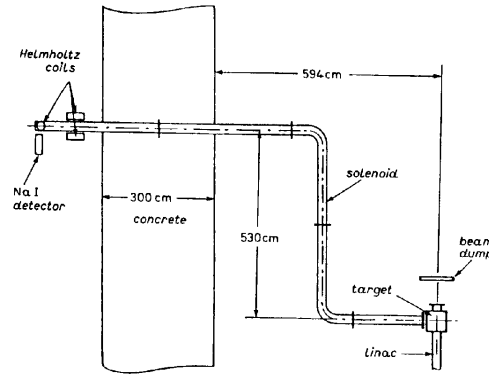
Figure 11.4:   Scheme of the slow-positron facility at University Mainz.[15]

radioactive sources is typically 10^{-3}). The positrons are accelerated with an extraction field to some keV and guided, electrostatically or magnetically focused (solenoid $\sim 10^{-3}T$) to the experiment.

The beam transport line of Fig. 11.4 indicates shielding requirements and bends, necessary to separate the positrons from gammas, neutrons and electrons. Note that the target assembly can easily be combined with the beam dump.

Brightness enhancement

In order to reduce the emittance of the positron beam a re-moderation can be performed: The beam is focused onto a moderator with the spot size as small as possible. The moderator takes the divergence out of the beam and hence re-emits a positron beam with reduced emittance. In a single step the emittance reduction is limited by the minimum attainable spot size, given by aberrations of the lens system.

However, the procedure can be repeated and is than limited by the unavoidable losses of the order of 30% - 50% occurring in each moderation stage.

With respect to brightness B, defined as:

$$B \; = \; \frac{I}{\theta^2 \times d^2 \times E}$$
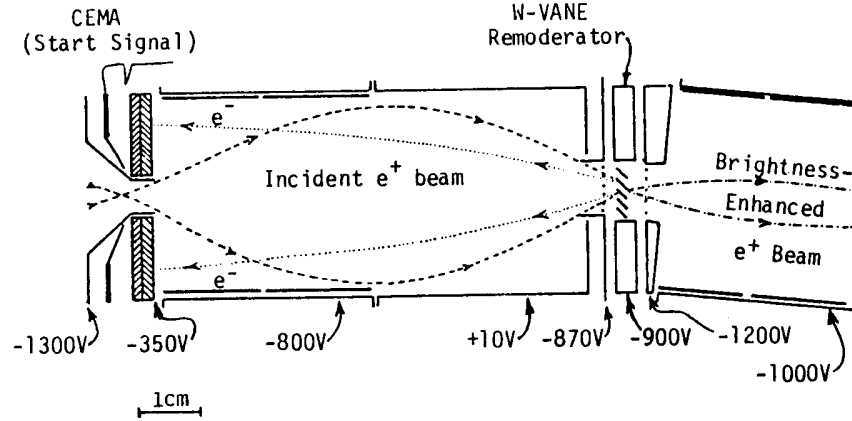
Figure 11.5: Brightness enhancement set up in transmission geometry.[27]

$$
\begin{aligned}
d &= \text{beam diameter} \\
\theta &= \text{angular divergence} \\
I &= \text{positron intensity (particles per second)} \\
E &= \text{kinetic energy of the beam}
\end{aligned}
$$

an improvement of a factor of ~ 500 has been achieved[28] Fig. 11.5 shows a brightness enhancement stage in transmission geometry. Instead of a vane moderator also a thin single-crystal foil can be used.[29]

The transmission geometry is advantageous from the beam optics point of view, but the moderator efficiency obtained so far is smaller than in a back-scattering geometry.

11.2.3   A slow-positron source at the TTF

The conversion efficiency of a linac based slow-positron source, defined as the number of slow-positrons divided by the number of incoming electrons,

---

[27]Van House, *A Brightness Enhanced, Timed, Slow-Positron Beam* in: International Workshop on Positron (Electron) Gas Scattering, Detroit (1985)

[28]K. F. Canter, in: Positron Studies of Solids, Surfaces and Atoms, World Scientific, Singapore 1986, Ed.: A. P. Mills Jr., W. S. Crane, K. F. Canter, p. 102.

[29]D. M. Chen, K. G. Lynn, R. Pareja, B. Nielsen, Phys. Rev. B31, p. 4123 (1985).

Table 11.3:   Parameters of a slow-positron source at the TTF.

Primary Electron Beam	
Energy MeV	400
Power kW	26.1
Slow-positron Beam	
Intensity $\frac{e^+ slow}{s}$	$(3.3 \pm 3) \times 10^9$
Pulse Width ps	~ 6
min. pulse distance ns	1000
Number of pulses $\frac{1}{s}$	8000

depends strongly on details of the source geometry and the moderator efficiency (surface roughness, surface contaminations etc.). In addition some uncertainty arises from the extrapolation to higher electron beam energies. A reasonably scaling for facilities above ~ 70 MeV is a simple scaling with the total beam power.[30] Table 11.4 summarizes the performance of five facilities. The average yield is $(1.22 \pm 1) \times 10^8 \frac{e^+}{s*kW}$. Taken this number an intensity of $3.3 * 10^9 \frac{e^+}{s}$ and peak intensities as high as $7.0 \times 10^{16} \frac{e^+}{s}$ can be reached at the TTF. Further source parameters are collected in Table 11.3. A comparison with existing and planned sources (Tables 11.4 and 11.5) indicates that a source driven by the TTF linac can compete with the sources of the next generation and may, for the near future, even become the source with the highest intensity in Europe. In addition the time structure matches very well the requirements of the positron time scale of Table 11.2. The bunch length of $\sim 6ps$ is much shorter than the positron or positronium lifetime in solids ($> 10^{-10}s$), respectively. The bunch spacing of $1\mu s$ on the other hand is much longer than all relevant lifetimes ($\leq 10^{-9}s$) and allows a full observation of all processes.

---

[30]C. Coceva, P. Giacobbe, ENEA report, Bologna (1984).

Table 11.4: Existing linac based slow-positron sources.

FACILITY	Beam Energy MeV	Intensity $\frac{e^+slow}{s}$	Pulse Width ns	Efficiency $\frac{e^+slow}{s \times kW}$
LLNL	100	3.0×10^9	< 20	0.9×10^8
Mainz	160	5.0×10^7	1 - 3000	3.1×10^8
ETL Tsukuba	75	1.4×10^7	?	0.5×10^8
ETL Tsukuba	75	1.0×10^7	?	1.3×10^8
JAERI Tokai	100	3.0×10^7	?	0.3×10^8

Table 11.5: Planned and existing slow-positron sources. As primary sources electron beams ($\diamondsuit$), bremsstrahlung photon beams ($\clubsuit$) and radioactive isotopes are used. The planned high intensity sources based on isotopes are located at high flux fission reactors.

FACILITY	Status	Intensity $\frac{e^+slow}{s}$	Pulse Width
Univ. of Michigan	existing	$4.0 \times 10^7 - 4.0 * 10^8$	continuous
BNL	planned	10^9	continuous
HFIR/ANS*	planned	$10^{10}/10^{12}$	continuous
Munich/Grenoble	planned ?	$10^{11} - 10^{12}$	continuous
ORNL $\clubsuit$	existing	10^8	2-30 ns
KEK-PF $\diamondsuit$	planned	4×10^8	$1\mu s$
KEK-PF $\diamondsuit$	planned	2×10^9	$1\mu s$
Positron Factory (IAERI)	planned	10^{10}	$2\mu s$
CEBAF $\diamondsuit$	planned	2.5×10^{10}	$\sim 1ps$

*High Flux Isotope Reactor/Advanced Neutron Source at ORNL

Appendix A

Parameter Lists

Table A.1: TESLA 500 – TTFL parameter comparison.

Parameter	TESLA 500	TTFL	
Linac Energy	250 GeV	500 MeV	
RF frequency	1.3 GHz	1.3 GHz	
Accel Gradient	25 MeV/m	15 MeV/m	
Q_0	5×10^9	3×10^9	
# Cryo modules	≈ 2500	4	
Energy spread, single bunch	1.5×10^{-3}	$\approx 10^{-3}$	
Energy variation, bunch to bunch	10^{-3}	$\approx 5 \times 10^{-3}$	
Bunch length rms	1 mm	1 mm	
Beam current	8 mA	8 mA	
Beam macro pulse length	0.8 ms	0.8 ms	
Lattice β typical	$\langle 66$ m$\rangle$	12 m max	
		Inj I	Inj II
Injection Energy	10 GeV	10 MeV	20 MeV
Emittances (x/y), $\gamma\sigma^2/\beta$	$20/1\mu$m	$\approx 5\mu$m	$\approx 20\mu$m
Beam size σ, end of linac	$50/12$ μm	250μm	500μm
Beam size σ, injection	$260/60$ μm	1.7 mm	3.5 mm
Bunch frequency	1 MHz	217 MHz	1MHz
Bunch separation	1 μsec	4.6 ns	1μsec
Particles per bunch	5×10^{10}	2.3×10^8	5×10^{10}

Table A.2: Injector I

Gun Energy	250	keV
Output Energy	9.9	MeV
Accel Gradient (Capture Cav)	10	MV/m
Frequency Capture Cav	1300	Mhz
Phase spread, gun	± 150	deg
Prebuncher Frequency	216.7	MHz
Bunch Population	2.3×10^8	per bunch
RMS Phase Width	0.77	deg
Total Phase Width	3.2	deg
RMS Energy Spread	0.078	MeV
Total Energy Spread	0.3	MeV
Emittance $(4\gamma\sigma^2/\beta)$	16.8	mm-mrad
RMS bunch length	0.49	mm
$\Delta E/E$ RMS	0.8	%

Table A.3:   Injector II: RF photoemission gun and accelerating section.

Bunch spacing	1	μsec
Bunches per macropulse	800	
Electrons per bunch	5×10^{10}	
Brightness	4.8×10^{12}	A/m^2
Emittance, $\gamma\sigma^2/\beta$	20	mm-mrad
RF frequency	1.3	GHz
RF power—gun	4.5	MW
Solenoid focusing	0.14	T
field on axis		
Beam radius at cathode	3	mm
Bunch length, σ	3.1	mm
before compression		
Bunch length, σ	1	mm
after compression		
Post gun energy	6	MeV
Injector output energy	20	MeV
Momentum spread	8	%
Longitudinal emittance	1.5	MeV-deg
Laser pulse FWHM	28	ps
Photocathode QE	1	%
Micropulse energy	> 5	μJ
Time jitter	< 1	ps
Amplitude jitter	< 5	%
Pointing stability	< 100	μrad
Laser wavelength	< 300	nm

Table A.4: RF cavity parameters for the TTFL

Frequency	1.3	GHz
Cells per cavity	9	
Cavity length	1.035	m
Iris radius	35	mm
R/Q	973	ohms/m
E_{peak}/E_{acc}	≈ 2.0	
RF power @ 25 MeV/m	206	kW/m
HOM k_{long}/cavity	8.5	V/pC (1mm bunch σ)
HOM k_{trans}/cavity	18	V/pC/m

Table A.5: Summary of the cryogenic system heat budget.

	Static Losses	Total Losses 15 MV/m $Q=3 \times 10^9$	Total Losses 25 MV/m $Q= 5 \times 10^9$
Summary—2 K			
2 K load, W/m	0.23	1.28	1.78
Budget, 5 modules, W	21	115	160
Summary—4.5 K			
4.5 K load, W/m	1.16	1.27	1.33
Budget, 5 modules, W	104	114	120
Summary—70 K			
70 K load, W/m	6.4	10.4	11.3
Budget, 5 modules	576	936	1017
w/o HOM	576	684	765

Table A.6:   Parameters of TESLA 500 and TESLA 1000 as of Jan 95. (
Parameters are under evaluation at time of printing.) Items
marked with a dagger (†) are analytical results, while items
marked with a double–dagger (‡) are the results of simula-
tions carried out by Schulte. N* is number of electrons (or
positrons) per crossing, produced with p_t >20 MeV/c and
angle > 0.15 rad.

Parameter	Units	Values	Values
(unchanged values from previous column not filled in)			
		TESLA 500	**TESLA 1000**
LINAC-Primary Parameters			
Energy (CM)	GeV	500	1000
Energy-Linac	GeV	250	500
N_b	10^{10}	5.14	.91
f_c	kHz	8	20.9
Rep Rate	Hz	10	5
# bunches/pulse		800	4180
bunch separation	μsec	1.0	0.2
Beam pulse	ms	0.8	0.836
$\epsilon_{n,x}$	m $\times 10^{-8}$	2000	520
$\epsilon_{n,y}$	m $\times 10^{-8}$	100	6.3
σ_z	mm	1	0.5

Parameter	Units	Values	Values
(unchanged values from previous column not filled in)			
		TESLA 500	**TESLA 1000**
Final Focus System			
σ_x^*	nm	1000	325
σ_y^*	nm	64	8
β_x^*	mm	24.5	20
β_y^*	mm	2	1
L_o-nominal	10^{33} cm^{-2}sec^{-1}	2.6	5.3
R		15.6	41
D_x		0.54†	0.24
D_y		8.5†	9.8
H		2.3‡	1.9‡
L with pinch	10^{33}cm^{-2}sec^{-1}	5.9	10.4
Υ		0.03‡	0.058‡
δE_{beam}	% av	3.1‡	2.7‡
Cross angle	mrad	0	
N_γ	/beam e	2.5‡	1.3‡
N*	/crossing	14.5‡	4.5†
LINAC-Secondary Parameters			
Gradient	MV/m	25	
RF freq	GHz	1.3	
2 linac RF length	km	20	40
cavity length	m	1.04	
2 linac # cavities		19328	38656
2 linac # klystrons		604	1208
# cavities/kly		32	32
Kly peak power req	MW	6.85	6.06
Kly pulse length	μsec	1.33	1.37
a/wave length		0.15	
P_b-beam power/beam	MW	16.5	15.2
P_{ac}-2 linac AC power	MW	155	170
P_{ac}-cryo	MW	58	79
P_{ac}-RF	MW	97	91
Damping Ring Energy	GeV	4.0	

Appendix B

Device Coordinates
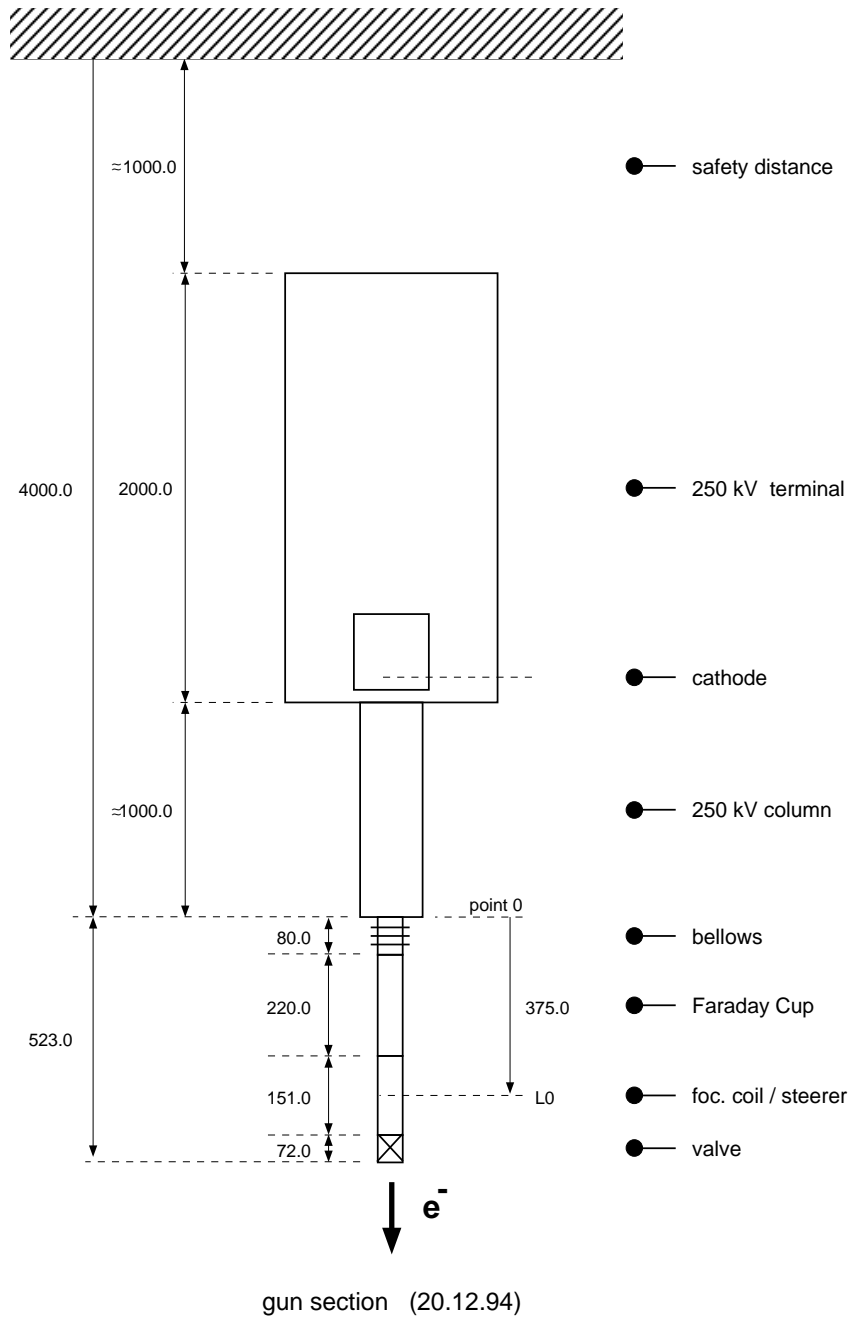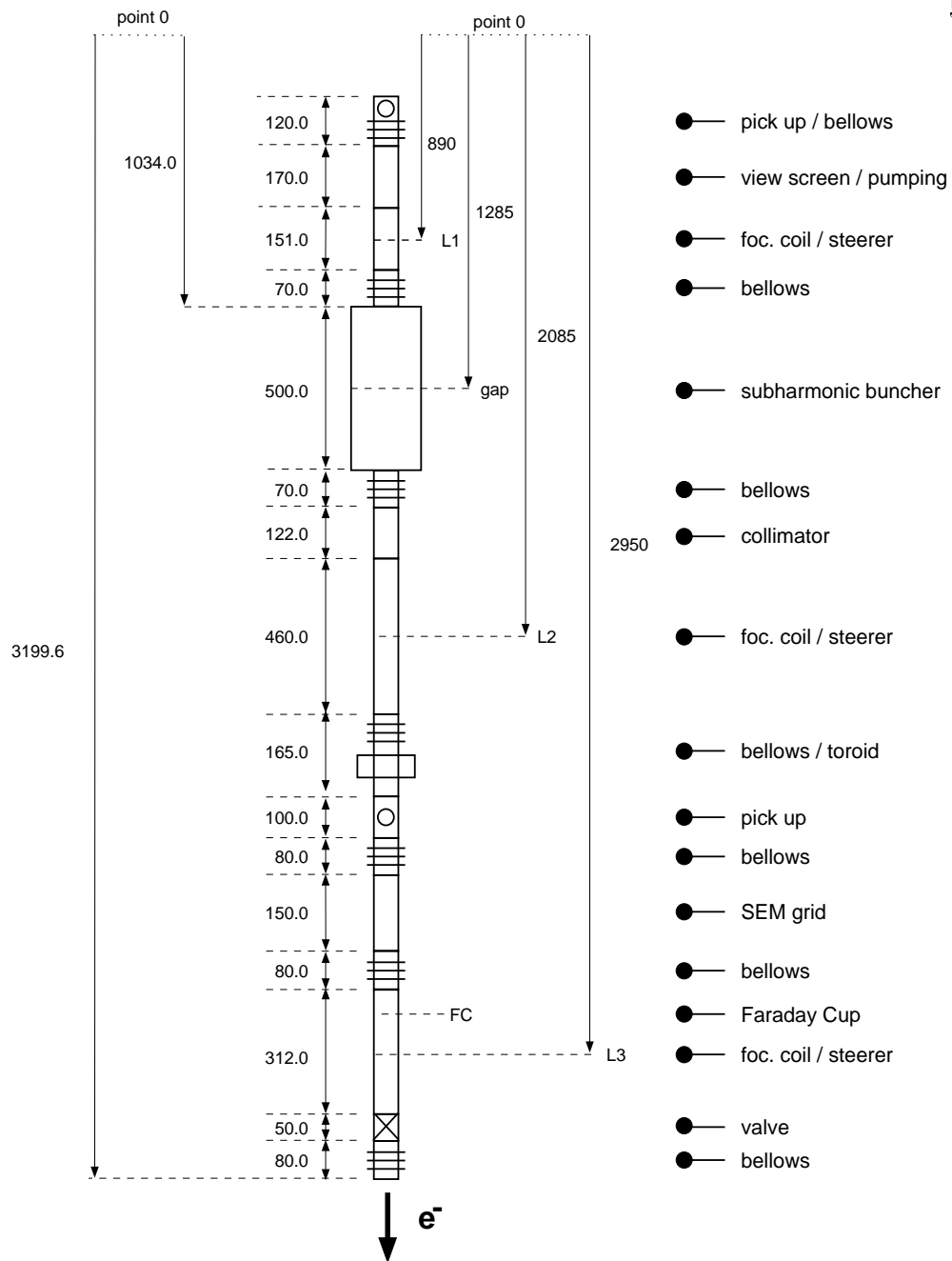
gun section   (20.12.94)

injector section 200 (20.12.94)

point 0

3199.6

122.0 — pumping port

35.0 — bellows

? — manual valve

— begin cryostat

3945.0

754.4

?

4980.2

— cut off tube

138.0

1035.2 — cavity #0

5819.6

2620.0

— cut off tube

102.0

?

?

?

— end cryostat

? — manual valve

? — pumping port

e⁻
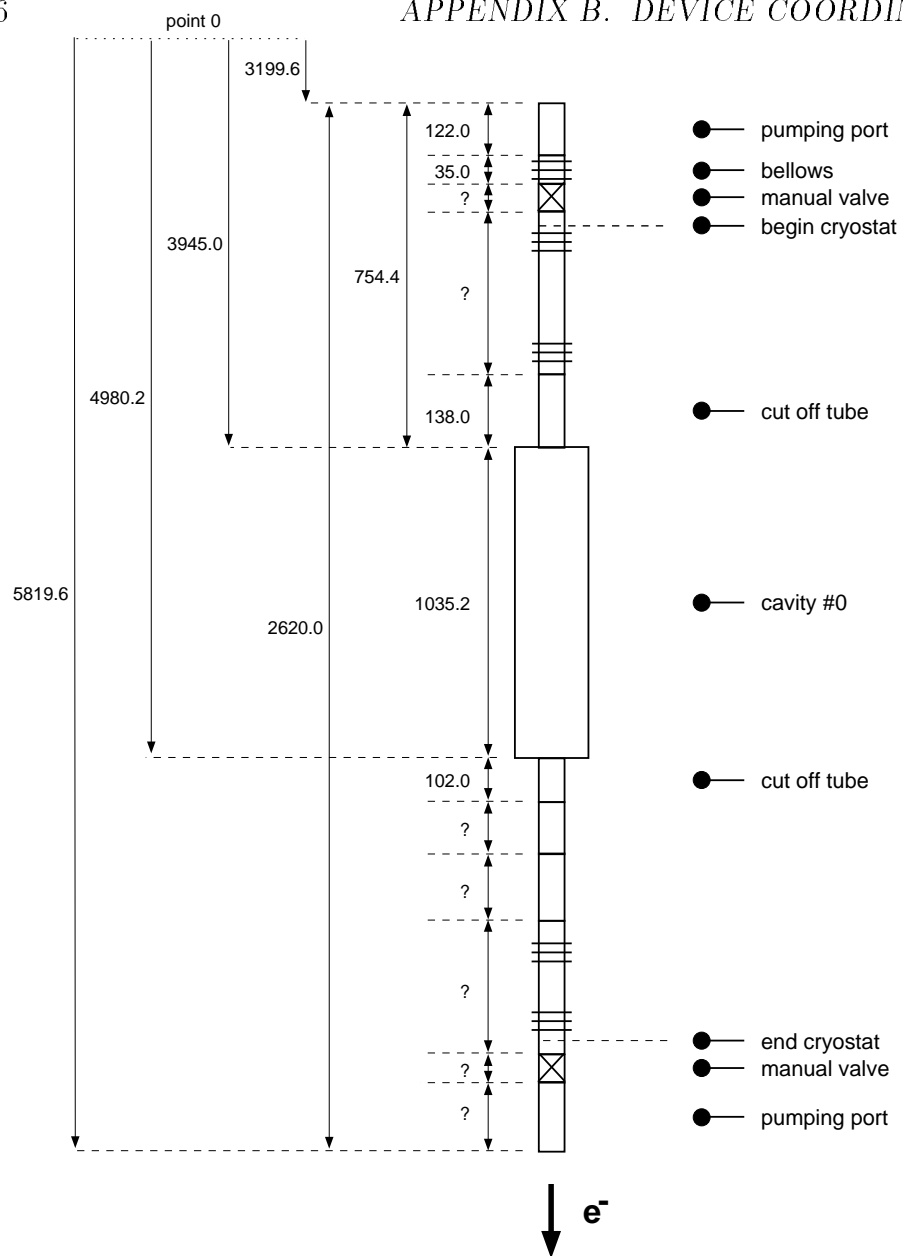
capture cavity section   (20.12.94)
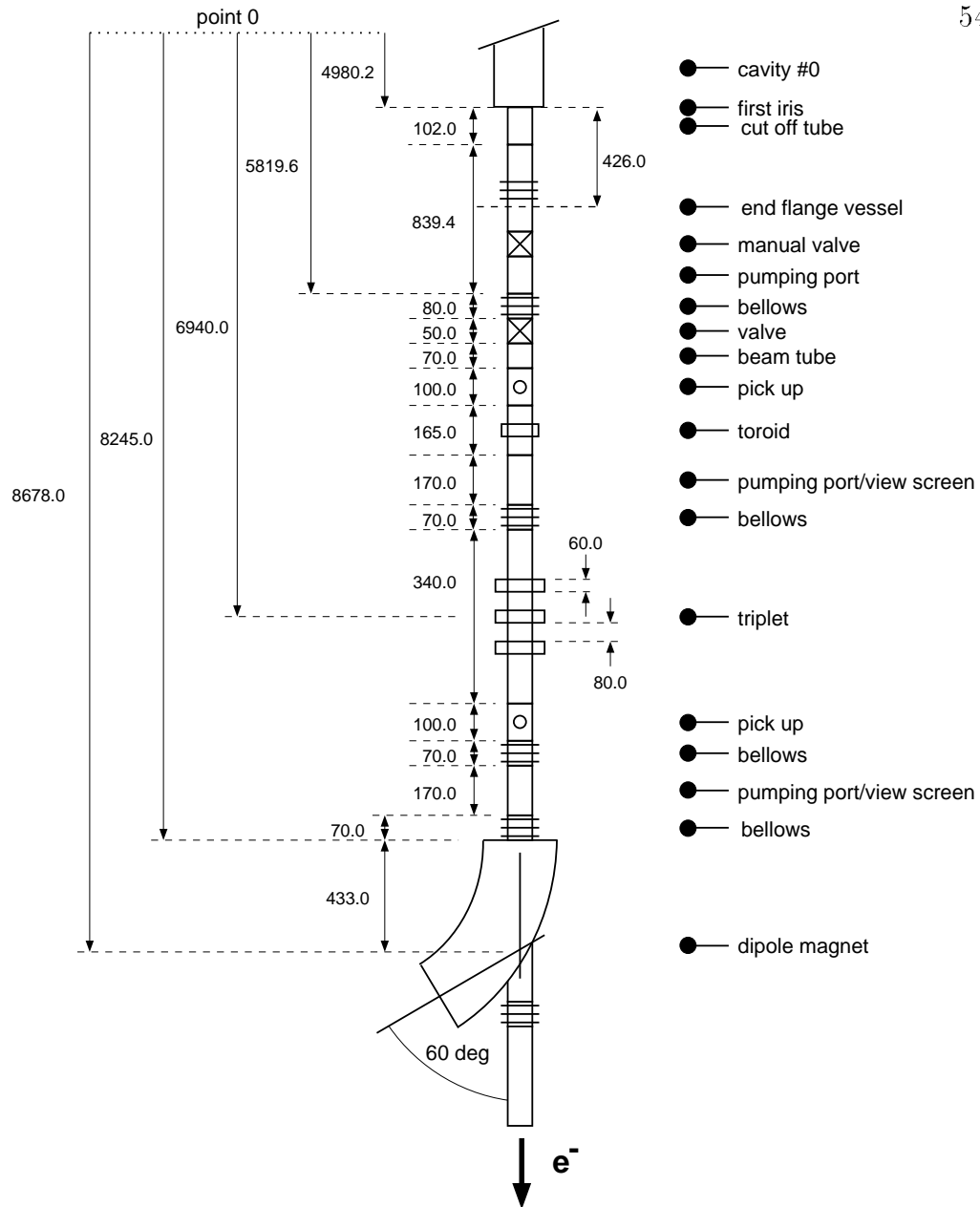
matching section between cavity #0 and dipole magnet (20.12.94)

point 0

8245.0

170.0

70.0

8678.0

433.0

9500.0

60 deg

60.0

80.0

12920.0

80.0

450.0

150.0

300.0

150.0

200.0

150.0

275.0

14000.0

300.0

275.0

150.0

210.0

300.0

150.0

e⁻

pumping port/view screen

bellows

dipole magnet

bellows

triplet

bellows

dipole magnet chicane

bellows

BPM

bellows

pumping port/view screen

bellows

horz./vert. steering

BPM

horiz./vert. steering

bellows

faraday cup

toroid

bellows

warm valve

cold valve

first iris

cavity #1

matching section between dipole magnet and cavity #1 (27.02.95)

point 0

8245.0

433.0

dipole magnet

1280.0

2280.0

SEM grid

3300.0

beam dump

e⁻

10 MeV dispersive section between dipole magnet and beam dump (20.12.94)

point 0

80.0

≈ 335

≈ 160

14000.0 | 1000.0

70 K

≈ 200

4.2 K

80.0

138.0

107.0

1187.0

815.0

245.0

● ——— valve

● ——— pumping port
● ——— begin feed cap

● ——— beam tube

● ——— bellows

● ——— beam tube

● ——— cold valve

● ——— first iris

● ——— begin outer vessel

● ——— cavity #1

e⁻

upstream end of cryo module (20.12.94)
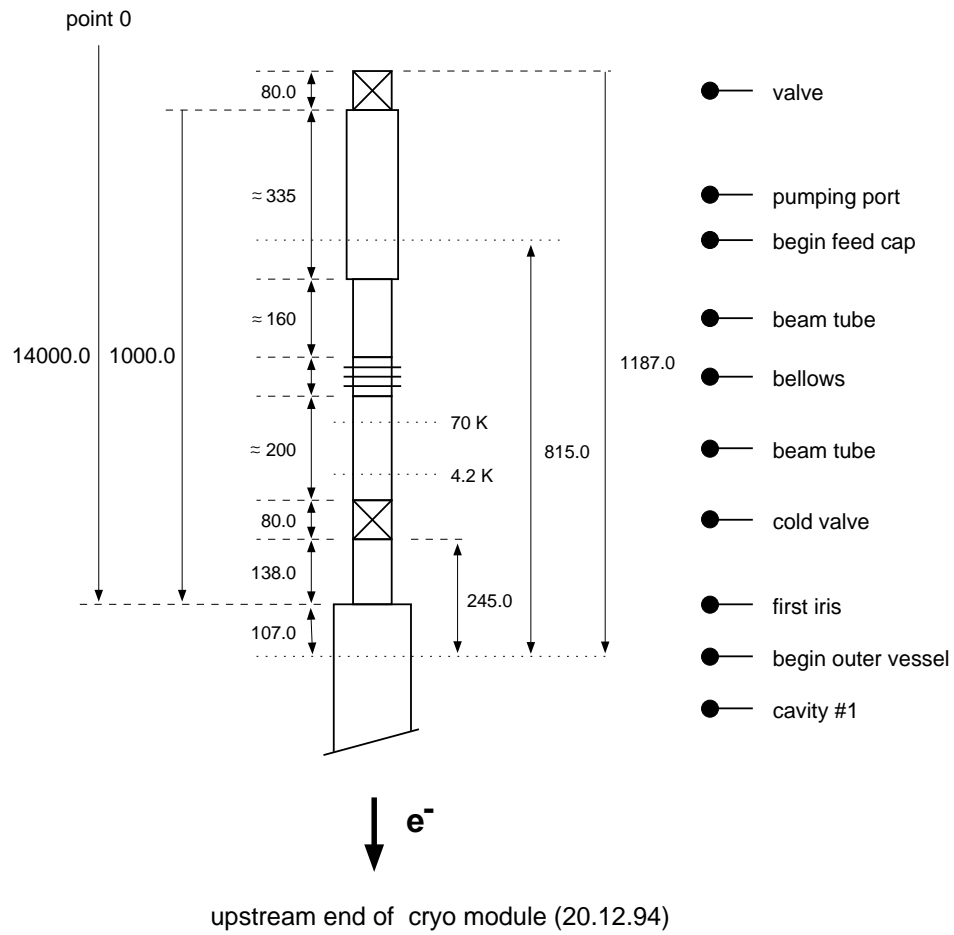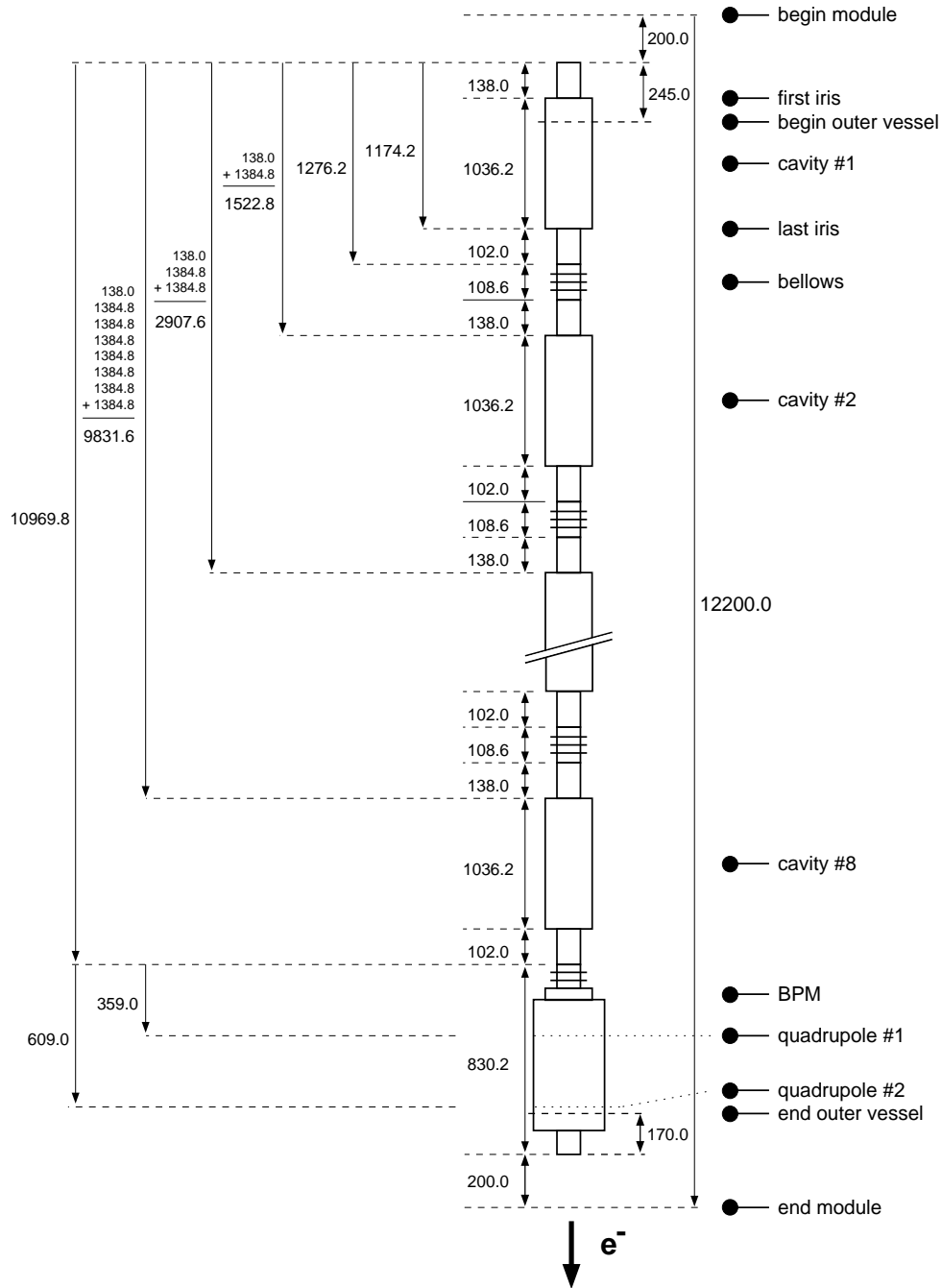
cavity string within cryo module (12.12.94)
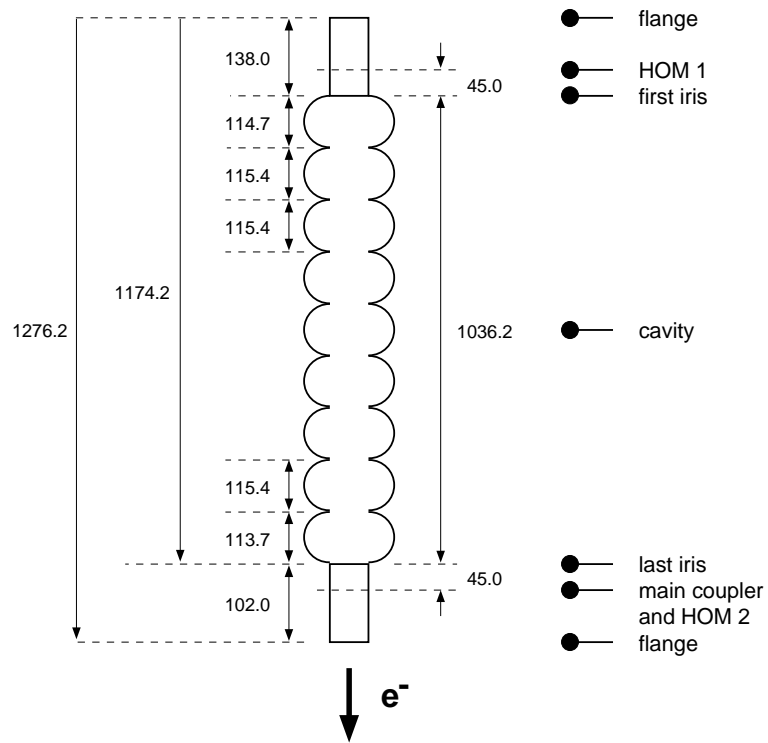
s.c. cavity TTF linac (20.12.94)
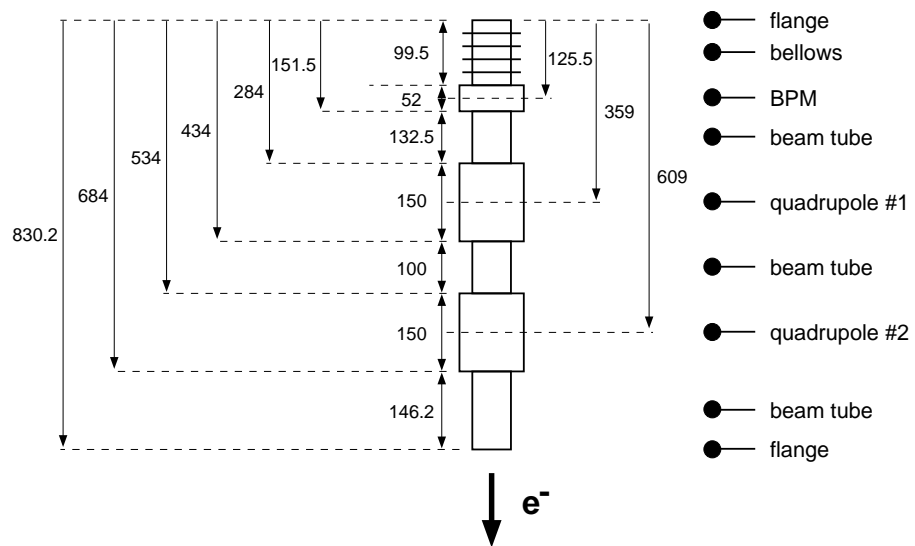
quadrupole module TTF linac (07.09.94)

quadrupole module

flange cryo module

145.0

80   cold valve

≈ 400   beam tube

4.2 K

≈ 360   ≈ 200   stripline ???

1700.0   70 K

≈ 195   end of end cap

≈ 400   warm beam tube

≈ 340   pumping port

valve

e⁻

downstream end of cryo module (20.12.94)

point 0

80480.0

81480.0

84610.0

86980.0

210.0 — laser port
500.0 — horizontal steerer
1000 — vertical steerer
500.0
70.0 — valve
150.0 — bellows
230.0 — TV/OTR-screen, pumping port
350.0 — position monitor
300.0 — current monitor
150.0 — bellows
1000.0 — 3130 — tube
150.0 — bellows
230.0 — TV-screen, pumping port
350.0 — position monitor
150.0 — bellows
650.0 — small bore quadrupole
650.0 — small bore quadrupole — 2370
1000.0 — tube

e⁻

experimental area 1-1 (13.02.95)
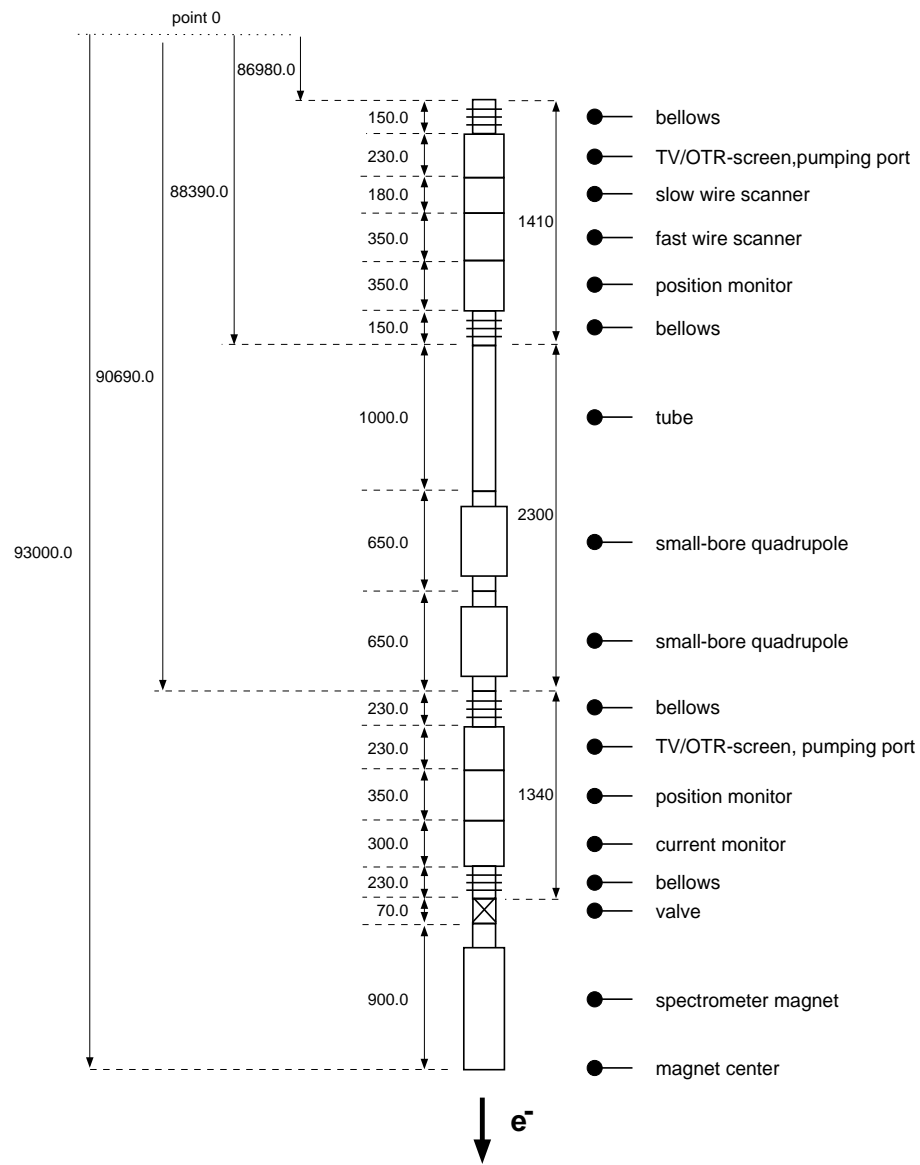
experimental area 1- 2 (20.12.94)

point 0

93000.0

94100.0

102200.0

1100.0

1000.0

300.0

70.0

230.0

6500.0

●——— magnet center

●——— spectrometer magnet

●——— beam tube

●——— szintillator, pumping port

●——— valve

●——— bellows

●——— beam tube, pumping port

●——— window, beam dump

e⁻
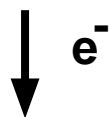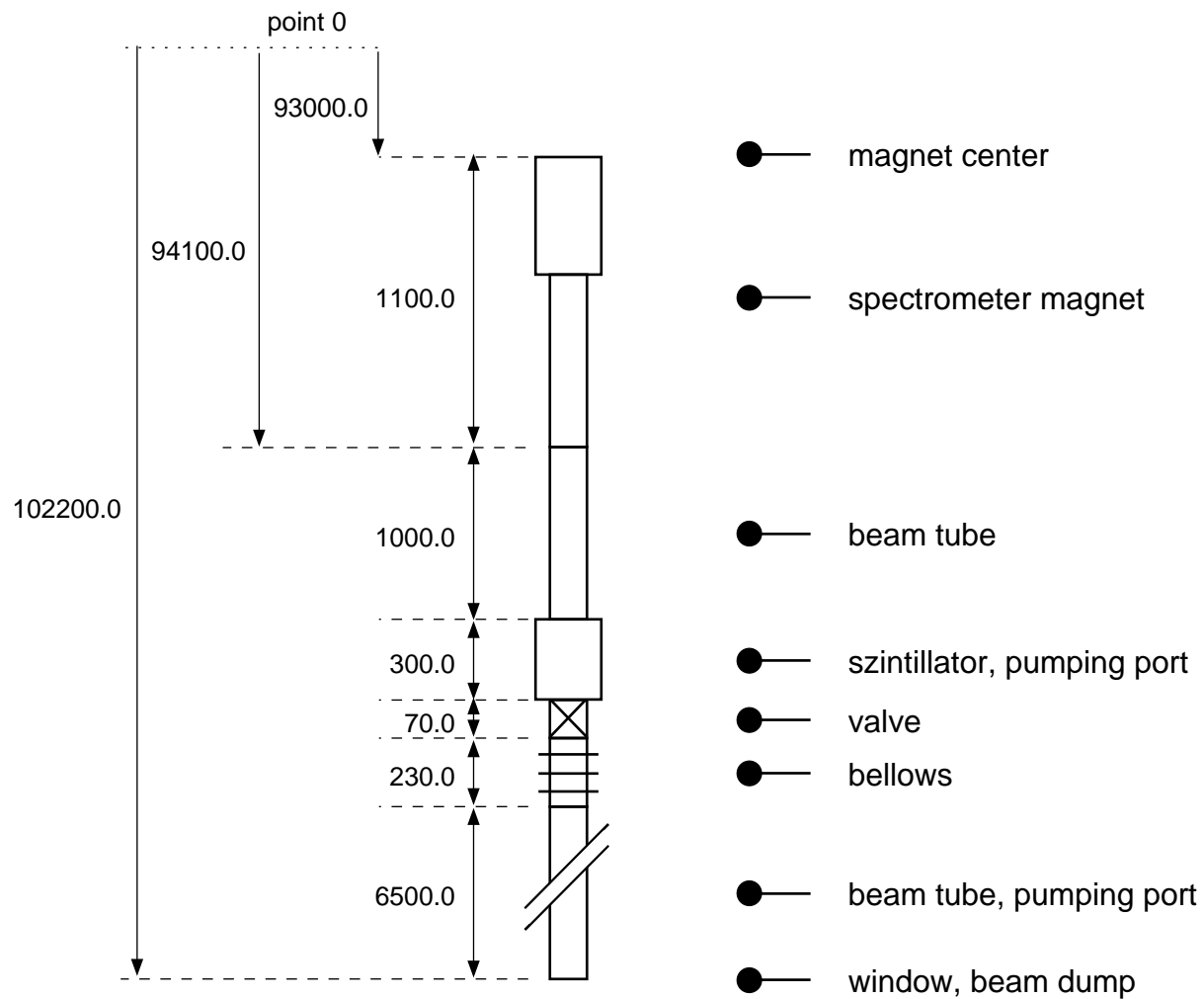
experimental area 2 (13.02.95)

point 0

93000.0

94075.0

1075.0   1075   ● magnet center

95895.0

1075.0   ● spectrometer magnet

97585.0

1400.0   1820   ● large-bore quadrupole

103055.0

350.0   ● tube, pumping port

70.0   ● valve

230.0   ● bellows

230.0   ● TV/OTR-screen, pumping port

350.0   ● SEM - grid

350.0   1690   ● position monitor

300.0   ● current monitor

230.0   ● bellows

1400.0   ● large-bore quadrupole

5470

70.0   ● valve

4000.0   ● tube, pumping port

● window, beam dump

e⁻

experimental area 3 (13.02.95)